NASA SP-406

POWERED-LIFT AERODYNAMICS AND ACOUSTICS

A conference held at
LANGLEY RESEARCH CENTER
Hampton, Virginia
May 24–26, 1976

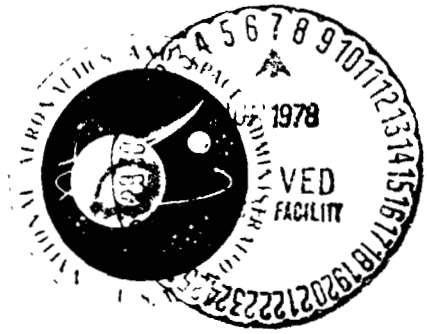

(NASA-SP-406) POWERED-LIFT AERODYNAMICS AND ACOUSTICS (NASA) 502 p HC A22/MF A01
CSCL 01A

N78-24046
THRU
N78-24076
Unclas
H1/02 17138

NATIONAL AERONAUTICS AND SPACE ADMINISTRATION

NASA SP-406

POWERED-LIFT AERODYNAMICS AND ACOUSTICS

A conference held at NASA Langley Research Center,
Hampton, Virginia, on May 24–26, 1976

Prepared by Langley Research Center

Scientific and Technical Information Office 1976
NATIONAL AERONAUTICS AND SPACE ADMINISTRATION
Washington, D.C.

PREFACE

This compilation consists of papers presented at a conference on Powered-Lift Aerodynamics and Acoustics held at the NASA Langley Research Center on May 24-26, 1976. The presentations were made in sessions subdivided according to subject matter as follows: I - High-Lift Aerodynamics, II - High-Speed and Cruise Aerodynamics, III - Acoustics, IV - Propulsion Aerodynamics and Acoustics, V - Aerodynamic and Acoustic Loads, and VI - Full-Scale and Flight Research.

The purpose of the conference was to provide an in-depth review of powered-lift technology generated by in-house and NASA sponsored research over the last several years. Papers were presented by members of NASA Centers, Universities, and Industry.

PAGE II INTENTIONALLY BLANK

CONTENTS

SESSION V - AERODYNAMIC AND ACOUSTIC LOADS

SESSION VI - FULL-SCALE AND FLIGHT RESEARCH

OVERVIEW OF POWERED-LIFT TECHNOLOGY

John P. Campbell
The George Washington University,
Joint Institute for Acoustics and Flight Sciences

SUMMARY

This introductory paper is intended to set the stage for the conference by reviewing progress to date in the powered-lift field. The concept and application of powered lift and the effects of some fundamental design variables are discussed. A brief chronology of significant developments in the field is also presented and the direction of research efforts in recent years is indicated. All powered-lift concepts are included, but emphasis is on the two externally blown schemes which involve blowing either above or below the wing and which are now being utilized in the YC-14 and YC-15 airplanes. This review deals primarily with aerodynamics and vehicle design, and only touches briefly on the areas of acoustics, propulsion, and loads.

INTRODUCTION

It is perhaps appropriate to start this review with a bit of historical background which illustrates one of the factors that spurred interest in powered lift back in the 1950's. Richard E. Kuhn brought out this point very well by the use of figure 1 which is a history of maximum lift development from the Wright Brothers to the present day. The upper solid line shows that with the introduction of trailing-edge flaps and with the continuing refinement and sophistication of these flaps, the maximum lift coefficient $C_{L,max}$ obtained in wind-tunnel tests increased at a rapid rate up until the 1940's but at a much more modest rate afterward. Of course, the values of $C_{L,max}$ attained with operational aircraft lagged well behind the wind-tunnel progress at first, but it later became apparent that airplanes would soon be using up most of the mechanical-flap high-lift technology developed in the wind tunnel. This trend was foreseen by researchers in the early 1950's who recognized that the ceiling on $C_{L,max}$ obtainable with mechanical flaps could be bypassed by making full use of the energy of the turbojet propulsion engines to augment wing lift, as indicated by the dashed line. Exploratory research on the jet-flap principle was therefore started in an effort to realize this potential.

In this jet-flap concept, a high-velocity jet sheet is turned downward by a trailing-edge flap and effectively increases the chord of the flap to produce higher lift. The total lift produced is made up of the three components shown in figure 2: the power-off lift produced by the wing and flap, the lift due to thrust deflection (that is, the vertical component of the thrust), and powered

circulation lift which is the additional circulation lift induced on the wing and flap by the presence of the jet sheet. The proportions of the three components can vary quite a bit, depending on the type of flap and the particular powered-lift concept used.

POWERED-LIFT CHRONOLOGY

A number of different concepts have been studied as indicated by the powered-lift chronology presented in figure 3. Dates are shown for the first research conducted on a given concept and for the first flight of an airplane incorporating the concept.

The blowing boundary-layer-control (BLC) scheme illustrated at the top is not usually considered a true powered-lift concept since it only uses engine bleed air and hence does not make full use of the available engine thrust. It is included here, however, because of its basic similarity to the jet flap and because some of the work on blowing BLC provided useful information in the development of the jet flap. Exploratory studies of blowing BLC were carried out as early as the 1920's but it was not until the 1940's and 1950's that systematic research was conducted that lead to application of the concept. Some of the most impressive work was done on the Navy's F9F-5 airplane in the early 1950's under the direction of John Attinello (ref. 1). A number of other aircraft with blowing BLC have been flown, including the Boeing 367-80 airplane which was used by NASA for low-speed flight research in the early 1960's. (See fig. 4.)

The principle of the jet flap was proposed and verified by Schubauer in 1932, but very little attention was given to the concept until 20 years later when Attinello's studies in the United States (ref. 1) and Davidson's studies in England (ref. 2) showed great promise for the jet flap. This work led to extensive research programs on the concept in England, France, and the United States. (For example, see refs. 1 to 4.) The Hunting jet flap research airplane (fig. 5) was built in the early 1960's to study the flight characteristics associated with the jet flap. (See ref. 5.) Unfortunately, the airplane had a number of deficiencies which limited its usefulness as a research aircraft.

In the late 1950's De Havilland of Canada initiated research on a variation of the jet flap called the augmentor wing. This concept incorporates a shroud assembly over the flap to create an ejector system which augments the thrust of the nozzle by entraining additional air. The augmentor wing was the subject of a comprehensive research program carried out jointly by NASA and the Canadian government starting in 1965. This program culminated in the design and construction of the C-8 augmentor wing research airplane by Boeing and De Havilland. (See fig. 6.) The aircraft was first flown in 1972 and since that time has been used in a joint NASA-Ames and Canadian flight research program. (See ref. 6.)

Both the augmentor wing and the jet flap proved to be very efficient aerodynamically in that they produced a large increase in wing lift with a given amount of engine thrust. But they are internally blown systems and hence suffer the disadvantage of requiring internal ducting which adds to the weight, cost, and complexity of the wing structure.

In an effort to eliminate internal ducting and to provide much simpler powered-lift systems, NASA Langley Research Center started work in the 1950's on the so-called "externally blown systems" - the externally blown flap used with conventional pod-mounted engines, and the upper surface blown flap. Exploratory research was first carried out on the externally blown flap in 1956 (ref. 7); research on the upper surface blown flap started about a year later (ref. 8). Initial results appeared to be promising for both concepts. A fairly extensive research program was carried out to develop the technology for the externally blown flap; but there were no indications of serious interest by the industry in applying the concept until Boeing incorporated it in its proposal for the C-5 competition. Although Boeing's entry did not win, this show of interest accelerated the research on the externally blown flap and led to an earlier build-up of the technology base required for application of the concept. The culmination of all this research is, of course, the McDonnell-Douglas YC-15 AMST (fig. 7) which has been flying since August 1975.

As pointed out earlier, the initial results obtained on the concept for the upper surface blown flap in 1957 appeared to be promising. The aerodynamic performance was comparable with that of the externally blown flap, and preliminary noise studies showed it to be a potentially quieter concept because of the shielding effect of the wing. (See ref. 9.) However, since the upper surface blowing arrangement involved a change in engine location away from the generally accepted underslung pods and since there was at that time no special concern with the noise problem, research on the upper surface blown flap was dropped after the initial studies. Research was resumed in the early 70's when it was becoming apparent that the externally blown flap might have difficulty meeting increasingly stringent noise requirements. Since that time, of course, research on the upper surface blown flap has been carried out at an accelerated pace; this research lead to the Boeing YC-14 AMST (fig. 8) which will make its first flight within a few months and to the NASA quiet short haul research aircraft (fig. 9) which should be flying in about 3 years.

As the conference proceeds, you will note that there is special emphasis on the upper surface blown flap, for this is the concept which has been researched most extensively since the last NASA powered-lift conference held in 1972.

PERFORMANCE

Now, let us turn to some general performance considerations for powered-lift aircraft. The landing performance will be considered since it is generally more critical than take-off performance for these aircraft. Some of the factors involved in landing-field length are illustrated in figure 10. On this plot of wing loading against approach speed and the corresponding operational field length, there is a family of curves representing different approach lift coefficients. The band of values for 1.5 to 1.8 is for conventional airplanes with mechanical flaps. Note that these values are approach lift coefficients which are considerably lower than maximum lift coefficients because of the various angle-of-attack and speed margins required for safety of operation. The hatched area represents typical powered-lift conditions in the higher wing loading range and extends from field lengths of about 609.6 m (2000 ft) to about 1371.6 m

(4500 ft). Aircraft which use the shorter field lengths, 609.6 m (2000 ft) to about 1066.8 m (3500 ft), are usually classified as STOL or short take-off and landing aircraft; whereas those using the 1066.8- to 1371.6-m (3500- to 4500-) field lengths are termed RTOL, or reduced take-off and landing aircraft. The approach lift coefficients can vary from values as low as 2 for the RTOL to values of 4 or 5 for the STOL. Of course, lower wing loadings can be used rather than higher lift coefficients to obtain the shorter field lengths, but this usage can lead to undesirable reductions in cruise performance and ride qualities.

Now, consider the additional power which must be installed in the airplane to obtain powered lift. Figure 11 shows the airplane thrust-weight ratios required to produce certain values of $C_{L,max}$ and approach lift coefficients for an externally blown concept. As an example of a high-performance STOL case, let us take an approach C_L of 4 which gives a landing field length of about 609.6 m (2000 ft) with a wing loading of 3830 N/m^2 (80 lb/ft^2). The thrust-weight ratio required in this case is about 0.5 or about twice the installed thrust-weight ratio for conventional jet transports. Of course, if the lower approach lift required for RTOL aircraft is used, the thrust-weight ratios required are much smaller. As has been indicated, these curves are for externally blown flaps. The more efficient internally blown flaps require less thrust-weight ratio, as indicated in figure 12 (data from ref. 10).

Figure 12 shows the static thrust-weight ratio required as a function of approach C_L for internally and externally blown flaps. The lower thrust requirement for the internally blown flaps is apparent. However, in order to obtain a meaningful comparison of the power requirements for the internally and externally blown flaps, it is necessary to consider the characteristics of the engines used with the two flap systems. This point is illustrated in figure 13 by combining the data of figure 12 with some engine information. The curve at the right illustrates the variation with engine fan pressure ratio of the static thrust-weight ratio available with a given design cruise thrust. The engines appropriate for use with externally blown flaps have a relatively low fan pressure ratio and, hence, provide much more static thrust than the engines for internally blown flaps designed for the same cruise thrust. The dashed lines with arrows indicate that this difference in engine characteristics almost balances out the difference in flap efficiency so that the overall performance, as indicated by the approach C_L obtained with a given cruise thrust, is not greatly different for the two flap systems.

Another important factor affecting the performance of the externally blown systems is the relationship of the engine exhaust to the flap. In the case of the externally blown flap (EBF), it has been found that the amount of powered lift obtained depends on how well the flap "captures" the engine exhaust and turns it downward.

This point is illustrated in figure 14 (data from ref. 11) which shows powered-lift increment as a function of slipstream capture ratio, z/D, where z/D is defined by the sketch. The lift increment appears to vary directly as the proportion of the slipstream captured and actually continues to increase beyond a z/D of 1 where the bottom of the engine exhaust would theoretically

coincide with the bottom of the flap. It has been found that this relatively simple factor z/D can satisfactorily account for changes in geometric design features such as longitudinal and vertical position of the nacelle, the incidence of the nacelle, and the relative size of the flap and engine nozzle. A paper by D. R. Hoad (ref. 12) in this conference will give more information on this subject.

In the case of the upper surface blown flap (USB), there are some other critical factors involved in the turning of the jet exhaust as indicated by figure 15 (taken from ref. 13). On this plot of engine fan pressure ratio against the ratio of jet thickness to flap turning radius, a boundary for good turning is shown. The boundary indicates that reductions in pressure ratio permit thicker jets to be used, but it has been found that even with low-fan-pressure-ratio engines, some special features are required for satisfactory turning. These special features include extreme flattening of the exhaust nozzle, a downward deflection of the nozzle, and the use of some flow control device such as boundary-layer control or vortex generators at the knee of the flap. The YC-14 AMST makes use of vortex generators along with a small nozzle deflection angle to obtain good turning. An illustration of the improvement in turning obtained with nozzle deflection angle is shown in figure 16. Note the favorable shift in the boundary with the deflected nozzle. The sketches in figure 17 (taken from ref. 13) illustrate how the deflected nozzle flattens the jet sheet to produce better turning. Since the jet sheet also spreads out, it covers a greater part of the flap span and results in improved lift performance.

It should be pointed out that the nozzle deflection angle illustrated in figures 16 and 17 may be referred to in later papers in the conference as deflector angle, kickdown angle, or nozzle roof angle. Definition of these angles may differ in detail but they all refer to a downward deflection of the exhaust over the top of the wing to flatten the jet sheet and make it turn better.

STABILITY AND CONTROL

Now let us turn from performance to stability and control considerations. A critical problem in this area for both externally blown concepts is maintaining lateral trim with an engine out. Of course, an attempt is made in the basic design of the aircraft to minimize the problem by locating the engines as far inboard on the wing as possible; but special provisions are still required to obtain lateral trim without prohibitive losses in lift. Typical engine-out rolling moments measured on EBF and USB models (refs. 13 and 14) are presented in figure 18 as a function of the engine-out lift loss. The solid line represents the rolling moments obtained by multiplying the loss in lift by the distance out to the dead engine (y/b), whereas the data points show the measured rolling moments. For both models, the fact that the measured moments are smaller than the calculated moments indicates that the center of lift induced by an engine is somewhat inboard of the engine. These measured moments, however, are still very large and require special attention on the part of the designer.

One satisfactory solution to the problem for the externally blown flap is illustrated in figure 19 (taken from ref. 14). Shown on a plot of rolling-moment coefficient against lift coefficient are the basic 4-engine $C_{L,max}$ condition, the engine-out condition with no lateral trim, and the trimmed conditions obtained with midspan differential flaps and spoilers. With both the spoilers and flaps deflected, the rolling moment is more than adequate for lateral trim; therefore, much of the spoiler effectiveness is available for maneuvering in roll.

This solution to the engine-out lateral trim problem did not work for the upper surface blown flap because of a basic difference in the flow patterns over the wing and flap, as illustrated in figure 20 (taken from ref. 13). For the externally blown flap, the flow impinges on the bottom surface of the flaps and spreads out spanwise through the flap slots so that the powered-lift effect extends well outboard of the engines. For the upper surface blown flap, the jet exhaust tends to roll up and contract, and thus pulls the lower velocity free-stream flow inward along the midspan. The midspan flap segment is therefore not very effective for providing roll trim. A much more effective roll trim for the USB configuration was found to be the use of asymmetrical boundary-layer control; that is, the use of BLC on the leading edge and aileron of the wing with the engine out but not on the other wing. Figure 21 shows some lateral trim data obtained with this method (ref. 13) which look very similar to the results obtained on the EBF model with the midspan differential flap and spoiler. This point will be covered in more detail by A. E. Phelps III and J. L. Johnson (ref. 15).

Another critical stability and control problem area for powered-lift aircraft is the design of the horizontal tail for adequate longitudinal trim and stability. Longitudinal trim is a problem because of the large nose-down pitching moments produced by powered-lift flaps at high thrust settings. The problem is illustrated in figure 22 (data from ref. 13) which shows the horizontal-tail size required to trim out these nose-down moments at various lift coefficients. Curves are shown for a 27° swept wing and an unswept wing having USB flaps. (Similar results would be expected with the EBF concept.) A tail arm (l_{tail}/c) of four wing chords and a tail lift coefficient $(C_{L,tail})$ of two have been assumed in calculating the curves. It is apparent that very large horizontal tails are required for trim at the higher lift coefficients obtained with powered lift, especially for the unswept wing. The trim requirements are smaller for the swept wing because with the engines located inboard, the powered-lift loads are acting further forward with respect to the center of gravity and therefore produce smaller nose-down moments. Even for the swept wing, however, the tail sizes required at the higher lift coefficients are much larger than the area of about 20 percent usually required for conventional transports.

This large horizontal tail must also be positioned properly on the aircraft to give satisfactory longitudinal stability, as illustrated in figure 23 (taken from ref. 14). These pitching-moment data, for a powered-lift approach condition, show the unstable tail-off curve with the large nose-down moments and two tail-on curves. With the high rearward tail location, the model is longitudinally unstable. Moving the tail forward in the high position makes the model stable, at least out to an angle of attack of 15°. Figure 24 (taken

from ref. 14) shows why moving the tail forward helped the stability. The trailing vortices originating at the wing tip or outboard end of the flap move inward so that a rearward-located tail tends to move into a region of destabilizing downwash as angle of attack is increased. Locating the tail farther forward gets it farther away from the vortices and into a region of less destabilizing downwash. It is apparent from this sketch and the two preceding data figures that sizing and locating the horizontal tail for satisfactory trim and stability can be a critical design problem for powered-lift aircraft.

Another important stability and control consideration for powered-lift aircraft is the stability of the Dutch roll oscillation, as illustrated in figure 25 (taken from refs. 13 and 14). Calculated Dutch roll characteristics for USB and EBF configurations with swept and unswept wings are shown with boundaries taken from an AGARD publication outlining STOL handling criteria (ref. 16). The plot on the left shows that with the swept wing, both the USB and EBF aircraft had unsatisfactory Dutch roll stability when the lift coefficient was increased from 1.5 to 5.0. Satisfactory damping could be obtained by doubling the basic roll and yaw damping of the EBF aircraft and tripling the roll and yaw damping of the USB aircraft. In contrast, the plot on the right for the unswept wing shows that increasing the lift coefficient from 1.5 to 5.0 makes the Dutch roll stability satisfactory even with the basic roll and yaw damping. The fact that the unswept wing looks so good from the standpoint of Dutch roll, while the swept wing was shown to require a much smaller horizontal tail for longitudinal trim (fig. 22) suggests that some intermediate sweep angle (between 0° and 27°) could be a good compromise.

ACOUSTICS AND LOADS

The areas of powered-lift acoustics and loads will now be considered. A good illustration of the severity of the noise problem for powered-lift STOL aircraft is shown in figure 26 (from ref. 17) which compares the noise requirements for STOL and CTOL (conventional take-off and landing) aircraft. First, the bars at the left show the present and proposed Federal Aviation Administration (FAA) sideline noise constraints (103 to 98 EPNdB) for a sideline distance of 0.56 km (0.35 mile) or 643 m (2100 ft). If these values are converted to a sideline distance of 151 m (500 ft) they become 124 and 119 EPNdB. The bar at the right shows that the tentative STOL noise goal for this same 151-m (500-ft) sideline distance is 95 EPNdB, which means the STOL must be 24 to 29 EPNdB quieter than a conventional airplane. This stringent requirement, of course, stems from the fact that STOL aircraft are intended to operate from airports which are closer to populated areas.

Although the STOL is required to be much quieter than a CTOL, it is actually potentially noisier because it has a much higher installed thrust and operates at high thrust values during approach and landing. The solution to this problem is obviously the use of a very quiet engine; and promising research and development have been going on in this area. Unfortunately, the externally blown flap produces additional noise which compounds the problem, as illustrated in figure 27 (from ref. 18). Noise radiation patterns are shown for engine alone, for

flaps retracted, and for a take-off flap deflection. There is a small increase in noise level even with flap retracted, and a very large increase when the flaps are extended down into the jet exhaust.

As indicated earlier, it was the severity of this flap impingement noise with the EBF which resulted in renewed interest in upper surface blowing. The benefit to be gained by having the exhaust flow above the wing to take advantage of the shielding effect of the wing is illustrated in figure 28 (from ref. 18) which compares noise radiation patterns and noise levels for EBF and USB flap systems with a landing flap deflection. The plot at the left shows that the USB produces more noise above the wing but produces much less noise below the wing, which is, of course, the important direction. The plot at the right shows the variation of noise with nozzle exhaust velocity for the two concepts. A substantial reduction in exhaust velocity is required with the EBF to give comparable noise levels with the USB; to obtain this lower exhaust velocity, an engine with a lower fan pressure ratio is required with the EBF. Recent developments which indicate solutions to the noise problems of both these concepts are covered in later sessions of the conference.

In the area of aerodynamic loads, one of the problems inherent in the externally blown concepts is the large static loads produced on the flaps as illustrated in figure 29 (taken from ref. 19). On this plot of the spanwise variation of flap normal force on the three flap segments, the peak loads are obtained directly behind each engine. These results were obtained on an EBF model; but similar peak values behind the engines occur for USB configurations as will be seen in a subsequent paper by B. Perry III and M. R. Mendenhall (ref. 20). Another loads problem for both of these concepts is high-intensity fluctuating loads which can induce high vibration levels and sonic fatigue. Figure 30 (taken from ref. 21) illustrates the principal sources of turbulent pressure fluctuations for both externally blown concepts. These pressure fluctuations can be generated within the engine by combustion, in the mixing region of the core or bypass exhaust jet, or in the flow impingement region by boundary layers or separated flow. The significance of the dynamic loads induced by these pressure fluctuations is illustrated in figure 31 (taken from ref. 22). The sound pressure levels of several sources of acoustic loading on aircraft are compared in bar graph form. For sound pressure levels above about 130 dB, sonic fatigue failures of light secondary structures have become a problem with the top four sources shown. It is therefore expected that blown flaps (both EBF and USB) will also be subject to sonic fatigue and that special attention must be given to this problem in the detailed design of the powered-lift system.

OTHER POWERED-LIFT CONCEPTS

Some other powered-lift concepts which have recently been receiving attention are illustrated in figure 32. First, at the top of the figure is the over-the-wing blowing arrangement which has potential application to conventional subsonic transports and supersonic transports. This concept differs from upper surface blowing in that the engine exhaust in cruising flight does not touch the upper surface of the wing. Thus, scrubbing drag is avoided and it might be

possible to position the engine so that the exhaust produces a favorable rather than a detrimental interference drag. For low-speed flight, tail-pipe deflectors turn the exhaust downward against the top of the wing. Research results on this concept will be given in a subsequent paper by P. L. Coe and P. G. Fournier (ref. 23).

Another concept, illustrated at the lower left, is spanwise blowing, a technique in which a jet of air is blown out along the upper surface of the wing in a direction essentially parallel to the leading edge in order to enhance the leading-edge vortex and thereby delay vortex breakdown and wing stall to higher angles of attack. (See ref. 24.) This concept appears to be promising as a means of increasing the maneuverability of fighter aircraft. Another means of increasing fighter maneuverability, which has also been studied recently, is the use of powered-lift maneuvering flaps such as illustrated at the lower right of figure 32. Flaps of this type can provide the substantial increase in lift desired for better maneuvering capability.

CONCLUDING REMARKS

In this overview of powered-lift technology, an attempt has been made to present in a very condensed form, an objective view of both the potential and the problems of powered lift. The papers to be presented during the remainder of the conference will complete the picture and will cover some of the latest developments in the field.

REFERENCES

1. Attinello, John S.: Design and Engineering Features of Flap Blowing Installations. Boundary Layer and Flow Control, Pergamon Press, 1961, pp. 463-515.

2. Davidson, I. M.: The Jet Flap. J. Roy. Aeronaut. Soc., vol. 60, no. 541, Jan. 1956, pp. 25-50.

3. Lowry, John G.; Riebe, John M.; and Campbell, John P.: The Jet-Augmented Flap. Preprint No. 715, S.M.F. Fund Paper, Inst. Aeronaut. Sci., Jan. 1957.

4. Malavard, L.; Poisson-Quinton, Ph.; and Jousserandot, P. (T. M. Berthoff and D. C. Hazen, transl.): Theoretical and Experimental Investigations of Circulation Control. Rep. No. 358, Dept. Aero. Eng., Princeton Univ., July 1956.

5. Harris, K. D.: The Hunting H.126 Jet-Flap Research Aircraft. Assessment of Lift Augmentation Devices, AGARD-LS-43-71, Feb. 1971.

6. Quigley, Hervey C.; and Innis, Robert C.: A Flight Investigation of the STOL Characteristics of an Augmented Jet Flap STOL Research Aircraft. NASA TM X-62334, 1974.

7. Campbell, John P.; and Johnson, Joseph L., Jr.: Wind-Tunnel Investigatic of an External-Flow Jet-Augmented Slotted Flap Suitable for Application to Airplanes With Pod-Mounted Jet Engines. NACA TN 3898, 1956.

8. Turner, Thomas R.; Davenport, Edwin E.; and Riebe, John M.: Low-Speed Investigation of Blowing From Nacelles Mounted Inboard and on the Upper Surface of an Aspect-Ratio-7.0 35° Swept Wing With Fuselage and Various Tail Arrangements. NASA MEMO 5-1-59L, 1959.

9. Maglieri, Domenic J.; and Hubbard, Harvey H.: Preliminary Measurements of the Noise Characteristics of Some Jet-Augmented-Flap Configurations. NASA MEMO 12-4-58L, 1959.

10. Hoad, Danny R.: Comparison of Aerodynamic Performance of Several STOL Concepts. STOL Technology, NASA SP-320, 1972, pp. 111-119.

11. Roe, Marshall H.: Air Force STOL Tactical Aircraft Investigation: Evaluation of Externally Blown Flaps. [Preprint] 730914, Soc. Automot. Eng., Oct. 1973.

12. Hoad, Danny R.: Externally Blown Flap Impingement Parameter. Powered-Lift Aerodynamics and Acoustics, NASA SP-406, 1976. (Paper no. 7 of this compilation.)

13. Johnson, Joseph L., Jr.; and Phelps, Arthur E., III: Low-Speed Aerodynamics of the Upper-Surface Blown Jet Flap. [Preprint] 740470, Soc. Automot. Eng., Apr.-May 1974.

14. Parlett, Lysle P.: Stability and Control of Externally Blown Flap Configurations. STOL Technology, NASA SP-320, 1972, pp. 55-69.

15. Phelps, Arthur E., III; Johnson, Joseph L., Jr.; and Margason, Richard J.: Summary of Low-Speed Aerodynamic Characteristics of Upper-Surface-Blown Jet-Flap Configurations. Powered-Lift Aerodynamics and Acoustics, NASA SP-406, 1976. (Paper no. 4 of this compilation.)

16. V/STOL Handling. I - Criteria and Discussion. AGARD Rep. No. 577, Dec. 1970.

17. Rulis, Raymond J. STOL Noise Sources and Fan Noise Treatment. Aircraft Engine Noise Reduction, NASA SP-311, 1972, pp. 247-258.

18. Dorsch, Robert G.; and Reshotko, Meyer: EBF Noise Tests With Engine Under-the Wing and Over-the-Wing Configurations. STOL Technology, NASA SP-320, 1972, pp. 455-473.

19. Greene, George C.; and Perry, Boyd, III: Aerodynamic Loads Measurements on Externally Blown Flap STOL Models. STOL Technology, NASA SP-320, 1972, pp. 121-130.

20. Perry, Boyd, III; and Mendenhall, Michael R.: Measured and Calculated Steady Aerodynamic Loads on a Large-Scale Upper-Surface-Blown Model. Powered-Lift Aerodynamics and Acoustics, NASA SP-406, 1976. (Paper no. 26 of this compilation.)

21. Mixson, John S.; Shoenster, James A.; and Willis, Conrad M.: Fluctuating Pressures on Aircraft Wing and Flap Surfaces Associated With Powered-Lift Systems. AIAA Paper 75-472, Mar. 1975.

22. Lansing, Donald L.; Mixson, John S.; Brown, Thomas J.; and Drischler, Joseph A.: Externally Blown Flap Dynamic Loads. STOL Technology, NASA SP-320, 1972, pp. 131-142.

23. Coe, Paul L., Jr.; and Fournier, Paul G.: Application of Powered-Lift Concepts for Improved Cruise Efficiency of Long-Range Aircraft. Powered-Lift Aerodynamics and Acoustics, NASA SP-406, 1976. (Paper no. 5 of this compilation.)

24. Campbell, James F.: Augmentation of Vortex Lift by Spanwise Blowing. AIAA Paper No. 75-993, Aug. 1975.

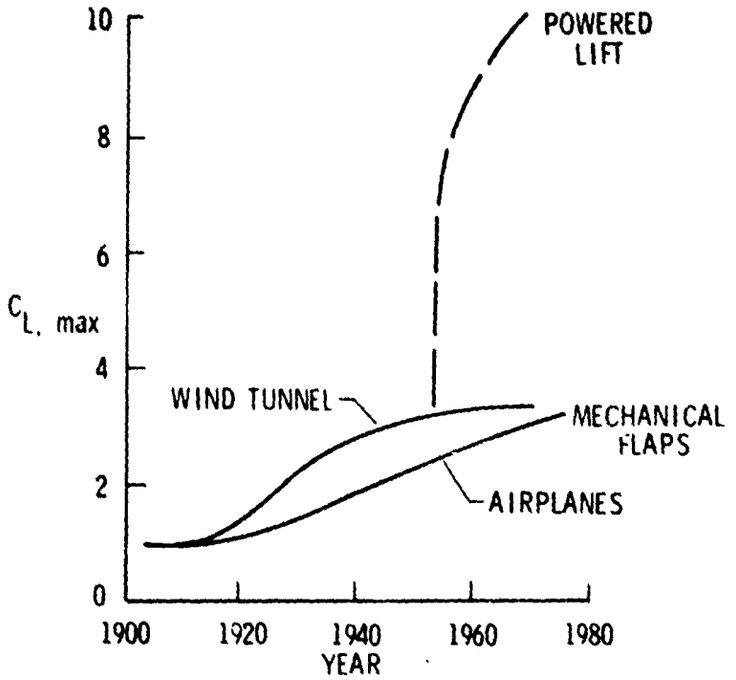

Figure 1.- Maximum lift history.

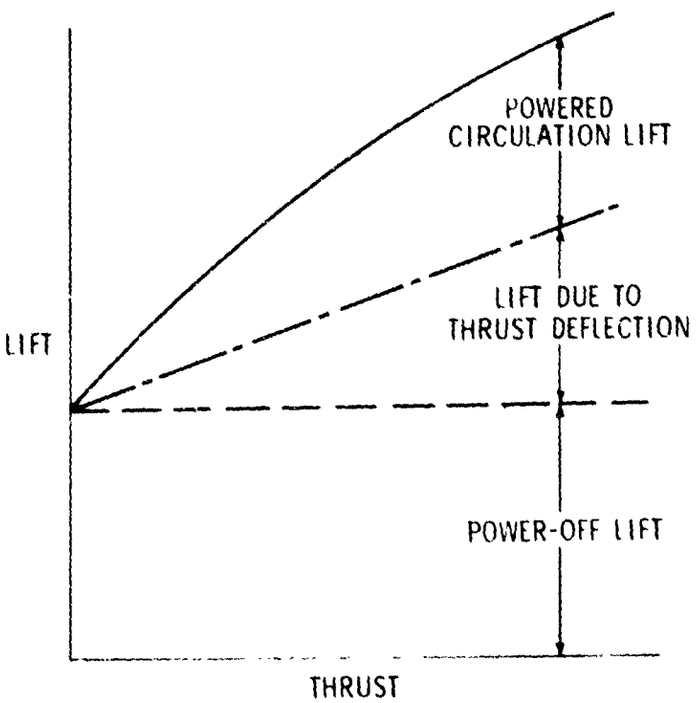

Figure 2.- Components of powered lift.

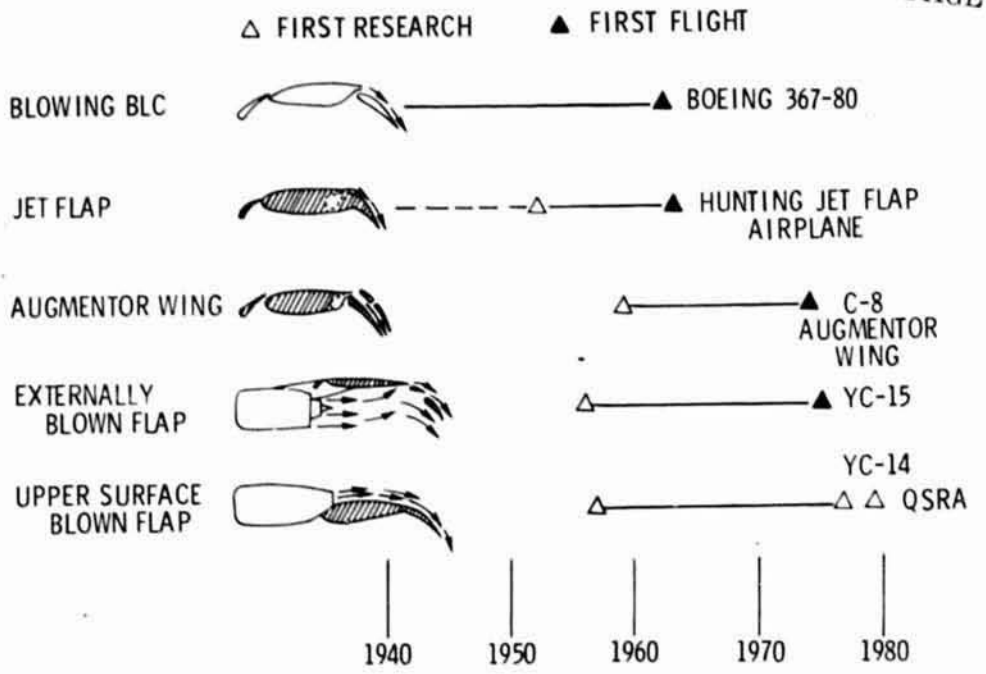

Figure 3.- Powered-lift chronology.

Figure 4.- Boeing 367-80 BLC airplane.

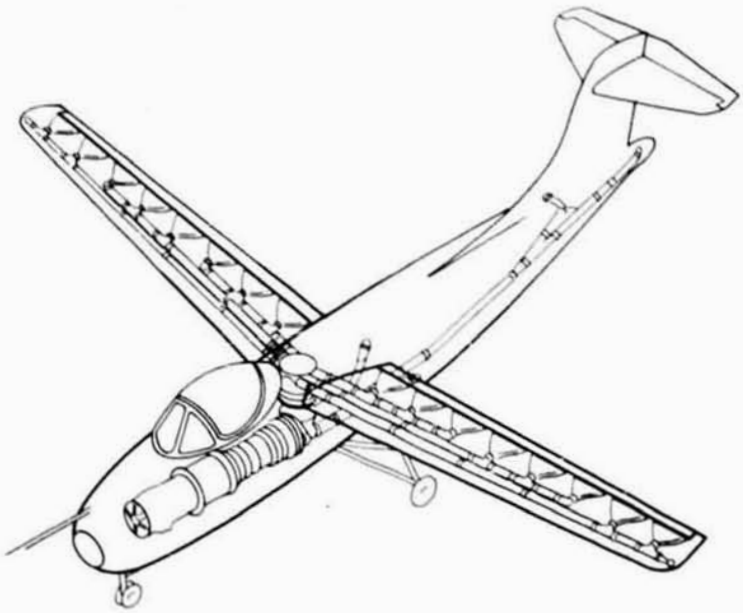

Figure 5.- Hunting jet-flap airplane.

Figure 6.- C-8 augmentor wing airplane.

Figure 7.- McDonnell-Douglas YC-15 airplane.

Figure 8.- Boeing YC-14 airplane.

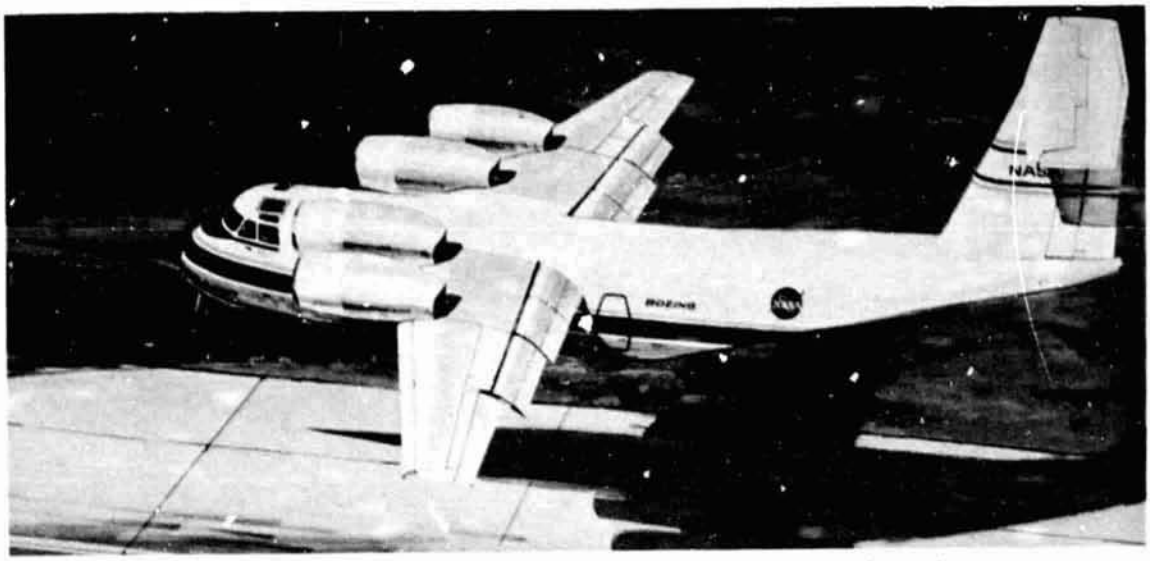

Figure 9.- Quiet short-haul research aircraft (QSRA).

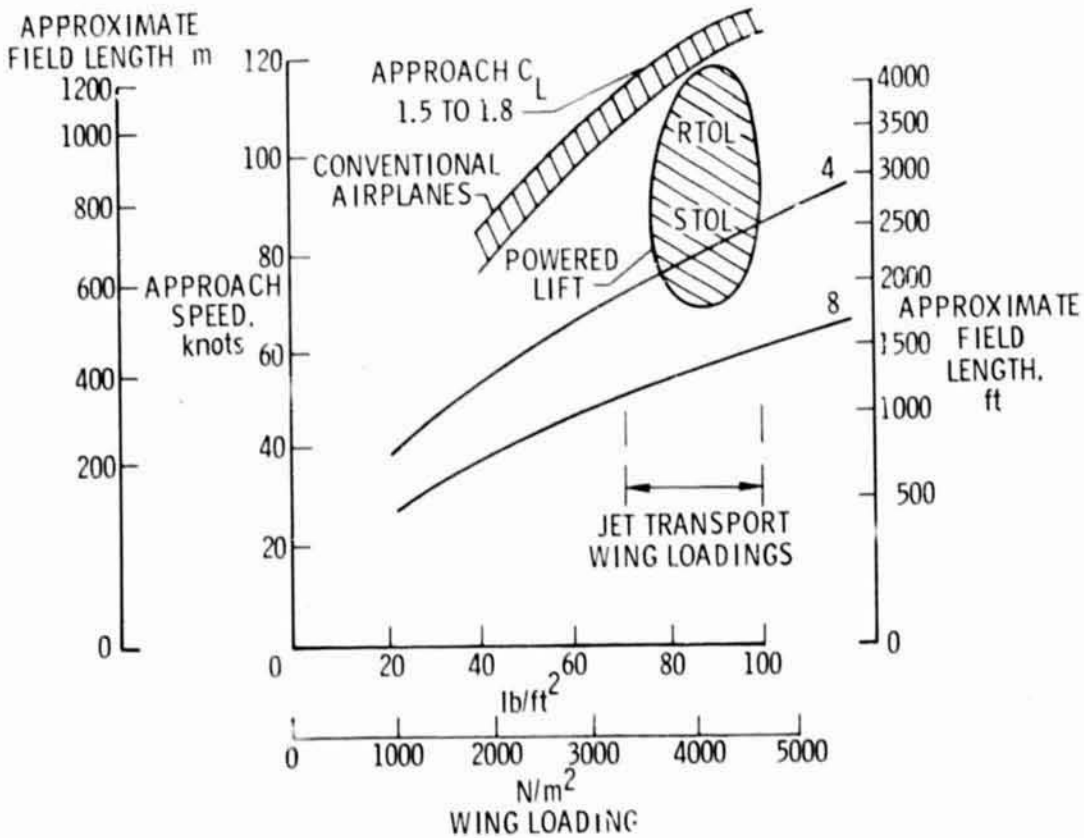

Figure 10.- Field length considerations.

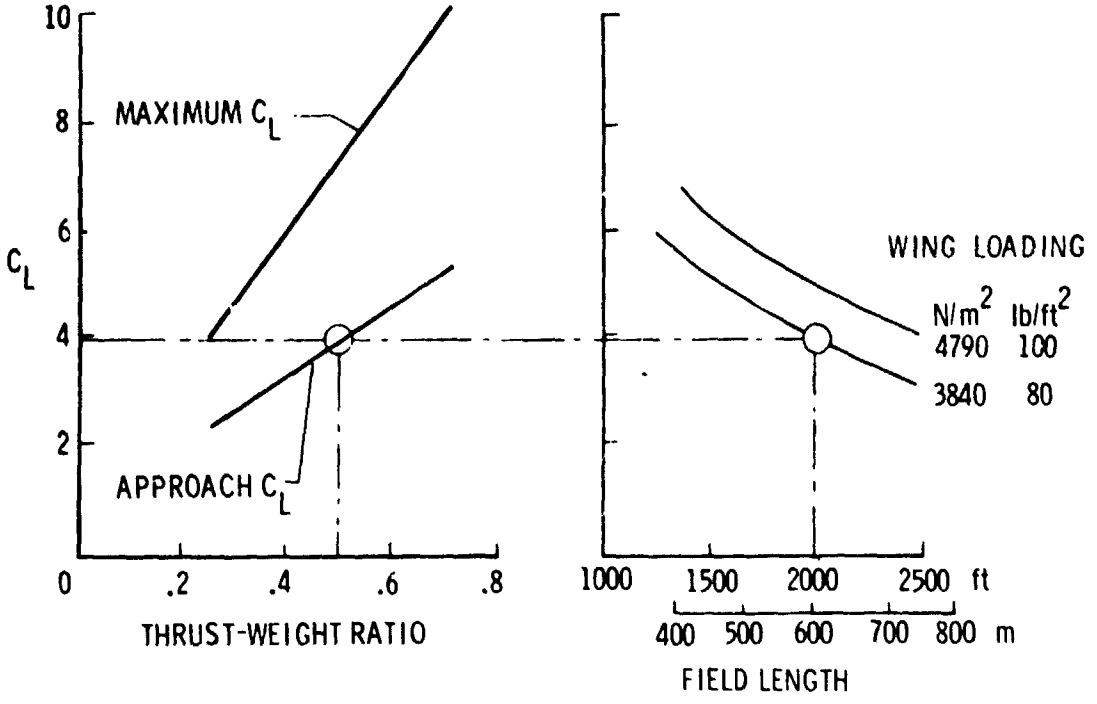

Figure 11.- Landing performance of powered-lift aircraft.

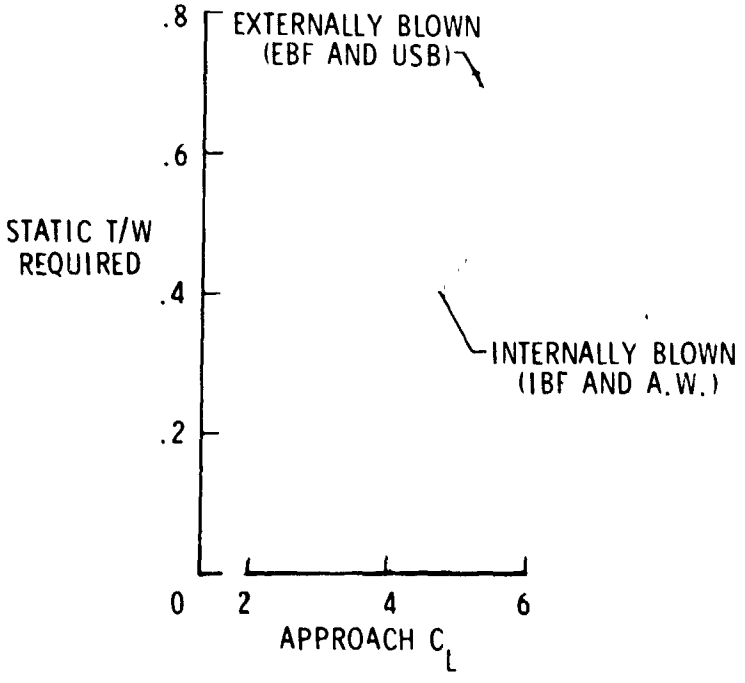

Figure 12.- Performance of externally and internally blown flaps.

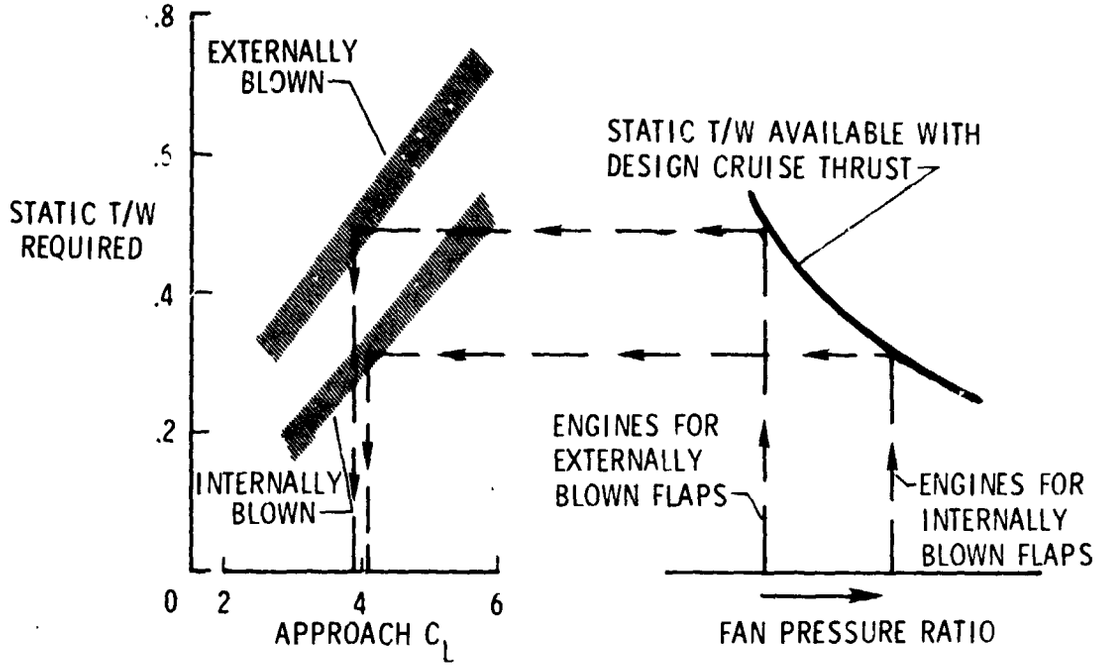

Figure 13.- Performance comparison including engine characteristics. Externally and internally blown flap systems.

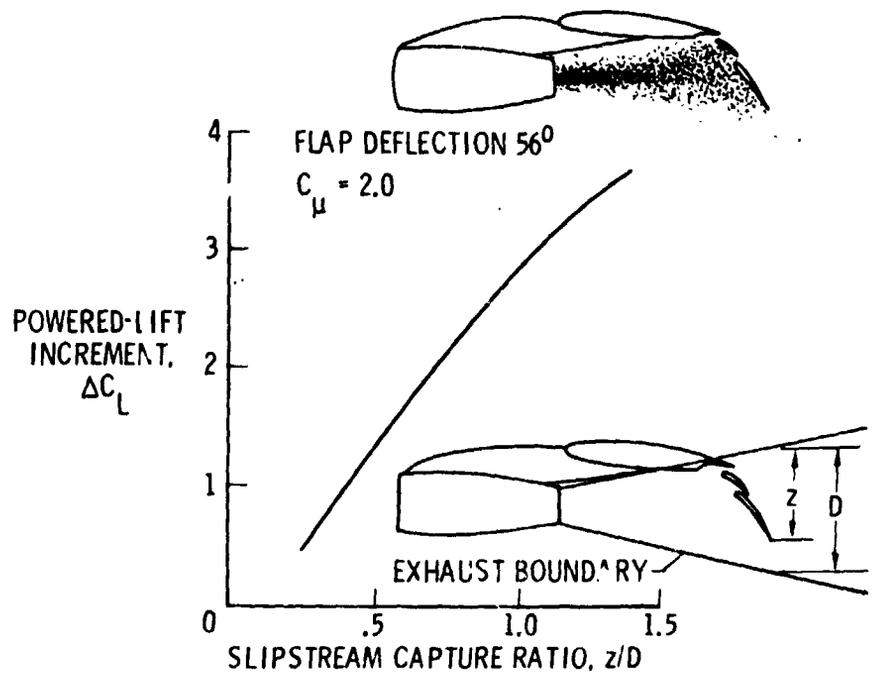

Figure 14.- Slipstream capture. Externally blown flap.

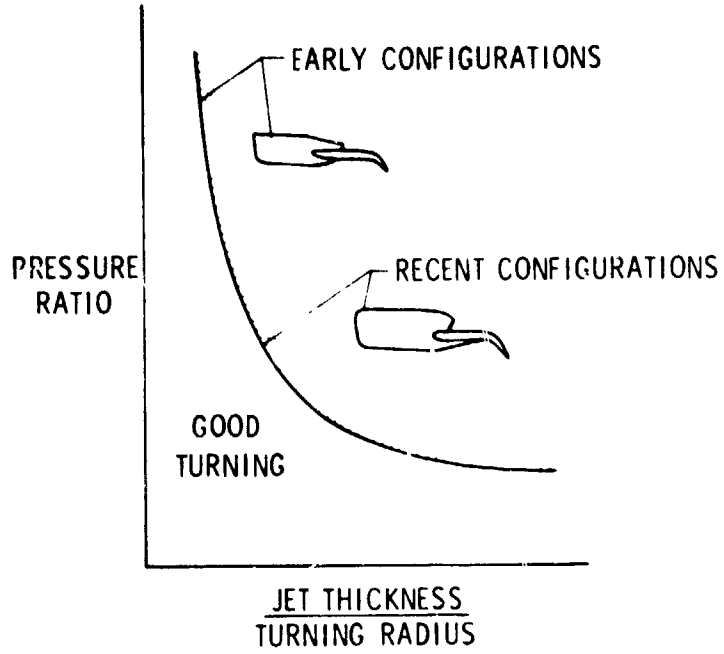

Figure 15.- Static turning.

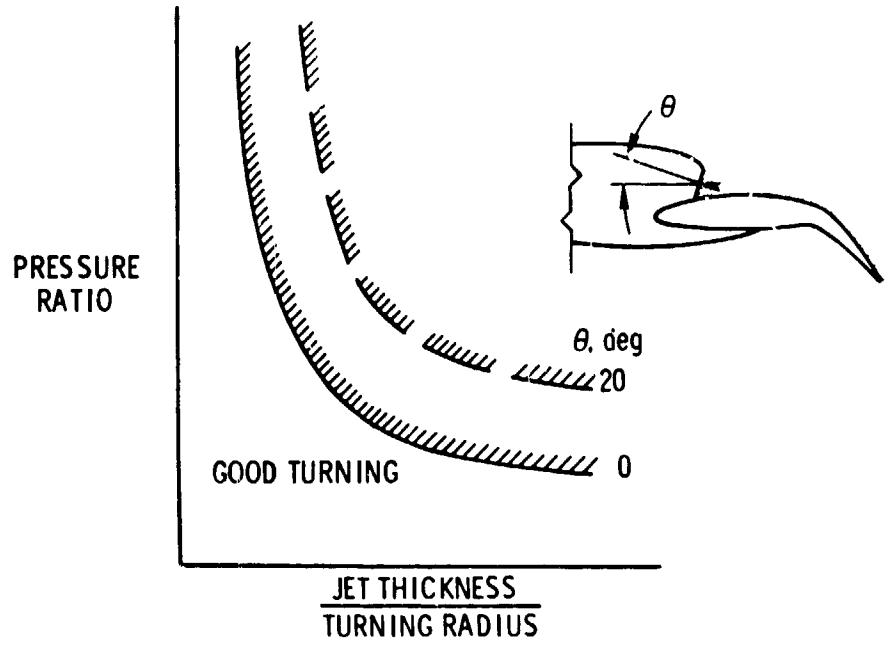

Figure 16.- Effect of nozzle deflection angle.

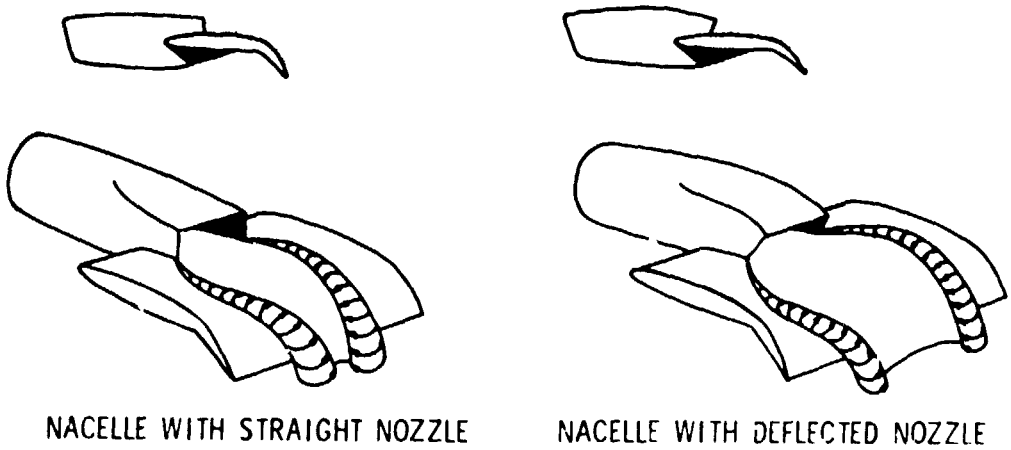

Figure 17.- Flow characteristics behind nacelles.

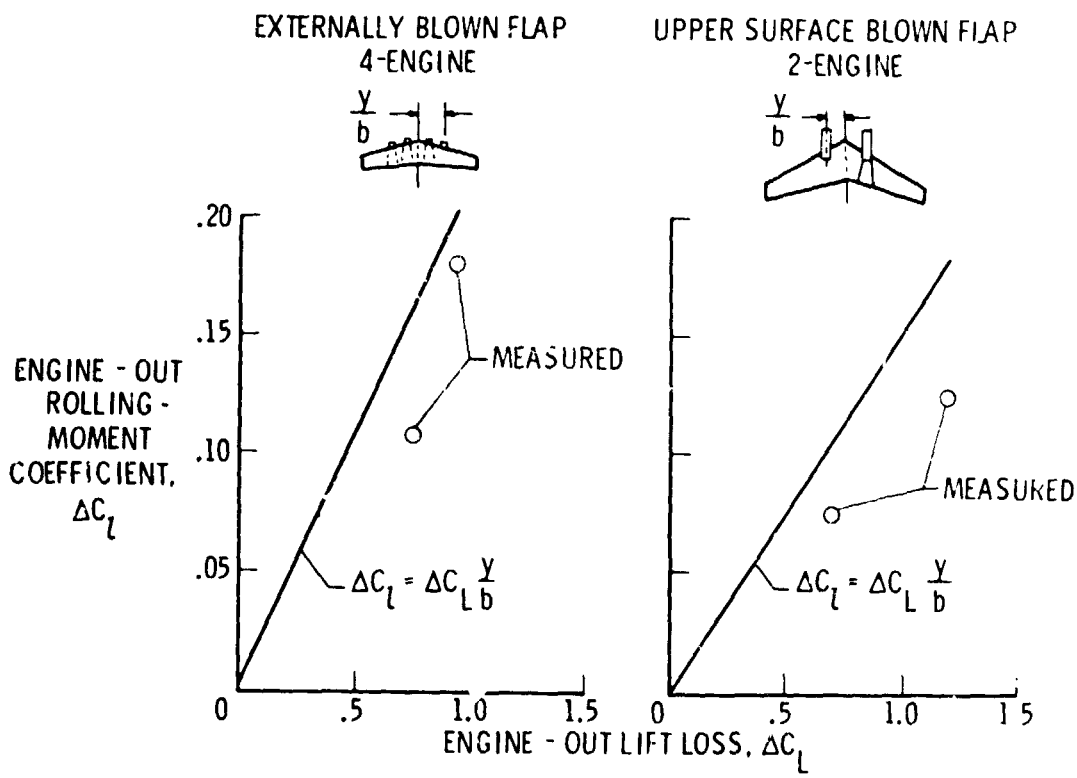

Figure 18.- Engine-out rolling moments.

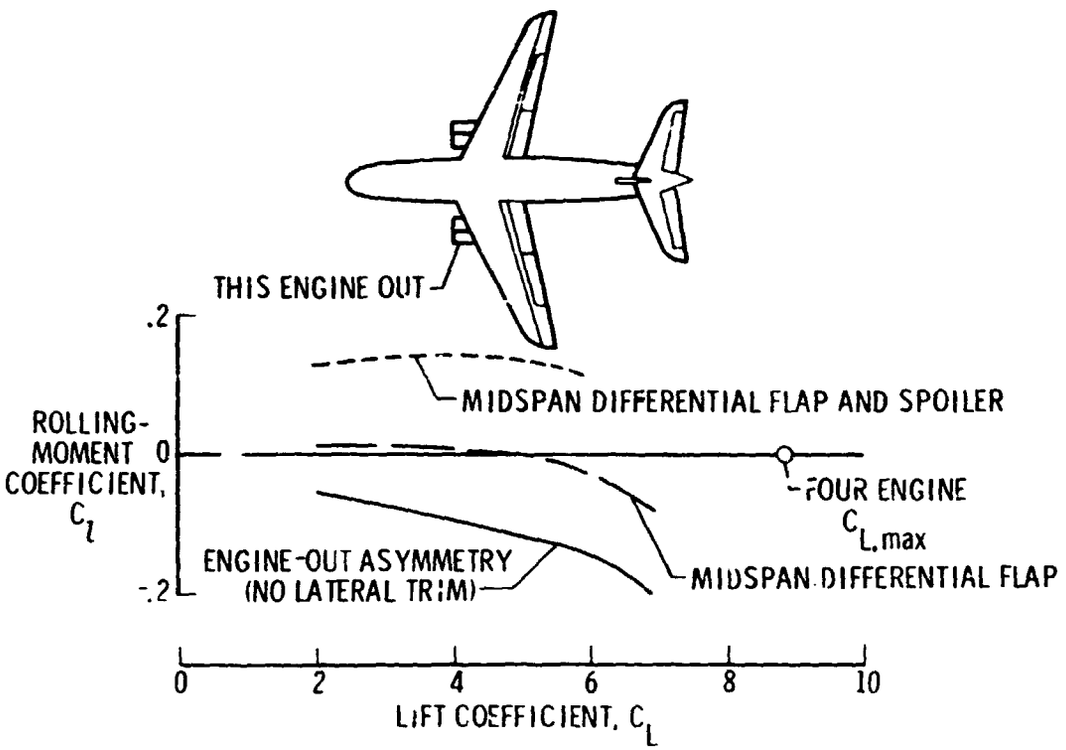

Figure 19.- Engine-out lateral trim. Externally blown flap.

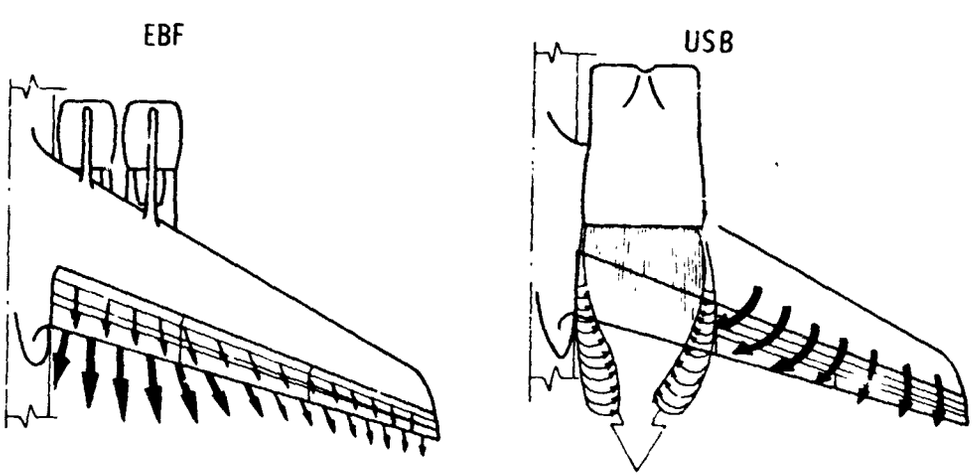

Figure 20.- Comparison of flow patterns for EBF and USB models.

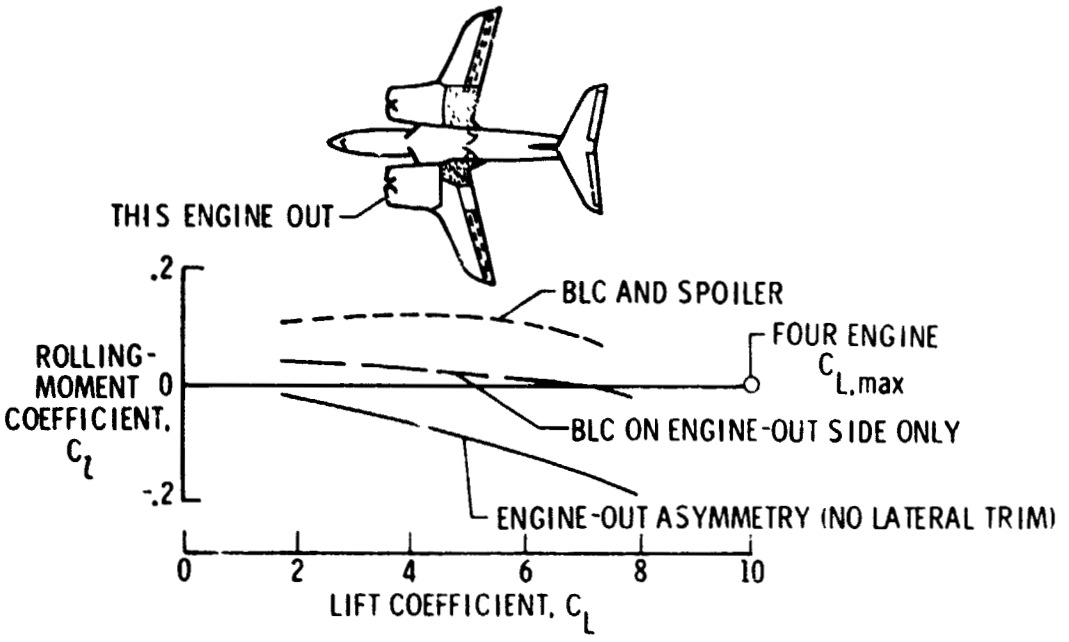

Figure 21.- Engine-out lateral trim.
Upper surface blown flap.

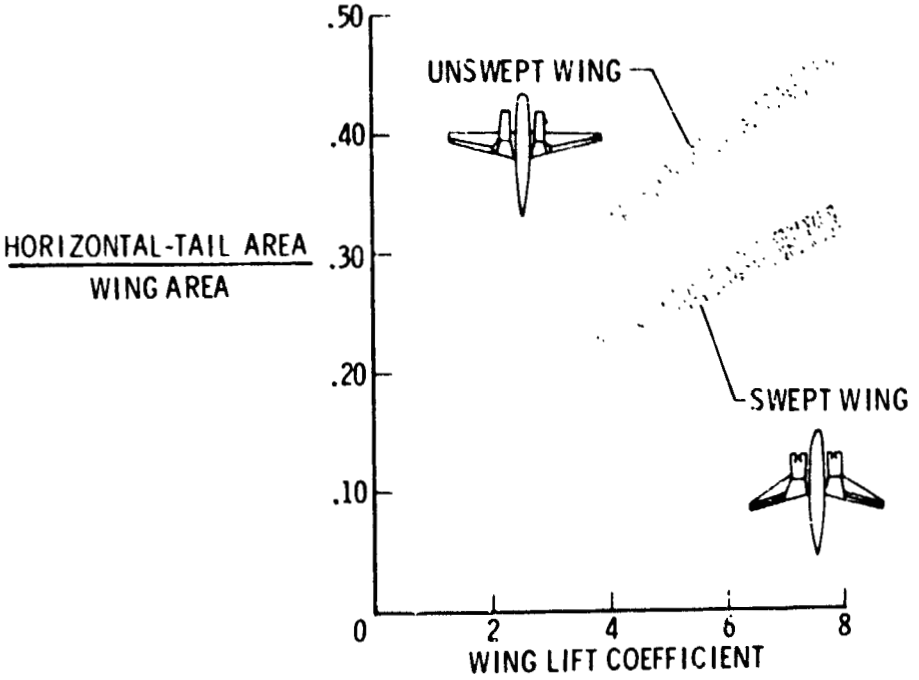

Figure 22.- Horizontal-tail size required for trim.
USB flap; $l_{tail}/c = 4$; $C_{L,tail} = 2$.

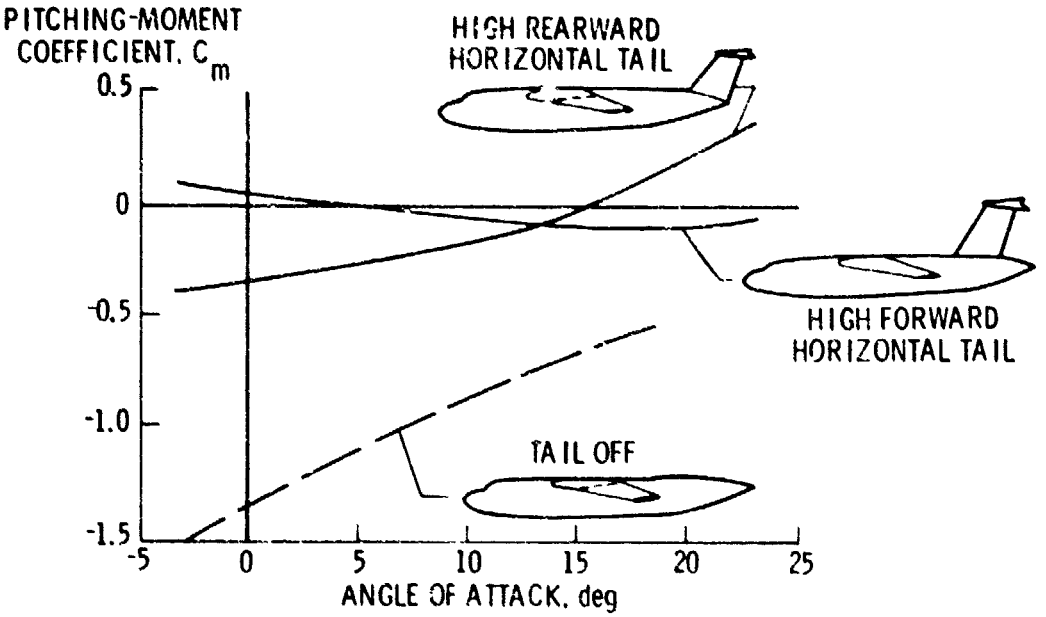

Figure 23.- Longitudinal stability.

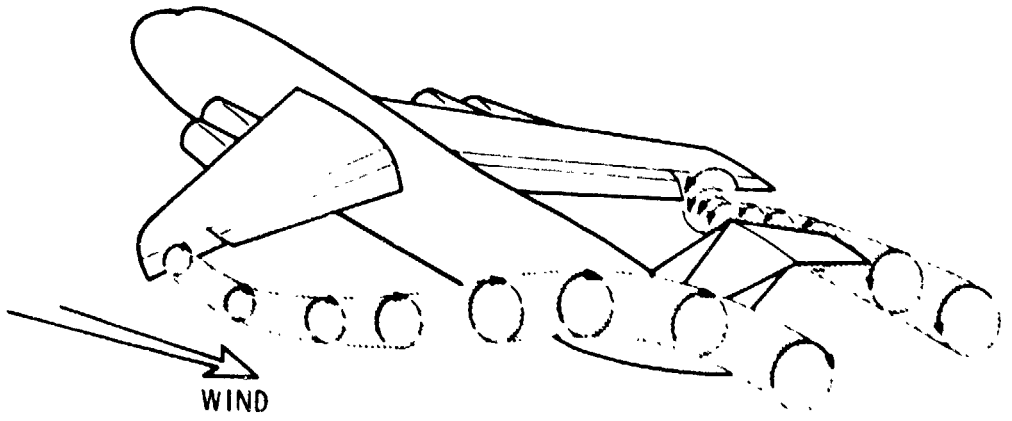

Figure 24.- Wing vortex flow.

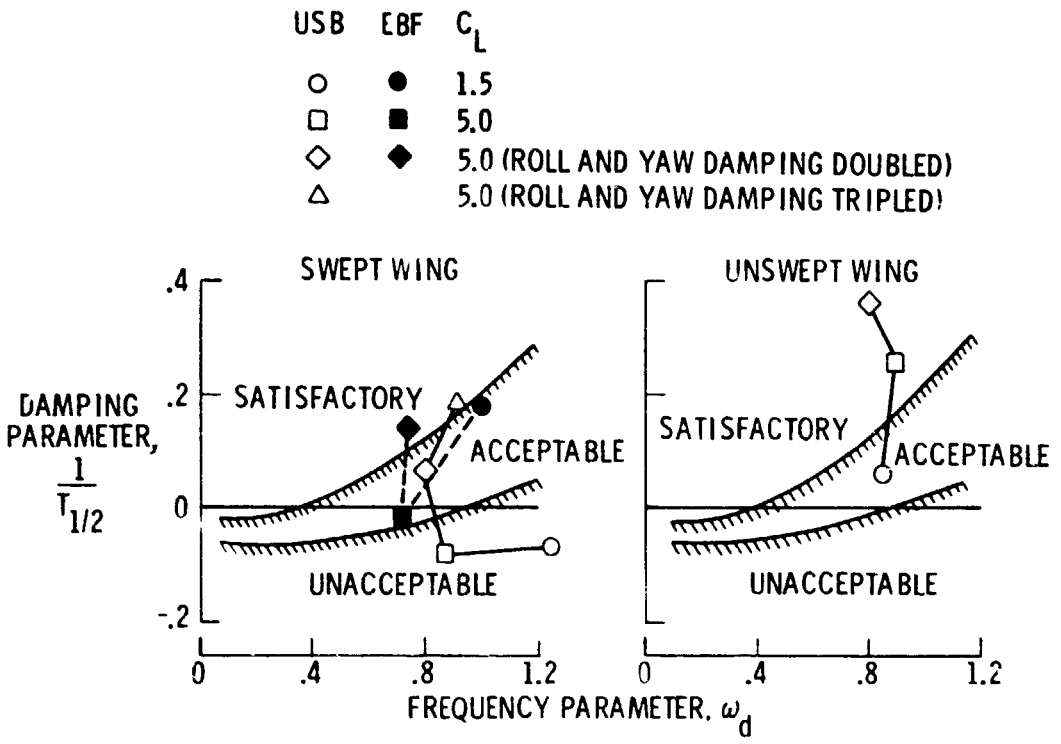

Figure 25.- Dutch roll characteristics.

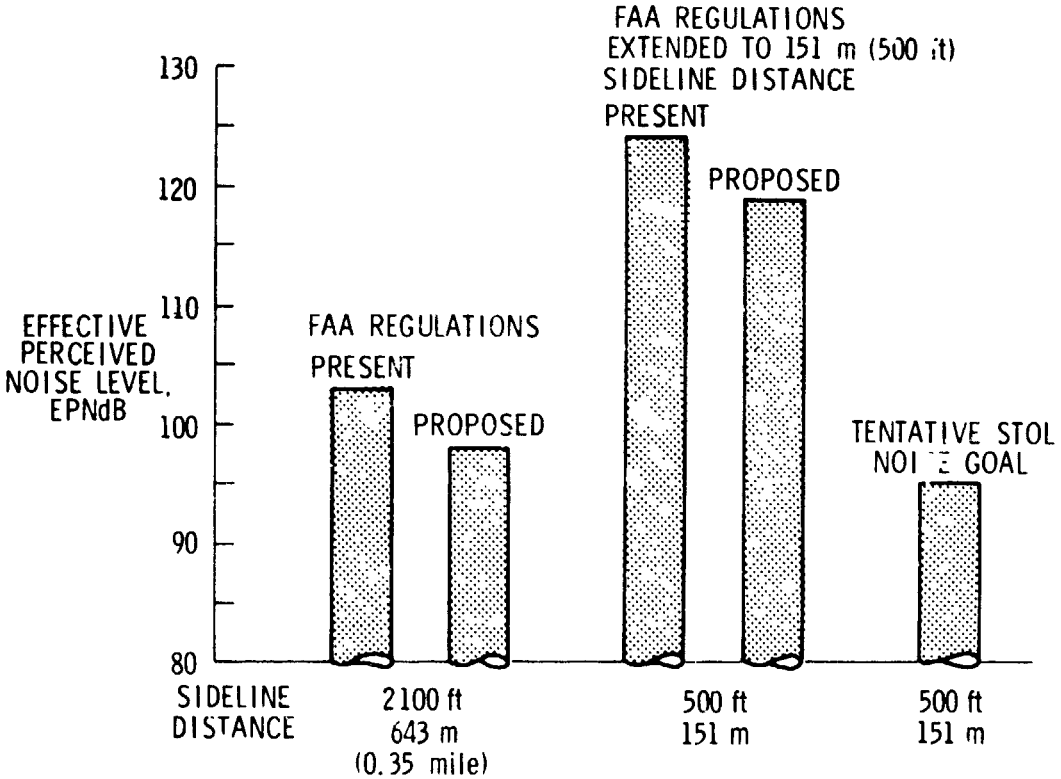

Figure 26.- CTOL and STOL noise requirements.
672 000 N (150 000 lb) aircraft.

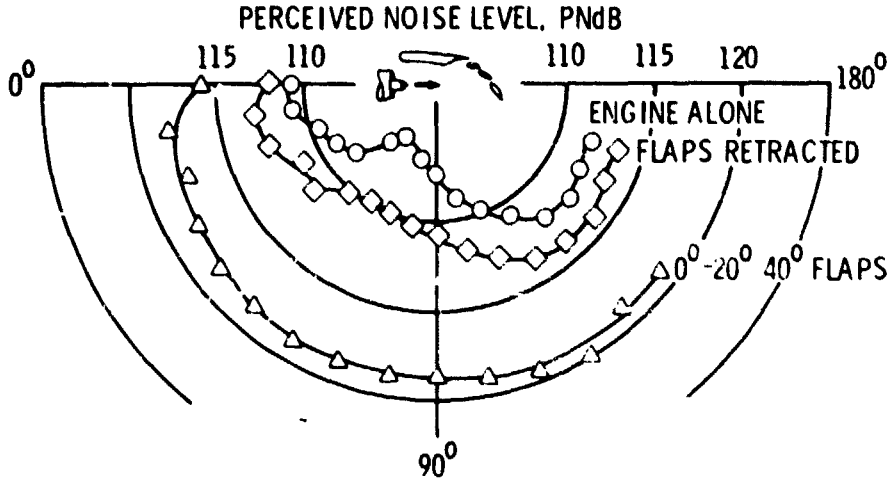

Figure 27.- EBF noise radiation patterns.
30.4 m (100 ft) from noise source.

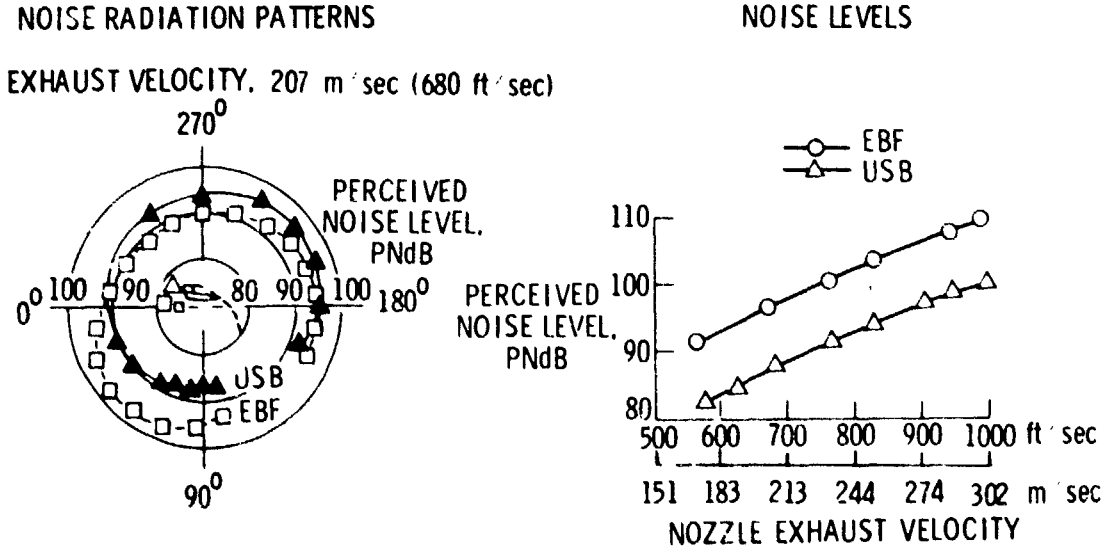

Figure 28.- Comparison of EBF and USB noise.
151 m (500 ft) from noise source; 30°/60° flaps.

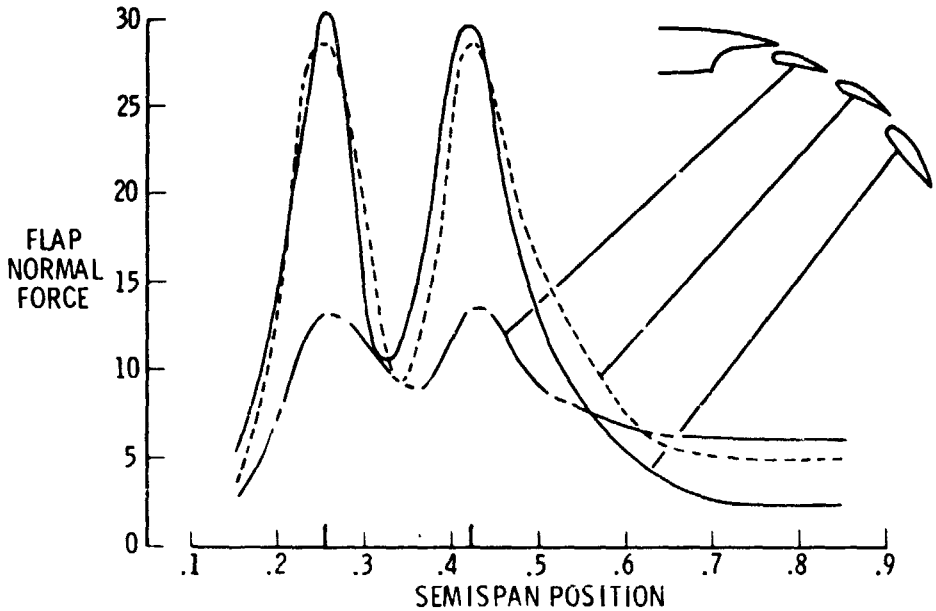

Figure 29.- Spanwise variation of flap normal force. 4-engine EBF, landing flaps (15°/35°/55°); α = 16°; C_μ = 4.0.

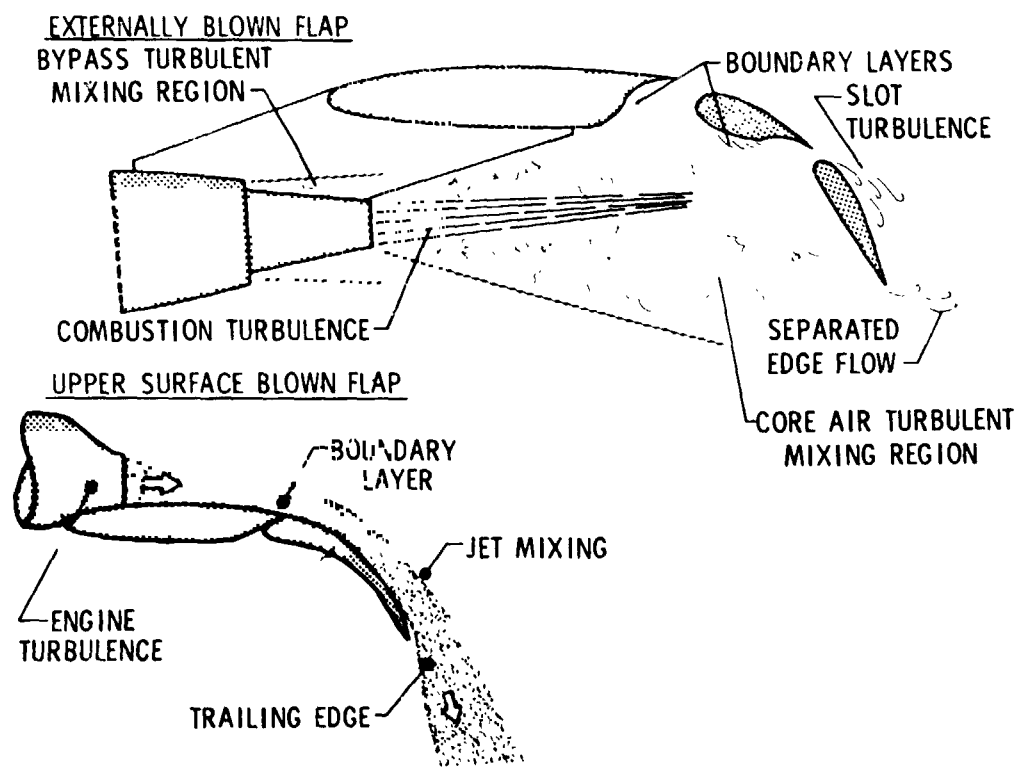

Figure 30.- Sources of fluctuating pressure on blown flaps.

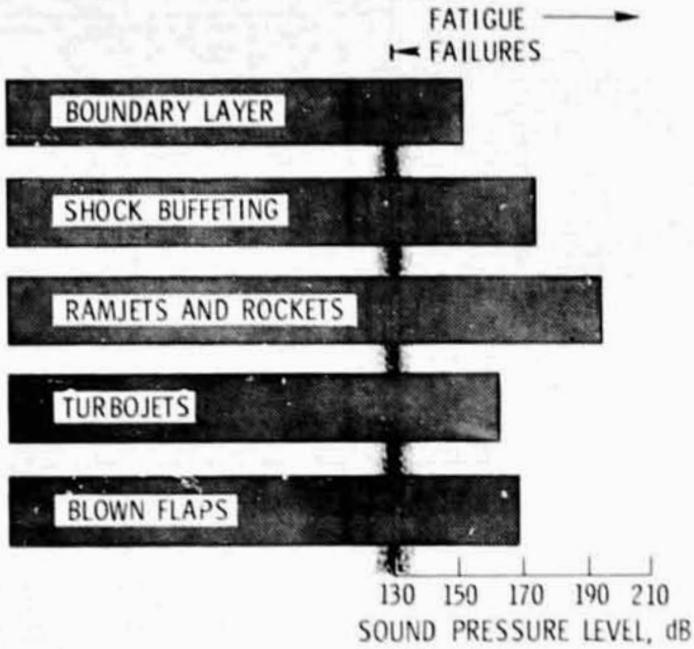

Figure 31.- Sound pressure levels of acoustic loading on aircraft structures.

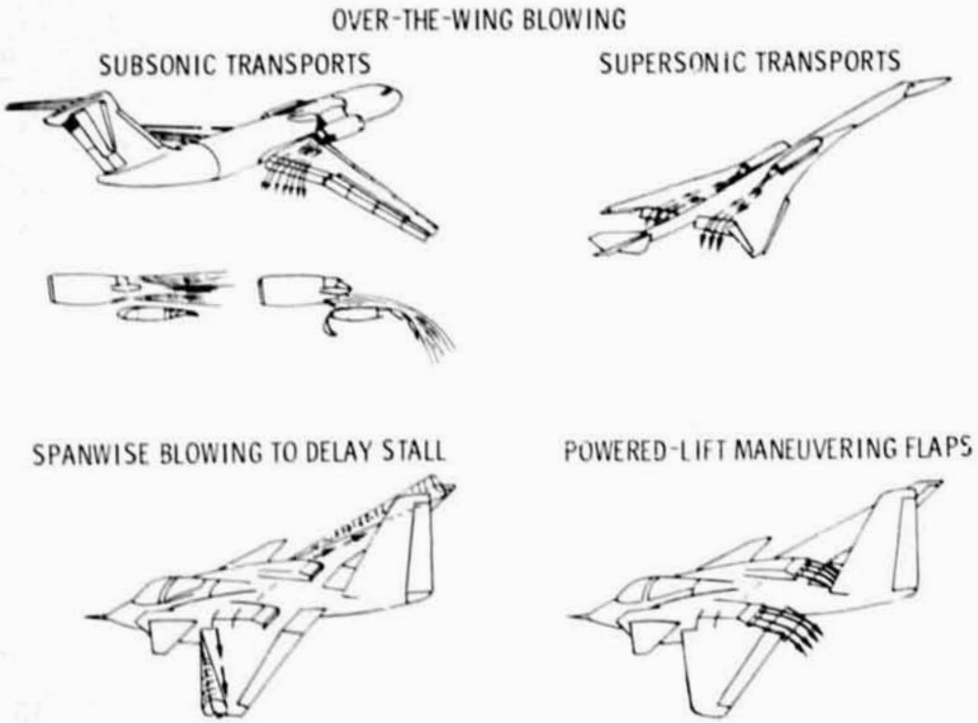

Figure 32.- Other powered-lift concepts.

N78-24048

UPPER-SURFACE-BLOWING FLOW-TURNING PERFORMANCE

William C. Sleeman, Jr.
NASA Langley Research Center

Arthur E. Phelps III
Langley Directorate, U.S. Army Air Mobility R&D Laboratory

SUMMARY

Jet-exhaust flow-turning characteristics were determined for systematic variations in USB (upper-surface blowing) exhaust nozzles and trailing-edge flap configuration variables from experimental wind-off (static) flow studies. For conditions with parallel flow exhausting from the nozzle, jet height (as indicated by nozzle exit height) and flap radius were found to be the most important parameters relating to flow turning. Nonparallel flow from the nozzle, as obtained from an internal roof angle and/or side spread angle, had a large favorable effect on flow turning.

Comparisons made between static turning results and wind-tunnel aerodynamic studies of identical configurations indicated that static flow-turning results can be indicative of wind-on powered-lift performance for both good and poor nozzle-flap combinations but, for marginal designs, can lead to overly optimistic assessment of powered-lift potential.

INTRODUCTION

The need for systematic study of upper-surface-blowing (USB) nozzle and flap variables has been recognized for identifying favorable combinations of primary variables that would provide good static flow turning and accompanying good wind-on powered-lift performance. The present parametric studies of USB nozzle and flap design variables were undertaken to fulfill this need for basic USB design information, as well as to improve understanding of the flow phenomena associated with generation of powered lift.

Static flow-turning studies offer a relatively simple and inexpensive means of evaluating the high-lift performance potential of a range of USB configuration variables. It is recognized that other factors, such as thrust recovery efficiency, are important to powered-lift performance; however, without good flow turning, a configuration has little chance of developing acceptable powered-lift characteristics. Static flow-turning data for a broad range of configurations can identify promising nozzle-flap configurations for subsequent powered-lift evaluation with forward speed effects in wind-tunnel tests. Past experience generally has shown that configurations with good static flow turning also provide appreciable lift increments due to power,

whereas configurations that showed poor flow turning at static conditions also had very little gain in lift due to power. One of the objectives of the work presented herein was to determine effects of a broad range of nozzle-flap configurations on static flow-turning angles. The second objective was to determine how well the wind-on lift characteristics of USB configurations could be inferred from static flow-turning characteristics.

Static tests were conducted on a USB nozzle-flap model that provided for systematic variations of basic design parameters over a nozzle-pressure-ratio range from about 1 to 3. Eight values of nozzle height, seven values of flap radius, and five values of run length ahead of the flap were investigated for parallel flow from the exhaust nozzle. The basic nozzle was modified internally to provide four internal roof angles and two side spread angles in addition to the basic parallel flow (0°) angles. Both static data and wind-on tests in the Langley V/STOL wind tunnel of a few complete models with rectangular exhaust nozzles and with full-span leading-edge blowing provided comparative information for assessing the applicability of static flow-turning results.

SYMBOLS

C_L	lift coefficient, $\frac{\text{Lift}}{qS}$
C_μ	thrust coefficient, $\frac{\text{Thrust}}{qS}$
H	nozzle height, height of nozzle roof above nozzle floor at exit
q	test dynamic pressure
R	flap radius, effective turning radius of USB flap at tangent point to upper surface of wing airfoil
S	reference wing area
α	angle of attack of wing chord line
δ_f	flap deflection, angle of flap chord line at trailing edge with respect to wing chord line
USB	upper-surface blowing

Notation:

Run length	length of straight flow run downstream of nozzle exit to beginning of flap curvature

Flow-turning angle	effective static turning angle of jet flow after passing over flap, as determined from wind-off force measurements, $\tan^{-1}\sqrt{\frac{\text{Normal force}}{\text{Axial force}}}$
Nozzle pressure ratio	ratio of total pressure in exhaust nozzle to ambient total pressure
Nozzle roof angle	internal angle of nozzle roof with respect to nozzle floor
Nozzle spread angle	internal spread angle of nozzle sides measured from nozzle center line (slanted to spread exhaust flow laterally over wing and flap)

STATIC TESTS OF NOZZLE-FLAP VARIABLES

Model Description

A photograph of the static test model is shown in figure 1 with half of the nozzle block removed to show some of the inside details. High-pressure air was supplied from a pipe and brought to the model through a special plenum. The whole model assembly was mounted on a strain-gage balance, and the static flow-turning characteristics were determined from the measured forces. All measured data were corrected for tares associated with the air-supply hookup.

A schematic drawing of the model is given in figure 2 to indicate configuration variables investigated. Eight values of nozzle height ranging from 0.635 cm to 5.080 cm were investigated by the use of interchangeable nozzle blocks. Five values of run length ahead of the flap were investigated over a range from 0 cm to 10.16 cm; seven values of flap radius from 2.54 cm to 20.32 cm were investigated with circular arc flaps. The arc length of the flap having the largest radius was 32 cm from the beginning of curvature to the trailing edge (fig. 2). This length was held constant for all smaller values of flap radius by the addition of straight segments that formed the flap trailing edge. (See figs. 1 and 2.)

The width of the exhaust nozzle remained constant while other nozzle parameters such as spread angle and nozzle height were varied. The span of the flap was sufficiently large to contain the flow for all conditions of the exhaust nozzle investigated (fig. 2). All tests of the model were conducted over a range of nozzle pressure ratios which varied from about 1.1 to 3.1 for nozzle heights equal to or less than 2.54 cm (nozzle aspect ratio of 7); for the largest nozzle height of 5.08 cm (nozzle aspect ratio of 3.5),

the maximum pressure ratio that could be obtained was limited to about 1.6 because of mass-flow and total-pressure limitations of the air-supply system.

Effect of Pressure Ratio on Flow Turning

The flap and nozzle variables investigated in the present study provided over 300 different configurations which were tested over a range of nozzle pressure ratios. This paper presents only selected portions of the vast amount of data obtained, to illustrate the principal findings and to summarize the results.

Data showing effects of nozzle pressure ratio on flow turning for various nozzle aspect ratios are presented in figure 3. Flap radius, flap turning angle (90°), and run length were held constant. The jet flow turning as illustrated in figure 3 is the angle of the jet flow after it passes over the wing and flap. The test results show turning angles that extended to about 50°, which indicates that the jet flow did not adhere to the 90° flap all along the flap but separated at some point ahead of the trailing edge.

The nozzle aspect ratio was changed by varying the jet exit height, and a decrease in the nozzle aspect ratio was accompanied by an increase in the height and attendant flow thickness. The results of figure 3 show an expected reduction in flow turning as the jet thickened (decreased nozzle aspect ratio). Also, as the jet height increased, conditions were reached where the flow could no longer negotiate the turn over the flap at higher pressure ratios and the abrupt loss in flow turning shown for some curves indicates sudden detachment of the flow. Past experience has shown that such sudden detachment can occur if the corner is too sharp (small turning radius), the jet is too thick, or the pressure ratio is too high.

Effects of pressure ratio on flow turning for a range of flap radius are shown in figure 4, where flap radius is expressed nondimensionally as a function of nozzle height. For these tests, the nozzle aspect ratio (and nozzle height) was held constant, as was the flap angle of 90°. Past experience would lead one to expect increases in flow turning with increasing turning radius (ref. 1); however, the data of figure 4 show progressive decreases in turning with increasing radius at pressure ratios up to 2.2. As mentioned previously, the smallest radius was too sharp for flow turning at high pressure ratios, and abrupt detachment was shown for pressure ratios above 2.2. Additional details on effects of flap radius, particularly in the lower range, will be discussed later.

The test results over a range of pressure ratio presented in figures 3 and 4 are fairly typical of the nature of the characteristics obtained for a wide range of nozzles and flap geometry, and most of the data showed only minor variations in turning angle with pressure ratio at low and moderate pressure ratios. The test results at low values (<1.5) of nozzle pressure

ratio were found to be indicative of the maximum flow turning to be expected from a given configuration. A nozzle pressure ratio of 1.4 has been selected as representative of a quiet, high-bypass-ratio propulsion system and will be utilized for the remaining discussion of the static tests of nozzle-flap variables.

Effect of Flap Radius on Flow Turning

Data which show effects of flap radius on flow turning for small increments over a broad range of nozzle aspect ratios are presented in figure 5. These results are for a nozzle pressure ratio of 1.4 and a constant run length. The flap radius is nondimensionalized by the nozzle height.

While radius-height ratios up to 32 were included in the results of figure 4, the results of figure 5 are concerned only with the lower end of the radius range (to values of about 8).

The results of figure 5 show the expected increase in flow turning with increasing radius at very low values of radius-height ratio, but a breakaway point is evident beyond which little or no increase in turning occurs as the radius increases (for each nozzle aspect ratio). Each nozzle aspect ratio had its own breakaway point except possibly for the aspect-ratio-28 nozzle, for which data were lacking. These test results also show that there is some upper limit to the flow-turning angle that can be obtained with a particular parallel-flow nozzle/flap combination.

The data of figure 5 were generally representative of data obtained at other pressure ratios and run lengths. Increasing the nozzle pressure ratio from the 1.4 value used for figure 5 to a value of 2.0 caused only a slight reduction in flow turning, while variations in flow turning with run lengths greater than zero were relatively small. Most of the data available from this investigation were used to develop the following figure (fig. 6) which accounts for second-order effects by shaded areas which replaced the discrete lines of figure 5. Breakaway points for several nozzle aspect ratios are indicated by the numbers shown on the rising shaded band in figure 6. This rising shaded band separates the region where flow turning is available from the region where flow turning is not available with parallel flow nozzles and 90° flaps. The rising band extends to about 60° flow turning for a flap radius ratio of around 4, but this good turning is obtained only with a very large nozzle aspect ratio.

Experience with USB nozzle-flap configurations in other studies has demonstrated that flow-turning angles equal to or better than the 60° shown in figure 6 have been obtained on models with relatively low-aspect-ratio nozzles. The question naturally arises as to why these low-aspect-ratio nozzles were able to provide such high turning. Since the high-aspect-ratio nozzle of the present study provides a very thin jet, the effective jet height at the start of turning is perhaps of more fundamental importance than nozzle

height. Low-aspect-ratio nozzles can turn flow if there is some means of thinning and spreading the flow. Several means for causing the exit flow to thin after leaving the nozzle have been used successfully and include the use of external deflectors, a large internal roof angle, and appreciable nozzle side flare.

Effects of Nozzle Internal Angles

The present nozzle-flap study included systematic variations in internal roof angle and side spread angle as shown schematically in the sketches in figure 7. Flap radius and run length were varied but the nozzle aspect ratio of 7.0 was held constant. Typical turning-angle results are also presented in figure 7 as a function of internal roof angle for three values of spread angle. These test results are for a nozzle aspect ratio of 7 and a radius-height ratio of 4. For parallel exit flow (see fig. 6), the flow turning at these values of aspect ratio and radius would be 25° to 30°, which is consistent with the flow turning shown in figure 7 at 0° roof angle and 0° spread angles. Attainment of 60° turning can be obtained either by increasing only the roof angle to 30° or by using 20° of spread angle and 0° roof angle (fig. 7). Combinations of roof angle and spread angle can provide up to 80° of flow turning. The trade-offs in roof and spread angle, as illustrated in figure 7, provide the designer with some freedom of selection to minimize problems such as high cruise drag associated with high boattail/roof angles.

WIND-TUNNEL TESTS OF COMPLETE USB MODELS

The preceding discussion has been concerned with wind-off static turning and design variables that influence flow turning for rectangular nozzles. The second part of this paper deals with forward speed effects for complete USB model configurations in wind-tunnel tests. Emphasis is given to the determination of how well the wind-on lift characteristics can be inferred from the static flow-turning characteristics.

Four-Engine Model With Radius Flaps

A photograph of the four-engine USB configuration in the Langley V/STOL tunnel is shown in figure 8. The wing had supercritical airfoil sections with a maximum thickness of 9.3 percent chord, a nominal quarter-chord sweep angle of 30°, an aspect ratio of 7.48, and a taper ratio of 0.247. Test results and a detailed description of this model are given in reference 2. This model provides a very good tie-in with the nozzle-flap study just discussed inasmuch as it used aspect-ratio-6 rectangular exhaust nozzles and a 90° radius flap. It should be noted that both the chord and area of the flap decreased as the deflection decreased from 90°; the arc length was proportional to flap deflection angle (i.e., the arc length of the 45° flap was half of that for the 90° flap).

Both static flow-turning and companion forward speed test results at 0° angle of attack are given in figure 9 for a range of flap deflections from 45° to 90°. Static test results presented in figure 9 show consistent increases in flow turning with increasing flap deflection, and the turning angles were essentially invariant with thrust. The level of flow turning was fairly good; that is, the nozzle-flap configuration turned the flow about two-thirds of the flap deflection (60° turning for 90° flap). Characteristics of the wind-on lift that could be inferred from these fairly good static flow-turning data are that lift should increase in a smooth and steady manner with increased thrust, and that lift should increase for a given thrust, proportionate to changes in flap deflection. These characteristics are certainly evident in the wind-on data of figure 9, and the static turning data can be considered indicative of the wind-on lift characteristics to be expected.

Four-Engine Model With Modified Slotted Flap

Representative test results on the same basic model just discussed but with different high-lift flaps are given in figure 10. The modified flap system is shown at three different deflections in the sketches at the top of figure 10. The flap was originally a double-slotted flap for an externally blown flap model; the flap was modified for upper-surface blowing by filling in the gaps between flap elements. The resulting flap-radius—nozzle-height ratios shown in figure 10 are judged to be the approximate effective values.

The static flow turning at low and moderate thrust appears to be fairly good, in that the flow angle was about equal to the flap deflection and was relatively invariant with thrust except for the first few data points at the lower flap angles. In the middle-to-high thrust range, however, abrupt detachment of the flow occurred for the highest flap deflection, as evidenced by the large decrease in flow turning. It could be inferred from these static results that the wind-on lift at low thrust would vary in proportion to the flap deflection but at high thrust would suffer a loss in lift in going to the highest flap deflection. The actual wind-on lift data, however, show that lift coefficients for the highest flap deflection were always lower than those for the lower flap deflections. The static data therefore are overly optimistic and not directly indicative of the wind-on characteristics obtained.

Previous experience with upper-surface-blown configurations has indicated that poor wind-on powered-lift characteristics almost always accompany poor static flow-turning characteristics. Likewise, good invariant static flow turning generally can be taken to indicate correspondingly good wind-on lift characteristics. Considerable uncertainty can exist between these extremes of very good and poor static turning; however, where appreciable variations in flow turning with static thrust occur, anomalies in the wind-on lift can generally be expected. The sudden detachment of the flow shown for the 65° flap deflection in figure 10 suggests that the flow at low thrust was only

marginally attached, and the addition of more thrust and/or addition of the free-stream velocity caused the jet flow to detach. In this last example, static flow-turning results gave some indication that the jet flow was only marginally attached for some configurations and, with forward speed, would be expected to detach. The question then arises as to the likelihood of a situation where the static flow-turning data gave no indication of marginal attachment, while in fact, forward speed effects would cause the flow to detach. The discussion in the next section deals with such a situation.

USB Model With Full-Span Leading-Edge Blowing

A photograph of the leading-edge-blowing model is shown in figure 11. The model had blowing over the upper surface of the wing from a small full-span slot located near the wing leading edge. The model had a double-hinge plain flap with a very small radius on the forward element. A sketch of the model airfoil, showing the blowing slot at 19 percent chord and the deflected flap, is given at the top of figure 12. The use of a double-hinged flap allowed a matrix of flap combinations to be investigated by setting the rear flap and varying the deflection of the forward element over a range of angles. In order to cover more model configurations than could be easily handled by the data presentation used with the previous figures, the data of figure 12 are presented as a function of total flap deflection.

Flow-turning angles and wind-on lift coefficients are presented in figure 12 as functions of total flap deflection for $C_\mu = 2.0$ with the wind on and for static thrust corresponding to $C_\mu = 2.0$ with the wind off. None of the basic wind-off flow-turning data showed unusual variations with static thrust. Static test results of figure 12 show that flow turning increased as the total flap deflection increased, and turning angles up to 85° were obtained at the highest flap deflection. The wind-on lift data of figure 12 show increases in lift with flap deflection up to a point and then a decrease in lift. It is interesting to observe that the lift peak always occurred at 45° deflection of the front flap (45° front + 0° rear = 45°, 45° front + 15° rear = 60°, and 45° front + 30° rear = 75°). These results indicate that good static flow turning may not always be indicative of correspondingly good power-on lift characteristics. An assessment of the lift potential based on the static turning data for this leading-edge-blowing model would be optimistic for flow-turning angles in excess of about 60°.

CONCLUDING REMARKS

Static test results obtained in an investigation of parallel-exit-flow USB nozzle and flap geometric variations over a range of nozzle pressure ratio from about 1 to 3 showed very little effect of pressure ratio on static flow turning for configurations with well-established flow. Test results obtained at low pressure ratios were indicative of the maximum flow-turning performance to be expected. Some gains in flow turning were even realized by the use of a

small (2.54 cm) run length ahead of the flap, but further increases in run length produced relatively small changes in turning. Flow-turning angles increased when the jet height decreased and increased with flap radius up to a point, beyond which little or no increase was evident. The jet height, as indicated by the nozzle exit height, and the flap radius were the most important parameters relating to flow turning for parallel flow from the nozzle. Non-parallel flow from the nozzle, as obtained from an internal roof angle and/or side spread angles, had a large favorable effect on flow-turning angles.

Static tests and wind-on tests of complete USB models in a wind tunnel indicated that the static flow-turning results can be indicative of wind-on powered-lift performance for both good and poor conditions. For marginal conditions, the static results can lead to an overly optimistic assessment of wind-on powered-lift potential.

REFERENCES

1. Phelps, Arthur E., III: Aerodynamics of the Upper Surface Blown Flap. STOL Technology, NASA SP-320, 1972, pp. 97-110.

2. Sleeman, William C., Jr.; and Hohlweg, William C.: Low-Speed Wind-Tunnel Investigation of a Four-Engine Upper Surface Blown Model Having a Swept Wing and Rectangular and D-Shaped Exhaust Nozzles. NASA TN D-8061, 1975.

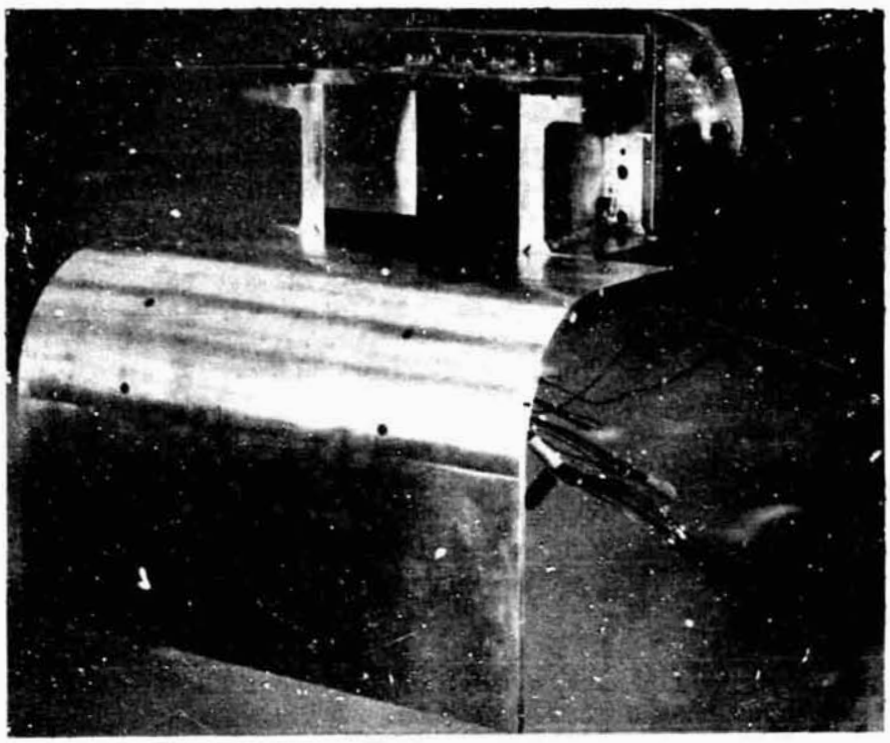

Figure 1.- Model used in static tests of USB nozzle and flap variables.

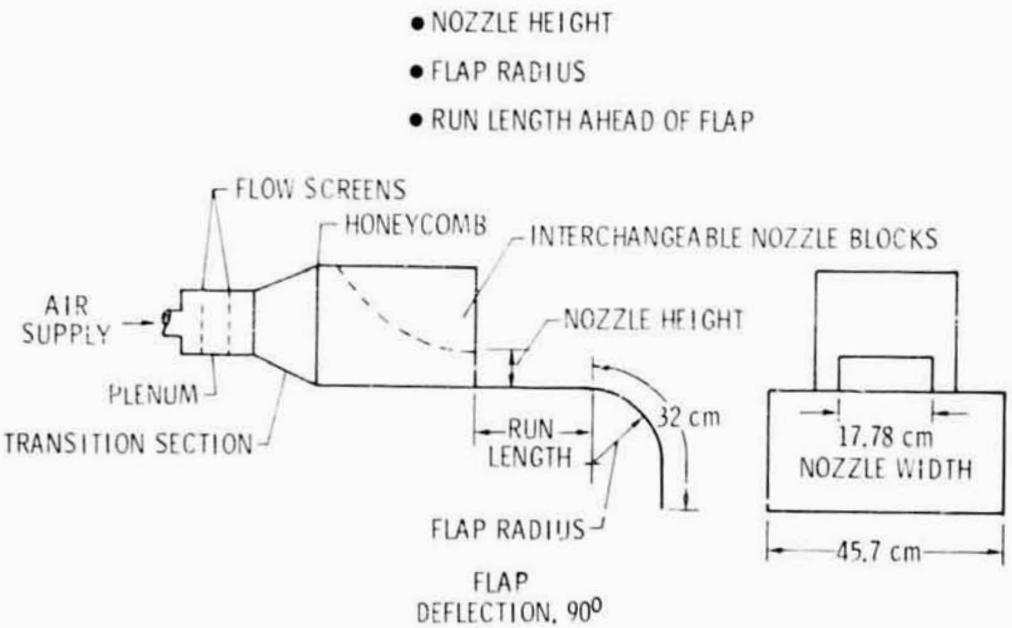

Figure 2.- Model configuration variables for parallel exit flow.

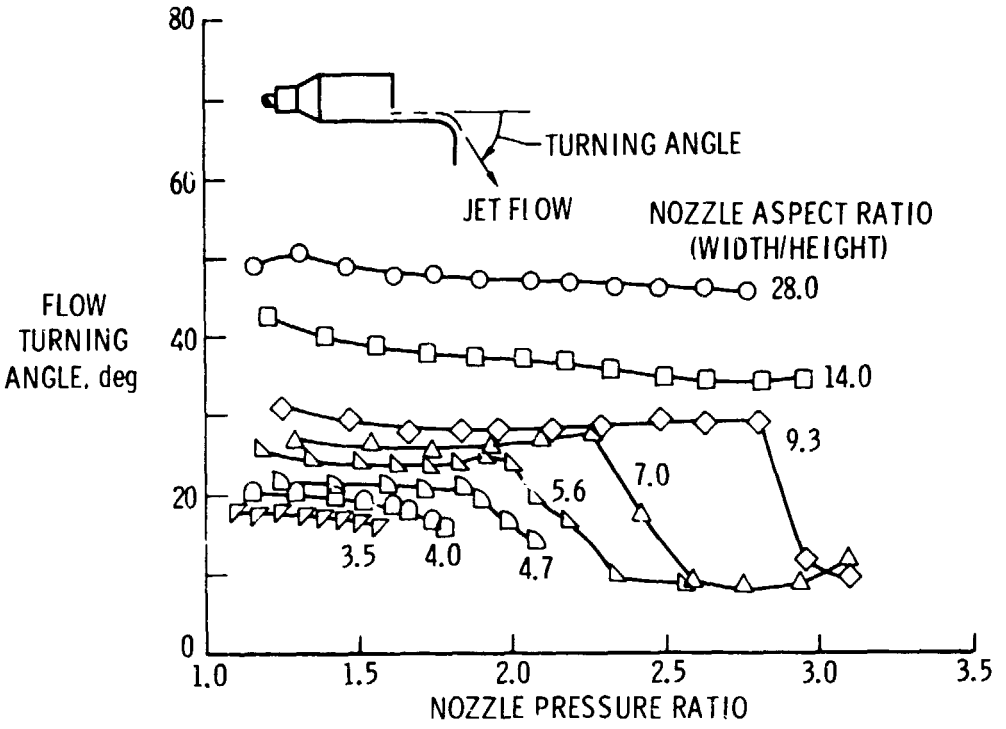

Figure 3.- Effect of pressure ratio on flow turning for various nozzle aspect ratios. Constant flap radius.

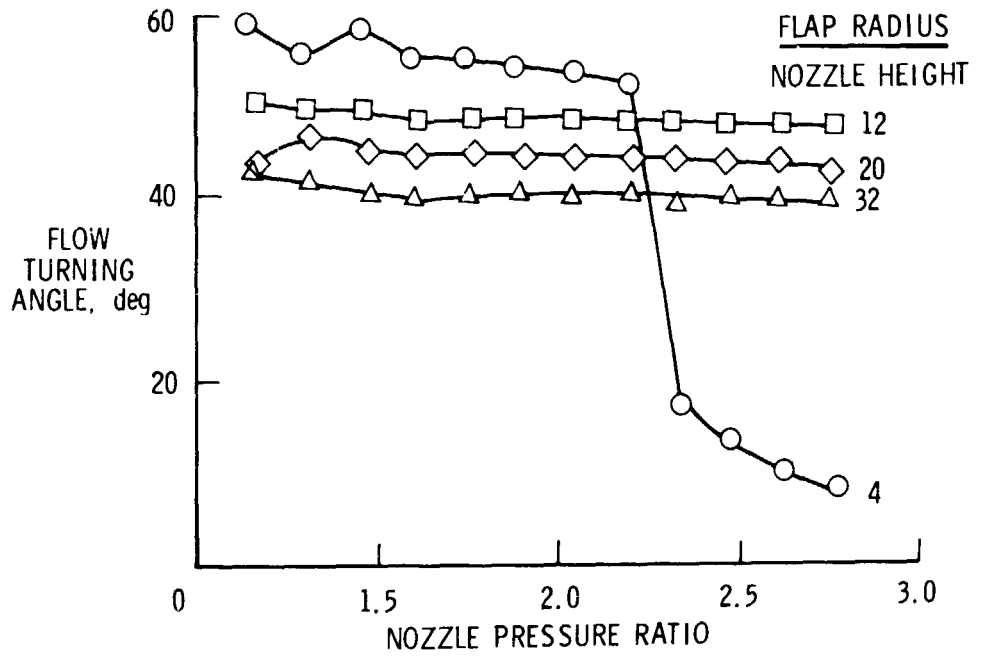

Figure 4.- Effect of pressure ratio on flow turning for a range of flap radius. Nozzle aspect ratio of 28.

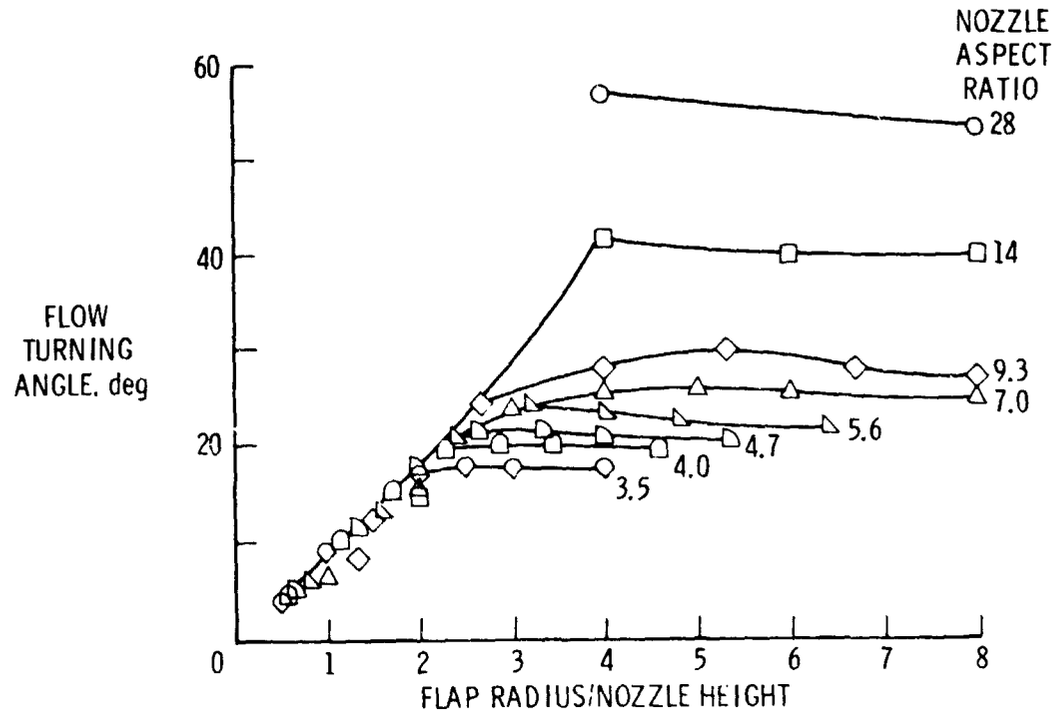

Figure 5.- Effect of flap radius on flow turning for a pressure ratio of 1.4 and a constant run length.

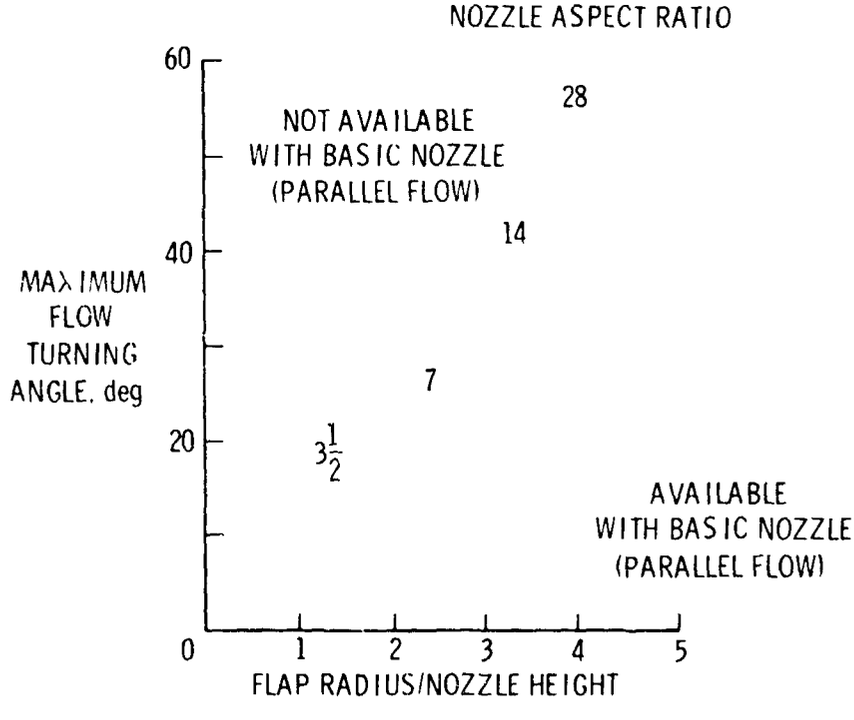

Figure 6.- Effect of flap radius on maximum flow turning for a range of pressure ratio and run length.

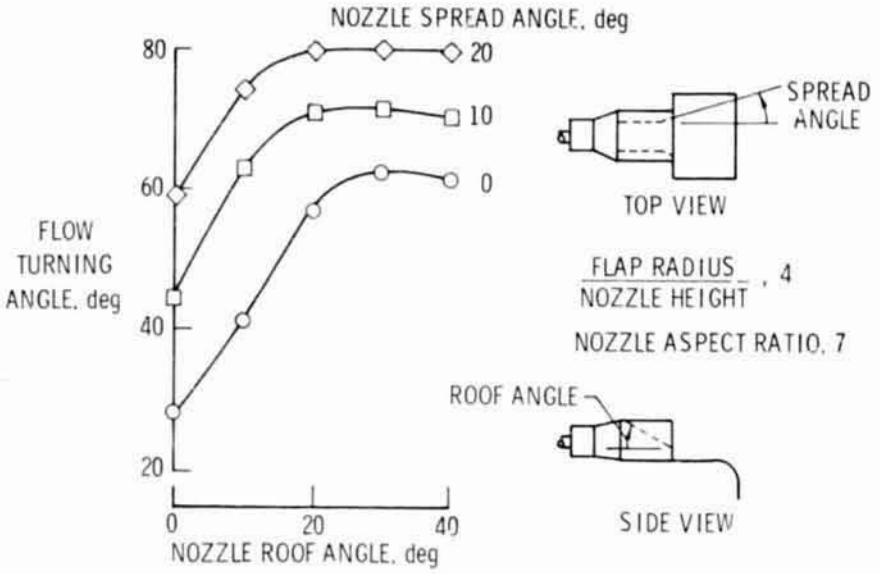

Figure 7.- Effects of nozzle roof angle and spread angle on flow turning.

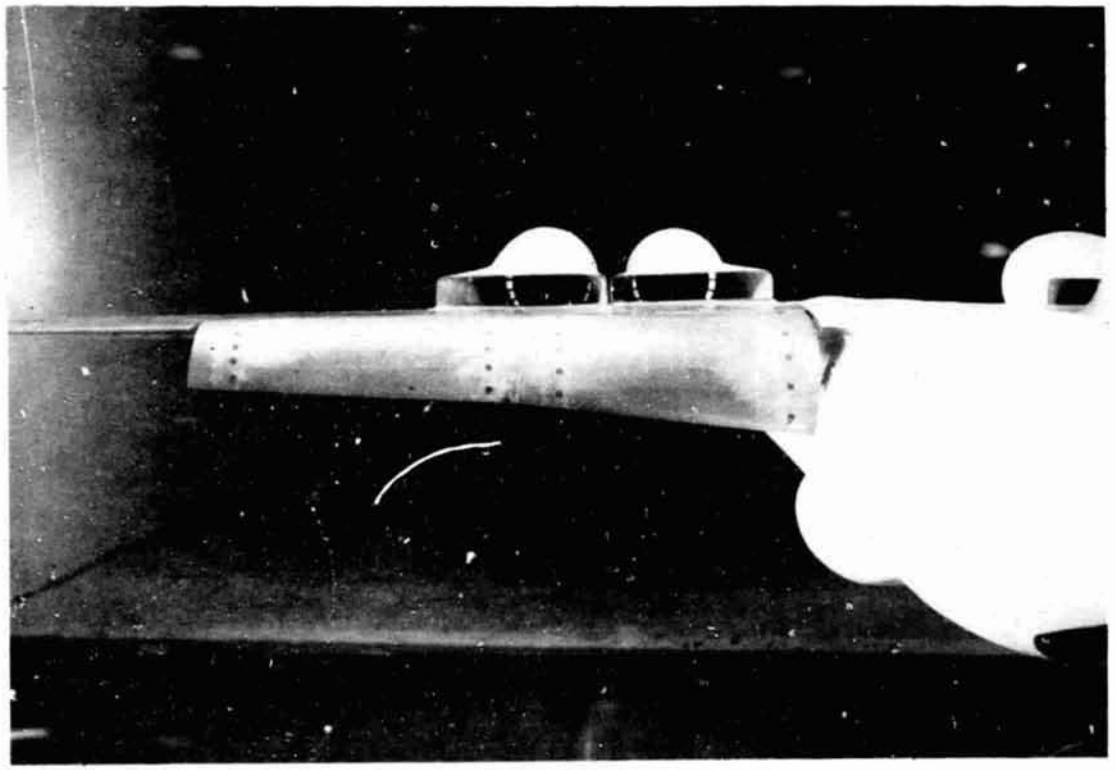

Figure 8.- Four-engine USB model with moderate-radius flaps in the Langley V/STOL tunnel.

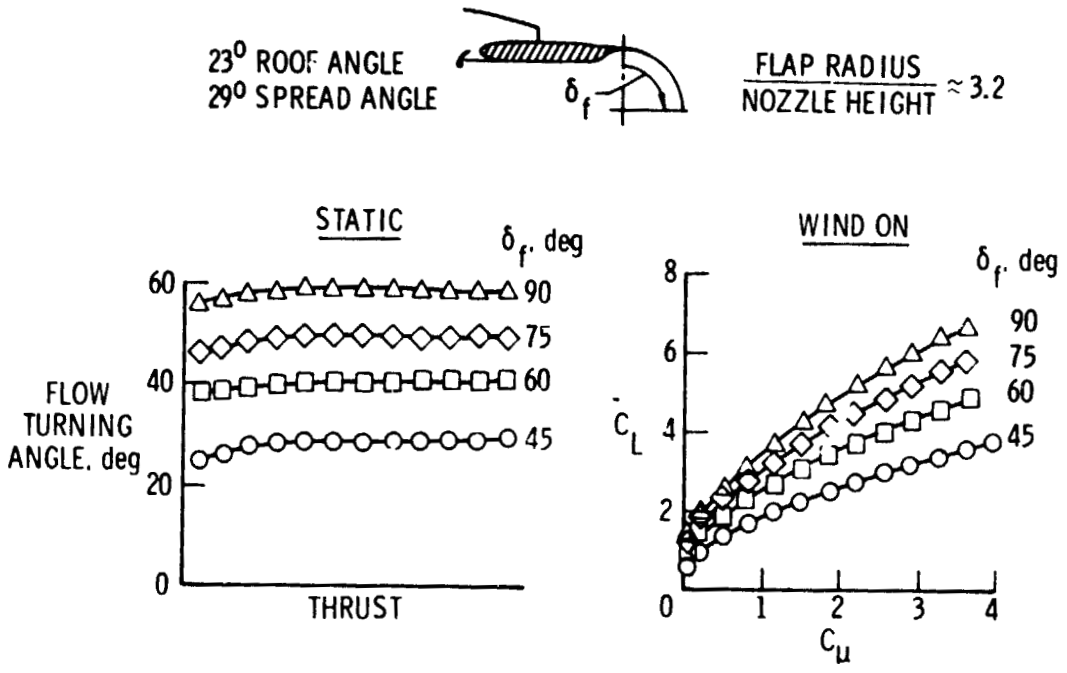

Figure 9.- Static turning and wind-on lift for moderate-radius flap. $\alpha = 0^\circ$.

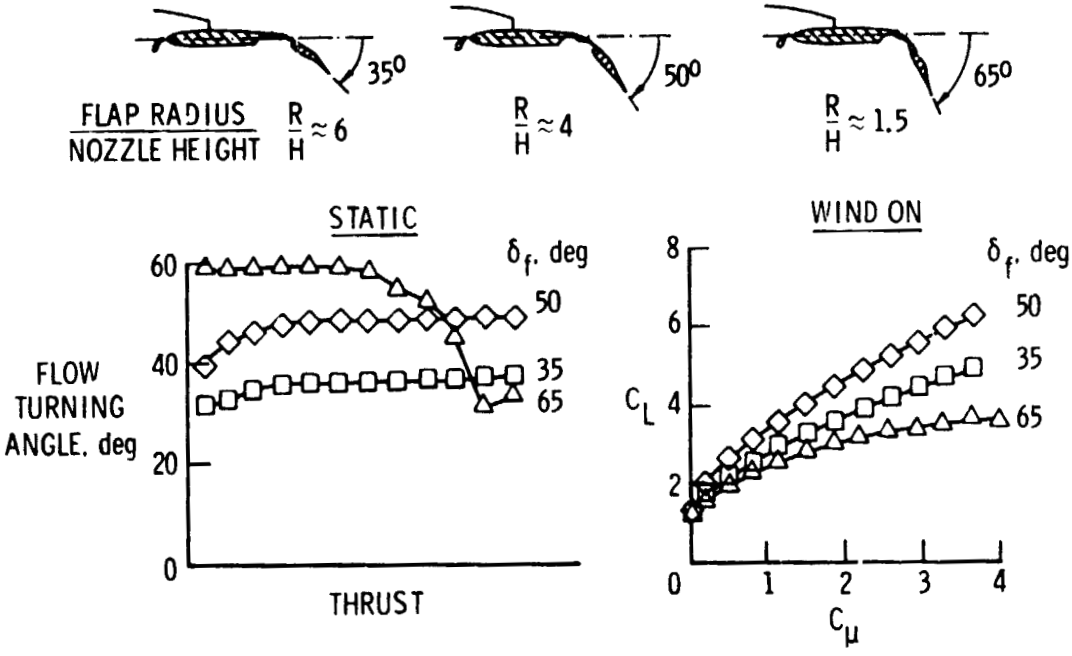

Figure 10.- Effect of flap radius and deflection on static turning and wind-on lift. $\alpha = 0^\circ$.

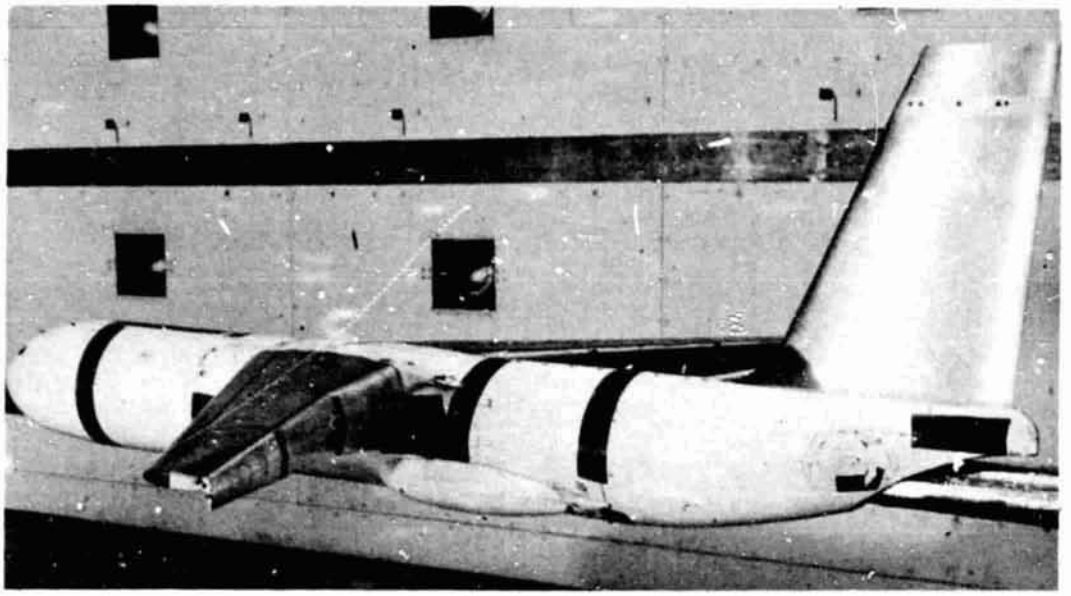

Figure 11.- Full-span leading-edge-blowing model with small-radius flaps in the Langley V/STOL tunnel.

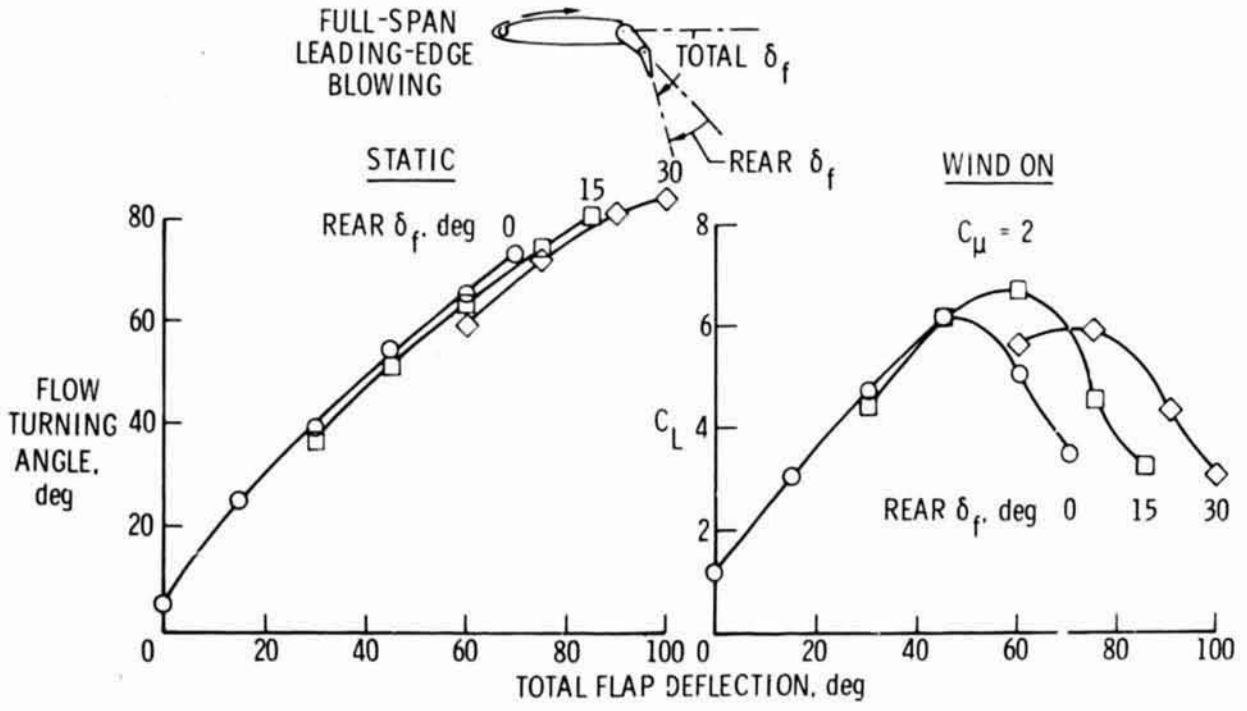

Figure 12.- Static turning and wind-on lift for small-radius flap. $\alpha = 0^\circ$.

N78-24049

RESULTS OF STATIC TESTS OF A 1/4-SCALE MODEL OF THE BOEING YC-14 POWERED-LIFT SYSTEM

James L. Hassell, Jr.
NASA Langley Research Center

3

SUMMARY

One-quarter-scale static ground tests of the Boeing YC-14 powered-lift system were conducted for correlation with full-scale test results. The 1/4-scale model utilized a JT-15D turbofan engine to represent the CF6-50D engine employed on the YC-14 advanced medium STOL transport prototype aircraft. The tests included evaluation of static turning performance, static surface pressure and temperature distributions, fluctuating loads, and accelerations of portions of the wing, flaps, and fuselage. Results are presented for the landing flap configuration over an appropriate range of fan pressure ratio as affected by several variables including ground height and vortex generator modifications. Static turning angles of the order of 60° were obtained. The highest surface pressures and temperatures were concentrated over the upper surface of the flaps in the region immediately aft of the USB nozzle.

INTRODUCTION

Past NASA research on the upper-surface blowing (USB) concept has progressed from tests of small-scale powered models for evaluations of low-speed powered-lift performance, stability, and control (refs. 1 to 4) to tests of large-scale models powered by real turbofan engines for evaluations of the operational environment produced on the upper wing and flap surfaces by the concept (refs. 5 to 7). The data base provided by this research has provided a valuable foundation for further development of the USB concept. As a result of increased interest in USB and the performance potential indicated for such a system, the Boeing Company recently incorporated the USB concept in the YC-14 advanced medium STOL transport prototype. As indicated in figure 1, the YC-14 utilizes Coanda flaps in conjunction with USB nozzles to provide low-speed powered lift. It will be noted, however, that the airplane uses D-nozzles to provide efficient performance during low speed operations and at cruise. The D-nozzle, which has a semielliptical exit shape, represents a marked change in design from the high-aspect-ratio, rectangular nozzles previously studied by NASA in large-scale tests (refs. 5 and 6).

The development program for the YC-14 included full-scale static tests of the powered-lift system components shown in figure 2. These components included the CF6-50D engine, the USB nozzle, a stub wing, the USB flaps, and

PAGE INTENTIONALLY BLANK

an adjacent boiler plate section of the fuselage. Some of the results of these full-scale tests at Boeing's Tulalip test facility are presented in reference 8.

Boeing's full-scale static test of the YC-14 powered-lift system provided the impetus for reduced-scale tests at Langley using a small turbofan engine — the primary objective being to evaluate scaling relationships for the various technologies involved. Other objectives were to conduct exploratory powered-lift research with a cruise-configured nozzle and to evaluate a broader range of variables than practical at Tulalip because of the constraints in time and cost.

Evaluation of the scaling relationships will be accomplished later; the present paper is limited to a discussion of some of the 1/4-scale test results.

SYMBOLS

$A_{primary}$ — geometric area of primary (hot flow) nozzle at mixing plane, cm^2 (in^2)

$A_{secondary}$ — geometric area of secondary (fan flow) duct at mixing plane, cm^2 (in^2)

F_A — axial force, N (lbf)

F_N — normal force, N (lbf)

h/b — ratio of height of wing upper surface at USB nozzle exit to wing span

$\frac{\Delta p}{p_{amb}}$ — surface static pressure ratio, $\frac{\text{Incremental local surface static pressure}}{\text{Ambient pressure}}$

T_{amb} — ambient temperature, ^{o}C (^{o}F)

$\frac{y}{b/2}$ — nondimensional spanwise location, $\frac{\text{Spanwise distance from airplane center line}}{\text{Airplane wing semispan}}$

$\frac{z}{b/2}$ — nondimensional normal location, $\frac{\text{Distance normal to local surface}}{\text{Airplane wing semispan}}$

δ_j — jet turning angle, $\tan^{-1}\frac{F_N}{F_A}$, deg

δ_{USB} tangency angle of the upper surface of the aft flap at the trailing edge measured with respect to wing chord plane, deg

η thrust recovery efficiency, $\frac{\sqrt{F_N^2 + F_A^2}}{\text{Thrust}}$

USB upper-surface blowing

DESCRIPTION OF MODEL

The Langley 1/4-scale model of the YC-14 powered-lift system and the static ground test apparatus is shown in figure 3. The model is powered by a JT-15D turbofan engine rated at 9786 N (2200 lbf) static thrust (as compared with 222.4 kN (50 000 lbf) thrust for the CF6-50D engine of the full-scale YC-14). The side door on the USB nozzle was tested only in the "door open" configuration corresponding to that used for powered-lift operation. This door has two functions: First, it provides the necessary nozzle area variation to obtain engine match conditions for both take-off and cruise, and second, in the open position for powered-lift operation, it helps spread the exhaust gas flow outboard over the Coanda flap span. Essentially all geometric details of the nozzle, wing, flaps, vortex generators, and fuselage are scaled from the YC-14. In this view the model is mounted at a scaled height above the ground corresponding to the full-scale test at Tulalip; the upper surface of the wing is 1.45 m (4.75 ft) above the surface, compared with 5.80 m (19 ft) for the full-scale configuration at Tulalip.

Figure 4 shows how the YC-14 USB nozzle was adapted to the JT-15D engine, which has a bypass ratio of 3.3 and a maximum fan pressure ratio of 1.4. (The CF6-50D engine has a bypass ratio of 4.4 and a maximum fan pressure ratio of 1.6.) These differences in engine characteristics forced a compromise in the 1/4-scale nozzle design; the primary and secondary areas at the mixing plane were adjusted to the values shown in figure 4 rather than being geometrically scaled. Basically, this design feature of the nozzle was compromised in order to match static pressures from the fan and core flows. All other geometric details of the YC-14 nozzle, such as the skewed plug primary, were retained in the 1/4-scale model. The purpose of the skewed plug primary is to direct the hot core flow to the top of the mixed flow nozzle and thereby minimize thermal problems on the wing and flaps.

Some of the characteristics of the JT-15D engine are compared with the CF6-50D engine in table 1. Aside from the very large difference in thrust, these two turbofan engines have somewhat similar characteristics. With both engines operating at a fan pressure ratio of 1.4, the fan and core velocities of the two engines correspond fairly well. This operating condition is about 66 percent maximum thrust for the CF6-50D engine. However, as a result of the

difference in bypass ratios, the exhaust flow in the 1/4-scale tests is composed of a larger proportion of core flow, resulting in the higher peak temperature at this operating condition. The temperature data of the 1/4-scale tests should therefore give conservative results as related to the YC-14 airplane.

A sketch of the 1/4-scale apparatus is presented in figure 5 to provide a description of the force measurement system. The entire model, including the bellmouth inlet, engine, nozzle, wing, flap, and fuselage, is supported on a floating frame which has strain gages forward and aft to measure normal force and a simple rod-rigged load cell to measure axial force. These measurements provide the magnitude and direction of the resultant force. The resultant force is the thrust recovered, and the direction of the resultant force is the jet turning angle δ_j. In order to determine thrust, the forward engine mounts are pivoted in pillow blocks which are instrumented with strain gages to measure engine axial force. The aft engine mount is supported by an adjustable link with rod end bearings at the top and bottom. The USB nozzle is mounted to the engine case but does not touch the wing, the fuselage, or any other part of the floating frame structure. A rubber seal isolates the face of the engine from the bellmouth inlet. The output of the engine axial-force strain gage was calibrated against measured thrust with the wing, flaps, and fuselage removed, and the calibration obtained was used to determine measured thrust during subsequent testing with the wing, flaps, and fuselage in place. Thrust recovery efficiency η is then defined as the ratio of the thrust recovered to the measured thrust.

Sensor locations for other types of data are shown in figure 6. Static pressure ports and thermocouples were distributed uniformly over the wings and flaps and also over appropriate areas of the fuselage. Surface microphones and accelerometers were also positioned on the wing, flaps, and fuselage, and are described in reference 9.

In addition, pressure and temperature rakes were installed in both the engine fan ducts and in the primary nozzle, and the bellmouth inlet was instrumented to measure inlet mass flow. This engine instrumentation provided for determination of ideal thrust and, when related to the measured thrust, permitted evaluation of the nozzle velocity coefficient.

The fluctuating loads and acceleration data are currently being analyzed and will not be presented. The data discussed will therefore be limited to static turning performance, surface pressures and temperatures, and flow surveys as affected by several of the more important variables for the landing flap configuration which has a trailing-edge upper-surface angle of 86.5°.

The test variables included a range of flap deflections, thrust corresponding to fan pressure ratios from 1.1 to 1.4, and heights above the ground corresponding to wheel contact height (5.80 m (19 ft) full scale), to an airborne height (9.14 m (30 ft) full scale), and to a free-air condition.

The effectiveness of vortex generators in aiding flow attachment is critical in this powered-lift concept where the designer has elected to avoid a high nozzle kickdown angle because of cruise performance considerations; the vortex generator configuration therefore was considered to be an important variable.

STATIC TURNING PERFORMANCE

Figure 7 shows the effect of vortex-generator deployment on static turning performance for the landing flap configuration. The data are presented in terms of the jet turning angle δ_j and the thrust recovery efficiency η as functions of fan pressure ratio. The pressure ratio range of interest for the YC-14 operating in the landing approach is between 1.25 and 1.4. The results presented were obtained for an h/b value of 0.147, the height corresponding to the YC-14 with wheels on the ground. For this particular comparison the gap between the nozzle and the wing was unsealed. The results indicate deployment of the basic vortex generators provides about 12° improvement in jet turning angle with a decrease in thrust recovery efficiency of about 5 to 6 percent. Also, values of jet turning angle tend to decrease with increasing fan pressure ratio. These results demonstrate the effectiveness of retractable vortex generators in providing improved jet turning angle without resorting to a high nozzle kickdown angle which might unduly compromise cruise efficiency. At this point it should be acknowledged that the full-scale static tests at Tulalip produced 5° to 6° better static turning angle with vortex generators retracted and about 8° better turning angle with vortex generators deployed. These discrepancies are possibly related to the juncture between the USB nozzle and the wing upper surface. On the full-scale YC-14 there is no juncture; the floor of the nozzle is formed by the upper surface of the wing.

Figure 8 shows the effect of height above the ground on static turning performance. For this comparison the basic vortex generators are in the up position, and the clearance gap between the edge of the USB nozzle and the upper surface of the wing has been sealed to better represent the full-scale YC-14 nozzle arrangement. Results are presented for two ground heights: h/b values of 0.147, corresponding to a wheel-on-the-ground condition, and 0.232, corresponding to a condition wherein the YC-14 wing is at a height of 9.14 m (30 ft) above the runway. The results indicate only about a 1° improvement in jet turning angle and a few percent better thrust recovery efficiency at the higher height. The infinite ground height condition is yet to be tested.

In order to assure an adequate level of powered-lift performance in the landing approach condition, further improvement in static turning performance to values approaching 60° was needed, especially at the higher fan pressure ratios. As shown in figure 9, two modifications to the basic vortex generators were made in an attempt to improve the turning. The first modification simply

doubled the span of the outside pair of vortex generators so that more of the jet efflux would be affected and thereby reenergize the boundary layer at the knee of the flap better than with the basic vortex generators. The second modification retained the same increased span and also increased the incidence angle 10° on the outside pair. The rationale for this second modification was to intensify the vortices produced by the outside pair of vortex generators so as to further energize the boundary layer and thereby promote better flow attachment toward the trailing edge of the flaps.

Figure 10 presents the static turning performance obtained with the two vortex generator modifications as compared with the basic vortex generators. Both modifications improved the jet turning angle, especially at the important higher fan pressure ratios. The second modification provided a significant 5° or 6° improvement in jet turning angle at a cost of about 4 percent in thrust recovery efficiency.

SURFACE PRESSURE AND TEMPERATURE DISTRIBUTIONS

Figure 11 provides a basis for understanding the flow characteristics on the upper surface of the wing and flaps. Surface pressure ratio contours are shown plotted on the upper surface of the wing and flaps in the region aft of the USB nozzle Negative values of pressure ratio indicate suction pressures and positive values indicate impact pressures. In addition to providing indications of good or poor flow attachment, this type of data is also valuable to the designer for the determination of steady-state static loads over portions of the wing and flaps. The case shown in figure 11 is for the landing flap configuration with the basic vortex generators deployed, for a value of h/b of 0.147 and for a fan pressure ratio of 1.36. Along the center line of the thrust axis, suction pressures occur almost to the trailing edge indicating excellent flow attachment, but regions of poor flow attachment are indicated both inboard adjacent to the fuselage and outboard toward the tip of the flap. A cross plot of the surface pressure ratios along the spanwise dashed line indicated on the aft flap in figure 11 provides a better indication of the degree of flow attachment.

Figure 12 presents the cross plot of aft flap pressures to show the effect of vortex generator modifications. Surface pressure ratio $\Delta p/p_{amb}$ is plotted against the nondimensional span parameter $\frac{y}{b/2}$ with negative values of pressure ratio upward. The locations of the center line and the side of the fuselage are indicated in the figure. The most dramatic improvement in flow attachment due to the vortex generator modifications occurs in the inboard area of the flaps adjacent to the fuselage. The jet turning angles for this pressure ratio of 1.4 (refer to fig. 10) are also indicated in figure 12 for the basic vortex generators and for each of the modifications. These pressure data therefore indicate that all the improvement in static turning angle resulted from the inboard vortex generator modification. The outboard modified vortex generator only penalized the thrust recovery efficiency.

Surface-temperature contours over the wing and flaps for the case with basic vortex generators deployed are presented in figure 13. The higher temperatures from the primary flow are concentrated near the center line, with peak values slightly above 204° C (400° F) on the flap system. Flap structures of suitable high-temperature-resistant alloys such as stainless steel should experience no problem in this environment. The surface temperatures in the region of wing structure present no problem, even for aluminum alloys. Although not presented in figure 13, temperatures on the side of the fuselage never exceeded 60° C (140° F).

FLOW SURVEYS

Various flow surveys were made to determine the extent of the jet efflux dispersion and to evaluate local flow conditions related to specific microphone locations. In order to obtain detailed velocity profiles of the flow adjacent to the wing and flap upper surfaces, a survey rake about 48.3 cm (19 in.) long having 25 total pressure probes and fewer static pressure and thermocouple probes was used. Discrete velocity measurements were obtained at each of the total pressure probe locations.

Figure 14 shows the results of some of the flow surveys for the case of vortex generators deployed at the highest fan pressure ratio. Velocity profiles near the center line are shown at the nozzle exit, at two locations on the flaps corresponding to microphone positions, and aft of the trailing edge of the flaps. The rake was positioned normal to the local surface for each location. The peak velocity at the nozzle exit was about 375 m/sec (1230 ft/sec) and decayed to about 251 m/sec (825 ft/sec) at the flap trailing edge. The profile begins to change appreciably on the forward flap and then shows considerable thickening over the aft flap element and at the trailing edge.

Figure 15 shows the results of rake surveys made over the span of the nozzle exit and the flap trailing edge with modified vortex generators deployed (modification 2). The data were also obtained at the highest value of fan pressure ratio of 1.4. In these plots the velocity data are presented in terms of constant velocity contours measured in the two planes indicated — at the nozzle exit and at the flap trailing edge. The plots are oriented to relate the spanwise extent of the USB nozzle to the flap span. The data show that the higher velocity flow from the primary nozzle is concentrated in the upper center of the USB nozzle, with some indication of spreading of the lower velocity fan flow beyond the projection of the nozzle due to the "door open" geometry. Much of the flow pattern at the nozzle exit is apparent at the flap trailing edge, and it should be noted that the higher velocity flow is still concentrated along a projection of the nozzle center line. The flow was thickened 3 to 4 times the nozzle depth but has spread very well across the flap span. Of particular interest is the further indication of good flow attachment at the flap trailing edge near the side of the fuselage which was brought about by the modified vortex generators.

CONCLUDING REMARKS

Preliminary results of static tests of the 1/4-scale Boeing YC-14 USB model indicate that the static turning performance of the landing flap configuration was improved appreciably by the use of the basic vortex generator design. Regions of poor flow attachment were noted near the trailing edge of the flap both inboard adjacent to the fuselage and outboard toward the tip. Improved flow attachment was obtained by tailoring the vortex generators which resulted in further improvement in static turning performance. Peak values of surface static pressures and temperatures were concentrated over the upper surface of the flaps along the center line of the thrust axis. These results together with results dealing with fluctuating loads, currently under analysis, will be correlated with full-scale YC-14 static data with an eventual objective of establishing appropriate scaling laws for the various technologies involved.

REFERENCES

1. Phelps, Arthur E.; Letko, William; and Henderson, Robert L.: Low-Speed Wind-Tunnel Investigation of a Semispan STOL Jet Transport Wing-Body With an Upper-Surface Blown Jet Flap. NASA TN D-7183, 1973.

2. Phelps, Arthur E., III; and Smith, Charles C., Jr.: Wind-Tunnel Investigation of an Upper Surface Blown Jet-Flap Powered-Lift Configuration. NASA TN D-7399, 1973.

3. Sleeman, William C., Jr.; and Hohlweg, William C.: Low-Speed Wind-Tunnel Investigation of a Four-Engine Upper Surface Blown Model Having a Swept Wing and Rectangular and D-Shaped Exhaust Nozzles. NASA TN D-8061, 1975.

4. Phelps, Arthur E., III: Wind-Tunnel Investigation of a Twin-Engine Straight-Wing Upper Surface Blown Jet-Flap Configuration. NASA TN D-7778, 1975.

5. Staff of the Langley Research Center: Wind-Tunnel Investigation of the Aerodynamic Performance, Steady and Vibratory Loads, Surface Temperatures and Acoustic Characteristics of a Large-Scale Twin-Engine Upper-Surface Blown Jet-Flap Configuration. NASA TM X-72794, 1975.

6. Shivers, James P.; and Smith, Charles C., Jr.: Static Tests of a Simulated Upper Surface Blown Jet-Flap Configuration Utilizing a Full-Size Turbofan Engine. NASA TN D-7816, 1975.

7. Carros, Robert J.; Boissevain, Alfred G.; and Aoyagi, Kiyoshi: Aerodynamic Characteristics of a Large-Scale Hybrid Upper Surface Blown Flap Model Having Four Engines. NASA TM X-62460, 1975.

8. Sussman, M. B.; Harkonen, D. L.; and Reed, J. B.: USB Environment Measurements Based on Full-Scale Static Engine Ground Tests. Powered-Lift Aerodynamics and Acoustics, NASA SP-406, 1976. (Paper no. 30 of this compilation.)

9. Schoenster, James A.; Willis, Conrad M.; Schroeder, James C.; and Mixson, John S.: Acoustic-Loads Research for Powered-Lift Configurations. Powered-Lift Aerodynamics and Acoustics, NASA SP-406, 1976. (Paper no. 26 of this compilation.)

Table 1.- Comparison of Engine Characteristics

	CF6-50D	JT-15D
Rated thrust, kN (lbf)	222.4 (50 000)	9.79 (2200)
Bypass ratio	4.4	3.3
Fan pressure ratio	1.6	1.4
Fan velocity, m/sec (ft/sec)	[a]255 (836)	255 (836)
Core velocity, m/sec (ft/sec)	[a]347 (1140)	375 (1230)
Peak exhaust gas temperature, K (^{o}R)	[a]700 (1260)	872 (1570)

[a]Values at 66 percent maximum thrust, corresponding to a fan pressure ratio of 1.4.

Figure 1.- Boeing YC-14 advanced medium STOL transport.

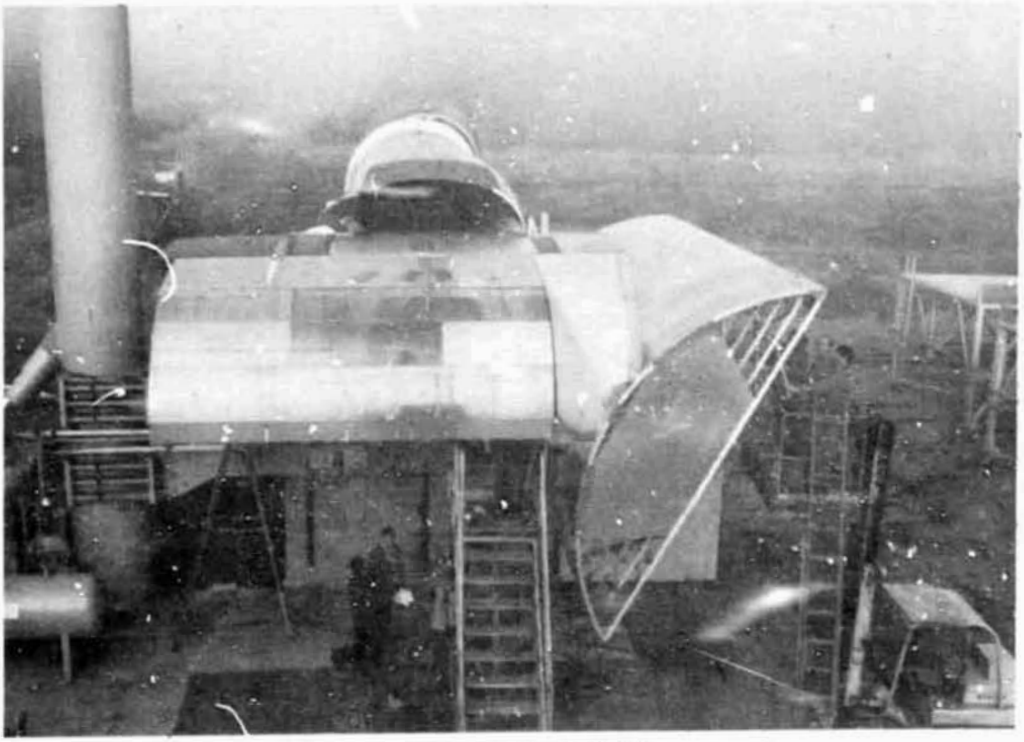

Figure 2.- Boeing's YC-14 Tulalip ground test.

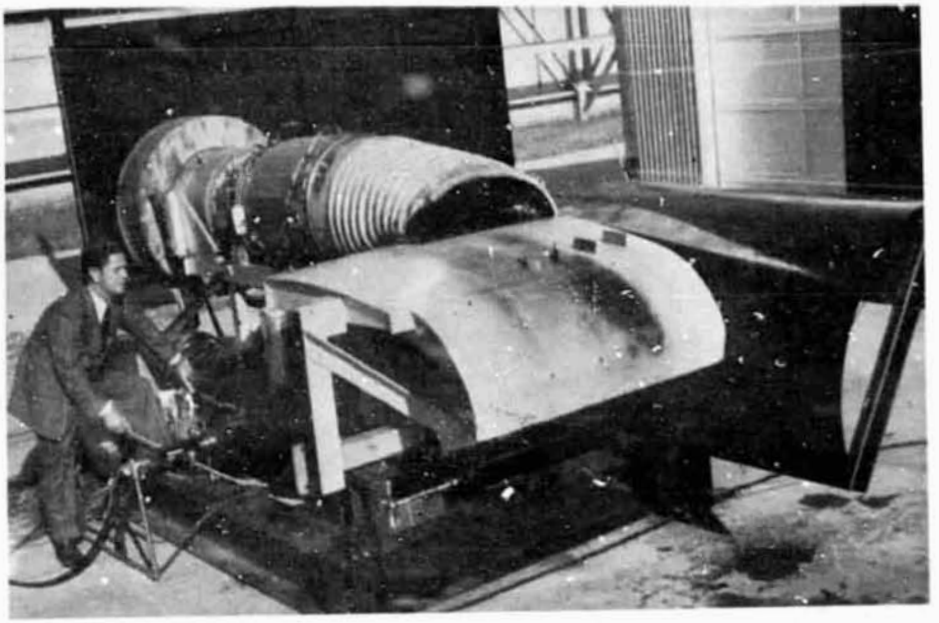

Figure 3.- 1/4-scale YC-14 ground test apparatus.

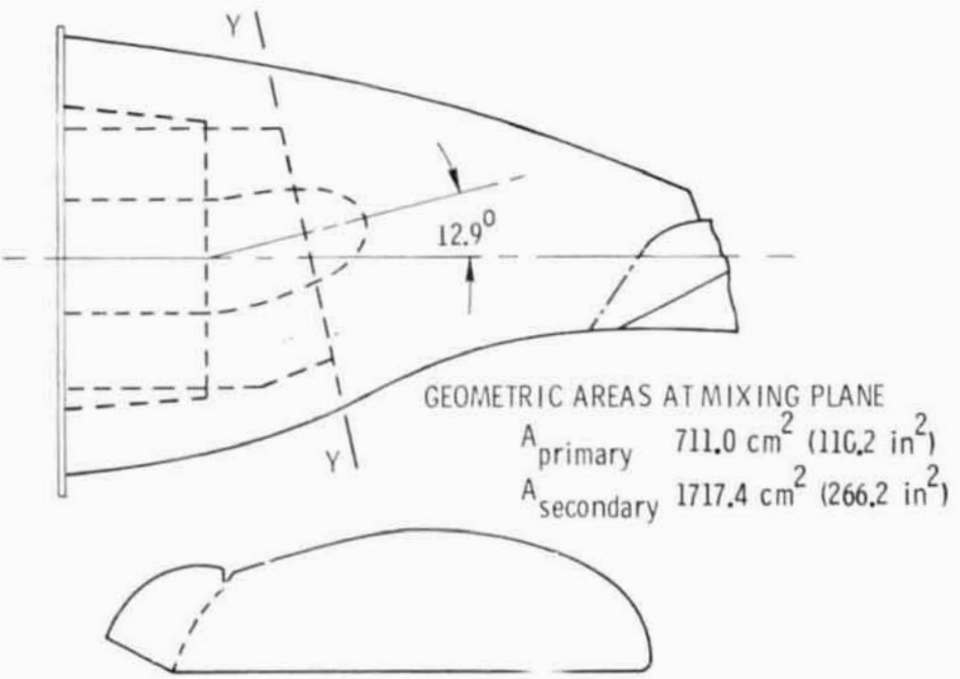

Figure 4.- YC-14 USB nozzle matched with JT-15D turbofan engine. Bypass ratio of 3.3; fan pressure ratio of 1.4.

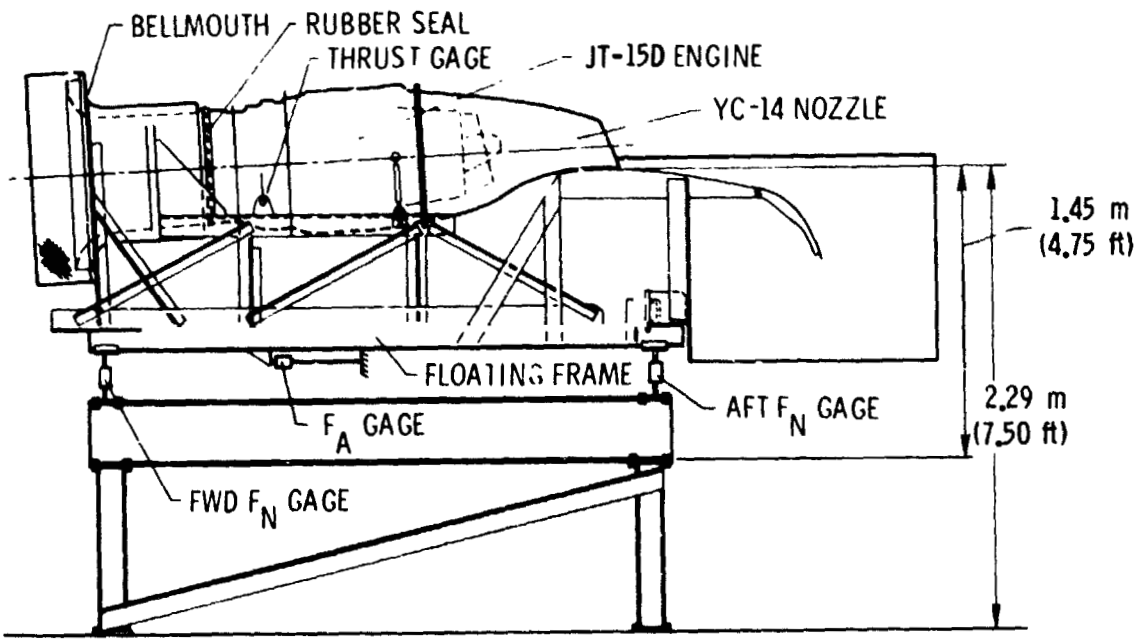

Figure 5.- Force measurement system for 1/4-scale ground tests.

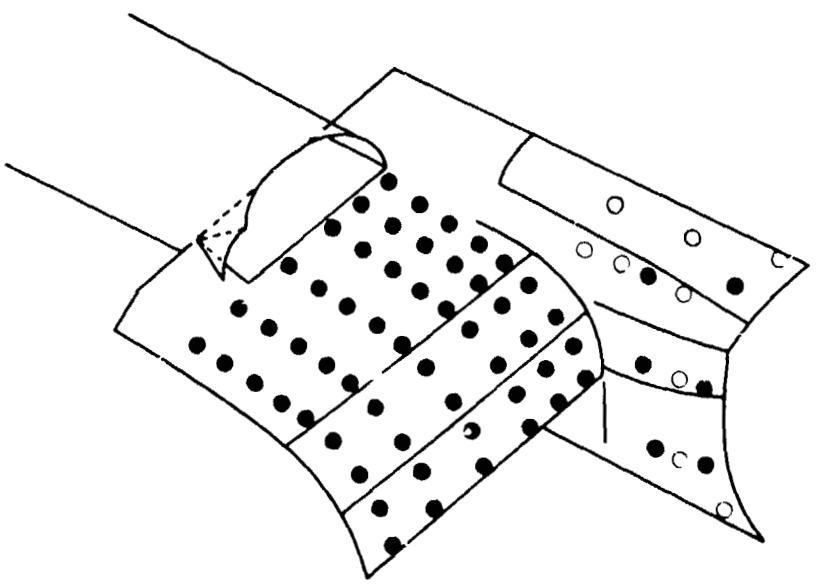

○ STATIC PRESSURE PORTS ONLY
● STATIC PRESSURE PORTS AND THERMOCOUPLES

Figure 6.- Sensor locations on wing, flaps, and fuselage.

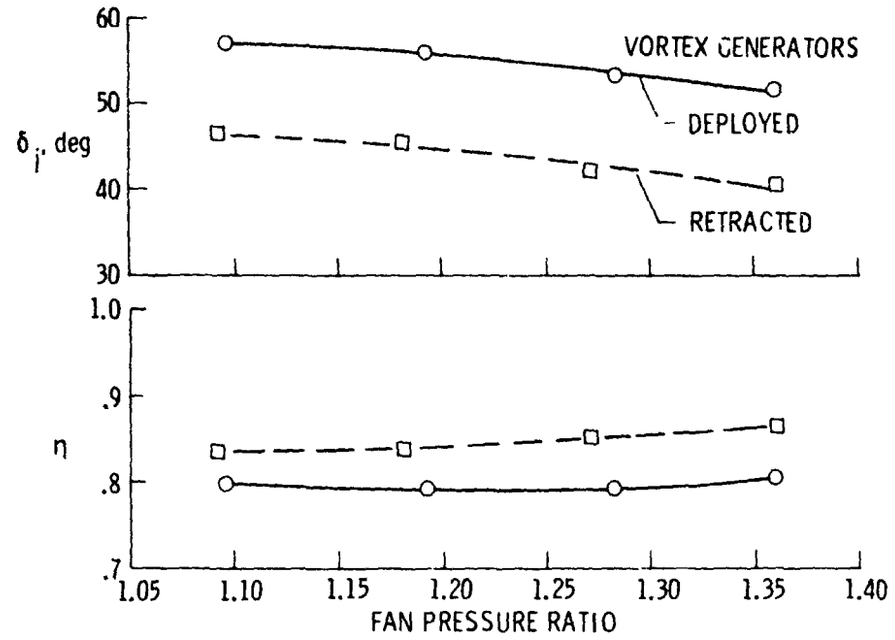

Figure 7.- Effect of basic vortex generators on static turning performance. h/b = 0.147; nozzle-wing gap unsealed.

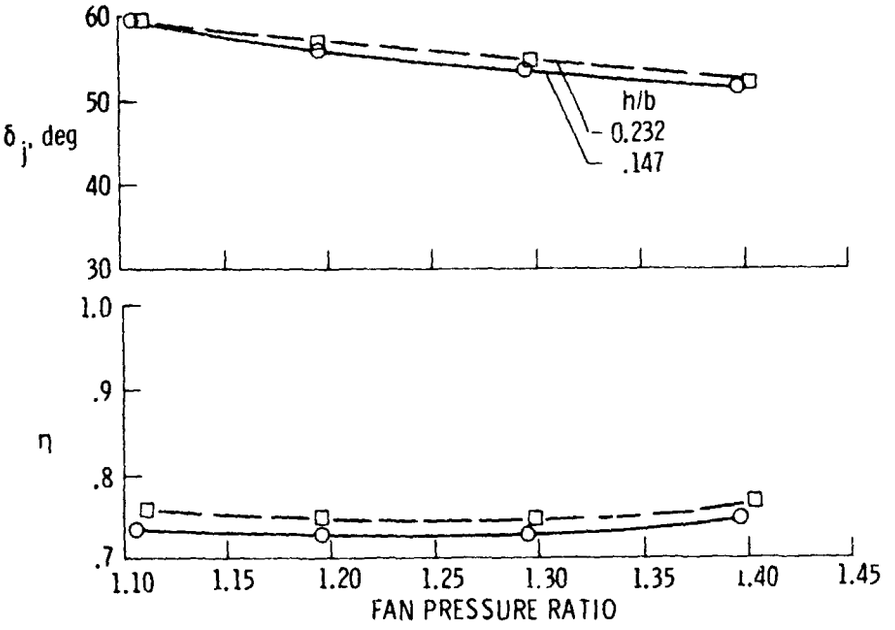

Figure 8.- Effect of height above ground on static turning performance. Basic vortex generators up.

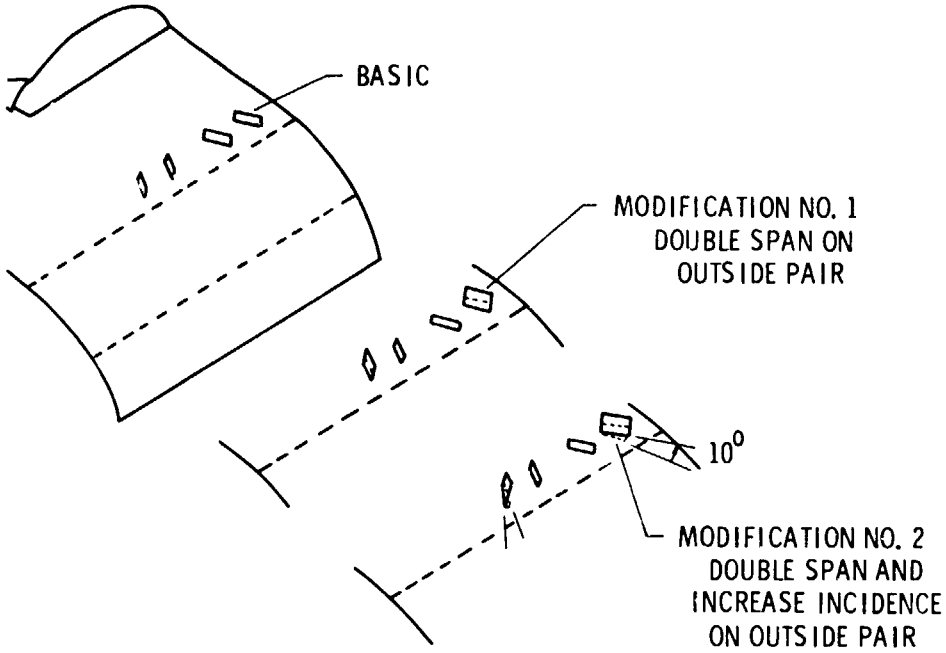

Figure 9.- Vortex generator modifications.

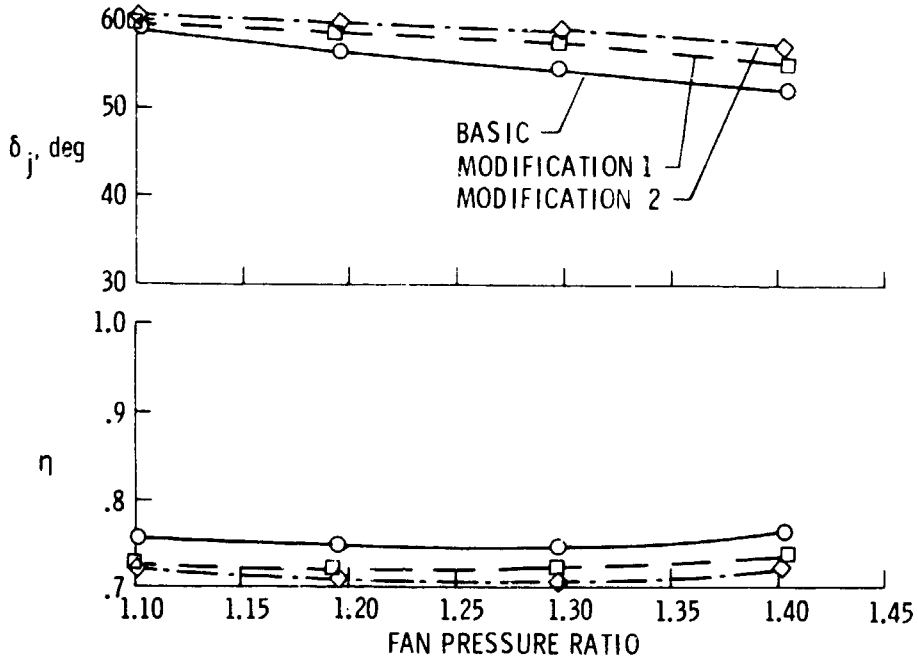

Figure 10.- Effect of vortex generator modifications on static turning performance.

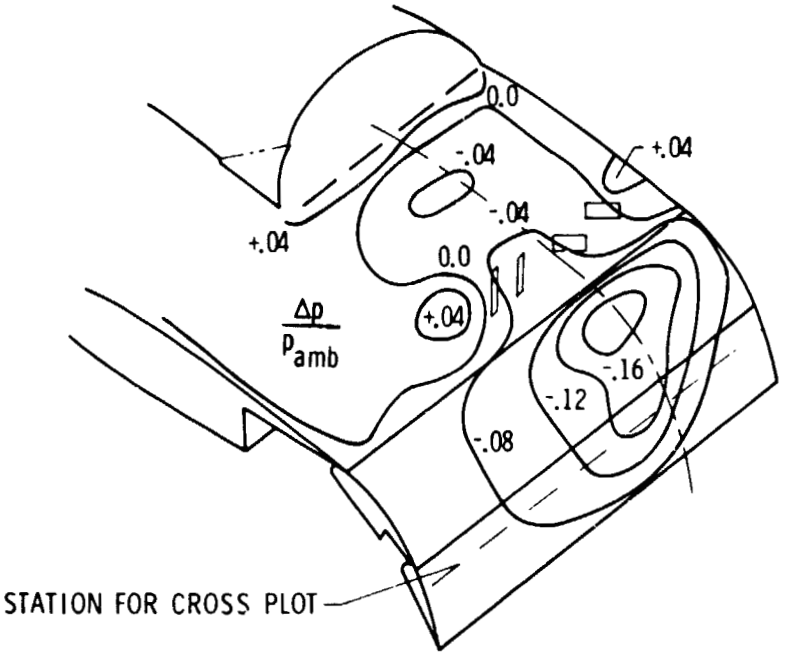

Figure 11.- Surface pressure ratio contours with basic vortex generators up. $\delta_{USB} = 86.5^{o}$; h/b = 0.147; fan pressure ratio of 1.36.

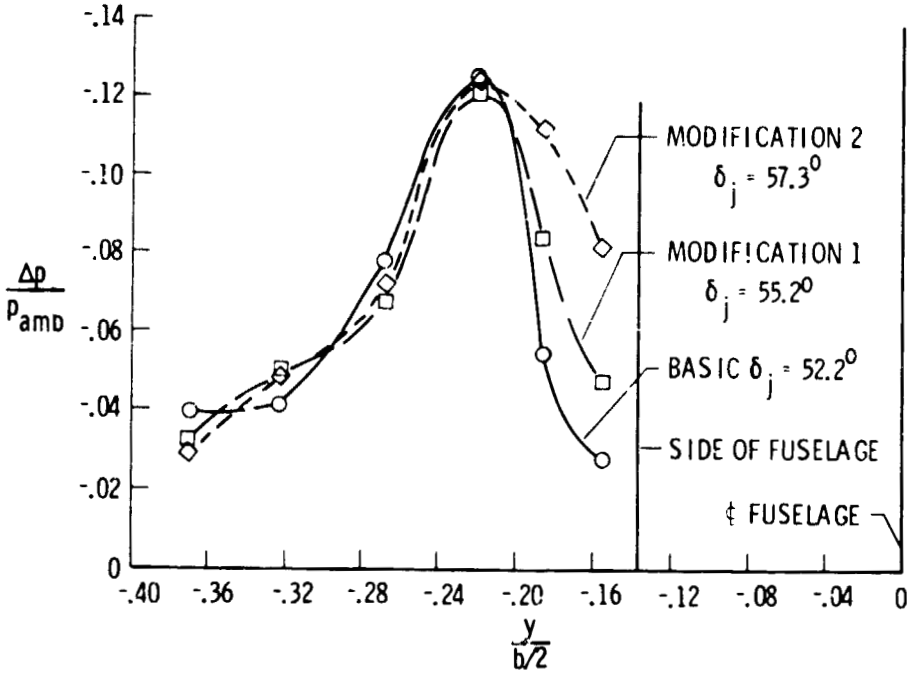

Figure 12.- Effect of vortex generator modifications.

°F	°C
100	38
200	93
250	121
300	149
350	177
400	204
420	216

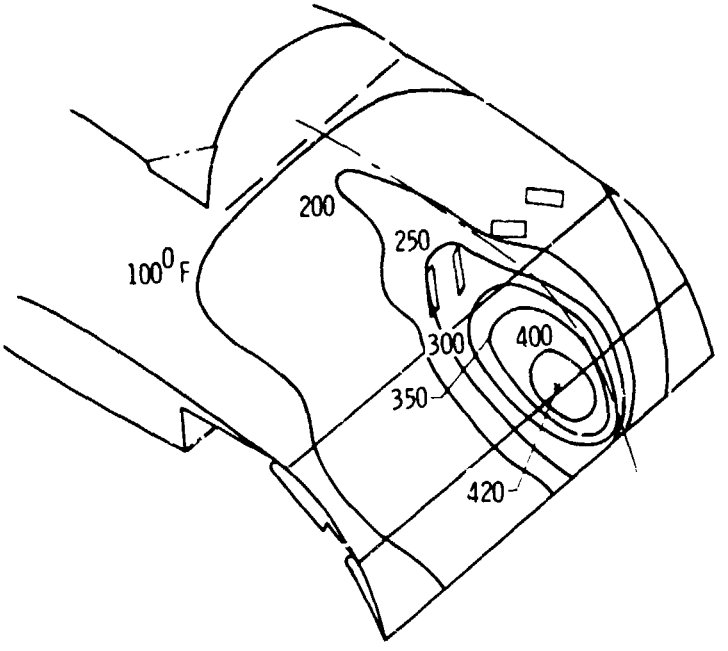

Figure 13.- Surface temperature contours with basic vortex generators up. δ_{USB} = 86.5°; h/b = 0.147; T_{amb} = 11° C (52° F); fan pressure ratio of 1.36.

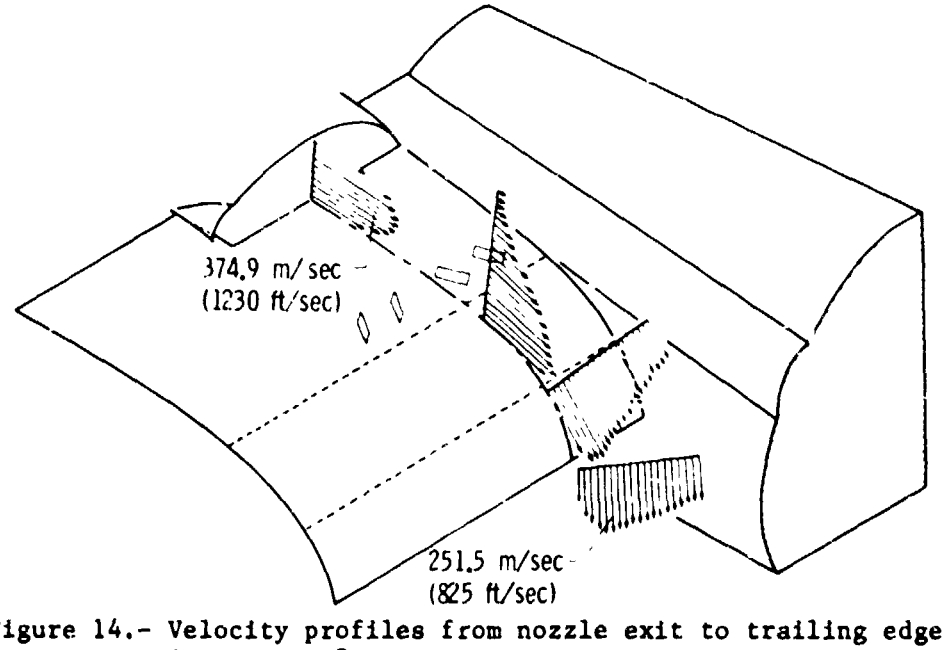

Figure 14.- Velocity profiles from nozzle exit to trailing edge. δ_{USB} = 86.5°; basic vortex generators up.

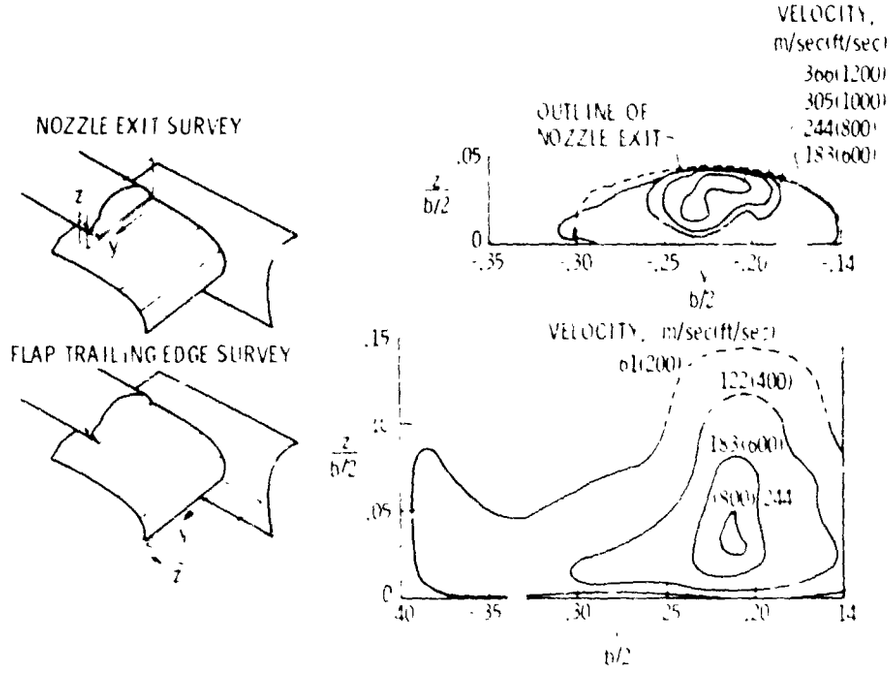

Figure 15.- Velocity contours at nozzle exit and flap trailing edge with modified vortex generators (modification 2). Fan pressure ratio of 1.4.

N78-24050

SUMMARY OF LOW-SPEED AERODYNAMIC CHARACTERISTICS OF UPPER-SURFACE-BLOWN JET-FLAP CONFIGURATIONS

Arthur E. Phelps III
Langley Directorate, U.S. Army Air Mobility R&D Laboratory

Joseph L. Johnson, Jr., and Richard J. Margason
NASA Langley Research Center

4

SUMMARY

The results of recent wind-tunnel investigations to provide fundamental information on the upper-surface-blown (USB) jet-flap concept demonstrated that the USB concept provides good high-lift performance. The low-speed performance appears to be mainly dependent upon the jet turning angle and turning efficiency and on the use of proper leading- and trailing-edge treatment to prevent premature flow separation. The best means of achieving good turning performance in any particular USB application must be determined from overall operational considerations in which high-speed performance, structures and noise, as well as low-speed performance, are evaluated. The large diving moments generated at high lift coefficients can be trimmed satisfactorily with a large, conventional horizontal tail; a high tail position is best from longitudinal stability considerations. Large rolling and yawing moments are introduced with the loss of an engine, but these moments can be trimmed satisfactorily through the use of asymmetrical boundary-layer control and through the use of spoiler and rudder deflection as needed.

INTRODUCTION

In recent years, considerable effort has been directed toward studies of the aerodynamic and acoustic characteristics of upper-surface-blown (USB) jet-flap configurations (refs. 1 to 7). The results of past aerodynamic investigations have indicated that the USB concept can provide the high lift necessary for efficient STOL operation; acoustic studies have indicated that the USB concept may provide beneficial noise reduction during flyovers because the wing shields ground observers from the noise produced at the engine exhaust nozzle. More recent studies have provided solutions to stability and control problems such as pitch trim, longitudinal stability at high lift, and lateral trim for engine-out conditions.

The present paper has been prepared to summarize some of the more important characteristics of USB configurations in the areas of performance, longitudinal stability and trim, lateral-directional stability, engine-out lateral trim, and dynamic stability and control. Although the discussion is directed toward USB configurations, certain problems such as pitch trim and longitudinal stability are common to all powered-lift STOL systems; the problem of engine-out lateral trim is common to other powered-lift concepts utilizing discrete blowing, such as the externally blown flap (EBF) arrangement. Therefore, the data presented

in the present paper for USB configurations may also be generally applicable to other powered-lift concepts.

SYMBOLS

A	aspect ratio
b	wing span
C_L	lift coefficient
C_{L_Γ}	power-induced lift coefficient
$C_{L,max}$	maximum lift coefficient
C_l	rolling-moment coefficient
C_{l_β}	effective dihedral parameter, $\partial C_l/\partial\beta$
C_m	pitching-moment coefficient
C_{m_α}	longitudinal stability parameter, $\partial C_m/\partial\alpha$
C_n	yawing-moment coefficient
C_{n_β}	directional stability parameter, $\partial C_n/\partial\beta$
C_μ	gross thrust coefficient, T/qS
$\bar{c}$	wing mean aerodynamic chord
F_A	axial force
F_N	normal force
l_t	tail length
T	thrust
$T_{1/2}$	time to damp to half-amplitude
W	weight
y,z	body axes coordinates
α	angle of attack
γ	flight path angle
δ_f	flap deflection

δ_j jet deflection

ϵ downwash angle

ω_d Dutch-roll damped frequency parameter

Abbreviations:

BLC boundary-layer control

EBF externally blown flap

USB upper-surface blown

V.G. vortex generator

PERFORMANCE

In a previous paper by William C. Sleeman and Arthur E. Phelps (ref. 8), it was shown that good static turning could be achieved with the USB concept. Figure 1 summarizes the static turning performance of a number of different USB configurations in terms of the ratio of normal force to thrust plotted against the ratio of axial force to thrust. The shaded band in figure 1 indicates representative values of static turning performance obtained with the USB concept and shows that efficiencies from about 80 to 90 percent can be obtained with high flap settings. For lower flap settings, efficiencies are generally much higher (95 percent or greater for flap angles below about 40°) and turning angles are within a few degrees of the upper surface tangency angle.

It has been determined from previous experience that a USB configuration with marginal static turning performance caused by regions of separated or partially separated flow will almost certainly exhibit poor lift performance in forward flight. Good static turning characteristics, on the other hand, have been shown to be a reliable indicator of good lift performance in forward flight. Figure 2 illustrates the effect of forward speed on the static pressure distribution and surface temperatures of a large-scale USB model with turbofan engines (ref. 3). Static turning tests of the configuration indicated good static performance. As shown in figure 2, forward speed had little effect on the magnitudes of the static pressures and surface temperatures along the engine centerline. Forward speed caused only slightly higher suction pressures and slightly cooler temperatures over the flap. Based on these results, it appears that structural and thermal design information may be determined for USB wing-flap systems on the basis of static tests which might be conducted with outdoor static rigs utilizing full-scale engines, nacelles, and wing-flap hardware.

Although tests have shown that the two major externally blown powered-lift concepts (EBF and USB) are generally comparable in overall performance, there are some fundamental differences in the exhaust jet flow fields between the two concepts at forward speed conditions. For example, in the EBF system the jet impinges on the lower surface of the flap and spreads spanwise, covering most

of the flap span. In the USB system, however, a different, more localized flow behavior occurs as indicated in figure 3. The sides, or edges, of the jet sheet produced by the engine exhaust roll up into vortices which enlarge and tend to thicken the jet as it turns over the trailing-edge flap. A number of factors influence the formation of these vortices, but the ratio of jet velocity to free-stream velocity and the thickness of the jet produced by the engine exhaust seem to be the most powerful. In addition to the vortex rollup of the jet sheet, there may be additional vortices produced by the external shape of the USB nozzle. This is especially true for a sharp-cornered rectangular nozzle; the nozzle vortices can be minimized by using a well-rounded or D-shaped nozzle. The overall effect of this vortex formation is to confine the jet influence to a highly localized region near the jet. In fact, the jet may actually entrain free-stream air in such a way as to cause spanwise flow inboard, rather than outboard. The significance of this flow characteristic will be discussed in subsequent sections of this paper.

Figure 4 presents high-lift data for a two-engine straight-wing USB configuration (ref. 4) over a range of Reynolds number and for power-off and power-on cases. The data show the anticipated large influence of Reynolds number on lift for the power-off case, but for the power-on case $(C_\mu = 3)$, the data show very little effect of free-stream Reynolds number. These results have also been observed in other investigations, indicating that for moderate to high thrust coefficients, the lift characteristics of the complete configuration are predominantly influenced by the exhaust jet rather than the free-stream flow; this factor may be related to the high level of turbulence of the jet as it impinges on the wing. From these results, it appears that small-model data may be used with confidence in the design of propulsive-lift systems.

Shown in figure 5 are data illustrating the effect of a leading-edge Krueger flap on the lift characteristics of a USB model with a high jet turning angle $(\delta_f = 60^o)$. The trailing-edge jet turning angle generates a strong upwash field ahead of the wing, and the need for leading-edge devices for adequate protection against leading-edge stall is clearly demonstrated by the data. As can be seen, a marked increase in maximum lift coefficient and in stall angle of attack resulted from the installation of a leading-edge Krueger flap.

One interesting point noted in tests of USB configurations is that close attention must be given to leading-edge stall in the vicinity of the nacelle. The very powerful upwash at the wing leading edge can pose serious problems when the nacelle is close to the fuselage or another nacelle (as in a four-engine arrangement). Figure 6 illustrates this problem for a two-engine straight-wing configuration and a four-engine swept-wing configuration. Both configurations were large-scale wind-tunnel models powered by JT15D-1 turbofan engines to provide a more realistic operational environment than that produced by small, cold jets. During tests of the two-engine straight-wing model (ref. 3), a very strong upwash field was observed between the nacelle and fuselage during power-on conditions. Without leading-edge treatment in this region (which was only about 2 percent of the wing span) the wing inboard of the jet and the entire top surface of the fuselage between the nacelles was badly stalled. Recontouring the lower surface of the nacelle to provide smoother flow transition and adding a leading-edge Krueger flap with blowing BLC between the nacelle and

fuselage resulted in a significant improvement in the flow quality over the fuselage. The left side of figure 6 shows the lift improvements resulting from the modifications to the original wing.

A similar problem was encountered in tests of the large four-engine swept-wing configuration of reference 9 which exhibited severe separation along the leading edge between the fuselage and inboard nacelle and between the inboard and the outboard nacelles. In this case, unsweeping the leading edges, recontouring the lower surface of the nacelles, and adding blown leading-edge Krueger flaps resulted in the improvements shown on the right side of figure 6. These data indicate a significant increase in both $C_{L,max}$ and stall angle of attack for the modified model.

The effects of partial- and full-span flaps on the lift characteristics of a two-engine USB configuration are presented in figure 7. The data show that a large increase in lift coefficient is obtained by extending the trailing-edge flap to full span. In order to determine the proportion of this lift increment due to power effects, the data were analyzed in terms of power-induced circulation lift coefficient C_{L_Γ} as a function of thrust coefficient, and the results are presented in figure 8. The data of figure 8 show that the benefit of power-induced circulation lift on the lift of a USB configuration with full-span flaps is minimal. Also presented in figure 8 are data for an internally blown jet flap in which the exhaust flow is distributed uniformly along the entire wing span (ref. 10). Generally speaking, the localized-flow USB configuration produces about 65 to 70 percent of the power-induced circulation lift available from an internally blown system.

Presented in figure 9 is a plot of the spanwise distribution of normal-force coefficient for the same model used to obtain the lift data of figure 8. The data of figure 9 are presented for power-off, power-on, and engine-out conditions at zero angle of attack. These data indicate that the influence of the exhaust jet on the wing is contained in a region extending approximately 1.75 nozzle widths outboard of the nozzle. In fact, for spanwise locations outboard of the 65-percent-semispan station, the power-off and power-on load distributions are very nearly the same. Of course, the actual spanwise location at which the engine-induced loads diminish to the power-off levels is configuration dependent, but arrangements in which the engines are located well inboard on the wing will generally exhibit this characteristic. From figure 9 it appears that the amount of lift to be gained by deflecting a flap on the outboard portion of the wing (beyond about 70 percent of the semispan) is primarily the lift available from unpowered flow conditions, and it is not likely to be greatly influenced by power-induced effects.

Figure 10 presents the lift characteristics of a number of USB configurations having different nozzle designs. Included are data for rectangular nozzles of three different width-height ratios, a fairly high kickdown D-nozzle; a low kickdown D-nozzle with vortex generators (ref. 11), and a D-nozzle with BLC (hybrid USB, ref. 12). The data presented have been plotted for a jet turning angle of 50°. These data indicate that at low to moderate thrust coefficients, such as those used on approach, there is very little difference in lift for the configurations tested. Thus, it appears that the lift characteristics

of USB configurations may be primarily a function of the jet turning performance, assuming adequate leading- and trailing-edge treatment to prevent premature flow separation. It has been shown (ref. 13) that the geometric nozzle characteristics which are desirable for good turning (such as high-aspect-ratio rectangular nozzles, large kickdown angles, and flare angles) are detrimental to cruise performance. It appears, therefore, that variable geometry features, such as nozzle deflectors or vortex generators, or BLC may be required to achieve optimum performance for both the high-speed and low-speed flight conditions. In any event, the design of a single nozzle to satisfactorily fulfill both the high-speed and low-speed requirements represents a significant challenge to the designer.

The foregoing discussion has centered on the lift performance of the USB concept. However, drag characteristics are also important from an operational viewpoint. A flight envelope relating glide path, lift coefficient, thrust-weight ratio, and angle of attack is very useful in relating lift and drag to overall performance because it serves to establish power requirements and speed margins for a given configuration. Figure 11 presents trimmed flight envelopes for a two-engine straight-wing USB configuration and for a four-engine swept-wing USB configuration. The lift data for these two configurations are contained within the bands shown on figure 10 and are therefore generally representative of USB configurations tested.

At the present time, there are no certified requirements for approach performance of powered-lift airplanes. For the data of figure 11, it is assumed that the aircraft will fly a 7.5° glide slope at a lift coefficient of 4.0. In the event of an engine failure, it must be possible to arrest the descent with full power on the remaining engines without changing flap setting or lift coefficient. From the data on the left side of figure 11 it can be seen that, for the two-engine configuration, the landing approach can be flown at a thrust-weight ratio of 0.21 with a stall margin of about 14°. In order to arrest the descent at this same flap setting, a thrust-weight ratio of 0.35 is required. It has been found with this model and with other USB (and EBF) models that such performance envelopes are almost the same with one engine out as with all engines operating. Hence it can be concluded that, for this two-engine configuration, a total installed thrust-weight ratio of about 0.70 is required.

A similar analysis of the data for the four-engine configuration shown on the right side of figure 11 indicates an approach thrust-weight ratio of 0.25, and an engine-out thrust-weight ratio requirement of 0.45. In the case of the four-engine configuration, only 25 percent of the available thrust is lost in an engine failure, so the four-engine aircraft requires an installed thrust-weight ratio of 0.60.

Based on such analysis, it appears that somewhat higher values of thrust-weight ratio are required for the two-engine configuration than for the four-engine configuration, as would be expected. The data of figure 11 have been found to be generally representative of both USB and EBF configurations; generally, both concepts require higher installed thrust-weight ratios than internally blown flap concepts (such as the distributed blowing concept which distributes the jet uniformly along the wing span). The simplicity of the

discrete-blowing, powered-lift systems, however, make them attractive for application to powered-lift STOL aircraft, as indicated by the selection of the USB and EBF concepts for use in the powered-lift prototype aircraft of the U.S. Air Force Advanced Medium STOL Transport program.

LONGITUDINAL STABILITY AND TRIM

It is a well-known fact that provision of adequate trim in pitch is a serious problem for powered-lift airplane configurations as illustrated in figure 12. The data show the variation of pitching moment with angle of attack for several thrust levels at high lift conditions for a swept-wing, two-engine USB configuration with the horizontal tail off. It should be noted that high thrust increases the longitudinal instability as well as the diving moments of the configuration.

The significance of the large diving moments produced by powered lift in terms of tail size required for trim is shown in figure 13. The figure shows the tail size required for trim as a function of tail lift coefficient following the procedure outlined in reference 14. The tail trim requirements were determined for a maximum wing lift coefficient of 8, a tail length of $3.5\bar{c}$. and a static margin of 10 percent. Figure 13 shows that for a plain elevator, the tail size required for trim is about 37 percent of the wing area, a value nearly double that required by conventional airplanes. The use of a slotted elevator can reduce the required tail size to about 30 percent of the wing area, but a considerably higher tail lift coefficient would be required to reduce the size of the tail to that for conventional airplanes.

The foregoing data have shown that the powered-lift configuration exhibits large pitching moments and that a large tail is required for trim. It should be pointed out that one very important factor which must be considered in sizing the tail is the tail location. As in the case of other powered-lift systems, the high lift generated in the USB concept results in very high downwash angles, particularly directly behind the engines. For this reason, care must be taken in locating the horizontal tail so as to avoid the high downwash region in which the tail could become ineffective. As an example of the flow characteristics behind a USB configuration, the variation of the downwash factor $1 - \frac{\partial \varepsilon}{\partial \alpha}$ with C_L for the two-engine configuration for three vertical locations of the horizontal tail is presented in figure 14. The data in figure 14 are for low-angle-of-attack conditions, and the increase in lift coefficient is obtained by an increase in thrust rather than by an increase in angle of attack. The data of figure 14 show that regardless of the tail location, the tail lost effectiveness as power was increased, but the high tail position was much better than the lower positions.

Flow survey work for USB configurations has not been as extensive as for EBF configurations, so earlier work performed on EBF models was used for guidance with regard to tail location. Stability and control studies of EBF configurations showed that with engines located inboard on the wing, a strong downwash

field was produced along the rear of the fuselage which made the low tail arrangement undesirable from stability considerations. Also, it was found that vortices shed from the wing tips and flaps did not trail straight backward but were drawn in sharply toward the centerline of the airplane. At high angles of attack, a horizontal tail located relatively far rearward and low would enter the vortex flow and become ineffective. For this reason, the horizontal tail was generally located high and forward to retain its stabilizing contributing for higher thrust levels and higher angles of attack. Limited flow survey work with the USB concept has demonstrated downwash characteristics similar to those of EBF concepts, and similar high-forward horizontal tail locations have proven desirable from longitudinal stability considerations.

In order to illustrate how the downwash data of figure 14 affect the contribution of the horizontal tail to stability, calculations have been made to determine the C_{m_α} contribution of the tail at the high and low tail locations of figure 14. The results are shown in figure 15 together with tail-off data. The tail contributions are based on a tail size of 35 percent of the wing area and a tail length of $3.5\bar{c}$. The data show that at low lift coefficients, the high tail position provided adequate stability. The low tail, however, provided very little stability at low lift coefficients and, as the lift coefficient was increased by increasing power, the combined effects of increased instability of the wing-fuselage combination and reduced tail effectiveness resulted in a very unstable configuration at high power settings.

LATERAL-DIRECTIONAL STABILITY

The lateral-directional stability discussion presented herein is based on results obtained for two USB model configurations which were flight tested in the Langley full-scale tunnel. Photographs of the two models mounted for static force tests are presented in figure 16. One model, with an unswept wing and two engines mounted close inboard to the fuselage, represented a 1/5-scale model of the large-scale USB Aero Commander configuration recently tested in the Langley full-scale tunnel. The second model was a four-engine, swept-wing USB configuration. Although the two models were different in planform and engine arrangement, the powered-lift characteristics for the two configurations were generally very similar, as illustrated by the data in figure 17. The lateral-directional stability characteristics for the two models, however, were considerably different, as shown in plots of the directional stability derivative C_{n_β} and the effective dihedral derivative C_{l_β} in figure 18. As shown by the data, the swept-wing configuration had relatively large values of positive effective dihedral which increased as lift coefficient increased. The directional stability was also relatively high and there was an increase in directional stability with increasing lift coefficient. The data for the straight-wing configuration show that the dihedral effect was relatively small and actually decreased with increasing power, but the directional stability increased very rapidly as power was applied. The differences in dihedral effect for the two configurations can probably be attributed to the differences in wing sweep angle. The differences in directional stability were primarily a result of differences

in the effect of the engine exhaust wake on the vertical tail. The engines were located much closer to the fuselage on the straight-wing configuration than on the swept-wing configuration, and the vertical tail was influenced much more by sidewash than on the swept-wing arrangement.

In order to illustrate how these differences in the static lateral-directional stability derivatives affect dynamic lateral-directional stability characteristics, period and damping characteristics were determined by using three-degree-of-freedom calculations for the two models; the results are presented in figure 19. The data show Dutch-roll characteristics in terms of the damping parameter $\frac{1}{T_{1/2}}$ and the damped frequency parameter ω_d. The handling quality boundaries were taken from an AGARD publication for STOL handling criteria (ref. 15). The plot on the left of figure 19 shows that the Dutch-roll oscillation for the swept-wing configuration was unstable and would be considered unacceptable with power off $(C_L = 1.5)$ or on $(C_L = 5.0)$. In order to achieve acceptable Dutch-roll characteristics, the damping in both roll and yaw would have to be doubled; even higher artificial damping would be required for satisfactory characteristics. In contrast to these results, the plot on the right side of figure 19 shows that the Dutch-roll mode for the unswept-wing configuration was stable and that increasing power resulted in increased Dutch-roll damping, with the result that satisfactory characteristics could be achieved without artificial stabilization.

ENGINE-OUT LATERAL TRIM

One of the major problems associated with powered-lift systems utilizing discrete blowing is that of restoring lateral trim in the event of the failure of one engine. This problem involves both roll and yaw, with the roll requirement being the more critical in an approach condition. One major objective of recent research on the USB concept was to determine effective means of providing roll trim for the engine-out condition. One method found to be effective for the USB configuration was that of asymmetrical boundary-layer control, that is, boundary-layer control on the leading edge and on the aileron of the engine-out wing. Some lateral trim data obtained with this method of trim are shown in figures 20 and 21 for the swept-wing and straight-wing flying models.

Figure 20 is a plot of yawing-moment coefficient and rolling-moment coefficient plotted against lift coefficient for the four-engine, swept-wing flying model. In a four-engine operation, the rolling moments were essentially zero and a maximum trimmed lift coefficient of 10 was achieved. With the failure of an outboard engine, the maximum lift coefficient decreased to about 8 and large out-of-trim rolling and yawing moments were introduced. By applying boundary-layer control to the failed engine side, it was possible to simultaneously provide roll and yaw trim. Additional moments produced by spoiler deflection could then be used for maneuver control.

The data of figure 21 show the engine-out rolling-moment and yawing-moment coefficients plotted against lift coefficient for the two-engine, straight-wing

flying model. In this case, the application of boundary-layer control to the failed-engine side reduced the out-of-trim rolling and yawing moments, but it was necessary to employ spoiler deflection and a blown rudder to achieve roll and yaw trim. Additional spoiler and rudder deflection were available for maneuver control.

MODEL FLIGHT TEST RESULTS

As part of the basic research program of USB jet-flap configurations, dynamic stability and control investigations have been made of the four-engine swept-wing configuration and the two-engine straight-wing configuration by using the free-flight model technique. This technique has proved to be useful in previous research in pointing out problem areas which might have been overlooked in conventional testing. The swept-wing model, shown in flight in figure 22, had a span of 3.05 m (10 ft) and was powered by four 13.97-cm-diameter (5.5 in.) turbofan engine simulators driven by compressed air. The horizontal tail incorporated a Krueger flap, and the elevator was deflected upward 50°. Longitudinal control was provided by deflecting the entire horizontal tail, and lateral-directional control was provided by spoilers and rudder. The two-engine straight-wing model was powered by turbofan engine simulators similar to those used on the swept-wing model and had a similar control system.

The free-flight technique is illustrated in figure 23. This figure shows a model being flown without restraint in the 9- by 18-m (30- by 60-ft) open-throat test section of the Langley full-scale tunnel and remotely controlled about all three axes by human pilots. Control surfaces are operated by remotely controlled pneumatic actuators. Pneumatic power and electric control signals are supplied to the model through a flexible trailing cable made up of electrical conductors and light plastic hoses.

The results of the free-flight model tests showed that with all engines operating and with artificial damping about the roll and yaw axes, the models were easy to fly even at lift coefficients up to 8.0. Without artificial stabilization, however, the swept-wing model exhibited a lightly damped Dutch-roll oscillation which made flying difficult. The straight-wing model exhibited good damping characteristics and was easy to fly without artificial stabilization. These results were in good agreement with the previously discussed dynamic stability calculations. With one engine inoperative, the models were trimmed laterally through the use of boundary-layer control on the leading edge and aileron of the engine-out wing and through the use of spoiler and rudder deflection as needed for additional lateral-directional trim. With artificial damping, the models were flown up to high lift coefficients, and the dynamic behavior with one engine inoperative was found to be generally similar to that for all engines operating.

CONCLUDING REMARKS

The results of recent wind-tunnel investigations to provide fundamental information on the upper-surface-blown (USB) jet-flap concept demonstrated that the USB concept provides good high-lift performance. The low-speed performance appears to be mainly dependent upon the jet turning angle and turning efficiency and on the use of proper leading- and trailing-edge treatment to prevent premature flow separation. The best means of achieving good turning performance in any particular USB application must be determined from overall operational considerations in which high-speed performance, structures and noise, as well as low-speed performance, are evaluated. The large diving moments generated at high lift coefficients can be trimmed satisfactorily with a large, conventional horizontal tail; a high tail position is best from longitudinal stability considerations. Large rolling and yawing moments are introduced with the loss of an engine, but these moments can be trimmed satisfactorily through the use of asymmetrical boundary-layer control and through the use of spoiler and rudder deflection as needed.

REFERENCES

1. Phelps, Arthur E.; Letko, William; and Henderson, Robert L.: Low-Speed Wind-Tunnel Investigation of a Semispan STOL Jet Transport Wing-Body With an Upper-Surface Blown Jet Flap. NASA TN D-7183, 1973.

2. Phelps, Arthur E., III; and Smith, Charles C., Jr.: Wind-Tunnel Investigation of an Upper Surface Blown Jet-Flap Powered-Lift Configuration. NASA TN D-7399, 1973.

3. Staff of the Langley Research Center: Wind-Tunnel Investigation of the Aerodynamic Performance, Steady and Vibratory Loads, Surface Temperatures and Acoustic Characteristics of a Large-Scale Twin-Engine Upper-Surface Blown Jet-Flap Configuration. NASA TM X-72794, 1975.

4. Smith, Charles C., Jr.; Phelps, Arthur E., III; and Copeland, W. Latham: Wind-Tunnel Investigation of a Large-Scale Semispan Model With an Unswept Wing and an Upper-Surface Blown Jet Flap. NASA TN D-7526, 1974.

5. Sleeman, William C., Jr.; and Hohlweg, William C.: Low-Speed Wind-Tunnel Investigation of a Four-Engine Upper Surface Blown Model Having a Swept-Wing and Rectangular and D-Shaped Exhaust Nozzles. NASA TN D-8061, 1975.

6. Reshotko, Meyer; Olsen, William A.; and Dorsch, Robert G.: Preliminary Noise Tests of the Engine-Over-the-Wing Concept. I. 30°-60° Flap Position. NASA TM X-68032, 1972.

7. Reshotko, Meyer; Olsen, William A.; and Dorsch, Robert G.: Preliminary Noise Tests of the Engine-Over-the-Wing Concept. II. 10°-20° Flap Position. NASA TM X-68104, 1972.

8. Sleeman, William C., Jr.; and Phelps, Arthur E., III.: Upper-Surface-Blowing Flow-Turning Performance. Powered-Lift Aerodynamics and Acoustics, NASA SP-406, 1976. (Paper no. 2 of this compilation.)

9. Koenig, David G.; and Aoyagi, Kiyoshi: Maximum Lift of Upper Surface Blowing STOL Aircraft With Swept Wings. AIAA Paper No. 75-868, June 1975.

10. Lowry, John G.; Riebe, John M.; and Campbell, John P.: The Jet-Augmented Flap. Preprint No. 715, S.M.F. Fund Paper, Inst. Aeronaut. Sci., Jan. 1957.

11. Wimpress, John K.: Upper Surface Blowing Technology as Applied to the YC-14 Airplane. [Preprint] 730916, Soc. Automot. Eng., Oct. 1973.

12. Carros, Robert J.; Boissevain, Alfred G.; and Aoyogi, Kiyoshi: Aerodynamic Characteristics of a Large-Scale Hybrid Upper Surface Blown Model Having Four Engines. NASA TM X-72460, 1975.

13. Skavdahl, Howard; Wang, Timothy; and Hirt, William J.: Nozzle Development for the Upper Surface-Blown Jet Flap on the YC-14 Airplane. [Preprint] 740469, Soc. Automot. Eng., Apr.-May 1974.

14. Johnson, Joseph L., Jr.: Wind-Tunnel Investigation of the Static Longitudinal Stability and Trim Characteristics of a Sweptback-Wing Jet-Transport Model Equipped With an External-Flow Jet-Augmented Flap. NACA TN 4177, 1958.

15. V/STOL Handling. I - Criteria and Discussion. AGARD Rep. No 577, Dec. 1970.

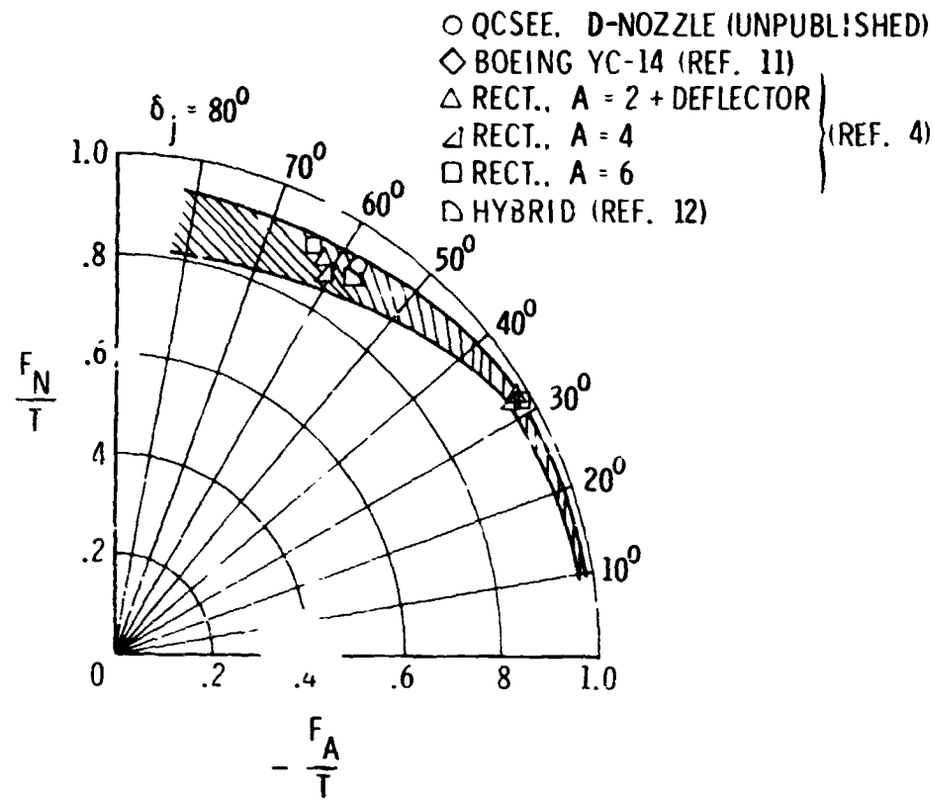

Figure 1.- Static turning characteristics of several USB configurations.

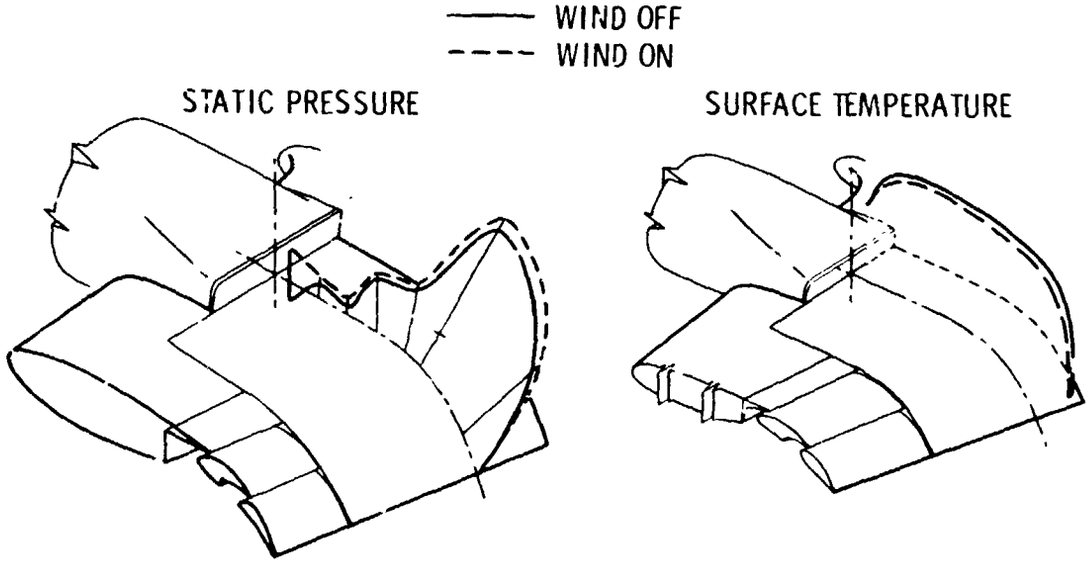

Figure 2.- Pressure and temperature profiles.

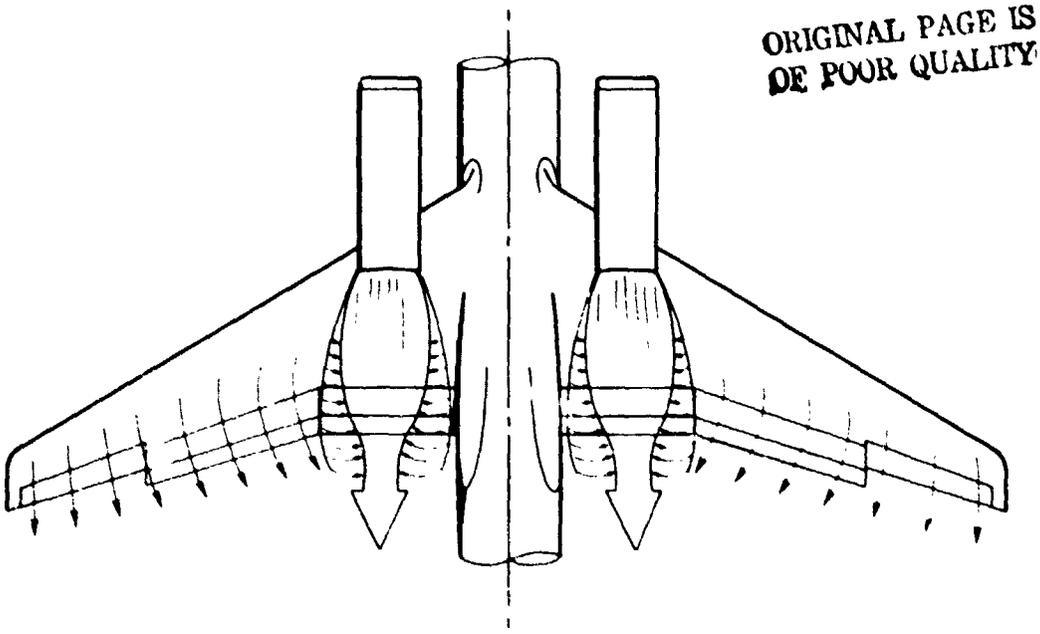

Figure 3.- USB flow characteristics.

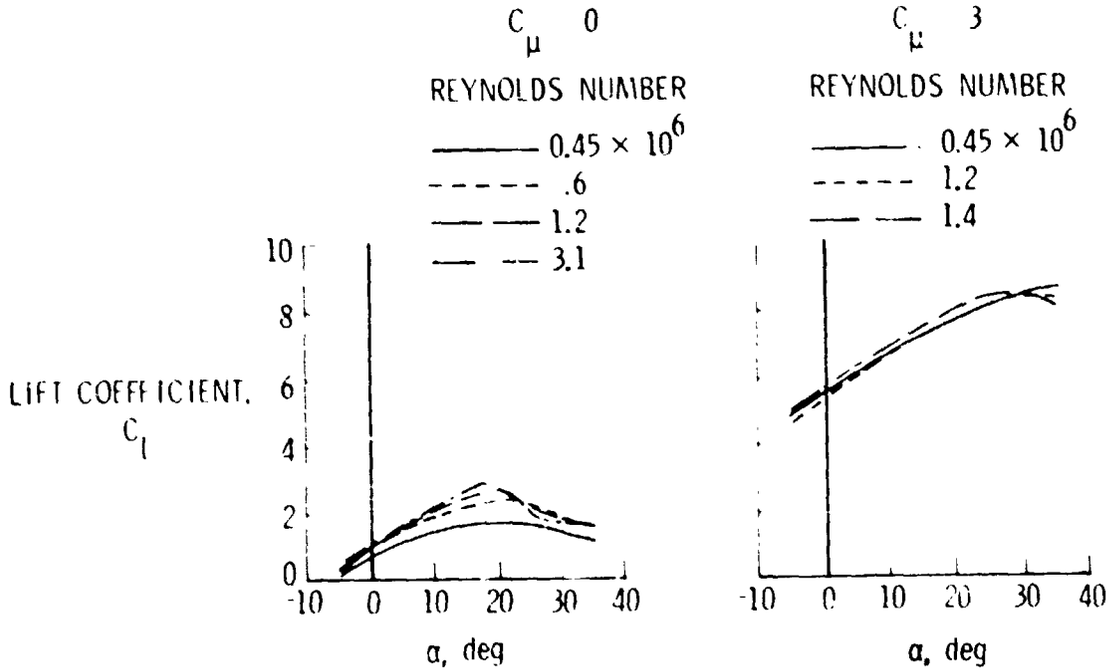

Figure 4.- Effect of Reynolds number on lift characteristics for two-engine straight-wing USB configuration.

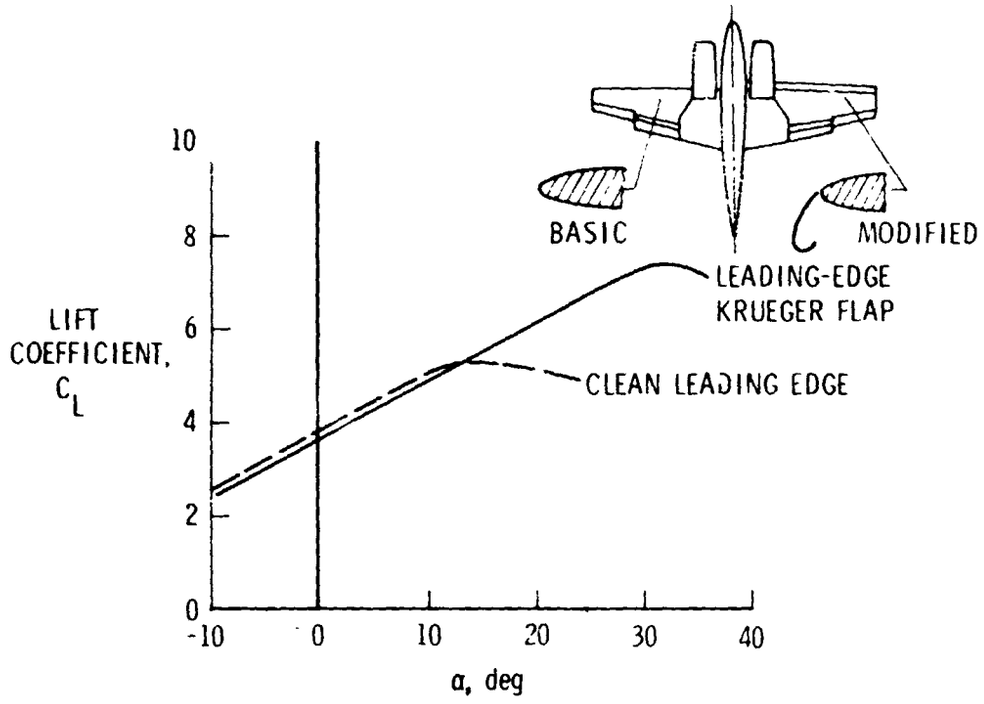

Figure 5.- Effect of leading-edge high-lift devices on lift. $\delta_f = 60^o$; $C_\mu = 2.0$.

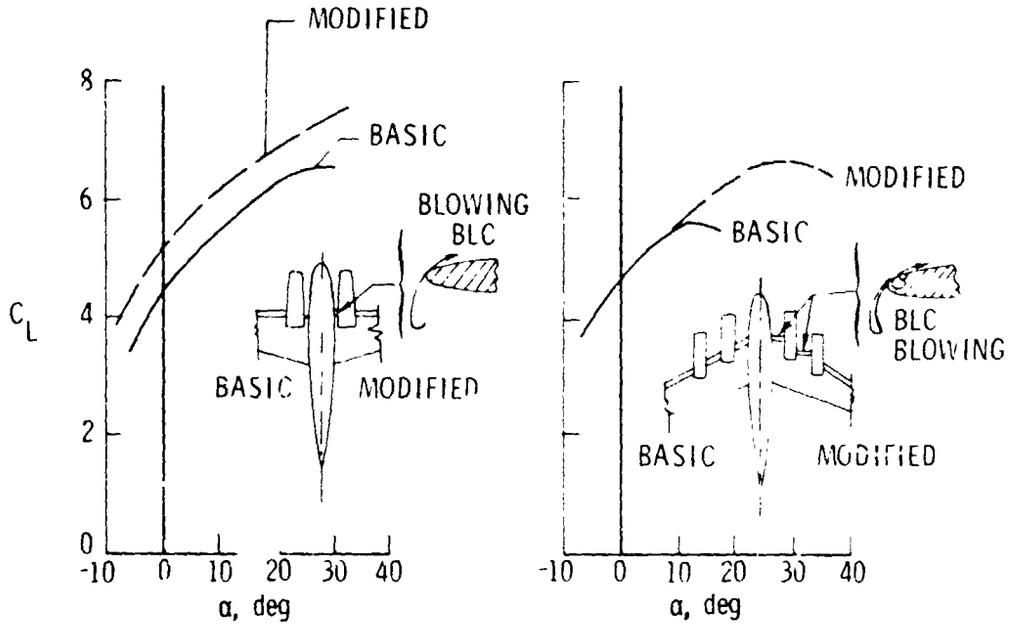

Figure 6.- Leading-edge treatment for two-engine straight-wing and four-engine swept-wing configurations.

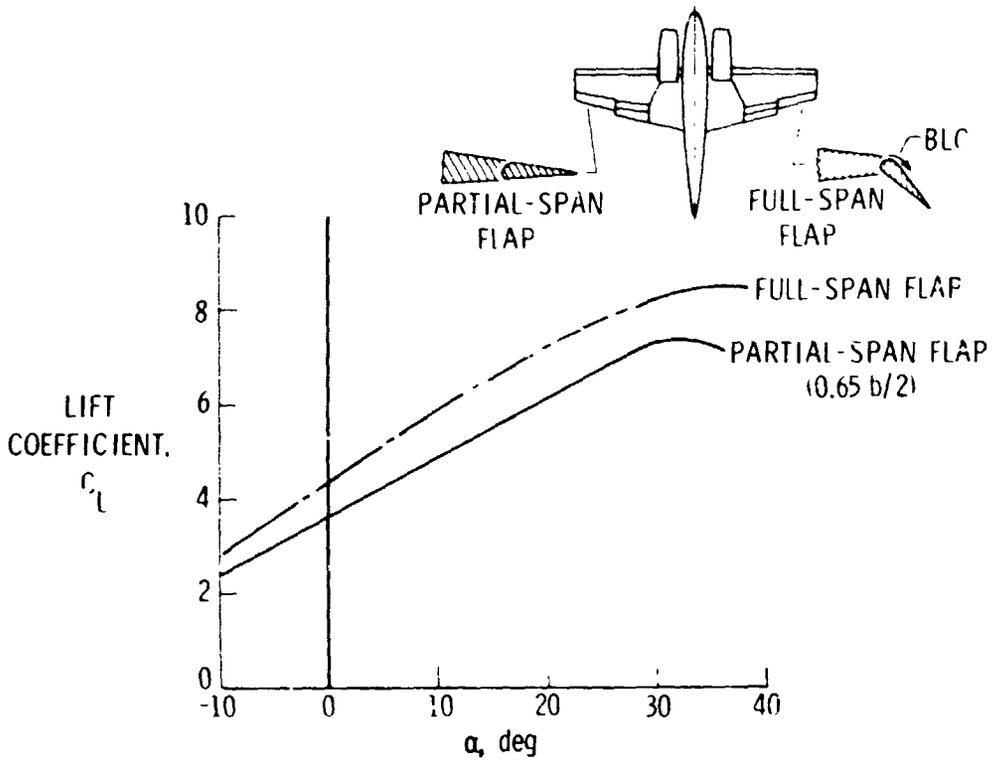

Figure 7.- Effect of trailing-edge flap span on lift. $\delta_f = 60^o$; $C_\mu = 2.0$.

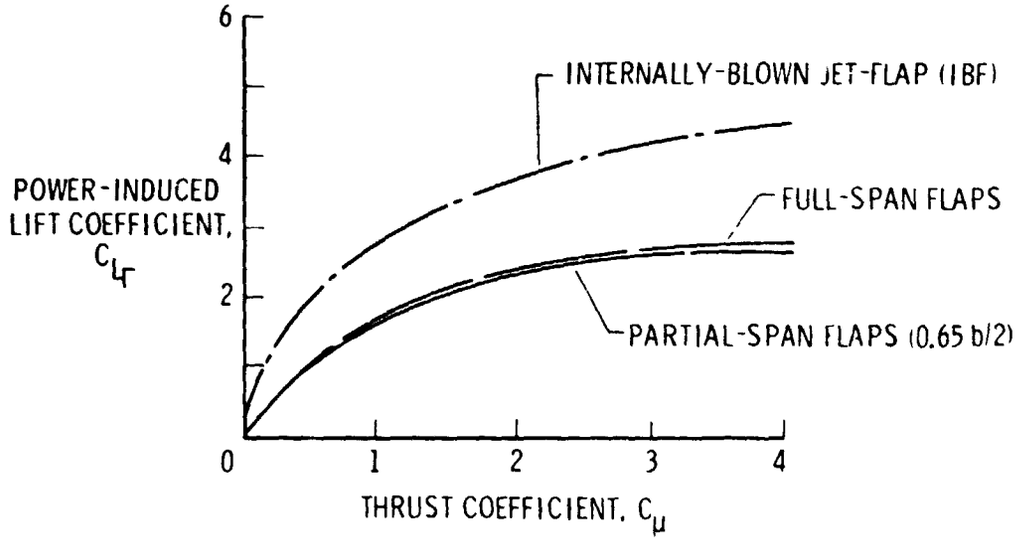

Figure 8.- Power-induced lift characteristics of two-engine straight-wing USB configuration. $\delta_f = 60^o$; $\alpha = 0^o$.

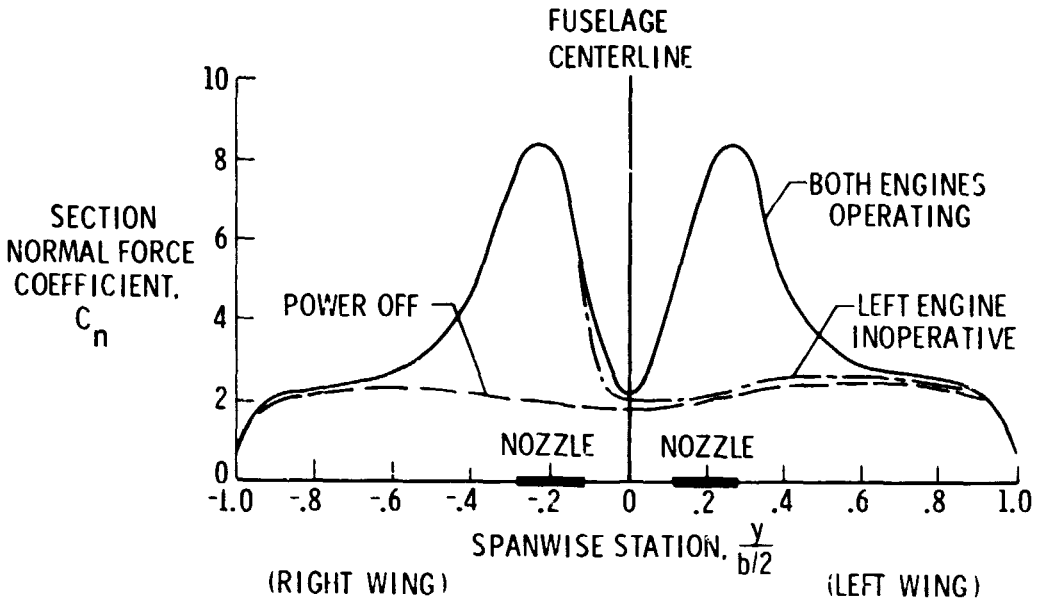

Figure 9.- Spanwise normal-force distribution for two-engine straight-wing USB configuracion. $\delta_f = 60^o$; $\alpha = 0^o$.

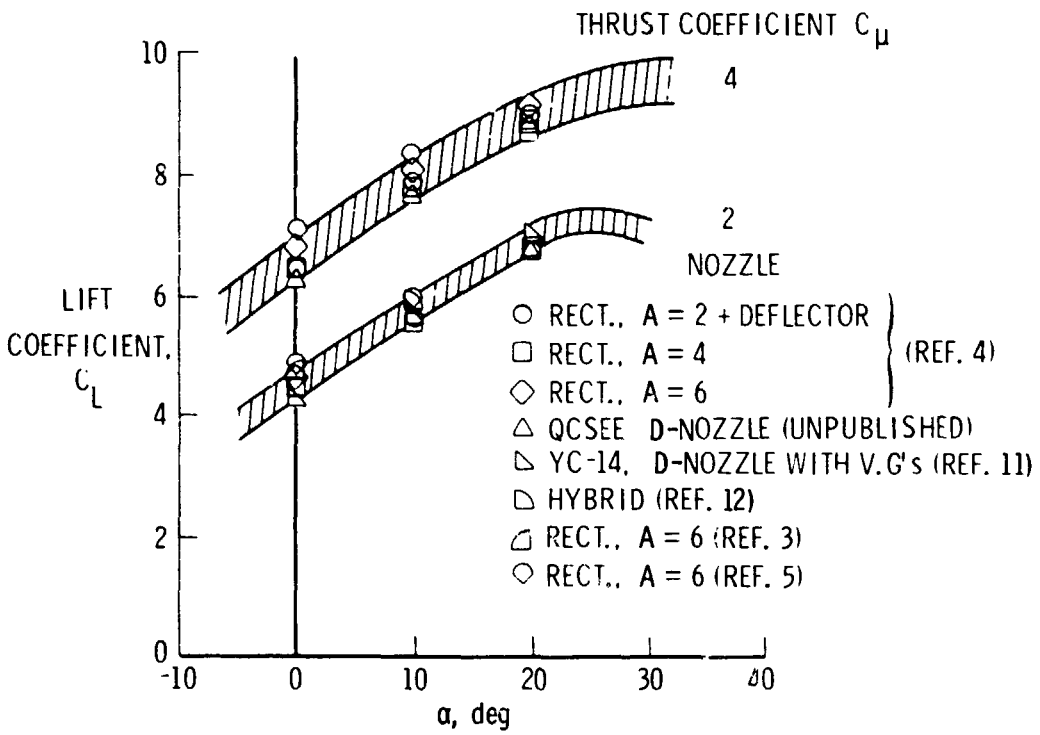

Figure 10.- Effect of nozzle geometry on lift for a number of USB configurations.

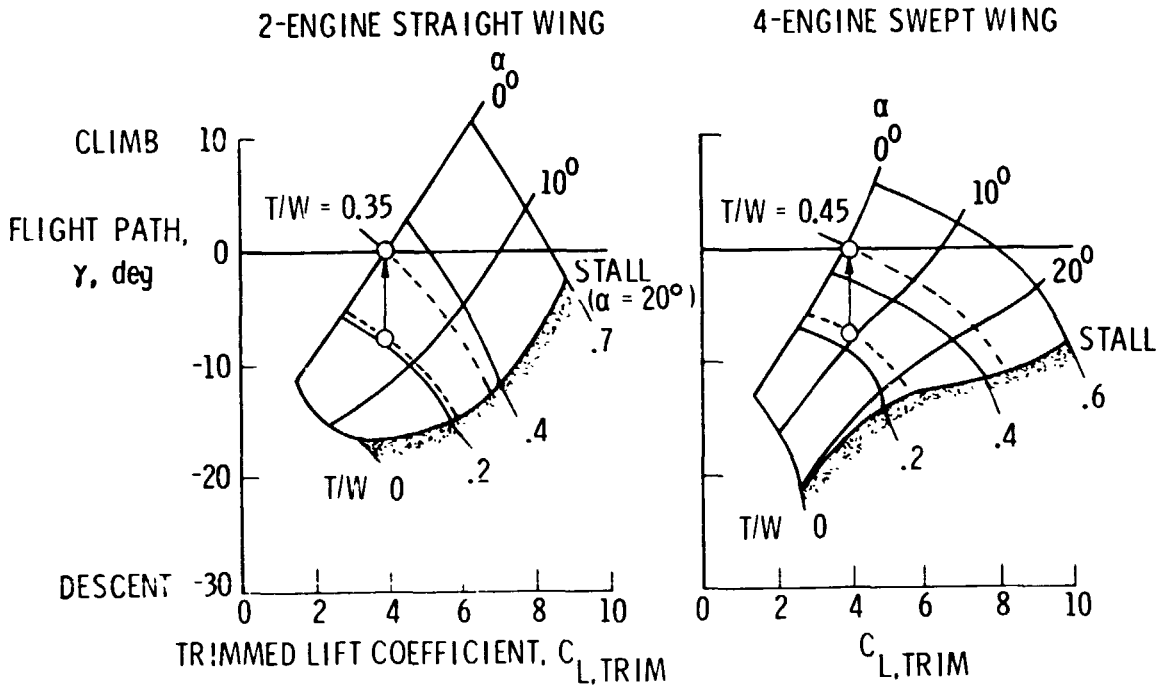

Figure 11.- Flight envelopes for two-engine straight-wing and four-engine swept-wing configurations.

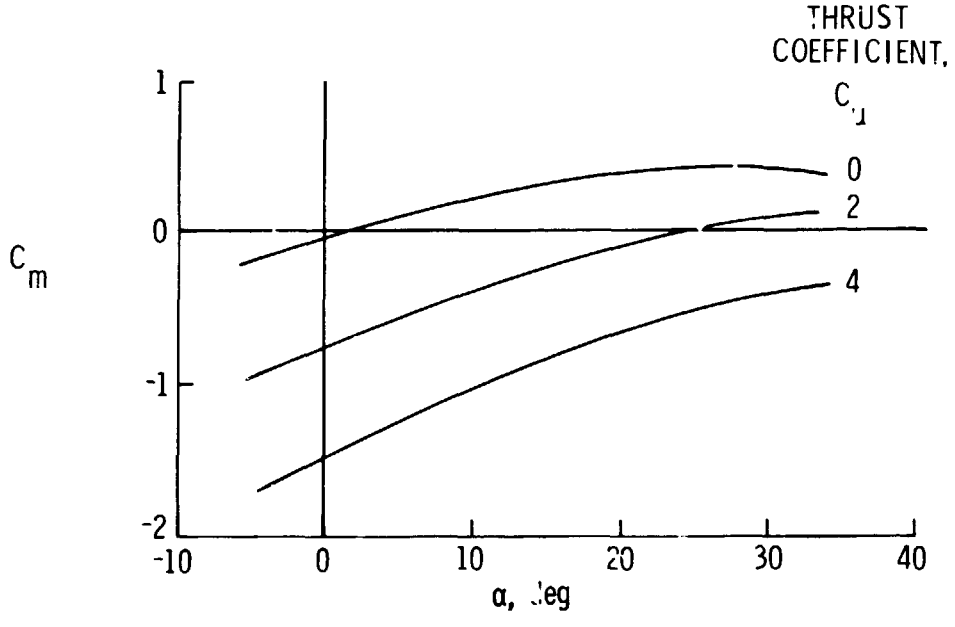

Figure 12.- Tail-off pitching-moment characteristics for four-engine swept-wing configuration. $\delta_f = 65^o$; tail off.

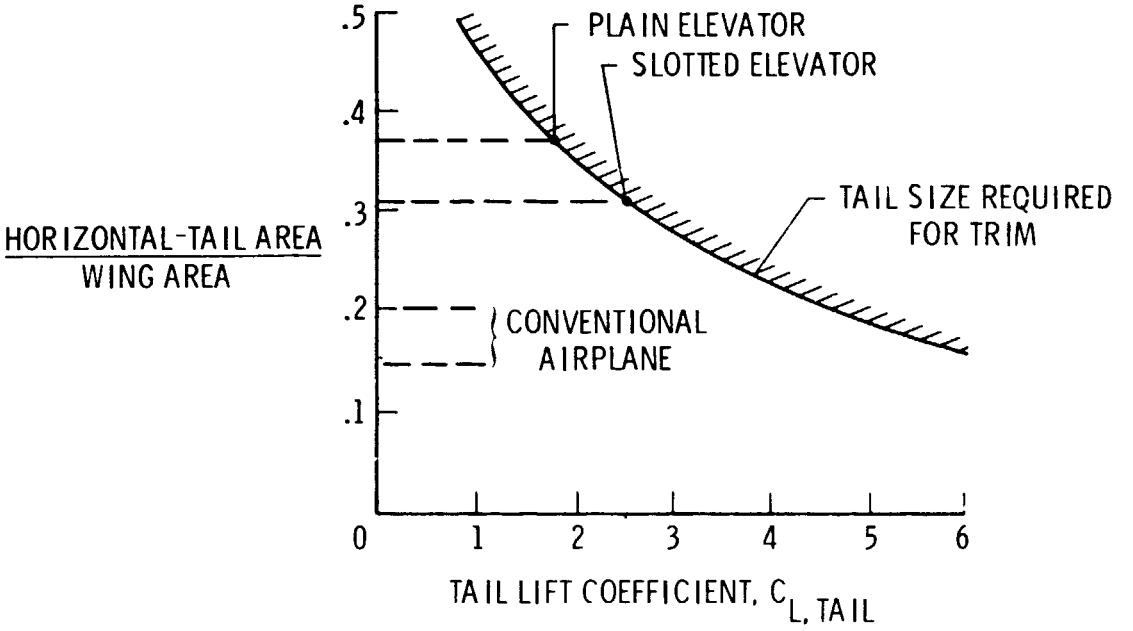

Figure 13.- Horizontal-tail requirements. $C_{L,wing} = 8.0$; $l_t = 3.5\bar{c}$; 10-percent static margin.

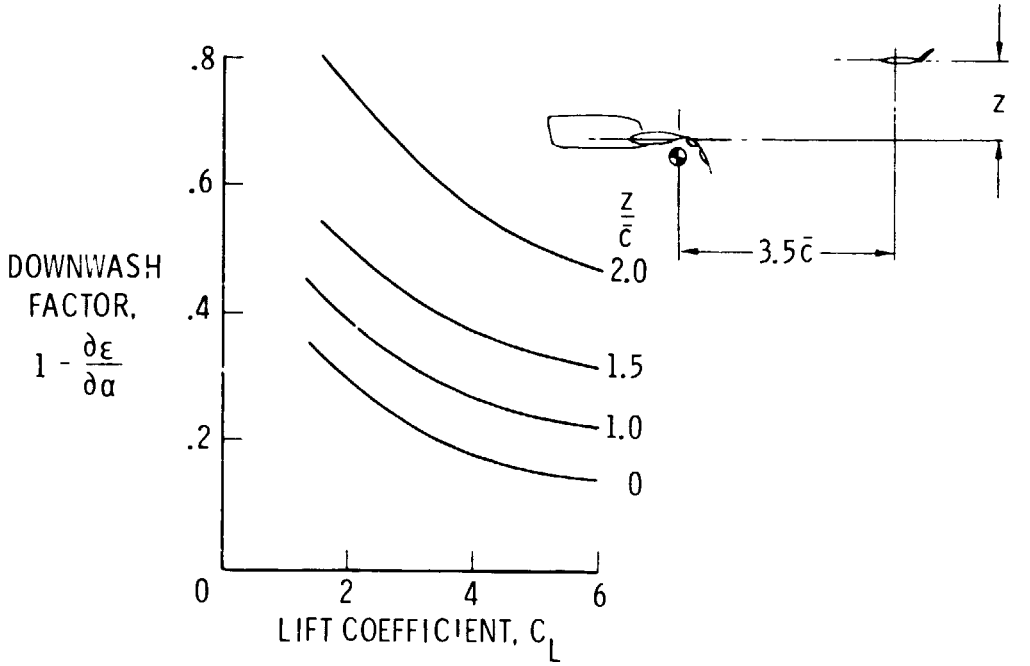

Figure 14.- Variation of downwash factor. $\delta_f = 69^o$.

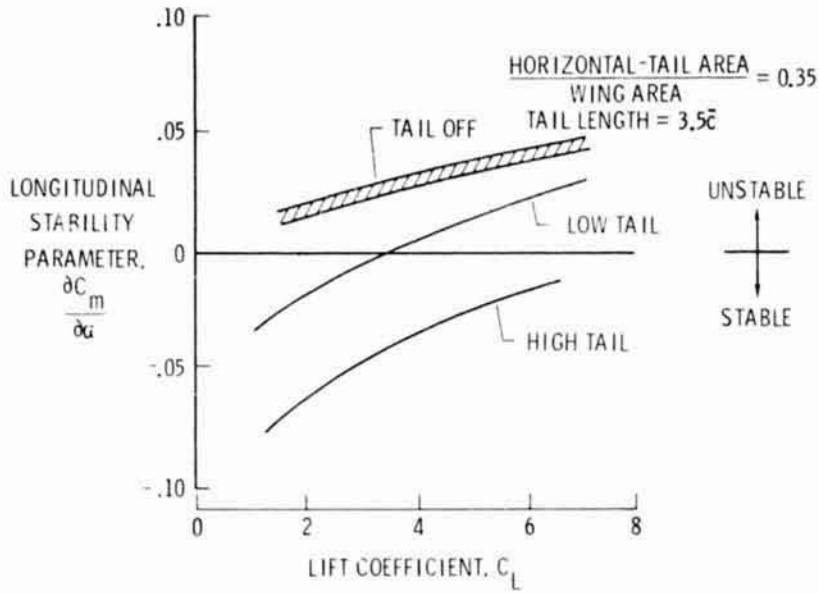

Figure 15.- Static longitudinal stability.

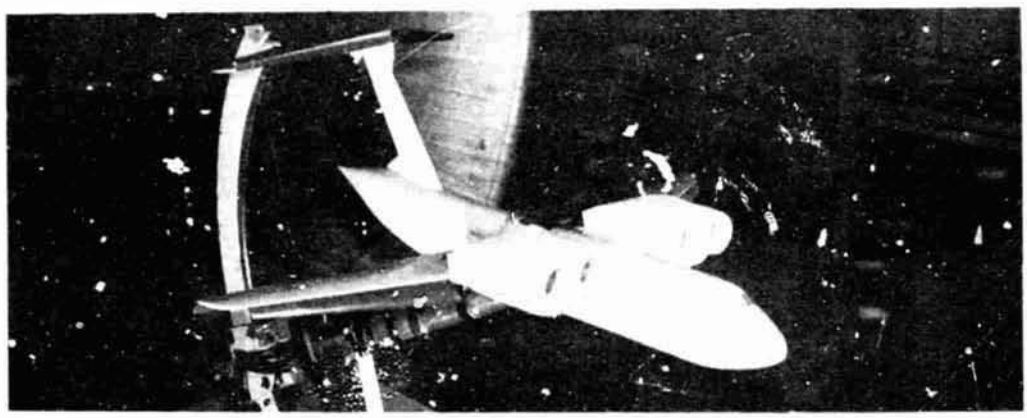

Four-engine swept wing

Two-engine straight wing

Figure 16.- Photographs of two-engine and four-engine USB models installed in the Langley full-scale tunnel.

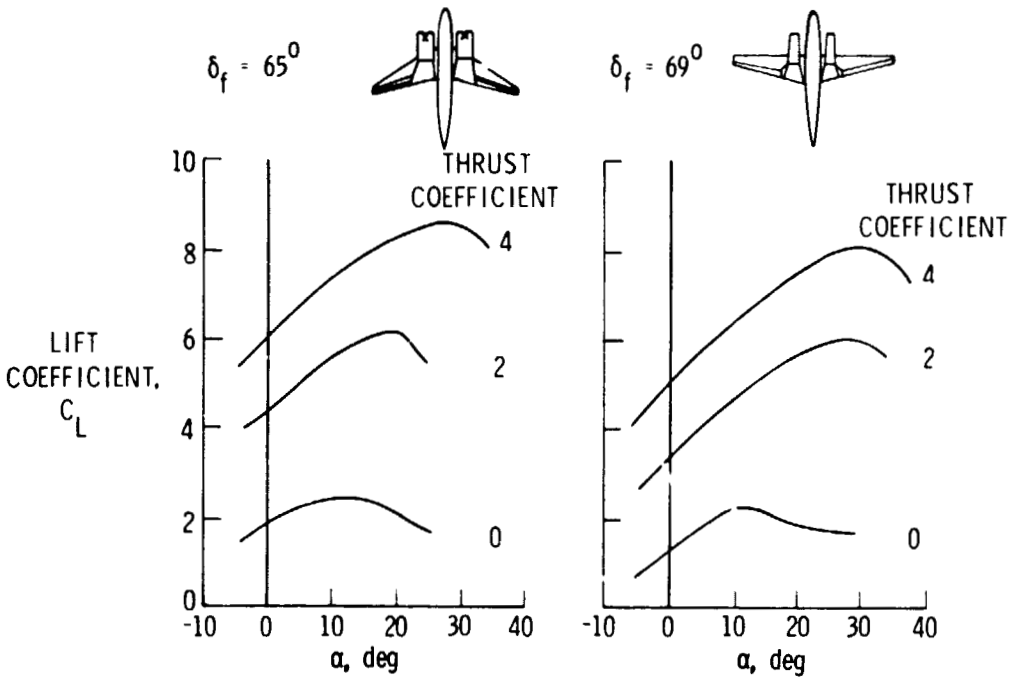

Figure 17.- Lift characteristics of two-engine and four-engine USB models.

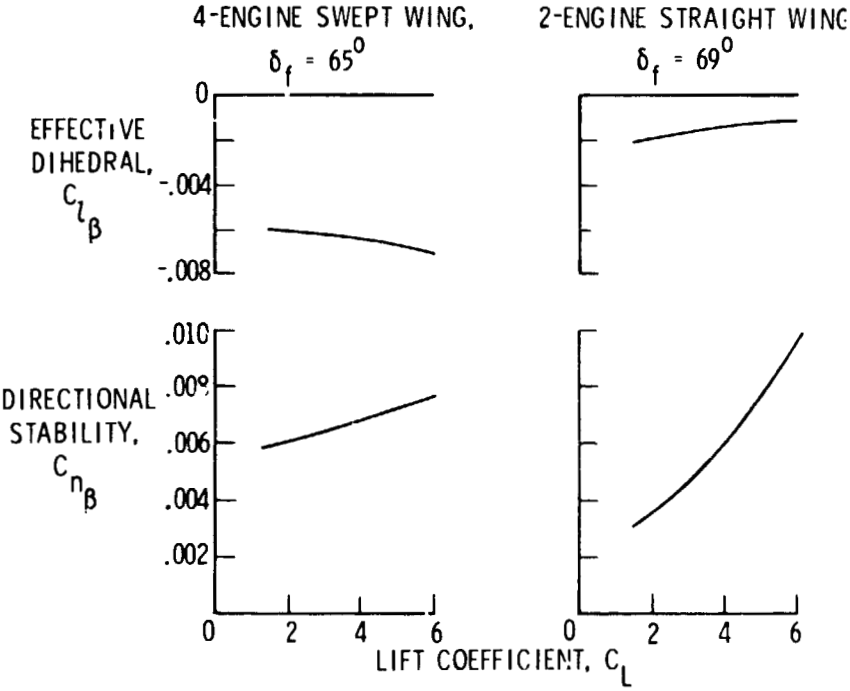

Figure 18.- Lateral-directional stability characteristics of two-engine and four-engine USB models.

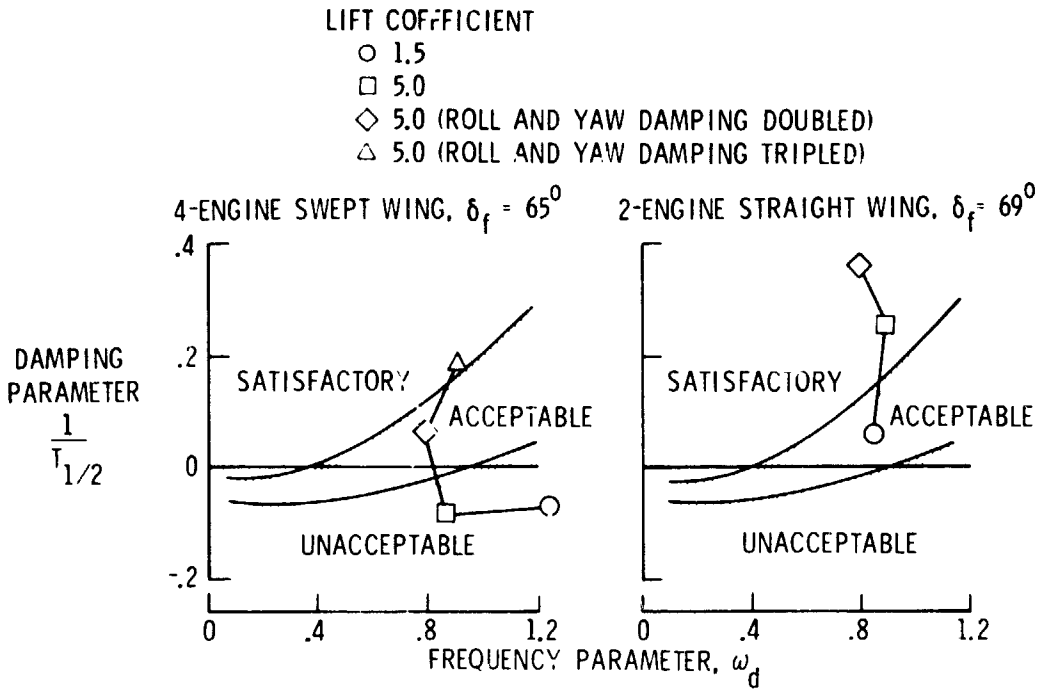

Figure 19.- Dutch-roll characteristics of two-engine and four-engine USB models.

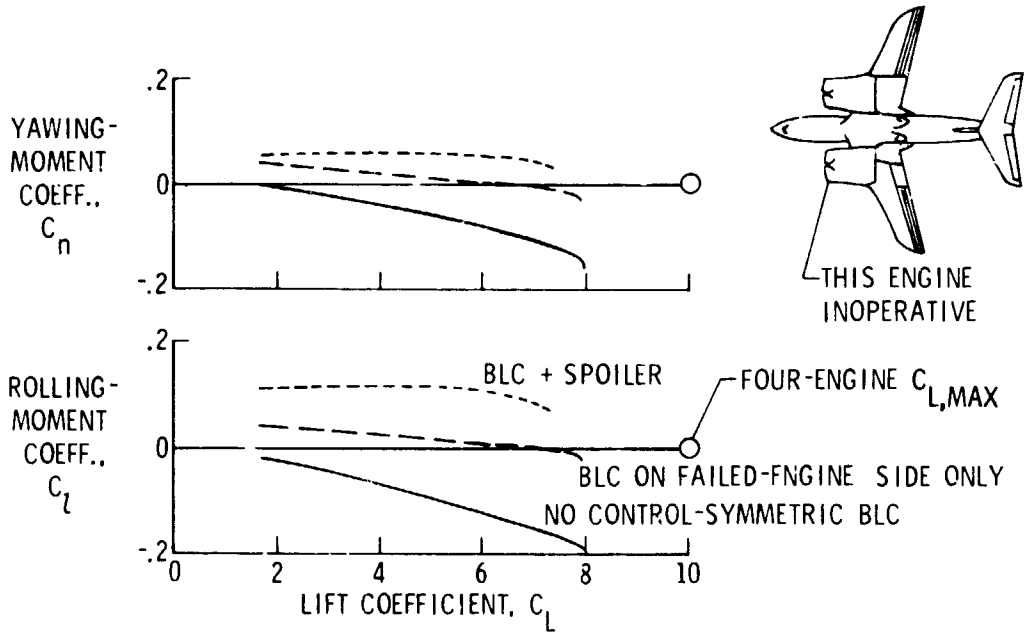

Figure 20.- Lateral trim characteristics for four-engine swept-wing USB model.

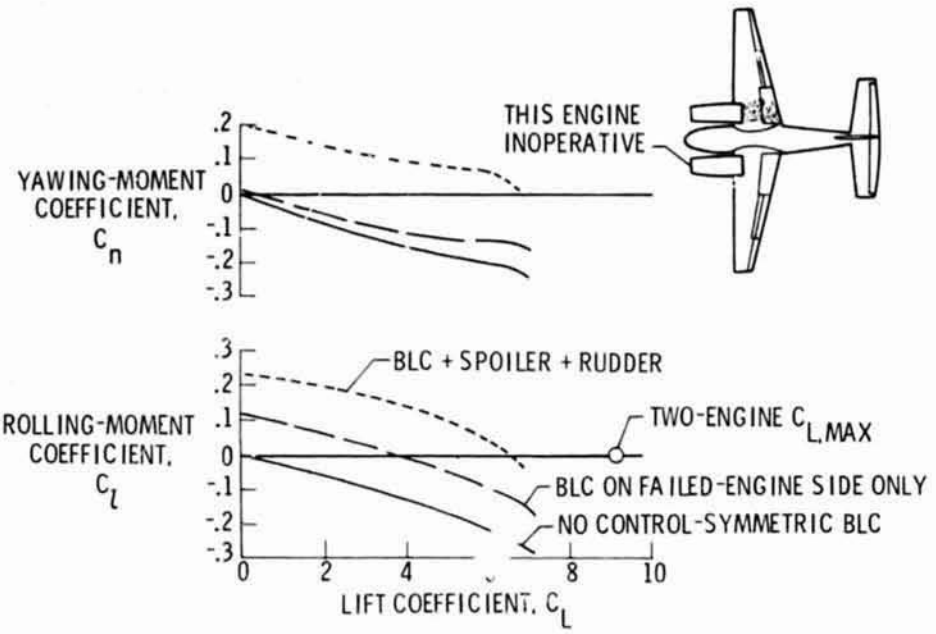

Figure 21.- Lateral trim characteristics for two-engine straight-wing USB model.

Figure 22.- Photograph of four-engine swept-wing free-flight USB model in the Langley full-scale tunnel.

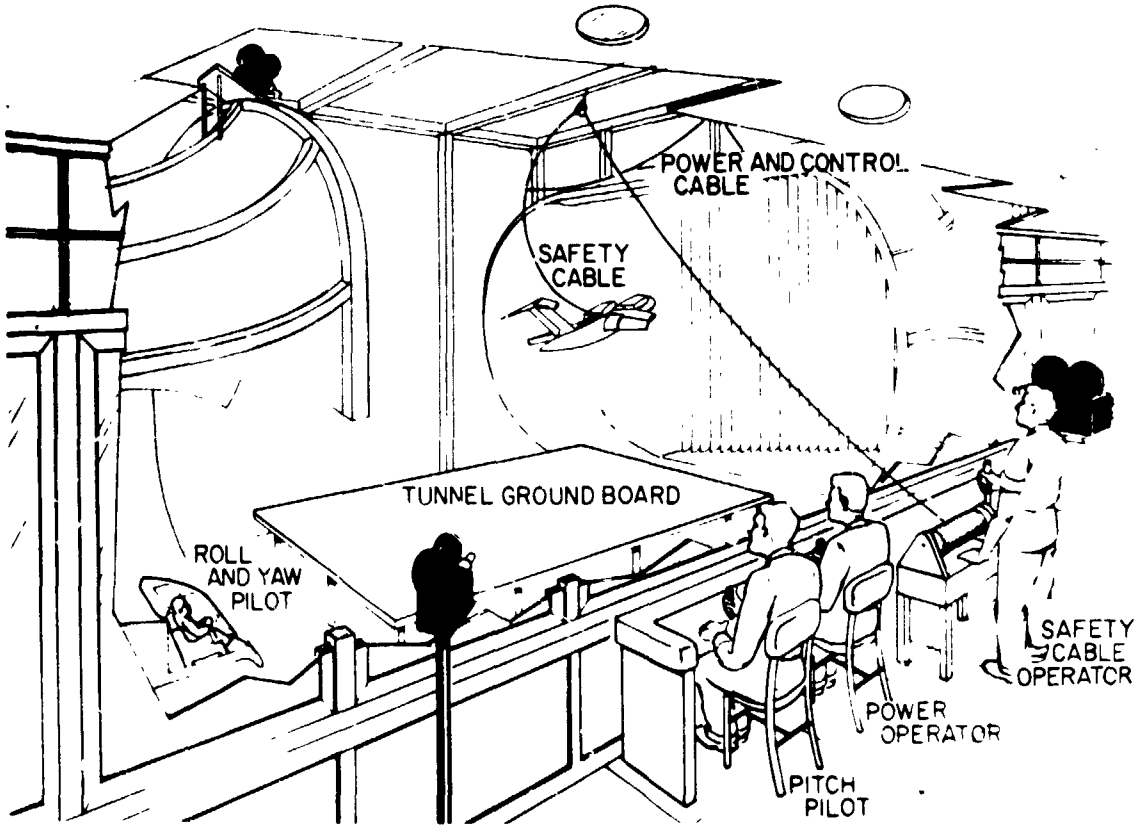

Figure 23.- Test setup for free-flight model testing in the Langley full-scale tunnel.

N78-24051

APPLICATION OF POWERED-LIFT CONCEPTS FOR IMPROVED CRUISE EFFICIENCY OF LONG-RANGE AIRCRAFT

Paul L. Coe, Jr., and Paul G. Fournier
NASA Langley Research Center

SUMMARY

The present paper summarizes results of recent studies conducted at the NASA Langley Research Center to explore the use of powered-lift concepts for improved low-speed performance of long-range subsonic and supersonic cruise vehicles. The results indicate that powered lift can provide significant improvements in low-speed performance, as well as substantial increases in cruise efficiency and range for both subsonic and supersonic cruise configurations.

INTRODUCTION

The NASA Langley Research Center is currently investigating the use of powered-lift concepts for improved low-speed performance of long-range subsonic and supersonic cruise aircraft. This research has been directed toward concepts which may provide substantial increases in lift for improved take-off and landing performance and, further, which may provide better engine-airframe matching for improved cruise efficiency and range.

The present paper summarizes results of recent studies of powered-lift concepts, conducted in the Langley V/STOL and full-scale tunnels. In particular, the paper discusses (1) the application of the over-the-wing blowing (OTWB) concept to an advanced subsonic cruise configuration and (2) the application of OTWB and thrust vectoring concepts to an advanced supersonic cruise configuration.

SYMBOLS

C_L	lift coefficient
$C_{L,\Gamma}$	additional circulation lift
C_m	pitching-moment coefficient
C_μ	thrust coefficient
D	engine nozzle diameter (see fig. 5)

h	height of engine nozzle above wing (see fig. 5)
i_c	incidence of canard
S	wing area
S_t	tail area
T	thrust
W	aircraft weight
α	angle of attack
δ_f	flap deflection angle

Abbreviations:

BLC	boundary-layer control
OTWB	over-the-wing blowing
USB	upper-surface blowing

POTENTIAL BENEFITS DERIVED FROM POWERED-LIFT CONCEPTS

One of the fundamental considerations in the design of a cruise efficient aircraft is the sizing of the configuration with regard to wing area and installed thrust requirements. It is recognized that the sizing process involves considerable compromise, and that low-speed performance plays a key part in the trade-off.

Presented in figure 1 is a classical "thumb print" plot which shows the variation of range with installed thrust-to-weight ratio T/W and wing loading W/S. Also shown in this figure is a typical take-off field length constraint which emphasizes the impact that low-speed performance has on engine-airframe sizing. The important point illustrated by figure 1 is the fact that for a specified configuration, optimum range is obtained with relatively low values of T/W and relatively high values of W/S, and that increasing T/W or reducing W/S from the optimum values in order to meet the take-off field length requirement results in a substantial reduction in vehicle range (or in an increase in aircraft weight, cost, and fuel consumption to achieve a given range).

Figure 2 illustrates the influence of take-off lift coefficient, T/W, and W/S on take-off field length requirements. This relationship was obtained from an empirical study and is discussed in detail in reference 1.

2.2

From figure 2 it is seen that a specified take-off field length can be obtained, with relatively low values of T/W and relatively high values of W/S, provided that sufficiently high values of take-off lift coefficient can be obtained. Therefore, the successful application of powered-lift concepts, which yield improved low-speed performance, will allow acceptable take-off field lengths to be obtained with values of T/W and W/S sized to obtain optimum cruise efficiency.

POWERED-LIFT CONCEPTS INVESTIGATED

The powered-lift concepts considered herein are described and discussed individually. Although the details differ, the fundamental consideration is the same for both subsonic and supersonic cruise vehicles; namely, to allow the wing area and installed thrust to be sized to provide optimum cruise efficiency while using powered-lift concepts to meet the low-speed operational requirements associated with conventional aircraft.

One particularly promising powered-lift concept, which may have near-term applications for long-haul subsonic transports, is over-the-wing blowing (OTWB). Figure 3 shows a photograph and a sketch of the concept applied to a subsonic transport configuration with an aspect-ratio-7.48 wing and a leading-edge sweep of 33.6°. The configuration is equipped with four, pylon-mounted, upper-surface engines with deflectable exhaust nozzles. Reference 2, which combined the analytical results of reference 3 and the experimental results of references 4 and 5, has shown that the OTWB concept with undeflected exhaust nozzles can provide substantial reductions in induced drag. The reduction in induced drag is provided by the jet exhaust which induces an upwash on the wing. The upwash rotates the wing force vector forward and effectively produces a negative increment in induced drag. Therefore, if it is possible to produce additional circulation lift by deflection of the exhaust flow downward onto the wing surface during take-off and landing, such an arrangement would provide not only improved low-speed performance but also improved cruise performance.

As was mentioned previously, powered-lift concepts have also been applied to supersonic cruise vehicles. Figure 4 shows a photograph of a large-scale advanced supersonic cruise arrow-wing configuration which has an aspect ratio of 1.72 and an inboard leading-edge sweep of 74°. The powered-lift concepts investigated for improved low-speed performance of this configuration are also sketched in figure 4 and include (1) boundary-layer control (BLC) for enhanced flap effectiveness and prevention of flow separation at high flap deflections, (2) OTWB for additional circulation lift (this concept also has another advantage in that the trailing-edge flap system may be continuous, rather than the segmented system necessitated by the use of the conventional underslung engines), and (3) thrust vectoring which provides increased lift by a combination of the direct vector component of thrust and by the additional circulation lift produced by flow entrainment.

LIFT CHARACTERISTICS

Subsonic Cruise Vehicles

Figure 5 shows the variation of additional circulation lift $C_{L,\Gamma}$, obtained with the OTWB concept, as a function of the ratio of the height of the engine above the wing to the engine diameter h/D. The data are presented for $\alpha = 0^{\circ}$ and $\delta_f = 45^{\circ}$. It should be noted that the exit nozzle deflection varied with h/D so that the jet would impinge at approximately the same chordwise location. From figure 5 it is seen that, as with other powered-lift concepts, relatively small values of thrust coefficient C_μ result in significant levels of additional circulation lift and that further increases in C_μ result in more gradual increases in $C_{L,\Gamma}$. Furthermore, from figure 5 it can be seen that there is only a slight increase in $C_{L,\Gamma}$ as h/D is increased from 0.5 to 1.0.

Figure 6 presents a comparison of the lift characteristics obtained for the OTWB concept with those for an upper-surface blowing (USB) concept applied to a configuration comparable with that used in the OTWB investigation (see ref. 6). The USB concept used rectangular exhaust nozzles having as aspect ratio of 6. On the basis of a comparison of the data for the OTWB and USB concepts, it would appear that both concepts produce essentially the same level of additional circulation lift. However, the reduction in induced drag provided by the OTWB concept in the cruise configuration indicates that such a configuration may have a higher level of cruise efficiency than a configuration with the USB concept.

In light of these considerations, the NASA Langley Research Center will be conducting tests with a large-scale model of the advanced OTWB subsonic transport configuration shown in figure 7. The configuration uses a supercritical airfoil with an aspect-ratio-12 wing and is designed for efficient cruise at Mach numbers of about 0.8. During the take-off and landing phases of flight, the exhaust is deflected downward onto the wing surface to provide the desired high lift for improved low-speed performance.

Supersonic Cruise Vehicles

Figure 8 summarizes the improvements in lift obtained with the various powered-lift concepts investigated for the advanced supersonic cruise vehicle. From figure 8 it is seen that the increment in lift provided by the plain trailing-edge flap is reduced for flap deflections above 20°, as a result of flow separation at the higher flap deflections. As would be expected, the application of BLC provides enhanced flap effectiveness and eliminates flap stall for flap deflections up to 40°. Figure 8 also shows that thrust vectoring provides an additional increment in lift; however, this increment was limited to the vector component of thrust. The fact that thrust vectoring failed to provide additional circulation lift is attributed to the relatively far aft position of the exhaust nozzles for the particular engine location considered. The data show further that the OTWB concept provides substantial additional increases in lift. This result is attributed to the continuous

trailing-edge flap system, permitted by the upper-surface-mounted engines, and the additional circulation lift produced by the concept.

The potential benefits obtainable from the application of powered-lift concepts to the supersonic cruise vehicle are illustrated in figure 9. The relatively low value of lift curve slope, associated with the low-aspect-ratio, highly swept, arrow wing, and the tail scrape angle are seen to constrain the take-off lift coefficient of the basic concept to values of only about 0.55. Furthermore, the relatively high angle of attack associated with this lift coefficient results in substantial drag which penalizes the low-speed performance. In addition, the relatively high rotation angle requires the use of a visor nose for acceptable pilot visibility and also requires an elongated landing gear installation which results in a weight and volume penalty.

Results of airframe-engine sizing studies have indicated that significant improvements in supersonic cruise efficiency and range can be obtained by reducing the wing size of this configuration by about 25 percent. Therefore, to obtain acceptable take-off field lengths, the resized vehicle would require approximately a 25-percent increase in lift coefficient, which corresponds to $C_L \approx 0.7$.

Figure 9 shows that thrust vectoring in combination with BLC provides the desired lift coefficient of 0.7 at $\alpha \approx 6^o$, whereas OTWB and BLC provides a lift coefficient of 0.7 at $\alpha \approx 1.5^o$. The use of OTWB or thrust vectoring therefore permits operation at reduced angle of attack which would result in a significant reduction in drag and thereby provide improved low-speed performance. Furthermore, the reduced angle of attack would allow a reduction in landing gear length and may also eliminate the requirement for a visor nose, both representing a significant weight savings. However, the most significant point is that with the increased value of lift, the wing size can be reduced toward the optimum size for increased supersonic range while maintaining acceptable take-off and landing performance.

It should be noted that the OTWB concept appears to provide better low-speed performance than the particular thrust vectoring concept investigated. However, it is considered that, through proper design, the thrust vectoring concept might be as efficient as the OTWB concept and that the thrust vectoring concept may offer some advantages over other high-lift concepts for achieving improved lateral control. For example, one promising thrust vectoring concept which uses a two-dimensional exit nozzle design is illustrated in figure 10. Such an arrangement should provide improved powered-lift characteristics and also allow significant, and needed, improvements in roll control by the introduction of differential thrust vectoring.

LONGITUDINAL TRIM

It should be noted that the data presented in the previous section correspond to untrimmed values of lift coefficient, and that extremely large nose-down pitching moments accompany the increases in lift provided by the powered-lift concepts. The problem of providing pitch trim for subsonic transport

configurations has been discussed in reference 7; therefore, the present discussion is limited to the problem of providing pitch trim for supersonic cruise vehicles.

Figure 11 shows the pitching moments produced by application of powered-lift concepts to the supersonic cruise vehicle. Relative merits of various means for providing pitch trim have been investigated for this configuration and the results are presented in figure 12. The analysis was conducted for a trim lift coefficient of 0.7 and a static margin $\left(dC_m/dC_L\right)$ of 3 percent. As would be expected, the use of a conventional aft tail for trim requires a download, whereas the canard concepts require an upload. Furthermore, both the conventional aft tail and the fixed canard require relatively high values of tail lift coefficient $\left(C_{L,tail}\right)$ and would therefore probably require a sophisticated high-lift system.

It is possible to achieve the favorable upload of the canard and to eliminate the requirement for a high tail lift coefficient by introducing a gearing arrangement which provides artificial stability by driving the canard surface so that the canard angle of attack is reduced as the aircraft angle of attack is increased. It should be pointed out that the geared canard requires the lowest lift coefficient per tail area ratio $\left(S_t/S\right)$ and may not require the sophisticated high-lift devices which would be associated with either the fixed canard or the conventional aft tail.

CONCLUDING REMARKS

The application of powered-lift concepts to advanced long-range subsonic and supersonic cruise vehicles appears promising for providing significant improvements in low-speed performance. The increased lift provided by the powered-lift concepts allows a reduction in both wing size and installed thrust requirements which yields a better engine-airframe match for improved cruise efficiency and range. The powered-lift benefits appear to be particularly significant for the supersonic cruise vehicle because of the inherently poor low-speed lift characteristics associated with the low-aspect-ratio, highly swept wing required for supersonic flight.

REFERENCES

1. Weirich, Robert L.: Analytical Determination of the Take-Off Performance of Some Representative Supersonic Transport Configurations. NASA TN D-2308, 1964.

2. Bower, Robert E.: Opportunities for Aerodynamic-Drag Reduction. NASA/University Conference on Aeronautics, NASA SP-372, 1975, pp. 323-352.

3. Putnam, Lawrence E.: An Analytical Study of the Effects of Jets Located More Than One Jet Diameter Above a Wing at Subsonic Speeds. NASA TN D-7754, 1974.

4. Putnam, Lawrence E.: Exploratory Investigation at Mach Numbers From 0.40 to 0.95 of the Effects of Jets Blown Over a Wing. NASA TN D-7367, 1973.

5. Ewald, B.: Airframe-Engine Interaction for Engine Configurations Mounted Above the Wing. Part II: Engine Jet Simulation Problems in Wind Tunnel Tests. Airframe/Propulsion Interference, AGARD-CP-150, Mar. 1975, pp. 26-16 - 26-32.

6. Sleeman, William C., Jr.; and Hohlweg, William C.: Low-Speed Wind-Tunnel Investigation of a Four-Engine Upper Surface Blown Model Having a Swept Wing and Rectangular and D-Shaped Exhaust Nozzles. NASA TN D-8061, 1975.

7. Phelps, Arthur E., III; Johnson, Joseph L., Jr.; and Margason, Richard J.: Summary of Low-Speed Aerodynamic Performance of the Upper-Surface Blown Jet-Flap Concept Powered-Lift Aerodynamics and Acoustics, NASA SP-406, 1976. (Paper no. 4 of this compilation.)

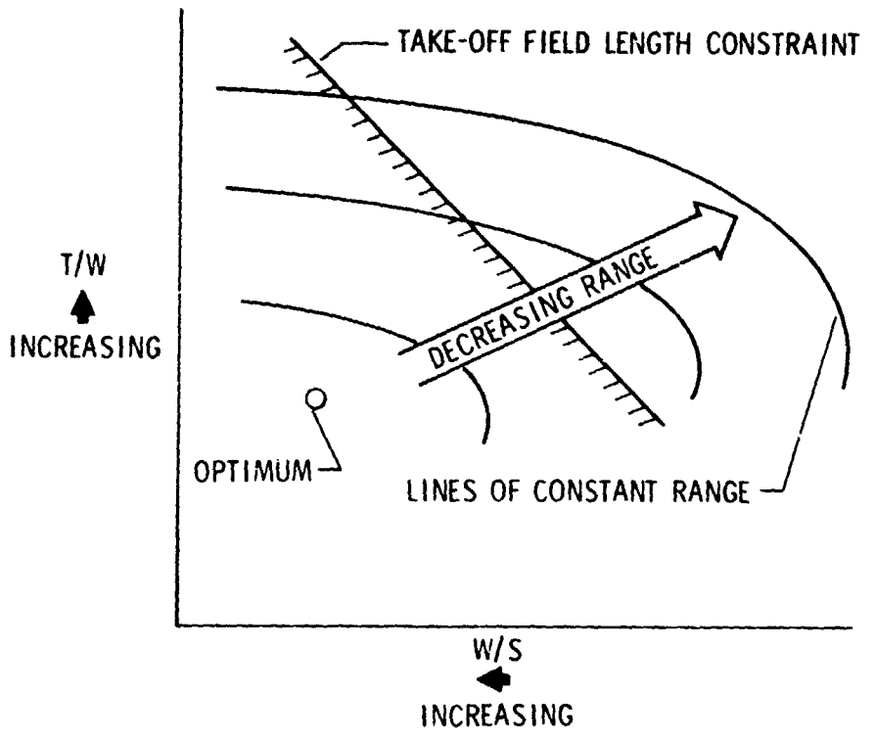

Figure 1.- Variation of range with T/W and W/S.

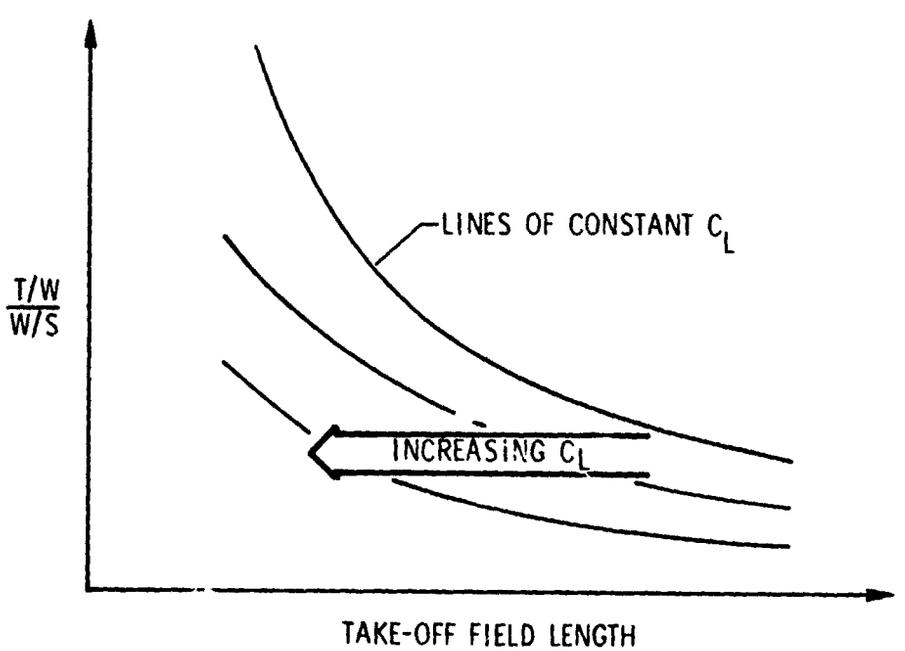

Figure 2.- Influence of C_L on take-off field length.

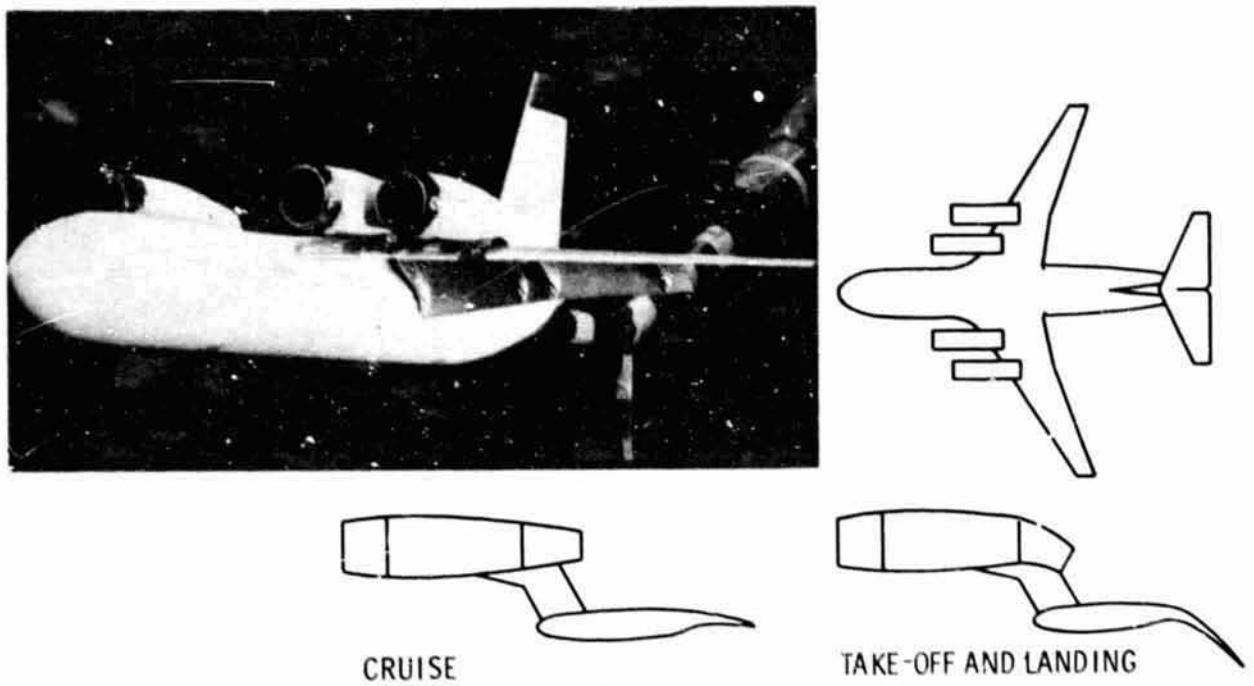

Figure 3.- OTWB concept applied to subsonic transport.

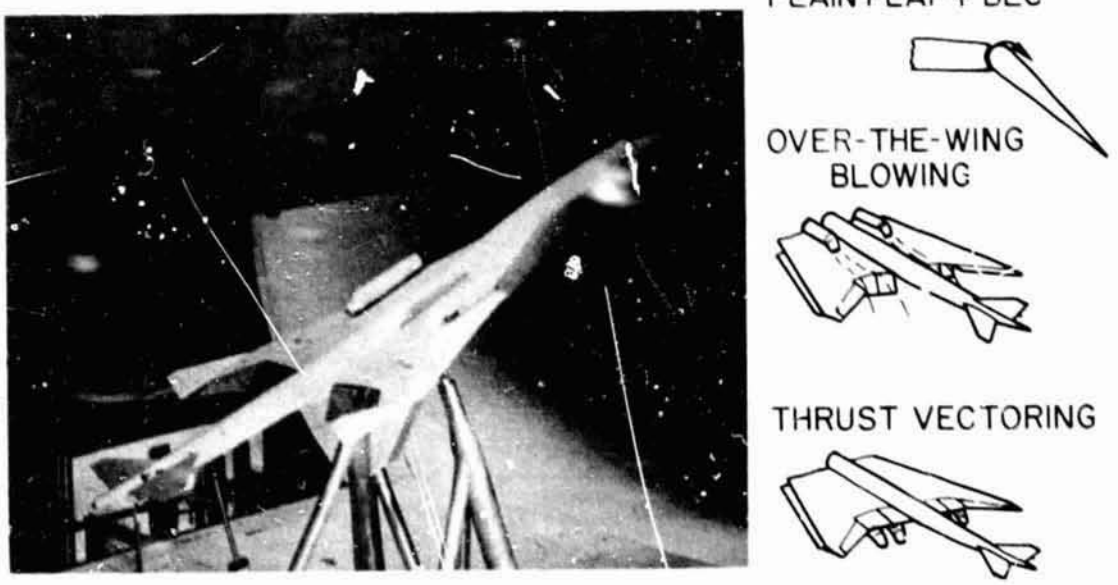

Figure 4.- Powered-lift concepts investigated for supersonic cruise configuration.

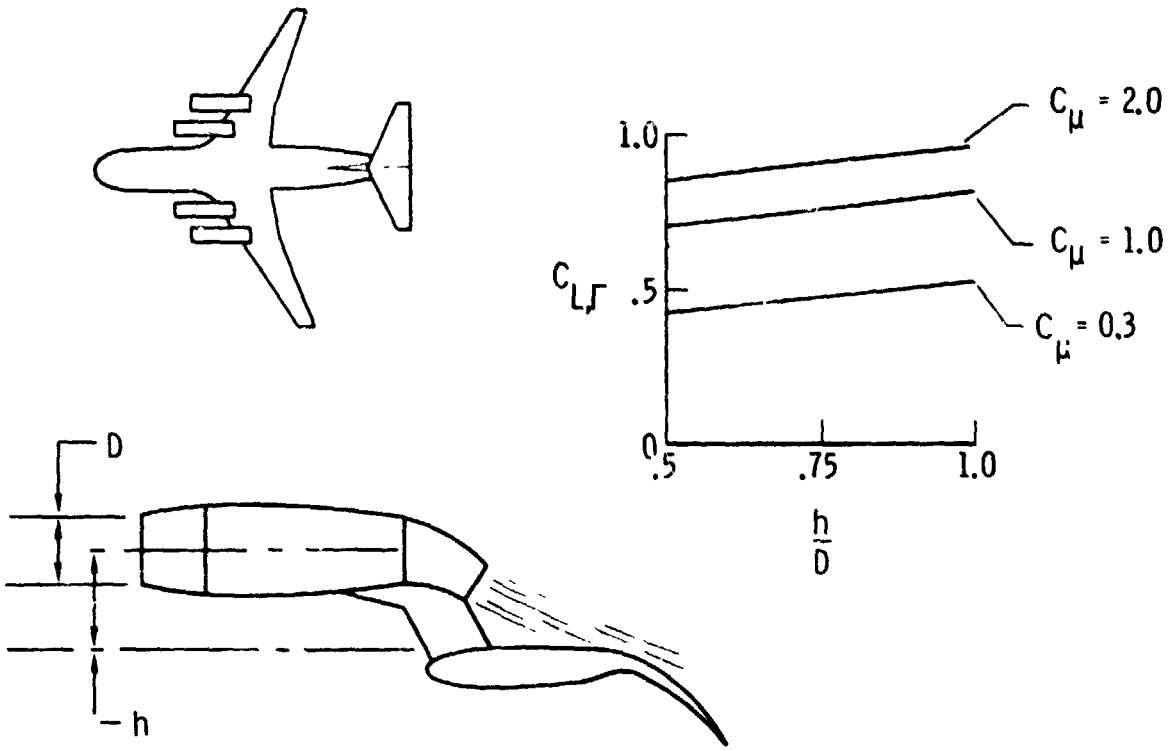

Figure 5.- Additional circulation lift produced by OTWB for subsonic cruise configuration. $\delta_f = 45°$.

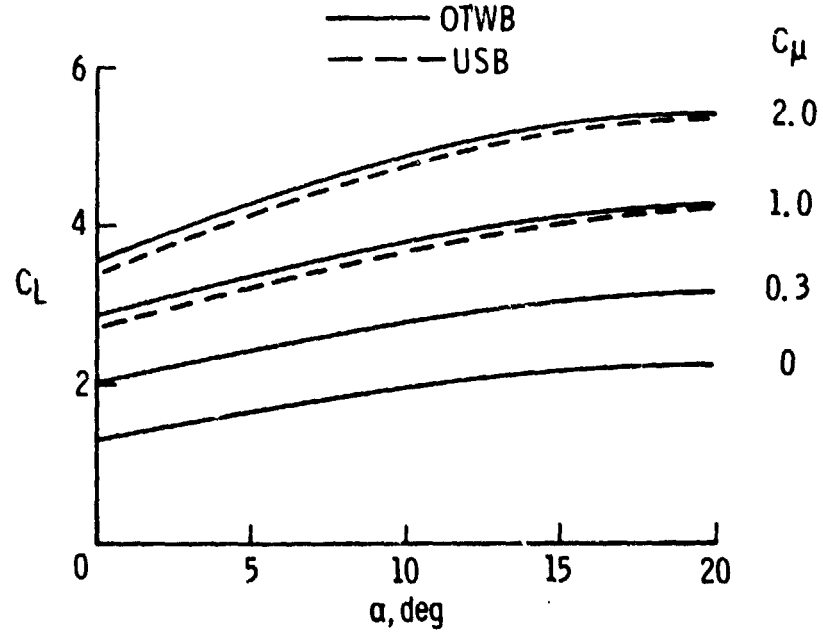

Figure 6.- Comparison of low-speed lift characteristics for OTWB and USB concepts applied to subsonic cruise configurations.

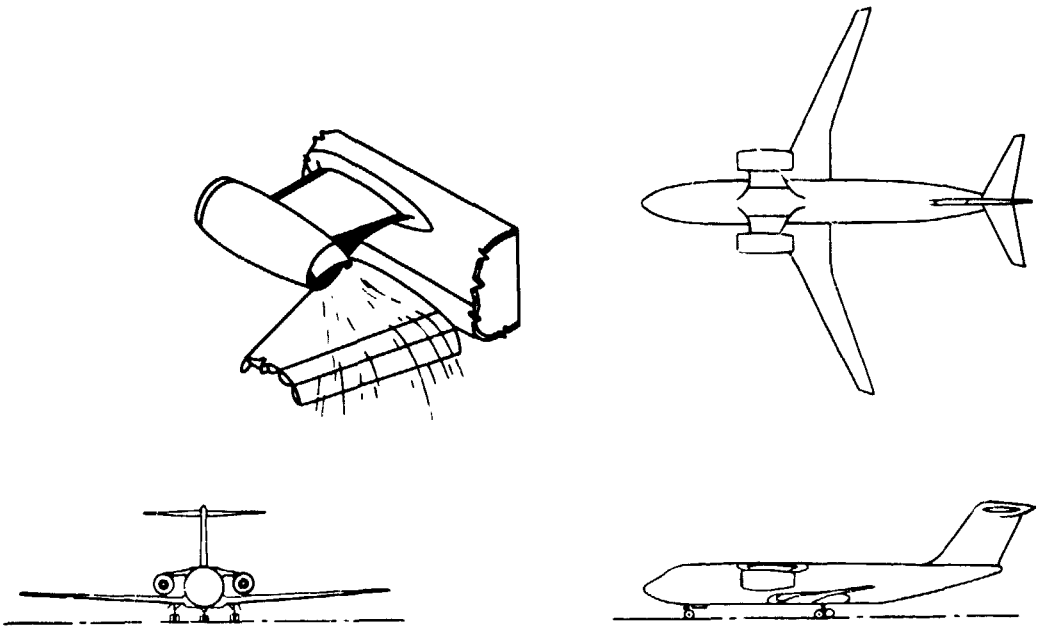

Figure 7.- Sketch of advanced long-haul subsonic transport with OTWB.

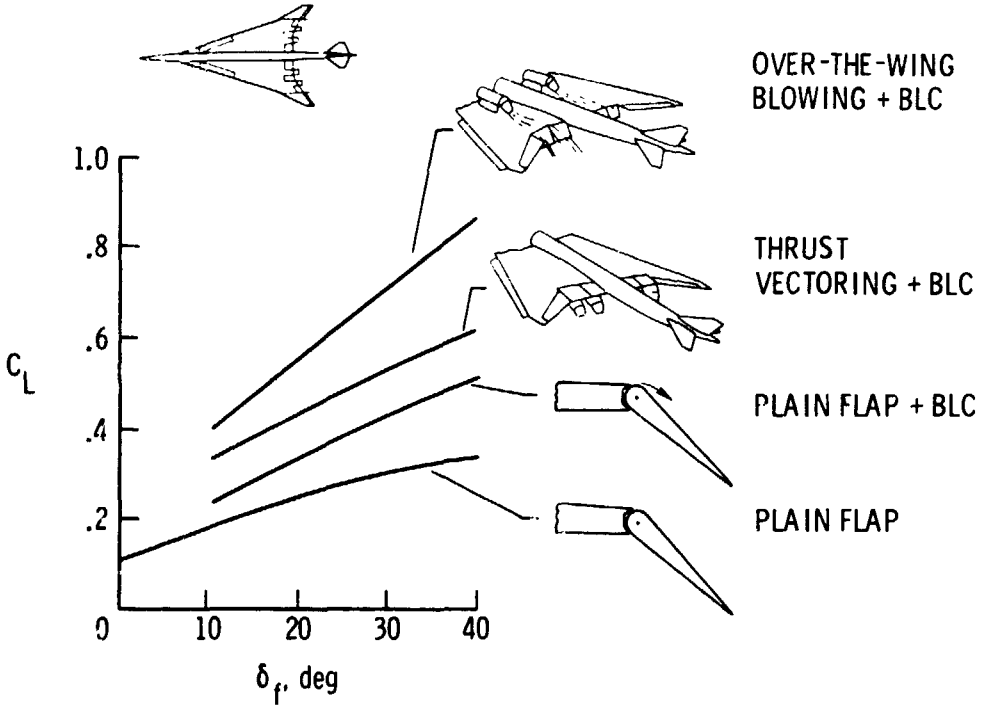

Figure 8.- Lift improvements due to powered-lift concepts for advanced supersonic cruise vehicle. $\alpha = 0^o$.

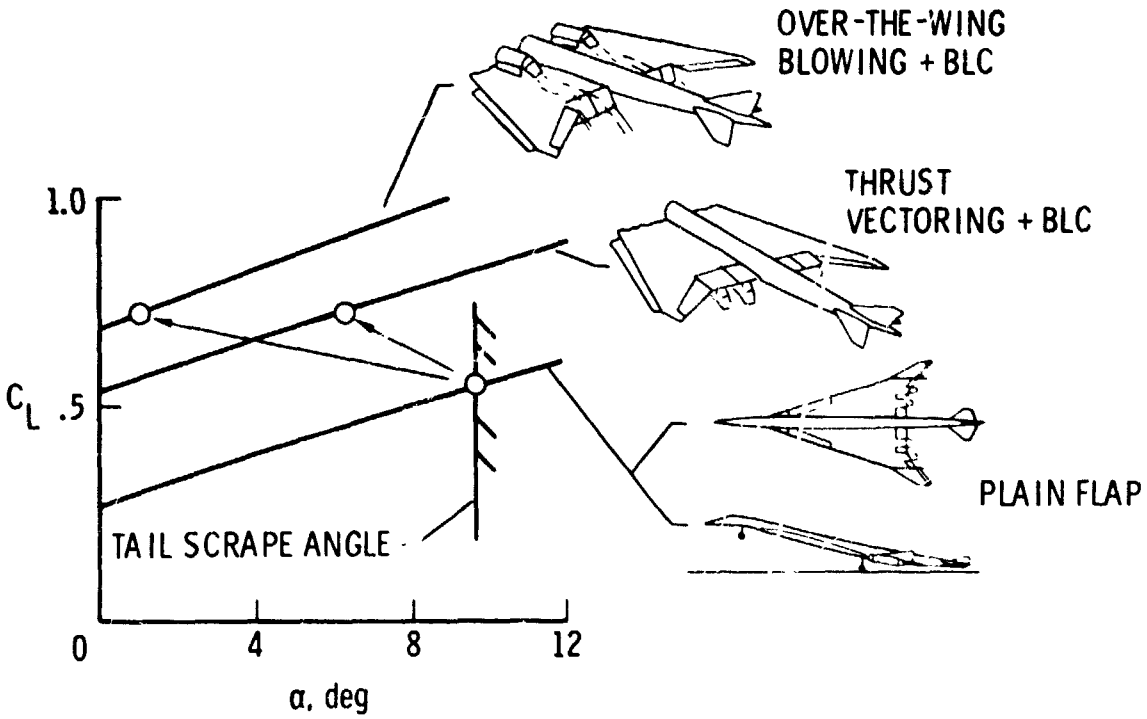

Figure 9.- Potential benefit of application of powered-lift concepts to supersonic cruise vehicle. $\delta_f = 30^o$.

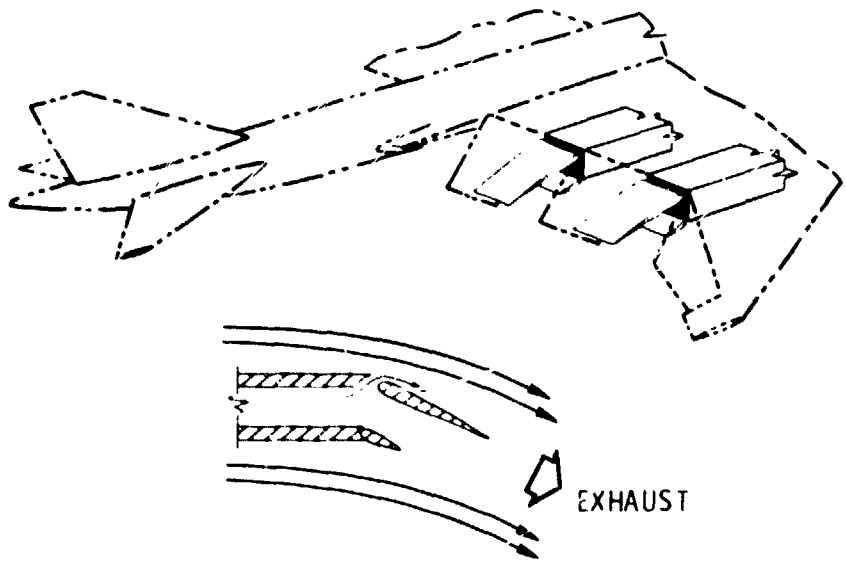

Figure 10.- Sketch of revised thrust vectoring concept for supersonic cruise vehicle.

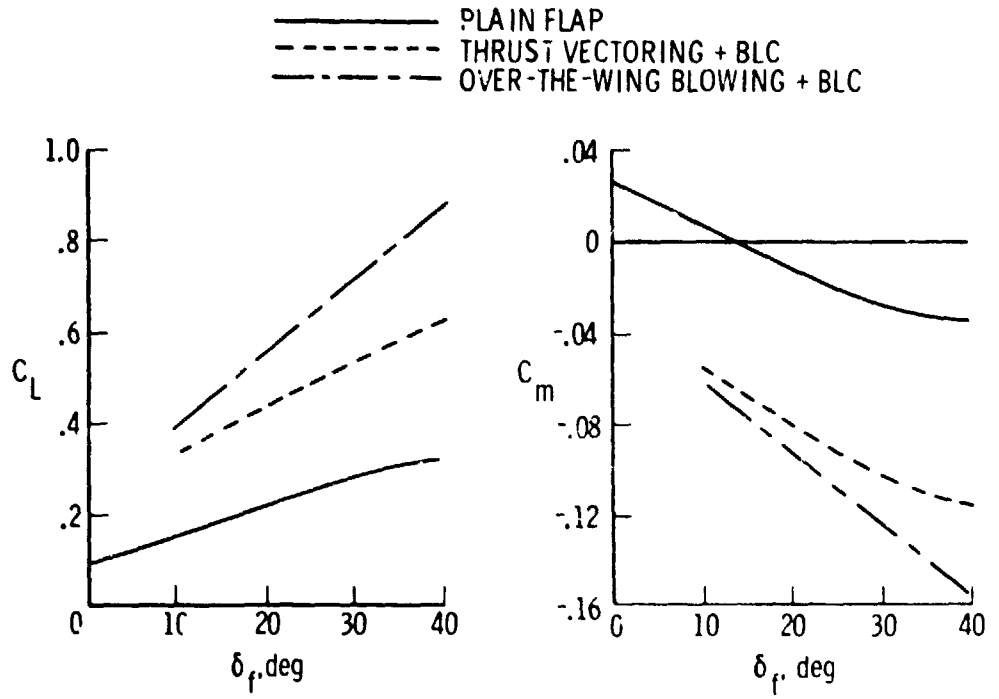

Figure 11.- Pitching moments introduced by application of powered-lift concepts to supersonic cruise vehicle. $\alpha = 0^o$.

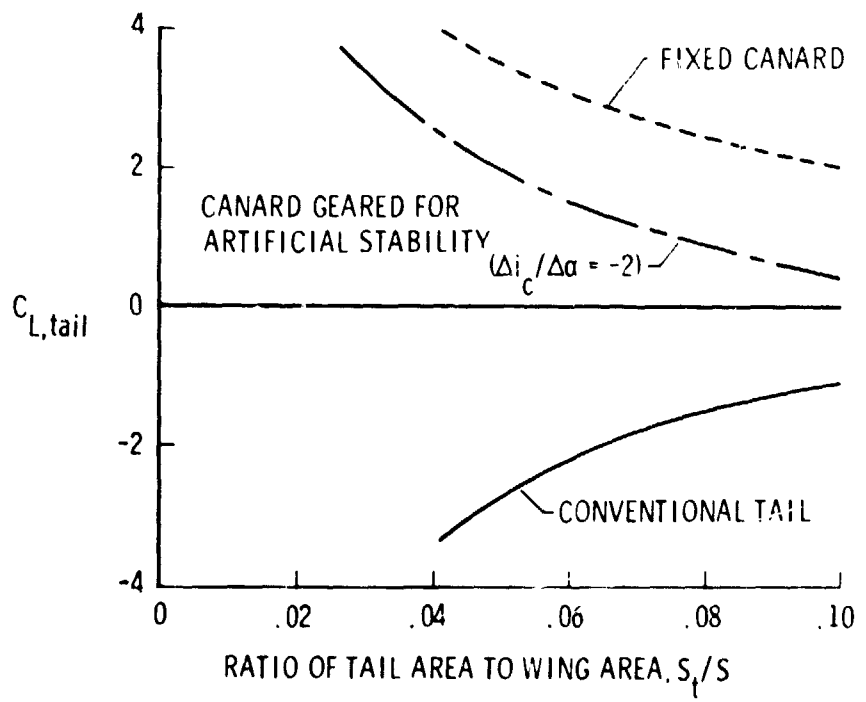

Figure 12.- Tail requirements to trim supersonic cruise vehicle. $C_L = 0.7$; 3-percent static margin.

N78-24052

COMPARISON OF AERODYNAMIC THEORY AND EXPERIMENT FOR JET-FLAP WINGS

Thomas G. Gainer, Long P. Yip, and Raymond D. Vogler
NASA Langley Research Center

SUMMARY

This paper compares aerodynamic theory predictions made for a jet-flapped wing with experimental data obtained in a fairly extensive series of tests in the Langley V/STOL tunnel. The predictions were made with the EVD (Elementary Vortex Distribution) program developed by Lopez, Shen, and Wasson at McDonnell-Douglas. The tests were made on a straight, rectangular wing and investigated two types of jet flap concepts: a pure jet flap with high jet deflection and a wing with blowing at the knee of a plain trailing-edge flap. The tests investigated full- and partial-span blowing for wing aspect ratios of 8.0 and 5.5 and momentum coefficients from 0 to about 4.

The total lift, drag, and pitching-moment coefficients predicted by the theory were in excellent agreement with experimental values for the pure jet flap, even with the high jet deflection. The pressure coefficients on the wing, and hence the circulation lift coefficients, were underpredicted, however, because of the linearizing assumptions of the planar theory. The lift, drag, and pitching-moment coefficients, as well as pressure coefficients, were underpredicted for the wing with blowing over the flap because of the failure of the theory to account for the interaction effect of the high velocity jet passing over the flap.

INTRODUCTION

Jet-flap theory is a relatively simple powered-lift theory developed by assuming that the jet exhaust that augments lift leaves the wing trailing edge at small angles as a thin sheet. The theory was first developed in two dimensions by Spence (ref. 1), then in three dimensions by Maskell and Spence and others. (See ref. 2.) More recently, lifting-surface programs patterned after those for conventional wings have been developed that can predict chordwise and spanwise loadings for complex wing planforms and arbitrary distributions of momentum coefficient and jet deflection. These programs include the EVD (Elementary Vortex Distribution) program (ref. 3) and the Vortex-Lattice Program for Jet-Flapped Wings (ref. 4).

Although the basic assumptions somewhat restrict the theory, it could have important applications. Designers are examining the jet-flap concept, for example, in connection with the two-dimensional nozzles being considered for

advanced supersonic aircraft. These nozzles would be mounted at the trailing edge of the wing and could be deflected to provide lift augmentation - either to improve performance or, in the case of fighters, to improve maneuvering; since these nozzles spread the exhaust into a fairly thin sheet, jet-flap theory would apply in their design. For many STOL applications, flow conditions may be outside the strict limitations of the theory; nevertheless, there are indications jet-flap theory could be used. Although the theory is based on small-disturbance concepts, the theory predictions have agreed for some cases with test data at high deflections. Jet-flap theories have also predicted aerodynamic characteristics of other configurations such as the augmentor wing and the externally blown flap (ref. 5).

The different applications of the theory have not been examined in detail, however, nor have the theories themselves been verified to any great extent because the necessary experimental data have not been available. For most of the powered-lift data available, the distributions of momentum coefficient and jet-deflection angle are not defined well enough to use in theory predictions. The data that have these distributions defined are limited to just a few blowing spans and jet deflections. Detailed pressure distributions are not generally available for comparison with theoretical predictions.

To provide some of the necessary data, Langley Research Center conducted a series of wind-tunnel tests that investigated a fairly wide range of jet-flap parameters. This paper compares predictions made with a representative jet-flap theory, namely the EVD theory (ref. 3) with these experimental data. The test model had a straight, untapered wing. It was tested with two powered-lift configurations which, while they do not quite agree with the assumptions of the theory, would be of interest in STOL applications. In one configuration the wing was equipped with a pure jet flap with high jet deflection, whereas in the other, the wing was equipped with blowing over a plain trailing-edge flap. Partial- and full-span blowing and two wing aspect ratios (8.0 and 5.5) were investigated. The model was tested through an angle-of-attack range from about -4° to 20° at momentum coefficients from 0 to about 4.

SYMBOLS

A	aspect ratio
a_{ij}	influence coefficient relating vorticity at a point j to downwash at a point i
b	span
C_D	net drag coefficient, based on model drag minus component of model thrust in drag direction
C_L	lift coefficient
$C_{L,jr}$	jet-reaction lift coefficient

$C_{L\Gamma}$	circulation lift coefficient
C_m	pitching-moment coefficient (referred to the wing apex)
C_μ	jet-momentum coefficient
c	wing chord
c_p	section pressure coefficient
Δc_p	difference between upper and lower surface pressures
c_μ	section jet-momentum coefficient
F_A	axial force
F_N	normal force
K	constant in thickness correction factor
k	thickness correction factor
S	wing area, m^2 (ft^2)
S_b	blown area of wing (blown span times wing chord), m^2 (ft^2)
t/c	wing thickness-chord ratio
T	thrust
w_i	induced downwash at a control point i
x	chordwise distance
y	spanwise distance
α	angle of attack, deg
γ	vorticity
δ_f	flap deflection, deg
δ_j	jet turning angle, deg
η	thrust efficiency factor; actual thrust divided by nominal calibrated thrust

MODEL AND APPARATUS

The test model is shown in the Langley V/STOL tunnel in figure 1. The fuselage was designed small enough to have negligible effect on the wing aerodynamic characteristics, yet large enough to contain the model balance, pressure gages, and associated tubing required in the tests.

Figure 2 shows some of the wing details. The wing had a 25.4-cm (10 in.) chord and an NACA 0018-64 airfoil section. It was tested as an aspect-ratio-8.0 wing (2.03-m (80 in.) span) with blowing over the full span, two-thirds of the span, or one-third of the span; then the outboard one-third of the wing was removed and it was tested as an aspect-ratio-5.5 wing (1.02-m (40 in.) span) with full- or half-span blowing. The leading-edge slat shown was used to prevent separation at the leading edge at high angles of attack and high jet deflections. Air for blowing was provided by the tunnel high-pressure air supply which was brought in through the sting.

For the pure jet flap (fig. 2), the wing remained in its basic airfoil shape, with the trailing edge undeflected, and air was ejected from a slot on the lower surface at the trailing edge. The air was ejected at an angle of approximately 60° with respect to the wing chord line.

For blowing over the flap (fig. 2), the part of the wing containing the jet flap was removed and replaced with a 25-percent-chord deflectable plain flap. A "slot" at the knee of the flap, consisting of 300 holes 0.159 cm (0.063 in.) in diameter and equally spaced along the span, provided the air for blowing. The flap was divided into three spanwise segments for different amounts of partial-span blowing, and only the flap segment along the blowing span was deflected. For example, with 1/3-span blowing, only the inboard 1/3-flap segment was deflected and the remaining two outboard segments were undeflected. Flap deflections of 0°, 15°, 30°, 45°, and 60° were investigated.

Model forces and moments were measured with a six-component strain-gage balance. Static pressures were measured at six spanwise stations on the right wing panel $\left(\frac{y}{b/2} = 0.15, 0.30, 0.45, 0.60, 0.78, \text{ and } 0.93\right)$ and, as a check on symmetry, at one station $\left(\frac{y}{b/2} = 0.30\right)$ on the left panel. There were 31 orifices on the wing at each station - 19 on the upper surface and 12 on the lower surface.

THEORETICAL CALCULATIONS

The theoretical calculations were made with the Elementary Vortex Distribution (EVD) program described in reference 3. The EVD program is a lifting-surface program that represents the wing and jet wake with a vortex sheet of varying intensity. The vortex strength on the wing is determined by satisfying the tangent flow boundary condition on the wing. This is done by setting the sum of the induced velocities w_i (fig. 3) equal to the components of

free-stream velocity normal to the wing surface so there can be no flow through the wing surface. The vorticity along the jet wake is determined by using the basic Spence relationship that expresses vorticity in terms of section momentum coefficient and the change in induced downwash with respect to downstream distance as follows:

$$\gamma_i = -\frac{cC_\mu}{2}\frac{\partial w_i}{\partial x}$$

The program has been linearized by assuming small perturbations and that all vorticity lies in the plane of the wing. The boundary conditions have been projected back to the plane of the wing. The camber, twist, and jet-deflection angles are assumed to be small.

The EVD program adds a degree of sophistication to the basic vortex scheme by assuming a continuously varying chordwise vorticity constructed from different types of basic vortex elements. The EVD uses overlapping triangular elements to obtain a linearly varying vorticity between two points on the wing, a square-root singularity at the leading edge, and logarithmic singularities at the flap hinge line and at the trailing edge where the jet exits from the wing. An "infinity" EVD, for which the vorticity goes to zero as one over the square of downstream distance, is used to represent the trailing jet sheet far downstream.

The EVD program accounts for wing camber and twist and allows for a trailing-edge flap, but the assumption is made that the jet is emerging from the trailing edge of the flap, not from a point on the upper surface of the wing. The program assumes a thin wing; however, thickness effects can be accounted for by multiplying circulation lift and wing pressure coefficients by the following correction factor:

$$k = 1 + K\frac{S_b}{S}\frac{t}{c}$$

where the constant K is usually taken to be 0.8 for airfoils with sharp trailing edges and 1.0 for cusped airfoils. The correction factors used varied from 1.144 with full-span blowing to 1.048 with 1/3-span blowing.

In making the EVD calculations, EVD elements were placed at 20 spanwise stations along the semispan for the aspect-ratio-8 wing and at 16 spanwise stations for the aspect-ratio-5.5 wing. There were six chordwise elements on the wing and five on the jet.

The momentum coefficient and jet-deflection angles needed to make the calculations were determined by static calibration, as shown in figure 4. For the blown-flap wing, a nominal thrust was first determined by calibrating the thrust at the blowing slot with the flap off. Then, with the flap on, force components were measured normal to and along the wing chord line and resolved into a

resultant force. An efficiency factor η, which is the ratio of the actual or resultant thrust to the nominal thrust, was then determined, as was the jet deflection or turning angle δ_j, which is the angle between the resultant thrust and the wing chordline. The wing with blowing over the flap had efficiencies varying from about 0.85 at $\delta_f = 0^o$ to between 0.75 and 0.79 at $\delta_f = 60^o$. The turning angle with blowing over the flap was about equal to the angle of the flap upper-surface deflection $(\delta_f + 13.5^o)$. The pure jet flap was calibrated the same way as the blown flap, except that it was calibrated with the jet flap in place so that the nominal thrust was equal to actual thrust and its efficiency factor was 1.0. The static results show that the jet-deflection angle for the pure jet flap was between 61^o and 63^o. In the calculations, the momentum coefficient and jet-deflection angles were assumed to be uniformly distributed over the blowing span.

RESULTS AND DISCUSSION

Pure Jet Flap

Comparison of total lift, drag, and pitching moment.- The lift, drag, and pitching-moment comparisons shown in figures 5, 6, and 7 indicate excellent agreement between theory and experiment for the pure-jet-flap wing. The results for full-span blowing with the aspect-ratio-8 wing $(\delta_j = 61.4^o)$ are given in figure 5; the results with 1/3- and 2/3-span blowing for this wing are given in figures 6 and 7, respectively. Except at $C_\mu = 0$, the theoretical predictions generally agreed closely with experiment through the C_μ range for the three blowing spans.

The poor agreement at $C_\mu = 0$ was caused by the fact that there was a good deal of separated flow on the wing without blowing. The leading-edge slat interfered with the flow at low angles of attack, and the flow was separated around the trailing edge at all angles of attack because the airfoil was relatively thick (t/c = 0.18). Just a moderate amount of blowing cleaned up the separated flow so that the theory was brought into close agreement with the experimental data.

The theory slightly underpredicted the lift at $C_\mu = 3.9$, but this disagreement between theory and experiment was not typical; data for other configurations showed good agreement at high C_μ. The fact that the agreement was as good as it was validates the thickness correction that was applied to the lift coefficients estimated by the thin-wing theory. Without this correction, the predicted lift coefficients would be noticeably lower than experiment throughout the C_μ range.

The drag coefficients shown are based on the net force in the drag direction measured by the model balance and, therefore, include the model thrust. The profile drag coefficient of the model (the value where the $C_\mu = 0$ curve intersects the $C_L = 0$ axis) was about 0.07, which was very small compared with the overall

level of drag being measured. Most of the drag developed was induced drag, and the results indicate the theory was able to predict the induced drag very accurately. The fact that the theory assumed 100-percent suction and gave good drag prediction indicates that the wing was experiencing full thrust recovery. Results for the aspect-ratio-5.5 wing are not presented, but there was excellent agreement between theory and experiment for this wing also.

Comparison of force components.- The fact that the theory gave good predictions of total force and moment coefficients at the high jet deflection, even though it has been linearized and assumes small jet-deflection angles, is consistent with some of the previous results for the jet flap, which also show good agreement with test data at high jet deflections. (See, for example, Spence's two-dimensional comparisons in reference 1 and also comparisons for an augmentor wing in reference 5.) This good agreement can be explained by examining the components of the forces and moments. It can be shown that while the predicted total forces and moments agreed with experiment, the components of the forces and moments did not agree. The following table compares the theoretical and experimental components of lift coefficient for the 2/3-span blowing case at a C_μ of 3.9 $(\eta C_\mu = 3.6)$ and $\alpha = 0^\circ$. The components shown (for no flap deflection and $\alpha = 0^\circ$) are the jet-reaction lift coefficient $C_{L,jr}$, which is the lift coefficient due to the thrust acting at the trailing edge, and the circulation lift coefficient C_{L_Γ}, which is the lift coefficient obtained by integrating the pressure distributions on the wing.

	C_{L_Γ}	$C_{L,jr}$	C_L
Planar theory	2.32	3.88	6.20
Experiment	3.15	3.17	6.32

Whereas the total lift coefficients agree within about 2 percent, the small-angle theory overestimates the jet-reaction lift coefficient: the small-angle value for $C_{L,jr}$ is $\eta C_\mu \delta_j$ (δ_j in radians), whereas the true jet-reaction lift coefficient is $\eta C_\mu \sin \delta_j$. The planar theory, on the other hand, will underestimate the circulation lift, and hence, the pressure distribution on the wing.

Comparison of pressure distributions.- The pressure distributions in figure 8 show the extent to which the linear theory underestimates the pressures on the wing, and hence, the circulation lift developed. Pressure distributions in figure 8 are for the pure-jet-flap wing with 2/3-span blowing at a C_μ of 3.9. The plots shown give the net pressure difference Δc_p between the upper and lower surfaces as a function of nondimensional chordwise distance along the wing. (In the EVD calculations $\Delta c_p = 2\gamma$, where γ is the vorticity at a given point.) The theoretical pressure distributions shown have been corrected for wing thickness effects. The pressure distributions are given for three spanwise stations; the two inboard stations have blowing, the one outboard

station has no blowing. It is seen that the theory underpredicts the pressures at the two inboard stations for which there is blowing $\left(\frac{y}{b/2} = 0.15 \text{ and } 0.45\right)$ but is in good agreement with experiment at the outboard station $\left(\frac{y}{b/2} = 0.78\right)$ where there is no blowing.

The lower wing pressures predicted by the theory can be attributed to the high jet deflections involved and to the fact that the theory satisfies boundary conditions in the plane of the wing rather than on the jet wake (see fig. 3). The effect of these planar assumptions is demonstrated by the results of a two-dimensional study in figure 9. Figure 9 shows pressure distributions calculated with a program developed by Clever (ref. 6) for a flat-plate two-dimensional wing with $C_\mu = 3.5$ and $\alpha = 0^\circ$. The nonplanar theory was developed without making linearizing assumptions; the planar theory assumes small angles and that vorticity lies in the plane of the wing. The comparisons show that at $\delta_j = 10^\circ$, there is no difference between the nonplanar and planar theories; at $\delta_j = 30^\circ$, which is about the limit of the small-angle assumptions, small differences start to appear. At $\delta_j = 60^\circ$, the linearized planar theory gives lower pressures than the nonplanar theory, particularly close to the wing trailing edge.

At both $\delta_j = 10^\circ$ and $\delta_j = 30^\circ$, the total as well as the components of lift coefficient were about the same for the nonplanar and planar theories. The table in figure 9 compares these lift coefficients at $\delta_j = 60^\circ$ and shows that, as was the case for the three-dimensional planar theory and experiment, total lift coefficient was about the same for the planar and nonplanar theories, even though the components did not agree. The planar theory overestimated the jet-reaction lift, but compensated for it by underestimating the circulation lift by about the same amount.

Wing With Blowing Over the Flap

Comparison of total lift, drag, and pitching moment.- Lift, drag, and pitching moments for the wing with blowing over the trailing-edge flap are shown in figure 10. The results are for the aspect-ratio-8 wing, full-span blowing, and $\delta_f = 30^\circ$. They are typical of those for all blown-flap configurations in that they show the theory consistently underestimated the lift and pitching moments for this wing throughout the C_μ range. The predicted lift-drag curves were in good agreement with experiment, but the drag at a given angle of attack was substantially lower for the theory than for experiment.

These results indicate there is a substantial interaction effect due to the jet exhaust passing over the flap that was not accounted for in the theory, which assumes the jet exhaust emerges from the trailing edge of the wing. This is substantiated by the pressure distributions for the blown-flap wing as described in the following section.

Comparison of pressure distributions.- Figure 11 shows the pressure distributions for the blown-flap wing for two flap deflections, 30° and 0°. These distributions, given at the 15-percent-semispan station, show both upper and lower surface pressures. These were obtained by solving the thickness problem for upper and lower surface velocities with no blowing, then adding these to the velocities determined for the thin wing with blowing from the EVD program. The velocities were then converted into pressure coefficients by using the incompressible Bernouli equation.

The pressure distribution for $\delta_f = 30^{\circ}$ indicates a high negative pressure peak around the flap hinge line and jet slot location (at 0.75c); the theoretical pressure distribution also has a negative pressure peak at this location because the flap is deflected. The pressures given by the theory around the hinge line, however, seem to be much lower than the experimental values, indicating that the high-velocity jet emerging from the slot also has a substantial effect. The effect of the jet is even more apparent at $\delta_f = 0^{\circ}$. The experimental data for $\delta_f = 0^{\circ}$ again indicates a very high negative pressure around the jet slot and hinge location; however, the theoretical distribution indicates no such peak because the flap is undeflected. The theory, in this case, treats the wing as though it were a pure jet flap with a jet deflection equal to the angle of the upper surface of the flap.

The fact that the effect of the jet appears as a singularity that is similar to logarithmic singularity caused by flap deflection indicates that it might be possible to modify this singularity to account for C_{μ} effects as well as flap effects. If this cannot be done, then a more general wing-jet interaction program (similar to ref. 7) would be needed to account for the jet flow over the flap.

CONCLUSIONS

Comparisons made between theory and experiment for a straight, untapered wing with two types of powered lift (a pure jet flap and blowing over the flap) indicated the following conclusions:

1. The lift, drag, and pitching-moment coefficients predicted by the linearized planar theory were in excellent agreement with the experimental values for the pure jet flap, even though the jet deflection was large (61° to 63°).

2. The planar theory underpredicted the pressure coefficients and hence the wing circulation lift. The lower circulation lift was compensated for by a higher jet-reaction lift, under the small-angle assumptions, so that total lift and pitching moments were close to the correct values.

3. The lift, drag, and pitching-moment coefficients as well as pressure coefficients at a given angle of attack were underpredicted for the wing with blowing over the flap because of the failure of the theory to account for the interaction effect of the high-velocity jet passing over the flap.

REFERENCES

1. Spence, D. A.: The Lift Coefficient of a Thin, Jet-Flapped Wing. Proc. Roy. Soc. (London), ser. A, vol. 238, no. 1212, Dec. 4, 1956, pp. 46-68.

2. Margason, Richard J.; Yip, Long P.; and Gainer, Thomas G.: Recent Developments in Propulsive-Lift Aerodynamic Theory. Aerodynamic Analyses Requiring Advanced Computers, Part II, NASA SP-347, 1975, pp. 871-895.

3. Lopez, Michael L.; Shen, Cheng-Chung; and Wasson, Norman F.: A Theoretical Method for Calculating the Aerodynamic Characteristics of Arbitrary Jet-Flapped Wings. Rep. No. MDC J5519 (Contract N00014-71-C-0250), McDonnell Douglas Corp., May 1973.

   Volume I - The Elementary Vortex Distribution Jet-Wing Lifting Surface Theory.

   Volume II - EVD Jet-Wing Computer Program User's Manual.

4. Clever, W. C.: A Vortex Lattice Program for Jet Flapped Airfoils. TFD-73-70, Los Angeles Div., North American Rockwell Corp., Jan. 26, 1973.

5. Lopez, M. L.; and Shen, C. C.: Recent Developments in Jet Flap Theory and Its Application to STOL Aerodynamic Analysis. AIAA Paper No. 71-578, June 1971.

6. Clever, W.: Linear and Nonlinear Two Dimensional Jet Flap Analysis. TFD-72-698, Los Angeles Div., North American Rockwell Corp., Nov. 22, 1972.

7. Lan, C. Edward; and Campbell, James F.: Theoretical Aerodynamics of Upper-Surface-Blowing Jet-Wing Interaction. NASA TN D-7936, 1975.

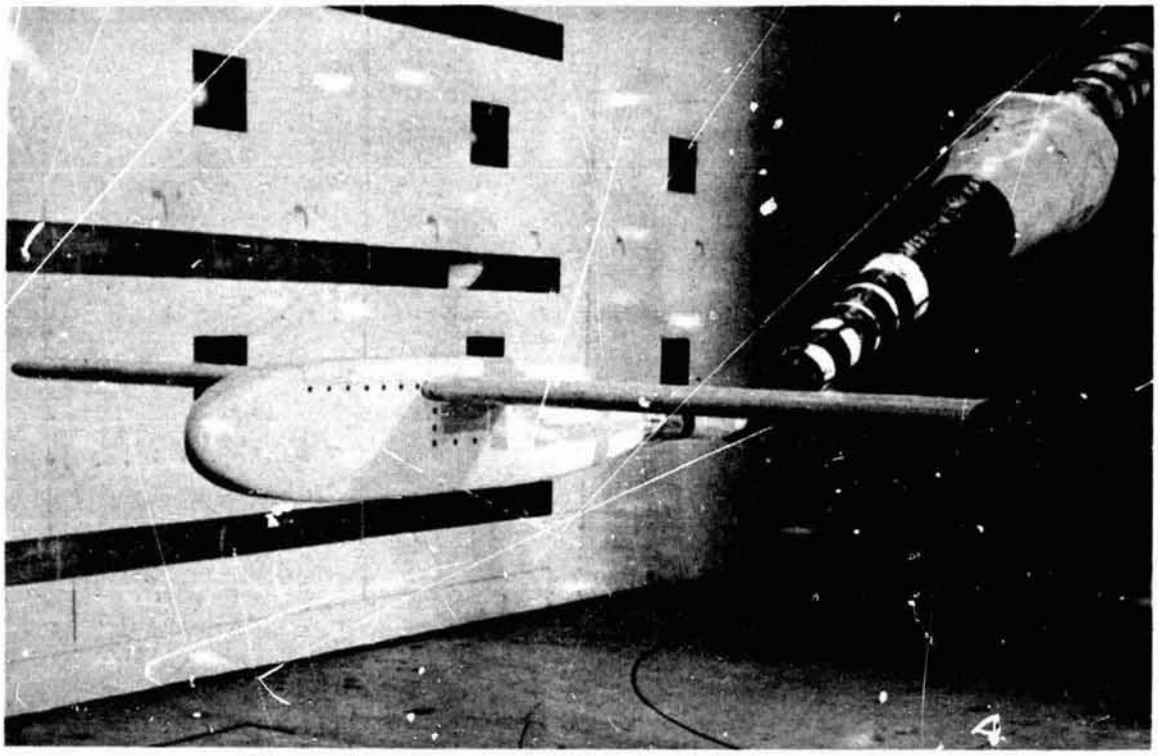

Figure 1.- Test model in the V/STOL tunnel.

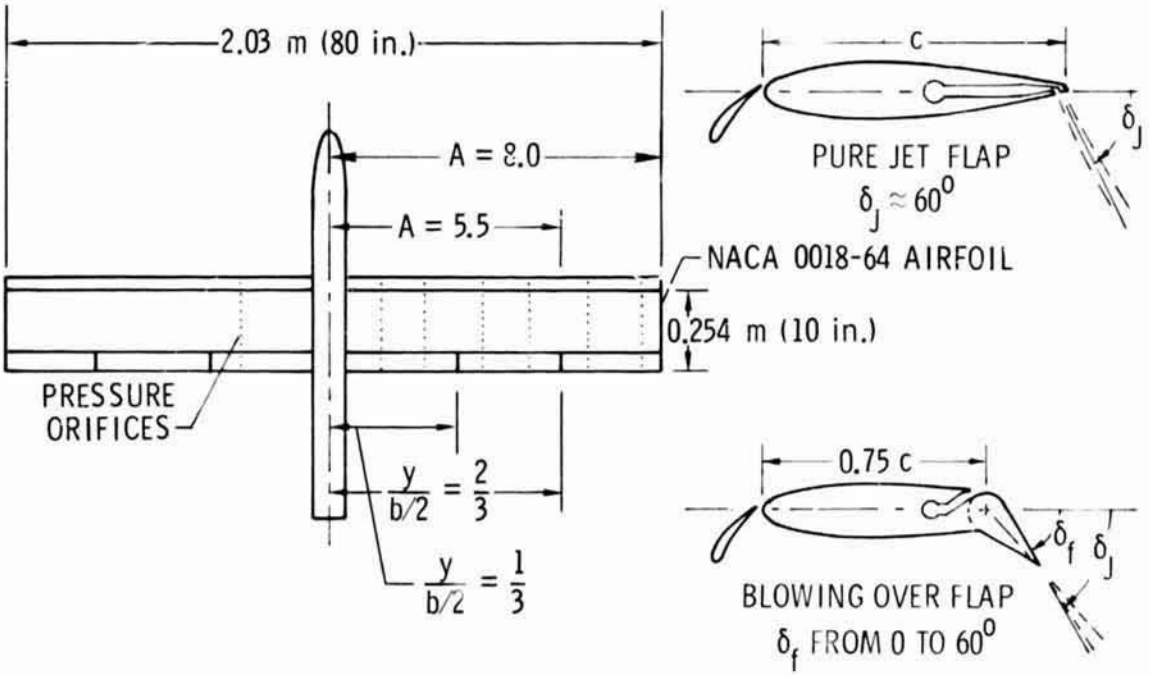

Figure 2.- Model details.

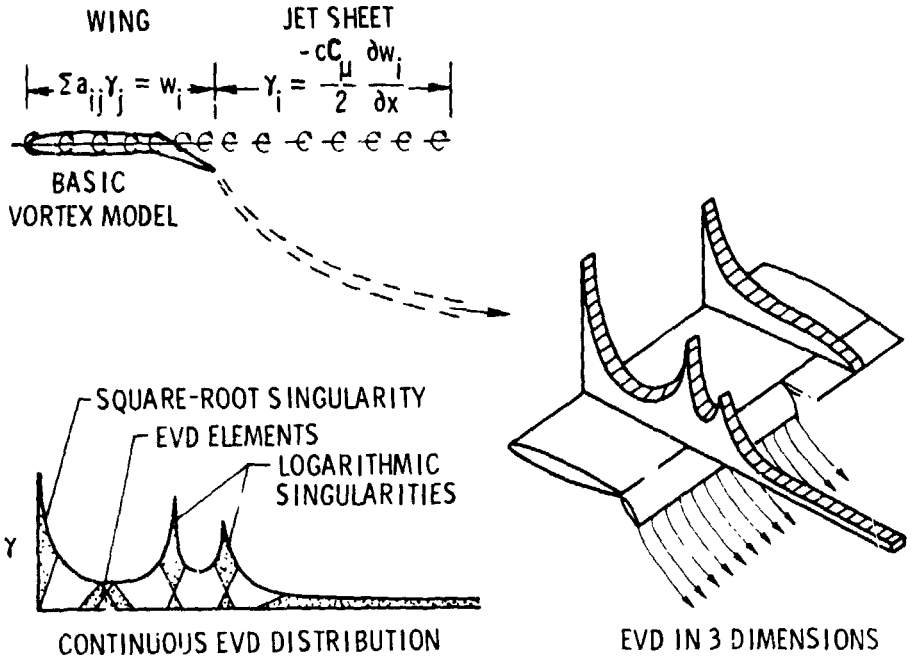

Figure 3.- Jet-flap lifting-surface theory.

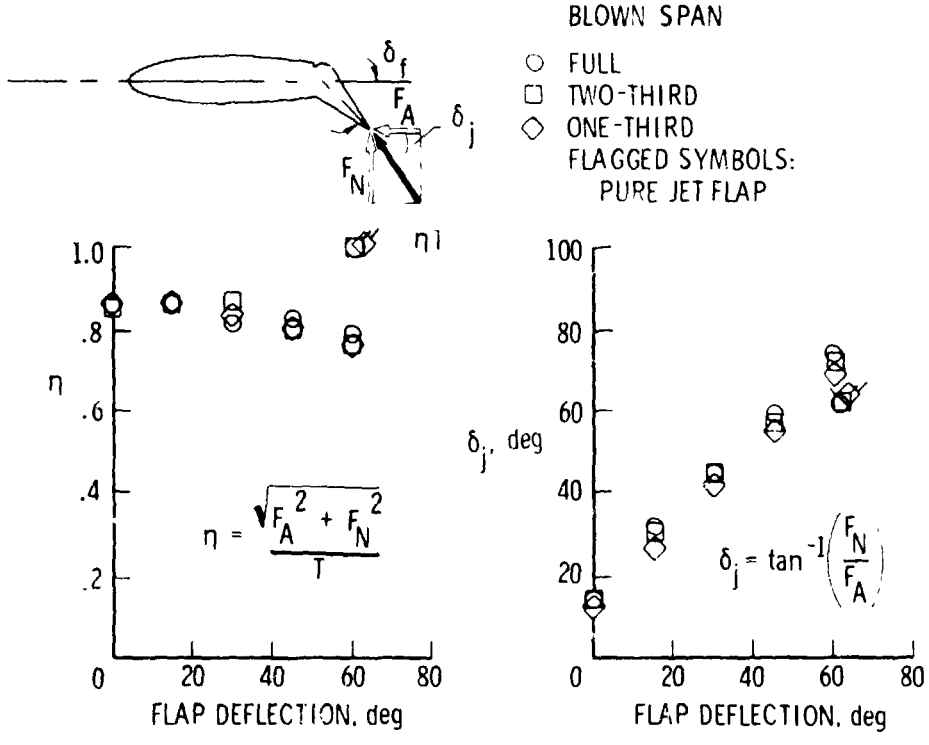

Figure 4.- Static turning characteristics.

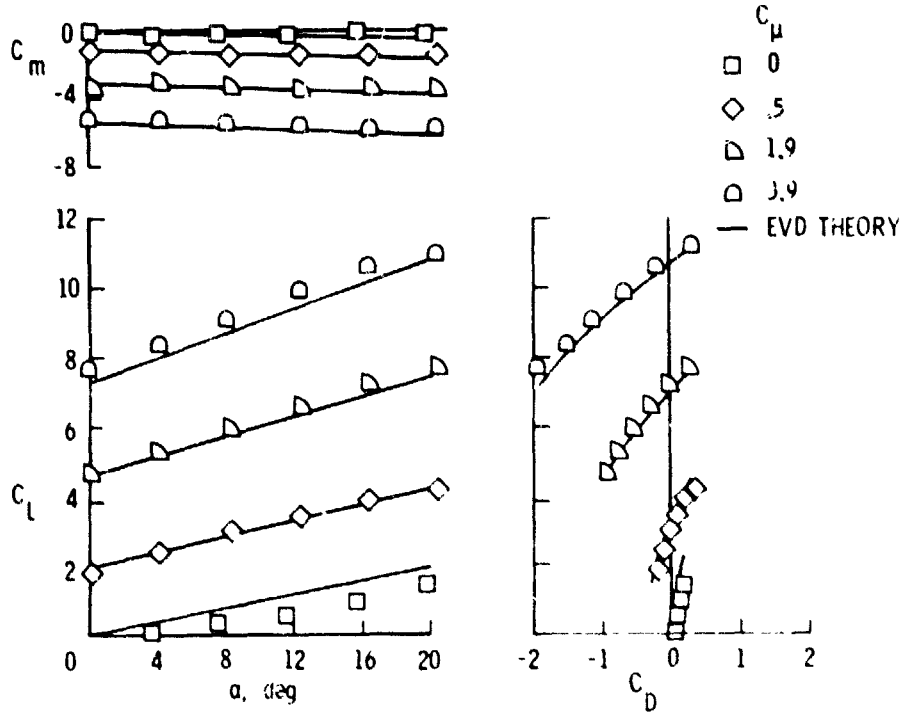

Figure 5.- Theory and experiment comparison for pure jet flap; A = 8; full-span blowing; $\delta_j = 61.4^\circ$.

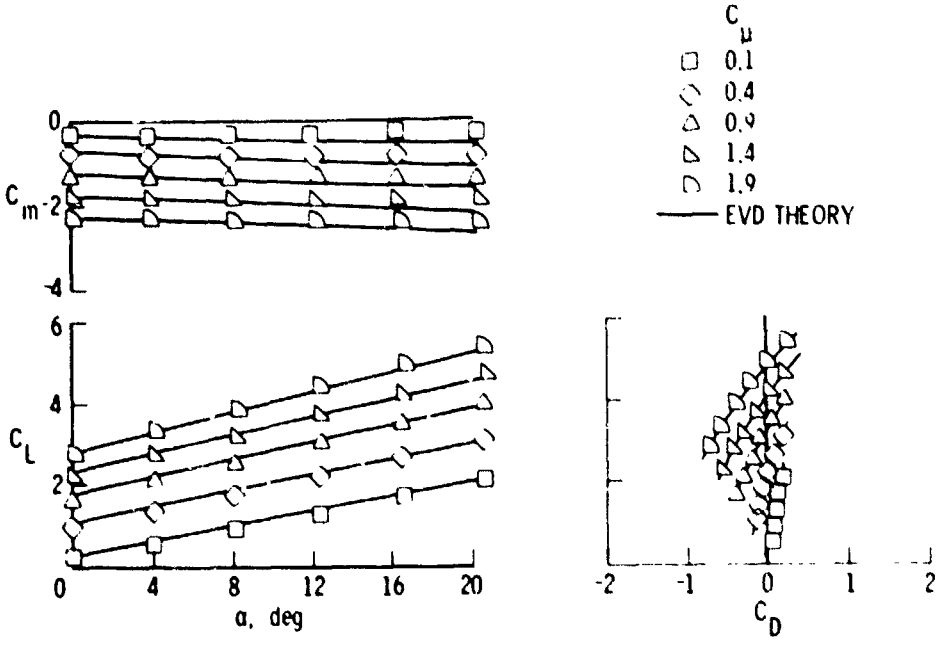

Figure 6.- Theory and experiment comparison for pure jet flap; A = 8; 1/3-span blowing; $\delta_j = 63.4^\circ$.

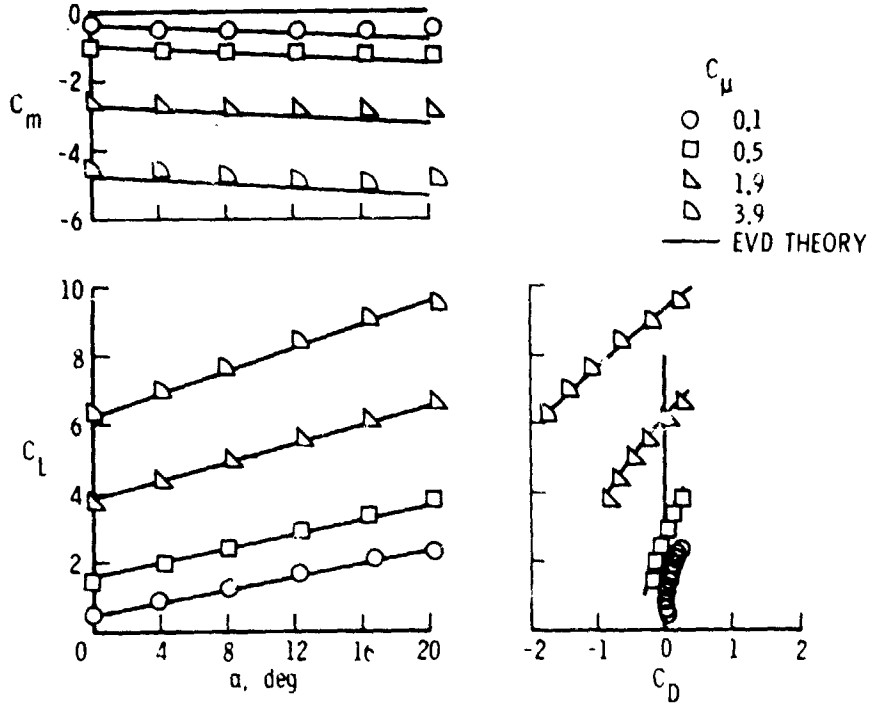

Figure 7.- Theory and experiment comparison for pure jet flap; A = 8; 2/3-span blowing; $\delta_j = 61.8°$.

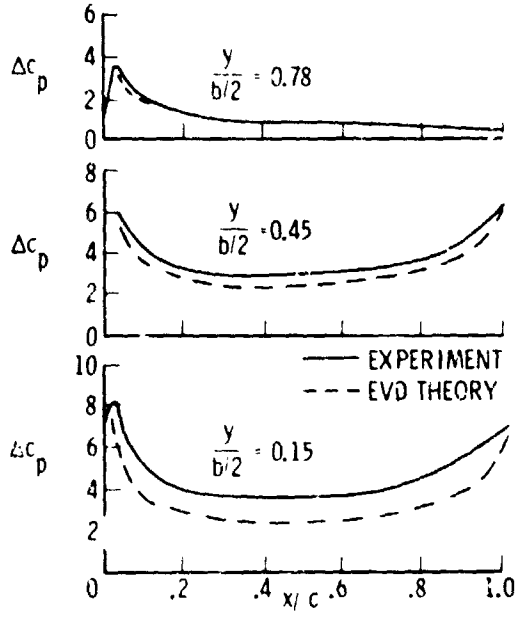

Figure 8.- Theoretical and experimental pressure distributions for pure jet flap. 2/3-span blowing; $C_\mu = 3.9$.

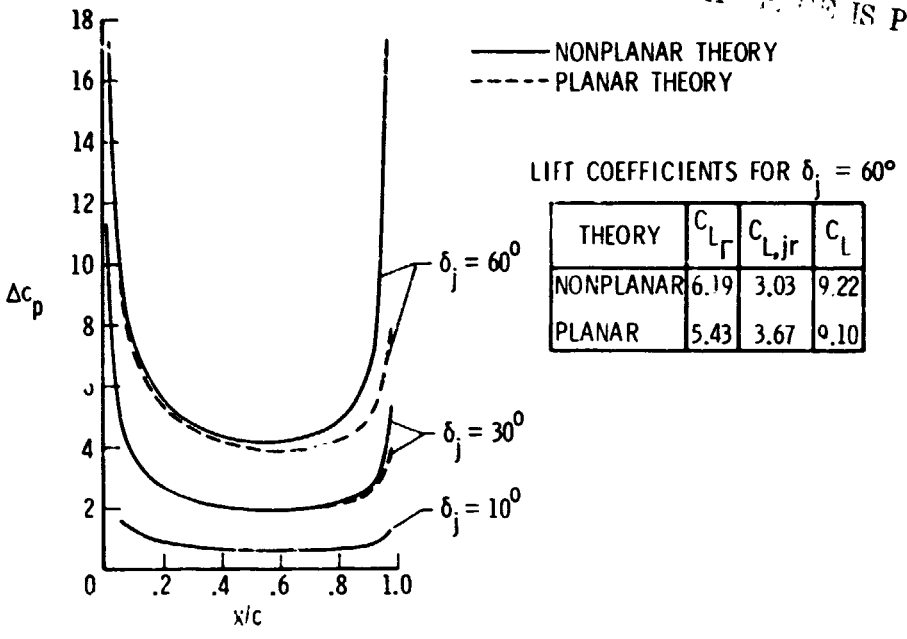

THEORY	C_{L_Γ}	$C_{L,jr}$	C_L
NONPLANAR	6.19	3.03	9.22
PLANAR	5.43	3.67	9.10

Figure 9.- Effect of planar assumptions in two dimensions (ref. 6). C_μ = 3.5; α = 0°.

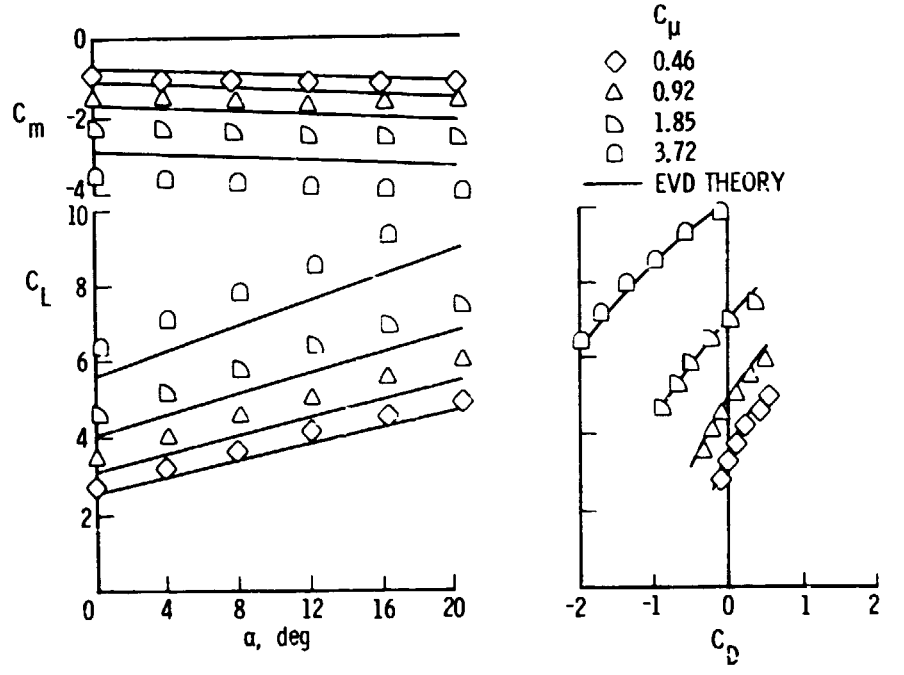

Figure 10.- Theory and experiment comparison for wing with blowing over flap A = 8.0; full-span blowing; δ_f = 30°.

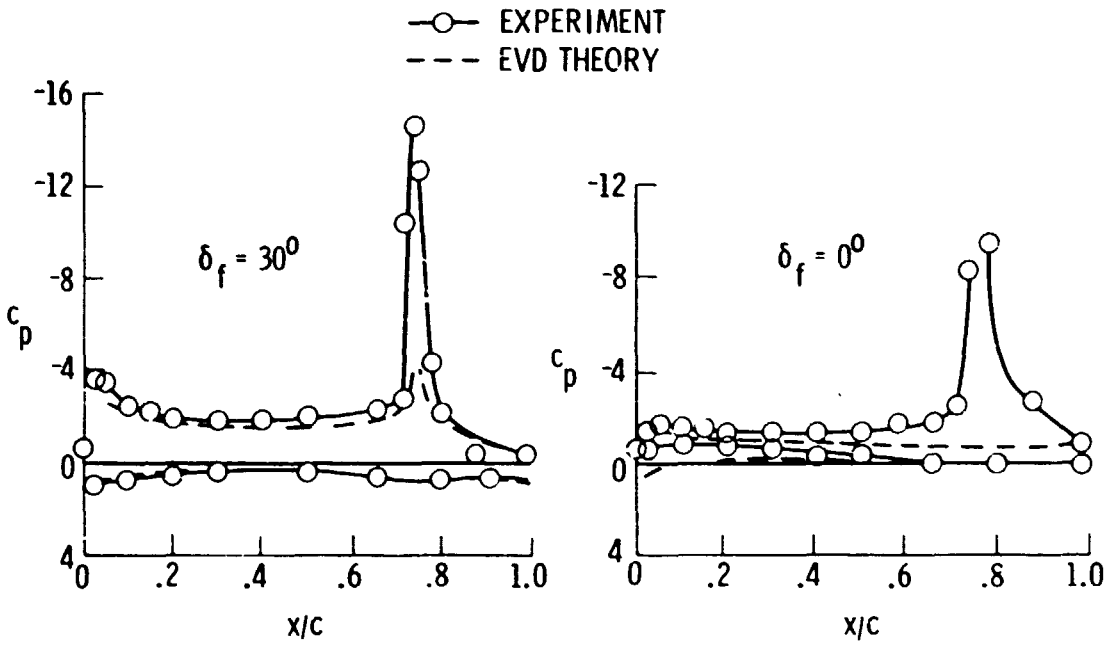

Figure 11.- Pressure distributions for wing with blowing over flap. 15-percent semispan station; $C_\mu = 3.9$.

EXTERNALLY BLOWN FLAP IMPINGEMENT PARAMETER

Danny R. Hoad
Langley Directorate, U.S. Army Air Mobility R&D Laboratory

SUMMARY

This paper presents a comparison of the performance of two externally blown flap (EBF) wind-tunnel models with an engine-exhaust flap impingement correlation parameter. One model was a four-engine EBF triple-slotted flap transport. Isolated engine wake surveys were conducted to define the wake properties of five separate engine configurations for which performance data were available. The other model was a two-engine EBF transport for which the engine wake properties were estimated. The correlation parameter was a function of engine-exhaust dynamic pressure at the flap location, area of engine-exhaust flap impingement, total exhaust area at the flap location, and engine thrust. The distribution of dynamic pressure for the first model was measured; however, the distribution for the second model was assumed to be uniform.

INTRODUCTION

Numerous concepts have been developed for achieving short-take-off-and-landing (STOL) performance. One approach which was selected for an advanced medium STOL transport (AMST) configuration, the YC-15, is the externally blown flap (EBF). Most EBF concept development has been achieved with experimental investigations (refs. 1 to 8) of various engine and airframe configurations. While very limited analyses (refs. 9 to 11) of these configurations have been attempted, some work has been done with an empirical analysis using a correlation parameter (impingement parameter) based on the vertical distance that the flap trailing edge extends into the jet exhaust from the engine center line and the radius of the jet exhaust at the flap trailing edge. (See ref. 12.)

The present paper describes the results of a relatively simple analysis based on an engine-exhaust flap impingement parameter, which is a function of the engine-exhaust dynamic pressure at the flap location, the area of engine-exhaust flap impingement, the total exhaust area at the flap location, and the thrust. Isolated engine wake surveys were conducted to define this parameter for one of the EBF models for which aerodynamic performance data were available (ref. 2). A uniform dynamic pressure profile was assumed to determine this parameter for the other EBF model. (See ref. 13.)

SYMBOLS

A_f total area of engine exhaust which impinges on flap, m^2

$A_{f,i}$ incremental area of engine exhaust which impinges on flap, m^2

A_j total area of engine exhaust at flap location, m^2

C_L lift coefficient, $\frac{\text{Lift}}{qS}$

$C_{L,tr}$ thrust-removed lift coefficient

C_μ thrust coefficient, $\frac{\text{Thrust}}{qS}$

c local wing chord, m

P_A engine-exhaust flap impingement parameter

q free-stream dynamic pressure, N/m^2

$q_{f,i}$ incremental dynamic pressure of engine exhaust which impinges on flap, N/m^2

q_j engine-exhaust dynamic pressure which impinges on flap, N/m^2

S wing area, m^2

T static thrust, N

z vertical distance, m

α angle of attack, deg

δ_f nominal flap deflection angle, deg

δ_j engine-exhaust deflection (measured from body axis), $\tan^{-1} \frac{\text{Normal force}}{\text{Axial force}}$, deg

η static-thrust recovery efficiency, $\frac{\sqrt{(\text{Normal force})^2 + (\text{Axial force})^2}}{T}$

Abbreviations:

BPR **bypass ratio**

EBF **externally blown flap**

MODELS

Two wind-tunnel investigations were conducted to determine the effect of different engine-exhaust characteristics on the performance of two separate EBF transport configurations (figs. 1 and 2).

A four-engine EBF transport (model 1, fig. 1) was tested in the Langley V/STOL tunnel. It had a 25° quarter-chord sweep, leading-edge slats deflected 50°, and triple-slotted full-span flaps whose elements were deflected 0°, 20°, and 40°, respectively, for the take-off configuration, and 15°, 35°, and 55°, respectively, for the landing configuration. The engines were simulated by a two-part ejector similar to that in figure 3. Each engine simulator was fitted with five separate cowl assemblies intended to represent five different engine configurations (fig. 4): (1) TF34 engine (BPR 6.2), (2) TF34 with noise suppressor nozzle (daisy nozzle), (3) stretched version of the TF34 (modified BPR 6.2), (4) JT15D engine (BPR 3.2), and (5) high-bypass-ratio engine (BPR 10). The modified BPR 6.2 engine was built so that the engine exit would be at the same chordwise location as the fan exit on the daisy nozzle. The BPR of these engine simulators does not describe in any way the size, horizontal position, or vertical position of the simulator, but is only intended to be a means of nomenclature. The important aspects of the simulator are not the characteristics at the exit, but the wake characteristics at the location of the flap as is evident subsequently in this paper. Since the exhaust and wake characteristics of the several full-scale engines represented are unknown, it is not possible to relate the present results to the performance of the full-scale engines. For further details of this model see reference 2.

A two-engine straight-wing EBF transport (model 2, fig. 2) was tested in the 5.18-m test section of the Langley 300-MPH 7- by 10-foot tunnel. It had a leading-edge slat deflected 40°, a double-slotted flap deflected 40° for the take-off configuration, and a triple-slotted flap deflected 60° for the landing configuration. The engines were simulated by a two-part ejector as presented in figure 5. The engine vertical position on this configuration was varied (to three positions) to determine its effect on the performance of the configuration (fig. 6).

TEST

Both models were mounted on a sting-supported six-component strain-gage balance for measurements of the total forces and moments. Isolated engine wake surveys were conducted for each engine configuration on model 1 so that the engine-exhaust flap impingement parameter could be determined. Dynamic pressure measurements were made with a pressure rake positioned so that the probes were alined along a radial line from the geometric center line. Four radial positions were chosen for the daisy nozzle and two radial positions were chosen for the other four engine simulators. These measurements were repeated at various downstream locations to obtain dynamic pressure profile characteristics. Isolated engine wake surveys were not available for the engine simulators on model 2. Since the same engine was used in all three positions, it was felt that assuming a 10° spread angle would be sufficient to determine the relative influence of the exhaust flap impingement parameter.

Jet deflection angles δ_j and static-thrust recovery efficiency η for both models were determined from measurements of the normal and axial forces made in the static-thrust condition with flaps deflected and leading-edge slat deployed.

CALCULATIONS

Isolated engine wake surveys were available for each engine configuration used on model 1. The flap impingement parameter was computed using the distribution of dynamic pressure at the flap location in the following manner:

$$P_A = \left(\sum_i q_{f,i} A_{f,i}\right) \frac{S}{TA_j} \sin \delta_f \qquad (1)$$

A schematic of exhaust impingement on the flap is presented in figure 7. The term $\sum_i q_{f,i} A_{f,i}$ can be seen as a summation of all the dynamic pressure measurements multiplied by the associated flap area on which they impinge In equation (1), A_j is the total area of engine exhaust at the flap impingement plane and δ_f is the nominal flap deflection angle. Since the term $\sum_i q_{f,i} A_{f,i}$ is a thrust or force term, the parameter was divided by thrust T and nondimensionalized by an arbitrary constant S (wing area).

Since isolated engine wake surveys were not available for the engine configuration used on model 2, the dynamic pressure was assumed to be uniform at the flap location. The exhaust was assumed to spread at an angle of 10° to determine the area of the exhaust at the flap location. The impingement

parameter in this case is slightly simplified in that the dynamic pressure is assumed constant over the flap; that is,

$$P_A = q_j A_f \frac{S}{TA_j} \sin \delta_f \tag{2}$$

The lift developed by a powered-lift system can be separated into three parts according to source: (1) the lift that would have been produced by the unpowered wing, (2) the lift due to the component of the jet which has been redirected by the flap system, and (3) the lift due to circulation induced by the blowing. If the portion of the lift due to the jet is removed from the total lift, a thrust-removed lift coefficient given by

$$C_{L,tr} = C_L - \eta C_\mu \sin (\delta_j + \alpha) \tag{3}$$

remains which can be related to the flap impingement parameter.

RESULTS AND DISCUSSION

The flap static turning effectiveness parameters for both models are presented in figure 8 in polar coordinate form. These parameters for the five engine simulators on model 1 and the three positions of the engine simulator on model 2 in the take-off and landing configurations are presented at a particular level of thrust. This was the thrust level used to obtain a thrust coefficient of 2 in the wind-tunnel test for each configuration.

The perpendicular distance from a data point in figure 8 to the horizontal axis would represent the lift component due to thrust at an angle of attack of 0°. If it were assumed that with zero power all engine simulator configurations had identical characteristics and that the only additions to the aerodynamic characteristics at an angle of attack of 0° were those components in figure 8, an assessment could be made as to the relative merit of the configurations. As discussed in reference 2, this assessment of the aerodynamic characteristics of an engine model configuration is not necessarily true. A more pertinent comparison based on the engine-exhaust flap impingement parameter is presented in this paper.

The flap impingement parameter is a correlation parameter which relates the engine-exhaust properties to the performance of the engine model configuration. The lift coefficient performance and impingement parameter are presented for several model flap combinations at an angle of attack of 0° as follows:

Figure	Model	Flap configuration
9	1	Landing
10	1	Take-off
11	2	Landing
12	2	Take-off

The effect of engine configuration for landing flap deflection on model 1 (fig. 9) indicates that the engine simulators which produce the largest impingement parameter (BPR 6.2 and modified BPR 6.2) provide the largest lift coefficient. The simulator which produces the smallest impingement parameter (BPR 3.2) provides the smallest lift coefficient. This impingement parameter is really a measure of the proportion of $q_j A_j$, or momentum, which impinges on the flap and, in turn, is deflected and induces circulation. This would indicate that the more momentum captured by the flap system, the better the combination will perform. The effect of engine configuration for take-off flap deflection on model 1 (fig. 10) is similar except for the relative performance and magnitude of impingement parameter for the daisy nozzle. The daisy nozzle has eight fan lobes and nine gas generator lobes. Since the wake survey for this engine included only two fan lobes and two gas generator lobes, it was not comprehensive enough to adequately define the profile.

The comparisons of performance and impingement parameter for model 2 with landing and take-off flap deflections are presented in figures 11 and 12. The results for the landing configuration indicate that moving the engine exhaust vertically toward the wing lower surface increases the proportion of $q_j A_j$, or momentum, which is captured by the flap system and, in turn, generates increased lift. Figure 12 for the take-off configuration indicates the same trend, although at a somewhat lower value because there is less flap projection to capture the exhaust.

To further relate this flap impingement parameter to the lift performance of the models, the thrust-removed lift coefficient at an angle of attack of 0° was computed for each configuration and is presented in figure 13 as a function of the impingement parameter. It is evident that the thrust-removed lift coefficient is the prime aerodynamic factor which can be related to the impingement parameter, because the data fit a straight line which intercepts $P_A = 0$ at the value of C_L which corresponds to the power-off condition. (In this case, P_A should be zero.) If the blowing did not induce supercirculation lift, these data points would be on horizontal lines. In each model, it can be seen that the landing configuration data describe a line with a larger slope than that for the take-off configuration. This is more evidence that since the landing flaps capture more of the exhaust flow, more circulation lift is induced. This again emphasizes the fact that the engine-exhaust flap impingement parameter is a measure of the proportion of momentum captured by the flap and provides a method to assess the relative performance of engine-wing combinations.

CONCLUDING REMARKS

This paper provides a technique to assess the relative performance of externally blown flap (EBF) configurations by means of an engine-exhaust flap impingement parameter. This parameter was determined to be a function of the proportion of momentum which is captured by the flap system.

The lift produced by an EBF configuration can be related to the proportion of momentum captured by the flap system. Furthermore, it has been shown that the thrust-removed lift coefficient can be directly related to this captured momentum, defined by the engine-exhaust flap impingement parameter.

REFERENCES

1. STOL Technology. NASA SP 320, 1972.

2. Hoad, Danny R.: Longitudinal Aerodynamic Characteristics of an Externally Blown Flap Powered-Lift Model With Several Propulsive System Simulators. NASA TN D-7670, 1974.

3. Parlett, Lysle P.; Freeman, Delma C., Jr.; and Smith, Charles C., Jr.: Wind-Tunnel Investigation of a Jet Transport Airplane Configuration With High Thrust-Weight Ratio and an External-Flow Jet Flap. NASA TN D-6058, 1970.

4. Smith, Charles C., Jr.: Effect of Wing Aspect Ratio and Flap Span on Aerodynamic Characteristics of an Externally Blown Jet-Flap STOL Model. NASA TN D-7205, 1973.

5. Parlett, Lysle P.; Smith, Charles C., Jr.; and Megrail, James L.: Wind-Tunnel Investigation of Effects of Variations in Reynolds Number and Leading-Edge Treatment on the Aerodynamic Characteristics of an Externally Blown Jet-Flap Configuration. NASA TN D-7194, 1973.

6. Aoyagi, Kiyoshi; Falarski, Michael D.; and Koenig, David G.: Wind-Tunnel Investigation of a Large-Scale 25° Swept-Wing Jet Transport Model With an External Blowing Triple-Slotted Flap. NASA TM X-62197, 1973.

7. Freeman, Delma C., Jr.; Parlett, Lysle P.; and Henderson, Robert L.: Wind-Tunnel Investigation of a Jet Transport Airplane Configuration With an External-Flow Jet Flap and Inboard Pod-Mounted Engines. NASA TN D-7004, 1970.

8. Vogler, Raymond D.: Wind-Tunnel Investigation of a Four-Engine Externally Blowing Jet-Flap STOL Airplane Model. NASA TN D-7034, 1970.

9. Johnson, William G., Jr.; and Kardas, Gerald E.: A Wind-Tunnel Investigation of the Wake Near the Trailing Edge of a Deflected Externally Blown Flap. NASA TM X-3079, 1974.

10. Goldhammer, M. I.; Lopez, M. L.; and Shen, C. C.: Methods for Predicting the Aerodynamic and Stability and Control Characteristics of STOL Aircraft. Volume I - Basic Theoretical Methods. AFFDL-TR-73-146-Vol. I, U.S. Air Force, Dec. 1973.

11. May, Fred; and Widdicon, Colin A.: STOL High-Lift Design Study. Volume 1. State-of-the-Art Review of STOL Aerodynamic Technology. AFFDL-TR-71-26-Vol. I, U.S. Air Force, Apr. 1971.

12. Roe, M. H.; Renselaer, D. J.; Quam, R. A.; et al.: STOL Tactical Aircraft Investigation - Externally Blown Flap. Volume II - Design Compendium. AFFDL-TR-73-20, Vol. II, U.S. Air Force, Apr. 1973. (Available from DDC as AD 770 110.)

13. Johnson, William G., Jr.: Longitudinal Aerodynamic Characteristics of a Wing-Body Combination Having a Rectangular, Aspect-Ratio-6, Slotted Supercritical Wing With Externally Blown Flaps. NASA TM X-2388, 1971.

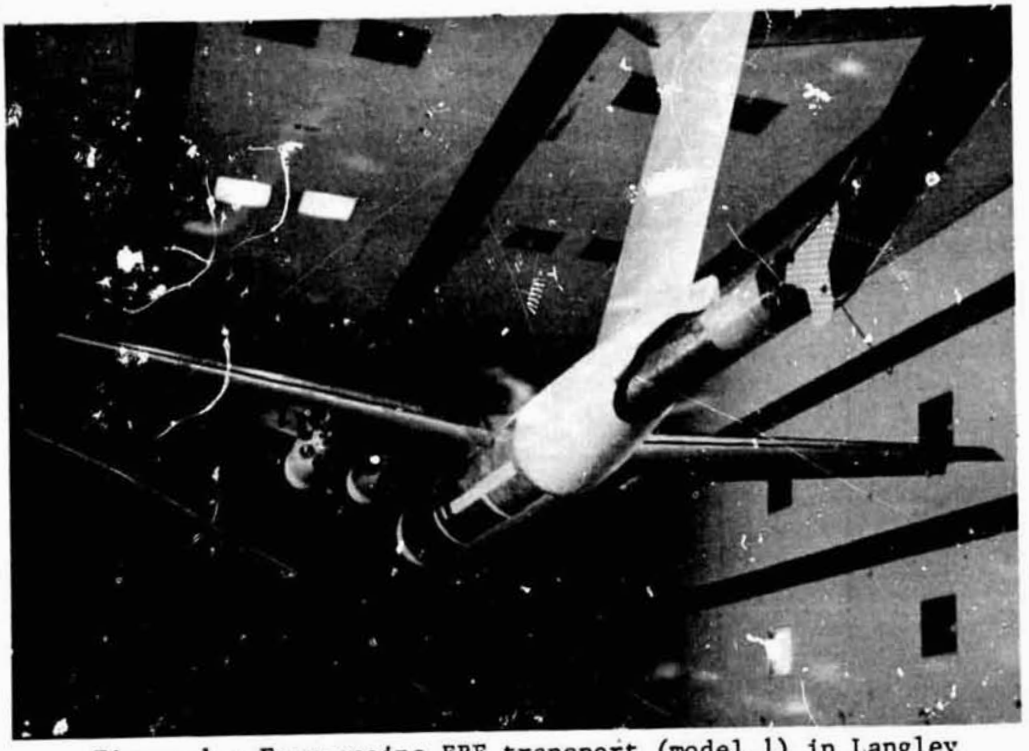

Figure 1.- Four-engine EBF transport (model 1) in Langley V/STOL tunnel.

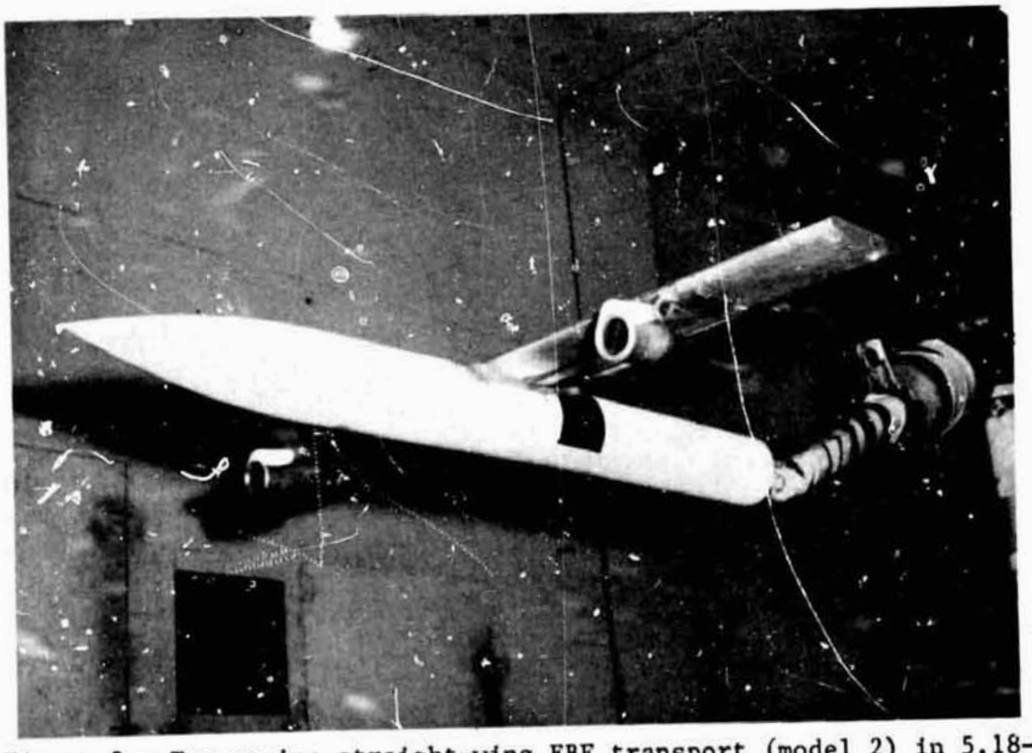

Figure 2.- Two-engine straight-wing EBF transport (model 2) in 5.18-m test section of Langley 300-MPH 7- by 10-foot tunnel.

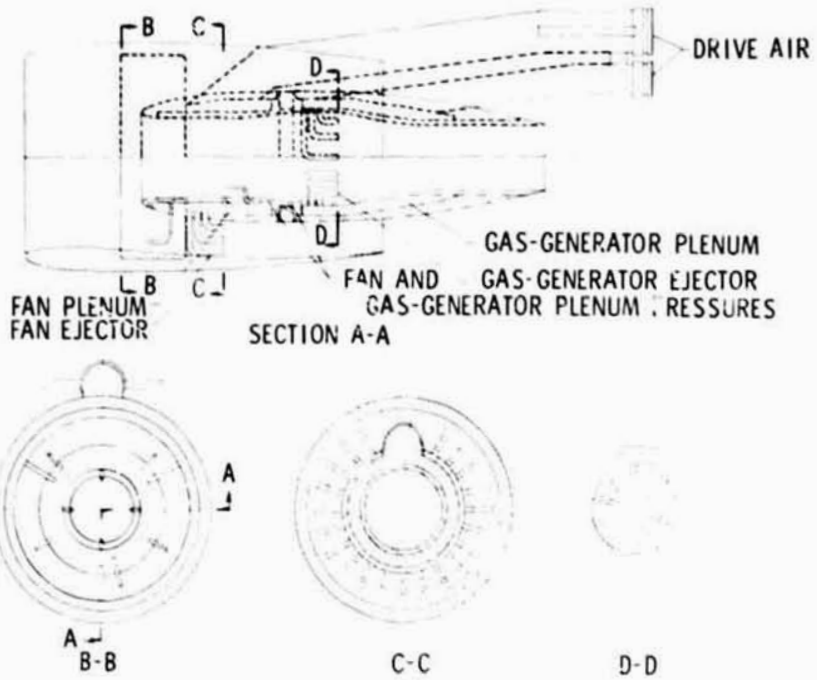

Figure 3.- Two-part engine simulator for model 1.

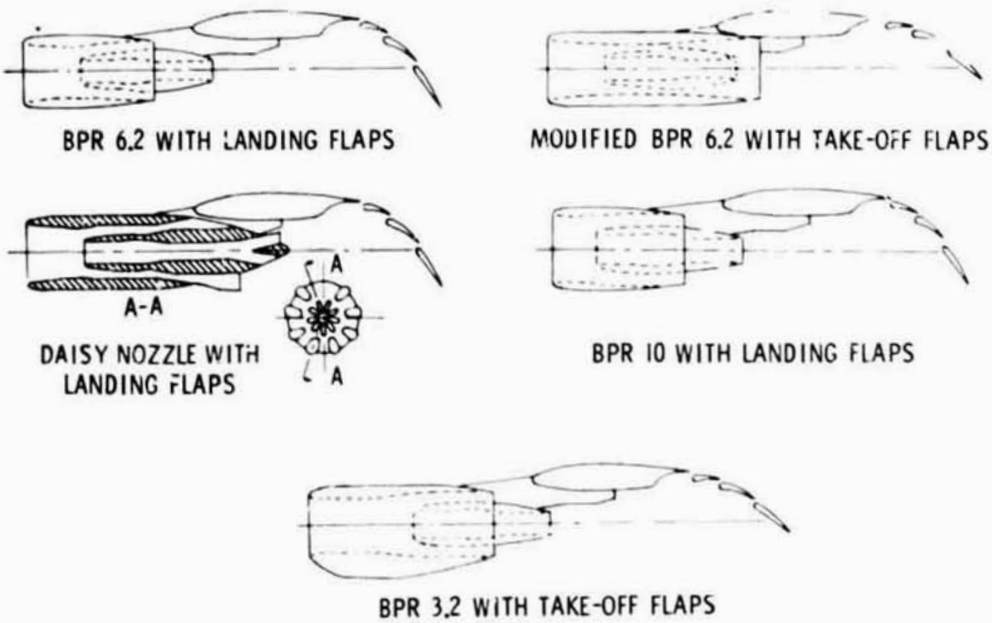

Figure 4.- Engine configurations used on model 1.

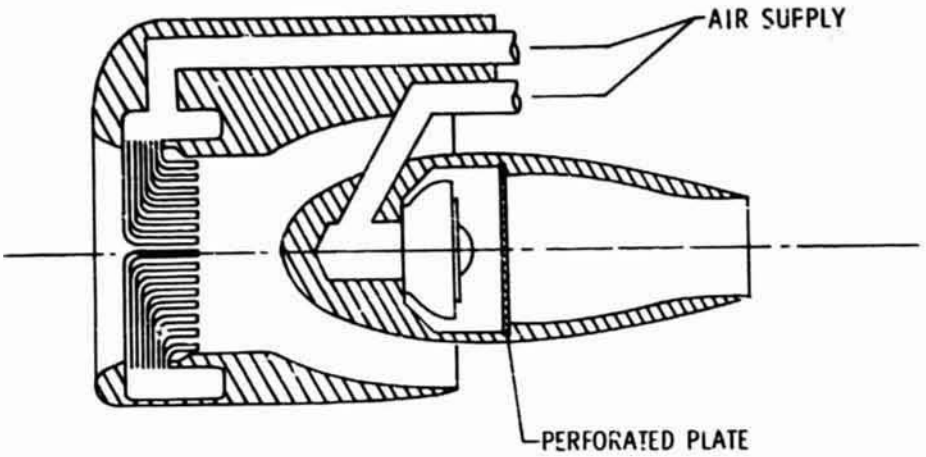

Figure 5.- Two-part engine simulator for model 2.

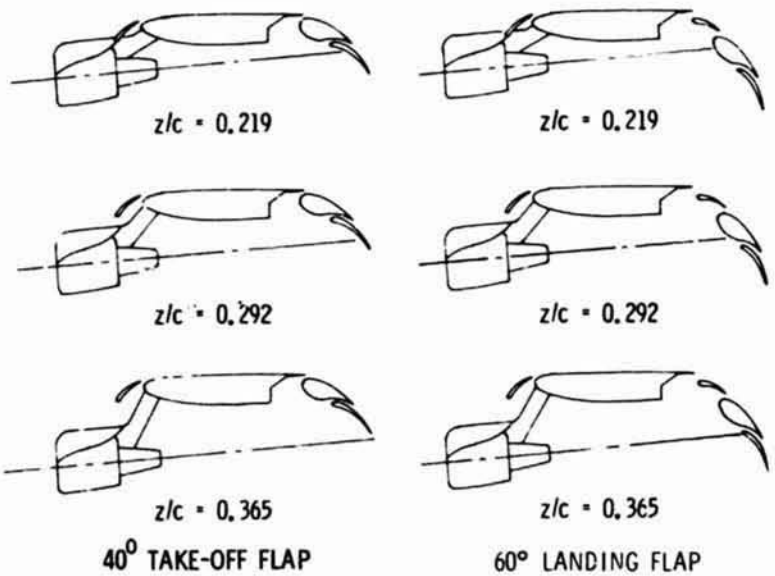

Figure 6.- Engine positions used on model 2.

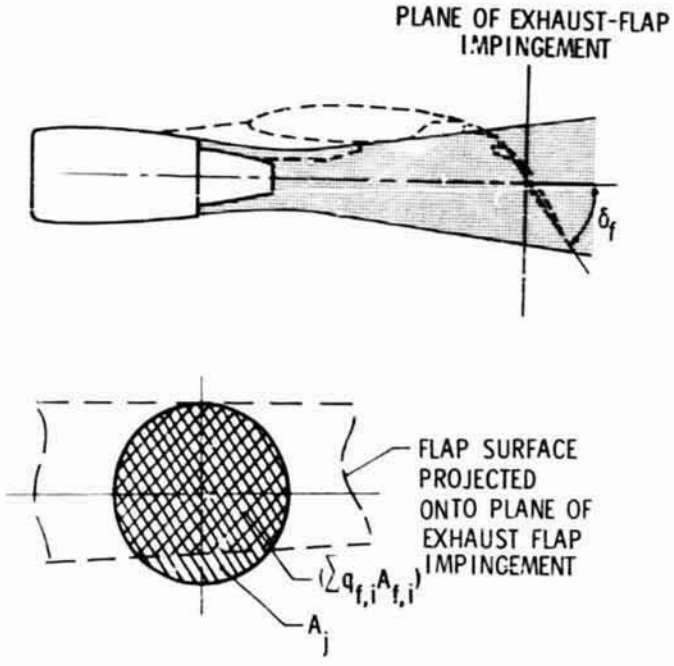

Figure 7.- Schematic of exhaust flap impingement.

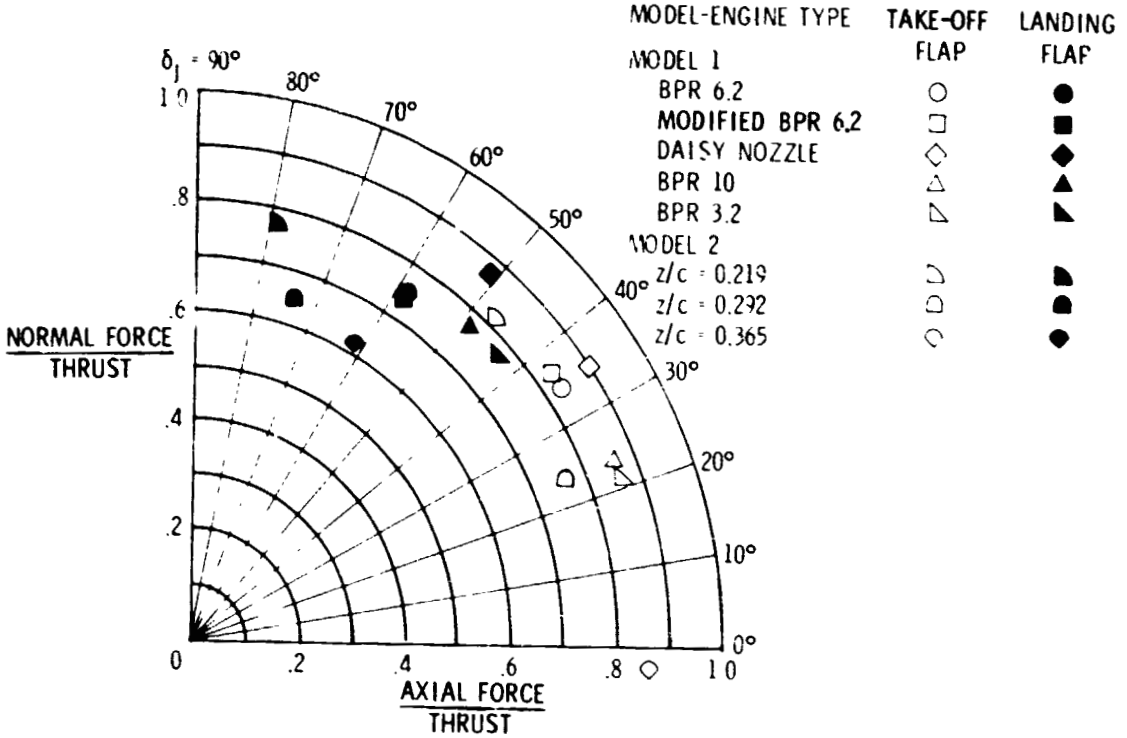

Figure 8.- Flap static turning effectiveness for models 1 and 2.

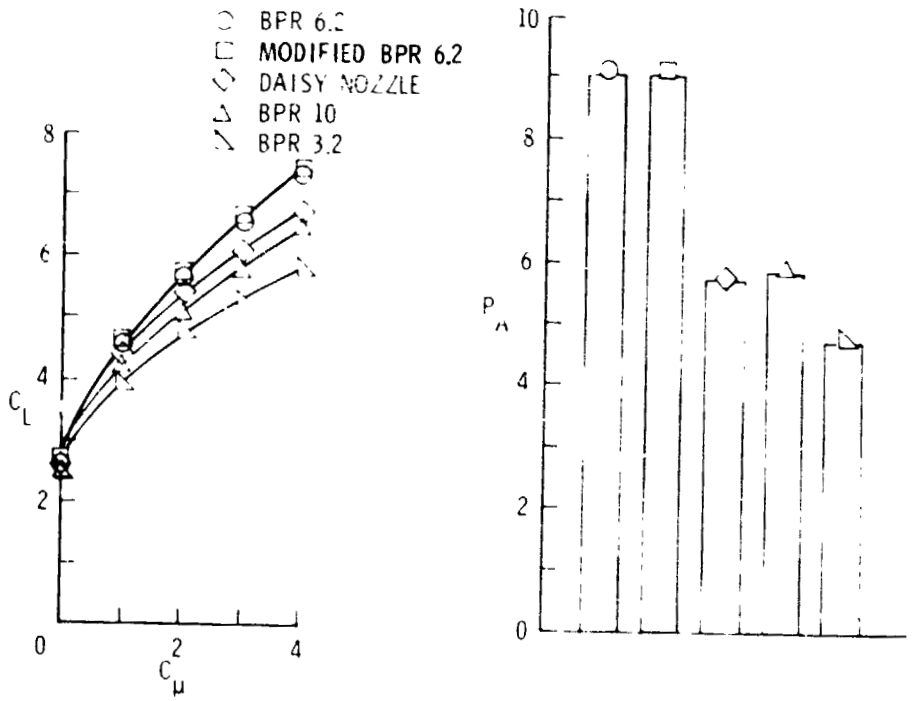

Figure 9.- Performance and impingement parameter for model 1 with landing flap deflection. $\alpha = 0°$.

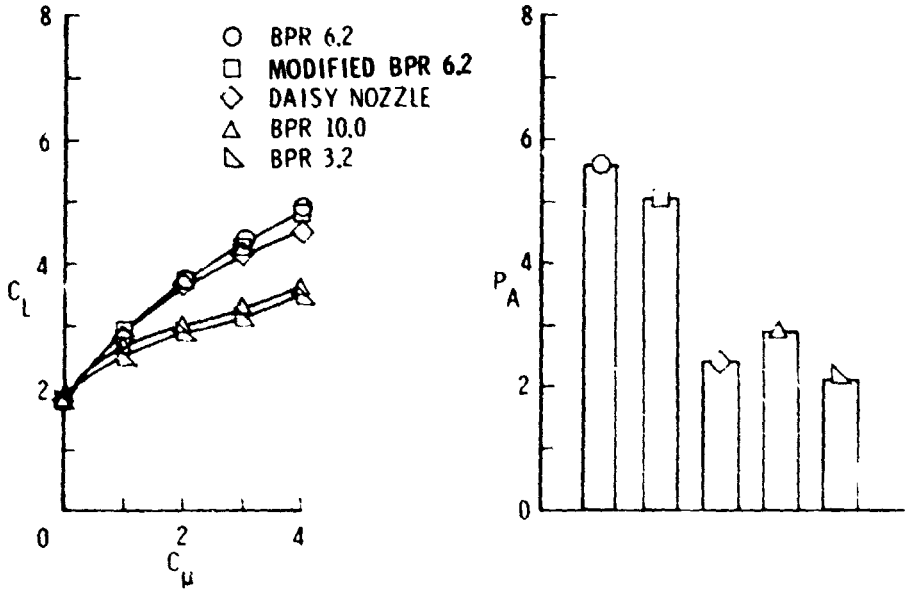

Figure 10.- Performance and impingement parameter for model 1 with take-off flap deflection. $\alpha = 0^\circ$.

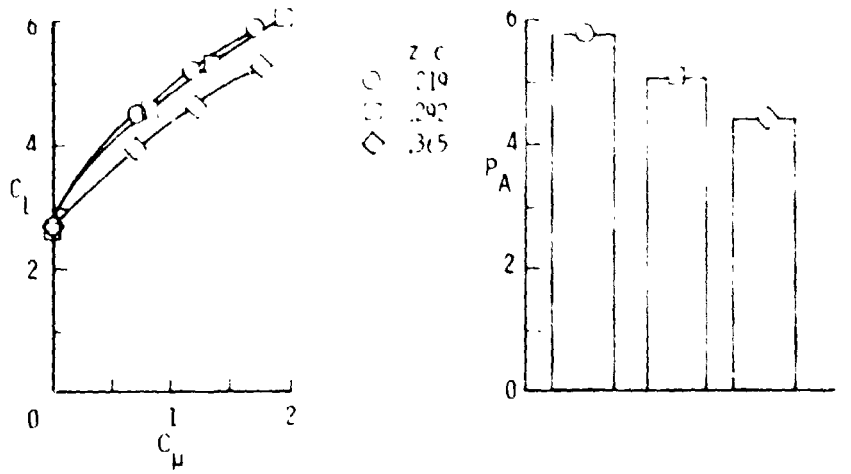

Figure 11.- Performance and impingement parameter for model 2 with landing flap deflection. $\alpha = 0^\circ$.

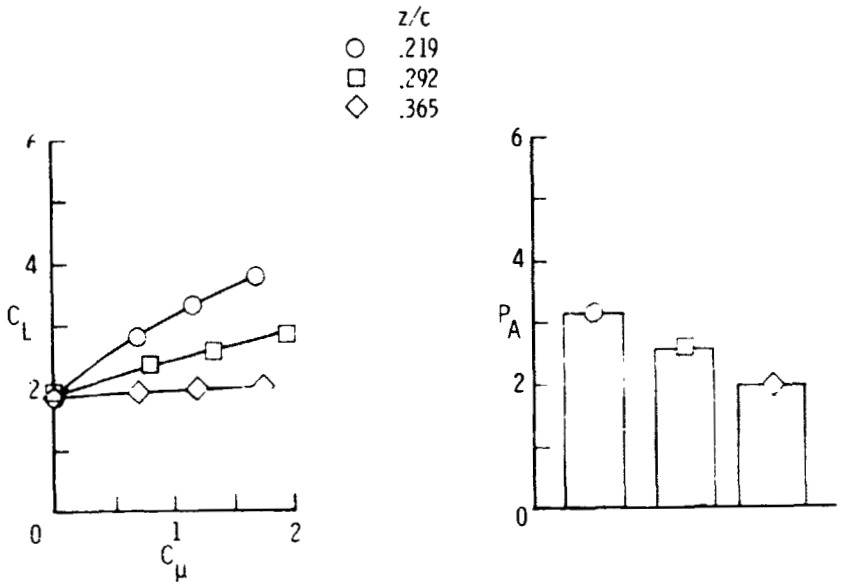

Figure 12.- Performance and impingement parameter for model 2 with take-off flap deflection. $\alpha = 0^o$.

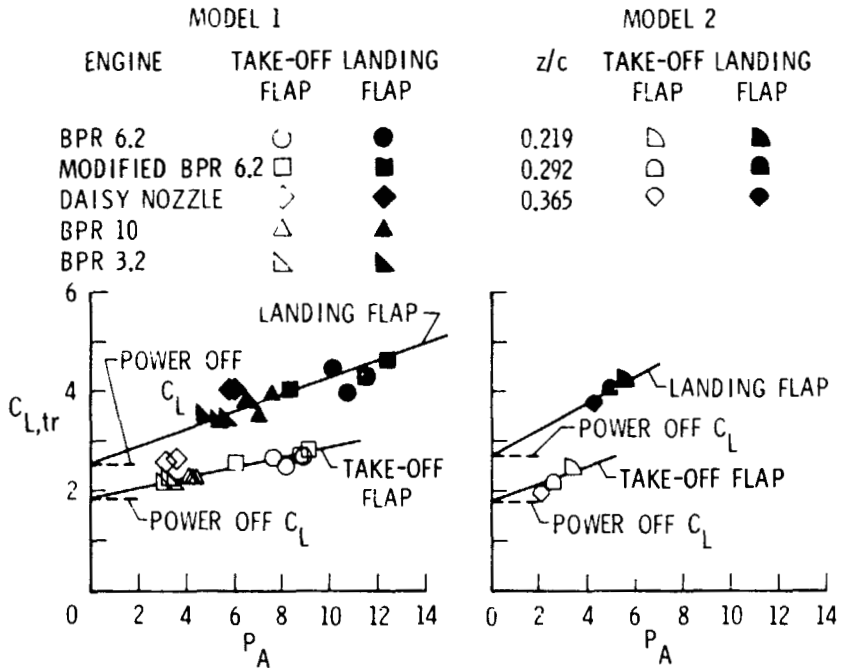

Figure 13.- Thrust-removed lift coefficient as a function of impingement parameter. $\alpha = 0^o$.

SOME MEASUREMENTS OF AN EBF POWERED-LIFT WAKE

William G. Johnson, Jr.
NASA Langley Research Center

SUMMARY

This paper discusses a summary of the analysis of results from a wind-tunnel investigation in which velocity vector measurements were obtained in the near wake of an externally blown flap powered-lift configuration. These measurements were used to develop spanwise distributions for the momentum strength and location of the engine exhaust stream tube with the results used as input parameters to one jet-flap analytical method.

This analysis showed that a comparison of the momentum coefficients obtained from forward speed wake surveys with the predicted values from static force data results in a good correlation, which verifies the use of the flap thrust recovery factor as a means of predicting the momentum strength at the flap trailing edge. Also, when wake survey distributions of momentum strength and direction are used as input parameters to one analytical jet-flap method, the results show reasonable agreement between the experimental data and analytical results.

INTRODUCTION

Powered lift is now being examined for application to conventional long-haul transports in order to enhance their take-off and landing performance as well as for short or reduced take-off and landing aircraft. To assist in the design of these aircraft, various analytical methods have been devised to predict the behavior of thick jet-flap powered-lift wakes. Experience has shown that these methods depend significantly on the descriptions of the wake momentum strength and location which are used as input parameters.

This paper will discuss a summary of the analysis of results from a wind-tunnel investigation (ref. 1) in which velocity vector measurements were obtained in the near wake of an externally blown flap powered-lift configuration. These measurements were then used to develop spanwise distributions for the momentum strength and location of the engine exhaust stream tube with the results used as input parameters to one jet-flap analytical method.

8

SYMBOLS

b wing span, m

c wing chord, m

C_L lift coefficient, $\frac{\text{Lift}}{q_\infty S}$

C_T thrust coefficient, $\frac{\text{Gross static thrust}}{q_\infty S}$

$C_\mu{}^*$ section momentum coefficient from wake surveys

C_μ total momentum coefficient from wake surveys

n number of velocity vectors in jet thickness

q_∞ free-stream dynamic pressure, Pa

S wing area, m^2

V magnitude of velocity vector, m/sec

V_j magnitude of specific velocity vector associated with $\delta_{j,l}$, m/sec

V_∞ free-stream velocity, m/sec

y distance along span of wing, m

α angle of attack, deg

δ_f flap deflection, deg

δ_j jet deflection angle, $\arctan \frac{\text{Normal force}}{\text{Axial force}}$, deg

$\delta_{j,l}$ local downwash angle minus wing angle of attack, deg

$\delta_j{}^*$ mean turning angle at any given survey station, deg

$\Delta\delta_j{}^*$ change in turning angle due to power, deg

η flap thrust recovery, $\frac{\text{Resultant force}}{\text{Static thrust}}$

τ jet thickness

DISCUSSION

The investigation was conducted in the Langley V/STOL tunnel on an existing externally blown flap model (ref. 2). As shown in figure 1, measurements were made at 11 spanwise stations between the edge of the fuselage and the

midsemispan station on the wing. The measurements were made with a split-film total vector anemometer which was capable of sensing the three velocity vector components (ref. 3). At each spanwise station, the probe was moved through a vertical arc through the wake and measured more than 100 velocity vectors at each survey station for each engine-power-off and engine-power-on condition.

Figure 2 shows a sample of the power-on velocity profiles taken at zero angle of attack and for thrust coefficients of 2.0 and 4.0. The profiles are shown at the two spanwise stations, $\frac{y}{b/2} = 0.227$ and $\frac{y}{b/2} = 0.376$, which are just inboard of the engine center lines. The outline of the wing-flap system is shown to locate the profiles relative to the 35° deflected flap and engine thrust center line. Units of free-stream velocity are indicated by dashed arcs within the profile. The profiles show higher than free-stream velocity flow above the wing and lower than free-stream velocity flow below the engine exhaust stream tube. The planform sketch in figure 1 shows that at the inboard station, the flap trailing edge is at a greater distance from the engine exhaust plane than at the outboard station. This greater distance results in the inboard exhaust stream tube being more diffuse than the jet sheet wake at the outboard station. Figure 2 shows that this wake characteristic holds for both thrust levels.

To establish the vertical bounds of the engine exhaust stream tube, a jet thickness τ was defined as the wake region in which the change in the local velocity vectors exceeded 0.3 m/sec. The magnitudes of the velocity vectors within the jet thickness were integrated to obtain a section momentum coefficient $C_\mu{}^*$ at each spanwise station by the following equation:

$$C_\mu{}^* = \frac{\int_0^\tau \left(V_{\text{power on}}\right)^2 d\tau - \int_0^\tau \left(V_{\text{power off}}\right)^2 d\tau}{\frac{1}{2} V_\infty{}^2 c}$$

This equation provides for the subtraction of the power-off momentum from the power-on momentum in coefficient form per unit area. The results of this integration are shown in figure 3 as a function of the spanwise location $\frac{y}{b/2}$. The data show that the peaks of the distributions have shifted significantly inboard of the engine center lines. This shift is contrary to the accepted thought that the engine exhaust spreads significantly outboard on a swept-wing configuration.

In addition to obtaining values for the distribution of the momentum strength and location along the flap trailing edge for analytical purposes, a comparison of a total momentum coefficient due to power from the forward speed-wake surveys and the predicted momentum coefficient obtained by use of static force data would be useful in verifying the technique generally used for defining the strength of engine exhaust momentum at the flap trailing edge. To obtain the wake survey value, the section momentum coefficient distributions were extrapolated to the edge of the fuselage $\left(\frac{y}{b/2} = 0.126\right)$ and to the most outboard extent

of the wing felt to be impacted by the spread engine exhaust flow $\left(\frac{y}{b/2} = 0.6\right)$. The distributions were then integrated spanwise to obtain the total momentum coefficient C_μ due to the engine exhaust at the flap trailing edge. The predicted value from static force data is obtained from the product of the static parameter η and the engine thrust coefficient C_T, where η is defined as the efficiency of turning the engine exhaust flow through some deflection angle. When the static force data are plotted as shown in figure 4, the value of η can be obtained as the radial distance from the origin to the data point. A comparison of the integrated values of engine momentum coefficient from the forward speed wake surveys with the product of the static values of η and C_T is shown in figure 5, and the result is a very good agreement for all of the thrust levels and angles of attack tested.

A mean turning angle $\delta_j{}^*$ was determined for each spanwise survey station by the following equation:

$$\delta_j{}^* = \frac{\sum_1^n V_j \delta_{j,l}}{\sum_1^n V_j}$$

where $\delta_{j,l}$ is the local downwash angle minus the wing angle of attack, V_j is the magnitude of the corresponding streamwise velocity vector, and n is the number of measured velocity vectors between the chosen limits. This equation weights $\delta_{j,l}$ by the velocity magnitude since it was felt that the higher velocity vectors had a stronger influence on the overall turning angle of the jet. The procedure was applied to the power-off and power-on data, with the resulting spanwise distributions shown in figure 6 by the circles and squares, respectively. These distributions show a change in the peak locations from those in the momentum distributions - the peaks are now shown on the engine center lines. This characteristic indicates that for this configuration $\left(\delta_f = 35^o\right)$, most of the engine exhaust is passing under the flap trailing edge with little turning. Since most jet-flap theories use the description of the jet-wake effects as an addition to basic wing theory, the local flow angle due to power was obtained by subtracting the power-off distributions from the power-on distributions. The results are shown in figure 7 as a function of spanwise station.

The distributions which were obtained for the momentum coefficients (fig. 3) and jet-deflection angles (fig. 7) were then used as input parameters to a jet-flap analytical method developed by Lissaman (ref. 4). The results of the computation are compared in figure 8 with the experimental lift coefficients as a function of wing angle of attack. The comparison indicates analytical results similar to the corresponding experimental data.

CONCLUSIONS

The analysis of results from a survey of the near wake of an externally blown flap configuration has resulted in the following conclusions:

1. A comparison of the momentum coefficients obtained from forward speed wake surveys with the predicted values from static force data results in a good correlation, which verifies the use of the flap thrust recovery factor as a means of predicting the momentum strength at the flap trailing edge.

2. When wake survey distributions of momentum strength and direction are used as input parameters to one analytical jet-flap method, the results show reasonable agreement between the experimental data and analytical results.

REFERENCES

1. Johnson, William G., Jr.; and Kardas, Gerald E.: A Wind-Tunnel Investigation of the Wake Near the Trailing Edge of a Deflected Externally Blown Flap. NASA TM X-3079, 1974.

2. Johnson, William G., Jr.: Aerodynamic Characteristics of a Powered, Externally Blown Flap STOL Transport Model With Two Engine Simulator Sizes. NASA TN D-8057, 1975.

3. Olin, J. G.; and Kiland, R. S.: Split-Film Anemometer Sensors for Three-Directional Velocity-Vector Measurements. Aircraft Wake Turbulence and Its Detection, John H. Olsen, Arnold Goldburg, and Milton Rogers, eds., Plenum Press, Inc., 1971, pp. 57-79.

4. Lissaman, Peter B. S.: Analysis of High-Aspect-Ratio Jet-Flap Wings of Arbitrary Geometry. NASA CR-2179, 1973.

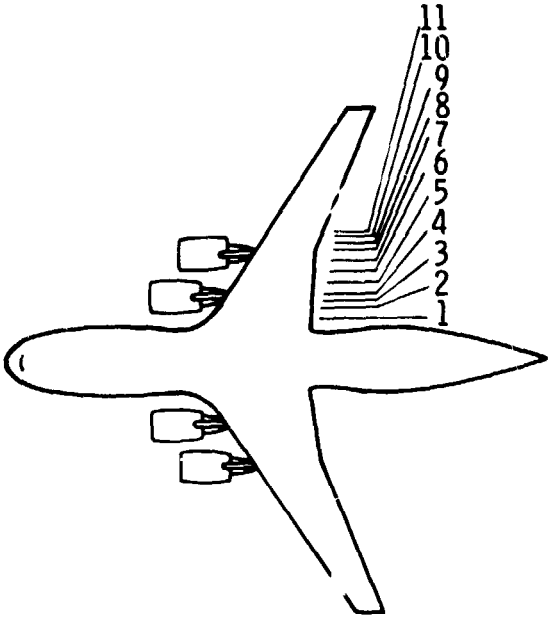

Figure 1.- Spanwise survey stations.

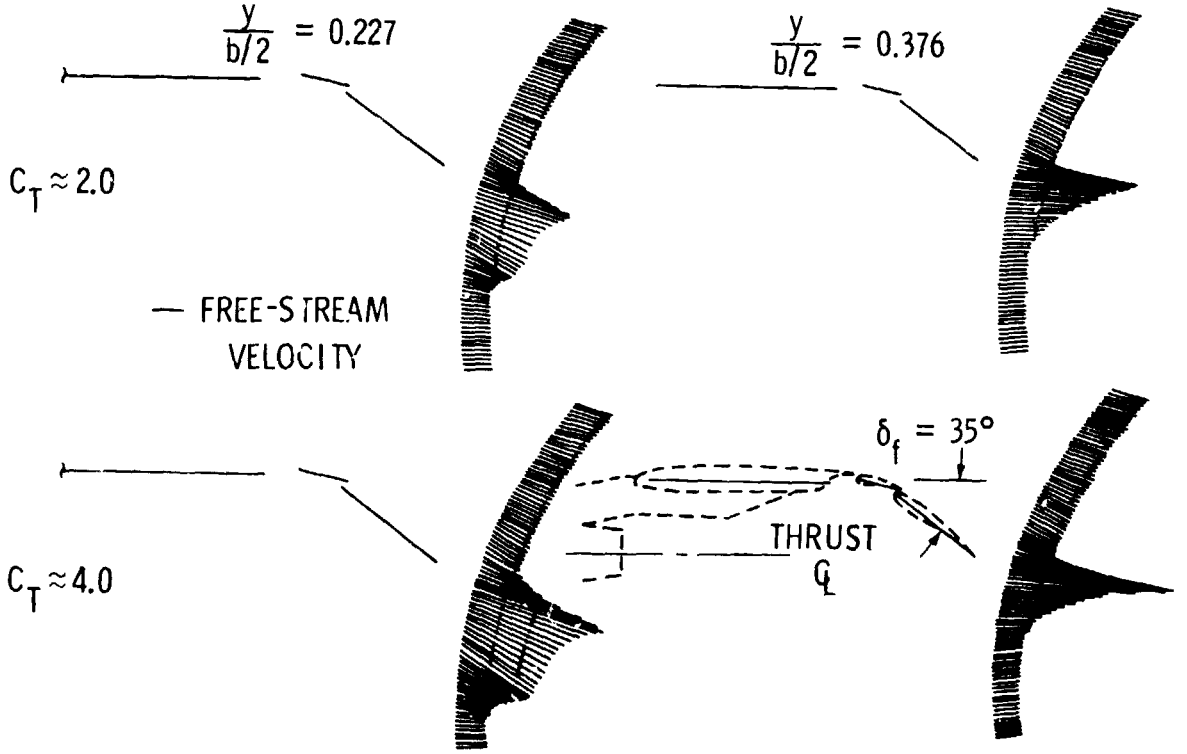

Figure 2.- Streamwise velocity profiles. $\alpha = 0^o$; V_∞ = 25.45 m/sec.

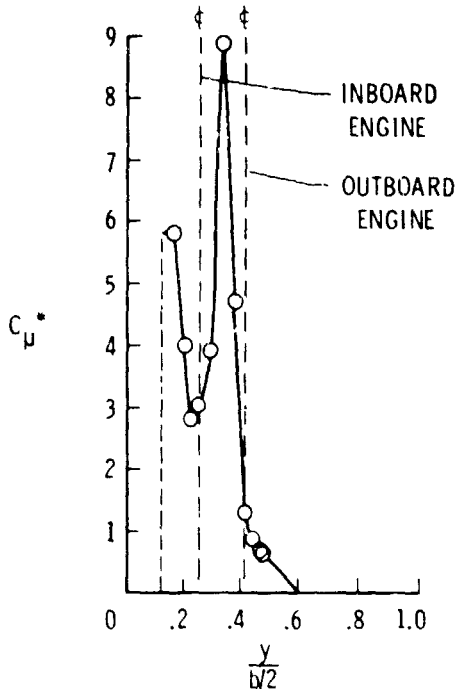

Figure 3.- Experimental momentum coefficient distribution. $\alpha = 0^o$; $C_T \approx 2.0$.

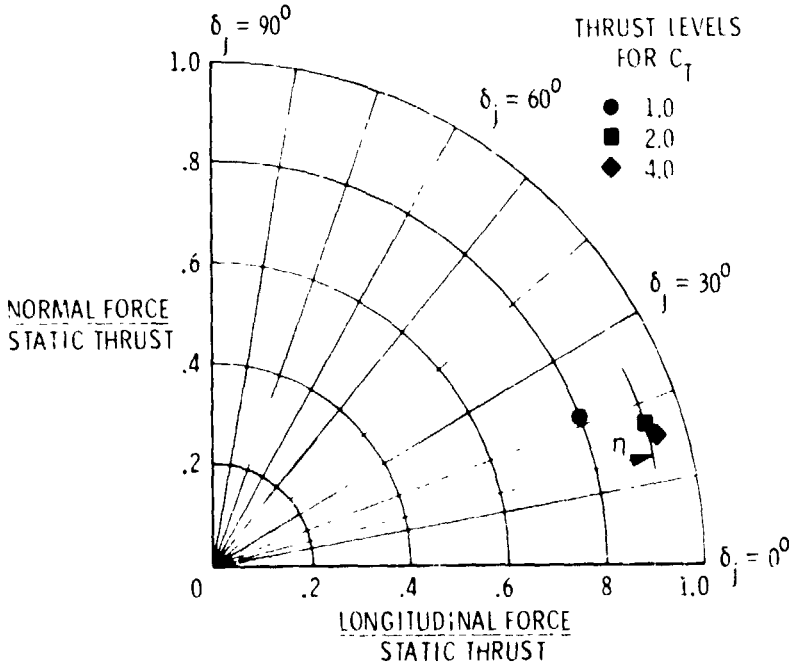

Figure 4.- Static turning angles and thrust recovery factor.

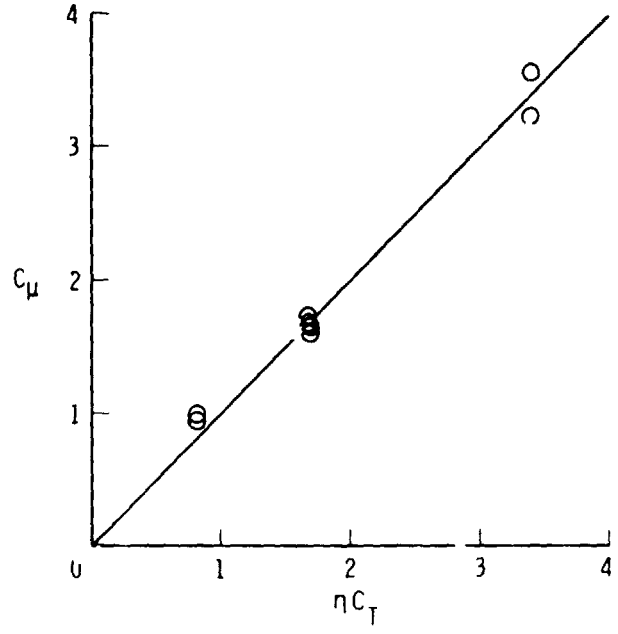

Figure 5.- Momentum coefficient from forward speed and static data.

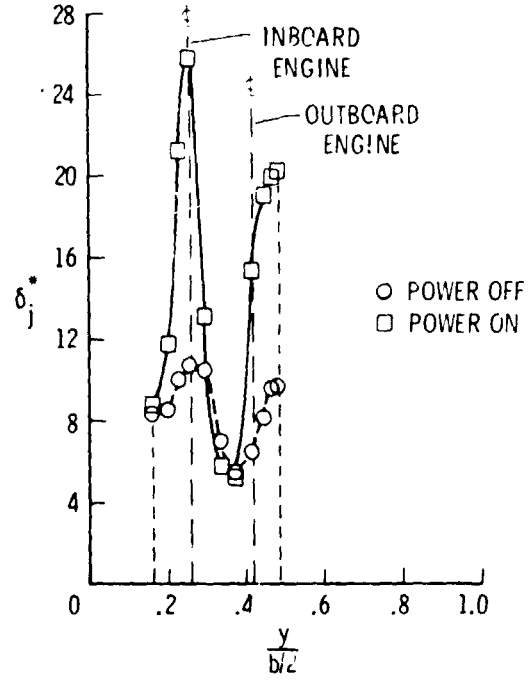

Figure 6.- Experimental distribution of jet-deflection angle. $\alpha = 0^o$; $C_T \approx 2.0$.

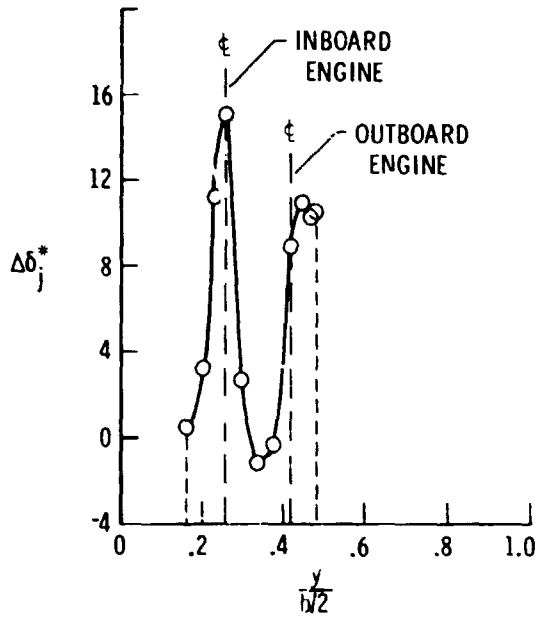

Figure 7.- Experimental jet-deflection angle due to power.
$\alpha = 0^{\circ}$; $C_T \approx 2.0$.

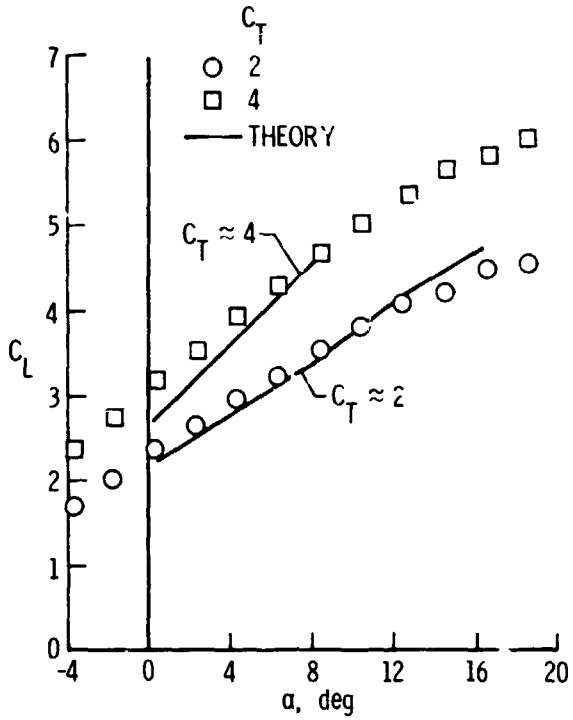

Figure 8.- Comparison of theory with experimental data for lift coefficient.

AERODYNAMIC CHARACTERISTICS IN GROUND PROXIMITY

James L. Thomas, James L. Hassell, Jr.,
and Luat T. Nguyen
NASA Langley Research Center

SUMMARY

Results from recent investigations in the Langley V/STOL tunnel of an externally blown flap and an upper-surface blown flap configuration in ground proximity are presented. Comparisons of longitudinal aerodynamic characteristics indicate that in ground proximity, drag is reduced for both configurations, but changes in lift are configuration dependent. Steady-state analyses of the landing approach indicate an increase in flight-path angle for both configurations in ground proximity because of the drag reduction. Dynamic analyses with a fixed-base simulator indicate that the resultant flight path during landing approach is dependent on the initial flight-path angle and the control technique used.

Effects of asymmetries, such as sideslip or roll and engine-out characteristics, in ground proximity were also available from the wind-tunnel tests. Sideslip characteristics were generally unaffected by ground proximity. Roll attitudes were unstable at heights near gear touchdown height, and no significant yaw-roll coupling was noted. Engine-out characteristics were unaffected by ground proximity.

INTRODUCTION

In 1969, an investigation (ref. 1) was conducted in the 17-foot test section of the Langley 300-MPH 7- by 10-foot tunnel to determine the aerodynamic characteristics in ground proximity of the four-engine externally blown flap (EBF) configuration shown in figure 1. Various combinations of the segmented full-span double-slotted flaps were tested. Typical flap deflections were 30° in a take-off configuration and 60° in a landing configuration. Both high and low positions of the wing were tested. Changes in lift, drag, and pitching moment in ground proximity were measured over a moving ground belt.

The results from that investigation were used as the basis for a study presented at the STOL Technology Conference in 1972 (ref. 2) of ground proximity effects on powered-lift landing performance. The conclusions of that study were that the lift loss in ground proximity for most powered-lift configurations could be correlated with the height of the flap trailing edge and the level of developed lift. The lift loss increased as the trailing edge of the flap approached

PAGE INTENTIONALLY BLANK

the ground and increased with increasing lift coefficient. The "adverse" ground effect was, therefore, greater for low-wing configurations. Steady-state and in-flight simulator analyses indicated that acceptable landings could be made with conventional applications of power and elevator although the landing task was more difficult for a low-wing as opposed to a high-wing configuration.

Since aerodynamic characteristics are a function of the height above the ground, there is a need to assess possible adverse effects of airplane position asymmetries, such as sideslip or bank angle, in ground proximity which might be critical during the landing approach. For the example of an airplane banked in ground proximity, the lift loss might increase on the wing closer to the ground and be reduced on the higher wing, thereby causing a rolling moment into the ground beyond the available control power. This consideration led to tests in the Langley V/STOL tunnel of the EBF model shown in figure 2. The model is a four-engine configuration with full-span triple-slotted flaps very similar in planform to the earlier EBF model tested. Flap trailing-edge deflection angles were 40° in a take-off configuration and 55° in a landing configuration. Forces and moments were measured over a moving ground belt with a boundary-layer removal system in the front of the test section over a range of test conditions. The tests allowed an assessment of the effect of airplane position asymmetries, including roll angle, sideslip angle, and combined roll and sideslip angles, in ground proximity as well as a comparison of longitudinal characteristics in ground proximity with those for the earlier EBF configuration.

The upper-surface blown (USB) concept is a rather different type of powered-lift concept for which little data in ground proximity are available and which might have unexpected changes in aerodynamic characteristics near the ground, particularly with one engine inoperative. This consideration led to tests in the Langley V/STOL tunnel over a moving ground belt of the USB model shown in figure 3. The model is the twin-engine configuration discussed by Phelps, Johnson, and Margason in reference 3. Trailing-edge deflection angles of the Coanda flap behind the engines were 20° in a take-off configuration and 60° in a landing configuration. Outboard of the Coanda flaps were double-slotted flaps and a blown drooped aileron. The wind-tunnel results allowed an assessment of the longitudinal and engine-out characteristics of the USB configuration.

This paper thus updates the previous study on powered-lift aerodynamics in ground proximity with recent research results in the V/STOL tunnel. Comparisons of longitudinal aerodynamic characteristics for the EBF and for the USB configurations in ground proximity are possible. Steady-state and dynamic analyses of the landing approach for a typical STOL airplane are made to indicate the consequences of the aerodynamic changes in ground proximity.

SYMBOLS

Measurements and calculations were made in U.S. Customary Units and are presented in both the International System of Units (SI) and U.S. Customary Units.

A	aspect ratio
b	wing span, m (ft)
C_D	drag coefficient
ΔC_D	incremental drag coefficient, $C_D - C_{D,\infty}$
C_L	lift coefficient
ΔC_L	incremental lift coefficient, $C_L - C_{L,\infty}$
C_l	rolling-moment coefficient
$C_{l\beta}$	effective dihedral parameter
C_m	pitching-moment coefficient
C_n	yawing-moment coefficient
$C_{n\beta}$	directional stability parameter
C_μ	static thrust coefficient
h	height of wing quarter-chord above ground, m (ft)
I_Y	moment of inertia about pitch axis, kg-m^2 (slug-ft^2)
m	mass, kg, (slugs)
V	velocity, m/sec (ft/sec)
α	angle of attack, deg
β	angle of sideslip, deg
γ	flight-path angle, deg
δ_f	flap deflection angle, deg
$\Lambda_{c/4}$	sweep angle at wing quarter-chord, deg
λ	taper ratio
ϕ	bank angle, deg

Subscripts:

o	initial value
∞	free-air condition

Abbreviations:

BLC	boundary-layer control
EBF	externally blown flap
L.E.	leading edge
USB	upper-surface blown

LONGITUDINAL AERODYNAMIC CHARACTERISTICS IN GROUND PROXIMITY

Both the EBF and the USB models tested in the Langley V/STOL tunnel were sting supported over a moving ground belt with a boundary-layer removal system ahead of the belt. However, the ground belt was not available during most of the EBF tests, although the boundary-layer removal system was always available. The variation of lift coefficient with the height-span ratio h/b is presented with the boundary-layer removal system operating and with the ground belt on and off. Results are presented for the EBF and USB models in the take-off configuration at constant angle of attack through a range of thrust coefficient. The shaded area represents the conditions given by Turner (ref. 4) for which a moving ground belt is required to simulate ground proximity correctly. The results indicate a slightly lower level of lift without the belt operating at free-stream velocity, although the trends are predicted very well. For the range of lift coefficient and height-span ratio, the ground proximity can be properly simulated with only a boundary-layer removal system in the test section.

The longitudinal characteristics in ground proximity of the recently tested EBF ($\delta_f = 55^o$) and USB ($\delta_f = 60^o$) models and the previously tested EBF ($\delta_f = 60^o$) model are presented in figure 5. The longitudinal forces and moments are presented as a function of h/b at constant angle of attack and at thrust coefficients appropriate for a free-air lift coefficient of about 4.25. Both EBF configurations show similar lift losses in ground proximity. The USB configuration shows a slight lift increase in ground proximity before losing lift at the lower heights. The lift is concentrated at the inboard sections of the wing for the USB configuration, whereas the lift is spread more outboard on the span for the EBF configurations. The differences in lift distribution may account for some of the differences in lift in ground proximity, although there are also differences in sweep between the configurations. Both EBF models are swept back 25^o at the quarter-chord and the USB configuration is unswept. All three configurations, however, show a decrease in drag associated with the reduction in jet deflection angle as the ground is approached.

The pitching-moment data of figure 5 are untrimmed at different settings of tail incidence and are presented only to show the trends in ground proximity. The EBF models show nose-down moment increments in ground proximity and the pilot will have to exert trim control during landing. The trim control is usually obtained from a download at the tail, so that the trimmed lift loss in

ground proximity is increased. The USB configuration indicates only a slight nose-down moment in ground proximity. The sweep differences between the configurations are probably the cause of the differences in pitching moment.

Presented in figure 6 are lift and drag as a function of height-span ratio for the EBF and USB configurations tested in the V/STOL tunnel. Results are presented with the flaps at reduced deflections corresponding to take-off conditions at two values of thrust coefficient. At the reduced flap settings the lift and drag in ground proximity change significantly less even though the lift levels are comparable to those given in figure 5 for the landing configuration. The pitching-moment changes, although not presented, were also reduced with the lower flap deflections.

ANALYSIS OF LANDING APPROACH

The changes in aerodynamic characteristics in ground proximity are most critical during the landing approach and the effects of these changes are considered in both steady-state and dynamic analyses. The aerodynamic inputs were those forces and moments measured in the Langley V/STOL tunnel for the EBF and USB configurations in ground proximity. Trimmed lift and drag polars in ground proximity were constructed and a typical variation of trimmed lift and drag in ground proximity, nondimensionalized by the free-air lift coefficient, are shown in the left side of figure 7. Flight-path angle and angle of attack in ground proximity for a constant-thrust, constant-speed approach corresponding to a trimmed lift coefficient of 4.0 and initial flight-path angle of -6° are shown on the right side of figure 7. The results indicate that the reductions in drag more than offset any of the lift changes to increase the flight-path angle in ground proximity. The angle of attack must be reduced slightly for the USB configuration and increased slightly for the EBF configuration to maintain constant trimmed lift. A similar increase in flight-path angle in ground proximity was noted at the 1972 STOL Technology Conference (ref. 2). Reductions of the flight-path angle to zero in a flaring maneuver were possible with application of elevator and power.

The steady-state analysis of the landing approach assumes that force and moment changes in ground proximity translate directly into flight-path changes. However, the mass and inertial characteristics must be considered in a dynamic analysis to properly simulate the actual airplane landing approach. The mass and inertial characteristics of a typical STOL aircraft (m = 24 993 kg (1711 slugs) and I_Y = 334 642 kg-m^2 (246 819 slug-ft^2)) were used as input to the fixed-base dynamic simulation program of reference 5. Approaches were simulated over a range of initial flight-path angle, free-air lift coefficient, and control technique. The fixed-base simulator results for a constant-thrust approach using a feedback control from the elevator to maintain speed are shown in figure 8 for the EBF and USB configurations. Free-air trimmed lift coefficient is 4.27 and results are presented as flight-path trajectories for initial flight-path angles of -6° and -1.5°. At the higher rate of descent, the steady-state results do not have time to influence the flight path, and neither the USB nor the EBF configuration deviates much from the initial flight path. As

a check on the results, the analysis was continued below gear touchdown height and eventually the flight-path angle was increased corresponding to the steady-state results. At the lower rate of descent, the changes in forces and moments in ground proximity have a chance to develop and both configurations perform self-flaring maneuvers at ground heights near 6.1 m (20 ft).

The flight-path changes in ground proximity are dependent on the particular type of feedback control system used. The results for a constant-thrust approach using a feedback control from the elevator to maintain attitude are shown in figure 9. Neither configuration deviates from the steep flight path in ground proximity. At the lower initial rate of descent, the USB configuration performs a self-flaring maneuver near 4.9 m (16 ft). The EBF configuration does not flare, although it never falls below the initial flight-path trajectory.

The drag reductions in ground proximity common to both the EBF and the USB configurations are most important in determining steady-state flight-path increases in ground proximity. The lift changes are configuration dependent and the extent to which the steady-state results are experienced on the actual airplane depends on the initial flight-path angle and the particular type of feedback control system used. None of the above analyses consider the flare maneuver which can be effected by application of either power or elevator.

SIDESLIP AND ROLL IN GROUND PROXIMITY

The EBF model in figure 2 was tested in the Langley V/STOL tunnel to determine the effect of sideslip angle, bank angle, and combined sideslip and bank angles in ground proximity. Results in figure 10 for the pure sideslip condition in ground proximity are presented as effective dihedral $\left(-C_{l_\beta}\right)$ and directional stability $\left(C_{n_\beta}\right)$ as functions of height-span ratio for several thrust coefficients at constant angle of attack. Through sideslip angles of $\pm 10^\circ$, the EBF model indicated strong stability with little change due to ground proximity. The directional stability shows the expected increase with thrust because of the increased dynamic pressure at the tail. The effective dihedral is increased slightly at the lower height-span ratios.

The effect of roll in ground proximity is presented in figure 11 at a constant angle of attack and constant thrust corresponding to a free-air lift coefficient near 4.0. Rolling moment as a function of height-span ratio is presented for various roll attitudes. The pure roll case is shown on the left side of the figure, and positive bank angles corresponding to right wing down give large unstable rolling moments at height-span ratios near gear touchdown height. The combined roll and sideslip condition is given in the right side of the figure. The increment in rolling moment due to sideslip at $\phi = 0^\circ$ arises from the strong positive effective dihedral. Positive and negative roll attitudes give unstable rolling moments at height-span ratios near gear touchdown height. The unstable rolling-moment increment due to roll attitude is about the same at $\beta = 0^\circ$ and $\beta = -10^\circ$, indicating no significant yaw-roll coupling.

ENGINE-OUT CHARACTERISTICS IN GROUND PROXIMITY

The lateral-directional characteristics of the twin-engine USB concept in the event of engine failure during a powered-lift approach have been a matter of some concern. A concerted effort has been made to develop lateral control systems for this concept sufficiently powerful to trim out lateral asymmetries due to engine failure. Figure 12 illustrates the effect of engine failure in ground proximity. Results are presented in terms of yawing moment and rolling moment as functions of angle of attack for both the free-air condition ($h/b = \infty$) and in ground proximity ($h/b = 0.2$). The results presented are for the landing configuration ($\delta_f = 60^o$) with the left engine inoperative and with the right engine at full thrust ($C_\mu = 1.80$). The left side of figure 12 illustrates engine-out characteristics with all controls neutral. Surprisingly, the rolling-moment asymmetry was unaffected by ground proximity; however, the adverse yawing moment due to engine failure was reduced at the higher values of angle of attack.

The right side of figure 12 illustrates a possible solution to the lateral asymmetry problem due to engine failure. The aileron on the engine-out side has been drooped 60^o and is augmented with blowing boundary-layer control (BLC). Also, the entire leading edge of the wing on the engine-out side is augmented with BLC to prevent flow separation at higher angles of attack. The results indicate that most of the rolling-moment asymmetry due to engine failure can be trimmed out with this lateral control system and that ground proximity had essentially no effect on the rolling-moment trim capability. Adverse yawing moment due to this lateral control is, in general, very slight (compare left- and right-hand yawing-moment data), and ground proximity causes the same reduction in yawing-moment asymmetry at higher values of angle of attack as was observed with lateral controls neutral. It should be mentioned that the twin-engine USB concept requires a double-hinged rudder capable of handling the yawing moments due to engine failure during take-off, and such a rudder control would be more than adequate to trim out the yawing moments shown in figure 12 for the landing configuration.

CONCLUSIONS

The following conclusions are drawn from the recent wind-tunnel investigations of powered-lift configurations:

1. Drag reductions in ground proximity are common to both EBF and USB configurations, whereas changes in lift are configuration dependent.

2. The extent to which the predicted steady-state flight-path increases in ground proximity are experienced on the actual airplane depends on the initial flight-path angle and the control technique used.

3. Lateral-directional characteristics due to sideslip are unaffected by ground proximity, whereas roll attitudes give unstable rolling moments near gear touchdown height.

4. Engine-out characteristics both with and without corrective control are unaffected by ground proximity.

REFERENCES

1. Vogler, Raymond D.: Wind-Tunnel Investigation of a Four-Engine Externally Blowing Jet-Flap STOL Airplane Model. NASA TN D-7034, 1970.

2. Hassell, James L., Jr.; and Judd, Joseph H.: Study of Ground Proximity Effects on Powered-Lift STOL Landing Performance. STOL Technology, NASA SP-320, 1972, pp. 199-213.

3. Phelps, Arthur E., III; Johnson, Joseph L., Jr.; and Margason, Richard J.: Summary of Low-Speed Aerodynamic Performance of the Upper-Surface-Blown Jet-Flap Concept. Powered-Lift Aerodynamics and Acoustics, NASA SP-406, 1976. (Paper no. 4 of this compilation.)

4. Turner, Thomas R.: Endless-Belt Technique for Ground Simulation. Conference on V/STOL and STOL Aircraft, NASA SP-116, 1966, pp. 435-446.

5. Grantham, William D.; Nguyen, Luat T.; Patton, James M., Jr.; Deal, Perry L.; Champine, Robert A.; and Carter, C. Robert: Fixed-Base Simulator Study of an Externally Blown Flap STOL Transport Airplane During Approach and Landing. NASA TN D-6898, 1972.

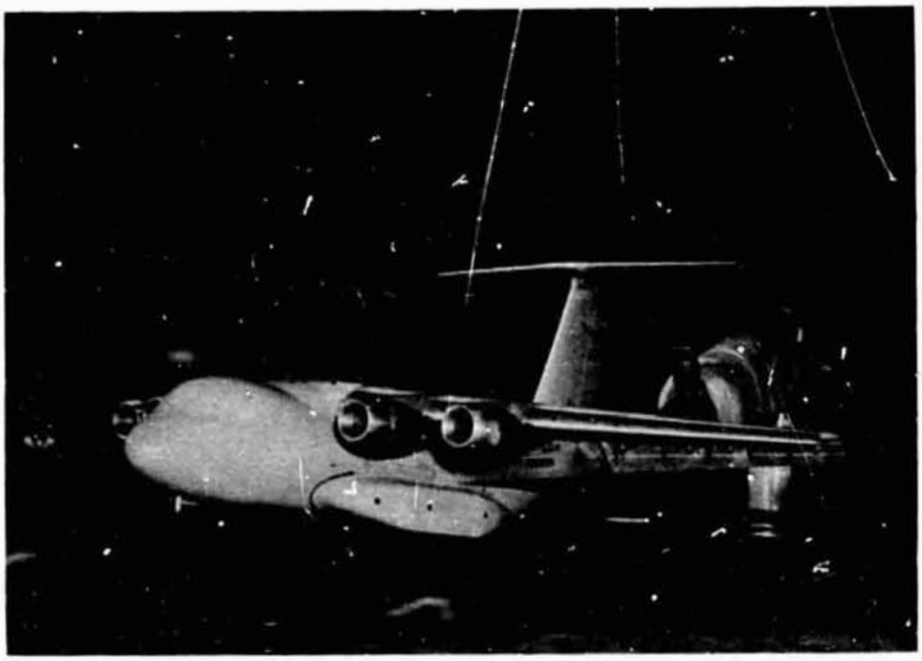

Figure 1.- EBF configuration tested in 17-foot test section of Langley 300-MPH 7- by 10-foot tunnel. A = 7.0; $\Lambda_{c/4} = 25^{o}$; $\lambda = 0.3$.

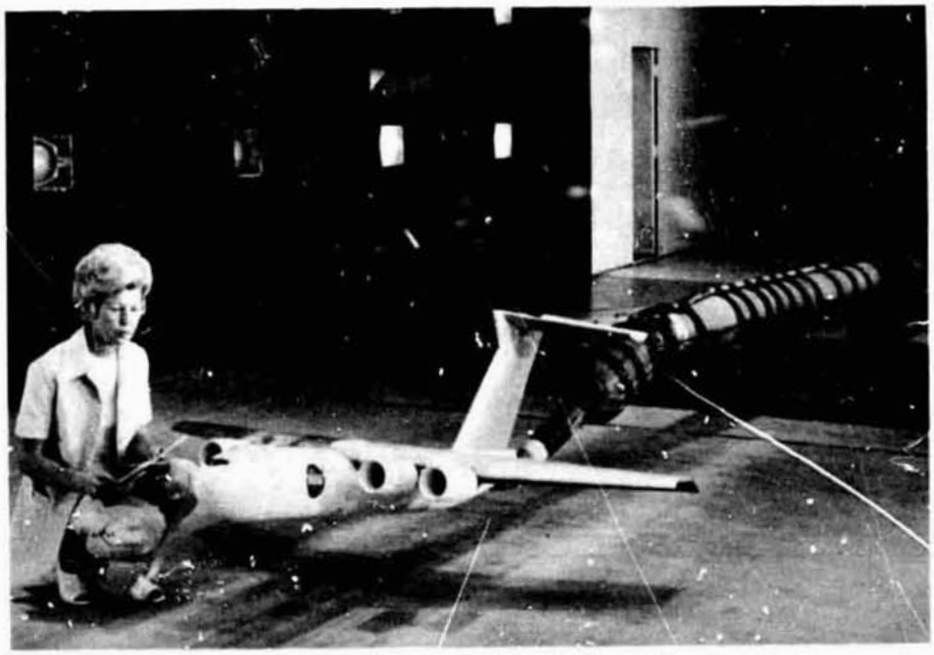

Figure 2.- EBF configuration tested in Langley V/STOL tunnel. A = 7.3; $\Lambda_{c/4} = 25^{o}$; $\lambda = 0.4$.

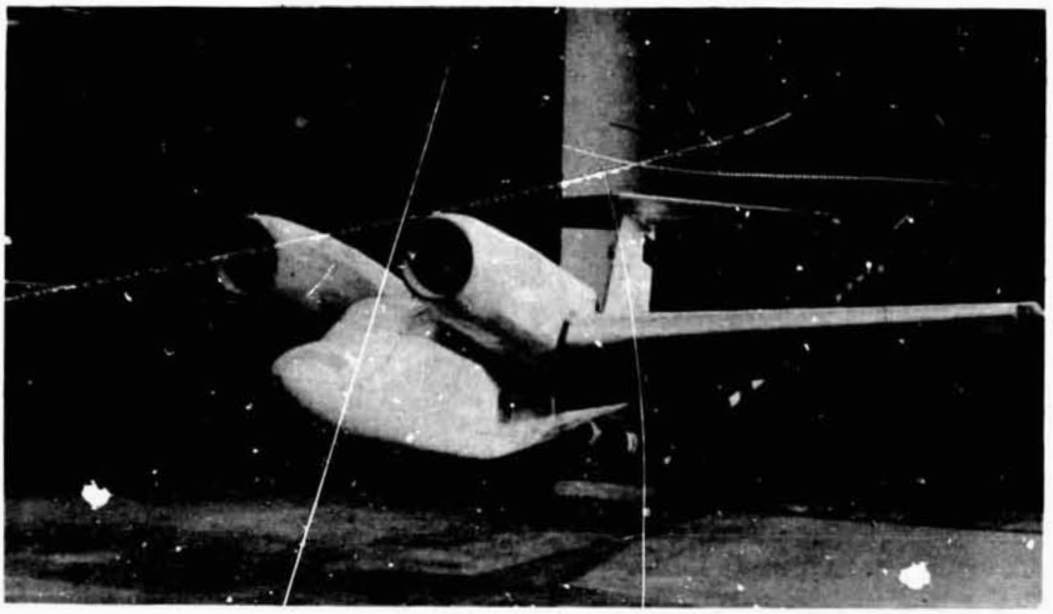

Figure 3.- USB configuration tested in Langley V/STOL tunnel. A = 8.2; $\Lambda_{c/4} = 0^{o}$; $\lambda = 0.3$.

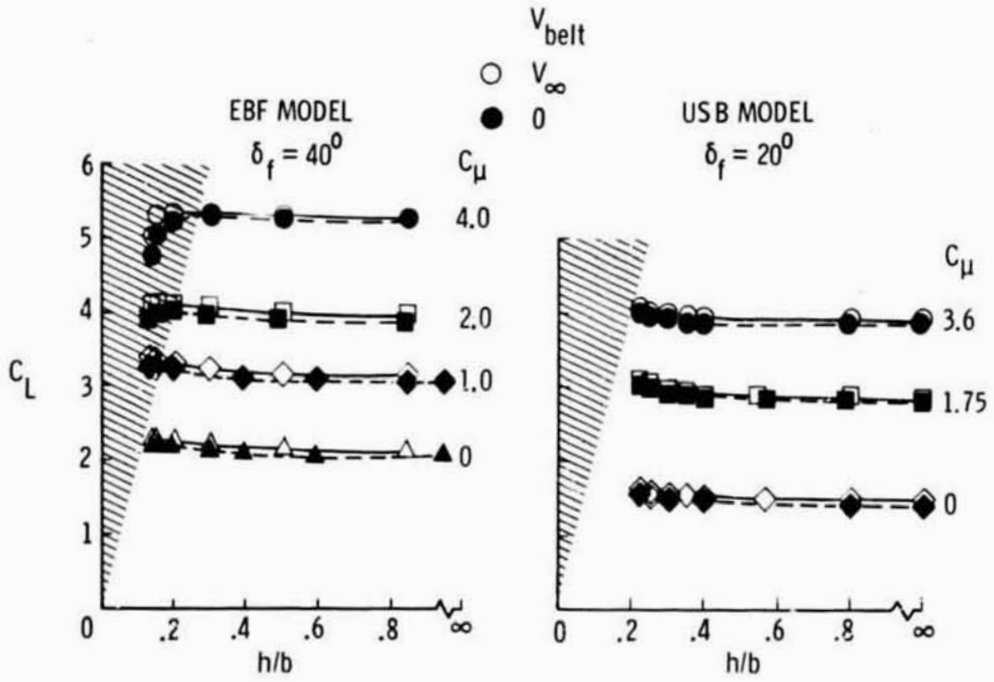

Figure 4.- Effect of moving ground belt on lift in ground proximity with boundary-layer removal system operating. $\alpha = 5^{o}$.

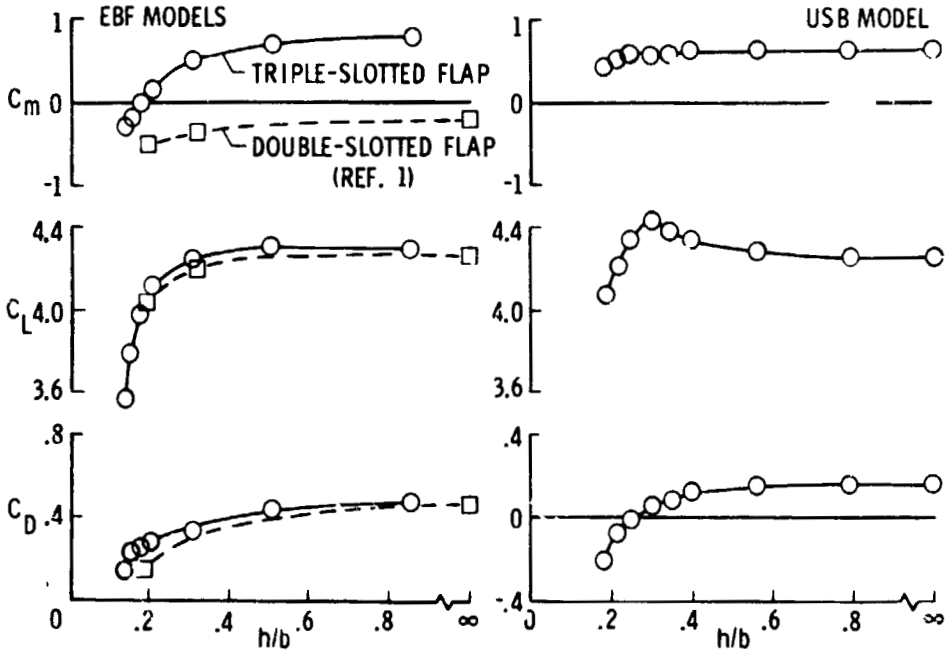

Figure 5.- Ground effect on longitudinal aerodynamics of landing configurations. $\alpha = 5^o$; C_μ = Constant; $C_{L,\infty} = 4.25$.

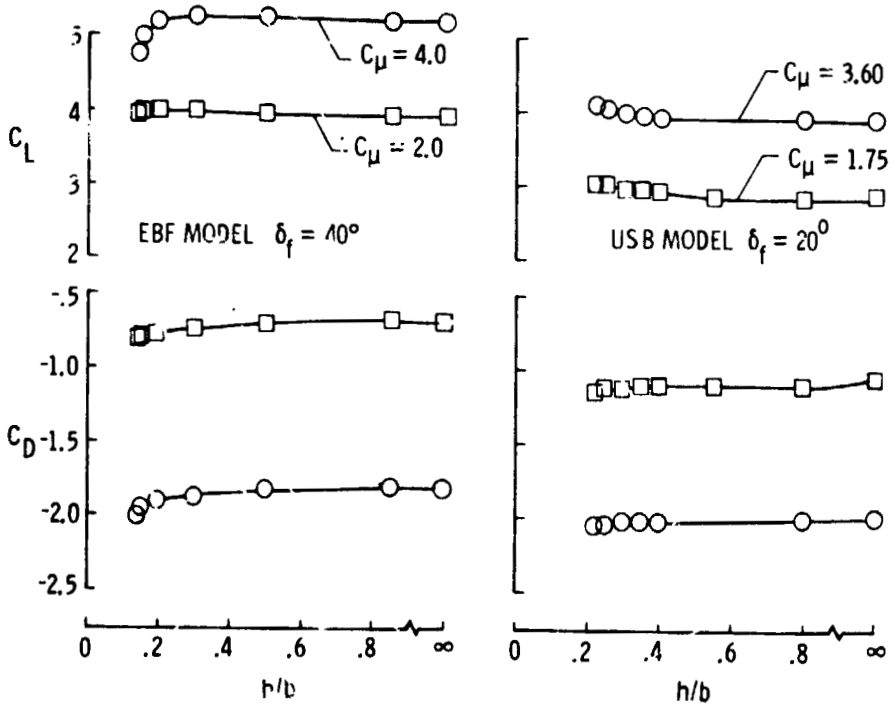

Figure 6.- Ground effect on longitudinal aerodynamics of take-off configurations. $\alpha = 5^o$.

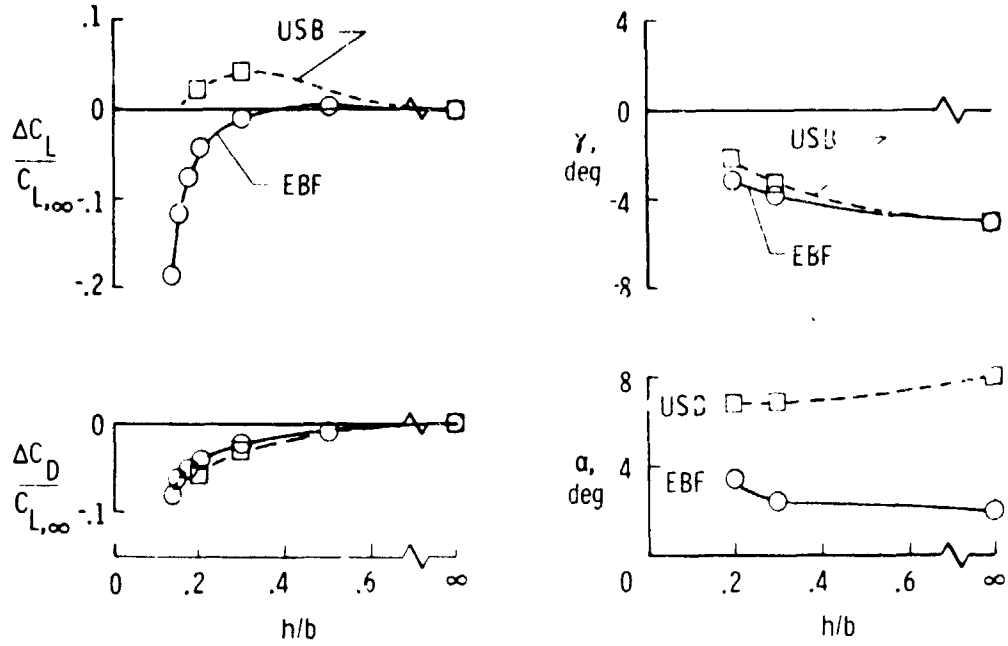

Figure 7.- Results from steady-state analysis of constant-thrust, constant-speed landing approach. $C_{L,trim} = 4.0$.

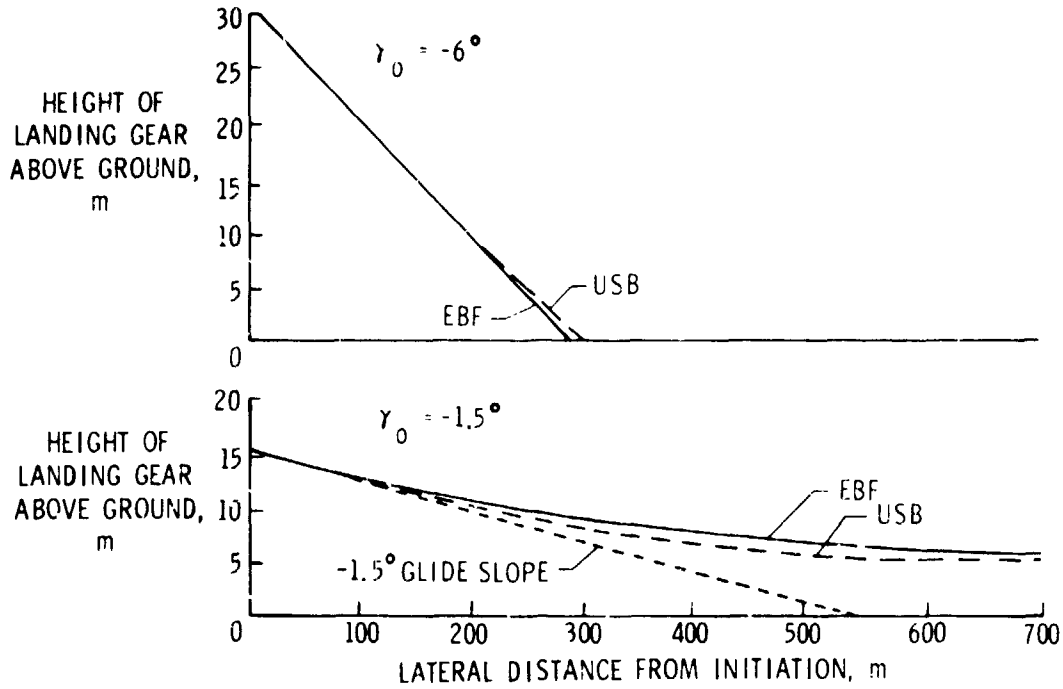

Figure 8.- Results from fixed-base simulator analysis of constant-thrust, constant-speed landing approach using elevator control. $(C_{L,trim})_\infty = 4.27$.

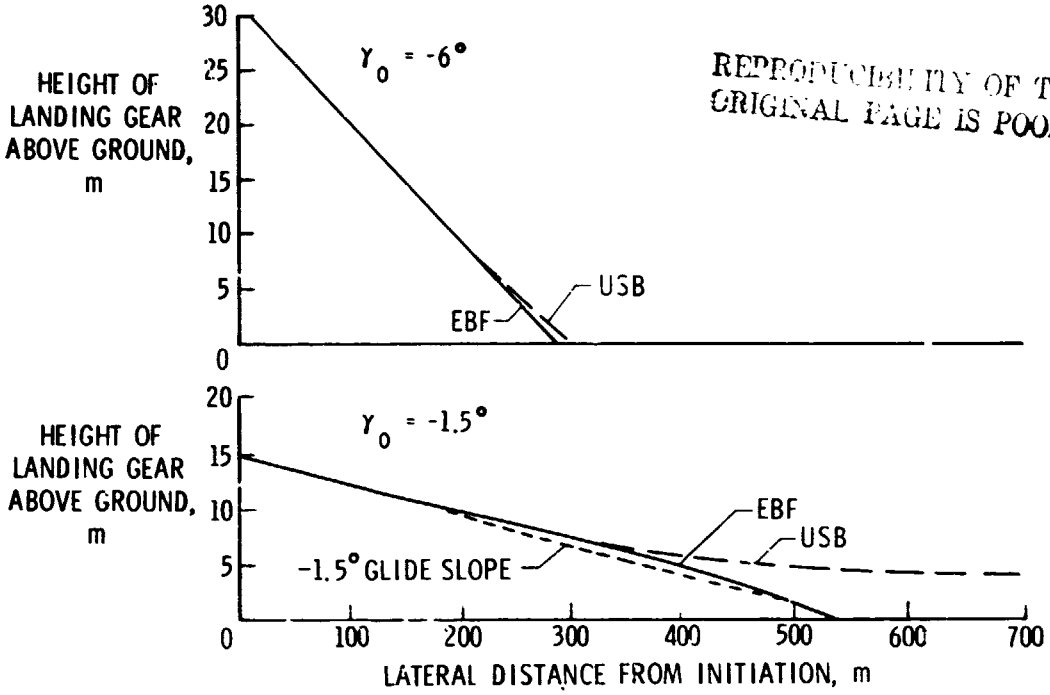

Figure 9.- Results from fixed-base simulator analysis of constant-thrust, constant-attitude landing approach using elevator control. $(C_{L,trim})_\infty = 4.27$.

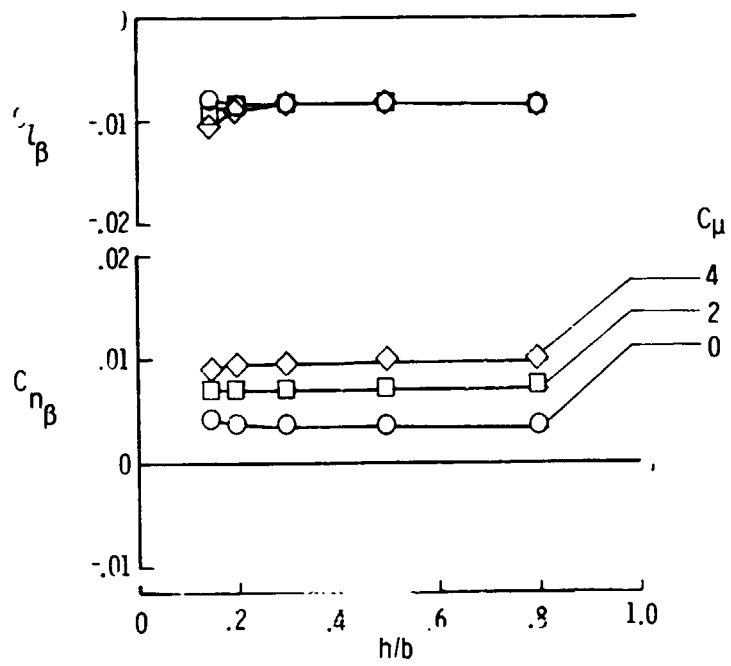

Figure 10.- Static lateral-directional characteristics in ground proximity. Triple-slotted EBF model; $\delta_f = 40^\circ$; $\alpha = 5^\circ$

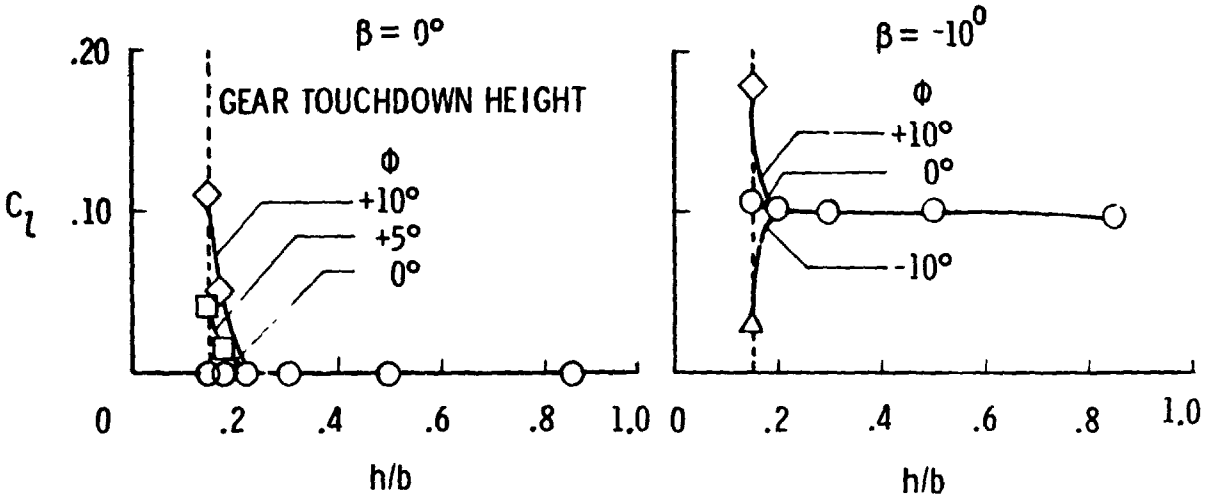

Figure 11.- Effect of bank angle in ground proximity. Triple-slotted EBF model; $\delta_f = 40^o$; $\alpha = 5^o$; $C_\mu = 2$; $C_{L,\infty} = 4.0$.

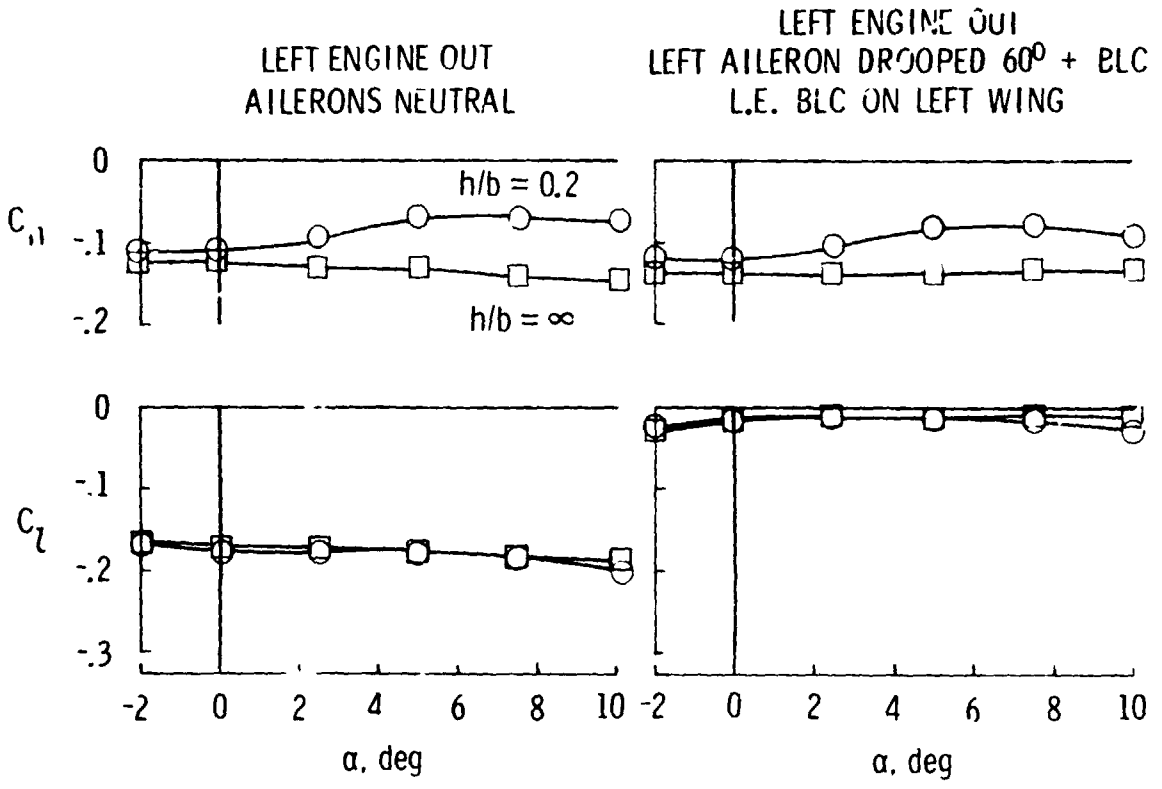

Figure 12.- Engine-out characteristics in ground proximity. Twin-engine USB configuration; $C_\mu = 1.80$; left engine out; $\delta_f = 60^o$.

DISTRIBUTED UPPER-SURFACE BLOWING CONCEPT

Paul G. Fournier and Paul L. Coe, Jr.
NASA Langley Research Center

SUMMARY

A low-speed investigation was conducted in the Langley V/STOL tunnel to determine the powered-lift aerodynamic performance of a distributed upper-surface-blown propulsive-lift transport model. The model used blowing slots across the span of the wing to produce a thin jet efflux near the leading edge and at the knee of the trailing-edge flap (internally blown jet flap). These concepts have both good propulsive-related lift and low drag-due-to-lift characteristics because of uniform spanwise propulsive thrust. The leading-edge blowing concept provides low-speed lift characteristics which are competitive with the flap-hinge-line blowing concept and does not require additional leading-edge treatment for prevention of abrupt stall.

INTRODUCTION

Several propulsive-lift concepts have been investigated recently in efforts to develop a quiet short-take-off-and-landing (STOL) aircraft. The upper-surface-blown (USB) jet-flap concept appears to offer an attractive solution for a quiet STOL aircraft. Most of the investigations to date have used configurations that direct the efflux from discrete engine nozzles over the wing upper surface and high-lift system to provide increases in lift by means of Coanda turning of the jet (ref. 1). These results indicated that the propulsive lift capabilities were greatly dependent upon the nozzle geometry and their [illegible]ion to the high-lift system, with thin well-spread jets giving the best Co[illegible] turning.

Another version of the USB concept utilizes full-span slot nozzles near the leading edge and flap hinge. These slot nozzles are beneficial in several ways. First, they improve the aerodynamic performance by distributing the propulsive efflux in the spanwise direction, which improves the induced lift and reduces the induced drag relative to that obtained with discrete USB nacelles. Second, this arrangement reduces the propulsive noise by the use of very high aspect-ratio nozzles which produce high-frequency noise that damps out quickly and by shielding the ground with the wing.

Figure 1(a) shows a photograph and a sketch of this distributed blowing concept applied to a subsonic transport configuration with an aspect-ratio-6.8 swept wing tested in the Langley V/STOL tunnel. The wing had internal plenums which supplied air to full-span slot nozzles located along the wing leading edge and along the flap hinge line. It is anticipated that this arrangement would

approach the upper limit for propulsive induced lift. However, such an arrangement would introduce weight and volume penalties and would require systems studies to determine if it is a practical concept for subsonic transport applications.

SYMBOLS

A	aspect ratio
C_D	drag coefficient, Drag/qS
C_L	lift coefficient, Lift/qS
$C_{L,jr}$	jet-reaction lift coefficient
$C_{L\Gamma}$	circulation lift coefficient due to power
C_μ	thrust coefficient, Thrust/qS
c	wing chord
q	free-stream dynamic pressure
S	wing area
α	angle of attack, deg
δ_f	flap deflection measured streamwise, deg (Dual notation indicates deflection of forward element with respect to the basic airfoil chord line, followed by the deflection of the rear element with respect to the chord line of the forward element. See fig. 1(b).)

DISCUSSION

The basic data for distributed blowing over the flap and at the leading edge for several flap deflections are presented in figure 2 for a nominal value of C_μ of 2.0. These data show that with blowing over the deflected trailing-edge flaps and with no leading-edge high-lift device, there was an abrupt stall near $\alpha = 12^o$. However, for the leading-edge blowing configuration, there was no stall through the angle-of-attack range tested.

The theoretical minimum drag-due-to-lift curve (ref. 2) is plotted along with the basic data for both blowing concepts in figure 2 and shows that the basic data approach this curve quite well.

T variations of lift coefficient with angle of attack for the two blowing concepts are presented in figure 3. All configurations had two element flaps

(fig. 1(b)) with the forward and aft elements deflected 45° and 15°, respectively. A comparison of the leading-edge and flap blowing indicates that at low angles of attack, the flap-hinge-line blowing results in somewhat higher values of C_L than the leading-edge blowing. Also, if the leading edge is dropped to 30° on the flap-hinge-line blowing configuration, it performs as well as, or better than, the leading-edge blowing configuration at the higher angles of attack.

Figure 4 presents the propulsive-related lift as a function of thrust coefficient for the distributed leading-edge blowing concept and a conventional USB concept. The propulsive-related lift is the combination of the jet-reaction lift $C_{L,jr}$ and the additional circulation lift due to power $C_{L\Gamma}$. The conventional USB concept (ref. 2) used rectangular exhaust nozzles having an aspect ratio of 6. The distributed leading-edge blowing concept produced much more propulsive-related lift than the USB concept.

CONCLUDING REMARKS

The distributed blowing concepts, with blowing at either the leading edge or flap hinge line, have both good propulsive-related lift and low drag due to lift because of the uniform spanwise propulsive thrust. The leading-edge blowing concept provides low-speed lift characteristics which are competitive with the flap-hinge-line blowing concept and does not require additional leading-edge treatment for prevention of abrupt stall.

REFERENCES

1. Sleeman, William C., Jr.; and Hohlweg, William C.: Low-Speed Wind-Tunnel Investigation of a Four-Engine Upper Surface Blown Model Having a Swept Wing and Rectangular and D-Shaped Exhaust Nozzles. NASA TN D-8061, 1975.

2. McCormick, Barnes W., Jr.: Aerodynamics of V/STOL Flight. Academic Press, Inc., 1967.

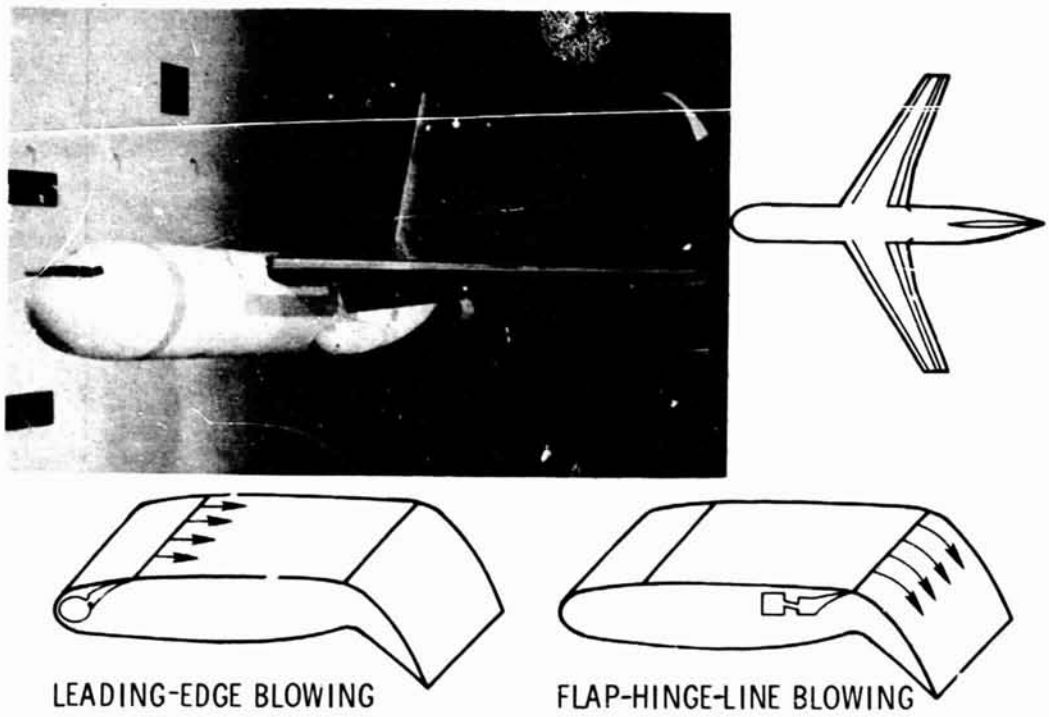

(a) Sketch and photograph of model.

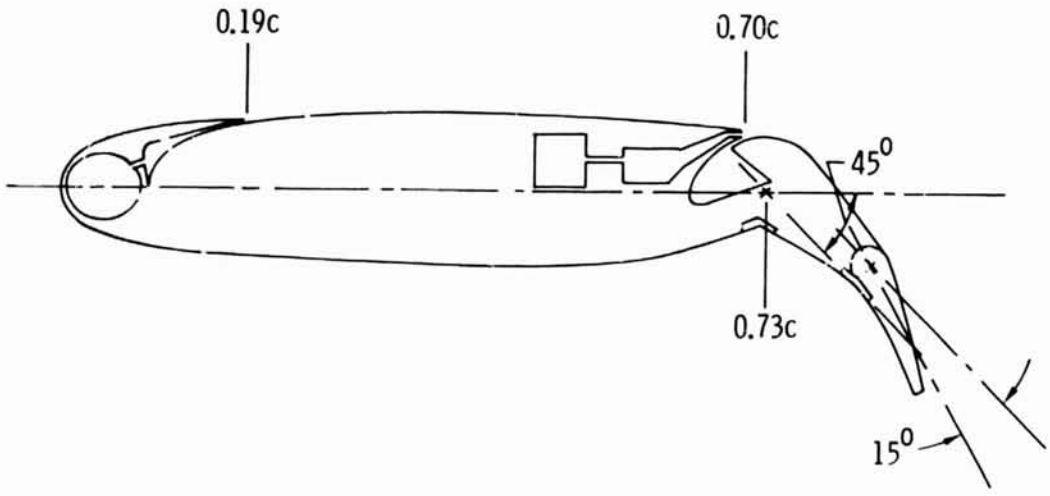

(b) Flap details.

Figure 1.- Distributed blowing concepts applied to subsonic transport.

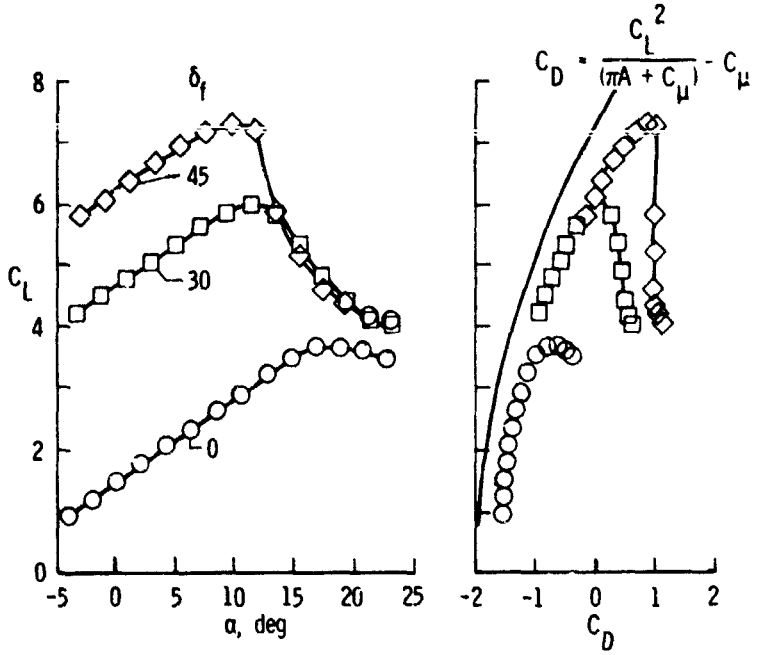

(a) Flap-hinge-line blowing. C_μ = 1.9.

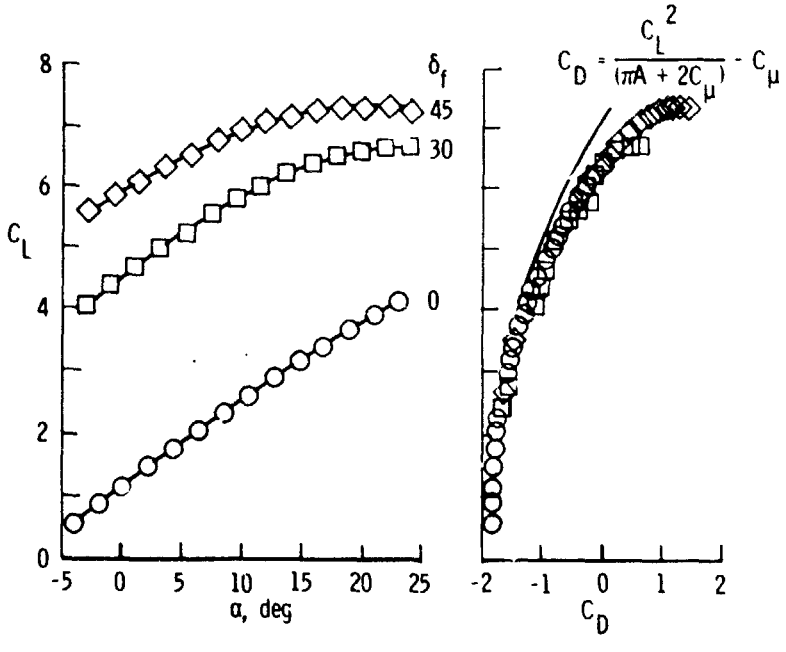

(b) Leading-edge blowing. C_μ = 2.0.

Figure 2.- Effect of flap deflection on lift and drag coefficients for model with distributed blowing concepts. Tail off; $\delta_f = 45^o$-0^o; $C_\mu \approx 2$.

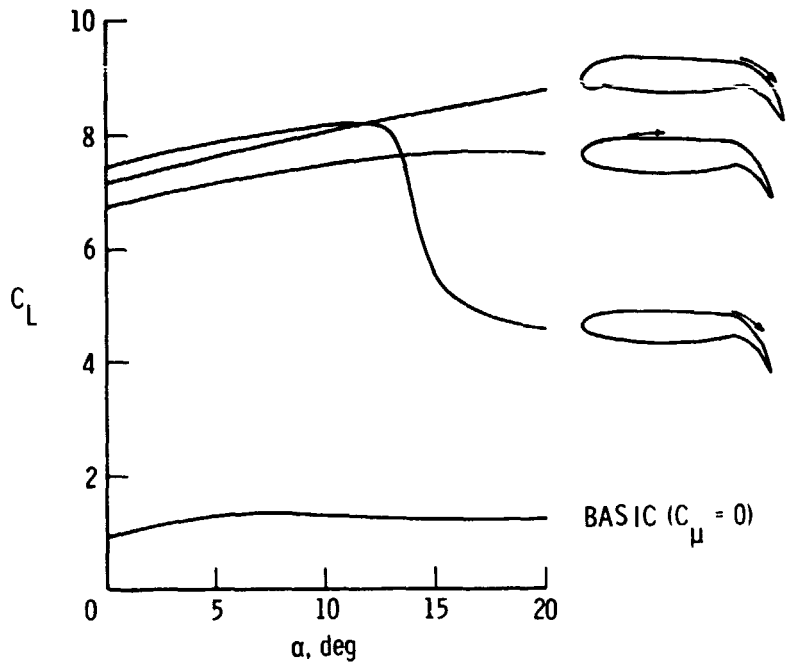

Figure 3.- Variation of C_L with α for the distributed blowing concepts. $\delta_f = 45^o\text{-}15^o$; $C_\mu = 2.0$.

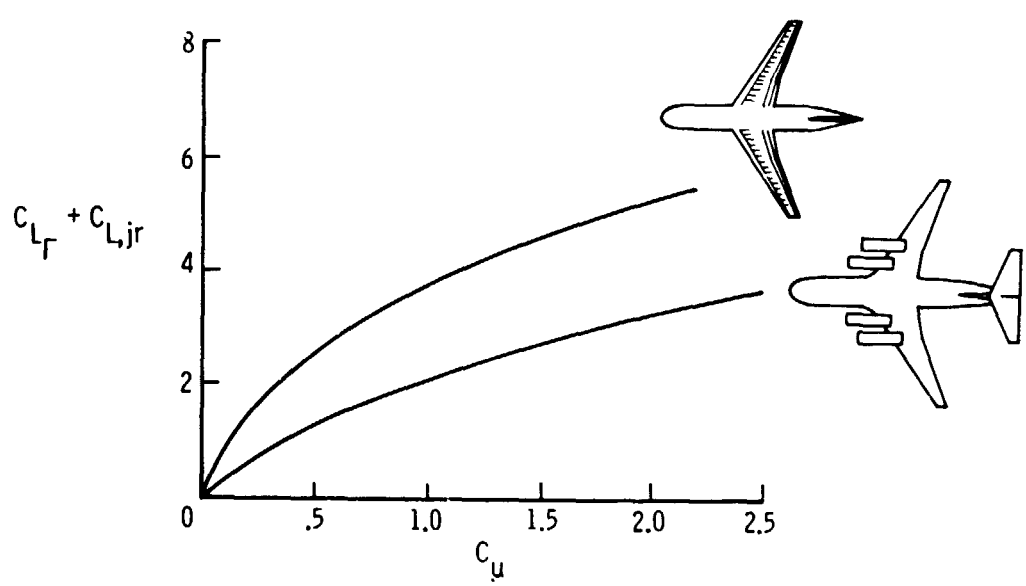

Figure 4.- Variation of propulsive-related lift with thrust coefficient for the distributed leading-edge blowing concept and a conventional USB concept.

CRUISE AERODYNAMICS OF USB NACELLE/WING GEOMETRIC VARIATIONS*

John A. Braden, John P. Hancock, and Kenneth P. Burdges
Lockheed-Georgia Company

SUMMARY

Experimental results are presented on aerodynamic effects of geometric variations in USB nacelle configurations at high-speed cruise conditions. Test data includes both force and pressure measurements on two- and three-dimensional models powered by upper-surface blowing nacelles of varying geometries. Experimental results are provided on variations in nozzle aspect ratio, nozzle boattail angle and multiple-nacelle installations. The nacelles are ranked according to aerodynamic drag penalties as well as overall installed drag penalties. Sample effects and correlations are shown for data obtained with the pressure model.

INTRODUCTION

Use of upper surface blowing (USB) engine installations, illustrated in figure 1, has been demonstrated as a viable means of STOL high-lift augmentation by both industry and government sponsored research over the past several years. Such studies have shown the system to be attractive for STOL application from a number of viewpoints. These include generally favorable acoustic characteristics for the terminal area environment, reasonably practical structural compatibility with the airframe, and acceptable flexibility for integrating with basic operational systems or sub-systems. These, of course, are in addition to the recognized potential for good STOL performance. In contrast to the low-speed accountability of the USB system, a comparable data base for the high-speed cruise regime has been lacking. To fill this need, the Lockheed-Georgia Company, under contract to the NASA, has conducted experimental investigations wherein USB nacelle/wing geometries and operating conditions are systematically varied in the $0.5 \leq M_o \leq 0.8$ cruise regime. The basic goal of this parametric investigation is to define those geometric properties and operating conditions indicative of minimum cruise-drag penalties and from which more refined USB configurations can evolve.

* Work performed under contract to the NASA; Contract No. NAS1-13871; "Cruise Performance of Upper Surface Blowing Configurations."

The present paper provides a brief over-view of the experimental program, currently still in progress, along with preliminary findings believed to be of general interest. The experimental work encompasses force-test evaluations, surface pressure measurements, and wake surveys behind powered configurations. A companion analytical effort is involved in the basic program, but an evaluation of math model capabilities via experimental correlation must await a more thorough examination of the test results.

SYMBOLS

Values are given in both SI and U.S. Customary Units. The measurements and calculations were made in U.S. Customary Units.

A_N	nozzle exit area, cm^2 (in^2)
AR	nozzle aspect ratio, w^2/A_N
b/2	wing semispan, cm (in.)
c	wing chord, cm (in.)
C_L	lift coefficient
C_μ	thrust coefficient
ΔC_D	incremental drag coefficient
D	drag, N (lb)
H	nozzle stagnation pressure, N/m^2 (lb/in^2)
H/P_o	nozzle pressure ratio
M_o	freestream Mach number
P_o	freestream static pressure, N/m^2 (lb/in^2)
q_o	freestream dynamic pressure, N/m^2 (lb/in^2)
S	wing area per semispan, cm^2 (in^2)
T	gross thrust, N (lb)

w	nozzle width, cm (in.)
X	chordwise distance from wing leading edge, cm (in.)
α	angle of attack, deg
β	boattail angle, deg
δ_j	jet turning angle measured statically, deg
η	thrust efficiency for wing/nacelle combination, T_{MEAS}/T_{ISOL}

Subscripts:

A, Aero	aerodynamic
F	friction
INT	interference
ISOL	isolated
ℓ	local
M, MEAS	measured
N	nacelle
TOT	total

EXPERIMENTAL OBJECTIVES

The objective of this experimental program is to establish a transonic experimental data base covering a wide variation of nacelle geometric parameters. An extensive array of nacelle/wing geometric configurations were developed so that experimental evaluation of the transonic force and surface pressure characteristics could be made. The geometric configurations were tested over a wide range of Mach number, angle of attack, and nozzle pressure ratio to establish an extensive data base from which summary "effects" are developed. The primary geometric variations in nacelle configurations, illustrated in figure 2, for which aerodynamic "effects" data are generated and aerodynamically ranked are:

- o nozzle exit aspect ratio
- o nozzle boattail angle

- o chordwise/vertical/spanwise positioning
- o size and number of nacelles

Secondary experimental objectives include the effects of:

- o wing sweep
- o wing camber modifications
- o inlet flow-field effects
- o jet deflectors
- o wing/nacelle filleting and streamlining

For the present discussion, only selected combinations of these geometric variations will be considered. In particular, nozzle aspect ratio, boattail angle and multiple-nacelle interference will be covered.

CFF TUNNEL TESTS

Test Facility

The experimental program is being conducted in the Lockheed-Georgia Compressible Flow Facility (CFF), which is a variable porosity, blowdown wind tunnel (Figure 3). Operating ranges are 0.2 to 1.2 Mach number and up to $164 \times 10^6/M$ Reynolds number in the transonic speed range. The test section, which is 50.8 cm (20 in.) wide, 71.1 cm (28 in.) high and 182.9 cm (72 in.) long, can be equipped with porous or solid walls to match particular test requirements. Model engine air supply is provided by an independent 2.068 MN/m^2 (300 lb/in^2) source. For powered force testing, air is supplied to the model through the force balance by a bellows arrangement.

Test Conditions

The Mach number range of interest in the experimental effort is $0.5 \leq M_o \leq 0.7$ for the unswept wing and $0.6 \leq M_o \leq 0.80$ for the swept wing model. Maximum nozzle pressure ratios (H/P_o) up to about 3.0 were tested over most of these speed ranges. Model angle of attack was varied from 0 degrees to 5 degrees encompassing all normal cruise settings. Flow visualization using titanium dioxide combined with oil was employed extensively to help understand the force and pressure test results.

Models

The test configurations are composed of a large number of interchangeable nozzles that fit the basic wing. There are two basic wings, swept and unswept, which have a removable tip allowing conversion from 2-D to 3-D configurations. The two-dimensional pressure models span the 50.8 cm (20 in.) horizontal width of the tunnel. For 3-D force testing, the wing is mounted vertically on the balance system in the tunnel floor. The semi-span-wing ($b/2 = 50.8$ cm (20 in.)) then spans 70 percent of the tunnel height (71.1 cm (28 in.)). Examples of the two force models, which illustrate unswept and swept 3-D wings, are provided in figures 4 and 5, respectively.

Figure 6 illustrates the build-up of a two-dimensional pressure model, using the unswept wing, along with the traversing wake rake. A supercritical-type of wing section is used for both the unswept and 25 degree swept wing. This airfoil section has a streamwise thickness ratio of 16 percent for the unswept wing application and 14 percent for the swept wing case; the wing chord is 17.8 cm (7 in.) in both instances. The wing design Mach numbers are about 0.7 and 0.8, respectively.

As illustrated, the nozzle air supply at 2.068 MN/m^2 (300 lb/in^2) is routed through the underwing duct and into a plenum formed by a faired-over forebody. The air is exhausted through a choke plate and exits from the nozzle at pressure ratios (H/P_o) ranging up to a maximum of 3.0. The same forebody is used with a number of interchangeable nozzles which have different exit shapes, but the same discharge area. Unpowered configurations may be built up by substitution of a flow-through inlet for the faired forebody.

Model instrumentation includes surface pressure taps at 5 spanwise positions on the wing and along the nozzle upper surface. A traversing wake rake provides the capability for sampling jet profiles and for evaluating momentum losses in the wing/nacelle wake.

RESULTS AND DISCUSSION

The force-test phase of the experimental program has recently been completed and pressure testing is currently in progress. For this reason, the present discussions emphasize force test results with limited reference to pressure testing, except where available data permits.

Aerodynamic Ranking

Following the convention established in low-speed, high-lift practice, the measured lift and accelerating force may be sub-divided into assumed components as shown in figure 7. The direct, or reactive thrust terms, $\eta C_\mu \sin(\alpha + \delta_j)$ and $\eta C_\mu \cos(\alpha + \delta_j)$ are removed from the measured data and the assumption made that the remainder represents the interactive

aerodynamic force and moment on the combined wing/nacelle. It is implicit in this approach that the statically determined thrust efficiency, η, representing scrubbing and vectoring losses, and turning angle, δ_i, are invariant with forward speed. It should also be noted that the loss represented by $(1 - \eta)$ is a constant increment of gross thrust and a much higher percentage of net thrust. The relationship between gross and net thrust is shown in figure 7.

Following the convention just discussed while holding constant circulation lift ($C_{L_A} = 0.40$) and Mach number (0.68), a comparison has been made of the aerodynamic interference drag for a D-duct nozzle to an AR = 6 nozzle, as shown in figure 8. Based on these aerodynamic interference drag levels, the wide (AR = 6) nozzle is superior to the semi-circular (D-duct) nozzle. However, this apparent aerodynamic advantage is gained at the expense of much greater penalty in scrubbing losses as indicated by the efficiencies shown at the top of the figure.

To obtain a more realistic ranking of these nozzles, a total interference drag coefficient is obtained by adding back in the losses associated with the assumed vectoring:

$$(\Delta C_{D_{INT}})_{TOT} = (\Delta C_{D_{INT}})_{AERO} + C_\mu [1 - \eta \cos (\alpha + \delta_i)]$$

This coefficient is compared in figure 9 for the same semi-circular and wide rectangular nozzles. In this comparison the semi-circular nozzle has the lowest drag. The magnitudes and rankings of these coefficients correspond to those which would be obtained by working only with the measured accelerating force reduced by the calibrated, isolated nacelle thrust and the clean wing/body drag plus nacelle friction. Therefore, ranking the nozzle geometric parameters in terms of the total interference drag rather than the aerodynamic drag alone is a basic process used throughout the present study.

Effect of Nozzle Aspect Ratio

Four characteristic exit shapes, three of which are illustrated in figure 10, form the basic variation in nozzle aspect ratio. The fourth shape is an aspect ratio 4 nozzle. This family of nozzles is designed with low boattail angles (6° - 12°) to prevent the effect of boattail angle from obscuring the true aspect ratio effects. Interference drag coefficients, which are inclusive of scrubbing losses and normalized to the drag of the circular nozzle are shown in figure 11. The Mach number and lift coefficients represent typical cruise conditions near the drag-rise Mach number of the unswept wing/nacelle combination. The pressure ratios (H/P_o) ranging from 1.85 - 2.55 are nozzle pressure ratios; corresponding fan pressure ratios for the indicated cruise conditions would be 1.36 - 1.88. The data shown in figure 11 show a pronounced drag advantage for the "D-duct" configuration. It is believed from preliminary analysis that this advantage stems from a lack of nozzle side flair and more rounded corners near the exit while simultaneously deriving some benefit through lift augmentation.

The better lift-generation capability of the wide nozzles is demonstrated in figure 12, which compares total lift across the pressure ratio range at typical cruise conditions of a constant angle of attack of 3 degrees and Mach number of 0.68. A comparison of the lift with clean wing values at the corresponding angle of attack shows that the circular nozzle provides very little lift augmentation, while the wide nozzles provide lift augmentation considerably in excess of the jet-supported lift. In fact, lift augmentation on the order of 3 to 5 times the direct lift due to thrust has been found to be characteristic of the wider nozzles. The "D-duct" generates lift augmentation ratios of about 2.5 at maximum blowing levels.

Effect of Boattail Angle

A second set of medium sized nozzles, spanning the aforementioned aspect ratio range, but characterized by high boattail angles (17° - 35°), is available in the model matrix. With the effect of nozzle aspect ratio on drag known from the previous evaluation, the effect of boattail angle on total interference drag may be determined. Figure 13 shows these results with the data again normalized to the circular nozzle drag. In the pressure ratio range 2.20 - 2.60, the maximum useable boattail angle appears to be about 20 - 21 degrees. There is an indication that the onset of boattail separation is delayed slightly at high blowing rates by the pumping action of the jet. The separated flow pattern near the exit of the aspect ratio 4 nozzle with a 35 degree boattail angle is shown in figure 14.

Effect of Multiple Nacelles

Both two- and four-engine nacelle configurations were tested on the swept wing. Figure 15 illustrates the increase in total interference drag for the four-engine airplane as compared to that obtained for twin-engine configurations tested separately with nacelles located at inboard and outboard wing positions. Although the nacelles are about 2 nacelle diameters apart, the increase in total interference drag is around 0.004, or equivalent to the drag of a single nacelle at low blowing levels. This drag diminishes by about 50% at the higher C_{μ} values. The interference drag also appears to be relatively insensitive to Mach number near the drag rise as indicated in the figure.

Pressure Test Results

A typical USB-pressure model is shown on figure 16 as mounted in the CFF. A sampling of data obtained with the traversing wake rake behind a circular nozzle is provided in figure 17. The basic effect of the wing on the jet cross section is seen to be a downward displacement of the contours as the jet tends toward wing attachment. Acquisition of similar data, both statically and wind-on, are in progress with nacelles of various shapes and sizes.

Additional results from the pressure tests are provided in figure 18. Wing surface pressures along the jet centerline of a D-duct nacelle are compared with results from a powered vortex-lattice modeling technique. The correlations afforded by the theoretical program and the pressure test results are providing significant insight into the aerodynamics of the USB system.

CONCLUSIONS

Based on preliminary evaluations of both force and pressure measurements obtained in the USB-Cruise experimental program, the following conclusions have been drawn:

- The semi-circular ("D-duct") nozzle is superior from the standpoint of the total installed drag penalty to either the circular nozzle or the wide (high aspect ratio) nozzles.
- Boattail angles of 20 - 21 degrees are permissible without large drag penalties.
- Tests of two adjacent nacelles have indicated the presence of an additional interference drag penalty, which amounts to about 25 percent of the total interference drag of the two nacelles tested separately.

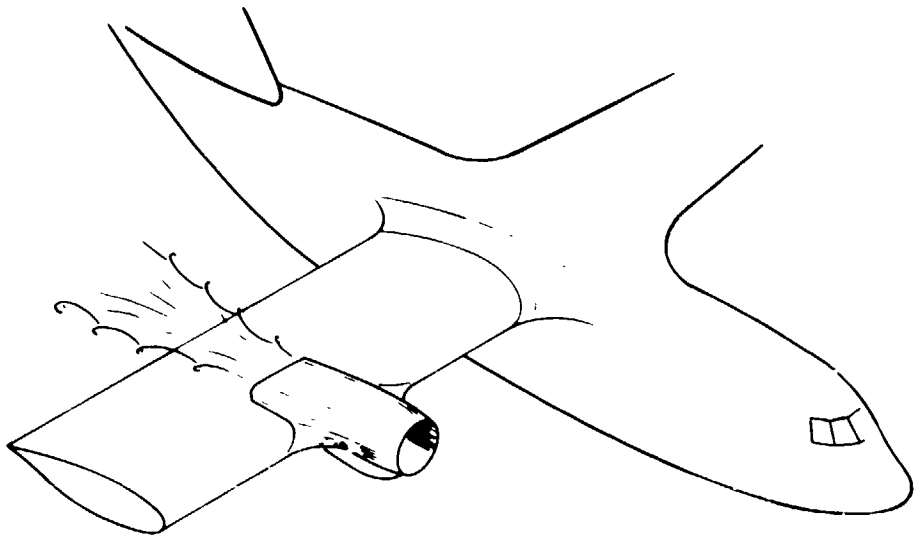

Figure 1.- Aerodynamic effects of USB nacelle/wing geometric variations.

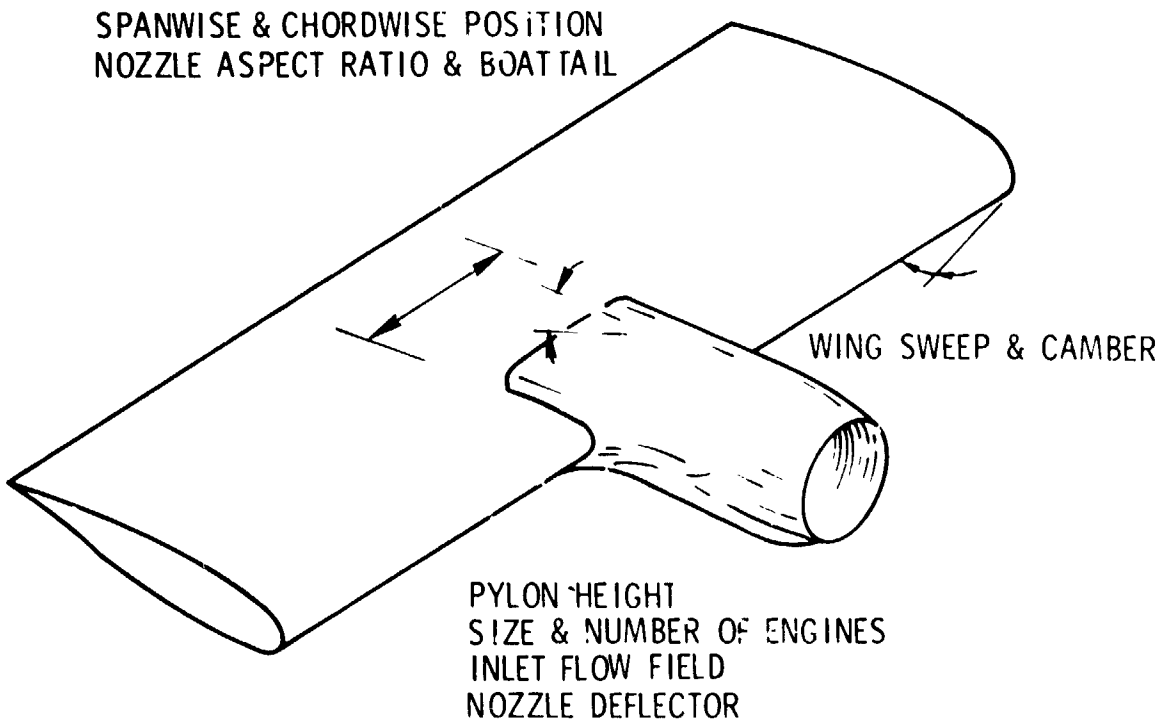

Figure 2.- Geometric effects. 2-D and 3-D.

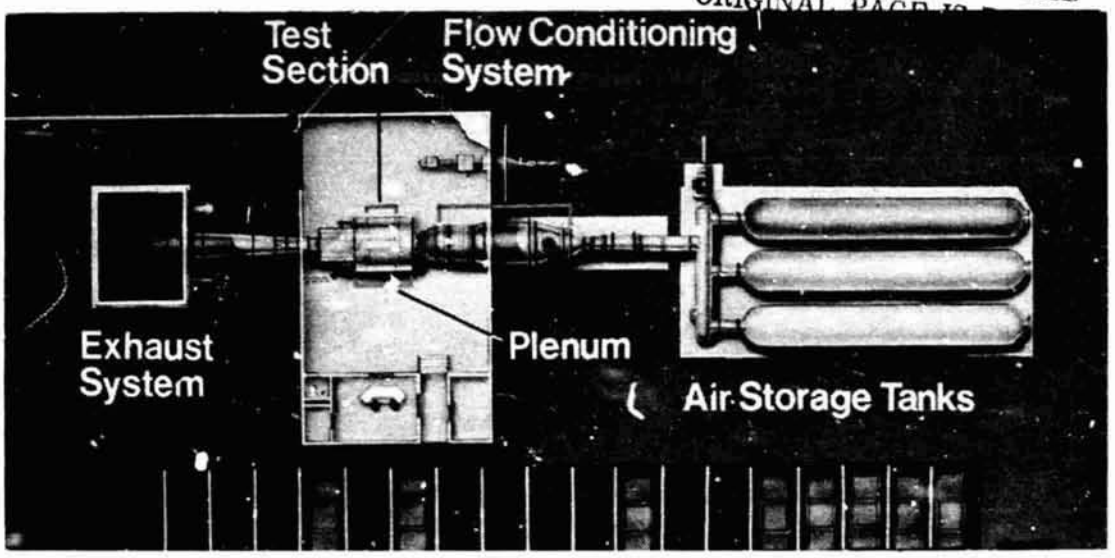

Figure 3.- Lockheed Compressible Flow Facility. Transonic blowdown tunnel ($0.2 \leqq M_o \leqq 1.2$); Reynolds number capability of 164×10^6/m; variable wall porosity; model blowing capability of 2.068 MN/m^2 (300 lb/in^2).

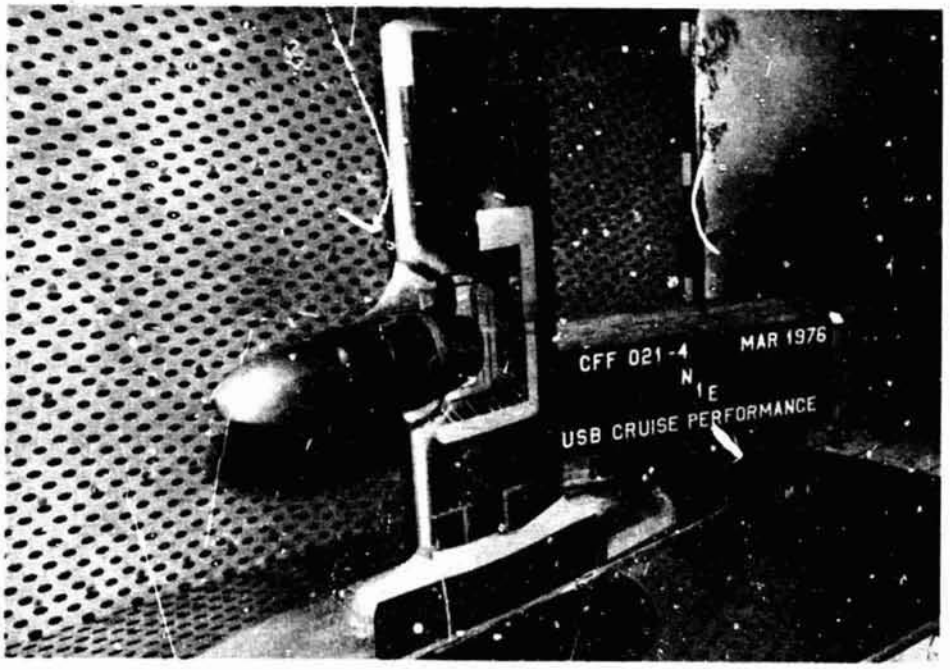

Figure 4.- 3-D unswept model.

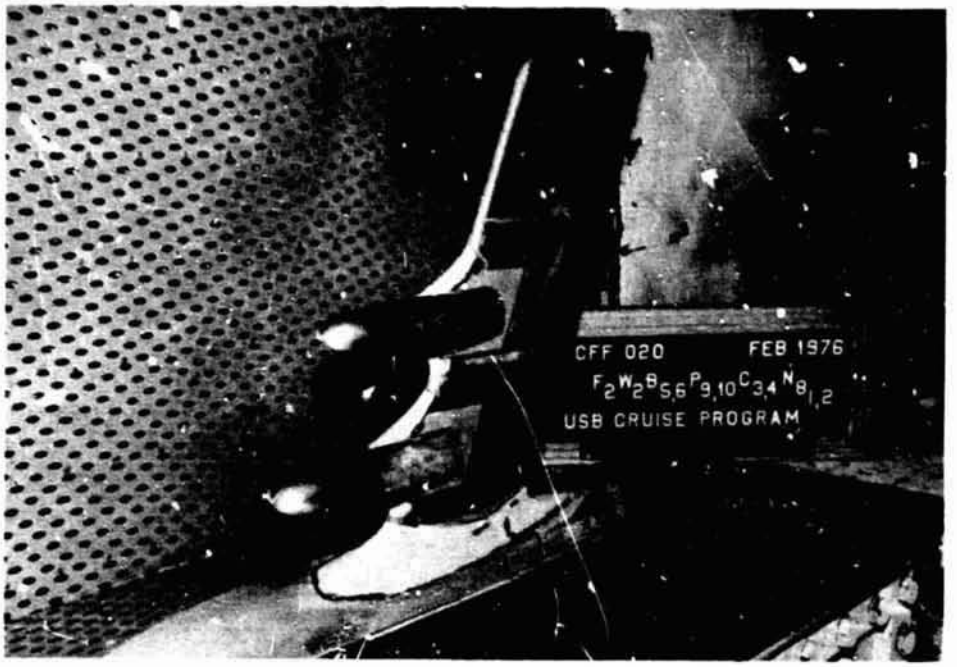

Figure 5.- 3-D swept model.

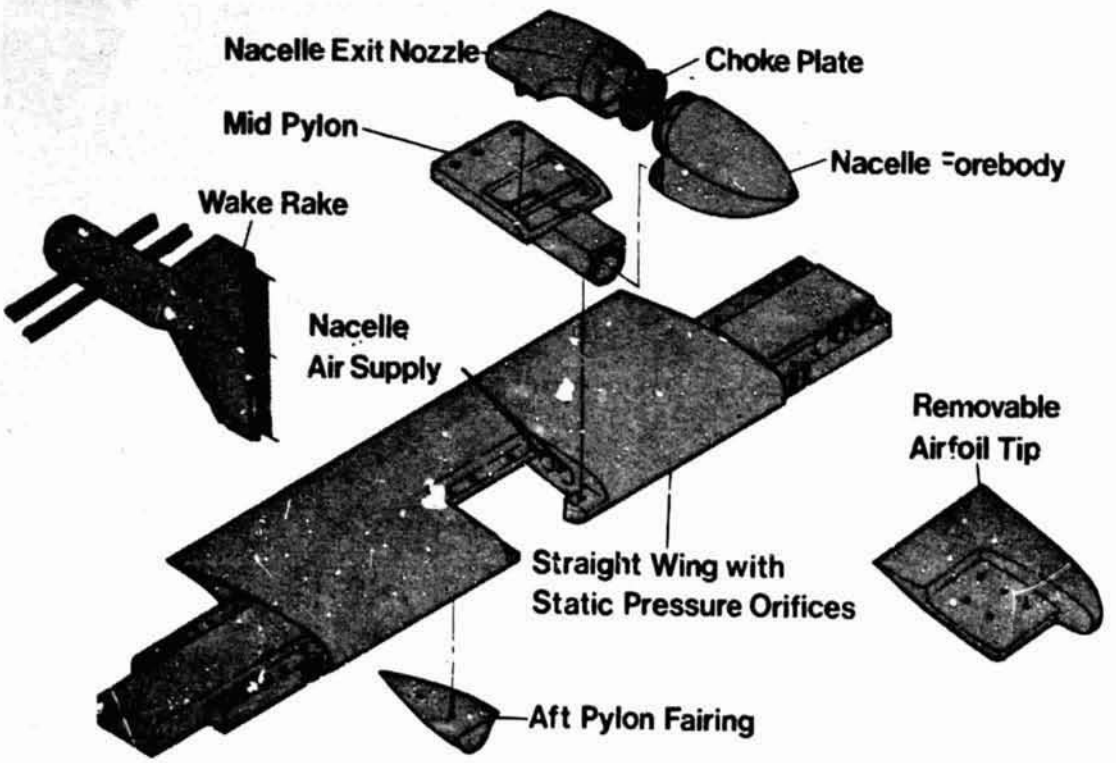

Figure 6.- Typical test model.

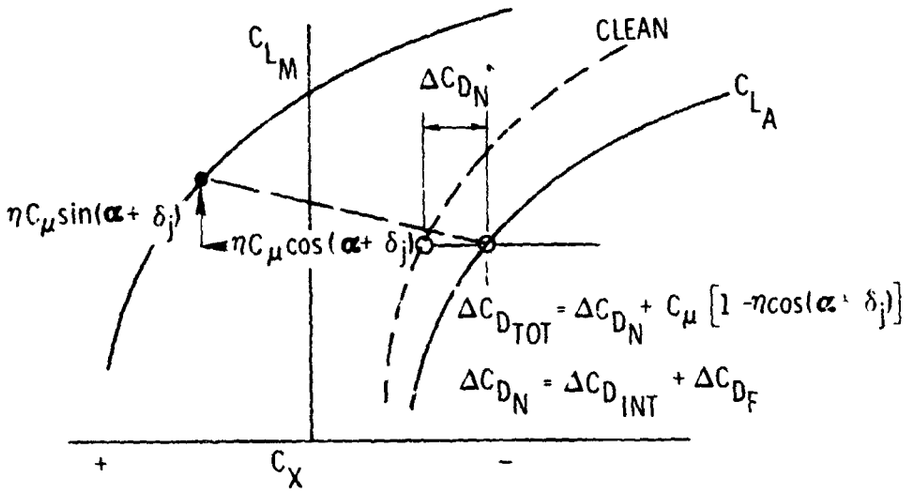

- ALL NOZZLES CALIBRATED ISOLATED
- δ_{jet}, EFFICIENCY (η) FROM STATIC WING + NACELLE CALIBRATION
- NET THRUST = GROSS THRUST - RAM DRAG

Figure 7.- Drag increment definition (C_X represents all coefficients shown).

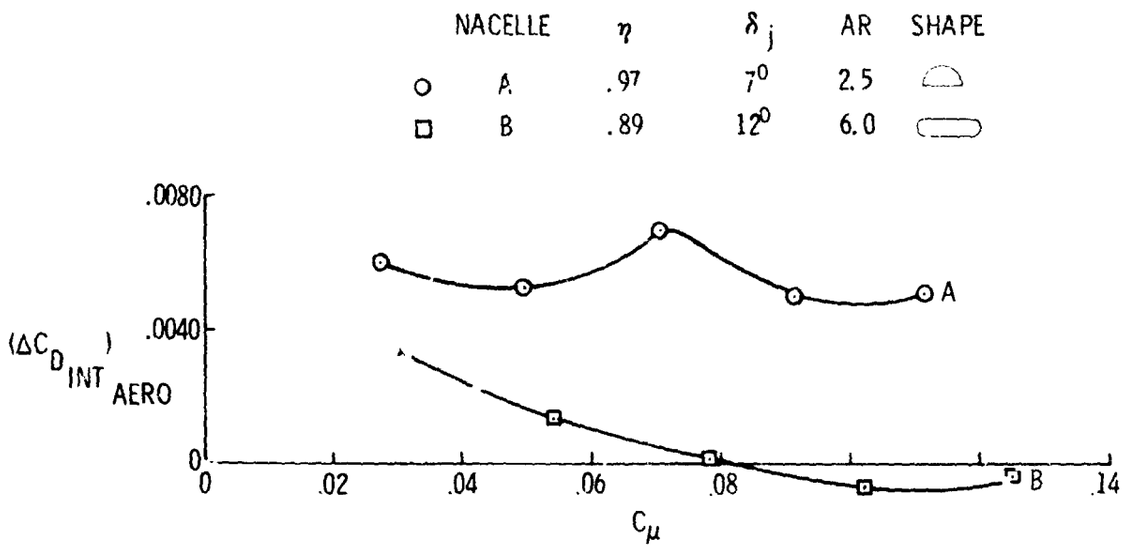

Figure 8.- Nacelle ranking; aerodynamic interference drag.

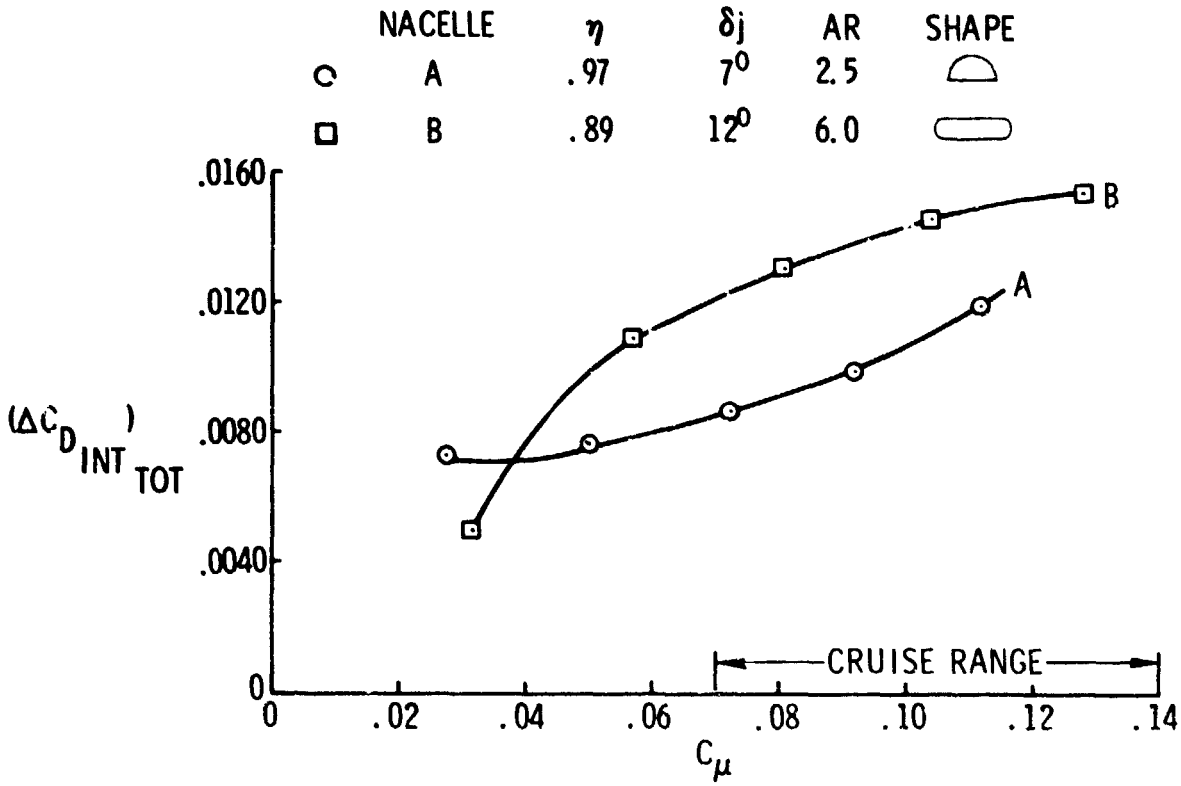

Figure 9.- Nacelle ranking; total interference drag.

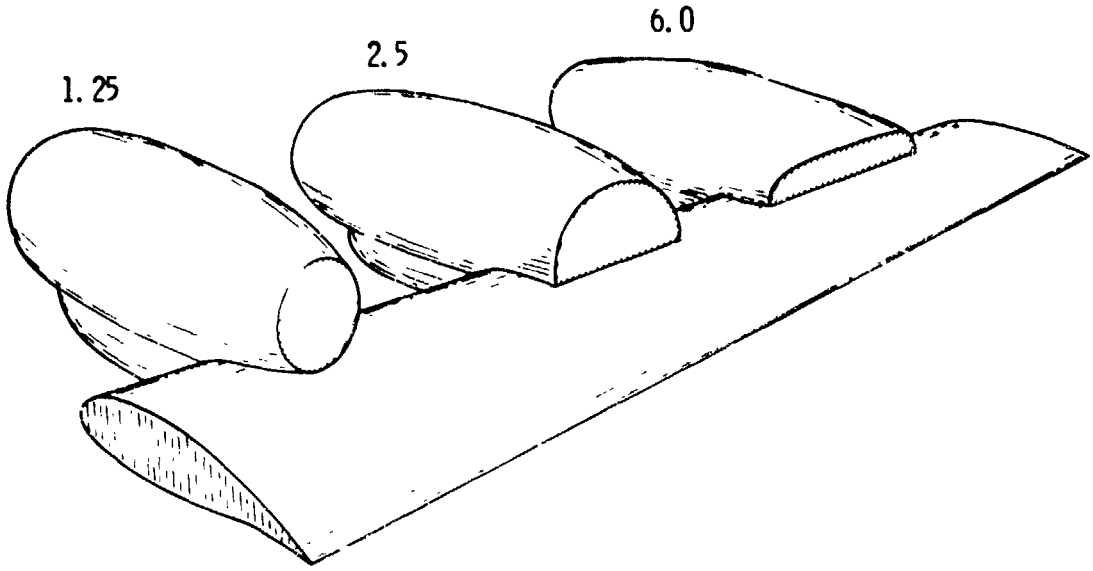

Figure 10.- Nozzle aspect ratio variation; $6^{\circ} \leq \beta \leq 12.5^{\circ}$.

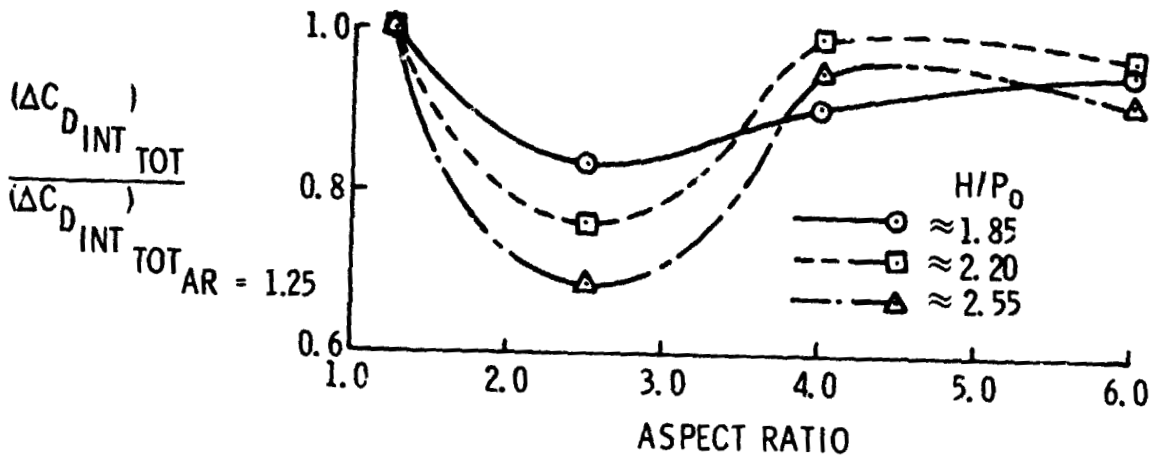

Figure 11.- Effect of nozzle aspect ratio on nacelle drag.
Unswept wing; $M_o = 0.68$; $C_{L_A} = 0.40$.

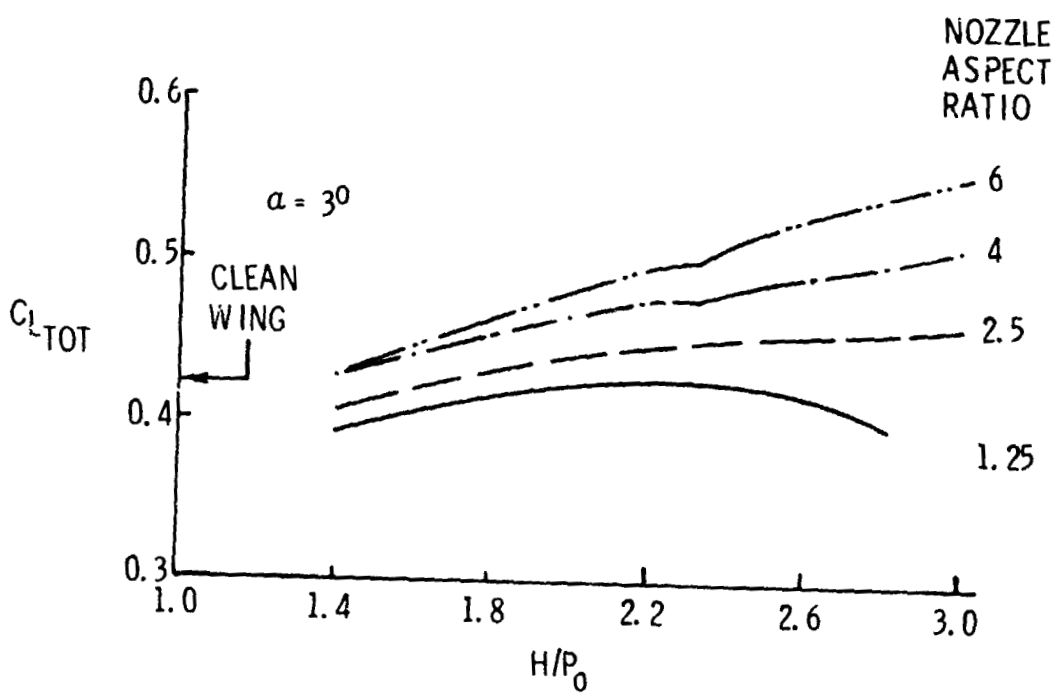

Figure 12.- Effect on total lift of nozzle aspect ratio variation.
Unswept wing; $M_o = 0.68$.

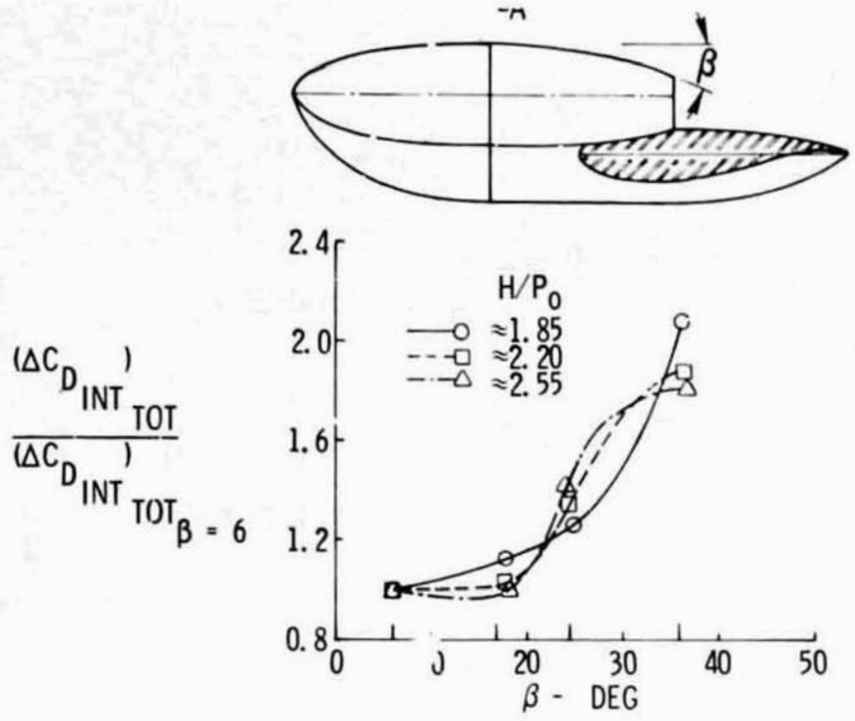

Figure 13.- Effect of nozzle boattail angle on nacelle drag. Unswept wing; $M_o = 0.68$; $C_{L_A} = 0.40$.

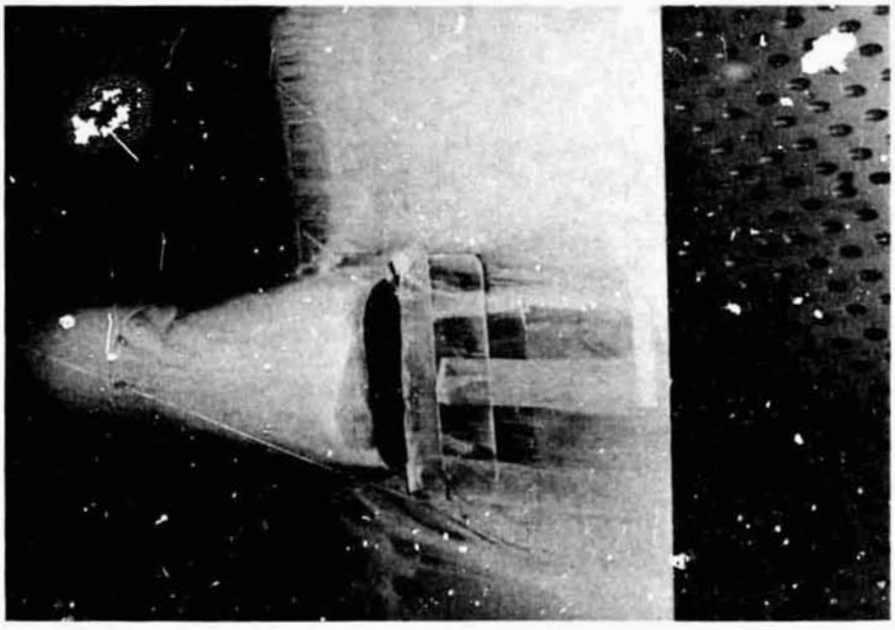

Figure 14.- Boattail separation.

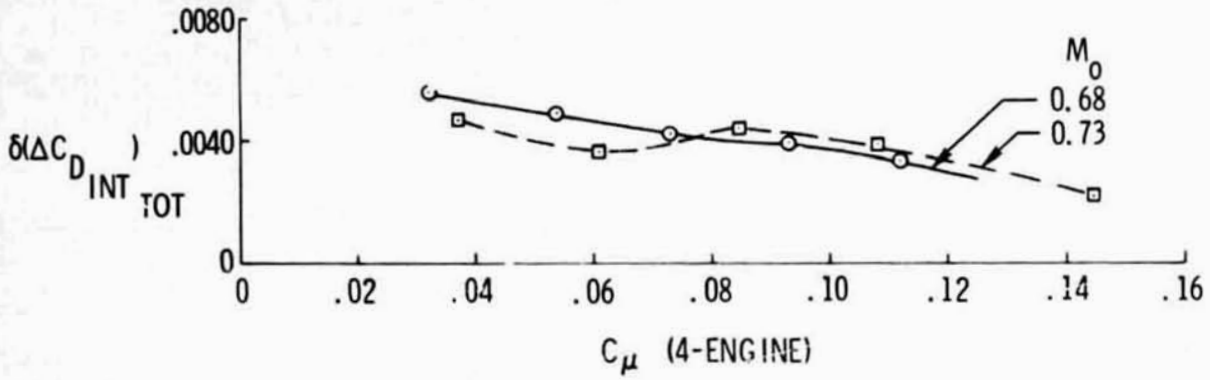

Figure 15.- Effect of multiple engines on interference drag. Swept wing; $(X/c)_{exit}$ = 0.2; D-duct nozzles; spacing between nacelles of 2 nacelle diameters.

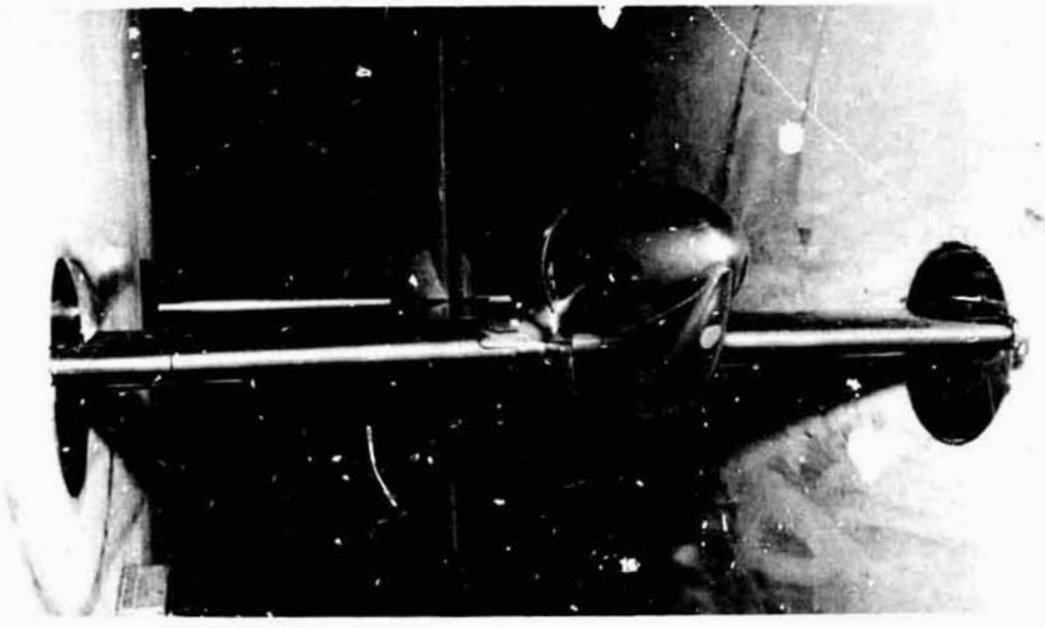

Figure 16.- Wing nacelle pressure model with traversing wake rake.

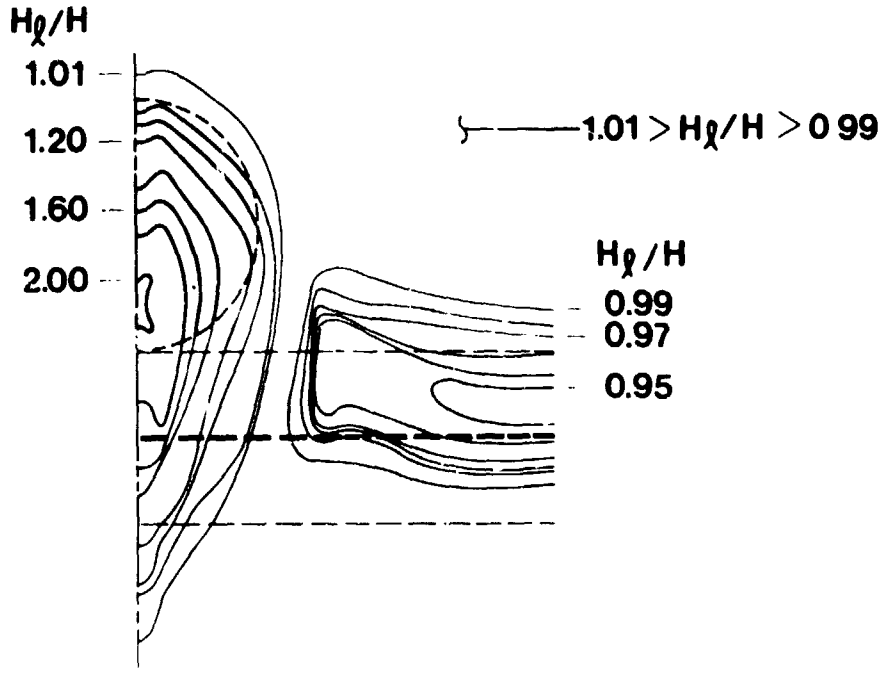

Figure 17.- Wake total pressure pattern. M_o = 0.68; $\alpha = 2.6^o$; H/P_o = 2.78.

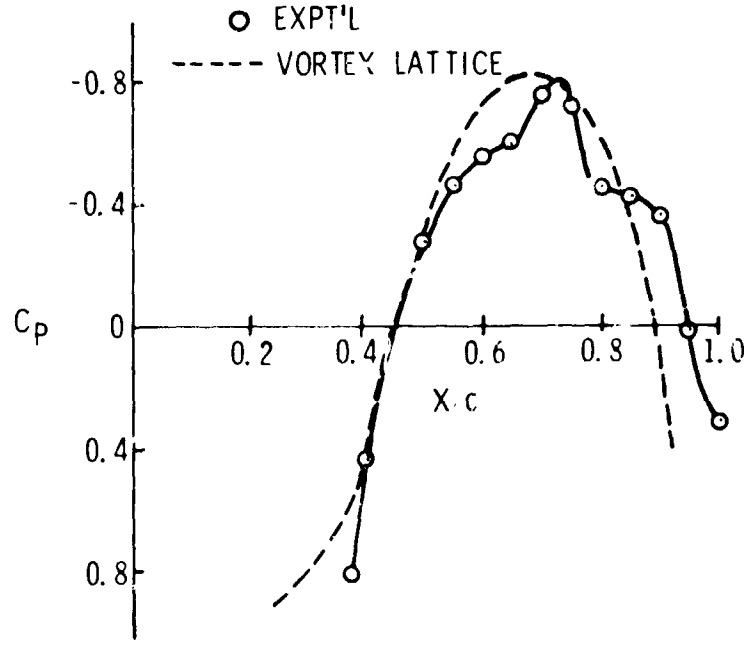

Figure 18.- Comparison of wing surface pressures along jet centerline of D-duct nacelle with values obtained from powered vortex-lattice modeling technique H/P_o = 2.1.

EFFECTS OF NOZZLE DESIGN AND POWER ON CRUISE DRAG FOR UPPER-SURFACE-BLOWING AIRCRAFT

Edward T. Meleason
NASA Lewis Research Center

SUMMARY

A high-speed wind-tunnel investigation was conducted on a series of upper-surface-blowing nozzles with D-shaped exits installed on a representative short-haul aircraft model. Both two- and four-engine configurations were investigated. Powered engine simulators were used to properly represent nacelle flows. Large differences in cruise drag penalties associated with the various nozzle designs were seen. Some geometric parameters influencing nozzle cruise drag are identified.

INTRODUCTION

Upper-surface-blowing (USB) nozzle design requirements present a conflict between good low-speed and high-speed performance, as noted in reference 1. At low speeds, a relatively wide, thin jet is desired for good flow turning and lift augmentation (ref. 2). This is usually accomplished by directing the nozzle jet onto the wing upper surface with a high boattail angle nozzle. Conversely, low boattail angles and minimal jet spreading appear desirable for low cruise drag. Previous investigators have reported (ref. 3) that compromising all the nozzle design parameters toward favorable low speed flow turning increased the cruise drag by as much as 20 percent of the airplane drag.

This earlier work involved the development of a USB nozzle for a configuration with twin high-pressure-ratio (low bypass ratio) engines. The present investigation was directed toward cruise nozzles for low-pressure-ratio USB engines similar to those being developed under NASA's QCSEE (Quiet, Clean, Short-Haul Experimental Engine) Program (ref. 4). A later paper by Ciepluch summarizes features of the QCSEE propulsion system. The different cruise nozzle exit geometries required for the different pressure ratio engines are shown in figure 1. The QCSEE nozzle exit is larger relative to its nacelle, producing a lower aspect ratio nozzle with sharper corners. In the present test, all experimental nozzles had this D-shaped low-aspect-ratio nozzle exit geometry. Cruise drag was evaluated for both low boattail angle nozzles designed specifically for good cruise drag and also for high boattail angle nozzles representing the QCSEE USB design. Both two- and four-engine configurations were tested.

SYMBOLS

A_{BT}	boattail projected area above the wing, cm^2 (in^2)
A_{EXIT}	nozzle exit area, cm^2
A_{NAC}	maximum circular cross-sectional area of nacelle, cm^2 (in^2)
AR_{EXIT}	exit aspect ratio, width/height
C_D	drag coefficient, $drag/q_0S$
C_L	lift coefficient, $lift/q_0S$
C_P	pressure coefficient, $(p-p_0)/q_0S$
M_0	free-stream Mach number
p_0	free-stream static pressure, N/cm^2
q_0	free-stream dynamic pressure, N/cm^2
S	wing area, cm^2 (in^2)
W	width, cm (in.)
β_{TOP}	external top centerline boattail angle at nozzle exit, deg
β_{SIDE}	external sidewall boattail angle at nozzle exit, deg
Δh	maximum displacement of external boattail corner, cm (in.)
θ_{KD}	average of top and bottom centerline flow deflection angles at nozzle exit

MODEL DESCRIPTION

Figure 2 is a photograph of the half-plane model installed in the Lewis Research Center's 8- by 6-Foot Supersonic Wind Tunnel. The 0.7-m (27.5-in.) semispan model was designed for Mach 0.7 cruise and had a cylindrical fuselage and straight supercritical wing. Wing sweep at the quarter chord was 5.6° and the aspect ratio was 7.0. The wing had a taper ratio of 0.3 and an average section thickness of about 13.5 percent. The entire aerodynamic configuration was mounted on a 6-component balance. Powered engine simulators, nominally 7.6 cm (3 in.) in diameter, were used to represent the nacelle flows. Flow-through nacelles were also used.

A typical nozzle installation on the wing is shown in figure 3. Inboard

nacelle centerline position was at 23 percent of semispan, with the outboard nacelle at 48 percent. The nozzle exits were located at 35 percent of the local chord, and the exit plane was unswept in the lateral direction.

The experimental nozzle designs are shown in figure 4. All had D-shaped exits with an aspect ratio (width/height) of about 2. The reference nozzle, designated N_{REF}, had a moderate external top (crown line) boattail angle of about 11° and an external side boattail of about 2°. The QCSEE-type nozzles, N_{QC}, featured a high external top boattail angle of 28° in order to obtain a high kickdown angle and to avoid internal flow restrictions at the larger exit area required at takeoff. Because of the high kickdown angle (average centerline kickdown angle, θ_{KD} = 12°), this type of nozzle would not require some type of flow deflector for good low-speed powered-lift performance as low-angle nozzles like N_{REF} would. The sidewall boattailing of the QCSEE N_{QC} nozzles (17° external, 10° internal) was designed to minimize jet spanwise pluming at cruise. Note that because N_{REF} is mounted lower on the wing than N_{QC} the boattail projected area above the wing is reduced.

There are two versions of the QCSEE nozzle, designated BL (baseline) and RC1 (recontoured no. 1). As discussed in an earlier paper by Sleeman and Phelps, the original baseline QCSEE nozzle was recently changed to the RC1 contour to improve its low-speed powered-lift characteristics. Note that the effect of the change was to flatten the top of the nozzle, increase the sharpness of the corners, and increase the effective boattail angle particularly at the corners. The terminal boattail angles on the top, β_{TOP}, and side, β_{SIDE}, remained unchanged. On the model, the external nozzle contours for $(N_{QC})_{BL}$ and $(N_{QC})_{RC1}$ correspond to the baseline and recontoured QCSEE configurations; however, the internal contours for both were for the baseline nozzle. In addition to these configurations, some modified versions of the N_{QC} nozzles were also tested.

The model N_{QC} nozzles were not an exact scaled representation of the full-scale QCSEE nozzle installation. During model design it became necessary to increase the nacelle maximum diameter to provide more room for instrumentation routing. As shown in figure 5, this added additional area to the forward part of the nozzle boattail and reduced the local curvature slightly. The high angle part of the boattail near the nozzle exit was duplicated exactly. The influence of this boattail area difference on the experimental results is addressed later in this paper.

POWERED SIMULATOR CONSIDERATIONS

Calibration

Prior to the wind-tunnel test, the propulsion nacelles with engine simulators were calibrated statically. A plate simulating the wing upper surface contour was attached to the nozzle through a separate balance, and its drag contribution was deleted. Nozzle thrust in the axial direction was calibrated as a function of nozzle pressure ratio for each experimental simulator/nozzle combination.

Drag Definition

Cruise drag results are presented in terms of a drag penalty which is described in figure 6. The drag penalty is the difference between the drag of the combined nacelle/wing-body configuration minus the separate isolated drags of the nacelle and wing-body. The total configuration drag with power consisted of the balance drag force corrected for the net thrust of the powered nacelles. The external nacelle drag was estimated for an assumed isolated nacelle at free-stream Mach number using an empirical technique based on nacelle fineness ratio. This estimate did not account for the increased pressure drag that would be present on an isolated high boattail nozzle such as the QCSEE nozzle. The drag of the basic wing-body without nacelles was measured. This drag was evaluated at values of Mach number and lift coefficient identical to those of the nacelle-on configuration. An additional correction was made to account for the drag increment of that portion of the wing covered by the nacelle. With these various drag components deducted from the original configuration drag, the remaining increment was considered a drag penalty which included any unfavorable interference effects. It should be noted that the scrubbing drag of the jet flow on the wing upper surface was not accounted for and would be included as part of the drag penalty.

Power Effects

Figure 7 is a typical comparison of drag results obtained with the powered simulators and with flow-through nacelles at Mach 0.7. The design point indicates the design lift coefficient of the model wing and the cruise fan pressure ratio of the QCSEE engine. For reference, a drag increment equivalent to 5 percent of cruise net thrust (airplane drag) is indicated, and it is seen that the power effect can exceed this value. Note that at the higher lift coefficient the jet flow has a favorable effect on drag. However, this favorable effect is small compared to the higher drag levels seen at this C_L.

RESULTS AND DISCUSSION

Two-Engine Configurations

Experimental drag penalties for the N_{REF} and $(N_{QC})_{BL}$ nozzle installations are shown in figure 8 for a two-engine airplane configuration (single nacelle installed on the half-plane wind-tunnel model). The powered nacelle was located at the inboard position (23 percent semispan), and data are shown for a fan pressure ratio of 1.37 and a lift coefficient of 0.4, corresponding to Mach 0.7 cruise design conditions. At these conditions, the nozzle pressure ratio was about 1.9 based on free-stream static pressure and about 2.2 based on local static pressure. At the design Mach number of 0.70, the reference nozzle N_{REF} had a small drag penalty of about 1.5 percent of net thrust (or airplane drag). Most of this penalty was probably associated with the additional scrubbing drag

of the jet on the wing. The high boattail angle baseline QCSEE nozzle $(N_{QC})_{BL}$ exhibited a considerably higher drag penalty at Mach 0.7, amounting to about 5 percent of net thrust. This penalty was partly associated with lower pressures over the nozzle boattail, as will be seen later. In addition, an enlarged region of supercritical flow was present on the wing upper surface with this nozzle. The wing shock was strengthened and moved aft toward the nozzle exit from its clean wing position.

Note that as Mach number increased beyond design, the reference nozzle developed a favorable interference effect while the drag of the N_{QC} nozzle continued to increase. Wing pressure data indicate that the reference nozzle acted to retard the development of supercritical flow above the wing as the wing entered drag rise, while the higher angle N_{QC} nozzle did not.

Four-Engine Configurations

Cruise drag results are presented in figure 9 for the four-engine configuration with reference nozzles N_{REF}, baseline QCSEE nozzles $(N_{QC})_{BL}$, and recontoured QCSEE nozzles $(N_{QC})_{RC1}$. A large difference in drag levels is evident. At Mach 0.70, the reference nozzles again had a relatively low drag penalty of less than 3 percent of net thrust. This is slightly less than twice the two-engine value for this nozzle, indicating the absence of any unfavorable nacelle-to-nacelle interference effects. The drag penalty with the N_{QC} baseline nozzles was about 12 percent of net thrust at Mach 0.7; twice the twin-engine value would be about 9 percent. Therefore, an additional drag penalty of about 3 percent is indicated due to nacelle-to-nacelle interference for this design. These mutual interference effects are also evident from the wing pressure data. With the N_{QC} nozzles, the addition of the outboard nacelle resulted in an accelerated supercritical flow region in the channel between the nozzles.

The change in external contour shape from the $(N_{QC})_{BL}$ configuration to the $(N_{QC})_{RC1}$ configuration produced an additional large drag increase (from 12 to 18 percent of net thrust at Mach 0.7). This was associated with extensive flow separation over the aft part of the $(N_{QC})_{RC1}$ boattail, as shown in figure 10. The crown line pressure distributions for the three nozzles are considerably different. A region of supercritical flow existed on the $(N_{QC})_{RC1}$ boattail, and extensive separation was present on the aft boattail, as indicated by the reduced pressure recovery at the trailing edge and shown on the tuft photograph. Flow over the $(N_{QC})_{BL}$ boattail approached the sonic level and only a small separation region was present. The N_{REF} boattail flow was at a nearly constant subsonic level.

Four-Engine Configurations with Modified Nozzles

The relatively high drag levels observed with the N_{QC} nozzles led to the development of modified N_{QC} nozzle configurations to further investigate drag behavior. These modified nozzles, shown in figure 11, were fabricated by add-

ing material externally to the boattail region of the N_{REF} nozzles. The external crown lines of the baseline and RC1 configurations were duplicated from the nozzle exit forward until fairing was required to match the maximum height of N_{REF}. As mentioned earlier, since N_{REF} was mounted lower on the wing than N_{QC}, a reduced boattail projected area above the wing resulted. Cross-sectional contours were similarly duplicated and shifted to match the very shallow sidewall boattail angles of N_{REF}. The resulting configurations thus had external boattail tops and corners quite similar to the N_{QC} nozzles, but with reductions in sidewall boattailing, boattail projected area, and flow kickdown angle on the wing. The modified nozzles are designated as $MOD(N_{QC})_{BL}$ and $MOD(N_{QC})_{RC1}$.

The combination of these changes produced a significant reduction in cruise drag at all Mach numbers. As shown in figure 12, a similar reduction occurs with the modified nozzles for both the RC1 and baseline boattails. In both cases the modifications alleviated the region of supercritical flow on the wing upper surface near the nozzles. Although not determined specifically, it appears probable that the mutual interference between nacelles was reduced with the modified configurations. It is seen from figure 12 that the external boattail change from baseline (BL) to the recontoured shape (RC1) produced similar large drag increases for both the unmodified and modified nozzles. Extensive boattail flow separation similar to that seen previously with $(N_{QC})_{RC1}$ was again observed on the $MOD(N_{QC})_{RC1}$ configuration.

Geometric Effects

The difference in external boattail geometry between baseline and recontoured configurations is predominantly an increased sharpness of the local nozzle corners. In figure 13 drag is correlated against a corner sharpness parameter $\Delta h/(W/2)$, where Δh is the maximum corner displacement from a line connecting the intersections of the nacelle centerlines with the nozzle crown line and side, and $W/2$ is the local nozzle half-width along the horizontal centerline. This parameter was evaluated at a location one maximum nacelle radius upstream of the nozzle exit, where the difference in corner sharpness is largest. The incremental drag change with corner sharpness for the N_{QC} and modified N_{QC} nozzles was quite similar.

As mentioned previously, the unmodified N_{QC} nozzles were not exact scale representations of the QCSEE flight nozzles but had additional boattail projected area present. The combination of geometrical changes inherent in the modified N_{QC} nozzles resulted in reduced boattail projected area above the wing. Relative values of this area and the associated drag levels are indicated in figure 14. It is not possible to isolate the effects of boattail area from the other geometric changes between the N_{QC} and modified N_{QC} nozzles, so figure 14 only indicates general trends. It is reasonable to assume that the drag penalty associated with the correct boattail area would lie somewhere between the full-scale mark and the N_{QC} point, depending on the relative effect of boattail area compared to the effects of changes in sidewall boattail angle and flow kickdown angle. The proximity of the modified N_{QC} points to the geometrically

correct boattail areas is of interest. This proximity suggests that the QCSEE nozzles with external sidewall boattailing reduced to 2° might obtain a cruise drag penalty somewhere near these levels if the effects of kickdown angle are not important. This would amount to drag penalties between 12 and 14 percent of net thrust for the RC1 nozzle and between 6 and 8 percent for the baseline nozzle.

CONCLUDING REMARKS

In summary, it was found that USB nacelles with moderate nozzle boattail angles could be installed on a high-wing short-haul aircraft configuration with only a small cruise drag penalty. This type of nozzle would not have good low-speed powered-lift performance without the development of a flow deflector and exit area variation system. A high boattail angle nozzle representing the QCSEE RC1 configuration, which was designed for good powered-lift performance without a flow deflector, displayed large cruise drag penalties associated with boattail flow separation and regions of accelerated supercritical flow on the wing upper surface. A similar nozzle with rounder corners and reduced powered-lift performance, representing the QCSEE baseline nozzle, had significantly lower cruise drag. Additional test configurations indicated the possibility of improving cruise drag levels of the QCSEE-type nozzles by reducing the sidewall boattail angles and the boattail projected area above the wing.

REFERENCES

1. Wimpress, J. K.: Upper Surface Blowing Technology as Applied to the YC-14 Airplane. SAE Paper 730916, Oct. 1973.

2. Johnson, J. L., Jr.; and Phelps, A. E., III: Low-Speed Aerodynamics of the Upper-Surface Blown Jet Flap. SAE Paper 740470, Apr. 1974.

3. Skavdahl, H.; Wang, T.; and Hirt, W. J.: Nozzle Development for the Upper Surface Blown Jet Flap on the YC-14 Airplane. SAE Paper 740469, Apr. 1974.

4. Ciepluch, Carl C.: QCSEE Program. Aeronautical Propulsion. NASA SP-381, 1975, pp. 65-80.

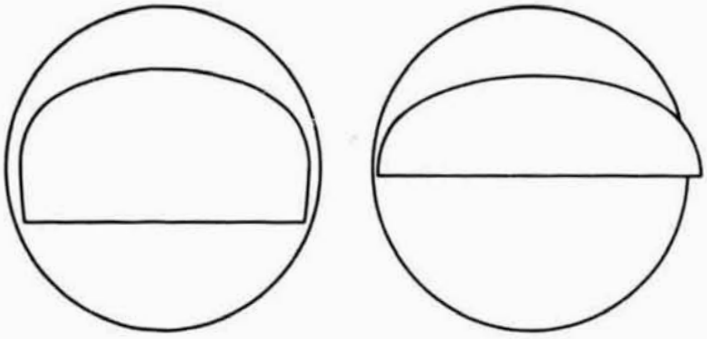

LOW-PRESSURE RATIO (QCSEE)	HIGH-PRESSURE RATIO (YC-14)
FAN P.R. = 1.37	FAN P.R. = 1.65
BYPASS RATIO = 10	BYPASS RATIO = 4
$\frac{A_{EXIT}}{A_{NAC}} = 0.5$	$\frac{A_{EXIT}}{A_{NAC}} = 0.3$
NOZZLE $AR_{EXIT} = 1.9$	NOZZLE $AR_{EXIT} = 3.2$

Figure 1.- Comparison of USB cruise nozzles.

Figure 2.- Wind-tunnel model.

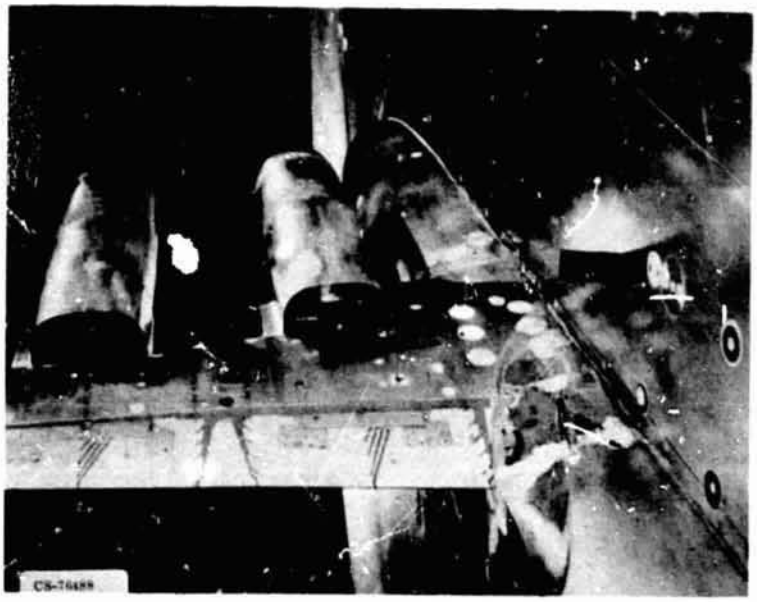

Figure 3.- Nozzle installation.

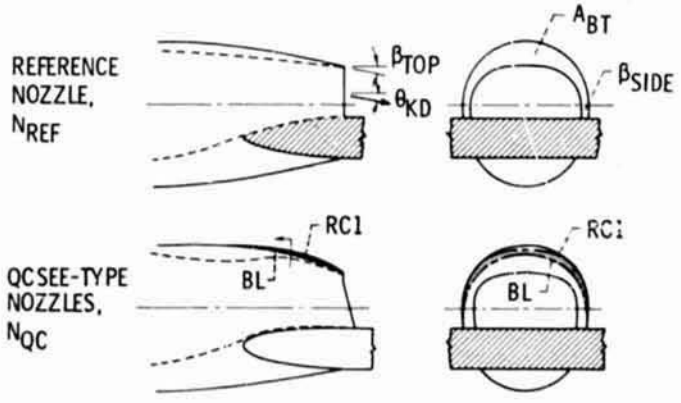

	β_{TOP}	β_{SIDE}	θ_{KD}	(A_{BT}/A_{NAC})
N_{REF}	11^0	2^0	3^0	0.214
$(N_{QC})_{BL}$	28^0	17^0	12^0	.282
$(N_{QC})_{RC1}$	28^0	17^0	12^0	.300

Figure 4.- Test nozzle configurations.

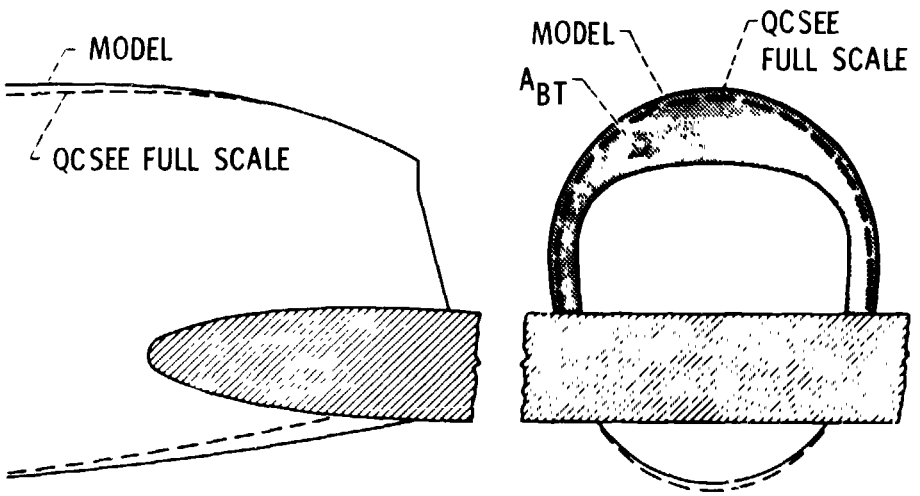

	$(A_{BT}/A_{NAC})_{MODEL}$	$(A_{BT}/A_{NAC})_{FULL\ SCALE}$
$(N_{QC})_{BL}$	0.282	0.237
$(N_{QC})_{RC1}$	.300	.252

Figure 5.- Comparison of model and QCSEE engine.

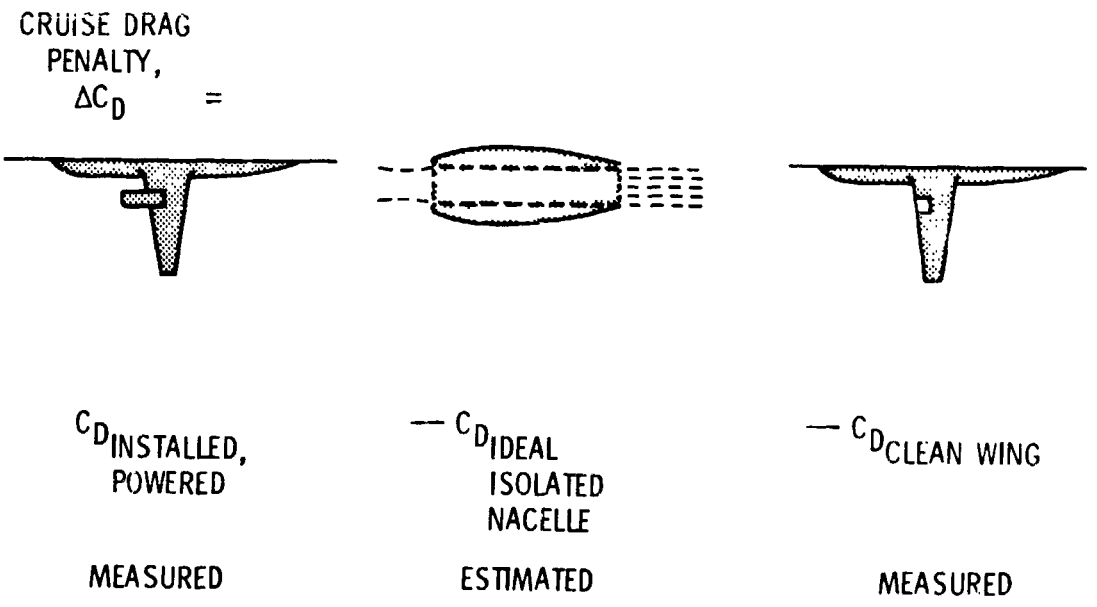

Figure 6.- Drag definition.

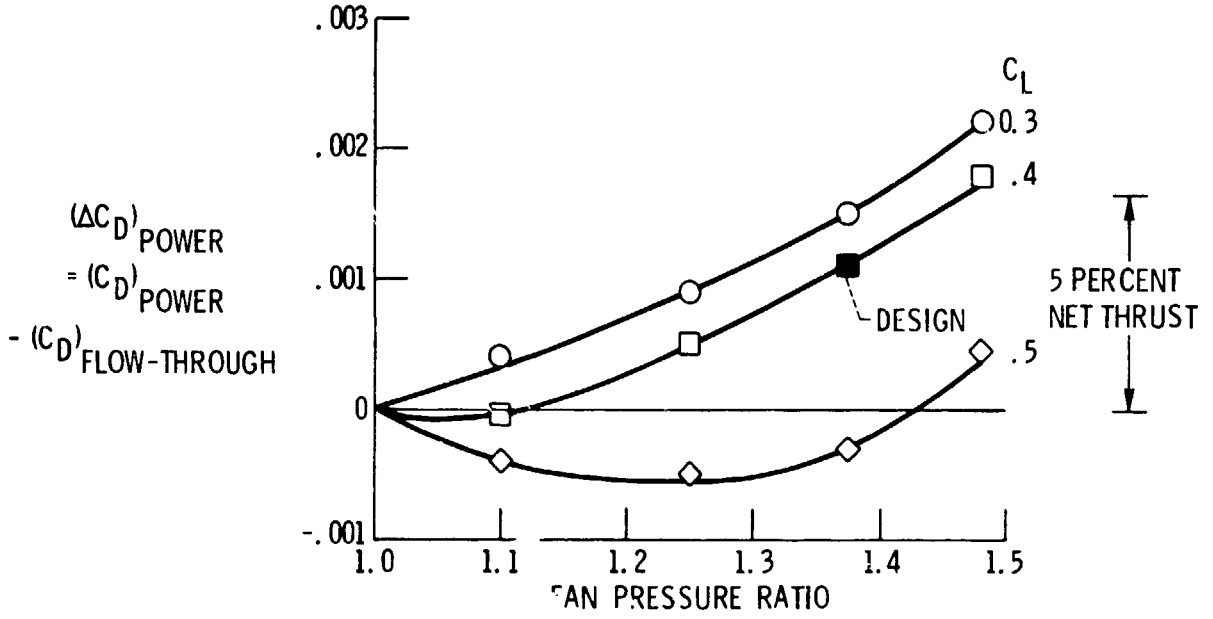

Figure 7.- Power effect; $(N_{QC})_{RC1}$ nozzles; 4-engine configuration; $M_0 = 0.7$.

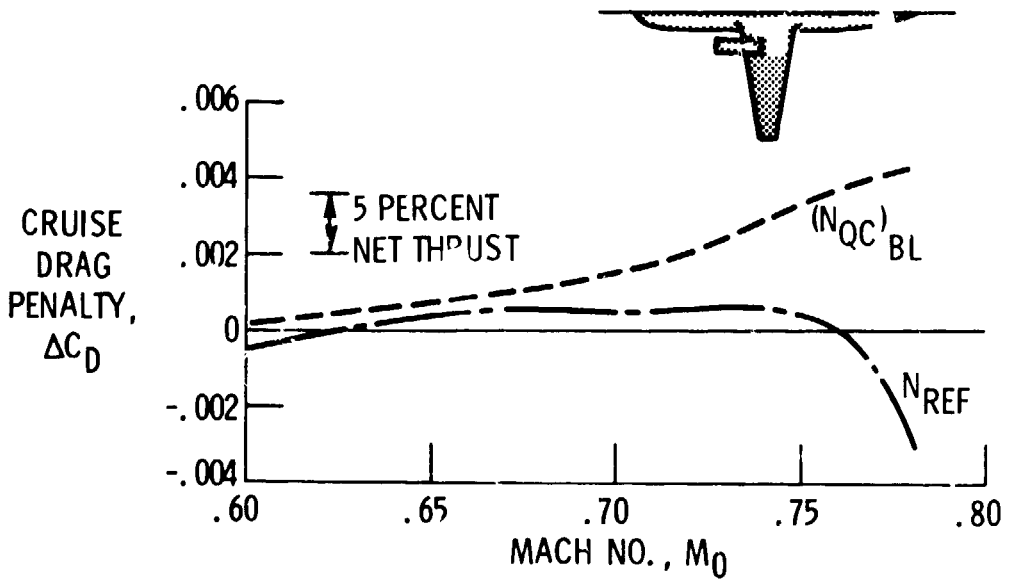

Figure 8.- Two-engine drag; FPR = 1.37; $C_L = 0.4$.

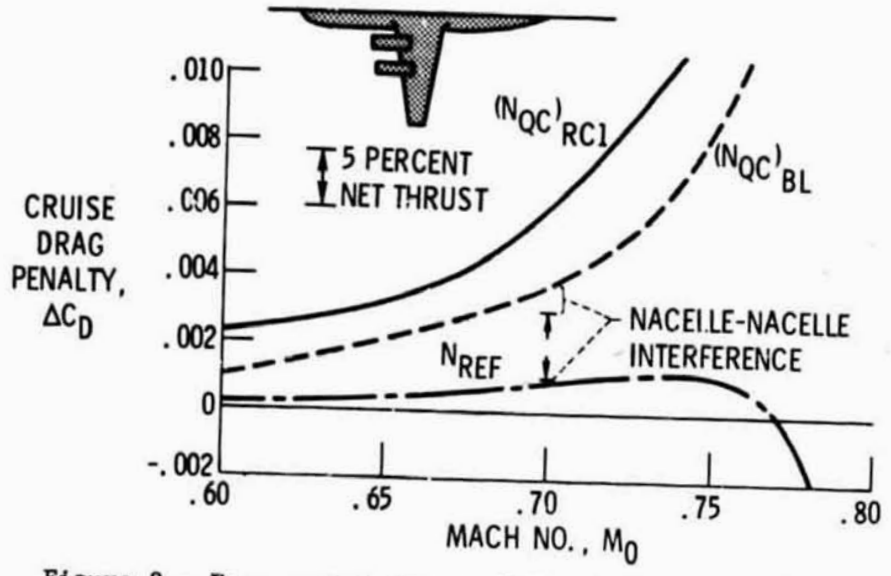

Figure 9.- Four-engine drag; FPR = 1.37; C_L = 0.4.

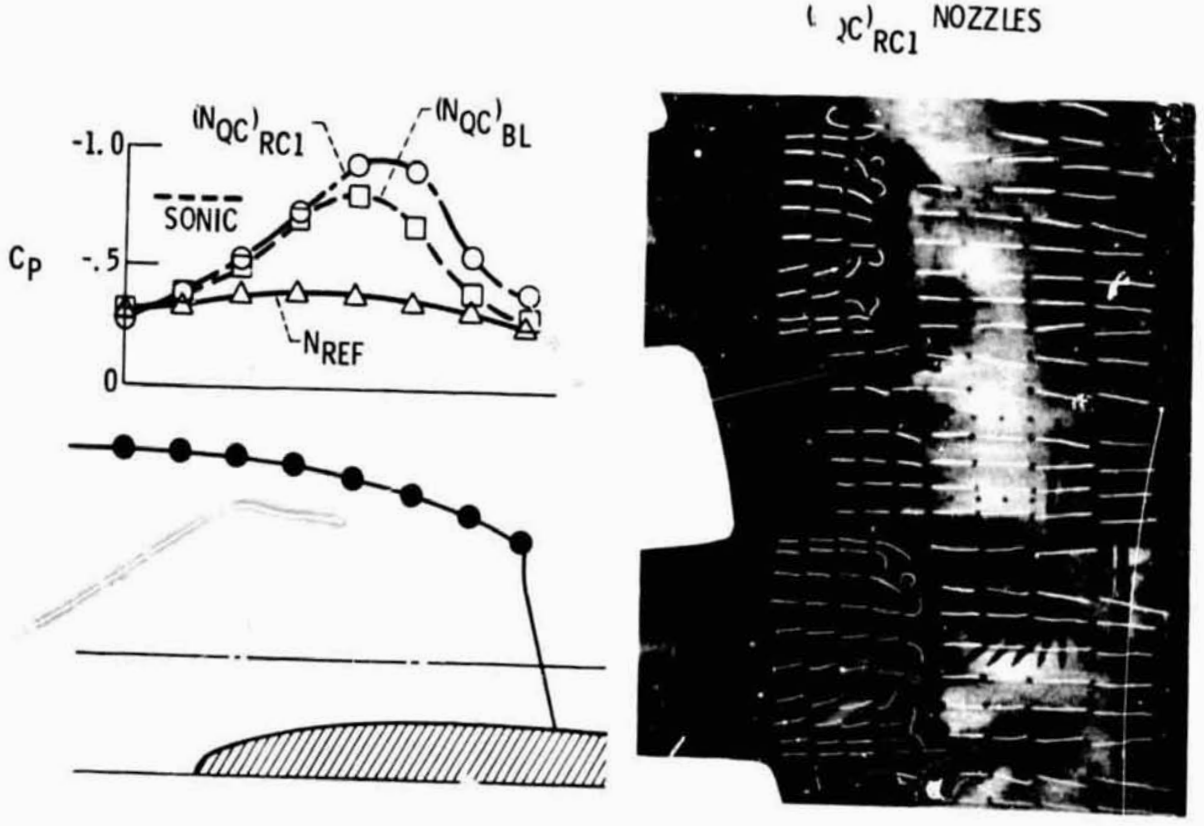

Figure 10.- Boattail separation; M_0 = 0.7; C_L = 0.4; FPR = 1.37.

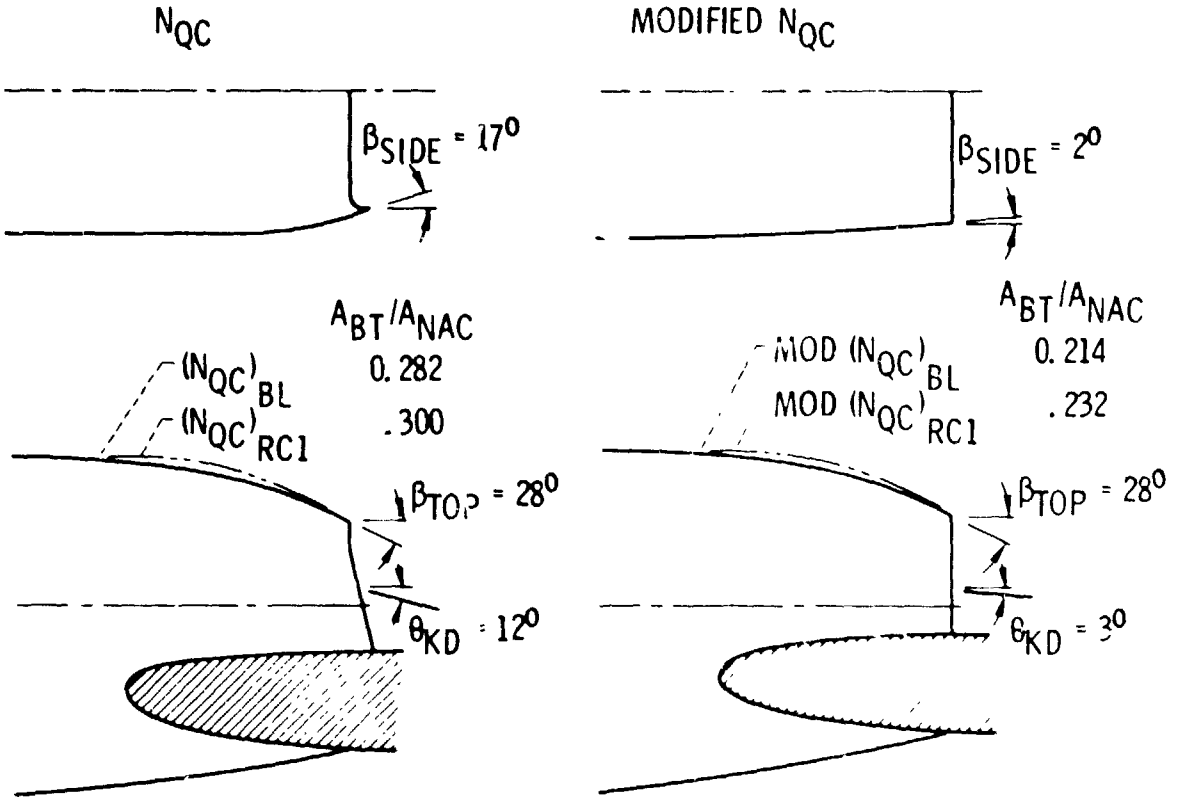

Figure 11.- Modified N_{QC} nozzles.

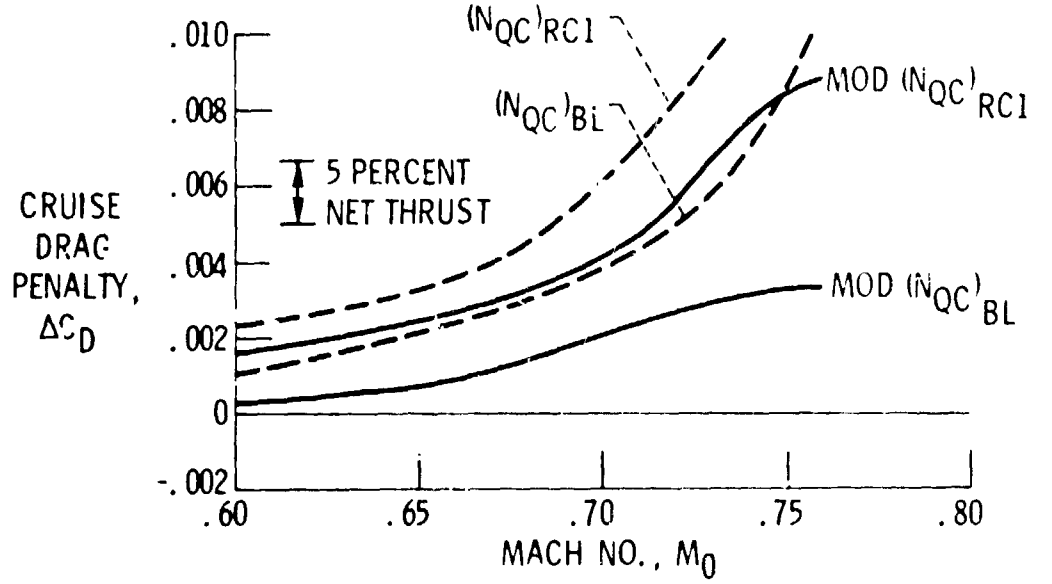

Figure 12.- Effect of N_{QC} nozzle modifications; 4-engine configuration; FPR = 1.37; $C_L = 0.4$.

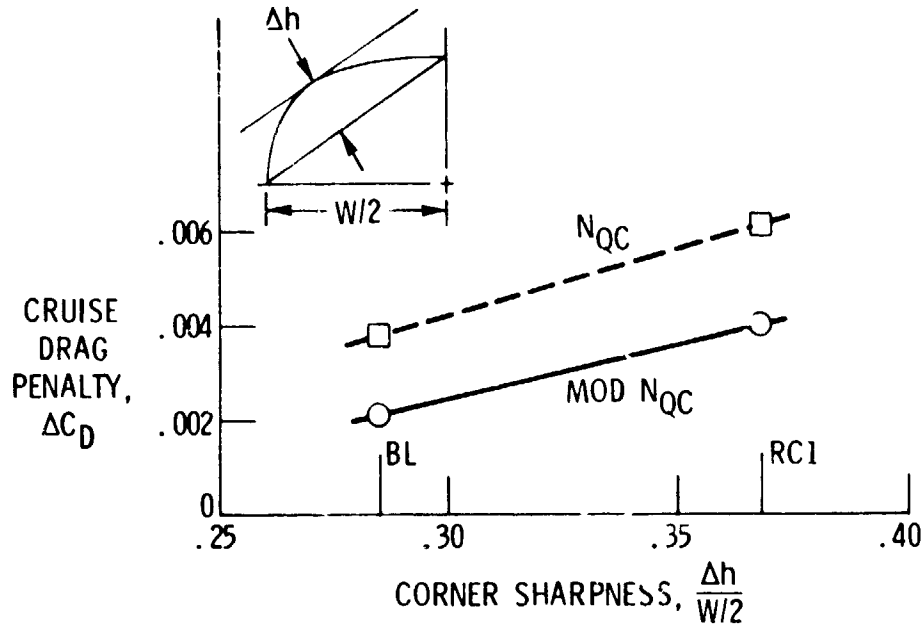

Figure 13.- Effect of corner sharpness; $M_0 = 0.7$; $C_L = 0.4$; FPR = 1.37.

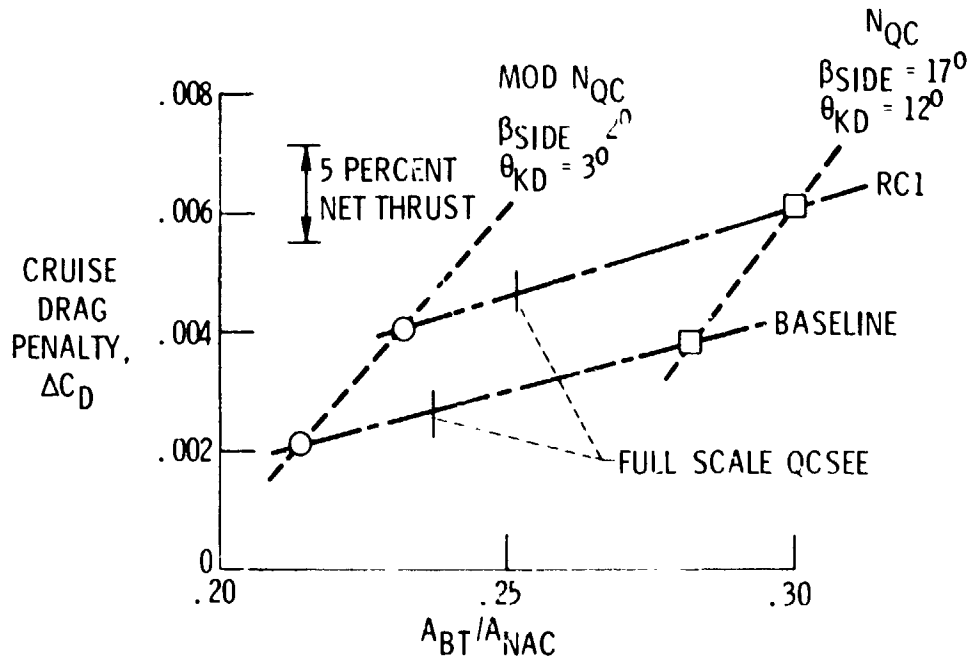

Figure 14.- Nozzle geometry effects; $M_0 = 0.7$; $C_L = 0.4$; FPR = 1.37.

THEORETICAL PREDICTIONS OF JET INTERACTION EFFECTS FOR USB AND OWB CONFIGURATIONS*

C. Edward Lan
The University of Kansas

James F. Campbell
NASA Langley Resear ı Center

13

SUMMARY

A wing-jet interaction theory is presented for predicting the aerodynamic characteristics of upper-surface-blowing and over-wing-blowing configurations. For the latter configurations, a new jet entrainment theory has also been developed. Comparison of predicted results with some available data showed good agreement. Some applications of the theory are also presented.

INTRODUCTION

When a wing is in close proximity to a jet, additional forces and moments will be induced on the wing. In the case of upper-surface-blowing (USB) configurations, where the relatively thick jet from the high bypass-ratio turbofan engines blows on the wing upper surface, these forces and moments can not be satisfactorily explained by the thin jet flap theory (ref. 1). With an over-wing-blowing (OWB) configuration, the conventional jet engine exhaust may be blowing aft or ahead of the wing leading edge and close to or away from the wing surface. It has been found that its wing aerodynamic characteristics are underpredicted by entrainment effects alone, in particular, when the jet is close to the wing surface (ref. 2). It is evident, then, that additional physical mechanisms for these effects must be identified. In this paper, they will be called the "jet interaction effects." By "interaction," it is implied that in the physical process, not only the wing flow field is perturbed in the presence of the jet, but also the jet flow is disturbed by the wing as well.

In the past, this jet interaction process has been applied mainly in the wing-slipstream interaction problem. For example, Shollenberger (ref. 3) developed a method wherein the jet shape distortion is allowed in predicting interaction effects. However, it is not applicable to the case where the jet Mach number is different from the freestream value (Mach number nonuniformity) and its applications to USB or OWB configurations have not been reported. On the other hand, Mendenhall et al. (ref. 4) used several circular jets with

*This work was supported by NASA Langley Research Center under grant NSG 1139 for the first author.

prescribed boundaries to approximate a rectangular USB jet without including the interaction process mentioned above.

In developing the analytical method for OWB configurations, Krenz (ref. 5) used sink panels on prescribed jet boundaries. No systematic method of computing the sink strength at arbitrary jet velocity ratios has been presented. To simulate the jet entrainment effect, Putnam (ref. 6) obtained the sink strength of a line sink distribution along the jet axis by Squire and Trouncer's method for incompressible, non-heated jets (ref. 7). In both studies, no interaction effects have been accounted for.

In this paper, results from a theoretical investigation of jet interaction effects for USB and OWB configurations in the past two years will be summarized. The present theory accounts for differences between the jet and free-stream dynamic pressures and Mach numbers. The jet shape can be rectangular or circular and the jet exit can be at an arbitrary location. However, the theory is a linear one so that the jet boundary distortion is not accounted for.

SYMBOLS

Values are given in both SI and U.S. Customary Units. The measurements and calculations were made in U.S. Customary Units.

AR	wing aspect ratio
c	chord length, m (ft)
$C_{D,i}$	induced drag coefficient
C_L	total lift coefficient
ΔC_L	difference in lift coefficients with jet on and off
C_m	pitching-moment coefficient
C_μ	jet-momentum coefficient
C'_μ	jet-momentum coefficient referred to p_∞
D_o	jet exit diameter, m (ft)
$\vec{e}$	unit vector tangent to jet path
$\vec{k}$	a unit vector along the z-axis

M_j	jet Mach number
M_∞	freestream Mach number
$\hat{n}$	unit vector normal to jet surface
r,s	jet axis system, normal and tangent to the jet surface, respectively
p_∞	ambient static pressure, N/m^2 (lb/ft^2)
$p_{t,n}$	nozzle total pressure, N/m^2 (lb/ft^2)
s	$= V_j/V_o$
S	wing area, m^2(ft^2)
T	$= \rho_\infty/\rho_j$
V_j	jet velocity, m/sec (ft/sec)
V_o	outer flow velocity, m/sec (ft/sec)
$\vec{V}_{je}$	jet-entrained flow vector, m/sec (ft/sec)
$\vec{V}_\infty$	freestream velocity vector, m/sec (ft/sec)
x,y,z	wing-fixed rectangular coordinates with positive x-axis along axis of symmetry pointing downstream, positive y-axis pointing to right, and positive z-axis pointing upward, m (ft)
x_j	jet exit coordinate, m (ft)
z_c	camber function, $z_c = z_c(x,y)$
z_j	height of jet axis above the wing plane, m (ft)
α	angle of attack, deg
Γ	vortex strength, m^2/sec (ft^2/sec)
δ_f	flap angle, deg
δ_j	jet-deflection, deg

λ	taper ratio
Λ_L	leading-edge sweep angle, deg
μ	$= V_\infty/V_j$
μ'	$= \vec{V}_\infty.\vec{e}/\vec{V}_j.\vec{e}$
ρ	density, kg/m^3 ($slugs/ft^3$)
$\bar{\phi}_j$	nondimensional velocity potential for the jet flow
$\bar{\phi}_o$	nondimensional velocity potential for the outer flow

DESCRIPTION OF THE METHOD

Basic Concept

Consider a two-dimensional inviscid, incompressible flow in which a jet is situated as shown in fig. 1, where a vortex Γ is assumed to exist in the outer flow. In order to satisfy the jet surface boundary conditions which require that the streamlines at both sides of the jet surface be parallel and the static pressures there be continuous, it is necessary to introduce additional vortices as has been shown by the image method (ref. 8). For the planar jet, the lower region in which the vortex Γ originates will receive additional disturbances represented by the vortex "A" (i.e., reflection effect). If the vortex Γ is now replaced by an airfoil, these additional disturbances on the airfoil will be in the form of upwash, thus increasing the lift. The vortex "B" represents the disturbance of the jet flow by the wing. Similar explanation can be given for a circular jet. It is seen, then, that the lift increment due to jet interaction is mainly due to the reflection of wing-created disturbances at the jet surface.

Three-Dimensional Formulation

In the three-dimensional case, the image method can not be used. However, the basic concept explained above remains applicable. That is, the additional upwash on the wing due to the jet surface reflection can be computed by satisfying the jet surface boundary conditions together with the wing tangency condition. In the linear theory, these conditions can be written as (ref. 2),

$$\frac{\partial \bar{\phi}_o}{\partial n} - \frac{\partial \bar{\phi}_j}{\partial n} = -\frac{\vec{V}_\infty.\vec{n}(1-\mu')}{\vec{V}_\infty.\vec{e}} \qquad \text{jet surface tangency condition} \qquad (1)$$

$$\frac{\partial \bar{\phi}_j}{\partial s} - T(\mu')^2 \frac{\partial \bar{\phi}_o}{\partial s} = 0 \qquad \text{jet surface pressure continuity} \qquad (2)$$

$$\frac{\partial \bar{\phi}_o}{\partial z} = \frac{\partial z_c}{\partial x} - \frac{\vec{V}_o \cdot \vec{k}}{\vec{V}_\infty \cdot \vec{e}} \qquad \text{wing tangency} \qquad (3)$$

where

$$\vec{V}_o = \vec{V}_\infty + \vec{v}_{je} \qquad (4)$$

and $\vec{v}_{je}$ is the jet-entrained flow vector. To satisfy eqs. (1)-(2), the jet surface is replaced by two vortex sheets -- one to account for the perturbations in the outer flow and the other for the jet flow. This is necessary because of the Mach number nonuniformity. Eq. (3) is satisfied in the usual manner with a wing vortex sheet. The results are then reduced to algebraic equations for unknown vortex strengths through the application of a quasi-vortex-lattice method (ref. 1). This vortex model is illustrated in fig. 2. Note that for USB configurations, the jet entrainment is not directly included. Instead, it enters the problem through the Coanda jet reaction, because the Coanda turning is due to the jet entrainment. The Coanda jet reaction is calculated here with the linear momentum principle and is illustrated in fig. 3. It is seen that the total lift component due to the Coanda jet reaction is

$$\begin{aligned} C_{L,R} &= 2C_\mu \sin(\delta_j/2) \cos(\delta_j/2 + \alpha) + C_\mu \sin\alpha \\ &= C_\mu \sin(\delta_j + \alpha) \end{aligned} \qquad (5)$$

Similarly, drag component due to the Coanda jet reaction is given by

$$\begin{aligned} C_{D,R} &= 2C_\mu \sin(\delta_j/2) \sin(\delta_j/2 + \alpha) - (C_\mu \cos\alpha - \mu C_\mu) \\ &= C_\mu [\mu - \cos(\delta_j + \alpha)] \end{aligned} \qquad (6)$$

where the thrust component is also included. The jet flap effect is also calculated in the present method as described in ref. 1.

On the other hand, for OWB applications, the jet entrainment is calculated according to a newly developed method (ref. 2) which is applicable to a compressible heated jet. To avoid nonhomogeneous jet propertics in the mathematical model, an equivalent uniform jet is used which satisfies the conserva-

tion of mass, linear momentum and heat content. If the jet does not intersect the wing, a circular jet is assumed. This circular jet is in turn approximated by a polygon for interaction computation. In case the jet intersects the wing, a rectangular or circular jet may be chosen in the calculation, depending on whether or not the jet would follow the wing surface and deflect at the trailing edge at some angle relative to the chord line. This deflection angle can only be determined empirically at present by correlation with experimental data.

COMPARISON WITH EXPERIMENTAL DATA

In comparing the USB data, the calculations were done with experimental jet deflection angles measured under wind-off conditions. The data of a transport-type configuration of Smith, et al. (ref. 9) with AR = 7.8, λ = 0.73 and Λ_L = 0° are compared in fig. 4. The moment arms for the Coanda forces are measured directly from fig. 3 of ref. 9. The skin friction and the scrubbing drags are not accounted for in the moment computation. It is seen that the predicted results agree reasonably well with the data. It should be noted that all results were obtained by adding the predicted jet-induced increments to the experimental jet-off values. Since the method also predicts the induced drag, its comparison can be made approximately by using the relation:

$$\Delta C_{D,(\alpha)} = (C_{D,i} + C_{D,R})_{(\alpha)} - (C_{D,i} + C_{D,R})_{(\alpha = 1°)} \qquad (7)$$

Eq. (7) approximately represents the incremental induced drag due to the angle of attack. The results are compared in the following table with good agreement:

δ_f	0°		20°		40°		60°	
	$\Delta C_{D,(\alpha)}$		$\Delta C_{D,(\alpha)}$		$\Delta C_{D,(\alpha)}$		$\Delta C_{D,(\alpha)}$	
α	Theory	Exp.	Theory	Exp.	Theory	Exp.	Theory	Exp.
6°	0.096	0.15	0.233	0.2	0.322	0.3	0.375	0.35
11°	0.227	0.3	0.5	0.5	0.658	0.6	0.752	0.65

The jet induced lift increments for a fighter, vectored-thrust (VT) configuration of AR = 3.7 given in ref. 10 are compared in fig. 5. Since the model airfoil is thin (5%) and the camber is of supercritical type but unknown, it was assumed to be a flat wing in the computation to simulate the

jet-off C_L as closely as possible. As the jet Mach number is mostly supersonic, which is not allowed in the present subsonic computer program, the jet Mach number is assumed to be M_∞ and an equivalent velocity ratio is used as described in ref. 6. If the static thrust coefficient is C'_μ nondimensionalized with the ambient pressure, then C_μ in terms of freestream dynamic pressure is given by

$$C_\mu = \frac{2C'_\mu}{\gamma M_\infty^2} \qquad 8)$$

where C'_μ is given in ref. 10 and γ is the ratio of specific heats. From the comparison, it is seen that the agreement is reasonably good.

The OWB data by Falk (ref. 11) and Putnam (ref. 12) are compared with the predicted results in figs. 6 and 7, respectively. From fig. 6, it is seen that ΔC_L decreases rapidly as the jet is moved upwards from the wing surface. This is because with the jet close to the wing, the interaction effects become important. In addition, if the jet intersects the wing, the jet flap effect due to the jet deflection at the trailing edge relative to the chord line will also be significant. Both effects diminish rapidly with the distance to the wing surface. It is also seen from both figs. 6 and 7 that jet entrainment alone will underpredict ΔC_L if the jet is close to the wing.

SOME ADDITIONAL RESULTS

As mentioned above, the jet interaction effects are mainly due to the jet surface reflection of wing-created disturbances which are proportional to the jet-off wing loading. Therefore, it is important in the interaction computation to simulate the jet-off lift as closely as possible. To see how the jet-off lift can affect the interaction effects, the configuration of Smith, et al. given in ref. 9, is again used under the conditions of $\alpha = 1°$, $\delta_f = 0°$, $\delta_j = 12°$ and $C_\mu = 2$. If NACA 64_2A215 ($a = 0.5$) and NACA 64_1A412 ($a = 0.5$) airfoils are used at the root and the tip, respectively, as shown in ref. 9, the theoretical jet-induced ΔC_L would be 0.826. On the other hand, if a symmetrical airfoil is used, ΔC_L becomes 0.688, a decrease of 19%. In addition, it has been shown that the jet flap effect (i.e., the effect of jet deflection relative to the chord) is always beneficial (ref. 1). That means that a thick airfoil with some trailing-edge angle will give better aerodynamic characteristics than a thin airfoil with little trailing-edge angle.

It has been shown experimentally and theoretically that the wing loading with USB has high peak in the jet region. Therefore, it is of interest to see how trade-offs can be made between lift capability and aspect ratio in cruise. Assume that $\alpha = 2°$ and $\delta_j = 10°$ without flap deflection and the jet is blowing from the leading edge. The results are shown in fig. 8. It is seen that although the lift will be decreased by 60% at $C_\mu = C$ when AR is reduced from 8 to 4, the decrease is only 42.7% in the circulation lift and 34.2% in the total lift (including the jet reaction) at $C_\mu = 1$. The decrease in the lift capability when the aspect ratio is reduced is seen to decrease as C_μ is increased.

One advantage of OWB configurations with the jet not intersecting the wing is that the jet scrubbing drag can be eliminated. Furthermore, the jet-entrainment created upwash will increase the loading and the leading-edge thrust. It is of interest to compare the interaction effects of rectangular jets with circular ones assuming the same cross-sectional area and entrainment. The jet axis is taken to be at $z_j/D_o = 1.2$ and the entrainment is computed assuming a circular jet. The results are shown in fig. 9. It is seen that both rectangular and circular jets perform equally well. However, it may be feasible to lower the rectangular jet to increase the performance without scrubbing the wing. It is also seen from the figure that the aerodynamic performance can be greatly improved by an over-wing-blowing jet, as has also been noted by Putnam (ref. 6).

CONCLUDING REMARKS

A theoretical method has been presented for predicting the aerodynamic characteristics of USB and OWB configurations. The predicted results show good agreement with some available data. The jet interaction effects have been shown to be important when the jet is on or close to the wing surface. Because of the nature of the interaction process, higher interaction lift can be achieved by increasing the jet-off lift. For a rectangular wing with USB in cruise, the total lift is shown to decrease by 34.2%, compared with 60% with jet off, when the aspect ratio is reduced from 8 to 4. It was shown for the OWB configurations that the interaction effects depend strongly on the distance of the jet surface to the wing.

REFERENCES

1. Lan, C. Edward; and Campbell, James F.: Theoretical Aerodynamics of Upper-Surface-Blowing Jet-Wing Interaction. NASA TN D-7936, 1975.

2. Lan, C. Edward: A Theoretical Investigation of Over-Wing-Blowing Aerodynamics. KU-FRL-700 (NASA Grant NSG 1139), The University of Kansas Center for Research, Inc., March 1976. (Available as NASA CR-144969.)

3. Shollenberger, C.A.: Three-Dimensional Wing/Jet Interaction Analysis Including Jet Distortion Influences. Journal of Aircraft, Vol. 11, No. 9, Sept. 1975, pp. 706-713.

4. Mendenhall, M.R.; Perkins, S.C. Jr.; Goodwin, F.K.; and Spangler, S.B.: Calculation of Static Longitudinal Aerodynamic Characteristics of STOL Aircraft with Upper-Surface-Blown Flaps. NASA CR-137646, April 1975.

5. Krenz, G.: Airframe-Engine Interaction for Engine Configurations Mounted above the Wing, Part 1. Interference Between Wing and Intake/Jet. AGARD CP-150, 1975.

6. Putnam, Lawrence E.: An Analytical Study of the Effects of Jets Located More Than One Jet Diameter Above a Wing at Subsonic Speeds, NASA TN D-7754, 1974.

7. Squire, H.B.; and Trouncer, J.: Round Jets in a General Stream. R.&.M. 1974, Brit. A.R.C., 1944.

8. Koning, C.: Influence of the Propeller on Other Parts of the Airplane Structure. Vol. IV, "Aerodynamic Theory," Ed. by W.F. Durand, Dover Publication.

9. Smith, Charles C. Jr.; Phelps, Arthur E. III; and Copeland, W. Latham: Wind Tunnel Investigation of a Large-Scale Semispan Model with an Unswept Wing and an Upper-Surface Blown Jet Flap. NASA TN D-7526, 1974.

10. Ishimitsu, Kichio K.: Investigation of Upper Surface Blowing Applied to High Speed Aircraft. AFFDL-TR-74-89, 1974.

11. Falk, H.: The Influence of the Jet of a Propulsion Unit on Nearby Wings. NACA TM 1104, 1946.

12. Putnam, Lawrence E.: Exploratory Investigation at Mach Numbers from 0.40 to 0.95 of the Effects of Jets Blown Over a Wing. NASA TN D-7367, 1973.

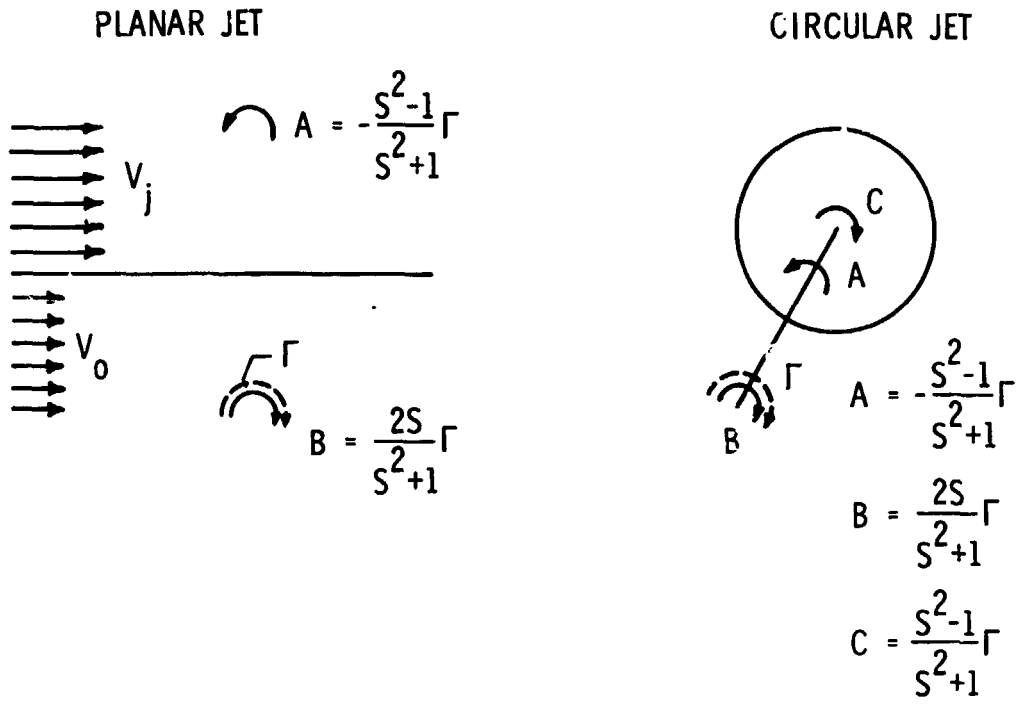

Figure 1.- Illustration of two-dimensional, inviscid jet interaction process.

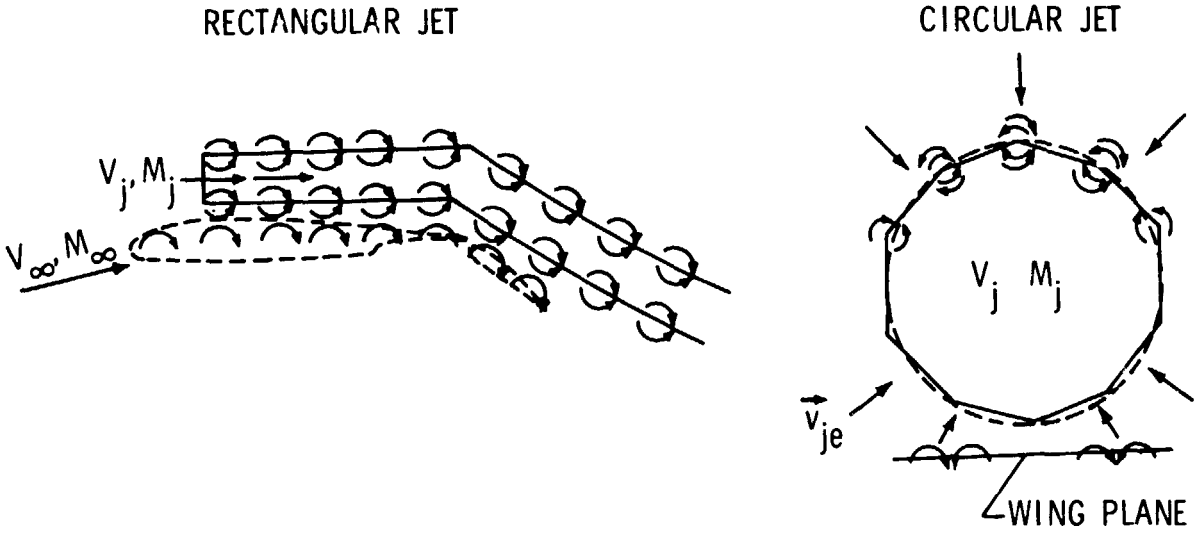

Figure 2.- Three-dimensional vortex model for jet interaction process.

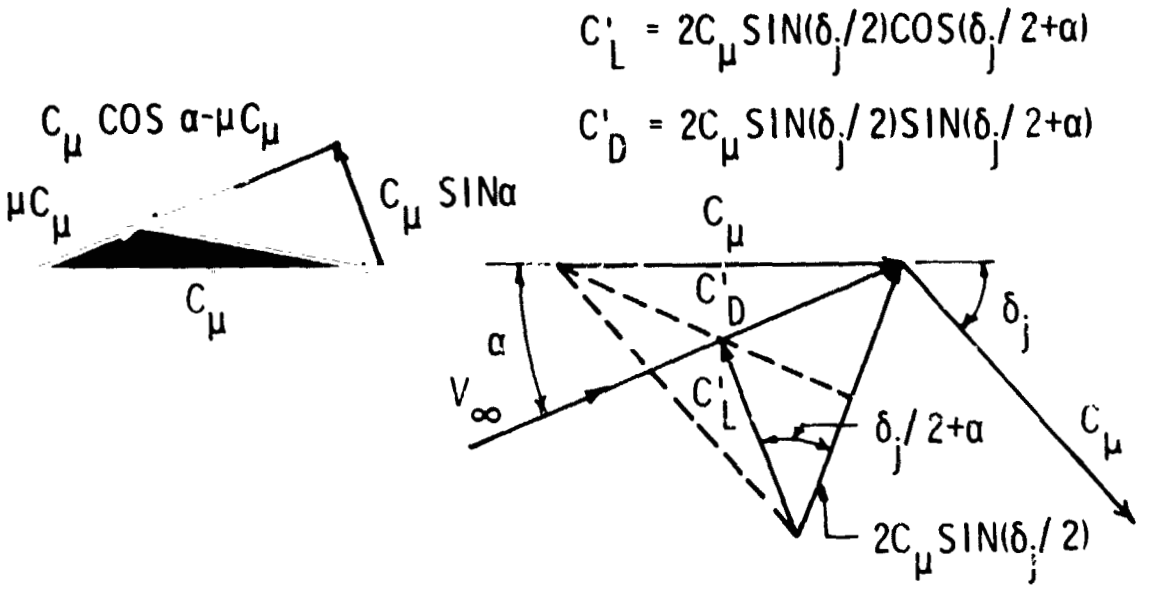

Figure 3.- Force components due to the Coanda jet reaction on USB configurations.

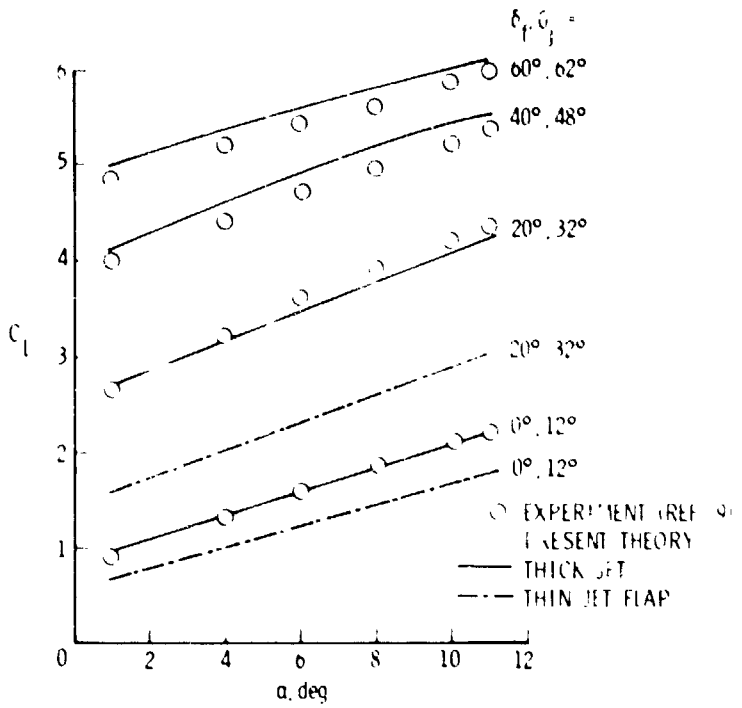

(a) Lift data.

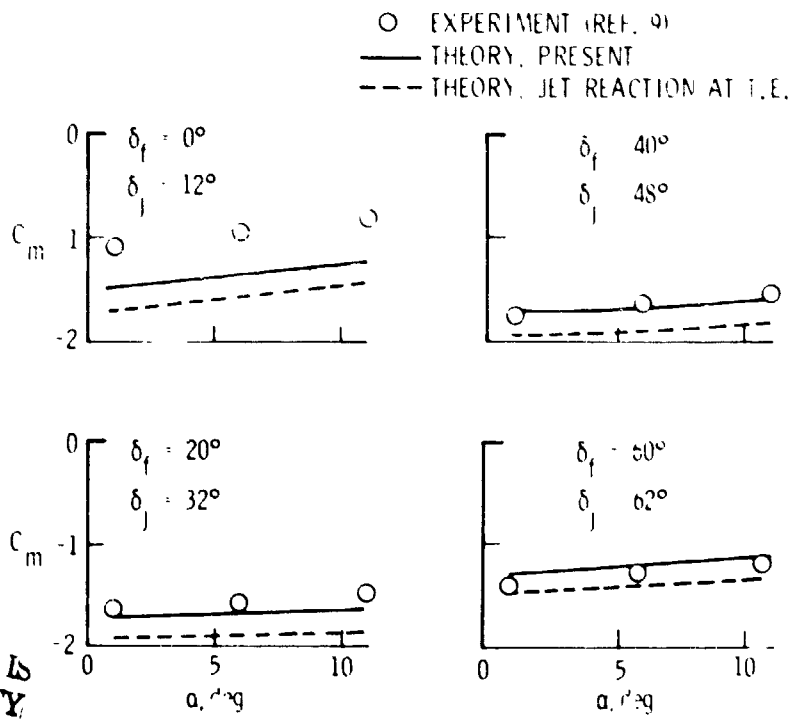

(b) Pitching moment data.

Figure 4.- Estimation of aerodynamic characteristics of a USB configuration for C_μ = 2 (results obtained by adding the predicted jet-induced values to the experimental jet-off values).

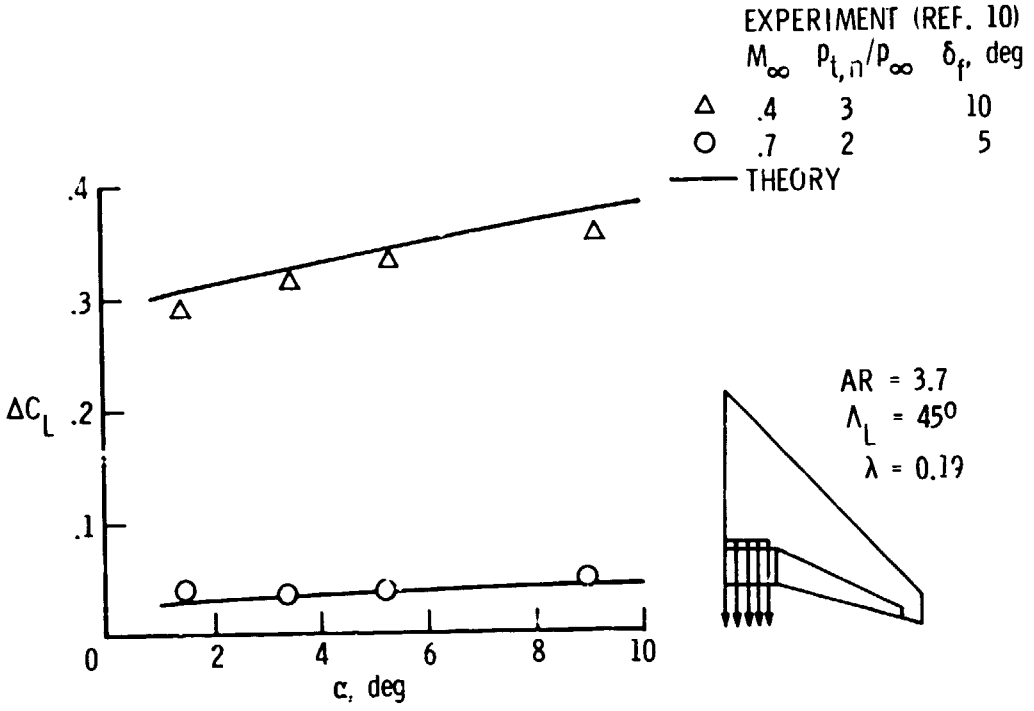

Figure 5.- Estimation of jet-induced lift for the vectored-thrust fighter configuration of reference 10.

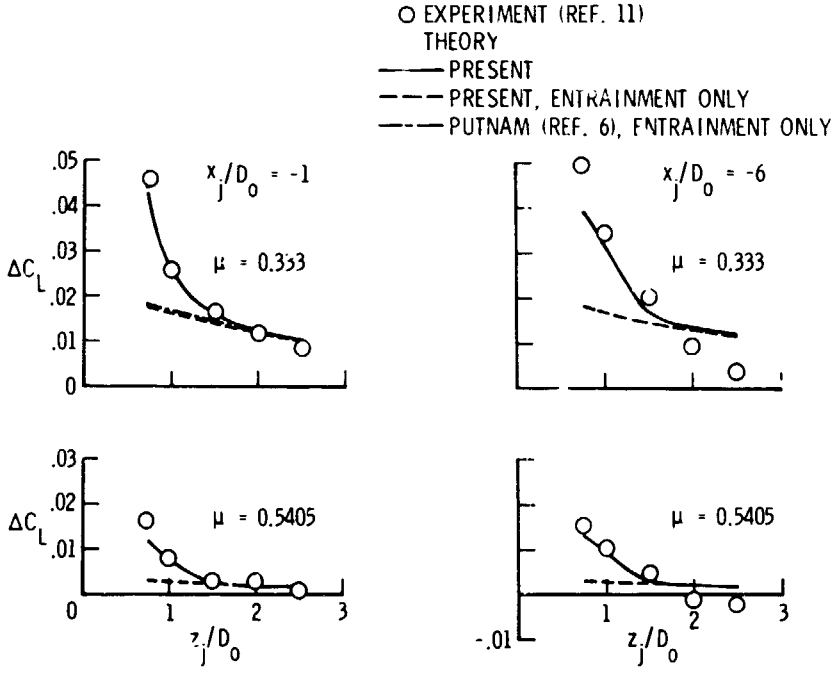

Figure 6.- Estimation of jet-induced lift for a rectangular wing having OWB. $\alpha = 0^o$; AR = 2.

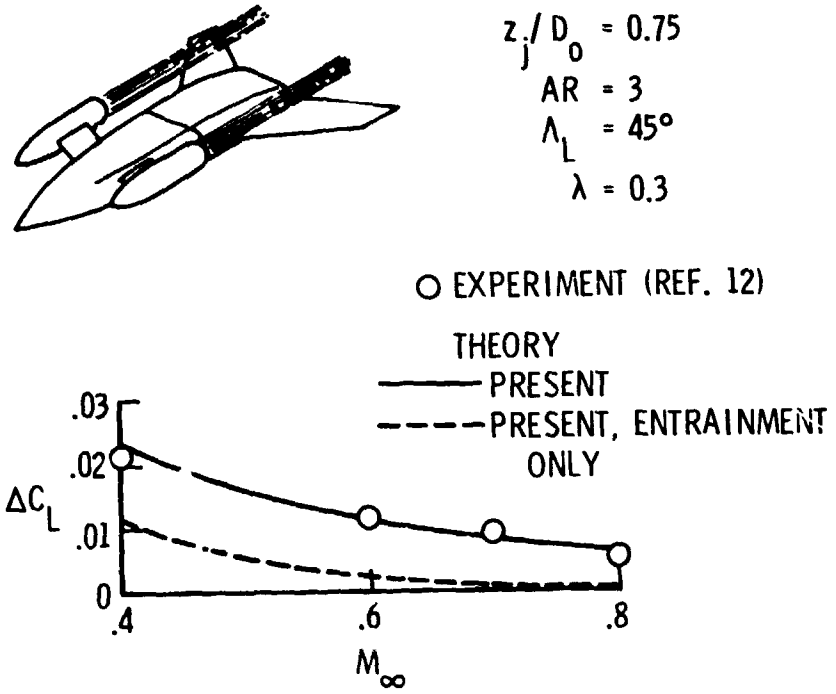

Figure 7.- Estimation of jet-induced lift for the OWB configuration of reference 12. $p_{t,n}/p_\infty$ = 1.9; α = 0°.

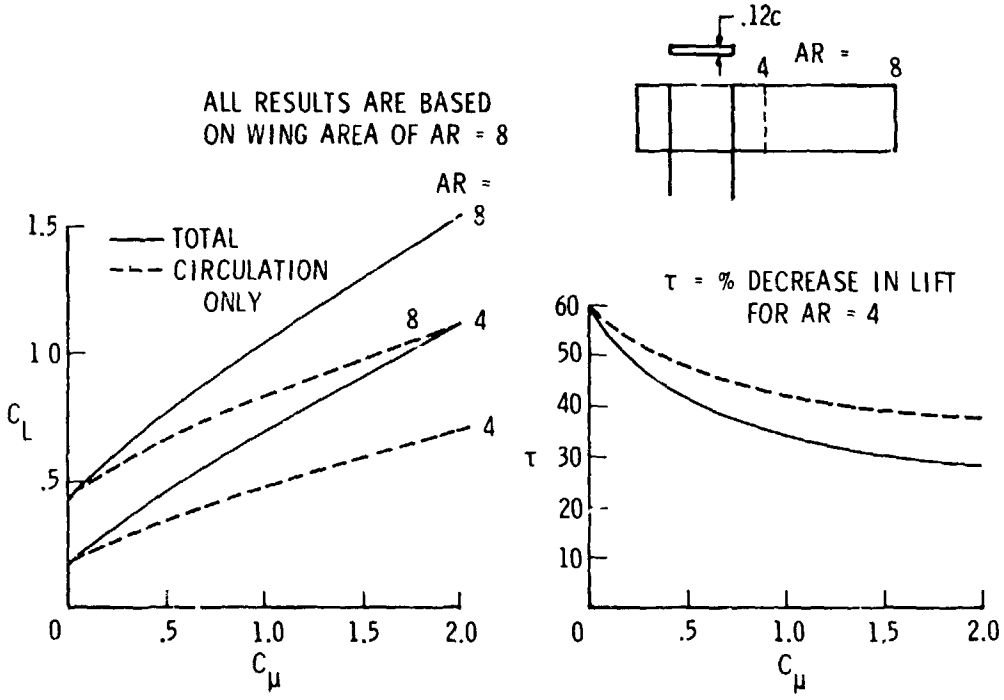

Figure 8.- Theoretical effect of aspect ratio on USB lift capability. $M_\infty = M_j = 0$; $\alpha = 2°$; $\delta_f = 0°$; $\delta_j = 10°$; NACA 65_1-412.

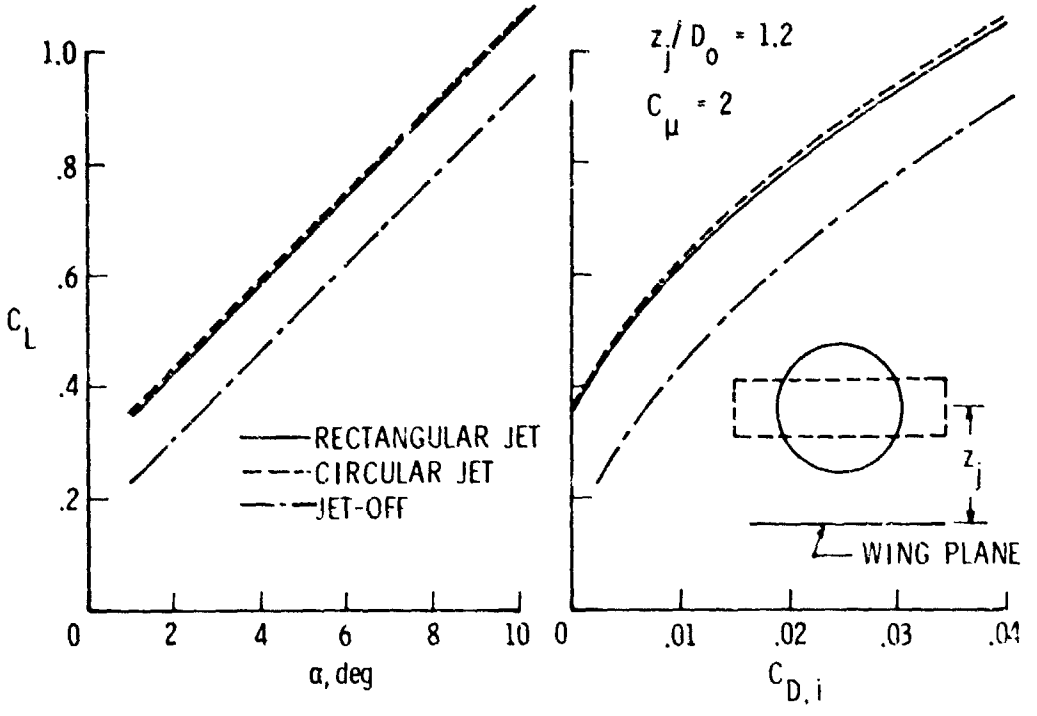

Figure 9.- Comparison of theoretical aerodynamics obtained by jets of rectangular and circular cross section on the configuration of reference 9. AR = 7.8; $\Lambda_L = 0^o$; $\lambda = 0.73$; $\delta_f = 0^o$.

USB FLOW CHARACTERISTICS RELATED TO NOISE GENERATION

W. H. Brown and N. N. Reddy
Lockheed-Georgia Company

SUMMARY

The effects of nozzle and flap geometry on USB flow field characteristics related to noise generation were examined experimentally using static models of two sizes. Flow attachment and spreading characteristics were observed using flow visualization techniques. Velocity and turbulence profiles in the trailing edge wake were measured using hot-wire anemometry, and the effects of the geometric variables on peak velocity and turbulence intensity were determined. Then, it is shown that peak trailing edge velocity is a function of the ratio of flow length to modified hydraulic diameter.

14

INTRODUCTION

Design concepts such as blown flaps, which provide high lift by turning and spreading the engine exhaust, necessarily produce more noise than would an undeflected jet. It is the problem of the designer to establish an acceptable balance between the performance of the aircraft and its noise. In this area, USB offers an apparent advantage over other techniques because the engine placement above the wing inherently provides noise shielding between the engine and the ground.

Performance and noise are directly related to flow characteristics. Performance evaluation generally involves only the gross properties of the flow field, such as mean velocity and pressure distributions, whereas noise evaluation requires knowledge of more detailed properties of the flow field, such as turbulence properties. The experimental work presented in this paper is directed toward understanding the role of turbulent flows interacting with rigid surfaces (wing and flap) in noise generation and propagation. Even so, some of the flow data obtained are applicable to performance evaluations. Radiated sound measurements and the analysis of noise sources given in references 1 and 2 provided some guidelines as to which flow characteristics might be pertinent in the determination of the noise characteristics of USB configurations. The results of flow visualizations, mean velocity and turbulence profiles, and the space-time cross correlations of fluctuating velocities in the trailing edge wake are presented.

EXPERIMENTAL MODEL AND APPROACH

Model designs and test conditions were kept general as befits an exploratory program and were selected to cover the range from CTOL through STOL aircraft. Nozzle and installation variables include nozzle size, shape, chordwise location on the wing, inclination and height above the wing. Flap variables include radius of curvature, deflection, and total flow-path length. Scale effects are provided by two model sizes.

The small-scale static model is shown in figure 1. This model, of 51 cm span, provided 5.08, 7.62, and 10.16 cm flap radii each at 30°, 45° and 60° deflection with provisions for a common flow length. The nozzle can be located off the surface or on the surface at any of three chordwise positions and at any desired impingement angle. Nozzles are provided in two sizes to simulate the range of engine by-pass ratio appropriate to the CTOL and STOL operation and in several shapes. Six nozzle shapes were used - circular, rectangular nozzles of aspect ratios 2, 4, and 4, D-shaped, and elliptical. The holes shown along the surface in this figure were used for surface static pressure measurements and with probe microphones to obtain space-time correlations of the fluctuating surface pressures.

The large-scale static model is shown in figure 2. This model, of 74 cm span, is approximately $2\frac{1}{2}$ times the linear scale of the small model (except in span). A constant ratio of flap-radius-of-curvature-to-nozzle-height is maintained between the two model sizes. The large model corresponds to the 7.62 cm radius small-scale configuration at 30° and 60° deflection angles with nozzles of aspect ratios 4 and 8. Circular nozzles were provided also.

Flow visualizations provide a useful point of departure by showing in a qualitative way the extent and intensity of the flow field. Photographs of surface oil flow show flow attachment and spreading characteristics. Schlieren, being sensitive to density gradients in the flow, shows attachment in another perspective in addition to showing turning shocks, the overall jet boundaries, and possible large-scale structure in the jet.

Previous studies have indicated that the major source of USB noise is located in the vicinity of the trailing edge. For that reason, mean velocity and turbulence profile measurements were concentrated there. Fairly extensive sets of wake velocity and turbulence intensity profiles were obtained using the small-scale static model and a single-channel linearized constant temperature anemometer. The hot-wire was positioned parallel to the trailing edge and moved normal to the upper surface of the flap. Centerline values received the most attention because they more nearly represent two-dimensional behavior (which is easier to handle analytically) and because the centerline flow is more firmly attached to the surface, thereby having steeper velocity gradients and higher turbulence levels generated near the surface.

Space-time correlations of fluctuating velocities were measured in the vicinity of the trailing edge. Correlations of each component of the fluctuating velocity would have provided a better understanding of the turbulence structure and its role in noise generation. However, component-by-component correlation was not feasible at the time because only two-channel anemometry capability was readily available and because the yawed-wire technique is too cumbersome. Therefore, useful correlation measurements were made using two linearized hot-wire channels with an on-line digital correlator.

RESULTS AND DISCUSSION

Flow Visualizations

Oil flow visualizations were used early in the investigation to determine which configurations had attached flow at the trailing edge. Typical visualizations of separated and attached flow are shown in figure 3. These oil flow photographs were made with the aspect ratio 2 nozzle touching the wing at the 20% chord location and the 5.08 cm radius 60° deflection flap. The flow at the trailing edge is seen to be separated at 0° impingement angle and attached at 10° and 20°.

For nozzles discharging at the surface, flow impingement angle clearly is an important variable relative to flow attachment. For nozzles located off the surface, the height of the nozzle above the wing is equally important. With the exception of the circular nozzle, attached flow was obtained from all nozzles at an impingement angle of 20°. The circular nozzle due to its narrow width (almost zero) at the wing surface and its high center of momentum required a 30° impingement angle to achieve attachment.

Some configurations which exhibit attached flow at the trailing edge have local separations over the curved flap section as evidenced by the bubble seen in the oil flow photograph for a 10° impingement angle. All nozzles except the aspect ratio 8 nozzle (the thinnest one) showed a tendency toward this kind of local separation. Nozzle location and nozzle height affect the tendency to form a separation bubble. Moving the nozzle aft from the 20% chord location toward the flap increases the tendency toward separation presumably by allowing less opportunity for flow spreading and for velocity decay before the high-curvature flap is encountered. Greater nozzle inclination angles tend to reduce or eliminate separation bubbles by promoting flow spreading.

Schlieren photographs taken in the spanwise direction more clearly show separation than do the oil flow photographs which suffer somewhat from the effects of inertia. Schlieren photographs provide a means for distinguishing between a weakly attached and a separated flow when the oil flow observations are inconclusive as often is the case when the oil streaks near the trailing

edge are approximately parallel and cover only a narrow span. The Schlieren visualizations in figure 4 cover the range from separated through attached flow with the aspect ratio 8 nozzle and the 7.62 cm radius 60° flap.

The oil flow photographs in figure 3 were used in an attempt to quantify flow spreading. A spreading parameter defined as the sum of the scrubbed widths measured at the nozzle exit, the start and end of curvature, and the trailing edge was evaluated for several configurations. The results, plotted in figure 5, show the strong influence of impingement angle, nozzle size, and nozzle location on flow spreading. The difference in scrubbed area between the 20% chord location and the 50% chord location actually is greater than that indicated on the figure because the spreading parameter ignores the area increase which results from increased flow path length.

Velocity and Turbulence Profiles

Mean velocity and turbulence intensity profiles for four different nozzles are shown in figures 6 and 7. These profiles were taken along the centerline behind a 5.08 cm radius 60° deflection flap. The nozzles were touching the wing at the forward (20% chord) location and were inclined 20° relative to the wing. The circular nozzle and the rectangular aspect ratio 4 and 8 nozzles are twice the area of the aspect ratio 2 rectangular nozzle - 20.26 sq cm as opposed to 10.13 sq cm. The aspect ratio 2 and 4 nozzles have a common nozzle height - 2.25 cm. The circular nozzle and aspect ratio 8 nozzles have heights of 5.08 cm and 1.58 cm, respectively. Several characteristics of USB flow can be seen in these profiles.

Consider the shapes of the mean velocity profiles in figure 6. The profiles for the AR2 and AR8 nozzles are broader than the other two profiles and have more rounded peaks than does the profile for the AR4 nozzle. The magnitudes of the peak velocities decrease in the order: circular, AR4, AR2, and AR8. The location (in nozzle heights) of the peak velocity moves away from the surface in the order: AR4, AR8, circular, and AR2. Thus, we see that the magnitudes and locations of the peak velocity do not vary systematically with nozzle size, height, or aspect ratio when these variables are taken individually.

The turbulence intensity profiles in figure 7 correspond to the previously discussed mean velocity profiles. These profiles, some with one peak and others with two peaks, are less similar in shape than the mean velocity profiles. The dip between the peaks is related to the extent of development of the flow mixing profile. A deep dip (as does a high peak velocity) indicates a region of flow relatively unaffected by mixing and by boundary layer growth. The rounded profiles for the AR2 and AR8 nozzles are characteristic of a more advanced state of turbulence profile development.

Effects of Geometric Variables on Peak Velocity

It is believed that practical considerations such as internal losses and structural compatibility ultimately will require nozzles of low aspect ratio, say less than four. This results in a jet-dimension-to-flow-path-length which is short in terms of flow field development. More importantly, the inner profile at the trailing edge is in the initial stage of transition from a boundary layer profile before the edge to a jet mixing profile some distance into the wake region. Therefore, similarity profiles are not expected. However, peak values of mean velocity should vary consistently with the major geometric and operational variables.

The peak velocity and the turbulence intensity value at the knee of the turbulence profile were examined at the trailing edge in the mid-span plane for attached flow cases. Knee turbulence is used because the peak value, particularly for longer flow lengths, often occurs far from the edge and far from the high shear area where the noise source is presumed to be. Figure 8 shows how peak velocity and knee turbulence vary with the nozzle installation variables. The measured values were found to be "well behaved" with respect to the chosen variables. Peak velocity decreases as impingement angle increases and increases as the nozzle is moved aft (toward the flap) along the wing while maintaining a constant flow length. The first tendency is believed to be the result of jet spreading which increases the effective length-to-diameter ratio of the jet flow. The reason for the increase in velocity with nozzle chordwise position is not clear, although it might be related to the partial development of the flow before the flap is reached.

The effects of flap variables on peak velocity are shown in figure 9. Peak velocity decreases with increasing flap deflection, flap radius, and flow length. Only the relatively small decrease with increasing flap radius is surprising. The intuitive thought prior to testing had been that, other things being equal, peak velocity would decrease with decreasing radius of curvature because of the higher radial acceleration of the flow, and its greater tendency to separate.

Jet velocity profiles are expected to be functions of a length-to-diameter ratio. In the case of non-circular jets, hydraulic diameter is used with free jets and nozzle height (or jet thickness) is used with wall jets. Length usually is measured from the nozzle exit along the jet axis. In USB configurations where the jet follows a curved surface, flow length along that surface from the nozzle to the trailing edge is an appropriate length variable. It was reasoned that pure hydraulic diameter was inappropriate because it failed to account for the reduction in mixing area caused by the presence of the surface. Ultimately a modified hydraulic diameter based on nozzle perimeter diminished by the nozzle width was successful with "well attached" flows from all the small-scale static tests and some of the large-scale tests. The results are seen in figure 10.

Correlation Measurements

A typical set of space-time cross correlations of fluctuating velocities is shown in figure 11. These correlation measurements are normalized to the maximum value of the auto-correlation for the upstream wire which was located 1.6 cm aft and 0.1 cm above the trailing edge. Both hot-wires were parallel to the trailing edge.

Two things can be learned from the peaks of the cross-correlation curves. The slope of separation distance plotted against delay time at which the corresponding correlation peaks occur is the convection velocity of the turbulent field. It represents the velocity at which the turbulent structure is convected past the measuring locations. The envelope of the peaks provides a measure of eddy lifetime. By following the peaks, the observer effectively is moving with the eddy. The eddies lose their identity or coherence by decay and by coalescence. The time required for the correlation coefficient to reach 1/e of its maximum is defined as the eddy lifetime. It is a measure of the length of time the turbulent structure maintains its spectral identity.

The cross correlations at zero time-delay provide a measure of the size and isotropy of the turbulent structure. The length scale for a typical eddy is defined as the area under the curve of the zero-time cross-correlation coefficients plotted against the corresponding separation distances. The length scale or eddy size is a measure of the distance over which the structure maintains an amount of coherence. These length scales are defined in all directions - lateral and transverse as well as longitudinal. The ratios of the scales are measures of the isotropy of the turbulence. A ratio of unity indicates isotropic turbulence; other ratios indicate deviance from isotropy. We have used the ratio of streamwise to spanwise eddy sizes as the scale of anisotropy of the turbulence.

The correlation measurements shown in figure 11 were made in the wake of the 7.62 cm radius 60° deflection flap with the AR8 nozzle inclined 20° relative to the wing at the 20% chord location. The measurements were made with a nozzle pressure ratio of 1.1. The corresponding peak trailing edge velocity is 74 m/s. The following values were obtained from that figure and a corresponding set of spanwise correlation measurements:

Convection Velocity	=	0.90 Peak Trailing Edge Velocity
Streamwise Length Scale	=	0.84 cm
Spanwise Length Scale	=	0.37 cm
Scale of Anisotropy	=	2.3

The use of these quantities in noise prediction is described in reference 2.

CONCLUDING REMARKS

It has been shown that the flow fields of realistic USB configurations are "well behaved" at least in respect to those gross characteristics, such as peak velocity, which are important in noise generation. Trends of peak velocity and turbulence intensity levels with respect to installational and operational variables appear to be reasonable and therefore should be usable in analyses of noise generation and of performance trends. These peak velocity trends when combined with a modified hydraulic diameter yielded a reasonable collapse of the peak trailing edge velocity data over a wide range of variables including model scale; flap radius, deflection, and length; and nozzle size, shape, location, and impingement angle.

The variation of trailing edge turbulence structure with geometric variables may be established with a more sophisticated experimental program using either four channel hot-wire anemometry or the four channel laser velocimeter developed recently at Lockheed.

REFERENCES

1. Gibson, J. S.; and Searle, N.: Characteristics of USB Noise. Powered-Lift Aerodynamics and Acoustics, NASA SP-406, 1976. (Paper no. 15 of this compilation.)

2. Reddy, N. N.; and Tam, C. K. W.: Analytical Developments for Definition and Prediction of USB Noise. Powered-Lift Aerodynamics and Acoustics, NASA SP-406, 1976. (Paper no. 16 of this compilation.)

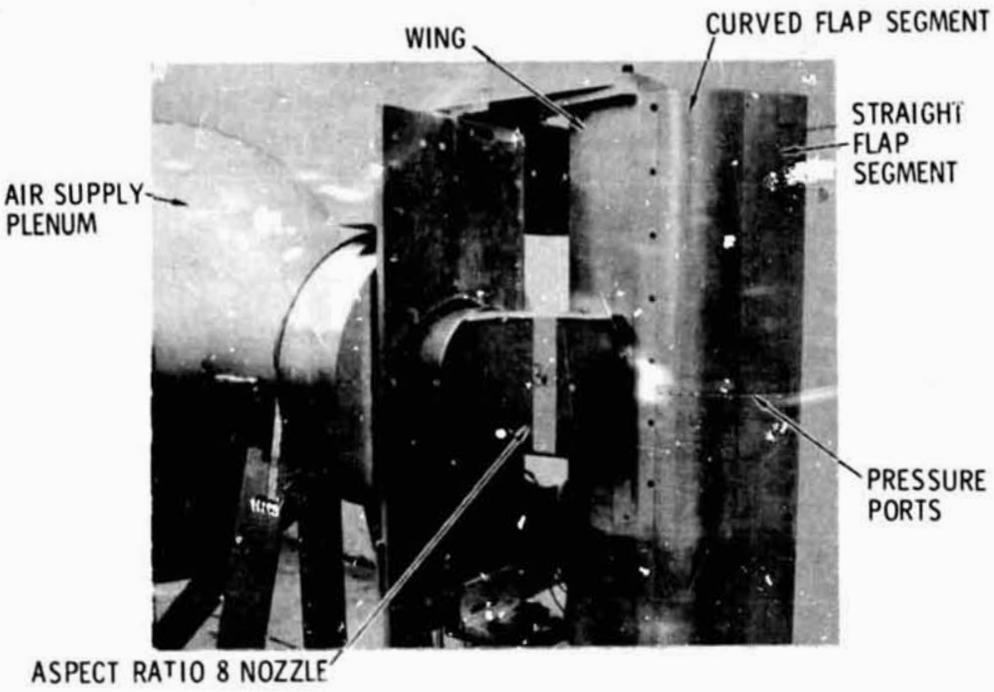

Figure 1.- Small-scale test apparatus.

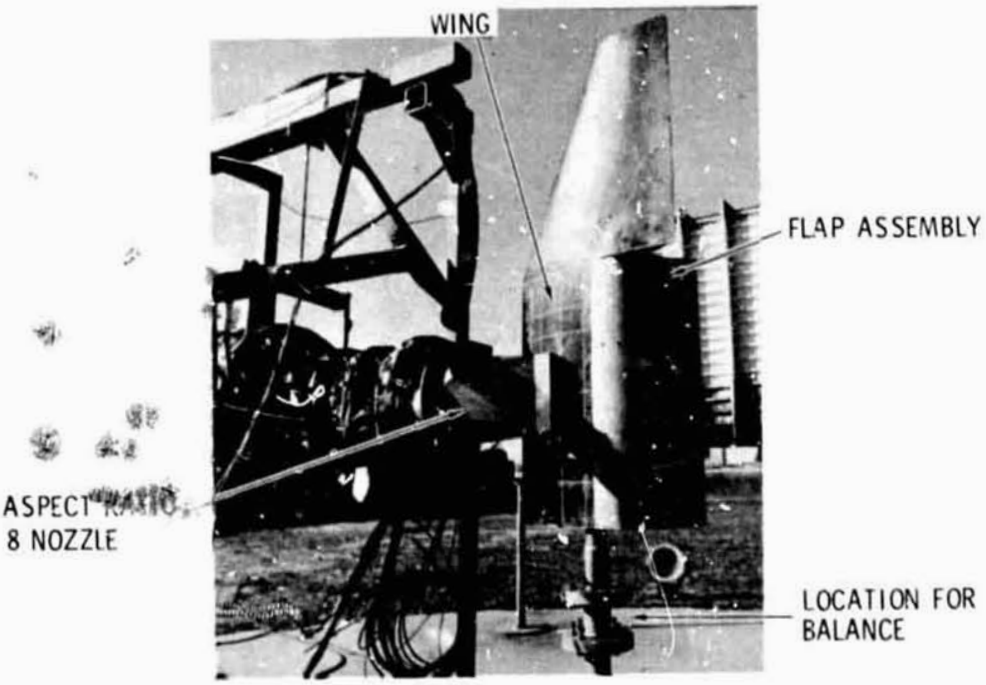

Figure 2.- Large-scale test apparatus.

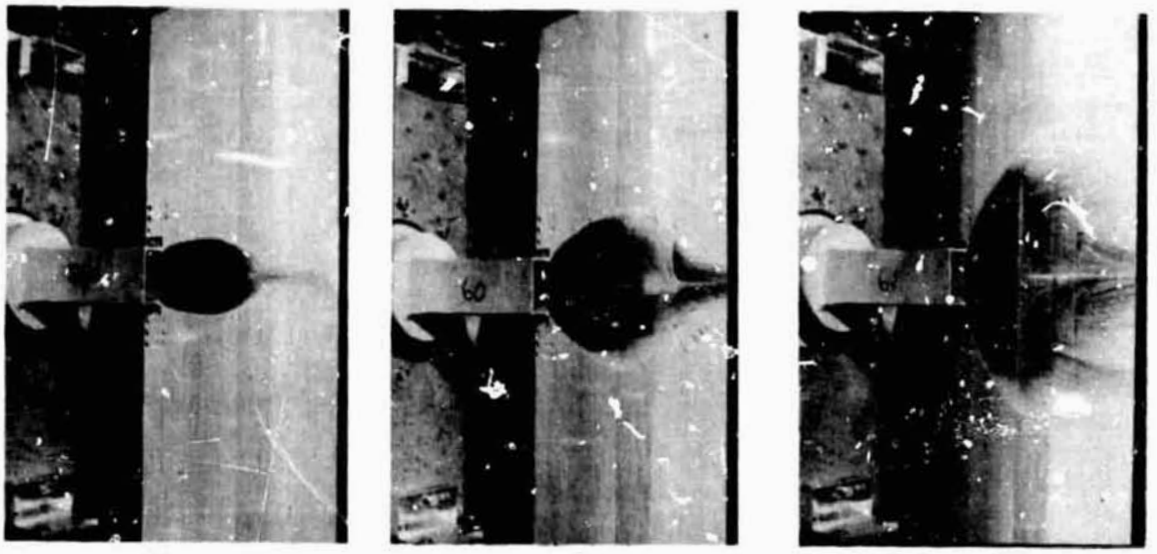

Figure 3.- Oil flow visualizations.

Figure 4.- Schlieren flow visualizations.

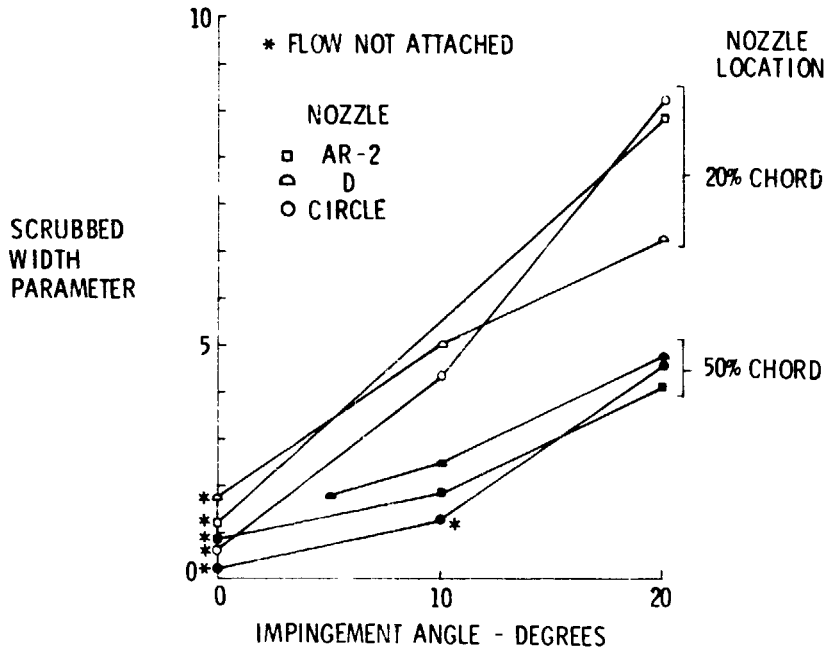

Figure 5.- Effect of nozzle variables on scrubbed width.

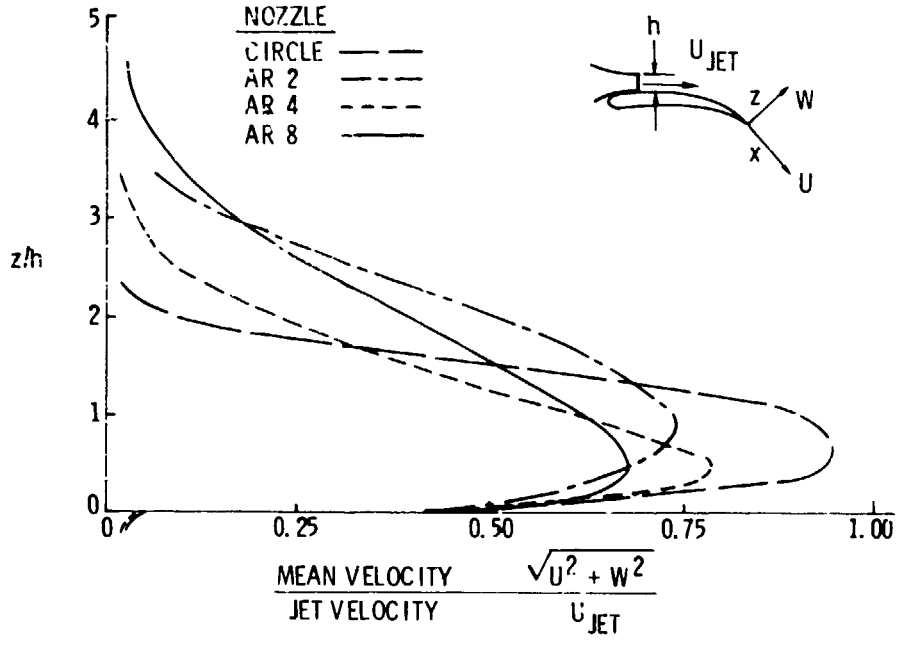

Figure 6.- Typical trailing edge mean velocity profiles.

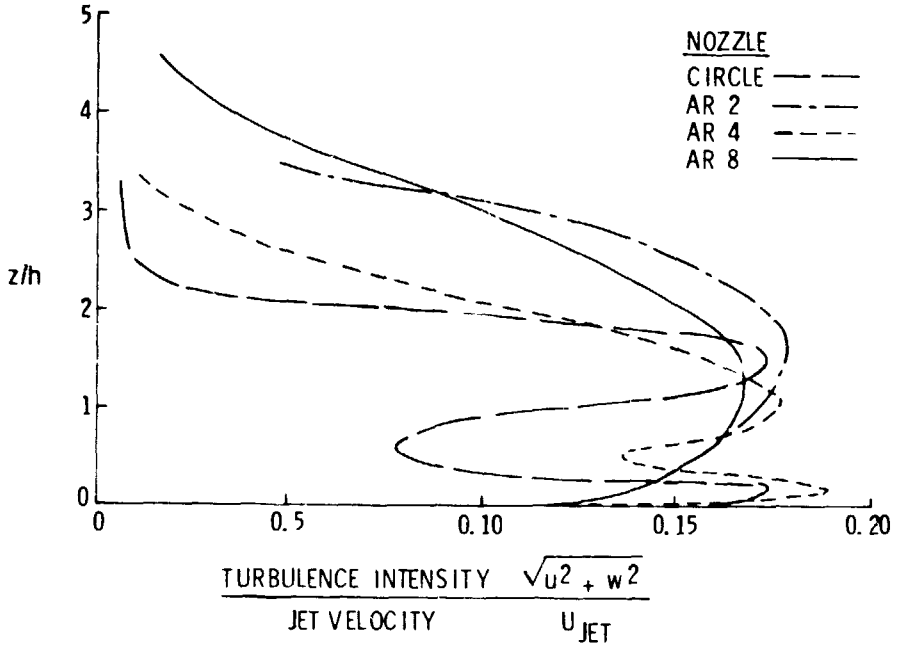

Figure 7.- Trailing edge turbulence profiles.

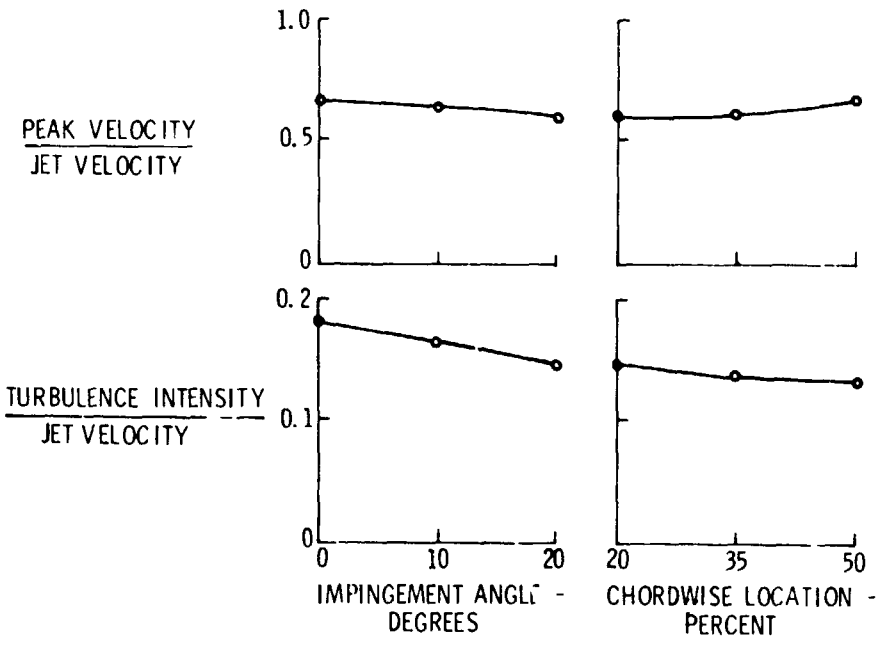

Figure 8.- Effect of nozzle installation variables.

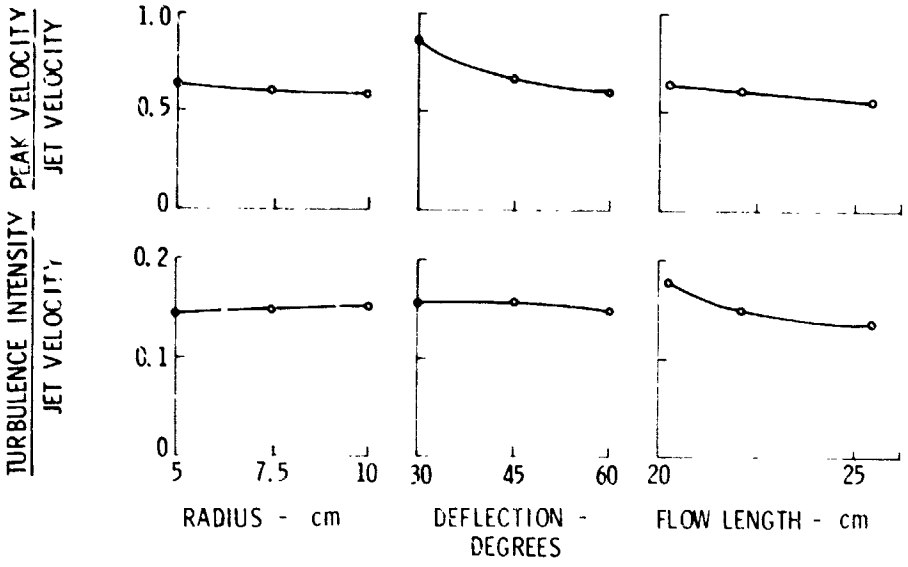

Figure 9.- Effect of flap variables and flow length.

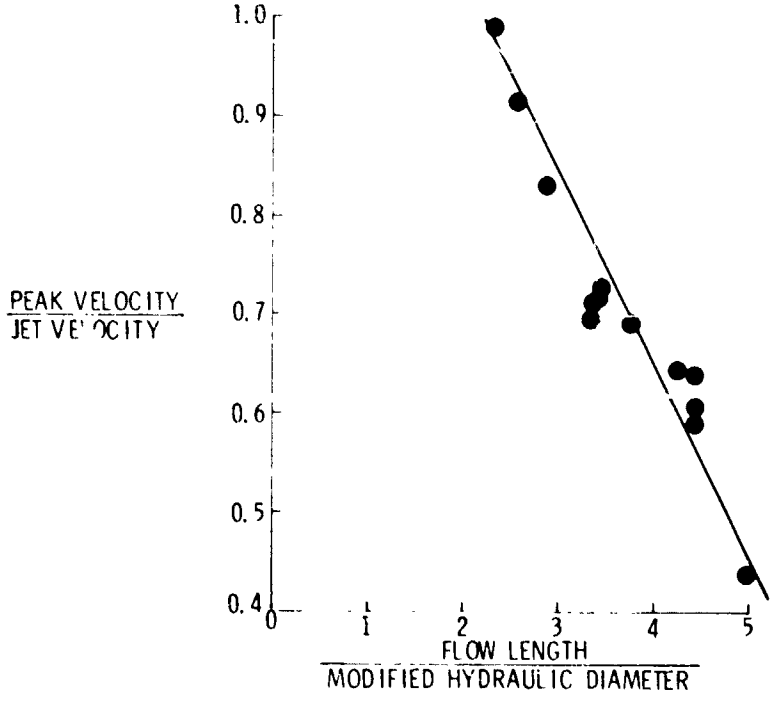

Figure 10.- Effect of nozzle and flap geometry on peak velocity.

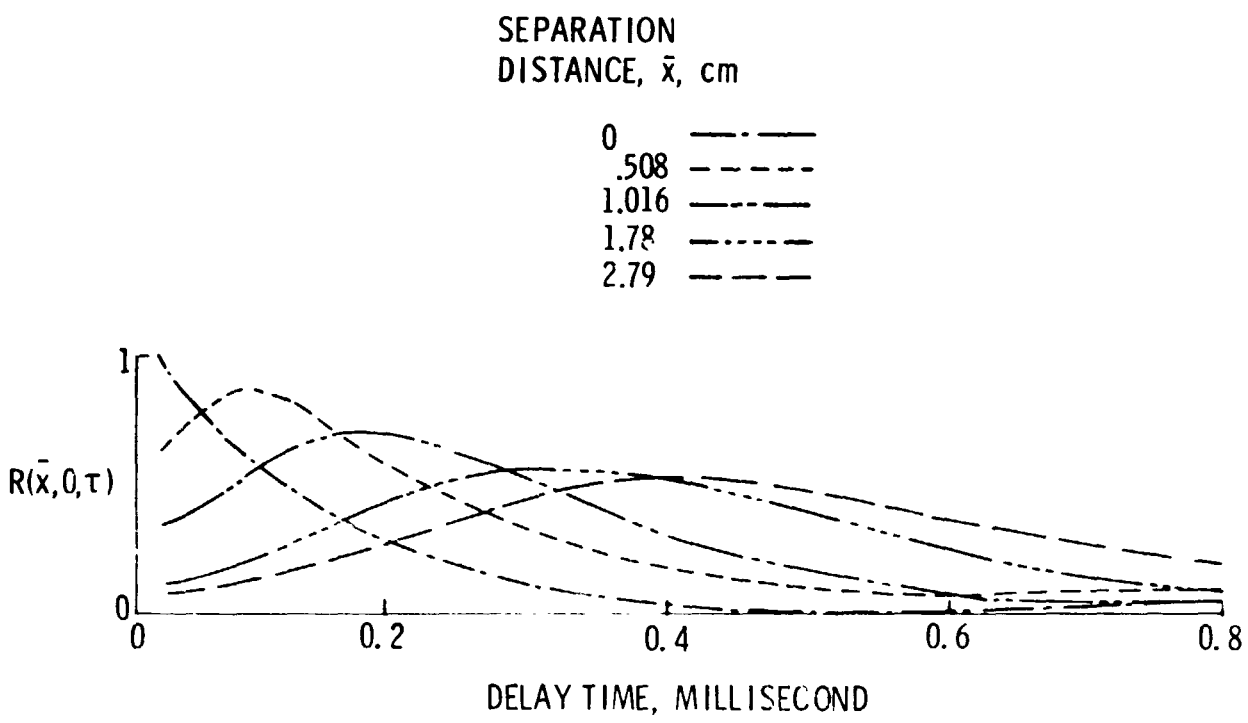

Figure 11.- Streamwise space-time fluctuating velocity cross correlation

CHARACTERISTICS OF USB NOISE*

J. S. Gibson and N. Searle
Lockheed-Georgia Company

SUMMARY

An extensive series of noise measurements, for a variety of geometric and operational parameters, have been made on models of upper surface blowing (USB) powered-lift systems. The data obtained have been analyzed and the effects and trends of parametric variation have been defined. From these results, insight can be gained into the behavior and nature of USB noise and the design of USB systems with low noise characteristics.

INTRODUCTION

This paper is concerned with the USB parametric acoustic evaluation program that is a companion effort to the flow field work described in the preceding paper, and the analytical acoustics work which is given in the next paper. In this discourse, primary emphasis is placed on observed far field acoustic effects and trends resulting from geometric and operational parameter variations. Most of the results to be covered relate to static, cold flow, blended nacelle, upper surface blowing configurations. The majority of the results are for attached flow cases; however, also briefly covered are some separated flow cases, as well as some vectored thrust cases, flow temperature effects, and forward speed effects.

EXPERIMENTAL FACILITIES

The majority of the acoustic data were obtained in an anechoic room, illustrated in figure 1. The small scale USB model which has a 51 cm (20 in.) wing span is shown inverted and mounted to the end of a foam-covered muffler and air pipe system. This is the same model that is described in the preceding paper. Several microphone arches, each on a 2.44 meter (8 ft.) radius, can also be seen, as well as the room itself. Noise measurements were made at many locations, but the typical experimental trends discussed in this paper were taken from the microphone directly opposite the bottom of the wing, unless otherwise stated. This location corresponds to an observer located directly under an aircraft.

* Work performed under NASA Contract NAS1-13870 with NASA-Langley Research Center.

The outdoor facility, which accepts models larger by approximately a factor of two and a half, is shown in figure 2. Parametric data primarily for scaling purpose were obtained at this facility. The model, also described in the preceding paper, is mounted in the center of the test pad, being fed by a muffled piped air supply. The moveable, motorized 6.1 meter (20 ft.) radius microphone arch, model air supply, and all data acquisition systems are remotely controlled from a control room located in the building in the background.

The final facility used in this program is the anechoic wind tunnel shown in figure 3. This is a 0.76 x 1.09 meter (30 x 43 inches), continuous free-jet type facility. Tunnel air flow is from left to right into the foam lined collector. The model, which is the same size and uses the same flaps as the static anechoic room and flow study model, can be seen mounted to a fairing just inside the tunnel flow field. The nozzle is fed from a muffled pipe which goes along the upstream tunnel centerline.

ATTACHED FLOW PARAMETRIC AND OTHER NOISE CHARACTERISTICS

The parametric results presented in this section are for attached flow conditions, except for those few cases discussed under the heading of "separated flow effects." As mentioned previously, the trends shown in the figures are derived from typical data at a location which simulates an observers position directly under an aircraft. Trends at this location, in most cases, are similar to trends at other points below the wing as well.

Nozzle Exit Velocity

Nozzle exit velocity has a major effect on USB noise. Both noise level and peak frequency increase as jet velocity increases. As indicated in figure 4, the peak frequency effect has been collapsed into non-dimensional form by converting the frequency scale to Strouhal number, where f is the frequency in Hertz, V_j is jet exit velocity, and L_f is nozzle to flap trailing edge flow length. The spectral data shown are for a series of jet velocities with all other parameters constant. In Strouhal form, the spectrum shapes are similar. The level of noise at any frequency is typically proportional to $V_j^{5.5}$ directly under the model; proportional to $V_j^{5.0}$ in the forward quadrant; and varies to $V_j^{7.5}$ in the extreme aft quadrant.

Nozzle Shape

Figure 5 shows the effect of nozzle shape. This figure is in conventional one-third octave band form. The very low and high frequency range of the spectra are essentially independent of nozzle shape. However, the relatively narrow peak frequency range is significantly affected. The trend is higher levels for lower aspect ratio nozzles. The variation is over about a 5 dB range between a round nozzle and an aspect ratio (AR) 8 rectangular nozzle. These effects are slightly greater in the aft quadrant. The conclusion

here is that the more spread out on the flaps a given amount of jet flow is, the less noise is generated in the peak frequency region. The reason why only the peak frequency range is affected is currently unknown. It may be associated with the flow field edge roll-up vortices, which are larger and stronger for lower nozzle aspect ratios.

It should be pointed out that these peak spectrum effects would occur at rather low frequencies on a full scale aircraft and may have more of an aircraft structural vibration and interior sound proofing impact than a community noise impact.

Nozzle Impingement Angle

The result of impinging the nozzle at successively higher angles with respect to the wing is somewhat similar to increasing nozzle aspect ratio. As the angle is increased, the flow is spread out more over the wing and flaps. The noise spectrum, as can be seen in figure 6, is affected significantly only in the mid-frequency range, where lower noise levels correspond to higher impingement angles. The peak noise level varies over about a 5 dB range as in the case of nozzle shape. These data, as well as the nozzle shape data, have been corrected to a constant flow rate.

Flow Path Length

The subject of flow path length is involved with two geometric parameters - nozzle horizontal location on the wing and flap trailing edge length. Either parameter changes the total flow path length between the nozzle exit plane and the flap trailing edge. As flow length increases, higher frequency noise decreases regardless of which of the two parameters' length was varied. As can be seen in figure 7, the data from several examples of nozzle location and trailing edge length variation collapse rather well when the frequency scale is converted to Strouhal number form with total flow length, L_f, as the characteristic dimension. The apparent exception is the noticeable peak in the 50% chord data. However, this peak is due to an aeroacoustic resonance phenomenon (a tone or whistle sound) that appeared sporadically in the experimental program. Resonances of this type were related to flow disturbances near the beginning of the flap radius section, feeding back energy to the nozzle exit plane instability area. They are apparently a function of wing-flap joint smoothness rather than any of the basic parametric variables. When the surface was smoothed, the tone disappeared and the anomalus peak then collapsed with the other data in figure 7.

Flap Radius of Curvature

While flow path length is an important parameter, the shape of the path is apparently not important at all to noise for attached flow. Over a wide range of flap knee radius of curvature, no systematic trend could be found and the variations observed were inconsequential. This corresponds to the results of the companion flow field study where radius of curvature had a small effect, in fact the smallest effect of any of the experimental variables.

Even in cases where flow separation "bubbles" were noted on the flap, no significant noise trend was seen as long as the flow reattached prior to leaving the trailing edge.

Flap Angle

Flap angle is one of the more obvious variables in a USB system, but it has a rather small effect on noise under the wing. There is mainly a low frequency shift, or increase, as indicated in figure 8. The sound field, or directivity pattern, moves with the flap as the flap is rotated downward. However, this directivity effect is relatively insensitive over the 60° range investigated.

Jet Temperature

A limited investigation of jet temperature was performed. As indicated in figure 9, when the temperature is increased from 24°C (75°F) over a range of jet velocities, the overall noise levels drop, stay the same, or increase. To convert these results to constant thrust conditions, the 93°C (200°F) data should be shifted up about 1 dB. Actually the velocity exponent is reduced when the temperature is increased, thereby changing the slope of the noise versus velocity curve. In this case, the low temperature curve was proportional to $V_j^{5.6}$ and the high temperature curve was proportional to $V_j^{4.8}$. These relationships are somewhat different at other microphone locations as were the basic jet velocity trends with location as mentioned previously.

Vectored Thrust

In addition to the blended type nacelle, the use of over-the-wing pylon mounted nacelles with vectored down jet flows for low speed performance shows promise as a viable powered lift configuration. Up to this point, only the blended or fully integrated nacelle and wing installations have been discussed. Figure 10 shows how a typical vectored installation compares with the blended type. In general, as the exhaust nozzle is brought up from the wing surface, and vectored downward, noise throughout most of the spectrum increases and the spectrum shape broadens. The largest changes occur in the high frequency range which could affect community noise since subjective noise ratings are more sensitive to high frequency noise. The example shown is for a nozzle vector angle of 40° where the nozzle height, or gap between the nozzle and wing surface, was 30% of the nozzle diameter. For lower vector angles and lower nozzle heights the noise increases are smaller. This is really a rather complex situation needing more study since our investigation was limited in the number of configurations tested.

Scaling Trends

Figure 11 indicates that, over the range of a factor of two and a half in model size that was utilized in this program, spectral scaling is rather good based on linear size and velocity factors for the frequency scale, and on 10 Log nozzle area ratio for the noise level scale (as was done in this figure). Therefore, basic USB noise scaling apparently behaves in the same manner as normal subsonic jet noise, a conclusion that has also been observed by other investigators.

We also had one case where the wing, flap, and other parameters were kept constant, except that the nozzle area was reduced by a factor of two (round nozzles in both instances). A negligible spectrum effect was noted and the overall noise level scaled as in the small versus large complete model example.

Separated Flow Effects

All of the results to this point have had flow attachment at the trailing edge and reasonably good flow turning. To determine what effect poor attachment and turning would have, a special series of test runs were made and the trends illustrated in figure 12. The upper curve is a typical attached flow case, where the nozzle was flush mounted on the wing with a nozzle impingement angle of 10°. The middle curve is for a case where everything is the same, except the nozzle impingement angle was reduced to 0°, causing the flow to separate just upstream of the trailing edge. These are low-and mid-frequency noise reductions, but the high-frequency range is about the same. This result helps to substantiate the idea that much of the low-frequency noise of a USB system is related to flow - trailing edge interaction. The lower curve is for a case where the nozzle is above the wing and the flow is not vectored down. This results in the jet flow being completely unattached and not turned down at all. The corresponding noise levels across the spectrum are reduced, due to no flow - structure interaction and no downward turning of the jet noise directivity pattern.

Effect of Forward Speed

A short series of tests were run in the anechoic wind tunnel to obtain some data on the effect of forward speed on USB noise. Typical results are as indicated in figure 13. At low frequency, up to the peak, there is a noise decrease with forward speed of several dB, about 4 dB in this particular case. However, throughout the mid- and high-frequency range, there is only about a 0.5 dB reduction. These trends are largely independent of observer location and are also similar for a 60° flap case, as well as for an over-the-wing vectored nozzle case that was run. The reasons for these results are still under investigation.

CONCLUDING REMARKS

It has been shown that the primary variables controlling far field noise for attached flow USB systems are jet velocity, flow path length, and nozzle vertical location. Other parameters, including flap angle, nozzle shape, nozzle impingement angle, and jet temperature also have noticeable and systematic effects, but are generally considered of secondary importance for far field or community noise. Those several parameters causing low-frequency noise increases, however, will undoubtedly increase the aircraft problems of structural vibration, sonic-fatigue, and passenger compartment noise.

Noise results have been presented independently of quantitative aeropropulsion performance effects. A study of the tradeoffs between low noise design features and good aircraft performance is a phase of the program that is not complete at the time of this writing. Therefore, the use of the noise trends alone in a USB aircraft design study should be done with care so that low noise features will not be offset by aircraft performance penalties.

Finally, it should be noted that not all the acoustic effects we have observed can be explained with any degree of satisfaction. There is still much to be learned about the basic nature of USB noise and realistic USB nozzle-wing-flap installations for optimum low noise airplane design.

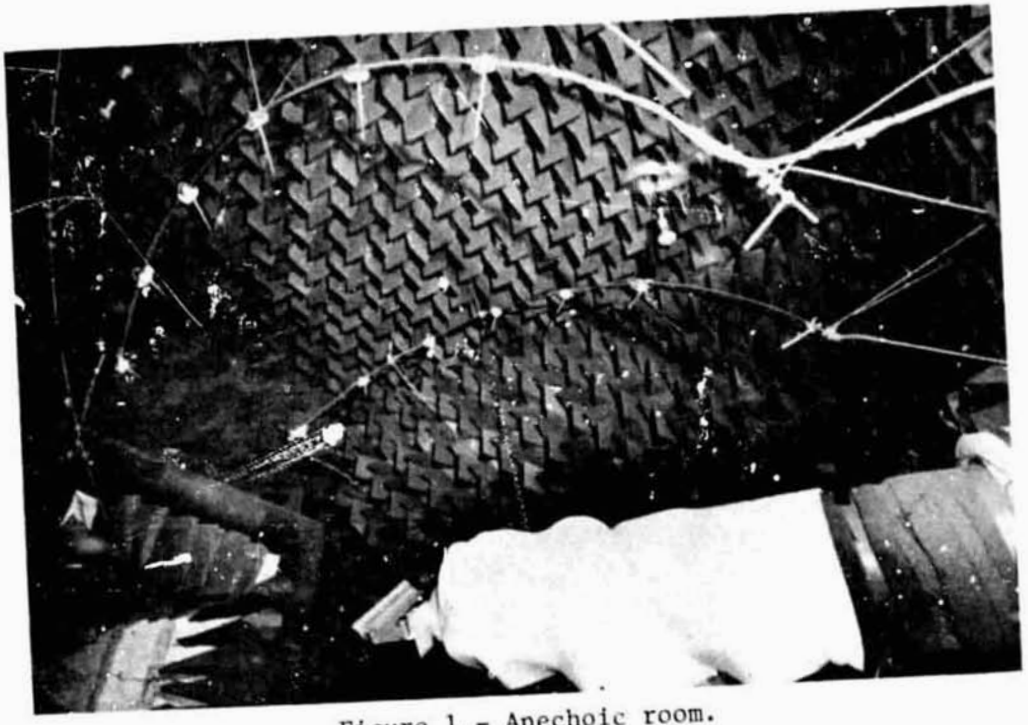

Figure 1.- Anechoic room.

Figure 2.- Outdoor facility.

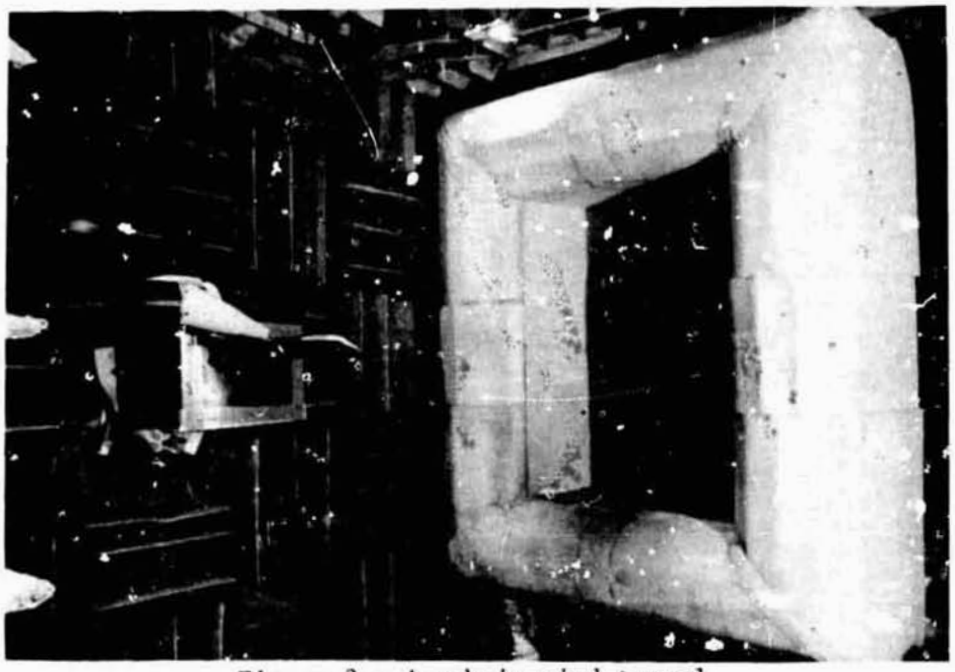

Figure 3.- Anechoic wind tunnel.

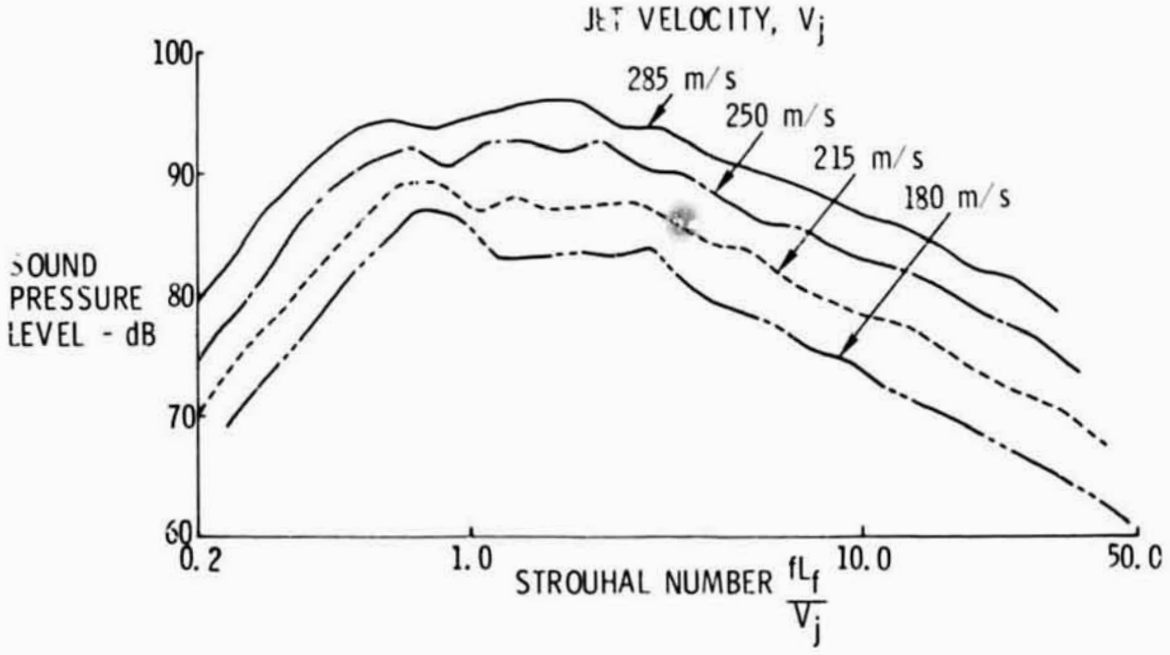

Figure 4.- Effect of jet velocity. AR4 nozzle; nozzle impingement angle 20°; nozzle location 20% chord; flap angle 30°.

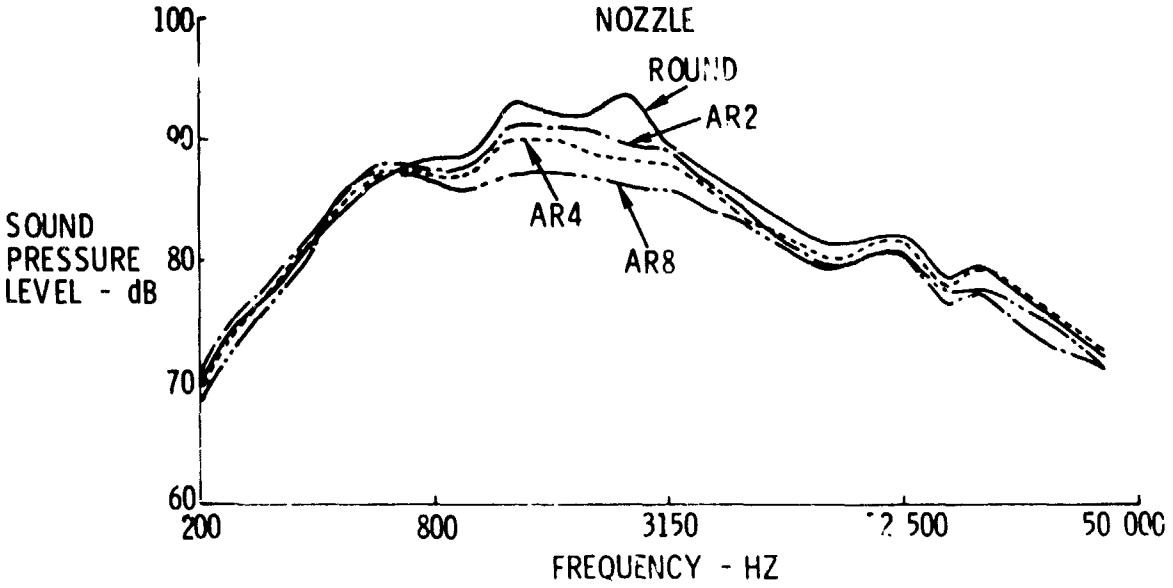

Figure 5.- Effect of nozzle shape. Jet velocity 215 m/s; nozzle location 20% chord; nozzle impingement angle 20°; flap angle 30°.

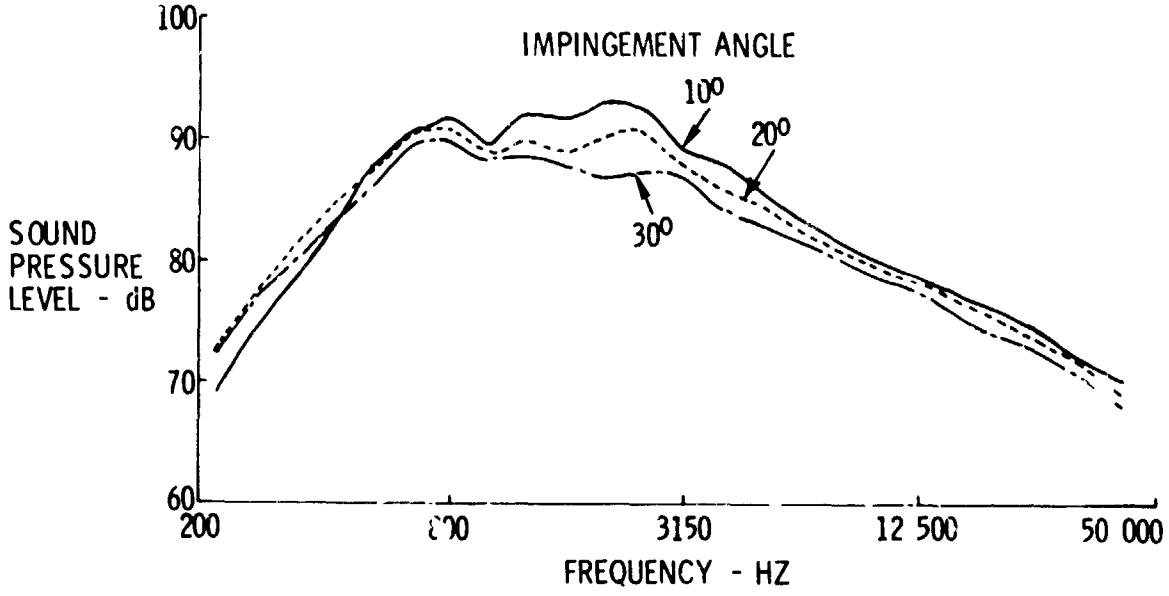

Figure 6.- Effect of nozzle impingement angle. AR4 nozzle; jet velocity 215 m/s; nozzle location 20% chord; flap angle 30°.

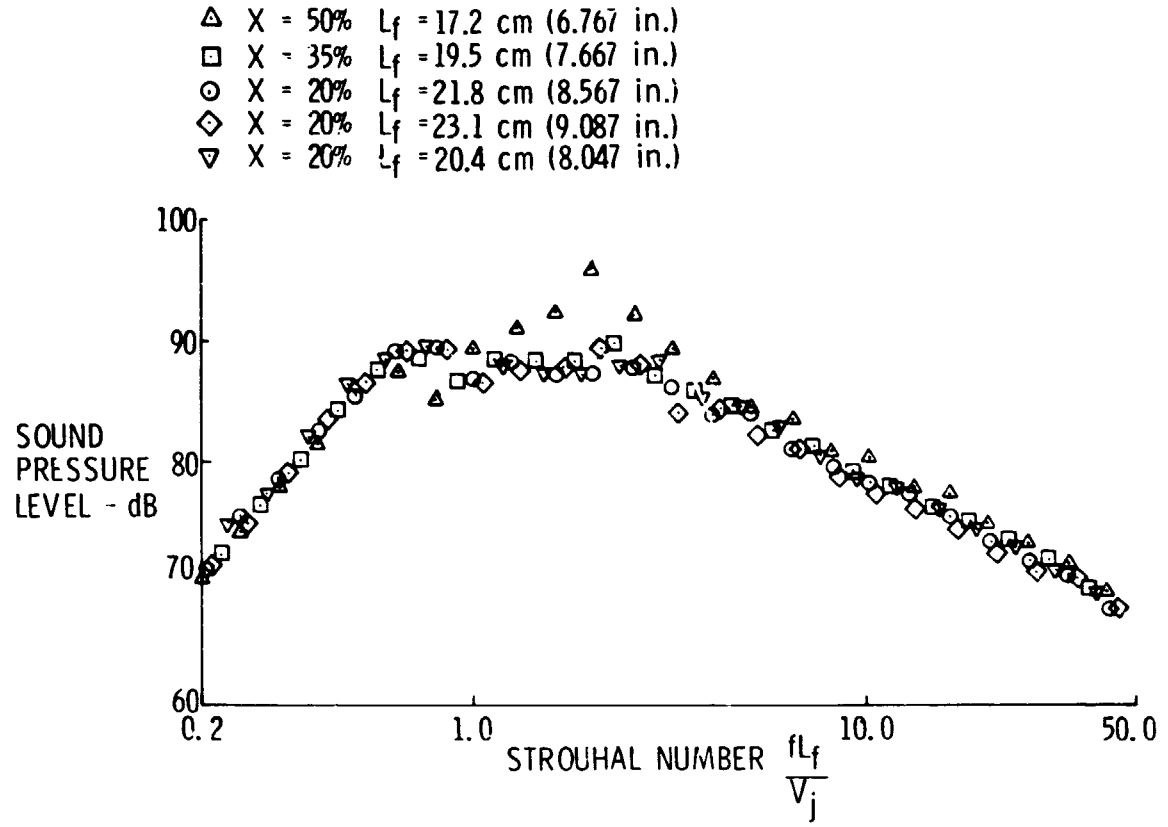

Figure 7.- Effect of flow path length. Jet velocity, V_j, 215 m/s; AR4 nozzle; nozzle impingement angle 20°; flap angle 30°; nozzle location, X, and flow path length, L_f, as indicated.

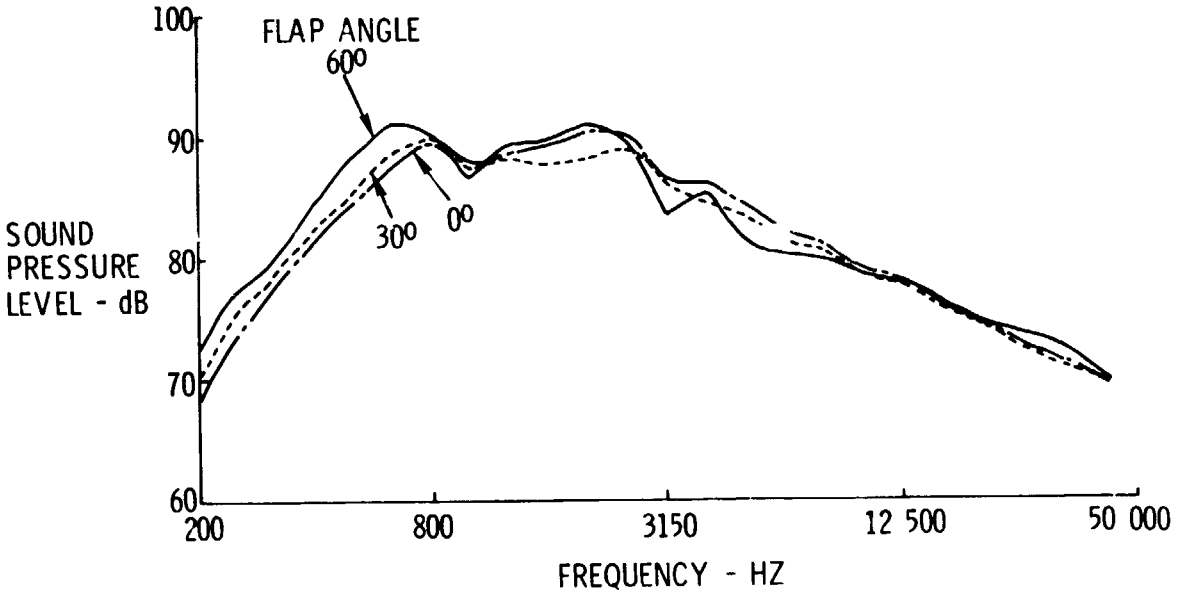

Figure 8.- Effect of flap angle. Jet velocity 215 m/s; AR4 nozzle; nozzle location 20% chord; nozzle impingement angle 20°.

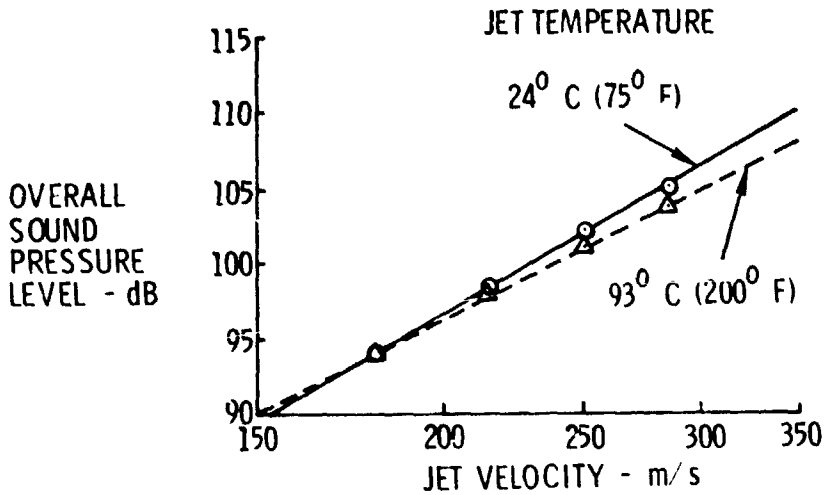

Figure 9.- Temperature trends. AR4 nozzle; nozzle impingement angle 20°; nozzle location 20% chord; flap angle 30°.

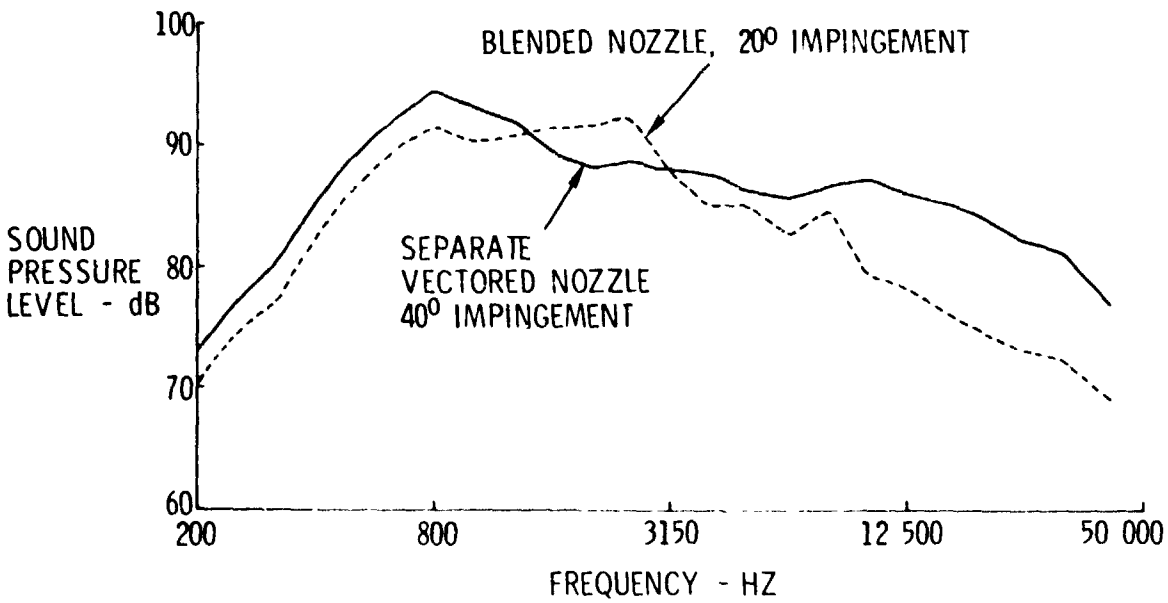

Figure 10.- Vectored thrust trends. Jet velocity 215 m/s; round nozzle; nozzle location 20% chord; flap angle 30°.

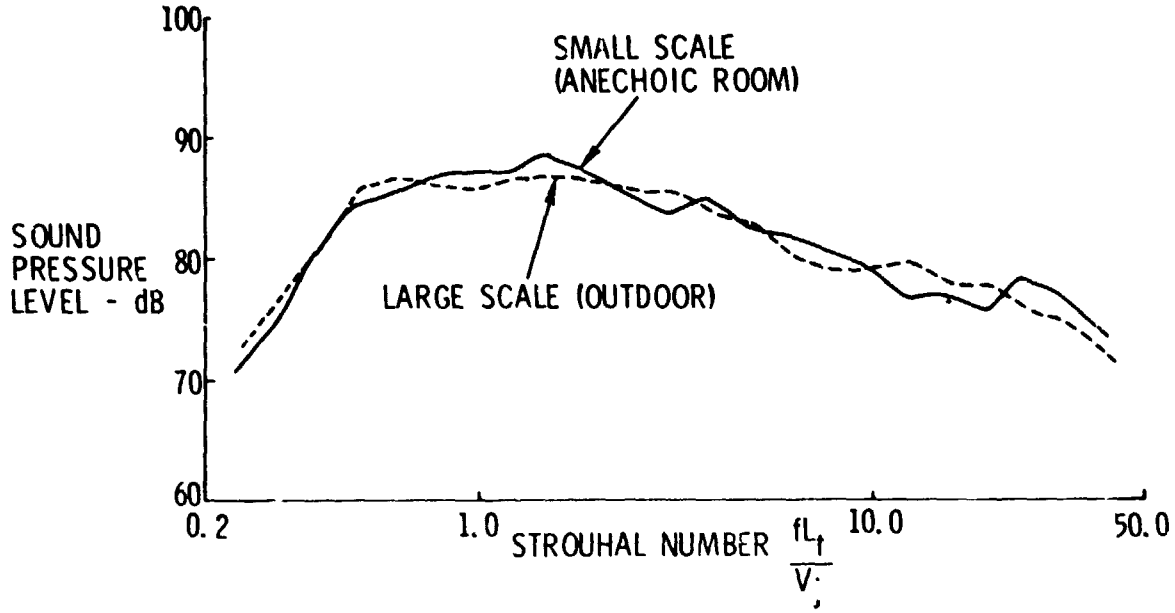

Figure 11.- Scaling results. Jet velocity 215 m/s; AR8 nozzle; nozzle impingement angle 20°; nozzle location 20% chord; flap angle 30°.

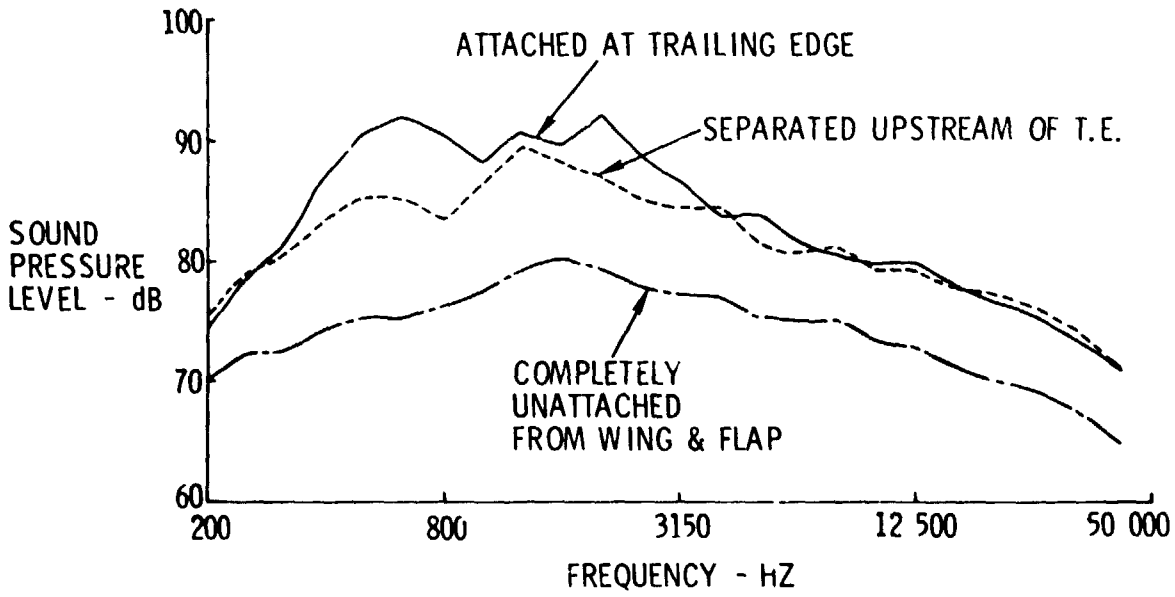

Figure 12.- Effect of flow attachment. Jet velocity 215 m/s; AR8 nozzle; nozzle location 20% chord.

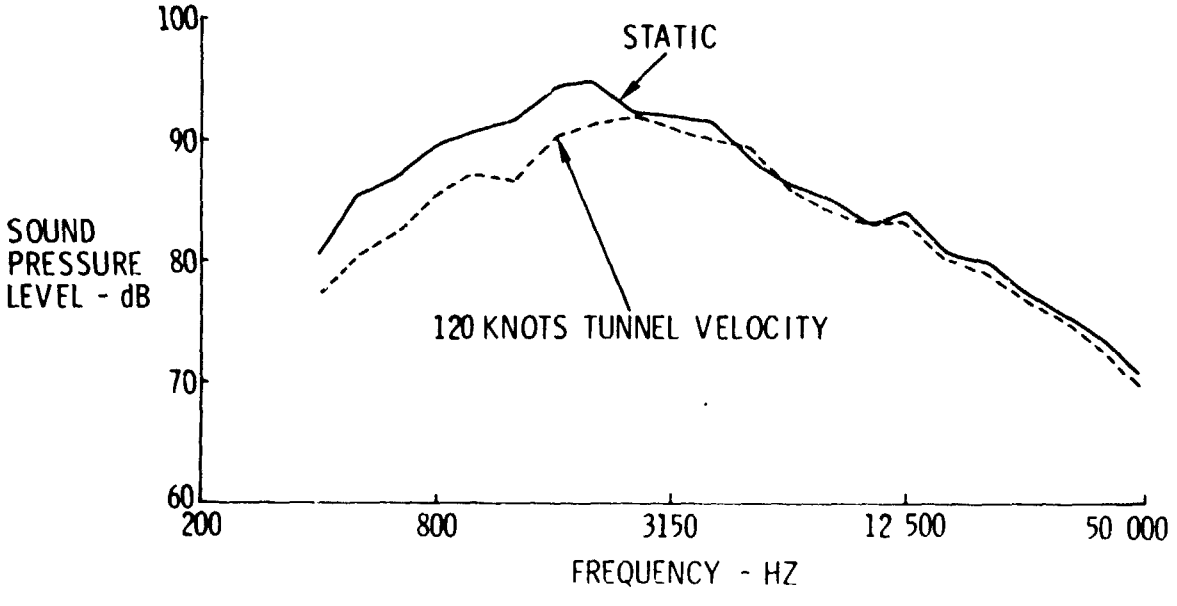

Figure 13.- Wind tunnel trends. Jet velocity 250 m/s; AR2 nozzle; nozzle location 20% chord; nozzle impingement angle 20°; flap angle 30°.

ANALYTICAL DEVELOPMENTS FOR DEFINITION AND PREDICTION OF USB NOISE*

N. N. Reddy and C. K. W. Tam**
Lockheed-Georgia Company

SUMMARY

A systematic acoustic data base and associated flow data were used in identifying the noise generating mechanisms of upper surface blown flap configurations of short takeoff and landing aircraft. Theory is developed for the radiated sound field of the highly sheared flow of the trailing edge wake. An empirical method is also developed using extensive experimental data and physical reasonings to predict the noise levels.

INTRODUCTION

It is clear from previous investigations (refs. 1-3) that most of the far-field sound field of upper surface blown flap configurations of STOL aircraft is from the interaction of turbulent jet flow with wing and flap surfaces. Analysis of the sound produced by interaction between turbulent flow and rigid surfaces, starting from the first principles, is very difficult if not impossible. Therefore, it is necessary to rely upon experimental data. Using the flow and noise data generated from a systematic experimental program at Lockheed under contract to NASA-Langley, the noise characteristics of USB are defined. The important source from a community standpoint is identified as the noise generated in the vicinity of the trailing edge. Therefore, theoretical analysis is performed for the sound field produced by the flow in the trailing edge wake, where the velocity gradient and turbulence intensity are large, using experimentally obtained flow characteristics. An empirical method is also developed using the noise data base and physical arguments which may be used to predict the noise levels — at least until the theory is developed further. addition, a brief discussion of the effect of aircraft motion and noise suppression is presented.

16

---

*Research performed under NASA Contract NAS1-13870.
**Professor, Department of Mathematics, Florida State University, Tallahassee, Florida.

PAGE INTENTIONALLY BLANK

NOISE MECHANISMS

The aerodynamic noise produced by the upper surface blown flap (USB) system may be summarized and idealized as the noise generated by the interference of a turbulent jet with finite rigid surfaces. Based upon the experimental and theoretical investigations, it is hypothesized that the propulsive lift related sound may be attributed to eight possible sources which differ in their geometric location and noise generation and propagation mechanisms. These sources are illustrated in figure 1.

Engine Internal Noise

Noise generated within the engine, which includes fan, compressor, and turbine noise, is known as internal noise. This propagates in the forward as well as in the aft directions. The forward-radiated noise is not peculiar to USB configurations, but most of the aft-radiated sound is shielded from the community by the wing and flap. This subject is really beyond the scope of this paper and thus will not be discussed in any detail.

Jet Mixing Noise

The jet flow prior to its impingement is defined as the USB jet mixing region. The noise generated in this region is called jet mixing noise. The fundamental flow mixing is modified by the presence of the rigid surface. Therefore, the noise generation process of flow mixing in this region may not be the same as free jet mixing without the presence of the wing. In the case of USB, however, this region of free jet mixing is close to the nozzle exit and above the wing. Therefore, most of this noise will be shielded from the community by the wing and flap as in the case of engine internal noise.

Jet Impingement Noise

When the jet is deflected onto the wing from an elevated position, as in the case of pylon-mounted engines, the jet exhaust flow impinges on the wing surface. This turbulent flow impinging on the surface generates additional noise generally known as "impingement noise." Even though the strength of this source could be significant (depending on the configuration), the radiated sound from this source below the wing for a typical aircraft configuration may be negligible because of its geometric location. In certain extreme cases, this noise may radiate toward the forward quadrant.

Wall Jet Boundary Layer Noise

The wall jet boundary layer on the wing and flap surface will have a high mean shear and can produce a high turbulence level, and noise is thus generated by the induced fluctuating pressures on the surface. The contribution of this

wall jet boundary layer noise to the community is very small because (1) the volume of turbulence of boundary layer is small compared to the volume of other noise-producing regions, and (2) the noise is generated above the wing and therefore shielded by the wing/flap.

Wall Jet Mixing Noise

The developed wall jet will be formed immediately after the impingement of the jet flow on the wing surface. The mixing of jet flow with the entrained air in this region results in fluctuating stresses similar to free jet mixing. The noise generated in this region is known as wall jet mixing noise. The introduction of curvature on the surface modifies the wall jet thickness and velocity decay rate and amplifies the turbulence levels in the flow. The contribution of sound from this source is primarily in the direction above the wing and possibly in the aft quadrant below the wing.

Trailing Edge Noise

Noise generated in the vicinity of the flap trailing edge is generally known as trailing edge noise. All the previous experiments and analyses indicate that the contribution of sound from this source, particularly in the direction below the wing, is dominating. However, there is no agreement among the various investigators about the noise-generating mechanism. For example, Hayden (ref. 4) has hypothesized that the turbulent flow leaving the surface at the trailing edge generates a strong dipole source with preferred axis perpendicular to the surface. Ffowcs Williams and Hall (ref. 5), on the other hand, analyzed the radiated sound field for quadrupole noise sources in the vicinity of the edge of a semi-infinite rigid surface. Both of these analyses gave essentially the same directivity and spectral distribution. However, closer examination of experimentally obtained, radiated sound field and flow-field data indicate that the trailing edge noise could be generated in the shear layer of the trailing edge wake. This will be discussed further under "Mathematical Model."

Wall Jet Roll-Up Noise

It is observed that the jet rolls up at the edges of the surface and grows as the axial distance from the nozzle increases. This roll-up phenomenon becomes stronger as the curvature increases and further amplifies as the aspect ratio of the nozzle decreases. The noise generated by this type of flow instability is known as wall jet roll-up noise. It appears that, for large aspect ratio nozzles or for the case where the jet flow spreads fairly well, the noise generated by roll-up is small. However, for small aspect ratio nozzles, this may not be negligible.

Flow Separation Noise

There are certain operational and geometrical configurations where the jet flow can separate before it reaches trailing edge. In fact, separation was observed in the wind tunnel experiments with forward speed for some cases where there is no separation during static tests. This phenomenon of separation obviously generates additional noise as discussed by Siddon (ref. 6). This separation noise could be significant in the aft quadrant, depending on the separation location.

In addition to the noise sources discussed so far, there may be acoustic feedback mechanisms which can result in large magnitudes of discrete frequency noise. Since it is observed that this type of noise is very sensitive to operational and geometric parameters, it is assumed that these conditions may be avoided with a careful design.

RADIATED SOUND FIELD

In order to identify the dominant noise source contributing in various directions, the spatial distribution of the one-third octave spectra is examined. Figure 2 illustrates the typical spectra in various directions in the flyover plane. It may be observed that, as the angle θ from the forward axis of the wing plane increases, the noise levels — particularly in the high-frequency range — increase. As we approach the direction above the flap surface (for $\theta > 150°$), the noise levels further increase and then start decreasing with the increase in θ. From these results and the results presented in the previous papers (refs. 7 and 8) and with the assumption that most of the noise generated upstream of trailing edge is shielded from radiating below by the wing and flap surfaces, it may be conjectured that the trailing edge noise is a dominant source from a community noise standpoint. In order to examine this hypothesis further, the sound pressure level spectra for different flap angles shown in figure 3 are studied. It may be observed that there are two peak sound levels at about 0.8 kHz and 2.0 kHz with a dip at 1.0 kHz. This type of spectral distribution is consistent with most of the tests, including tests at NASA (refs. 3 and 9). This observation led some investigators to conjecture that two sources, with low- and high-frequency dominance, contribute to the radiated sound in this direction. But closer examination of the experimental data indicates that the frequencies of these humps and dip are independent of flap angle, as shown in this figure, and they are also independent of jet velocity as shown in figure 4. It is suspected that the sound generated in the trailing edge wake and diffracted by the wing leading edge and rigid surfaces of the test rig, such as nozzle flange and the wing/flap end plates (as seen in one of the model descriptions of ref. 8), could cause the reinforcement and cancellation of radiated sound at certain frequencies. These possibilities are explored further experimentally by using sound absorbent material on several of these surfaces. The results are shown in figure 5. As can be seen, the humps and dip are eliminated in the frequency range of 500 to 2000 Hz by avoiding the surface diffraction. Therefore, it may be inferred that the spectral

distribution of radiated sound without diffraction is broad-band type at least in the low-frequency range up to 2000 Hz.

From these results, it is postulated that only the trailing edge is a dominant source contributing below the wing, and some of the other aeroacoustic sources discussed in the previous section — including the trailing edge noise — could contribute above the wing. Since the noise characteristics below the wing are more pertinent from community noise standpoint, further analysis is made on the trailing edge noise source.

MATHEMATICAL MODEL

A closer examination of the experimentally measured sound and flow field revealed that there was no clear-cut evidence to associate the trailing edge noise to either dipole model, as depicted by Hayden (ref. 4), or the diffracted quadrupole, as formulated by Ffowcs Williams and Hall (ref. 5). The typical flow characteristics just downstream of the trailing edge wake which are shown in figure 6 indicate that the velocity gradient and turbulence intensity are very large near the edge. In fact, it may be observed that the turbulence intensity is maximum where the velocity gradient is maximum. Experience tells us that the by-product of turbulence generation is noise generation or a noise source. Therefore, a mathematical model was developed for the turbulent mixing noise of the highly sheared trailing edge wake flow. In this model, the sheared flow downstream of the trailing edge is assumed to be locally two-dimensional and spatially homogeneous with respect to any plane parallel to the shear layer. These assumptions are justified experimentally, as discussed in reference 7. In addition, it is also assumed that the fluid within the shear layer is incompressible, which is reasonable for the flow velocity very much smaller than sonic velocity. With these assumptions and the equations of motion (Poisson's equation), the pressure fluctuations associated with turbulent mixing are found in terms of unsteady velocity components with the use of the Fourier transform. This result is then used to form the space-time near-field pressure cross-correlation function. Assuming only the shear components are important for radiated noise, these terms alone are retained.

This analysis illustrates that, for a practical upper surface blown flap configuration, the turbulent mixing in the vicinity of the trailing edge is a dominant noise source. The radiated noise is primarily a function of the flow parameters in the trailing edge wake. However, the typical streamwise space-time cross-correlation function of fluctuating velocities in the trailing edge wake, shown in figure 7, exhibit similar characteristics as in the shear layer close to the nozzle exit of the free jet. A function of the following form is derived as given by Maestrello (refs. 10 and 11):

$$R_w(\bar{x},\bar{y},z',z'',\tau) = G(z',z'')e^{\bar{x}/\lambda\delta} \sum_{i=1}^{n} \frac{\alpha_i A_i}{\alpha_i^2 + \left[\frac{\bar{U}}{U_c\delta}\right]^2 [(\bar{x} - U_c\tau)^2 + \beta^2\bar{y}^2]} \qquad (1)$$

where (see appendix for additional symbols)

$\bar{x} = \lvert x' - x'' \rvert$	streamwise (longitudinal) separation distance
$\bar{y} = \lvert y' - y'' \rvert$	spanwise separation distance
z', z''	lateral measurement locations
τ	delay time
λ	longitudinal decay rate of the cross-correlation function
δ	the shear layer thickness
U	maximum velocity in the trailing edge wake
U_c	eddy convection velocity
β	scale of anisotropy (ratio of longitudinal to the lateral length scales)
$G(z', z'')$	transverse correlation function of zero time delay
α_i and A_i	the empirical constants to describe the shape of the power spectrum of the fluctuating velocities

The far-field sound pressures were calculated by considering the fluctuating pressure components with supersonic phase velocity as given by Tam (ref. 12). The detailed discussion of the analysis of radiated sound from the trailing edge wake sheared layer of USB using experimentally obtained fluctuating velocity characteristics is presented in a paper to be presented in the AIAA aeroacoustics conference in July 1976 (ref. 13). The final expression for the radiated sound pressure per unit area of shear layer per unit solid angle in the direction ψ from the flow direction and per unit frequency at a frequency of ω, $D(\psi,\omega)$ is given as

$$\frac{D(\psi,\omega)}{\rho U^2 \delta} = \frac{\frac{U_c}{U}\left(\frac{\omega\delta}{U}\right)}{2\pi^2 \beta \lambda} M^3 \sin\psi \cdot \frac{\sum_{i=1}^{3} \left\{ \frac{A_i \alpha_i \nu_o \left(\alpha_i \frac{\omega\delta}{U}\right)}{\frac{1}{\lambda^2} + \left(\frac{\omega\delta}{U}\right)^2 \left(M\cos\psi - \frac{U}{U_c}\right)^2} \right\}}{\sum_{i=1}^{3} \frac{A_i}{\alpha_i}}$$

$$\cdot \left\{ \frac{1}{\bar{U}^4} \int_{-\delta}^{0}\int \frac{d\bar{U}}{dz'} \frac{d\bar{U}}{dz''} \cdot G(z',z'')\, dz'dz'' \right\} \qquad (2)$$

where

M is the flow Mach number based on ambient speed of sound

$K_0(x)$ is the zeroth order modified Bessel function

$d\bar{U}/dz'$ is the velocity gradient in the sheared layer.

The flow characteristics were measured using two single hot wires for a configuration shown in figure 8 in the mid-span just downstream of the trailing edge. A rectangular nozzle with aspect ratio of 8 and exit area of 20.26 square centimeters was used. The wing and flap consisted of 60° flap angle with 7.62 cm radius of curvature. The flow length, defined as the length between the nozzle exit to the trailing edge of the flap, was 21.8 cm. The following values were obtained from the hot-wire correlation and velocity and turbulence intensity measurements for maximum velocity, convection velocity, and length scales:

$$U = 74.4 \text{ m/s}$$

$$U_c = 67 \text{ m/s}; \qquad U_c/U = 0.9$$

$$L_x = 0.85 \text{ cm}$$

$$L_y = 0.35 \text{ cm} \qquad L_x/L_y = 2.4$$

$$\delta = 0.8 \text{ cm}$$

Shear layer thickness δ is defined as the height from 10% to 90% of maximum velocity.

A_i's and α_i's are determined using the measured auto correlation function shown in figure 9 as

$$A_1 = 0.7, \qquad A_2 = 6.3, \qquad A_3 = 3.0$$

$$\alpha_1 = 0.32, \qquad \alpha_2 = 1.4, \qquad \alpha_3 = 20.0$$

One-third octave band sound pressure levels are calculated using these values of flow properties in equation (2) in various directions at center frequencies of 400, 1600, and 6300 Hz. These results are compared with the measured radiated sound in figure 10. Comparison is also made in figure 11 between measured and calculated one-third octave band sound pressure level spectra in the direction of 10° to the flow. It may be observed from these two figures that there is a favorable agreement, particularly in the high-frequency region. The theoretical calculations may be improved if the turbulence properties are measured more precisely by considering the components of each direction. This may be accomplished with more sophisticated hot-wire system or laser velocimeter developed recently at Lockheed.

This analysis illustrates that, for a practical upper surface blown flap, the turbulent mixing in the vicinity of trailing edge is a dominant noise source. The radiated noise is primarily a function of the flow parameters in

the trailing edge wake. However, in order to estimate the effect of geometric and operational parameters on noise characteristics, it is necessary to establish the relationship between the trailing edge flow characteristics and the various parameters. But, to do so would require extensive experimental measurements which are not available at the present time. Therefore, using the systematic far-field sound measurements for various configurations and with the physical reasonings, an empirical method of USB noise-prediction method has been developed.

EMPIRICAL METHOD OF NOISE PREDICTION

In developing a noise-prediction program, an attempt is made to generalize the observations made in the extensive flow and acoustic data base and to incorporate them in the empirical model. Since the primary interest is in the direction below the wing, it is assumed that the dominant noise is from the trailing edge source. Therefore, the noise levels should be correlated with the gross parameters in the trailing edge wake such as velocity, turbulence, and jet thickness at the trailing edge. However, at the present state of the art, it is not possible to relate these trailing edge parameters to operational and geometric parameters. Thus, the empirical relations are derived using the readily available engine and wing/flap parameters. General variation of noise characteristics as a function of geometric and operational parameters is discussed briefly.

Nozzle Area and Shape

The radiated sound intensity is found to be directly proportional to the nozzle area. Generally, the noise levels increase as the aspect ratio decreases. For noise prediction, spectral shape is assumed independent of shape.

Nozzle Exit Velocity

The sound intensity is found to increase as the jet velocity increases; the velocity exponent varies from 5.0 to 7.5 depending on the direction as shown in figure 12. The frequency is directly proportional to the jet velocity.

Radius of Curvature

The magnitude and spectral characteristics are independent of radius of curvature, which means the sound intensity and spectral distribution do not depend on the sharpness of the flow turn provided that the flow was completely turned and attached to the complete longitudinal length of the flap surface without flow separation.

Flow Length

Flow length appears to be an important parameter. As the flow length increases, both the sound intensity and the frequency of the spectrum decrease. This is due to the reduction in velocity and perhaps due to increase in the jet thickness at the trailing edge.

Flap Angle

For a constant angle with respect to the flap (flow direction in the trailing edge wake), the sound intensity is independent of the flap angle. However, the peak frequency of the spectrum is reduced as the flap angle is increased. Again, this may be due to increase in the jet thickness as the flap angle increases.

An illustration of nondimensional spectral distribution derived from the data to develop the prediction procedure is given in figure 13. Here, it is assumed that the sound pressure varies as jet velocity raised to the power 7, and the nondimensional frequency is a function of flow length, jet velocity, and flap angle. It may be observed in this figure that the data collapse very well using these variables for different jet velocities, flow length, and flap angles.

The development of this empirical method for USB noise prediction is still in progress. However, the preliminary formulation using the data from small-scale model static tests with the jet flow at ambient temperature is given below.

$$S_N = \frac{f_c L_F}{V_J} \left[1 + \delta_f\right]^{1/3}$$

$$SPL(S_N) = 10 \log \left(\frac{V_J}{V_o}\right)^{n,(\theta'',\phi)} + 10 \log \frac{A_N}{A_o} - 20 \log \frac{R}{R_o}$$

$$- 10 \log \left[(AR_N)^{1/3} \frac{L_F}{D_H}\right] + K_1(\theta'') + k_2(\phi) \qquad (3)$$

where

S_N nondimensional frequency (Strouhal number)

f_c center frequency of one-third octave band

δ_f flap angle (radians)

$n(\theta'',\phi)$ velocity exponent as a function of direction, θ'' and ϕ (for definition of θ'' and ϕ see figure 12)

V_J	jet velocity (m/s)
V_o	reference velocity = 180 m/s
A_N	nozzle exit area (m^2)
A_o	reference nozzle area = 1 m^2
R	distance from nozzle to measurement location (m)
R_o	reference distance = 1 m
AR_N	aspect ratio of nozzle (width-to-height ratio)
D_H	hydraulic diameter of the nozzle exit (m)

The noise levels are calculated using equation (3) for small scale model and large scale model static cases. These results are compared with the measured data in figures 14 and 15. The agreement is very reasonable.

Until more data are available and analyzed, the effect of aircraft motion may be incorporated in the same way as given in reference 13. The preliminary indications of the recent data from Lockheed's Acoustic Free-Jet facility are that the spectral characteristics of sound change as the free-stream flow is introduced. The high-frequency noise does not reduce in the aft quadrant. The examination of the flow characteristics revealed that the jet flow separated from the surface just ahead of the trailing edge with the forward speed. Therefore, it is necessary to consider this aspect of the problem in analyzing and interpreting the data on the forward speed effect.

CONCLUDING REMARKS

An empirical noise prediction method has been developed using the extensive acoustic experimental data for USB configuration. The method is simple to use and correlates reasonably well with the available static test data. The effect of forward speed and the ground reflections for the case of aircraft in flight may be easily incorporated in the program.

It is conjectured from the experimental data that the noise generated in the vicinity of the trailing edge is a dominant source contributing to the radiated sound field in the direction below the wing. A mathematical model has been developed to predict the directivity and spectral distribution of the noise generated in the sheared layer of the trailing edge wake. These results are in good agreement with the experimentally measured data, which indicate the dominant noise is generated by the flow mixing where the velocity gradient is very large.

The results presented here indicate that one of the ways of reducing USB noise is to modify the shear layer and thus modify the turbulence generation in

the trailing edge wake. Accomplishment of this noise reduction requires more experimental and theoretical study.

More exploratory study is necessary to evaluate the flow characteristics in the trailing edge in order to correlate the relationship between the trailing edge flow and the geometric and operational parameters. This would yield a better analytical approach to predict the noise levels and also reveal the ways of controlling USB noise.

APPENDIX

SYMBOLS

Additional symbols used in the text and in figures are defined in this appendix.

AR	aspect ratio
C	chord
h	nozzle height
L_F	flow length
L_x	longitudinal length scale of eddy
L_y	spanwise length scale of eddy
R_c	flap radius of curvature
R_w	correlation function
$\bar{U}$	mean velocity
U_J	jet exit velocity
X	nozzle location
$\bar{x}$	separation distance
x'	streamwise location of first hot wire
x''	streamwise location of second hot wire
y'	spanwise location of first hot wire
y''	spanwise location of second hot wire
z'	lateral position of first hot wire
z''	lateral position of second hot wire
Θ	angle from forward axis of the jet in the flyover plane
Θ'	angle of the wing surface in the flyover plane
Θ''	angle from trailing edge surface in the flyover plane (see fig. 12)

Θ_N	nozzle impingement angle
ρ	density of the flow
ϕ	azimuthal angle (angle from the wing plane)

REFERENCES

1. Reddy, N. N.; and Brown, W. H.: Acoustic Characteristics of an Upper-Surface Blowing Concept of Power-Lift System. AIAA Paper 75-204, Jan. 1975.

2. Reddy, N. N.: Propulsive-Lift Noise of an Upper Surface Blown Flap Configuration. AIAA Paper 75-470, March 1975.

3. Von Glahn, U.; and Groesbeck, D.: Acoustics of Attached and Partially Attached Flow for Simplified OTW Configurations with 5:1 Slot Nozzle. NASA TMX-71807, Nov. 1975.

4. Hayden, R. E.: Sound Generation by Turbulent Wall Jet Flow Over a Trailing Edge. M.S. Thesis, Purdue University, 1969.

5. Ffowcs Williams, J. E.; and Hall, L. H.: Aerodynamic Sound Generated by Turbulent Flow in the Vicinity of Scattering Half Plane. *J. Fluid Mech.*, vol. 40, pt. 4, 1970, pp. 657-670.

6. Siddon, T. E.: Surface Dipole Strength by Cross-Correlation Method. *J. Acous. Soc. Am.*, vol. 53, no. 2, 1973.

7. Brown, W. H.; and Reddy, N. N.: USB Flow Characteristics Related to Noise Generation. Powered-Lift Aerodynamics and Acoustics, NASA SP-406, 1976. (Paper no. 14 of this compilation.)

8. Gibson, J. S; and Searle, N.: Characteristics of USB Noise. Powered-Lift Aerodynamics and Acoustics, NASA SP-406, 1976. (Paper no. 15 of this compilation.)

9. Olsen, W. A.; Dorsch, R. G.; Miles, J. H.: Noise Produced by a Small-Scale, Externally Blown Flap. NASA TN D-6636, March 1972.

10. Maestrello, L.: Measurement and Analysis of the Response Field of Turbulent Boundary Layer Excited Panels. *J. Sound Vib.*, vol. 2, no. 3, 1965.

11. Maestrello, L.: Use of Turbulent Model to Calculate the Vibration and Radiation Responses of a Panel With Practical Suggestions for Reducing Sound Level. *J. Sound Vib.*, vol. 5, no. 3, 1967.

12. Tam, C. K. W.: Intensity, Spectrum, and Directivity of Turbulent Boundary Layer Noise. *J. Acous. Soc. Am.*, vol. 57, 1975, pp. 25-34.

13. Tam, C. K. W.; and Reddy, N. N.: Sound Generated in the Vicinity of Trailing Edge of an Upper Surface Blown Flap. AIAA Paper No. 76-503, July 1976.

14. Dorsch, R. B.; Clark, B. J.; and Reshotko, M.: Interim Prediction Method for Externally Blown Flap Noise. NASA TM X-71768, 1975.

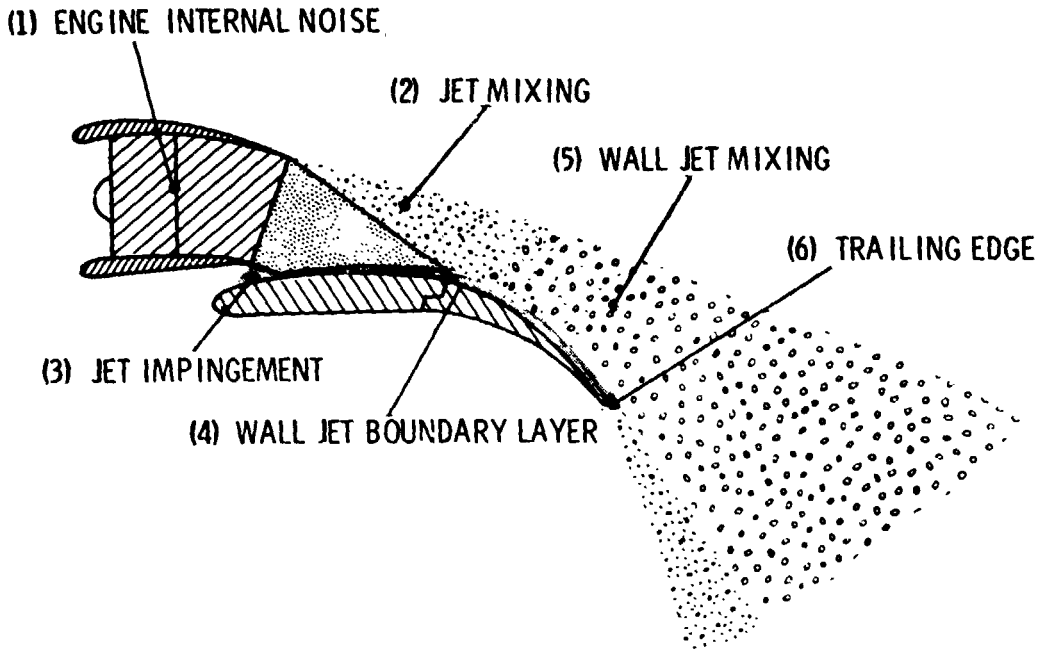

Figure 1.- USB noise source mechanisms.

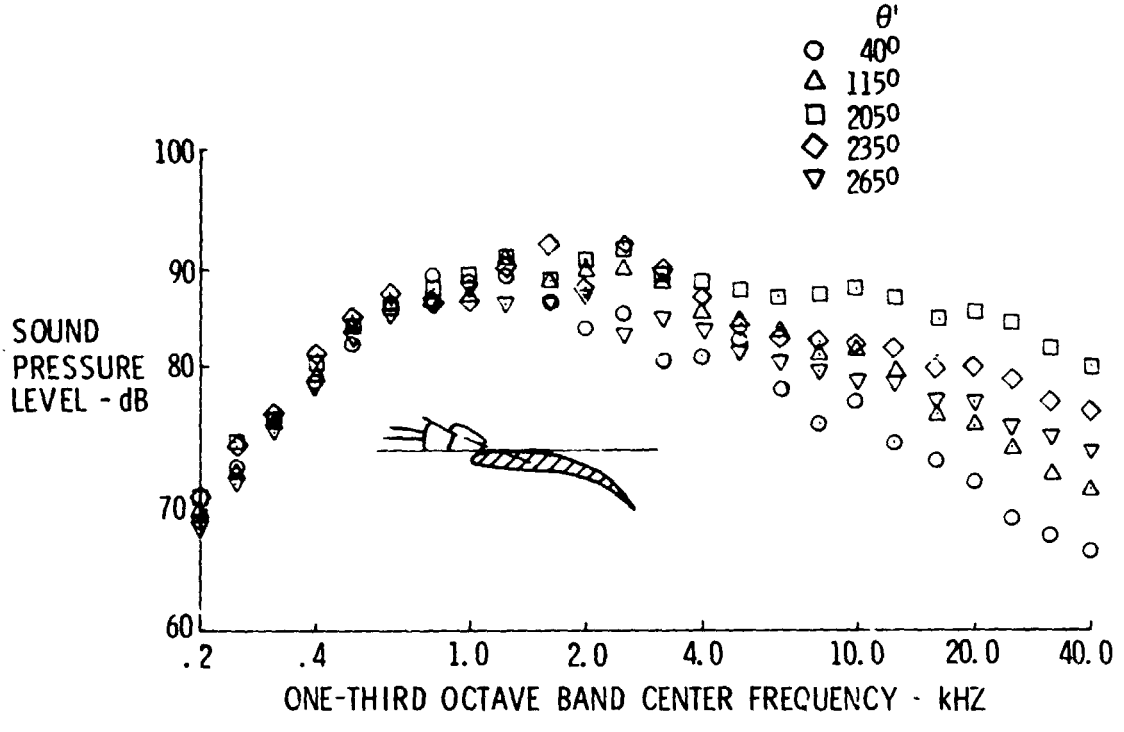

Figure 2.- Typical spectral distribution as a function of various angles in the flyover plane.

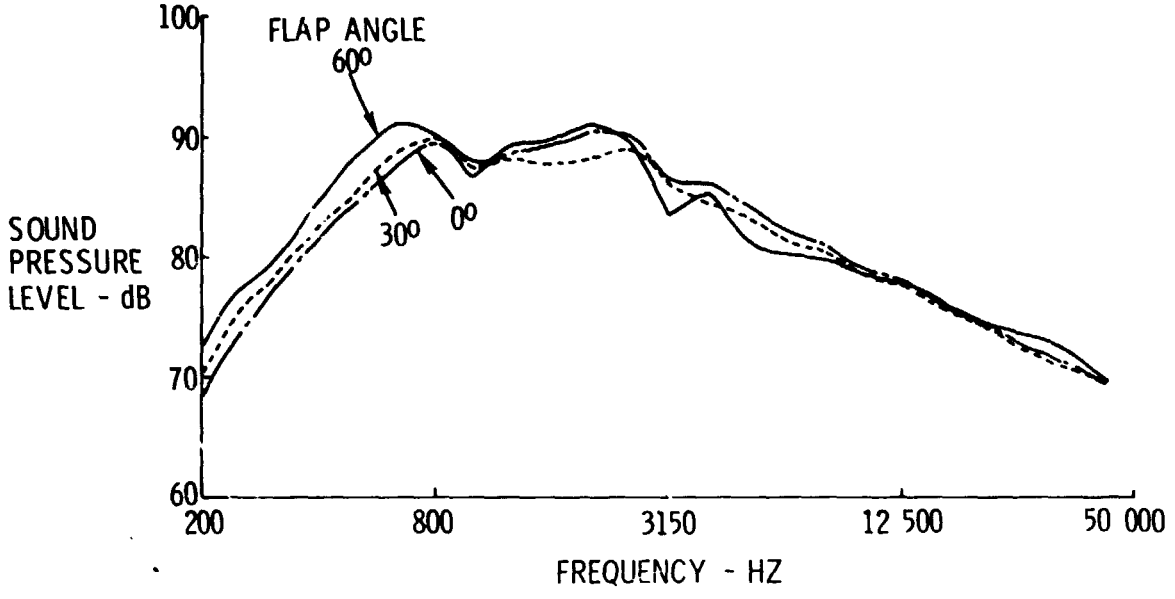

Figure 3.- Effect of flap angle on sound spectrum in flyover plane. $\Theta = 90^{\circ}$; $R_c = 7.62$ cm; $L_F = 22.66$ cm; $V_J = 215$ m/s; AR of nozzle = 4; X = 20% C; $\Theta_N = 20^{\circ}$.

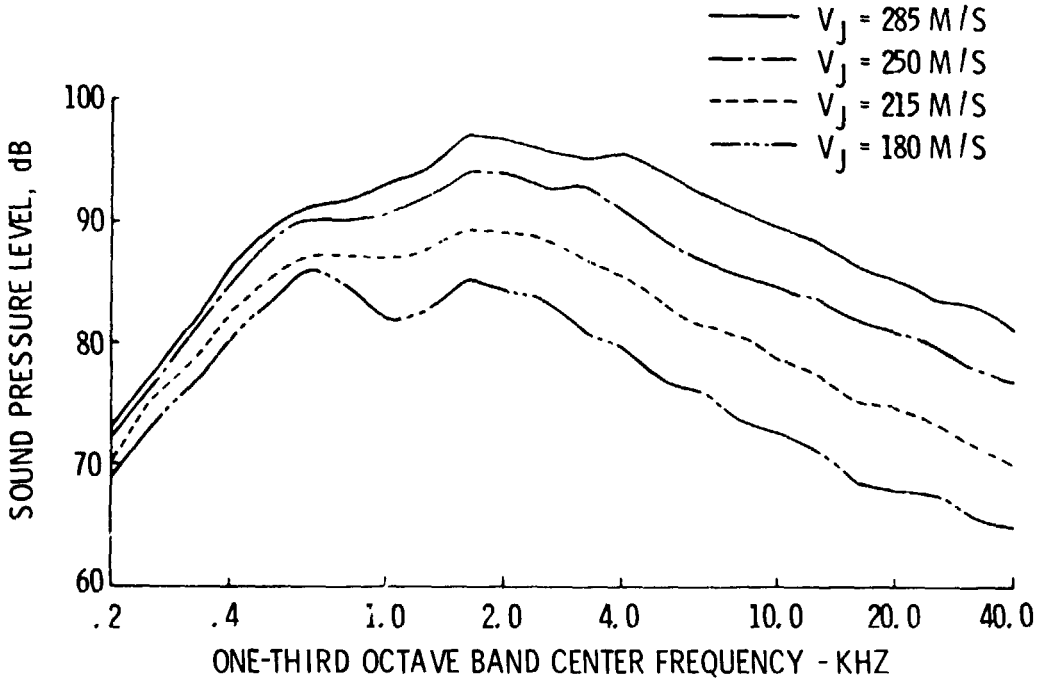

Figure 4.- Effect of jet velocity on spectral distribution in flyover plane. $\Theta = 90^{\circ}$; $R_c = 7.62$ cm; $L_F = 22.66$ cm; AR of nozzle = 4; X = 20% C; $\Theta_N = 20^{\circ}$.

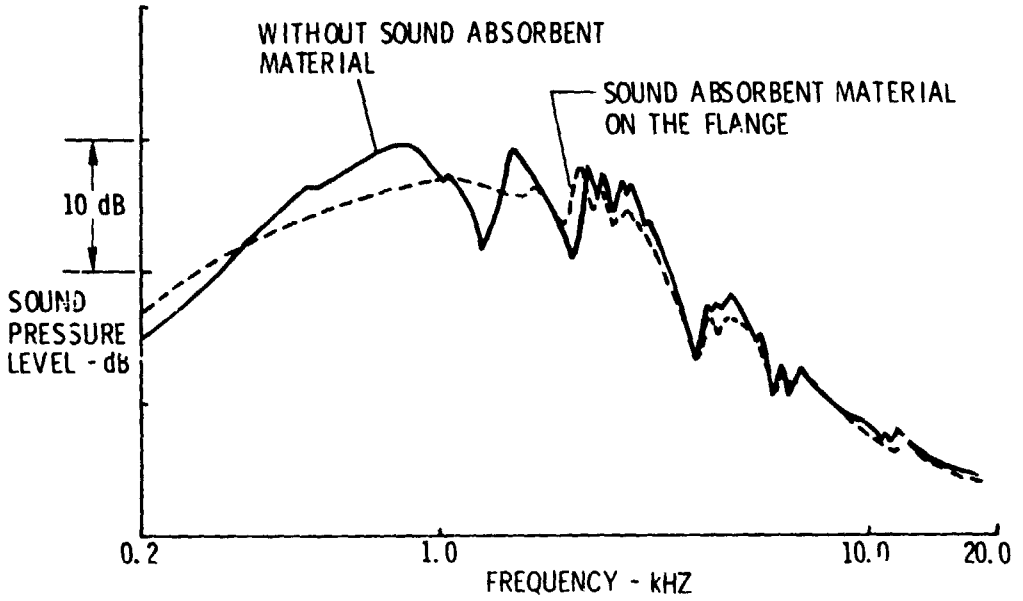

Figure 5.- Effect of nozzle surface diffraction on radiated sound in narrow-band analysis. $\Theta = 90^{o}$; $R_c = 7.62$ cm; $L_F = 22.66$ cm; AR of nozzle = 4; X = 20% C; $\Theta_N = 20^{o}$; $V_J = 215$ m/s.

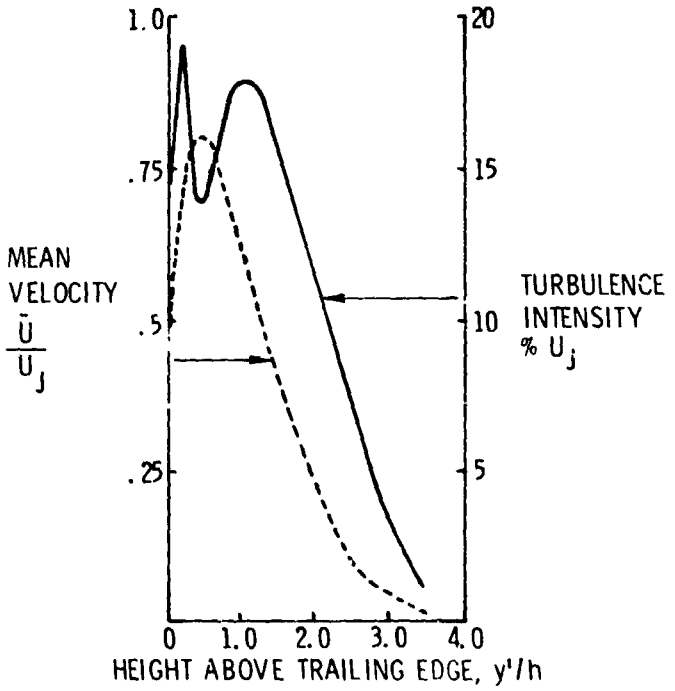

Figure 6.- Typical velocity and turbulence intensity profiles just downstream of trailing edge.

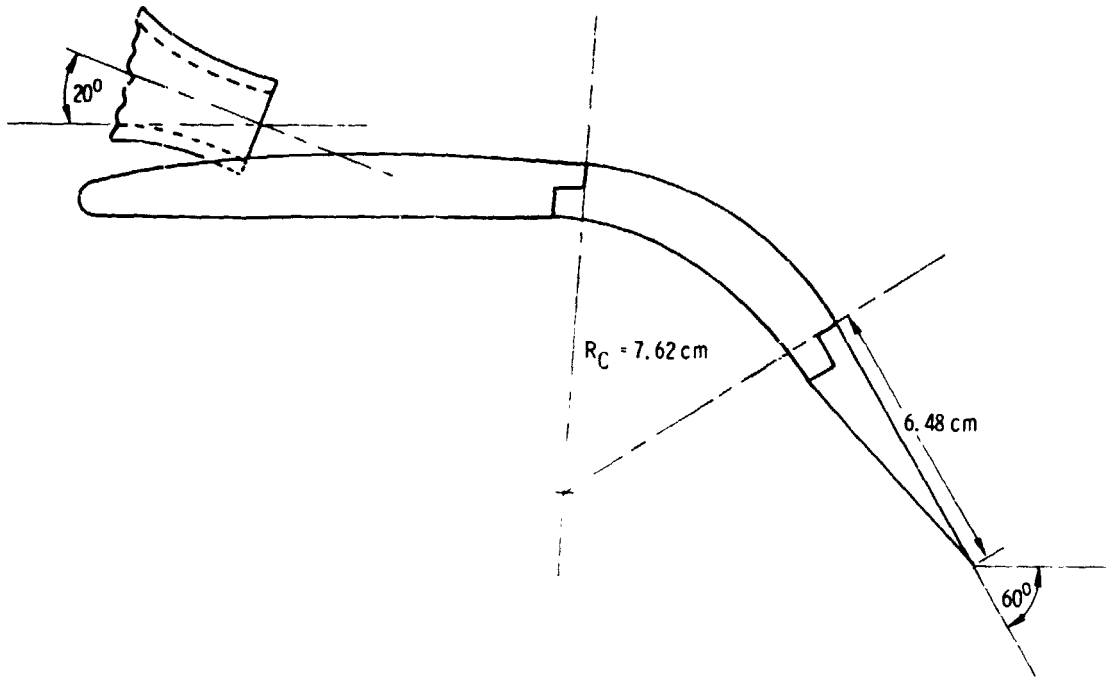

Figure 7.- Typical streamwise space-time cross correlations in the trailing edge wake.

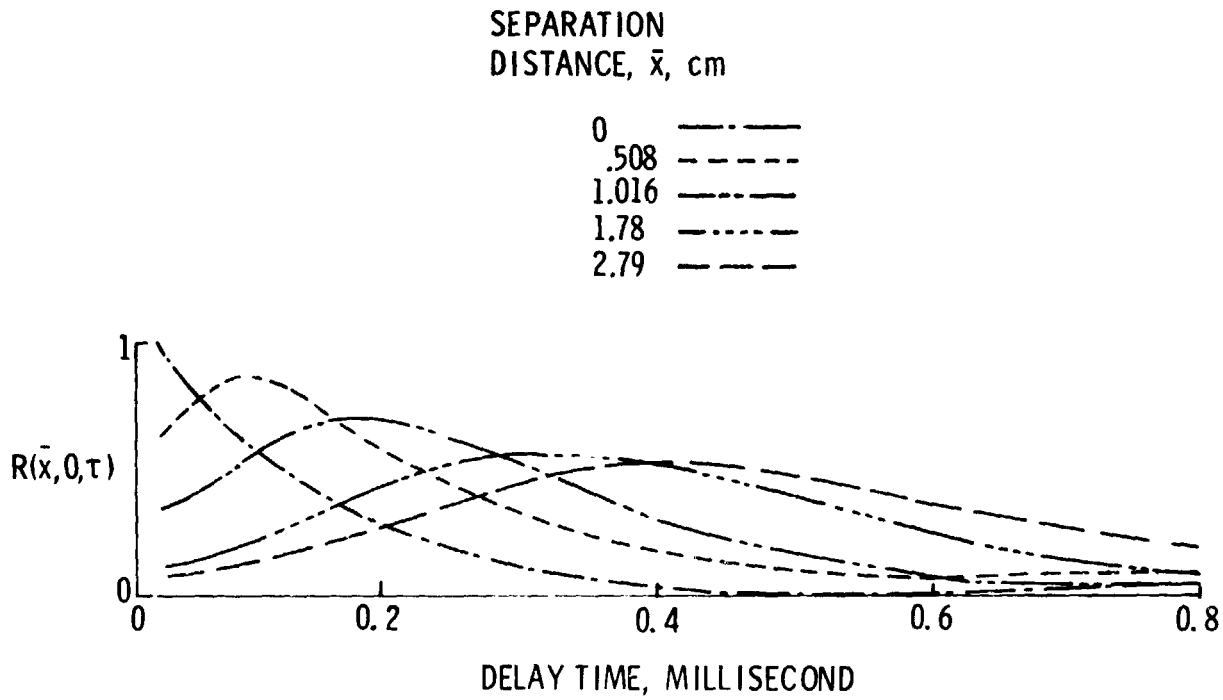

Figure 8.- USB configuration used for flow measurements.

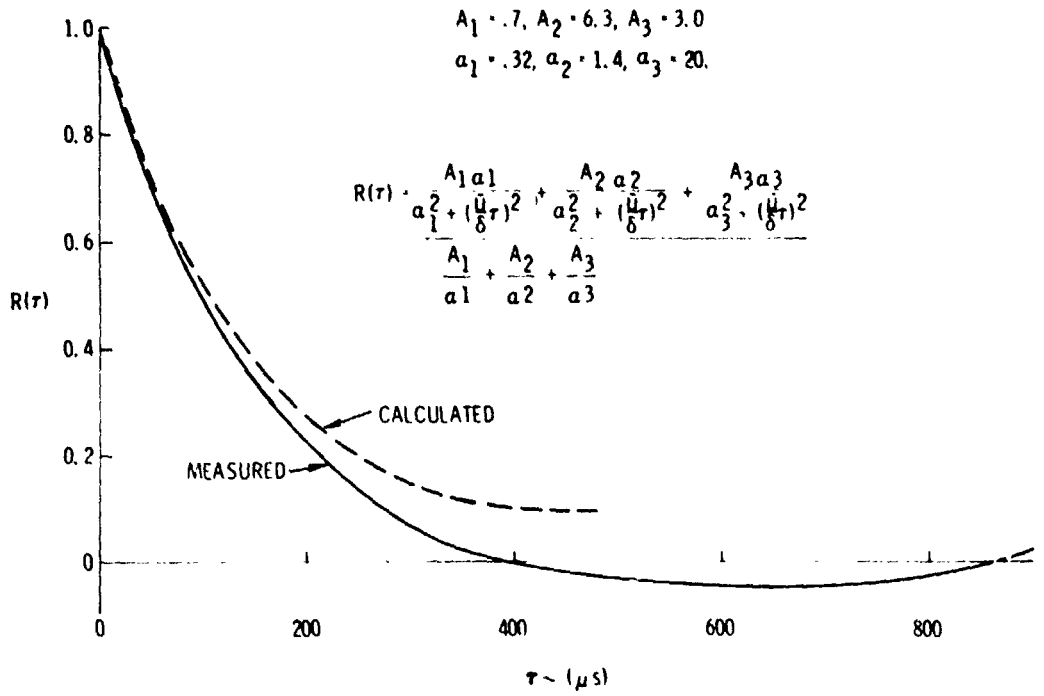

Figure 9.- Autocorrelation function of turbulence just downstream of trailing edge.

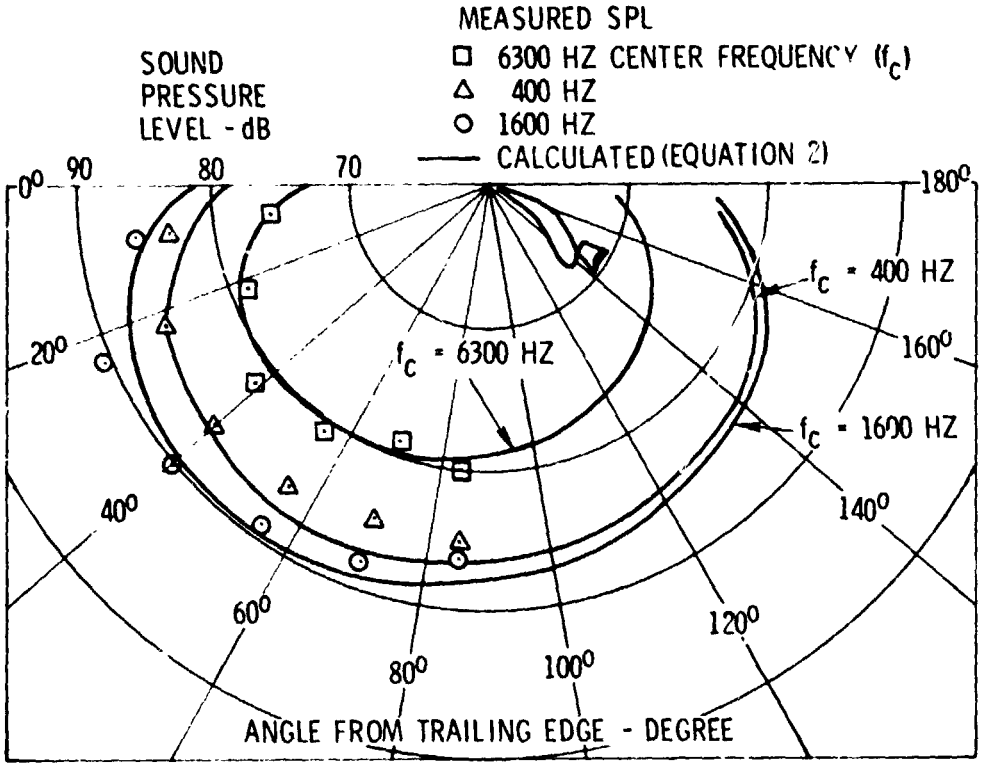

Figure 10.- Comparison between calculated and measured sound.

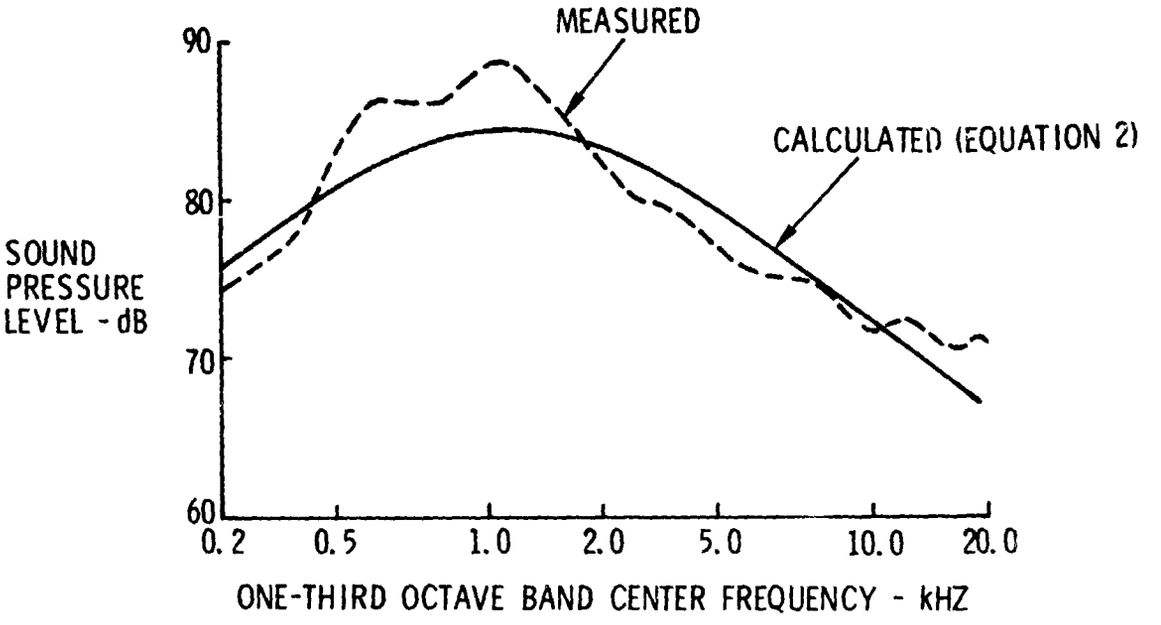

Figure 11.- Comparison between calculated and measured spectra.

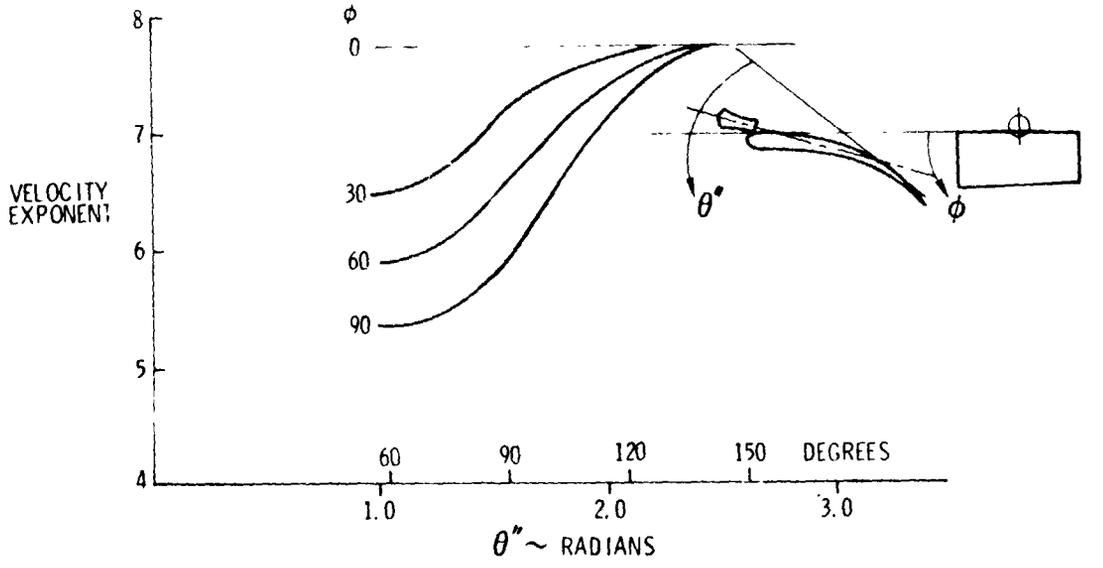

Figure 12.- Velocity exponent for USB noise.

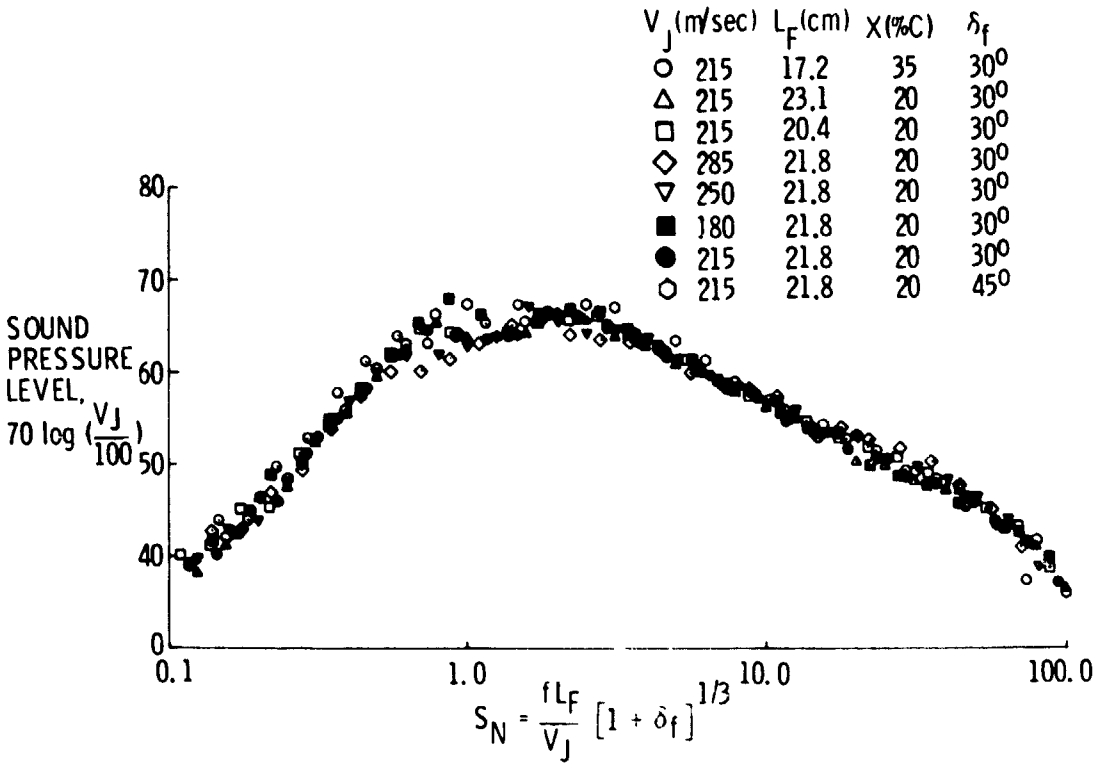

Figure 13.- Normalized spectra for USB noise. $\Theta'' = 115^\circ$.

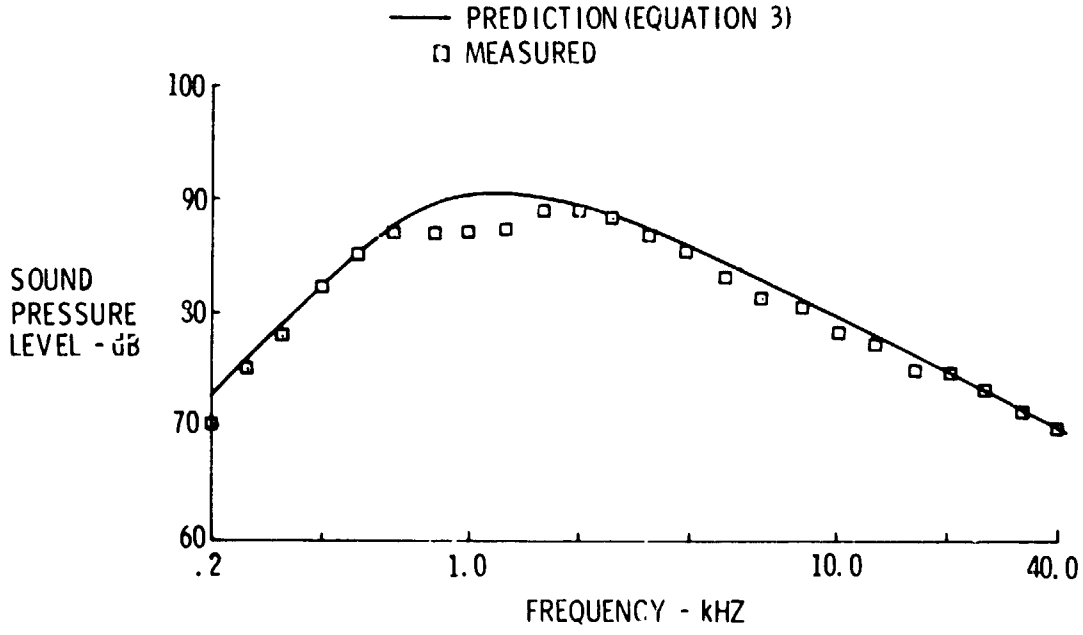

Figure 14.- Comparison of empirical prediction with experimental data in flyover plane. $A_N = 20.25$ cm^2; AR of nozzle = 4; $\delta_f = 30^\circ$; $\Theta = 85^\circ$.

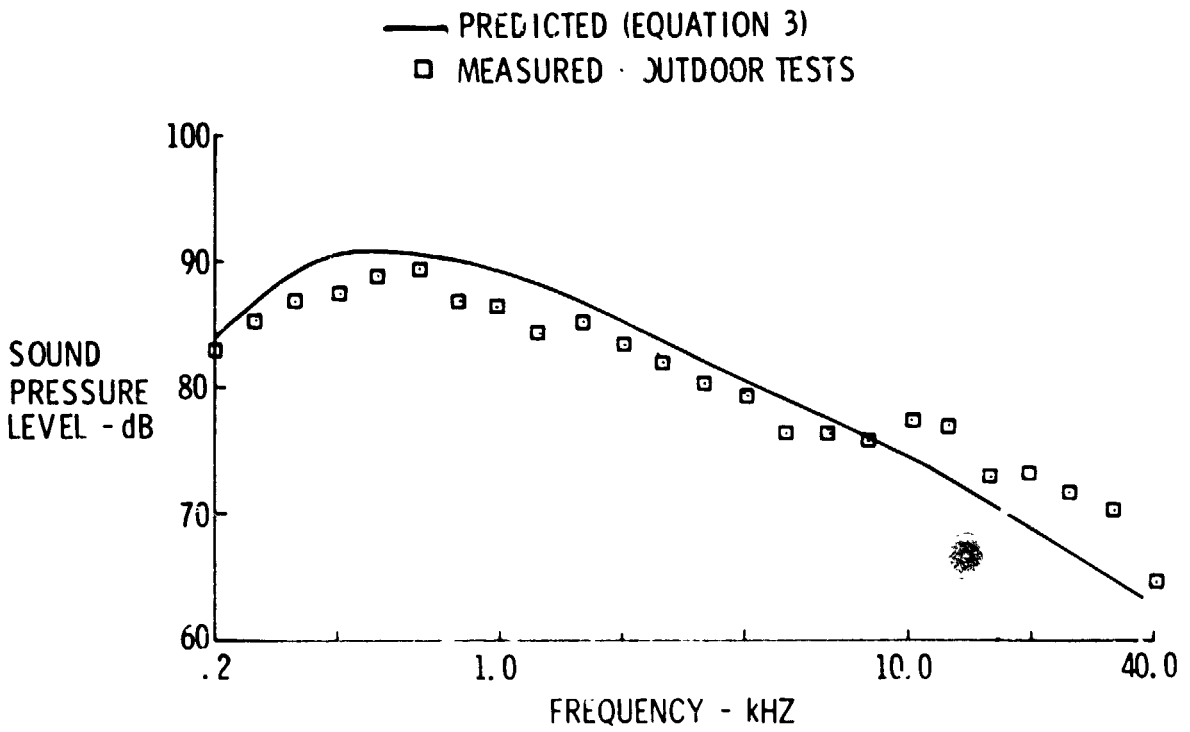

Figure 15.- Comparison of empirical prediction with experimental data in flyover plane. A_N = 113.8 cm^2; AR of nozzle = 4; $\delta_f = 30^\circ$; $\Theta = 130^\circ$.

N78-24063

ANALYTICAL MODELING OF UNDER-THE-WING EXTERNALLY BLOWN FLAP POWERED-LIFT NOISE

Daniel J. McKinzie, Jr.
NASA Lewis Research Center

SUMMARY

The sound field produced by the interaction of a subsonic jet with a large-scale model of the under-the-wing externally blown flap in an approach attitude was analyzed. The analysis was performed to obtain a better understanding of the dominant noise sources and the mechanisms governing the peak sound-pressure-level frequencies of the broadband spectra. An analytical expression is derived which incorporates two available theories and experimental data; the expression predicts the sound field along a circular arc of approximately 120° measured from the upstream jet axis in the flyover plane. The analysis compares favorably with test results obtained from two large-scale models, one using cold air from a conical nozzle and the other using hot gas from a TF-34 turbofan engine having a conical exhaust nozzle with a 12-lobe internal forced mixer. The frequency at which the peak sound pressure level occurs appears to be governed by a phenomenon which produces periodic formation and shedding of large-scale turbulence structures from the nozzle lip.

17

INTRODUCTION

The engine exhaust of the under-the-wing (UTW) externally blown flap (EBF) short takeoff and landing (STOL) aircraft is deflected downward by the wing flaps during takeoff and approach. Noise levels from 10 to 18 decibels greater than the jet noise are generated by the impingement of the jet on the flap surfaces (refs. 1 and 2).

NASA has conducted experimental research and development work to measure and define the flap interaction noise field for a variety of UTW configurations, as discussed in reference 3. After a review of the noise characteristics produced by each configuration, reference 3 notes that the overall sound pressure level was dependent on the sixth power of the peak impingement velocity and on the first power of the impingement area for each of these configurations. Thus, the dominant noise sources were not significantly altered or eliminated by the differences in the configurations. These results established a need for greater understanding of the dominant noise source mechanisms

in order to help develop noise suppression techniques that might be used to reduce the noise sources and thus meet noise goals.

In references 4 and 5 presentations are made of correlation and scaling-law techniques used to predict jet flap interaction noise for UTW EBF configurations. Although these techniques are presented as functions of geometric and gas dynamic variables, they do not adequately explain how or by what mechanisms the sound is produced. In reference 6 however, a mechanistic approach is taken in analyzing the noise generated by the interaction of a jet exhaust impinging on flat and curved plates. This approach is extended in reference 7 to large-scale test results of a UTW EBF configuration in which active and passive noise suppression techniques were studied.

The primary objective of this paper is to present, in summary form, the results of the UTW EBF analysis reported in reference 7 and to compare calculated estimates of the overall sound pressure level with two sets of test results. One set of data was obtained from a large-scale two-flap, non-swept-wing, cold-flow model of a UTW EBF configuration in an approach attitude (fig. 1). The second set of data was obtained from a full-scale, three-flap, swept-wing version of a UTW EBF configuration in an approach attitude using a TF-34 turbofan engine (ref. 8).

Although the prediction of the sound directivity for the UTW EBF takeoff configuration is not considered in this paper, the models of the noise sources presented are believed qualitatively applicable to the takeoff configuration.

SYMBOLS

A	actual correlation area, m^2
A_c	ideal correlation area, m^2
$(C_L)_\nu$	steady-state effective lift coefficient slope, deg^{-1}
c	speed of sound, m/sec
D	nozzle exit diameter, m
F'_L	fluctuating lift force, N (fig. 4)
f	frequency, Hz
f_r	characteristic frequency of fluctuating lift forces, Hz
M_j	jet exit Mach number
M_l	local Mach number evaluated on jet axis

N	magnitude of velocity exponent
OASPL	overall sound pressure level, dB re 20 $\mu N/m^2$
P_{ref}	reference sound pressure, 20 $\mu N/m^2$
r	distance between observer and trailing edge, m (fig. 3)
SPL	sound pressure level, dB re 20 $\mu N/m^2$
U	mean flow velocity, m/sec
U_l	local mean flow velocity evaluated on jet axis, m/sec
U_m	maximum mean velocity of free shear layer at trailing edge of flap, m/sec (fig. 3)
v'/U_l	turbulence intensity in direction normal to airfoil chord and leading edge
W	one-half of spanwise width of velocity profile between points where local velocity is equal to $U_m/2$ at trailing edge of flap, m (fig. 3)
x, y, z	Cartesian coordinates (fig. 3)
α	normalized turbulence intensity (ref. 11)
β	angle between fluctuating force vector and observer, deg (fig. 4)
δ	thickness of boundary layer, m (fig. 3)
θ	radiation angle measured from nozzle inlet axis, deg (fig. 5)
ρ	density of undisturbed fluid, kg/m^3
ρ_l	density of fluid evaluated at point where U_l is determined, kg/m^3
φ	angle, deg (fig. 3)
ψ	angle, deg (fig. 3)

Subscripts:

impact	impact
impinge	impingement
inflow	inflow
j	jet exit condition
l	local
TE	trailing edge

ANALYSIS OF JET-FLAP-INTERACTION NOISE

In figure 2 the jet impingement on an EBF two-flap wing in an approach attitude is depicted by the dashed lines. The major noise sources, shown in figure 2, are assumed to be the result of oblique jet impingement, surface scrubbing, jet interaction with the leading and trailing edges, free shear layer mixing over the surface of the deflected flaps, and inflow about the most downstream (second) flap.

In reference 6, the noise resulting from oblique jet impingement, surface scrubbing, and free shear-layer mixing is termed impact noise. Impact noise $OASPL_{impact}$ is defined as all the noise produced on a flat surface that is sufficiently large to exclude leading- and trailing-edge noise. The noise produced by inflow about the wing or flaps is referred to in this paper as inflow noise. Leading-edge noise is not considered because it is estimated to be less than trailing-edge noise, as reported in reference 9. Thus, it is assumed that trailing-edge noise, impact noise, and inflow noise are dominant. By assuming that these sound sources are uncorrelated (as proposed in refs. 6, 7, and 10), one may approximate their combined sound field by superposition. Therefore, the total jet-flap impingement OASPL is expressed as the logarithmic sum of the impact, trailing-edge, and inflow contributions:

$$OASPL_{impinge} = 10 \log\left[10 \exp\left(\frac{OASPL_{impact}}{10}\right) + 10 \exp\left(\frac{OASPL_{TE}}{10}\right) + 10 \exp\left(\frac{OASPL_{inflow}}{10}\right)\right] \quad (1)$$

This summation is referred to in this paper as impingement noise. The following sections present analytical expressions (in SI units) used to estimate trailing-edge, inflow, and impact noise.

Trailing-Edge Noise

Trailing-edge noise may be estimated from the theoretical approach of reference 11 in the form presented in reference 6, where the details of the derivation are presented. This noise source has a velocity dependence of U^5. Figure 3 is a sketch, used in the derivation of reference 6, which shows the coordinate system. The overall sound pressure level of trailing-edge noise $OASPL_{TE}$ for zero sweep angle is given (ref. 6) as follows:

$$OASPL_{TE} = 10 \log \frac{W\delta U_m^5}{r^2} + 10 \log \cos^2 \frac{\psi}{2} + 10 \log \frac{1.15\times10^8 \, \alpha^2 \rho^2}{c} \qquad (2)$$

The angle ψ was determined graphically in reference 6 as a function of the acoustic radiation angle θ.

Inflow Noise

A derivation of the noise produced from inflow effects is given in reference 7. The derivation is based on reference 12, in which the large-scale turbulence structures of the jet flow field (ring vortices) are assumed responsible for what is referred to as inflow noise. Figure 4 is a sketch of the coordinate system used in the derivation of reference 7. The overall sound pressure of inflow noise $OASPL_{inflow}$ is given in reference 7 as follows:

$$OASPL_{inflow} = 10 \log \left[\frac{(C_L)_\alpha \rho_l U_l^2}{r} \sqrt{\frac{}{}} \right]^2 + 10 \log \left(A_c \frac{A}{A_c} \right)$$

$$+ 10 \log \left[\frac{A}{A_c} \left(\frac{\pi}{\frac{7.559}{M_l^2} + 1} \right) \right] + 10 \log \left[\frac{\left(\frac{v'}{U_l} \right)}{8\pi P_{ref}} \right]^2$$

$$+ 10 \log \cos^2 \beta + 10 \log (0.23 f_r) \qquad (3)$$

The angle β was determined graphically in reference 7 as a function of the acoustic radiation angle θ.

Impact Noise

Although the specific mechanism which produces impact noise is not known, it is assumed as in reference 6 that impact noise is produced, in part, by the large-scale turbulence structures of the jet flow field impacting the flaps. In reference 13 the noise field produced when a 5.2-centimeter-diameter jet impacts a very large smooth flat board is presented. In the absence of an explicit theoretical expression and as

proposed in reference 6, these small-scale test results of reference 13, reproduced in figure 5, were used to estimate impact noise. The noise data shown in figure 5 did not include leading- and trailing-edge noise, but did include the remaining noise sources (i.e., oblique jet impingement coupled with surface viscosity effects, surface scrubbing, reflection by the surface, free jet mixing, and free shear-layer mixing over the deflected flat surface). The test conditions of reference 13 included nondimensional geometric and fluid flow conditions similar to those of the cold-flow test described in this paper. Therefore, the data of reference 13 were used after interpolation for the appropriate Mach number and normalized for differences in nozzle diameter D and microphone location r according to geometric scaling laws of reference 14.

COMPARISON OF CALCULATED AND MEASURED JET-FLAP-INTERACTION NOISE

Overall sound pressure levels representing the total jet-flap impingement noise (eq. (1)) are compared with two sets of experimental data: first, the large-scale, cold-flow, two-flap model data of reference 7; and second, the unpublished full-scale, hot-flow, three-flap model data obtained by using a TF-34 turbofan engine. Each configuration was positioned with the flaps in an approach attitude.

Cold-Flow, Two-Flap Model

The cold-flow model tests of reference 7 were conducted at the large-scale test facility schematically shown in figure 6. A primary airflow system supplied air to the 33-centimeter-diameter conical nozzle. The nozzle was located 7.33 nozzle diameters upstream of the flaps. Sound data were taken at nozzle exit Mach numbers of 0.5, 0.7 and 0.8 along the circumference of a 15.24-meter-radius microphone circle over a smooth blacktop ground plane.

The cold-flow model OASPL data are plotted as a function of radiation angle θ measured from the nozzle inlet axis in figure 7. Discrete ground reflection effects were eliminated by matching acoustic data taken at ground level and at 3.58 meters above it. This procedure produced spectra which were essentially free-field plus 2.58 decibels. As shown in figure 7, the data were taken along an arc of the microphone circle from 10° to 115°. The data are restricted to this range of θ because these are the limits of the useful impact noise data obtained in reference 13. A disproportionate increase in noise level with increased jet exit Mach number M_j is clearly shown between $70^{\circ} \leq \theta \leq 115^{\circ}$.

Overall-sound-pressure-level data taken at a jet Mach number M_j of 0.7 (from fig. 7) are compared in figure 8 with the total jet-flap impingement noise calculated from equation (1) (solid curve). Also included in figure 8 are estimates of each noise which contributes to the total impingement noise. These include trailing-edge noise applied to the second flap (eq. (2)), inflow noise applied to the two flaps and wing (eq. (3)), and the empirical estimate of the impact noise. The local gas properties and turbulence intensities used in the calculations were estimated, as in reference 7, from velocity decay profiles and small-scale turbulence intensities available in the literature.

From $\theta = 10^o$ to 80^o in figure 8, inflow noise from the second flap (having a U^6 dependence) dominates the noise field; however, trailing-edge noise from the second flap (having a U^5 dependence) is also a significant contributor. In the region from 90^o to at least 120^o impact noise (having a U^8 dependence) is dominant, and inflow noise and trailing-edge noise do not significantly affect the noise level. The agreement between the measured data and the curve representing impingement noise (eq. (1)) in figure 8 is considered good.

In the lower portion of figure 8 the velocity exponents determined from the experimental data indicate that OASPL varies nominally as $U^{5.6}$ for the range of θ between 10^o and 70^o. Above 80^o, however, OASPL varies as $U^{6.6}$, $U^{8.4}$, and $U^{7.3}$ at radiation angles of 85^o, 100^o, and 115^o, respectively. Comparing these results with the curves representing the dominant sound sources indicates general agreement with the expected values based on the present analysis.

Sound-pressure-level spectra. - A typical spectral plot for the cold-flow EBF configuration is presented in figure 9 (from ref. 7) for a radiation angle θ of 85^o. These data demonstrate the distinct broadband character of the sound field for values of jet exit Mach number M_j of 0.5, 0.7, and 0.8. Also shown in figure 9 are two tick marks positioned along each curve. These tick marks represent the frequencies at which two modal forms of the large-scale turbulence structures in a jet flow field are predicted to occur (ref. 15). Tick mark (1) represents the fundamental axisymmetric vortex mode (applicable at $M_j < 0.35$), and tick mark (2) represents the first harmonic of the axisymmetric vortex mode. The parameters upon which these modes depend are given in reference 6.

The possibility that the large-scale turbulence structures in a jet flow field are associated (through transfer functions) with the dominant noise produced during jet impingement on a flat plate is considered in reference 6. It is shown in reference 6 that the first harmonic mode of these structures occurs at approximately the same frequency as the peak value of the far field sound pressure level. In figure 9, as with the flat plate data of reference 6, the data show that the first harmonic mode of these vortex structures (tick mark (2)) occurs at approximately the same frequency as the peak value of the spectra. Thus, the dominant noise produced by jet impingement on the

flaps appears to be associated with the large-scale turbulence structures in the jet flow field.

Plugs in slots. - In order to test the noise source model further, an effort was made to reduce substantially or eliminate the noise produced by inflow of the jet about the wing and flaps. Short spanwise covers, referred to as plugs, were placed over the slots between the wing and the first flap and between the first and second flaps with the flaps deployed (fig. 10). These plugs were smooth fairings positioned on the flaps and centrally located in relation to the intersection of the nozzle axis with the flaps. They had spanwise lengths of approximately 2 and 3 nozzle diameters (fig. 10) and were designed to prevent most of the impinging jet flow from passing through the spaces between the wing and the flaps. Thus, they redirected the jet flow over and downstream on the impingement side of the flaps and effectively reduced local inflow of the jet about the wing and flaps. The rest of the flap system in the spanwise direction was unaltered, which permitted normal aerodynamic operation of the flaps.

The OASPL distribution for the cold-flow model with plugs in the slots between the wing and flaps is presented in figure 11 (ref. 7). The calculated trailing-edge noise (eq. (2)) is also shown, along with the empirically based estimate of impact noise and the logarithmic sum of impact and trailing-edge noise $OASPL_{impact,\,TE}$ (from eq. (5) of ref. 7), which is expressed by the following equation:

$$OASPL_{impact,\,TE} = 10 \log\left[10 \exp\left(\frac{OASPL_{impact}}{10}\right) + 10 \exp\left(\frac{OASPL_{TE}}{10}\right)\right] \qquad (4)$$

Inflow noise is not included in equation (4) because of the assumption that the plugs effectively eliminate noise from this source.

At a jet Mach number of 0.7 (fig. 11) close agreement is shown between the measured data and the curve of $OASPL_{impact,\,TE}$. Trailing-edge noise (eq. (2), U^5 dependence) is dominant between $\theta = 10^\circ$ and 40°, while impact noise (U^8 dependence) dominates from 80° to 115°. The dominance of these two noise sources is supported by the velocity exponents determined from the measured data and shown at the bottom of the figure.

Hot-Flow, Three-Flap Model

Figure 12 shows the full-scale, three-flap, swept-wing (25° sweep angle) UTW EBF in an approach attitude (first, second, and third flaps in 15°, 35°, and 55° position, respectively, ref. 8), using a TF-34 turbofan engine having a conical exhaust

nozzle with a 12-lobe, internal forced mixer. The axis of the nozzle intersected the leading edge of the third flap at approximately 4 nozzle diameters downstream from the exit plane of the nozzle. Also, the trailing-edge was oriented so that the included angle between a tangent to the flap surface and the jet axis was approximately 55°. The orientation of the engine to the three-flap swept-wing UTW EBF configuration was, therefore, not the same as that of the cold-flow model discussed in the preceding sections.

Overall-sound-pressure-level data taken at a jet Mach number of 0.5 are compared in figure 13 with the calculated estimate of the total jet-flap impingement noise (eq. (1)). The calculated impingement noise (solid curve) includes free-field estimates of trailing-edge noise applied to the third flap (eq. (2)), inflow noise applied to each of the three flaps (eq. (3)), and impact noise estimated from the data of reference 13. No velocity profile data were obtained at the trailing edge of the third flap in reference 8; thus the velocity profiles from the two-flap, cold-flow test data of references 6 and 7 were scaled up to estimate the boundary-layer height used in the calculations of trailing-edge noise. The local gas properties required in the calculations were determined from jet velocity profile and total temperature profile data for a conical exhaust nozzle with a 12-lobe internal forced mixer (unpublished data obtained from J. A. Schoenster of the Langley Research Center and N. E. Samanich of the Lewis Research Center). The local turbulence intensities in the vicinity of the flaps were estimated from the literature, as was done for the cold-flow model. The acoustic data were obtained by using 1.27-centimeter-diameter condenser microphones positioned on the ground.

In the region between $\theta = 40^{\circ}$ and 80° in figure 13, inflow noise from the third flap (having a U^6 dependence) dominates the noise field; however, trailing-edge noise from the third flap (having a U^5 dependence) is also a significant contributor. In the region 90° to 120° impact noise (having a U^3 dependence) is dominant, and inflow noise and trailing-edge noise do not significantly affect the total impingement noise level. For the three data points shown the calculated total impingement noise (eq. (1)) is within ± 1.5 decibels of the measured data.

In the lower portion of the figure the velocity exponents determined from the experimental data indicate that OASPL varied as $U^{5.6}$ at radiation angles of 70° and 90°, but at 110° the dependence increased to $U^{6.8}$. Comparing these results with the curves representing the sound sources at 70°, 90°, and 110° indicates that these nominal results and trend would be expected on the basis of the present analysis.

A spectral plot of the noise is presented in figure 14 for a radiation angle θ of 90° and a jet exit Mach number M_j of 0.5. Also shown in figure 14 are the two tick marks representing the large-scale vortex modes discussed previously for the cold-flow model. The value of the jet exit velocity used in the calculations of the vortex mode frequencies is based on mass average flow conditions computed in the exit plane

of the nozzle. It is shown that the first harmonic mode of the large-scale turbulence structures in the jet flow field (tick mark (2)) occurs at approximately the same frequency as the peak value of the sound spectra. Thus, as with the cold-flow model, the dominant noise produced by jet impingement on the flaps appears to be associated with the large-scale turbulence structures in the jet flow field.

CONCLUDING REMARKS

An analytical expression has been developed which approximates the overall sound pressure level and directivity of data obtained from two large-scale UTW EBF configurations in an approach attitude. Three dominant noise sources are modeled; two are based on analytical theories, and the third is based on scaled experimental data. The noise sources include the following: first, impact noise produced by the jet exhaust impinging on the surface of the most downstream flap; second, inflow noise, produced by the jet exhaust flow about the wing and flaps, which in turn produces a fluctuating lift response to an upwash disturbance; and third, trailing-edge noise, produced by the jet flow passing over the trailing edge of the most downstream flap.

The analysis was compared with experimental data obtained by using a subsonic cold-air jet impinging on a two-flap wing and a subsonic hot-gas jet from a TF-34 turbofan engine impinging on a three-flap swept wing. The agreement between the analytical expression and the data is considered good in both cases.

The dominant noise at 90° under the wing appears to result from the jet impact (eighth power dependence on jet velocity) rather than a fluctuating lift dipole (sixth power) or a trailing-edge disturbance (fifth power).

The frequency at which the peak sound pressure level occurred appears to be governed by the periodic formation and shedding of large-scale turbulence structures (ring vortices) from the outlet of the jet nozzle.

REFERENCES

1. Maglieri, Domenic J.; and Hubbard, Harvey H.: Preliminary Measurements of the Noise Characteristics of Some Jet-Augmented-Flap Configurations. NASA Memo 12-4-58L, 1959.

2. Dorsch, R. G.; Krejsa, E. A.; and Olsen, W. A.: Blown Flap Noise Research. AIAA Paper 71-745, June 1971.

3. Dorsch, R. G.: Externally Blown Flap Noise Research. SAE Paper 740468, Apr.-May 1974.

4. Fink, Martin R.: Prediction of Externally Blown Flap Noise and Turbomachinery Strut Noise. (United Technologies Research Center; NAS3-17863) NASA CR-134883, 1975.

5. Dorsch, Robert G.; Clark, Bruce J.; and Reshotko, Meyer: Interim Prediction Method for Externally Blown Flap Noise. NASA TM X-71768, 1975.

6. McKinzie, Daniel J., Jr.; and Burns, Robert J.: Analysis of Noise Produced by Jet Impingement Near the Trailing Edge of a Flat and a Curved Plate. NASA TM X-3171, 1975.

7. McKinzie, Daniel J., Jr.; Burns, Robert J.; and Wagner, Jack M.: Noise Reduction Tests of Large-Scale-Model Externally Blown Flap Using Trailing-Edge Blowing and Partial Flap Slot Covering. NASA TM X-3379, 1976.

8. Samanich, N. E.; Heidelberg, L. J.; and Jones, W. L.: Effect of Exhaust Nozzle Configuration on Aerodynamic and Acoustic Performance of an Externally Blown Flap System with a Quiet 6:1 Bypass Ratio Engine. AIAA Paper 73-1217, Nov. 1973.

9. Fink, M. R.: Mechanisms of Externally Blown Flap Noise. AIAA Paper 73-1029, Oct. 1973.

10. Guinn, Willy A.; Blankey, Dennis F.; and Gibson, John S.: V/STOL Noise Prediction and Reduction. LG73ER0062, Lockheed-Georgia Co. (FAA-RD-73-145), 1973.

11. Ffowcs, William, J. E.; and Hall, L. H.: Aerodynamic Sound Generation by Turbulent Flow in the Vicinity of a Scattering Half Plane. J. Fluid Mech., vol. 40, pt. 4, Mar. 1970, pp. 657-670.

12. Hayden, Richard E.: Noise from Interaction of Flow with Rigid Surfaces: A Review of Current Status of Prediction Techniques. NASA CR-2126, 1972.

13. Olsen, William A.; Miles, Jeffrey H.; and Dorsch, Robert G.: Noise Generated by Impingement of a Jet Upon a Large Flat Board. NASA TN D-7075, 1972.

14. Dorsch, R. G.; Kreim, W. J.; and Olsen, W. A.: Externally Blown-Flap Noise. AIAA Paper 72-129, Jan. 1972.

15. Neuwerth, Gunther: Acoustic Feedback Phenomena of the Subsonic and Hypersonic Free Jet Impinging on a Foreign Body. NASA TT F-15719, 1974.

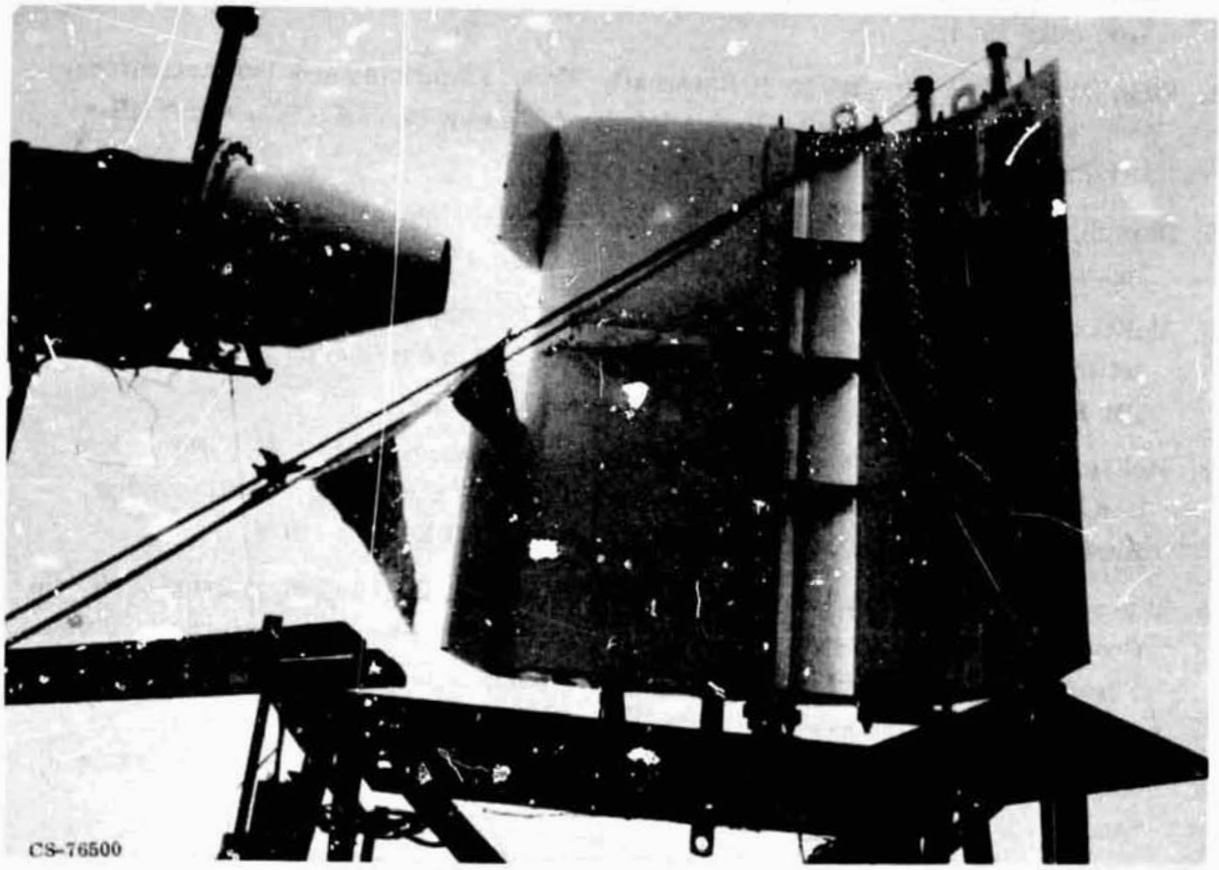

(a) Test installation.

(b) Approach attitude.

Figure 1.- Cold-flow model of two-flap EBF with conical nozzle.

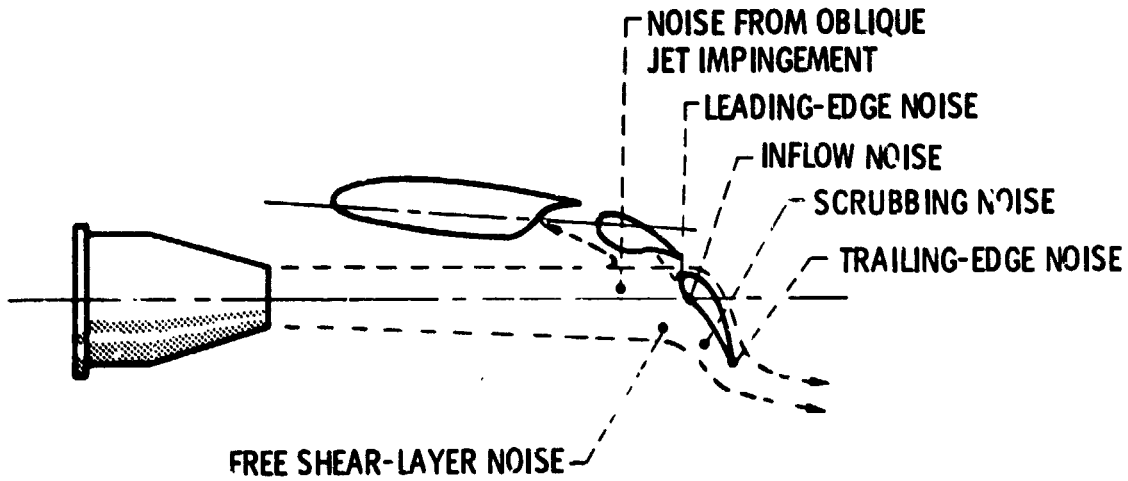

Figure 2.- Noise sources resulting from jet impingement on EBF two-flap wing in its approach attitude.

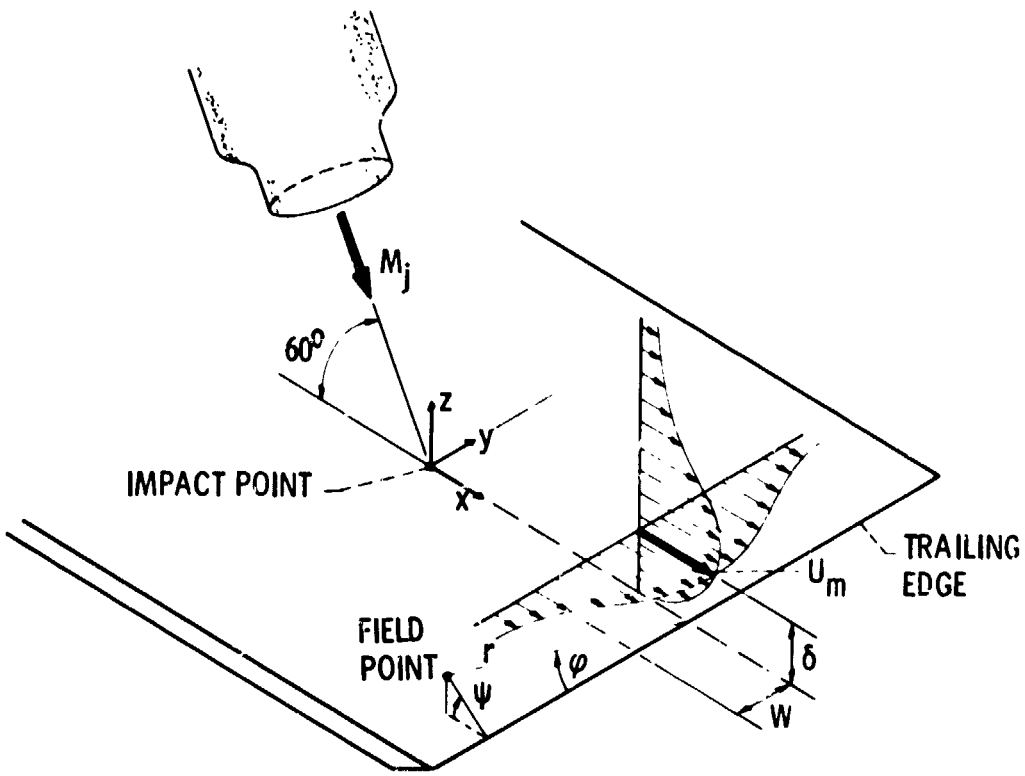

Figure 3.- Coordinate system of jet impinging on semi-infinite half-plane near its trailing edge (ref. 6).

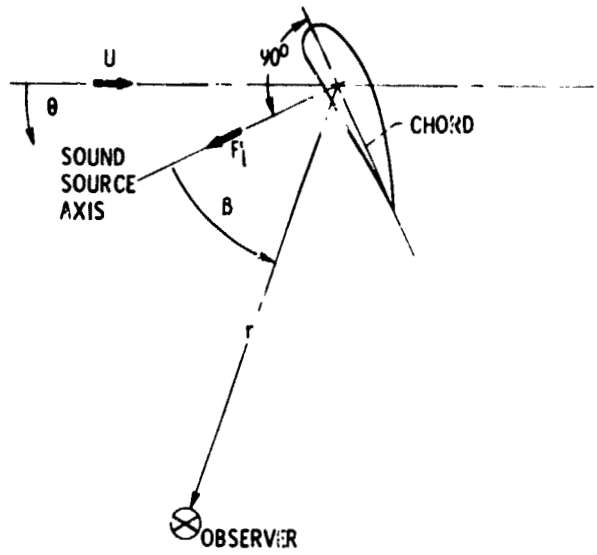

Figure 4.- Coordinate system for inflow noise (ref. 7).

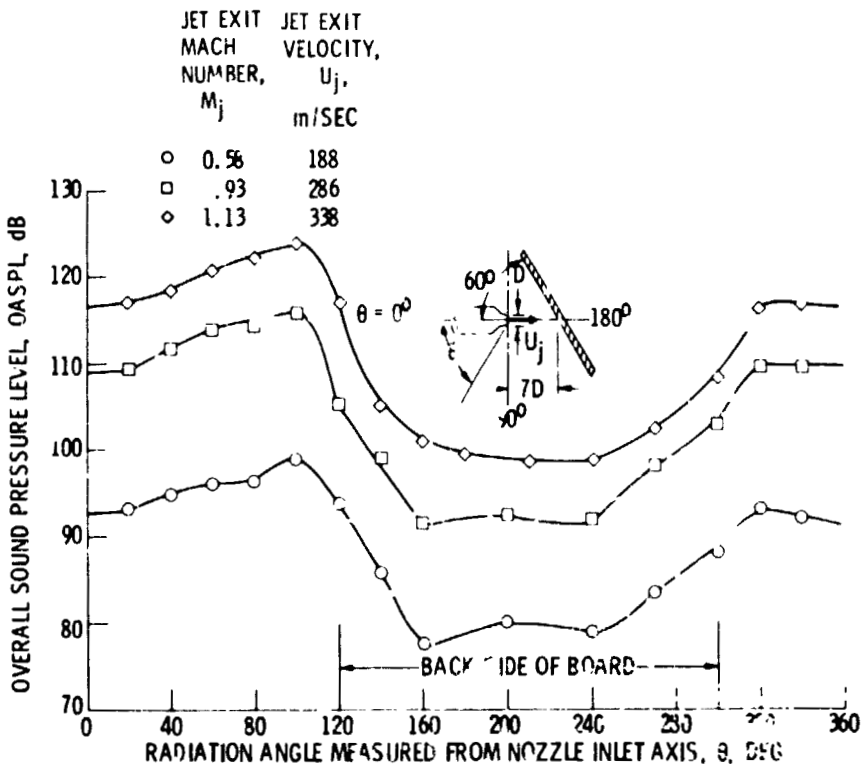

Figure 5.- Overall-sound-pressure-level distribution for large flat board. D = 5.2 m; microphone radius, 7.05 m; azimuthal angle, 0° (ref. 13).

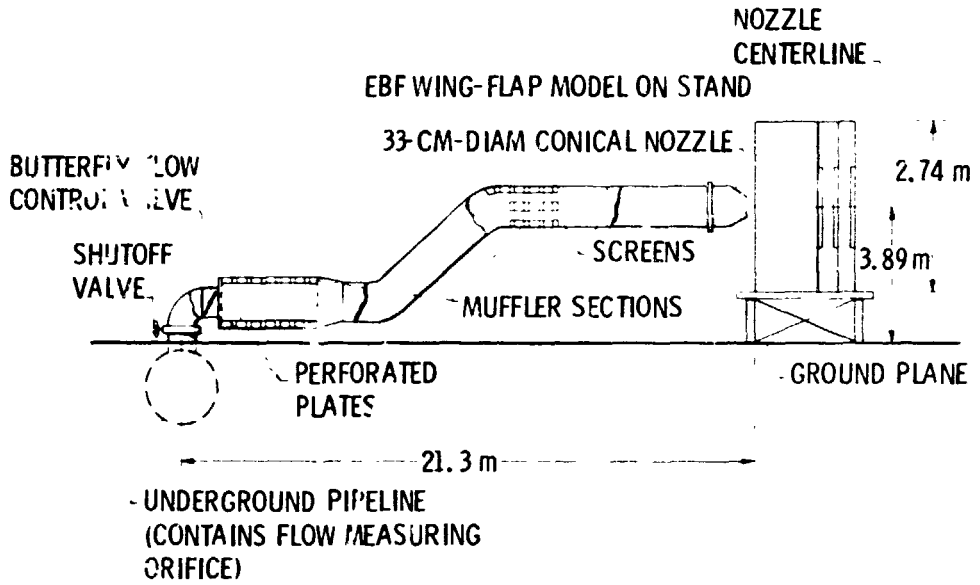

Figure 6.- Diagram of EBF large-scale test facility showing primary airflow system (ref. 7).

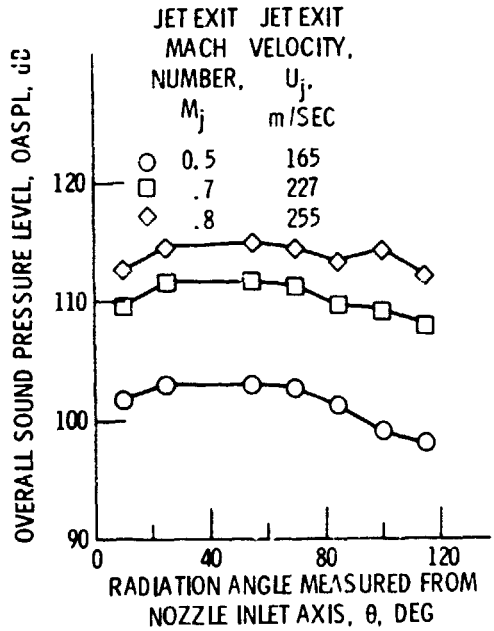

Figure 7.- Overall-sound-pressure-level distribution for two-flap EBF cold-flow configuration with 30° to 60° flaps (approach attitude). Microphone radius, 15.24 m.

C-4

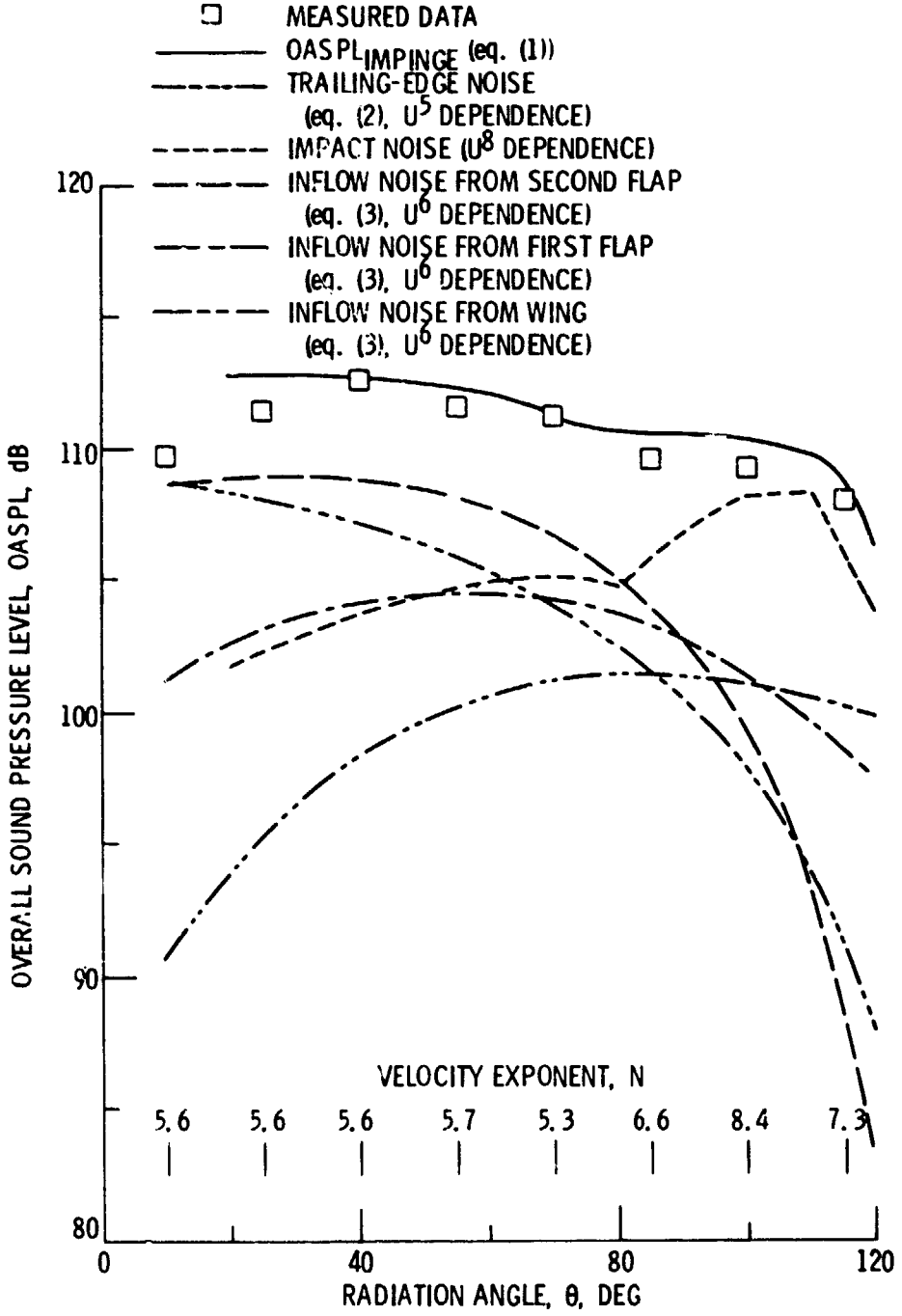

Figure 8.- Comparison of measured and calculated overall sound pressure level for cold-flow configuration (approach attitude). M_j = 0.7; U_j = 227 m/sec (ref. 7); microphone radius, 15.24 m.

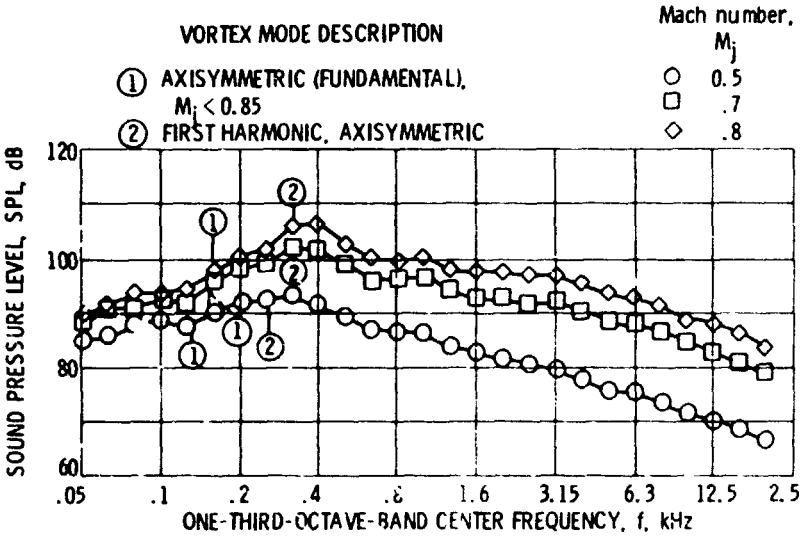

Figure 9.- Sound-pressure-level spectra for two-flap EBF cold-flow configuration with 30° to 60° flaps (approach attitude). $\theta = 85°$ (ref. 7); microphone radius, 15.24 m.

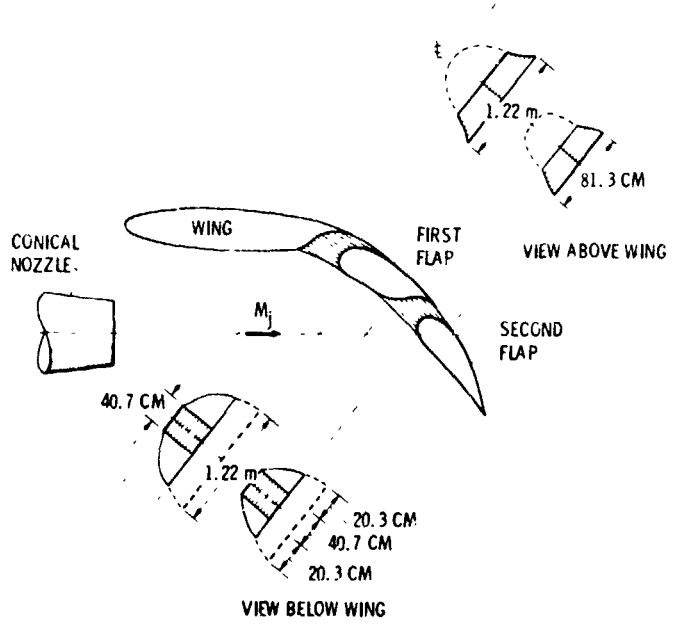

Figure 10.- Plug fairings in slots between wing and first flap and first and second flaps (ref. 7).

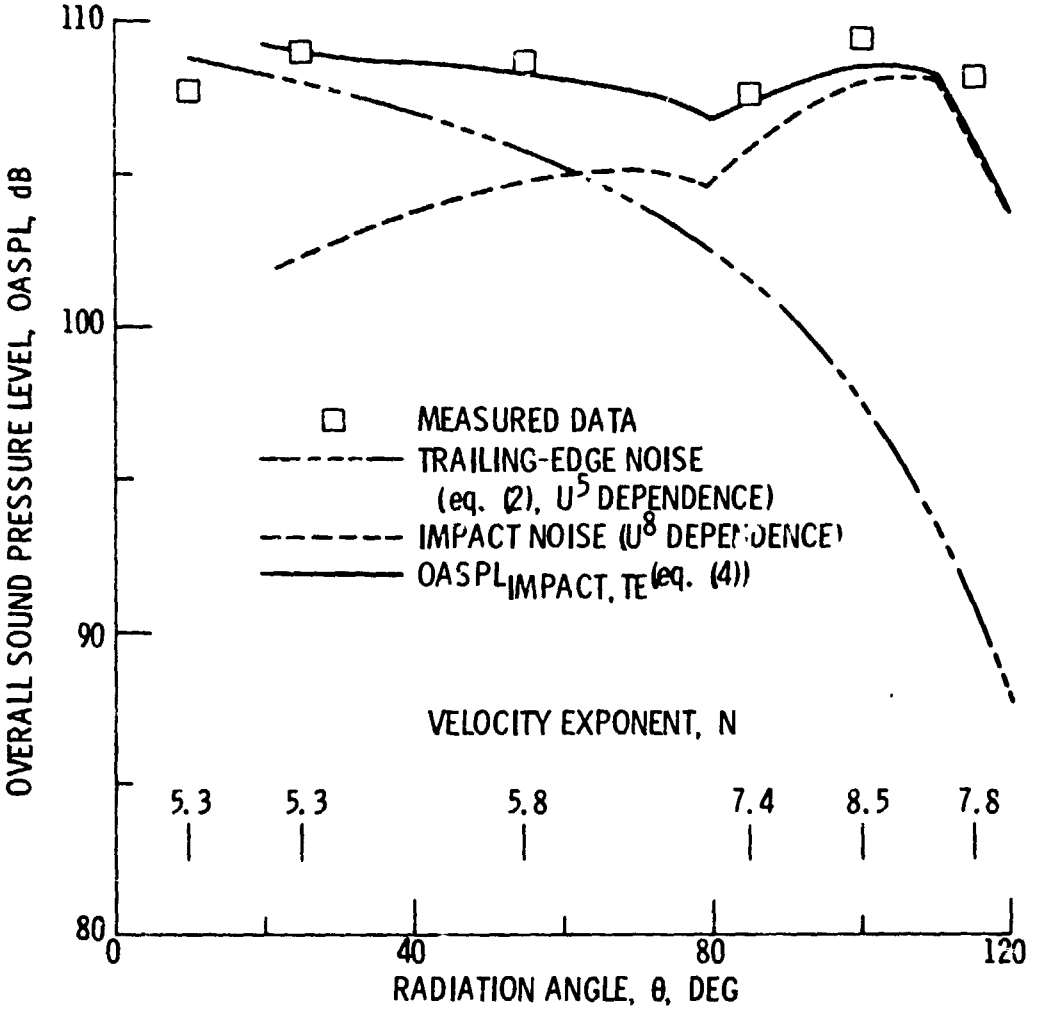

Figure 11.- Comparison of measured and calculated overall sound pressure level for cold-flow configuration with plugs (approach attitude). $M_j = 0.7$; $U_j = 227$ m/sec (ref. 7); microphone radius, 15.24 m.

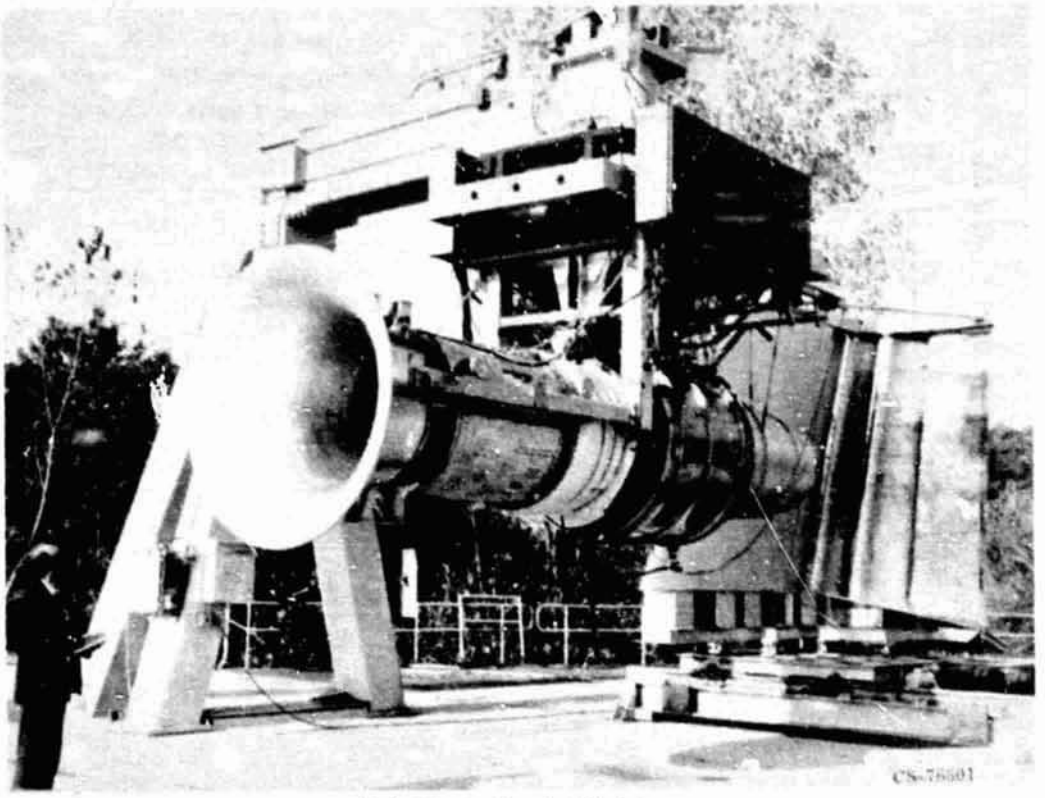

(a) Test installation.

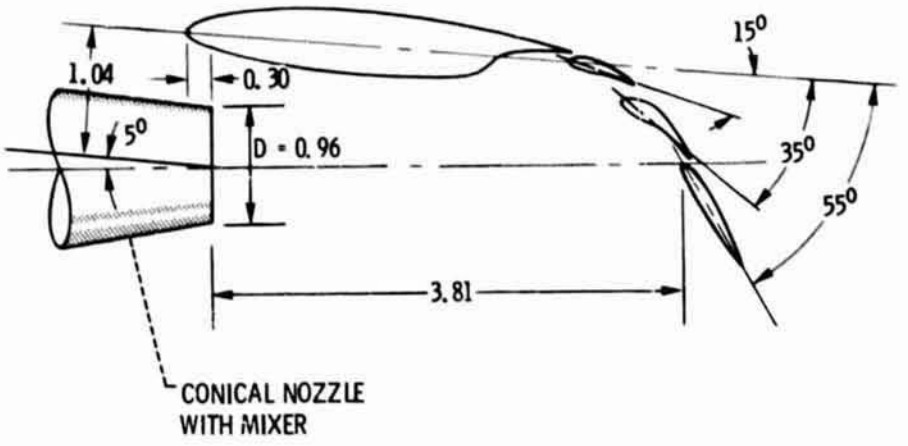

(b) Approach attitude.

Figure 12.- Hot-flow model of three-flap EBF with TF-34 turbofan engine (ref. 8). (All dimensions in meters.)

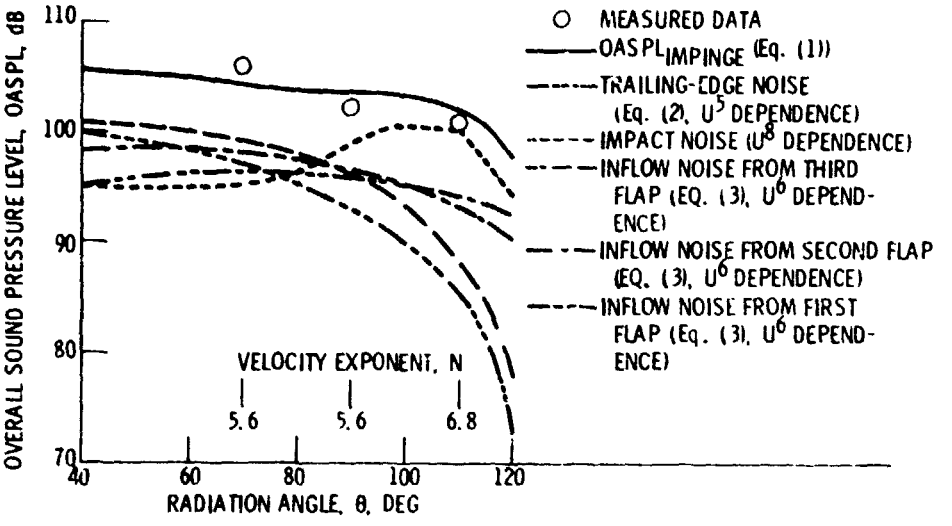

Figure 13.- Comparison of measured and calculated free-field overall sound pressure level for full-scale three-flap configuration with TF-34 turbofan engine (approach attitude). $M_j = 0.5$; jet exit core velocity, 250 m/sec; core temperature, 749 K; microphone radius, 30.48 m.

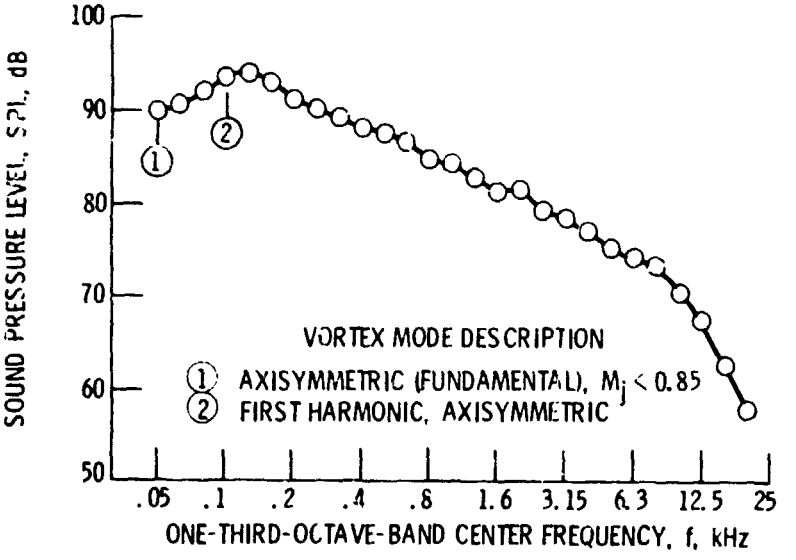

Figure 14.- Measured free-field sound pressure level spectra for full-scale three-flap configuration with TF-34 turbofan engine (approach attitude). $M_j = 0.5$; $\theta = 90^\circ$ (ref. 8); microphone radius, 30.48 m.

USB NOISE REDUCTION BY NOZZLE AND FLAP MODIFICATIONS

N78-24064

Richard E. Hayden
Bolt Beranek and Newman Inc.

SUMMARY

Upper surface blown (USB) system configuration parameters are chosen with both takeoff and cruise performance in mind. Indications are that configuration requirements for cruise may compromise the ability to derive low takeoff and landing noise from USB designs by selection of nozzle/flap locations and designs which are inherently quiet. Thus, additional noise reduction at the source will be required.

This paper reviews the development of concepts for reducing USB flap noise at the source through flap modifications and special nozzles. In particular, recent results obtained on the aerodynamic and acoustic performance of flaps with porous surfaces near the trailing edge and so-called multi-slotted nozzles are reviewed. Considerable reduction (6-10 dB) of the characteristic low frequency peak has been shown. The aerodynamic performance is compared with conventional systems, and prospects for future improvements are discussed.

INTRODUCTION

Upper surface blown powered lift aircraft appear to be attractive from an aerodynamic point of view. However, these aircraft incur noise problems associated with the basic physical phenomena responsible for the powered lift attachment of the engine exhaust flow to a single flap, or series of flaps. Because of the stringent community noise goals set for propulsive lift aircraft, much attention is being focussed on the flap noise problem in the aircraft concept development stage. The problem peculiar to USB aircraft is a pronounced low frequency peak in the radiated noise spectrum. This peak contributes to, but does not dominate the commonly accepted measure of community noise

18

from aircraft - the perceived noise level (PNL or PNdB). However, the low frequency peak is expected to produce a community noise impact due to secondary effects such as transmission into and excitation of building structures. Thus, significant reduction of the low frequency peak is desired. The high frequency sound levels produced by typical USB systems appear to be within a few dB of the desired goal and, thus, will require a lesser degree of reduction.

Cabin interior noise is an important area for both commercial and military aircraft applications. The USB powered lift system produces significantly higher source levels of low frequency noise than conventional jet aircraft, with a resultant increase in noise levels inside the cabin. Thus, due to the relatively poor noise-attenuating capabilities of conventional airframe structures at low frequencies, considerable attention must be given to reducing the levels of the source in the low frequency range.

TYPICAL USB NOISE CHARACTERISTICS

Figure 1 illustrates typical flyover noise spectra for a USB system under static conditions. The levels and frequencies are scaled from model data (Ref. 1) to a "full scale" (26,800 N (6000 lb) thrust) engine/flap configuration at a 152 m (500 ft) flyover distance. The nozzle pressure ratio (1.38) is representative of the upper part of the range currently being considered for powered lift aircraft. The single 26,800 N (6000 lb) engine/flap noise levels scale to about 95 PNdB at the 152 m (500 ft) distance. Four such engines and flaps would add 6 dB to these levels. [Note that a single 88,960 N (20,000 lb) thrust engine, identically mounted on a flap system whose dimensions were scaled to the nozzle diameter, would produce a noise spectrum 5 dB higher in level, and one octave lower in frequency than the single 26,800 N (6000 lb) engine.]

The pronounced low frequency peak is evident in Fig. 1. Levels in both the low and high frequency range are typically within a 5 dB range at all azimuths in the flyover plane, except in the immediate area of the deflected exhaust. Nozzle and flap details will affect the details of the far field sound spectra, so the data in Fig. 1 should only be regarded as typical examples.

Figure 2 compares predicted cabin internal noise levels with those actually measured on a range of CTOL jet aircraft (including all positions in the aircraft). The estimates for

the USB system were made from fuselage sidewall fluctuating pressure data measured on an actual USB configuration (Ref. 1) combined with analytical and empirical estimates for acoustic and aerodynamic transmission loss of actual aircraft fuselage structures (Ref. 2).

For the USB model tested, the jet exhaust noise alone (as measured with flaps removed) shows a significantly lower level and compares favorably with levels inside current CTOL passenger jets. From these comparisons, it is clearly evident that both flap source noise reductions at low frequencies and fuselage structural design changes will be needed to reduce USB cabin noise levels to an acceptable range.

Figure 3 shows measured continuous-traverse directivity of an unmodified USB flap system (60° flap setting) in the flyover plane. The evidence is that the flap sources are not strongly directional. Other measurements have shown that the directivity is even weaker (i.e., more uniform), except at those azimuths in the vicinity of the deflected flow axis. The directivity pattern has been observed to rotate with the flap deflection which clearly implicates the flaps as a major source of noise. From these and extensive similar data, it is concluded that one cannot rely on utilizing directivity effects in developing low noise design strategies.

NOISE REDUCTION AT THE SOURCE

Identification of Physical Parameters

Noise reduction of flap sources involves first identifying the physical parameters responsible for sound generation and then developing concepts which modify the most important parameters. Figure 4 shows schematically how USB fluid mechanical parameters combine to radiate sound. The problem can be summarized by stating that the far field sound intensity [$I(r,\theta)$] is related to the spanwise sum of individual source intensities whose strength is a function of the fluctuating fluid forces F, frequency ω of the fluctuating forces, and the directivity $D(\theta)$ of the local source.

$$I(r,\theta) \propto \sum_{W} \left(\overline{F^2}\ \omega^{i\pm}\ D(\theta) \right)$$

Examination of each element of Fig. 4 will lead to identification of the physical parameters which can be modified by nozzle and flap design changes. The fluctuating forces can be viewed as

a product of fluctuating pressures and the respective correlation area of various pressures. The fluctuating pressures on a USB flap are intense, often being as high as .03 - .1 of the local dynamic pressure q_o, and may vary significantly with location on the flap. The characteristic side shear layers of a USB flap system produce intense low frequency pressures, while the attached flow along the nozzle centerline has greater high frequency content. The frequency ω of the fluctuating forces with respect to a stationary observation point on the flap is a ratio of the local convection velocity of turbulent eddies U_c, to the eddy length scale in the streamwise direction ℓ_x (i.e., $\omega \propto U_c/\ell_x$). The correlation areas are simply the product of the local streamwise and spanwise length scales, which are in turn proportional to the local shear layer thickness, δ. Both the fluctuating pressures and correlation areas can be reduced by flap and nozzle modifications. Diagnostic cross-correlation studies have shown that the acoustically important flap pressures on a USB system occur between the knee of the flap and the trailing edge, with the high frequency components being concentrated at the trailing edge.

The fluctuating hydrodynamic forces must accelerate the acoustic medium to cause far field sound. The efficiency of conversion of fluctuating hydrodynamic forces to far field sound increases with frequency, usually as the square of the frequency, except at values greater than unity of the ratio of flap or wing chord (C) to acoustic wavelength λ ($\lambda = c_o/\omega$). This acoustic "transfer function" can be influenced by flap modifications through varying the rate of change of surface flow resistance in the vicinity of the trailing edge or by producing a reactive component of unsteady surface pressure in the noise producing regions near the trailing edge.

The directivity of the flap sources (Fig. 4) is maximum at a direction $\approx 90°$ from the plane of the flap surface near the trailing edge and minimal in the downstream direction aligned with the flap surface. In the upstream direction, the pressure of the wing surface leads to significant sound radiated forward. Little can be done to affect the basic directivity characteristics of the flap sources. However, the flap and wing may be used effectively to shield sound from sources located above the flap surface, as is also shown in Fig. 4. Such sources include the free shear layer near the nozzle, the nozzle lip and deflector, blowing slots, and engine internal noise.

To arrive at the total far field noise spectrum, one must add up the contribution of all individual sources, including source strength, radiation efficiency, directivity, and shielding. The effective number of sources, m, on a USB system increases with frequency, approximately linearly. In developing noise reduction

concepts, it must be kept in mind that devices for reducing source strength at a given frequency may lead to increasing the number of sources contributing to the far field, thus leading to a lesser amount of noise reduction than expected from source strength reduction.

Source Noise Reduction Strategy

The above discussion may be summarized in the form of a "strategy" for developing noise reduction techniques as follows:

- Reduce forcing function
  - fluctuating pressures
  - turbulence length scales
- Reduce transfer function between hydrodynamic forces and radiated sound
  - make surface discontinuity more gradual at trailing edge
  - add reactive interference with sources
- Take advantage of shielding benefits
  - move sources away from trailing edge or substitute high frequency sources away from edge for low frequency sources

The latter point may be implemented with a penalty in the number of effective sources contributing to the far field.

NOISE REDUCTION CONCEPTS

Several noise reduction concepts have been developed from the above-described source reduction strategy. In this section, the applications of flap surface modifications and nozzle modifications to USB source reduction are discussed.

Porous Flap Surface Concept

The basic idea of the porous surface (or variable impedance surface) concept is to replace the acoustically rigid flap surface with a porous surface with appropriate backing air cavities, over *all* areas of significant sound generation on the flap. Figure 5 illustrates the application of this concept to a simplified USB flap.

The effects of a porous surface are both hydrodynamic (source reduction) and acoustic (modification of transfer functio), although the relative effects of each have not been conclusively determined.

Variations on the basic porous edge design are also shown in Fig. 5. These are:

(1) Fully porous tapered edge with a constant flow resistance per unit thickness; the tapering gives a decreasing flow resistance toward the trailing edge

(2) Constant impedance porous surfaces only, on upper and lower flap surfaces

(3) Porous upper surface with a simple cavity formed by the rigid lower surface

(4) Porous upper surface with individual compartments formed by flap lower surface and flap internal structure; such compartments can be tailored to acoustic and aerodynamic details, if they are known for a given configuration

Noise reduction has been achieved on a wide range of configurations ranging from a simple airfoil to an aerodynamically optimized USB flap at high turning angle setting (Fig. 6). Figure 7 summarizes these results. The airfoil shown was operated in the cone of a free jet and had a simple tapered porous edge. Noise reduction of the low frequency noise arising from free jet shear layer interaction with the trailing edge and of the airfoil's discrete frequency wake noise was achieved. A simple wall jet has been tested by both BBN and Bohn of Boeing (Ref. 3). The noise reduction shown is a typical reduction which was maximum at the Strouhal peak and less at high frequencies. Peak reductions of at least 10 dB were commonly achieved. Early tests on the potential applicability of porous edges to USB systems were conducted by BBN (Ref. 4) on a small scale (~1/20) USB turning flap with a 10:1 AR nozzle kicked down at about 15°. As shown in Fig. 7, the flyover noise reduction at the Strouhal peak was substantial for both a simple porous edge and one with a simple cavity backing. However, the cavity reduced the flyover noise levels in the high frequency regime and was qualitatively found to improve turning.

Recently-completed exploratory tests on an aerodynamically optimized USB configuration (Fig. 6) were conducted by BBN under NASA Langley contract (Ref. 1). The objective of the study was to show that significant noise reduction could be achieved without impairing the aerodynamic performance of the USB system. It was also desired to develop a data base to improve the understanding of the important parameters influencing noise reduction.

A sampling of key results from the Aero Commander USB tests are shown in Fig. 7. Noise reduction was achieved over a wide range of frequencies at all observation points under the wing and along the sideline. Curves are shown for a simple porous flap with the

entire flap surface treated with a 0.9 ρc flow resistance* material, the same surface treatment with a solid lower flap surface in place, and a cavity-backed configuration where only the last 20% of the flap chord was treated. The latter configuration had superior aerodynamic performance as is discussed below. The peak noise reduction was about the same for all flap configurations, while high frequency noise reduction was better for the fully porous treatments than for those with the last 20% only treated. In cases where a large area was treated, the flow failed to stay attached at high exhaust velocities. This led to an apparent increase in high frequency noise, such as is shown at the 110° position. In fact, the high frequency noise was merely the free jet from the nozzle, being almost identical in level and frequency to the spectra with the flaps removed.

From these tests, it may be concluded that porous surface treatment may be successfully applied to an aerodynamically satisfactory USB configuration to achieve around 6 dB of reduction of the low frequency peak and 3-6 dB reduction of high frequency levels. Further optimization studies could improve the noise reduction through spatial variation in surface impedance and better matching of cavity geometry to local pressure field details.

USB NOZZLE MODIFICATIONS

The detailed flow parameters previously shown to influence flap-radiated noise are a function of the USB configuration details, namely:

- Nozzle shape, aspect ratio, kickdown angle
- Nozzle axial location
- Flap radius and length.

These details affect the intensity of turbulent pressure fluctuations and the scale at the trailing edge. The side shear layers are primarily responsible for the characteristic low frequency peak in both community noise and interior noise. Thus, if the intensity and scale of turbulence can be reduced, the source strength will be reduced, and the characteristic frequency will increase, thus taking advantage of shielding benefits for community

---

*ρc = density × sound speed of ambient medium
= acoustic impedance of air

noise, and improved transmission loss of the fuselage for high frequency noise.

Several baseline variations on USB nozzles (such as deflectors) can produce up to 5 dB reduction of the low frequency peak, but cause a comparable increase in high frequency levels (Ref. 1). This section describes a class of multi-segment nozzles which when integrated with turning flaps have shown considerable potential. Figure 8 shows the basic concept which combines ideas derived from concentric cylinder low noise free jet nozzles (Ref. 5), and flap trailing edge blowing (Ref. 6).

The expected benefits of multi-segment, or multi-slot nozzles, are both hydrodynamic (reduce intensity and scale of turbulence) and acoustic (replace low frequencies with high frequency sources above the wing to take advantage of shielding). Aerodynamically, high turning angles can be achieved with a short flap chord. All configurations involve using a small flap with three or more tangential blowing slots at the knee and trailing edge blowing slots. The fixed nozzle is either a single low aspect ratio nozzle with deflector ("split flow") or a series of fixed slots deployed during the powered lift mode of flight ("7-slot" nozzle or "14-slot" nozzle). The principal objectives of these integrated nozzle/flap designs were to reduce the low frequency noise peak and achieve high turning angles with a short flap. The results of several test programs (Refs. 7-9) are summarized below.

All three multi-segment nozzles were compared with a 6:1 AR Coanda nozzle and flap. The baseline nozzle/flap system had a 10° kickdown but no deflector and thus cannot be considered the most advanced design. Figure 9 shows typical reductions of community noise with various multi-slot nozzles. The low frequency peak was reduced by 10 - 15 dB, while high frequency levels increased by up to 5 dB in the important frequency range. Above the wing, high frequency levels increased by up to 15 dB, but sound radiation to the hemisphere above the wing is inconsequential. The seven slot nozzle was the quietest overall at the sideline position. Also shown in Fig. 9 is a significant reduction of cabin noise in the low frequency regime. The interior noise curves were based upon analytical estimates of the sound in the nearfield of the nozzles and not upon actual sidewall pressure measurements as was the case for the curves presented in Fig. 2. Due to shielding effects of the flow, the actual high frequency levels might be lower than shown in Fig. 9.

From the tests summarized above, it is concluded that the integrated multi-segment nozzle/slotted flap system offers

potential noise reduction of over 10 dB for both low frequency community noise and interior noise. Since the noise reduction with the 14-slot nozzle was not significantly greater than the simpler split flow nozzle, it may be concluded that the tangential multi-slot blowing at the high curvature region of the flap is the most important aspect of the noise reduction concept. It is also noted that porous edge treatment described earlier would provide additive noise reduction of edge sources producing the high frequency noise.

AERODYNAMICS

The practical feasibility of flap and nozzle modifications proposed for noise control purposes depends upon the ability of the system to produce acceptable aerodynamic performance without excessive weight penalties. The porous flap and multi-slot nozzle concepts have been studied with aerodynamic performance and noise reduction treated simultaneously. In both cases, the aerodynamic performance of many configurations is comparable with baseline USB systems. A sample of the findings is given below.

Porous Flaps

The porous flap configurations were tested for aerodynamic performance by measuring axial (A) and normal (N) forces as a function of nozzle pressure ratio. The baseline solid flap produce a linear variation of both axial and normal force components as a function of nozzle pressure ratio. All porous flap configurations followed the linear variation of A and N forces with pressure ratio at low pressure ratios, and many were linear through the lateral range of nozzle pressure ratio. However, some of the highly porous configurations underwent flap separation prematurely; an example of the raw data curves obtained in Ref. 1 is shown in Fig. 10. For those configurations for which flow separated, noise was evaluated at pressure ratios on both sides of the stall point. Those configurations treated on the last 20% of the flap did not stall and, as described above, produced 4 - 8 dB of noise reduction over a wide frequency range.

The static turning of porous flap configurations tested is summarized in Fig. 11. It can be seen that the turning efficiency and turning angle performance are acceptable for most configurations except the simple porous flap with no backing. No forward speed tests have been conducted to date.

Multi-Slot Nozzles

The integrated multi-slot nozzle/flap configurations were generally characterized by excellent turning performance at all flap settings, including 90°, for both static and forward speed tests. Tests were conducted by the Los Angeles Aircraft Division (LAAD) of Rockwell International Corp. (Ref. 9) on the same models tested acoustically by BBN in the low noise acoustic wind tunnel.

The static turning characteristics of the three nozzle/flap configurations described earlier are shown in Fig. 12. The split flow nozzle with slotted turning flap performed the best at high flap settings.

Figure 13 summarizes some of the forward speed performance of the multi-slot nozzles on a low aspect ratio swept wing. Again, the split flow nozzle appears to have excellent performance. Comparable data for the simple Coanda flap are not available, but these data may serve as a useful baseline for comparison with other flap systems.

Conclusions

The limited aerodynamic studies conducted to date on the porous flap and multi-slot nozzle have shown that these noise reduction concepts can have aerodynamic performance which is comparable to unmodified USB nozzle/flap systems. Further aerodynamic diagnosis and optimization could enhance the performance of USB systems using these concepts.

CONCLUDING REMARKS

This paper has presented data which show that significant noise reduction of USB flap sources can be achieved with flap and nozzle modifications, without serious compromise of aerodynamic performance. The porous flap concept can be used to reduce noise from any baseline level achieved through primary configuration variables. The porous flap and multi-segment nozzles can undoubtedly be optimized further to improve both noise reduction and aerodynamic performance.

APPENDIX

SYMBOLS AND ABBREVIATIONS

A	area
AR	aspect ratio
A/C	aircraft
BB	Bolt Beranek and Newman
C	flap or wing chord
C_D	drag coefficient
C_L	lift coefficient
$C_{L_{max}}$	maximum lift coefficient
C_{L_o}	lift coefficient at $\alpha = 0$
C_T	thrust coefficient
c	sound speed of ambient medium
c_o	speed of sound
F	fluctuating fluid force
f	frequency
I	intensity
ℓ_x	eddy length scale in streamwise direction
m	effective number of sources
N,A	normal and axial force, respectively
N_2	14-slot nozzle
N_3	7-slot nozzle
N_4	split flow partially slotted nozzle

p_R	pressure ratio
p_s	surface pressure
p_T	total pressure
q	dynamic pressure
q_{max}	maximum dynamic pressure
q_o	local dynamic pressure
r	radial distance
T	thrust
USB	upper surface blown
U	velocity
U_c	local convection velocity of turbulent eddies
U_e	exit velocity
w	span
α	angle of attack
δ	local shear layer thickness
δ_F	outboard flap angle
δ_N	turning flap angle
θ	angle between flow direction and observer direction
λ	acoustic wavelength
ρ	density of ambient medium
ρ_c	acoustic impedance of air
ω	frequency of fluctuating forces

REFERENCES

1. Hayden, R.E.: "Exploratory Investigation of Aeroacoustic Optimization of the Variable Impedance Edge Concept Applied to Upper Surface Blown Configurations," BBN Report No. 3245, Feb. 1976.

2. Wilby, J.F., and Scharton, T.D.: "Acoustic Transmission Through a Fuselage Sidewall," BBN Report No. 2742, July 1974.

3. Bohn, A.J.: "Edge Noise Attenuation by Porous Edge Extensions," AIAA Paper 76-80, Jan. 1976.

4. Hayden, R.E., Scharton, T.D., Kadman, Y., Wilby, J., and Rudd, M.J.: "A Preliminary Evaluation of Noise Reduction Potential for the Upper Surface Blown Flap," BBN Report No. 2478, Nov. 1972 (NASA CR-112246).

5. Scharton, T.D., White, P.H.: "Simple Pressure Source Model of Jet Noise," J. Acous. Soc. Amer., vol 52, Nov 1972.

6. Scharton, T.D., Pinkel, B., and Wilby, J.F., "A Study of Trailing Edge Blowing as a Means of Reducing Noise Generated by the Interaction of Flow with a Surface," BBN Report No. 2593, Sept. 1973 (NASA CR-132270).

7. Kadman, Y., Hayden, R.E., and Scharton, T.D.: "Noise Characteristics of Conventional and Multislotted Upper Surface Blowing-Nozzle Concepts With and Without Forward Speed," BBN Report No. 2889, Sept. 1974.

8. Kadman, Y.: "Small Scale Noise and Wind Tunnel Tests of Upper Surface Blowing Nozzle Flap Concepts; NASA CR-137748, 1976.

9. Renselaer, D.J., Nishida, R.S., and Wilkin, C.A.: "Small Scale Noise and Wind Tunnel Test of Upper Surface Blowing Nozzle Flap Concepts," Volume I. "Aerodynamic Test Results." NASA CR-137747, Dec. 1975.

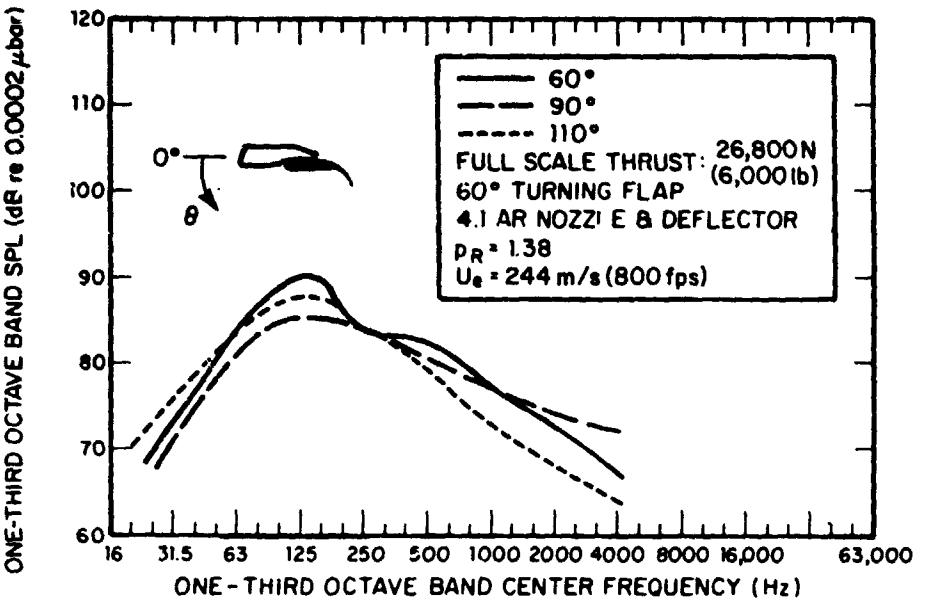

Figure 1.- Typical farfield USB sound spectra.

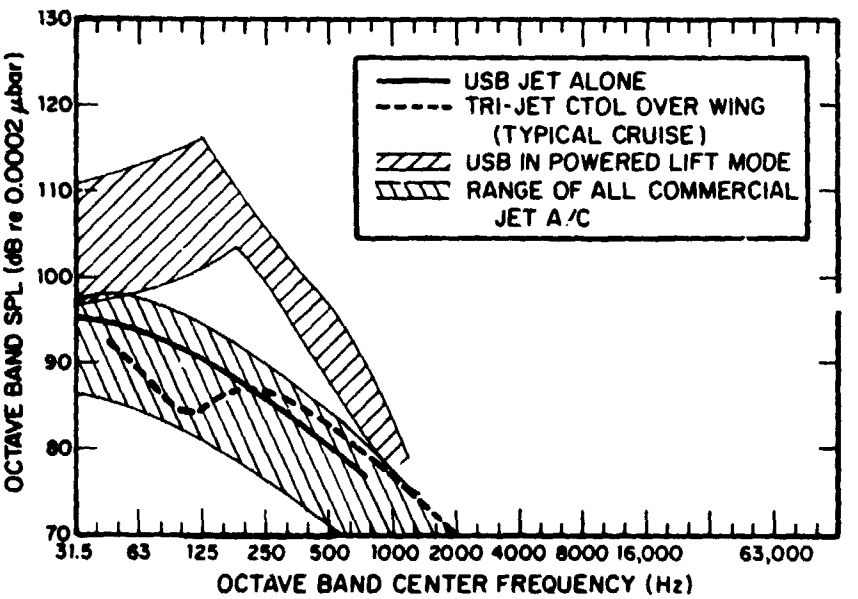

Figure 2.- Typical cabin noise levels.

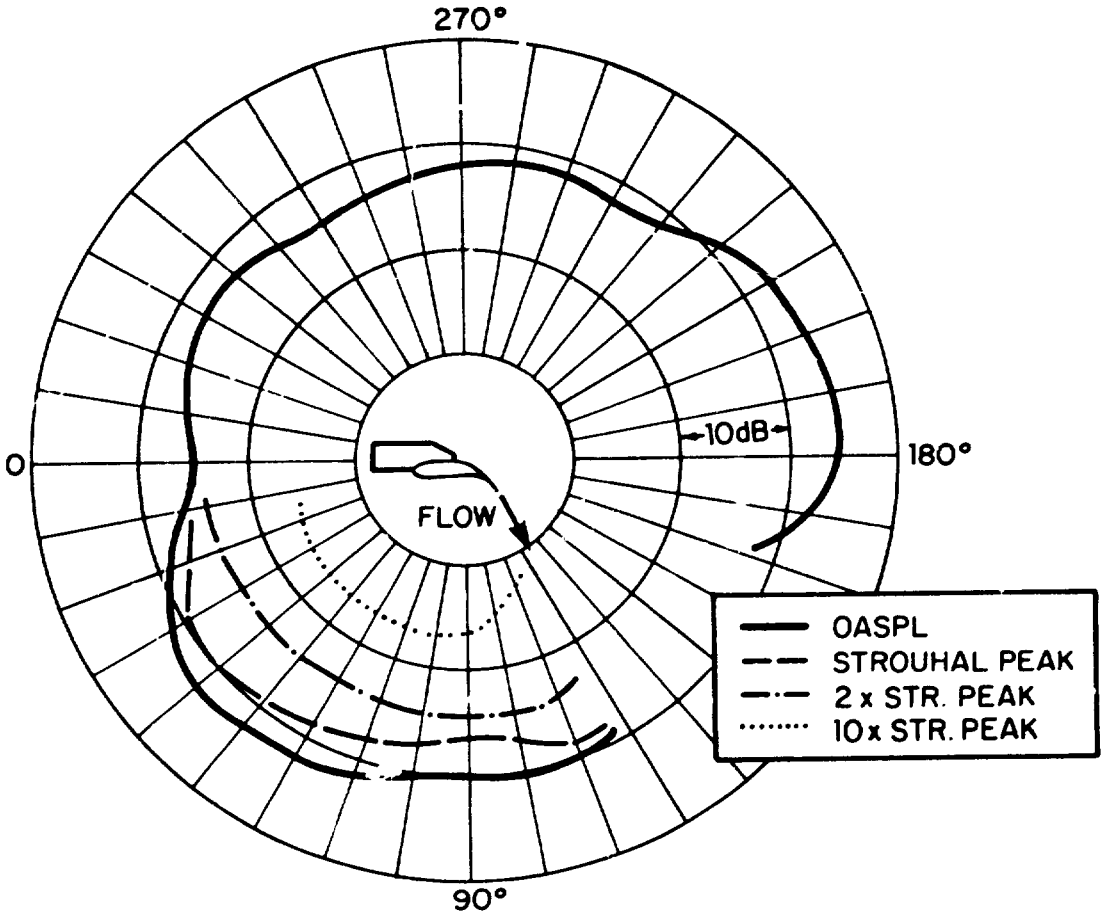

Figure 3.- Typical directivity in flyover plane.

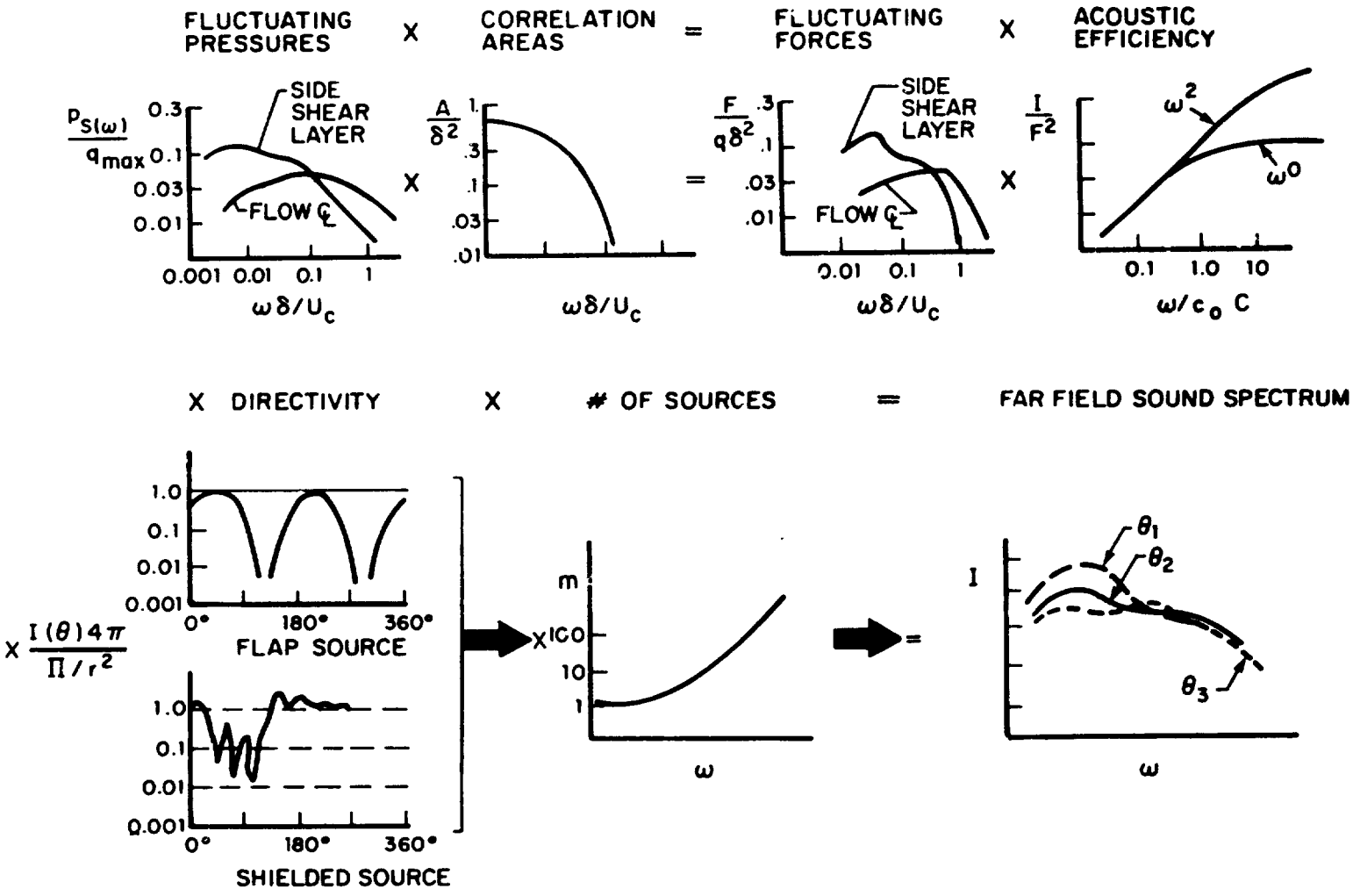

Figure 4.- Noise-producing parameters to be reduced.

FLAP MODIFICATION - POROUS FLAP

EFFECTS OF POROSITY

HYDRODYNAMIC: SOURCE STRENGTH REDUCTION

ACOUSTIC: IMPEDANCE MATCHING

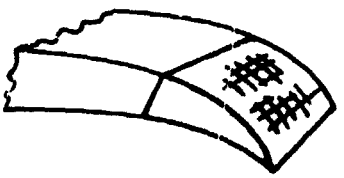

SCHEMATIC OF BASIC CONCEPT

USB-TYPICAL CONFIGURATIONS

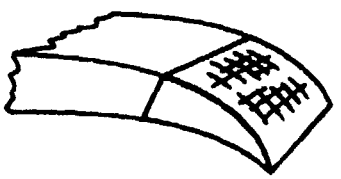

SIMPLE POROUS EDGE

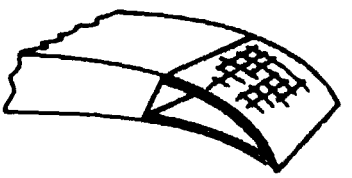

POROUS SURFACES ONLY

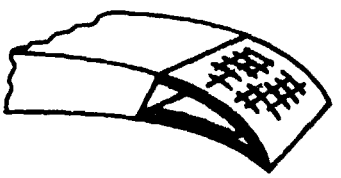

POROUS SURFACE WITH SOLID BACKING

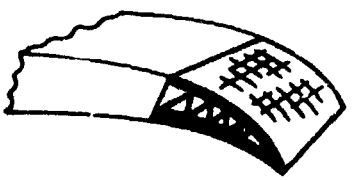

POROUS SURFACE WITH SOLID BACKING WITH COMPARTMENTS

Figure 5.- Noise reduction concepts.

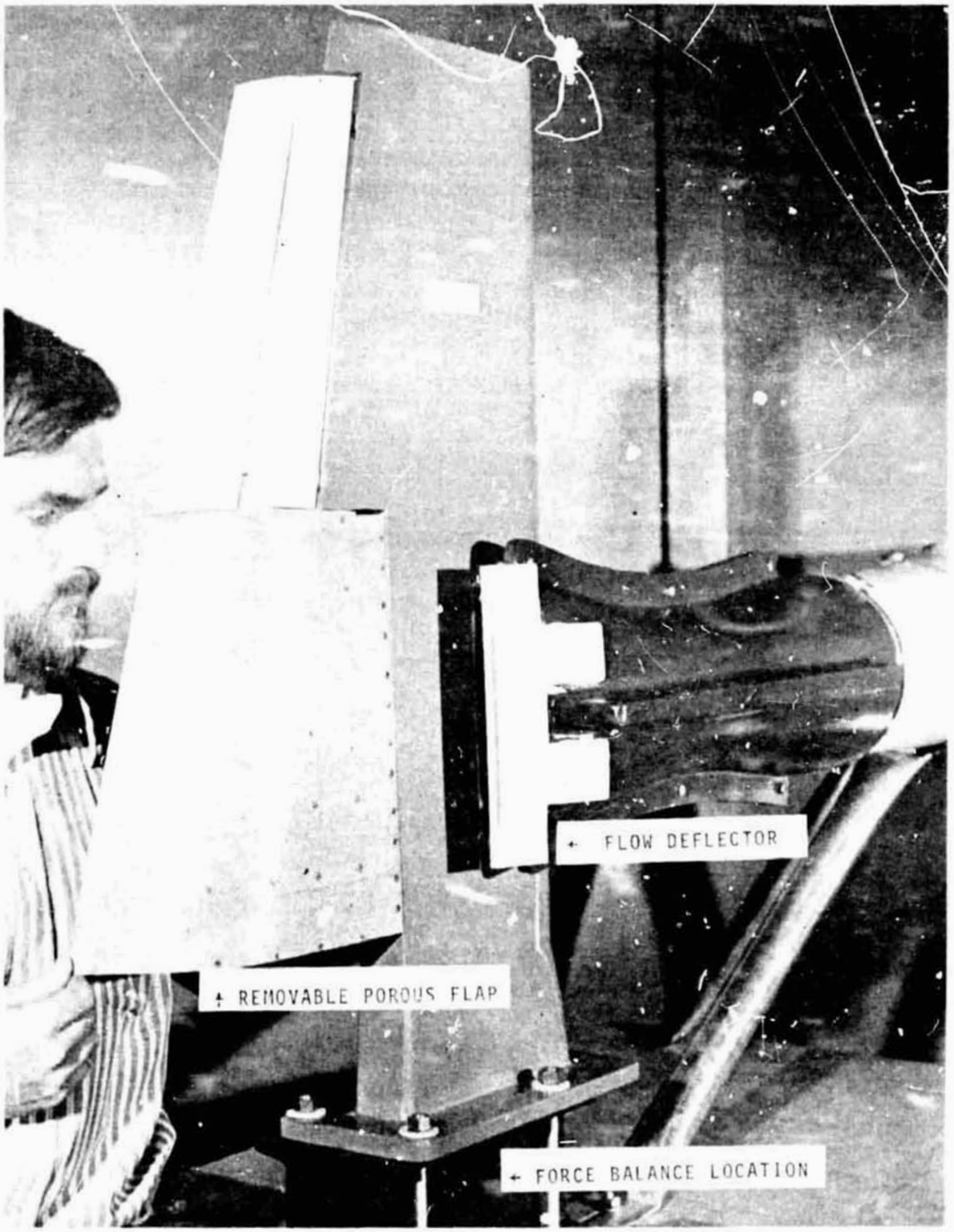

Figure 6.- Aero Commander USB model.

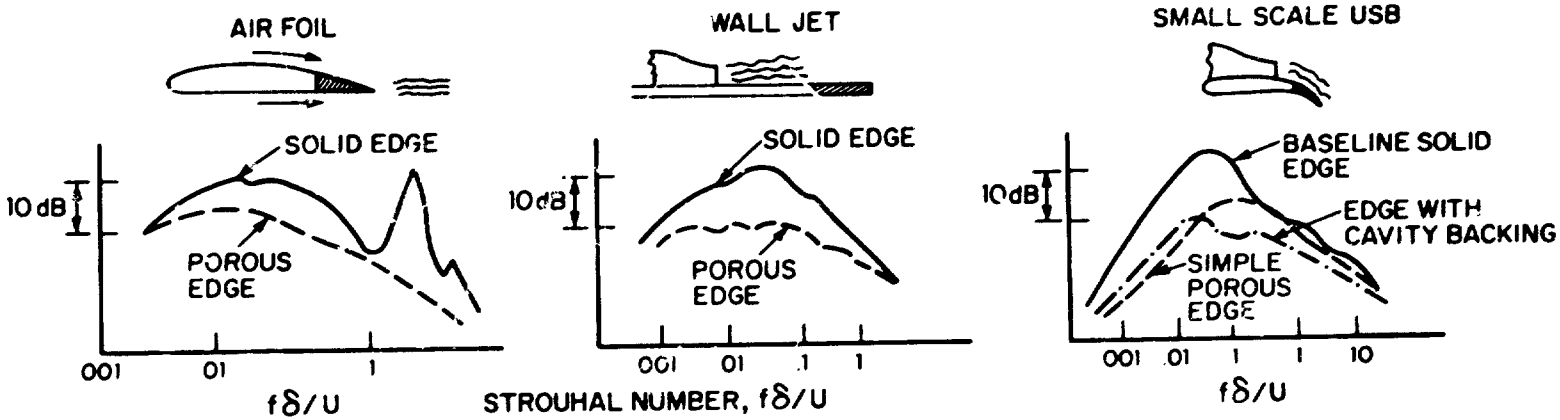

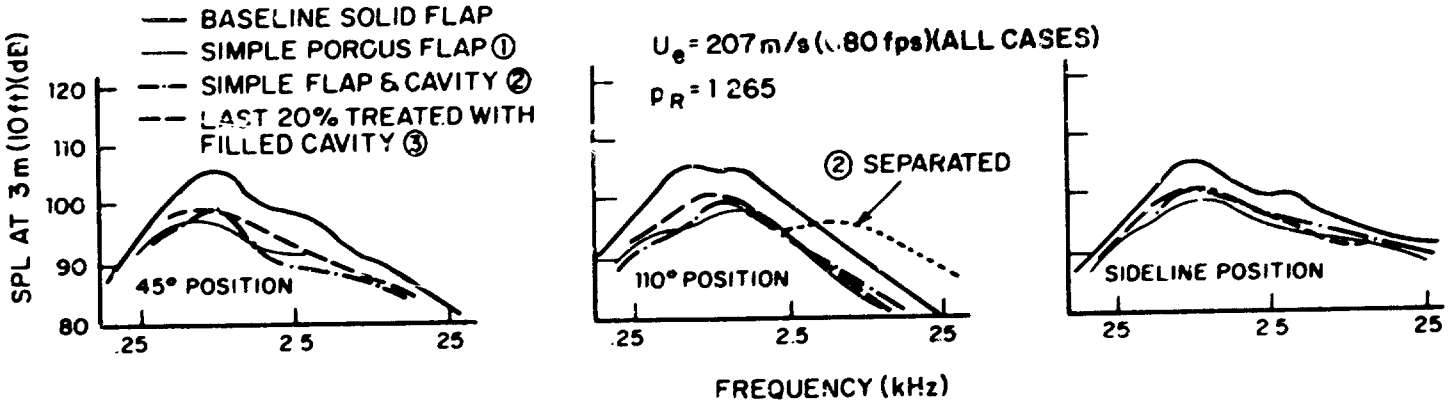

Figure 7.- Summary of noise reduction with porous edges.

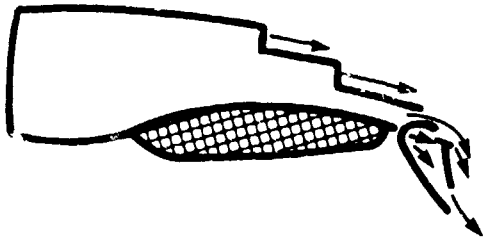

SCHEMATIC OF BASIC CONCEPT

HYDRODYNAMIC: RATE OF MIXING CHANGED TO REDUCE LARGE VORTEX PAIR.
- REDUCES TURBULENCE SCALE

ACOUSTIC: HIGH FREQUENCY NOISE CAN BE SHIELDED.

EFFECTS OF SLOTS

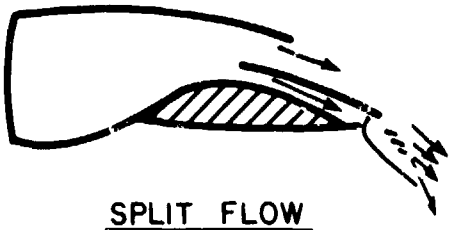

SPLIT FLOW NOZZLE

TURNING FLAP DETAIL

7 SLOTS

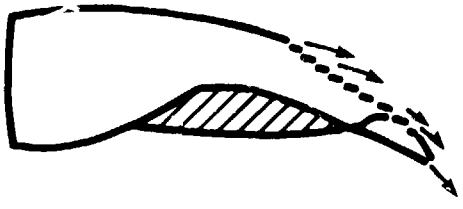

14 SLOTS

MULTI-SLOT NOZZLES

Figure 8.- Nozzle modifications.

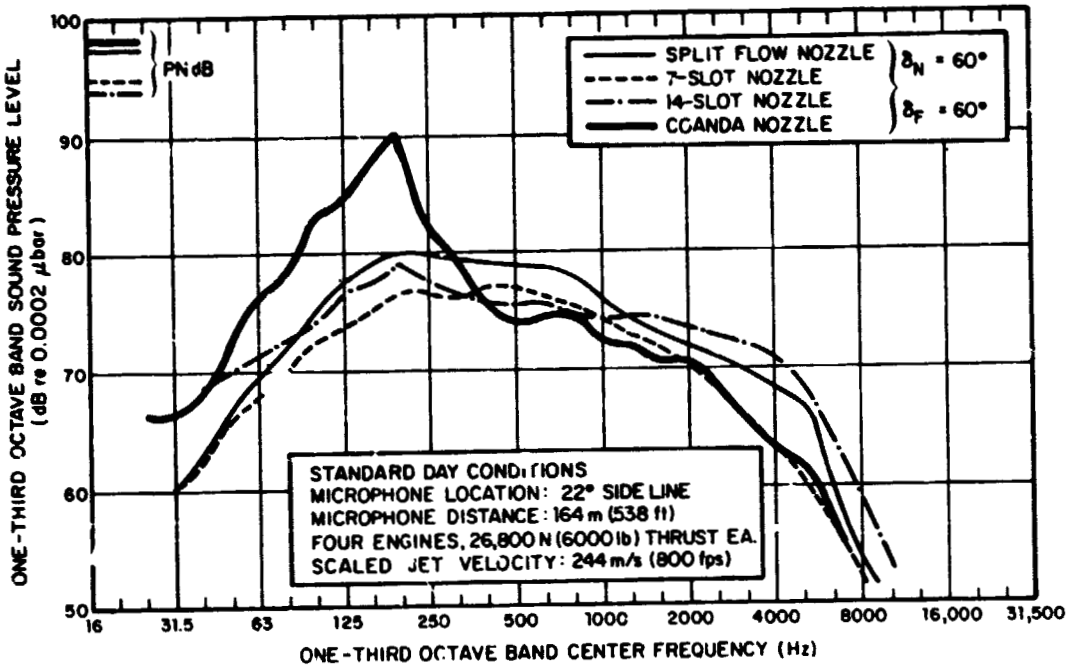

(a) Community noise.

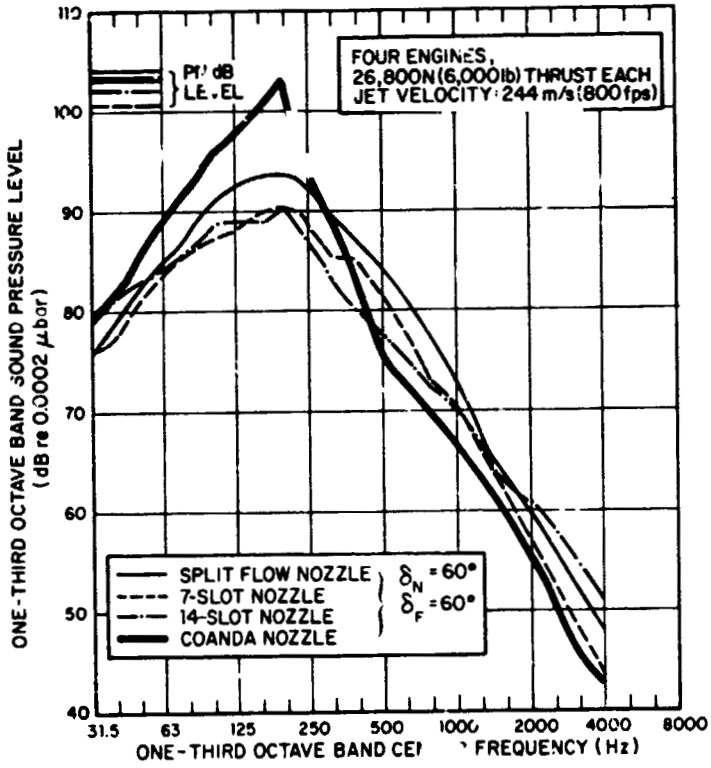

(b) Cabin interior noise.

Figure 9.- Noise reduction with multi-slot nozzles.

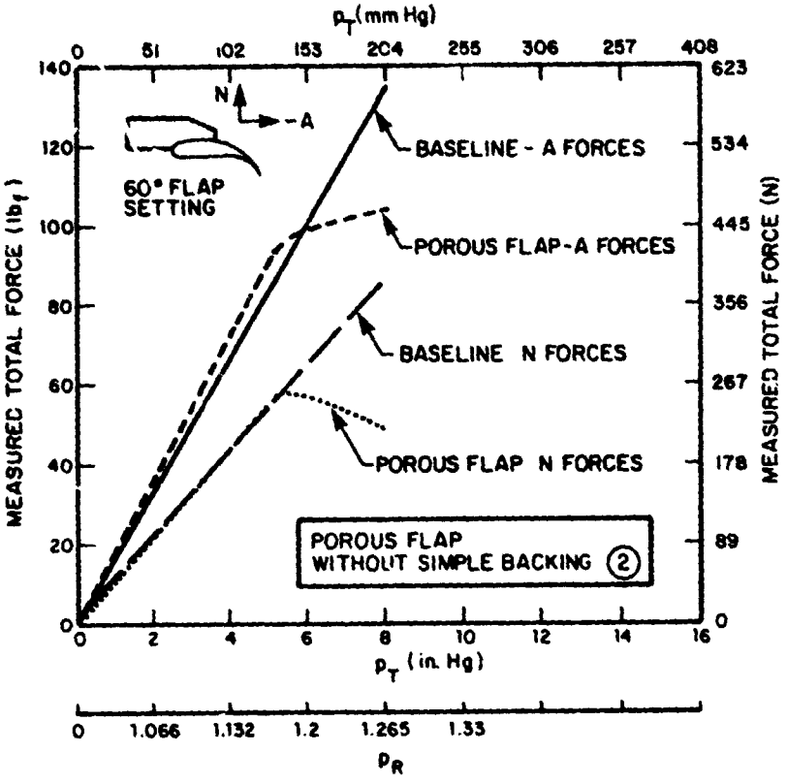

Figure 10.- Velocity dependence on porous flap forces.

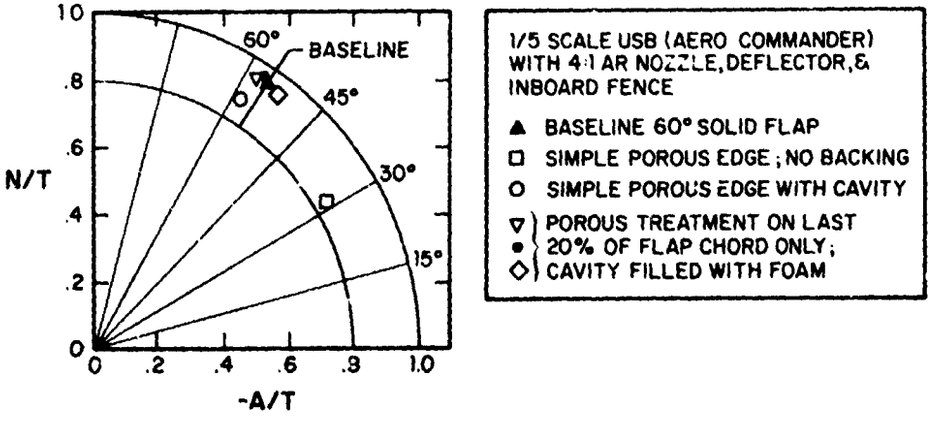

Figure 11.- Static turning of porous flap configuration.

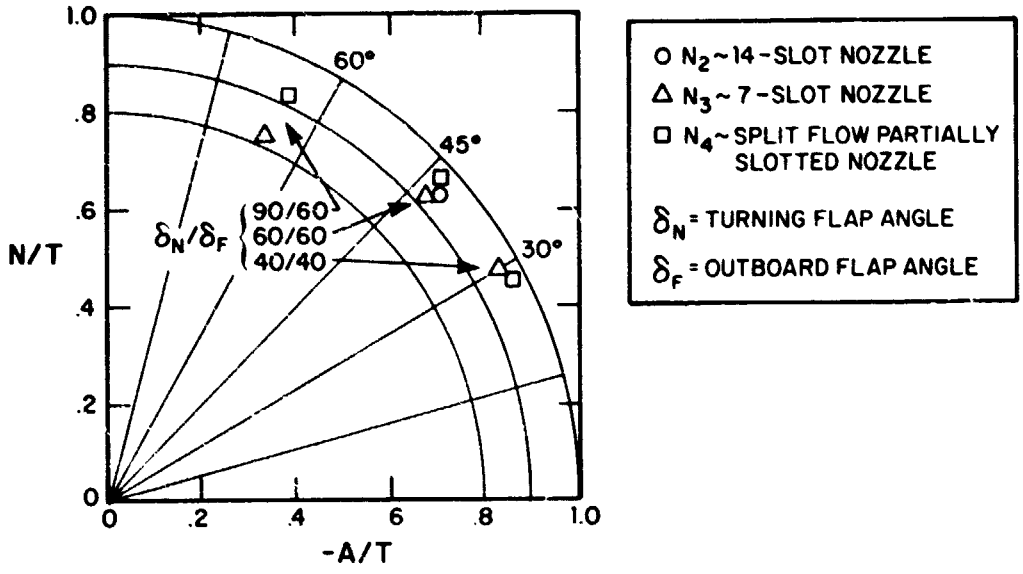

Figure 12.- Static turning of multi-segment nozzles on USB configuration.

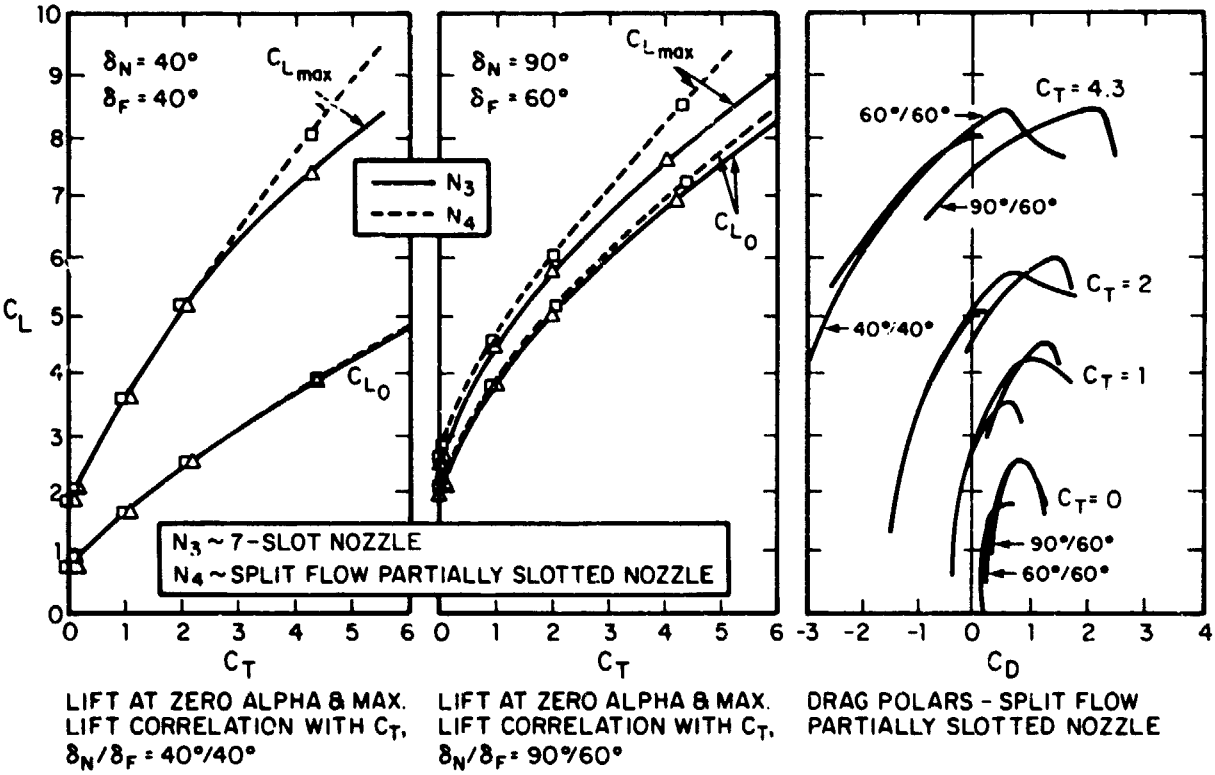

LIFT AT ZERO ALPHA & MAX. LIFT CORRELATION WITH C_T, δ_N/δ_F = 40°/40°

LIFT AT ZERO ALPHA & MAX. LIFT CORRELATION WITH C_T, δ_N/δ_F = 90°/60°

DRAG POLARS - SPLIT FLOW PARTIALLY SLOTTED NOZZLE

Figure 13.- Aerodynamic performance of multi-segment nozzle on USB configuration.

EBF NOISE REDUCTION THROUGH NOZZLE/FLAP POSITIONING*

Y. Kadman and K.L. Chandiramani
Bolt Beranek and Newman Inc.

SUMMARY

Results are presented of an experimental and analytical study of the dependence of Externally Blown Flap (EBF) noise on the relative position and shape of engine exhaust nozzle. Tests, conducted on a 1/15 scale model of a triple-slotted EBF system, indicate that a significant reduction (of up to 10 to 15 dB for no forward speed case and of up to 5 to 10 dB for forward speed case) is possible in the low frequency (around 63 Hz) region of the noise spectrum of the full scale device for small nozzle/flap separation distances. The overall acoustic performance, measured in PNdB, does not exhibit significant reductions. The analysis of the EBF noise is carried out for two limiting cases: (1) a turbulent jet being turned by a rigid corner, and (2) an isolated airfoil in a free jet. The analytical results also suggest that low frequency noise can be reduced by placing the nozzle close to the flow-turning elements.

INTRODUCTION

The noise from an integrated propulsive lift system arises from the engine and from the exhaust flow interacting with lift-augmenting flaps. Noise goals established for jet-powered STOL aircraft incorporating the propulsive lift concepts of under-the-wing externally blown flap (EBF), over-the-wing (OTW) blown flap (Coanda flap), internally blown flap, augmentor wing, or modifications of the above concepts require that the noise from the exhaust flow/lifting surface interactions be reduced substantially. Since muffling of these sources is not feasible, the generation of noise must be minimized. This requires an understanding of how noise is generated by turbulent flow interacting with flap-like surfaces, and what physical parameters (such as jet velocity, eddy size, etc.) affect the noise. Such an understanding is now sufficiently in hand to allow one to systematically seek methods for modifying the appropriate physical parameters in order to accomplish a reduced source level. However, one must be constrained in this pursuit by the fundamental necessity of maintaining adequate lift augmentation of the engine/flap system.

It is within these constraints that the present effort was undertaken to explore the effect of one parameter - the nozzle/flap separation - on the acoustic and aerodynamic performance of an EBF system.

19

*The above work was supported by contract from the NASA Lewis Research Center.

PAGE INTENTIONALLY BLANK

The experimental part of this effort was carried on a 1/15 scale model of a triple-slotted EBF system. The acoustic performance of the model was measured for a range of X/D from 0 to 3. Two exhaust nozzles - one round and one rectangular (Aspect ratio = 3.5) - were tested. All the acoustic data were compared at constant lift force.

The test results show that a reduction of up to 15 dB is possible in the low frequency (around 63 Hz) region of the noise spectrum of the full scale device for small nozzle/flap separation distances. The overall acoustic performance, when measured in PNdB, did not exhibit significant reductions.

The achieved large reductions of low frequency noise are considered important since one of the main problems associated with EBF systems is the high levels of noise and vibration inside the aircraft.

The analysis of the EBF noise problem was carried out for two limiting cases. The first case is that of a turbulent jet being turned by a rigid corner, and the second case is that of an isolated airfoil in a free jet.

The results of the analysis for both cases show that reduction of low frequency noise can be achieved by placing the nozzle close to the flow-turning elements.

Flap noise for EBF systems is dominated by three noise source mechanisms:

- Fluctuating forces on the whole flap (i.e., large scale fluctuations)
- Small scale pressure fluctuations at the leading edge of those flaps exposed to high velocity
- Trailing-edge noise from the flaps turbulent boundary layer and wake.

Secondary mechanisms are thought to be reflections of jet noise and surface-generated flow noise.

We expect the large scale fluctuations to determine the low frequency noise under investigation.

EXPERIMENTAL STUDY

Facility, Model and Instrumentation

The experimental phase of this effort was carried out in BBN's large wind tunnel facility in Cambridge, Massachusetts. For these experiments, the wind tunnel was fitted with a 28- by 40-in. nozzle which allows open jet velocities of up to 92 m/s (300 ft/sec). A compressor, with flow capacity of 3 m^3/min (6000 ft^3/min) at 103 400 Pa (15 psi) overpressure, supplied the high pressure air to the propulsive nozzle. A muffler on the high pressure line assured quiet flow to the EBF model. The tunnel test chamber was in the anechoic mode of operation. A detailed description of this high performance acoustic/aerodynamic test facility is given in reference 1.

The EBF model used in these tests was a triple-slotted type with 0.4-m (16-in.) flap span. Figure 1 is a drawing of the flap arrangement, showing both the takeoff (0^o-20^o-40^o) and landing (15^o-35^o-50^o) flap configurations. Only the takeoff configuration was tested in these series of experiments.

The model is a 1/15 scale model of an inboard engine nacelle and wing section designed and tested previously by NASA Langley Research Center. Table I summarizes the important dimensions.

The size of the nozzles that simulated the engine jet was arrived at by assuming that the full scale engine will produce 44 480 N (10 000 lb) of thrust at engine jet velocity of 244 m/sec (800 ft/sec) (pressure ratio of 1.35).

For cold flow of air, the above requirements will dictate a full scale nozzle area of 0.62 m^2 (6.67 ft^2) or a diameter of 0.89 m (35 in.). The model nozzle area will then be 0.003 m^2 (4.4 in^2).

Two nozzles were tested, a circular one, having a diameter of 0.06 m (2.37 in.) and a rectangular one, 0.03 by 0.1 m (1.12 by 3.9 in.), having an aspect ratio of 3.5. The maximum thrust that these equal area nozzles can develop at jet speeds of 244 m/sec (800 ft/sec) is 198 N (44.5 lb).

For the experiments, the EBF model was mounted on an extension of the wind tunnel nozzle floor and the high pressure air was ducted to the propulsive nozzle through an airfoil shaped duct so that interference between the main tunnel jet and ducting would be kept to a minimum. The location of the EBF model with respect to the stationary nozzle was varied by using the X-Y table, and an additional rotating table was used to adjust the angle of attack.

The instrumentation used in the tests consisted of two Band K 1/4 in. type 4135 microphones, one located 2.4 m (8 ft) below the wing and the other at an angle of 22^o below the wing planform, at a distance of 3.05 m (10 ft). This second location corresponds to a side line test point as defined in reference 2.

Test Description

Two series of tests - one static and the other with forward speed - were performed. The investigation was confined to the range X/D = 0 to 3, with Y/D between 1/2 and 1. Larger values of Y/D are impractical since part of the flow misses the flaps and the lift decreases drastically.

The forward speed tests were performed with simulated forward velocity of 44 m/sec (145 ft/sec) and nozzle flow velocity of 152 m/sec (500 ft/sec) and 192 m/sec (630 ft/sec). All tests were carried out with the round nozzle and then repeated with the rectangular nozzle.

Criteria for EBF Performance Evaluation

The basic premise that underlies the present effort is that when a parametric noise study of a propulsive lift device is conducted, the results should be compared at constant lift force. Although a more comprehensive evaluation scheme that includes power requirements and the size of the various elements

of the system may be more useful, the constant-lift comparison is a first step in that direction.

Since the lift coefficient of different systems - and even of the same system under different geometric conditions - vary, the lift force was corrected in all tests to 198 N (44.5 lb) - which corresponds to the maximum possible lift force which can be obtained from the nozzles used at 244 m/sec (800 ft/sec). This value is somewhat arbitrary but it only serves as a common basis for comparison of the acoustic performance.

The effects of the lift corrections on the noise generated by the EBF model was computed by using scaling laws. One has two options of calculating the effects of these lift corrections on the noise. The first is to assume increased jet speed (and a higher pressure ratio) and the second is to increase nozzle area at a constant jet speed.

The thrust, or lift, and the noise from an EBF obey approximately the following:

$$\text{Thrust} \propto (\text{nozzle area})\ (\text{jet velocity})^2$$

$$\text{Noise} \propto (\text{nozzle area})\ (\text{jet velocity})^6$$

Doubling of the thrust, if achieved by increasing the velocity by a factor of $\sqrt{2}$, will "cost" 9 dB in additional noise, whereas by doubling the nozzle area the price will be only 3 dB.

It was decided therefore that the lift correction will be done at constant velocity (244 m/sec (800 ft/sec)) for all nozzle/flap configurations.

It should be noted here that the above procedure contains the implicit assumption that the lift coefficient C_L does not change with the nozzle area increase, but this is true only for small area changes. If the velocity is manipulated to increase the lift, no such assumption has to be made.

The implications of these lift correction methods on the power plant of the aircraft and the relative merit of each needs further study.

Test Results

Table II summarizes the predicted community noise in two locations, flyover and sideline - both at a distance of 152 m (500 ft) from a 88 960-N (20 000-lb) thrust engine. Inspection of the table shows that when the noise is measured in PNdB, the acoustic performance of the EBF improves as one progresses to larger X/D. One should note, however, that the differences between the lowest and highest PNdB values are small (on the order of 2 dB or less) and are comparable to the experimental spread.

The individual pressure spectra for all of the 64 cases indicated in table II are reported in reference 3. Here, only a few selected spectra are displayed in figures 2 through 7. As in table I, the spectra refer to the full

scale situation (distance of 152 m (500 ft) from a 88 960-N (20 000-lb) thrust engine) and were obtained from the model spectra by the following procedure:

$$SPL_F(f_F) = SPL_M(f_M) + 60 \log \frac{U_{J,F}}{U_{J,M}} - 20 \log \frac{r_F}{r_M} + \log \frac{A_F}{A_M} \quad (1)$$

$$\frac{f_F}{f_M} = \frac{U_{J,F}}{U_{J,M}} \frac{d_M}{d_F} \quad (2)$$

Here, subscripts F and M refer to the full scale and model variables. SPL is the sound pressure level, f is the frequency, U_J is the jet velocity. r is the distance to the observation point, A is the nozzle area and d is the characteristic nozzle dimension.

Each of the figures 2 through 7 shows the variation in the noise level as a function of the nozzle/flap separation for a constant Y/D value. As mentioned before, the flaps were set at takeoff configuration (0°-20°-40°). Figures 2, 3, and 4 refer to the case of no forward speed, whereas figures 5, 6, and 7 refer to the case of a forward speed of 44 m/sec (145 ft/sec) for the same configurations.

The effect of nozzle/flap separation is evidenced clearly in the low frequency region of these spectra - a region which contributes little to the PNdB scale. The range of variation spans about 15 dB with no forward velocity and about 10 dB with forward velocity, and offers promise for significant alleviation of the interior noise and vibration problems.

The X/D dependence of overall noise (in PNdB) and of low frequency noise in one octave band (31.5 Hz to 63 Hz) is compared in figures 8 and 9 for the configurations selected for figures 2 through 7. Figure 8 shows the comparison for the case of no forward speed, and figure 9 shows the comparison for the case of a forward speed of 44 m/sec (145 ft/sec). As is evident from these figures, the reduction in low frequency noise with lower X/D is significantly larger than the associated slight increase in overall noise.

The nozzle shape did not seem to affect the noise. Some improvement in the low frequency region was detected but further study is needed to confirm these trends.

The effect of forward velocity was also found to be about the same on both nozzle shapes and, in general, reduced the noise by about 2 to 5 dB. As reported earlier (ref. 4), forward speed effects depend on the flap angles and, in general, do not reduce the noise by what may be expected from relative velocity arguments.

ANALYTICAL STUDIES

Predominant EBF noise generation mechanisms are dipole-like force fluctuations of the entire flap or fluctuations at the leading edge. Additional

sources, especially in the high frequency range occur at the trailing edge of the flaps. In the present effort, the analytical studies of the EBF noise were carried out on two limiting cases: (1) sound radiated by gross turning forces due to a turbulent jet being turned by a rigid corner, and (2) sound radiated by fluctuating lift at the leading edge of a thin isolated airfoil in a free jet.

These analyses are described in detail in reference 3. Here, we merely outline the basic ideas behind the analyses and present the calculated results.

Sound from Fluctuations in Gross Turning Forces

The EBF configuration is modelled as a simple smoothly faired corner with a jet against the concave part of the corner (fig. 10). It is assumed that in turning the corner, the only major change suffered by the total momentum flux across the jet cross-section is the change in its direction by angle ψ, with no substantial change in its magnitude or in its various statistics. On the basis of this assumption, the spectral density $\Phi_F(\omega)$ of the fluctuating force experienced by the flap is related to the spectral density $\Phi_M(\omega)$ of the fluctuating momentum flux in the flow direction by:

$$\Phi_F(\omega) = \Phi_M(\omega) \left\{2 \sin\left(\frac{\psi}{2}\right)\right\}^2 , \qquad (3)$$

where ψ is the turning angle of the flow. The above relation is likely to be valid only for large eddies, i.e., for low frequencies.

Next, the experimental data for round, subsonic jets (refs. 5 through 8) are used to estimate $\Phi_M(\omega)$ for various values of the dimensionless parameter X/D, where X is the axial location of the turning point and D is the nozzle diameter. For a given value of X/D, $\Phi_M(\omega)$ is a function of the flow dynamic head, the mean velocity profile; the spectral density of the fluctuating velocity in the axial direction; and a typical correlation area over the jet cross section, of the axial velocity fluctuations.

Finally, for estimating the noise radiated to the observation point $\underline{r}$, the fluctuating force on the flap is modelled as a whole-body, coherent, acoustic dipole source, possibly compact. Spectral density $\Phi_p(\underline{r},\omega)$ of the radiated pressure is given by:

$$\Phi_p(\underline{r},\omega) = \frac{\Phi_F(\omega)}{16\pi^2 r^2} \quad \frac{k_a^2}{1 + k_a^2 b^2} \quad D(\theta) , \qquad (4)$$

where k_a is the acoustic wavenumber at frequency ω, $D(\theta)$ is the directivity factor equal to $\cos^2\theta$ when θ is referred to the force axis and b is a typical dimension (semi-chord) of the source.

Figure 11 shows the estimated noise for the following conditions: nozzle diameter D = 0.9 m (3 ft); flap X/D = 2,4,6; turning angle $\psi = 60^{o}$; exit velocity = 213 m/sec (700 ft/sec), observation point 152 m (500 ft) radius (flyover).

Sound from Fluctuating Lift at Leading Edge

An airfoil of chord 2b and infinite span is considered to lie in a round turbulent jet (see sketch in fig. 12). The airfoil is assumed to lie in the x-y plane (i.e., z = 0). Its leading edge coincides with the x-axis and is at a distance X downstream of the jet nozzle.

A typical wave of fluctuating velocity w(x,y,t) in the vertical z direction in the jet impinges on the airfoil and creates a corresponding wave of fluctuating lift on the airfoil, concentrated mainly at the leading edge. The velocity wave is given by:

$$w(x,y,t) = w_0 \exp \{i(k_1 x + k_2 y - \omega t)\} \quad , \tag{5}$$

and the corresponding lift L(y,t) (of dimension force/length) is given by:

$$(L(y,t) = 2\pi\rho b w_0 \; U \; T(\tfrac{\omega}{U} ,k_2) \quad \exp \{i(k_2 y - \omega t)\} \quad , \tag{6}$$

where w_0 is the amplitude of the incident upwash wave, k_1 and k_2 are the wavenumber components of the wave, ρ is the medium density, $U = \omega/k_1$ is the mean velocity of the jet (dependent on the nozzle/airfoil separation X, and on the spanwise direction y) and $T(k_1,k_2)$ is the dimensionless response function (taken from ref. 8).

The experimental data of references 5 through 8 are used again to generate a statistical model of the wavenumber spectrum $\Phi_w(k_1,k_2)$ of the upwash disturbance and the corresponding spectrum $\Phi_T(k_2)$ of the leading edge fluctuations.

Finally, the radiated noise is calculated on the basis of regarding the leading edge lift fluctuations as statistically independent distribution of point dipoles of spanwise varying dipole strength. For high frequencies (for which $2b/\lambda > 1$, λ = acoustic wavelength) a correction factor similar to that in equation 4 accounting for noncompact nature of lift distribution in the chordwise direction (only) is introduced.

Figure 12 shows the estimated noise for the following conditions: nozzle diameter D = 0.9 m (3 ft); chord 2b = 0.9 m (3 ft); X/D = 2,4,7.5,10; exit velocity = 244 m/sec (800 ft/sec); observation point 152 m (500 ft) radius (flyover).

Discussion

Both figures 11 and 12 indicate the same trend for low frequencies, i.e., less noise for closer nozzle/flap separations. For higher frequencies both the

figures indicate trends not suggested by experimental data. Figure 11 suggests higher high frequency noise for larger X/D, contrary to experiments. The assumption, and elementary estimation, of the whole body force is undoubtedly not valid for high frequencies where a typical eddy size is smaller than the flap dimensions. Although high frequency noise is seen to be less dependent on X/D in figure 13, the noise levels estimated are higher than those indicated by data. Likely reasons for higher estimated noise are: (1) In the approximate calculations performed, adequate account could not be taken of relatively rapid decay, with high $|k_2|$, of the lift response function $|T(k_1,k_2)|$ (this aspect is of less critical importance at lower frequencies). (2) $T(k_1,k_2)$ of reference 9 (and of related work) is based on the assumption that the impinging gust is infinitely extended in the z direction. Such an assumption may not be valid for small scale jet turbulence involved at higher frequencies.

CONCLUSIONS

The noise output of an EBF system in takeoff configuration was shown to be strongly dependent on the flap/nozzle configuration only at the low frequency region on the spectrum. The high frequency region, which dominates the various measures of community noise levels is only weakly affected by the nozzle/flap separation or the nozzle shape.

It is found that simple analytical models produce good approximations and trend predictions for the so-called "whole body dipole" noise source of an EBF system. This source dominates in the low frequency part of the spectrum and presents severe noise and vibration problems to the aircraft.

REFERENCES

1. Kadman, Y. and Hayden, R.E.: Design and Performance of High-Speed Free-Jet Acoustic Wind Tunnel. AIAA Paper 75-531, Hampton, Va., 1975.

2. Noise Standards: Aircraft Type and Airworthiness Certification. Federal Aviation Regulations, pt. 36, FAA, June 1974.

3. Kadman, Y., *et al.*: Exploratory Study of EBF Noise Reduction through Nozzle/Flap Positioning. BBN Report No. 2894, January 1976.

4. Dorsh, R.E.: Externally Blown Flap Noise Research. SAE Air Transportation Meeting, Dallas, Texas, 1974.

5. Laurence, J.C.: Intensity, Scale, and Spectra of Turbulence in Mixing Region of a Free Subsonic Jet. NACA Report 1292, 1956.

6. Bradshaw, P., Ferriss, D.H., and Johnson, R.F.: Turbulence in the Noise-Producing Region of a Circular Jet. AGARD Report 450, April 1963.

7. Wooten, D.C., *et al.*: A Study of the Structure of Jet Turbulence Producing Jet Noise. NASA CR-1836, July 1971.

8. Davies, P.O.A.L., Fisher, M.J. and Barratt, M.J.: The Characteristics of the Turbulence in the Mixing Region of a Round Jet. *J. of Fluid Mechanics*, 15, 1963.

9. Filotas, Y.T.: Theory of Airfoil Response in a Gusty Atmosphere, Part I - Aerodynamic Transfer Function. UTIAS Report No. 139, October 1969.

TABLE I.- EBF MODEL AND FULL SCALE DIMENSIONS

	Wing chord at inboard nacelle		First flap chord		Second flap chord		Third flap chord	
	m	in.	m	in.	m	in.	m	in.
Full scale aircraft	153	3.83	22.96	0.58	30.6	0.78	34.43	0.87
Model	10.2	.26	1.53	.04	2.04	.05	2.30	.06

TABLE II.- EBF NOISE AT CONSTANT LIFT (IN PNdB)

[88 960-N (20 000-lb) thrust engine at 152 m (500 ft) distance; U_J = 244 m/sec (800 ft/sec). Lift corrections performed by changes in nozzle area]

	No Forward Speed							
	Round Nozzle				Rectangular Nozzle			
	Flyover		Sideline		Flyover		Sideline	
X/D	Y/D		Y/D		Y/D		Y/D	
	1/2	1	1/2	1	1/2	1	1/2	1
0	100.4	99.4	96.2	96.4	100.8	96.8	95.2	96.1
1	99.9	98.5	95.8	96.0	99.4	96.1	94.8	95.7
2	99.4	97.6	95.3	95.6	98.0	95.5	94.4	95.4
3	98.8	96.8	94.8	95.2	96.6	94.8	94.0	95.1

	With Forward Speed U_∞ = 44 m/sec (145 ft/sec)							
	Round Nozzle				Rectangular Nozzle			
	Flyover		Sideline		Flyover		Sideline	
X/D	Y/D		Y/D		Y/D		Y/D	
	1/2	1	1/2	1	1/2	1	1/2	1
0	98.6	98.3	96.8	96.3	99.5	98.4	96.9	94.8
1	97.3	96.9	94.9	94.7	99.0	97.0	94.8	93.9
2	97.0	96.0	93.9	93.5	98.2	95.8	94.1	93.1
3	96.3	95.2	93.2	92.8	97.0	95.3	93.9	92.7

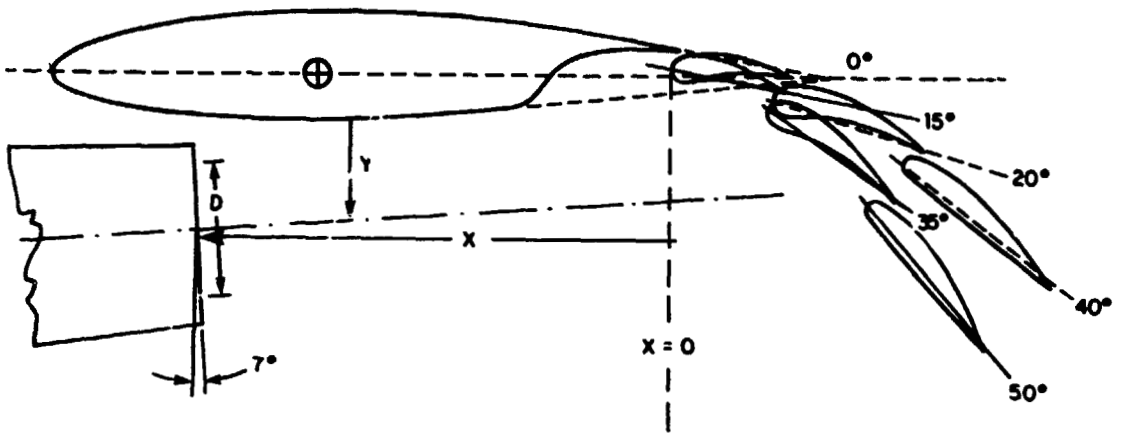

Figure 1.- EBF model geometry.

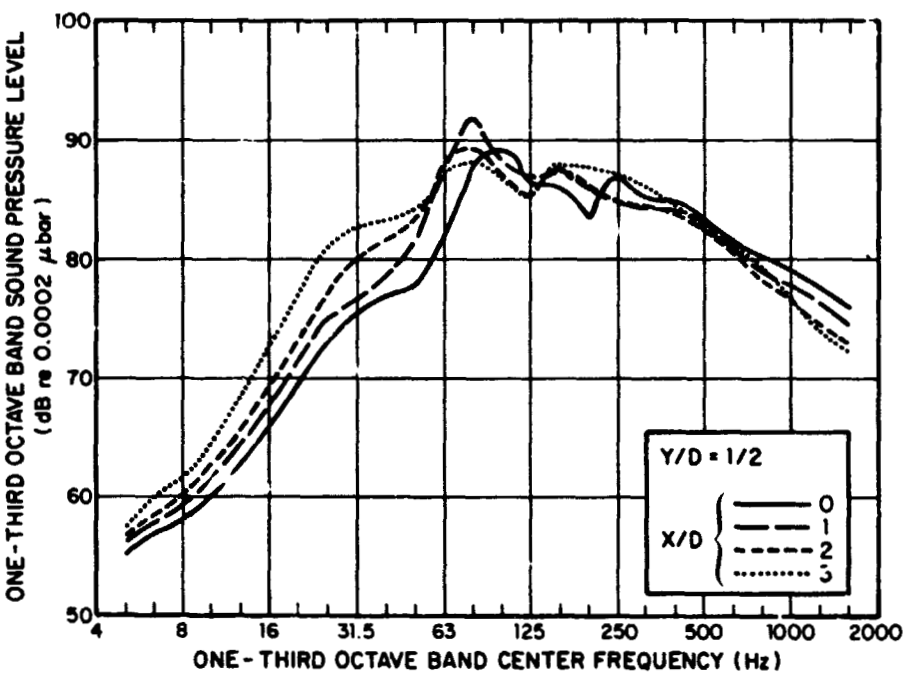

Figure 2.- Flyover noise spectra. Round nozzle; no forward speed; U_J = 244 m/s (800 ft/sec).

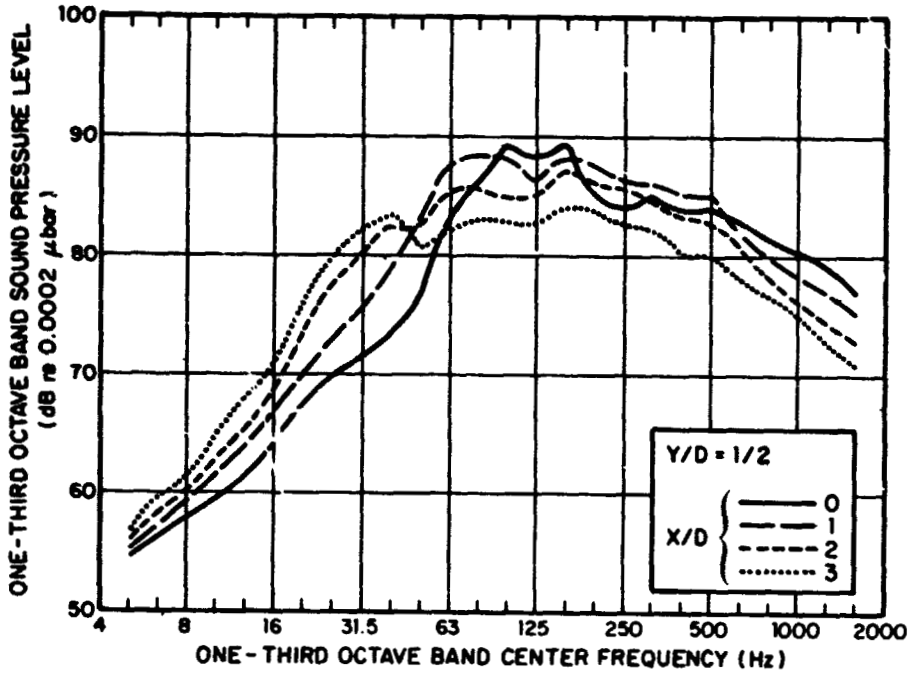

Figure 3.- Flyover noise spectra. Rectangular nozzle; no forward speed; U_J = 244 m/s (800 ft/sec).

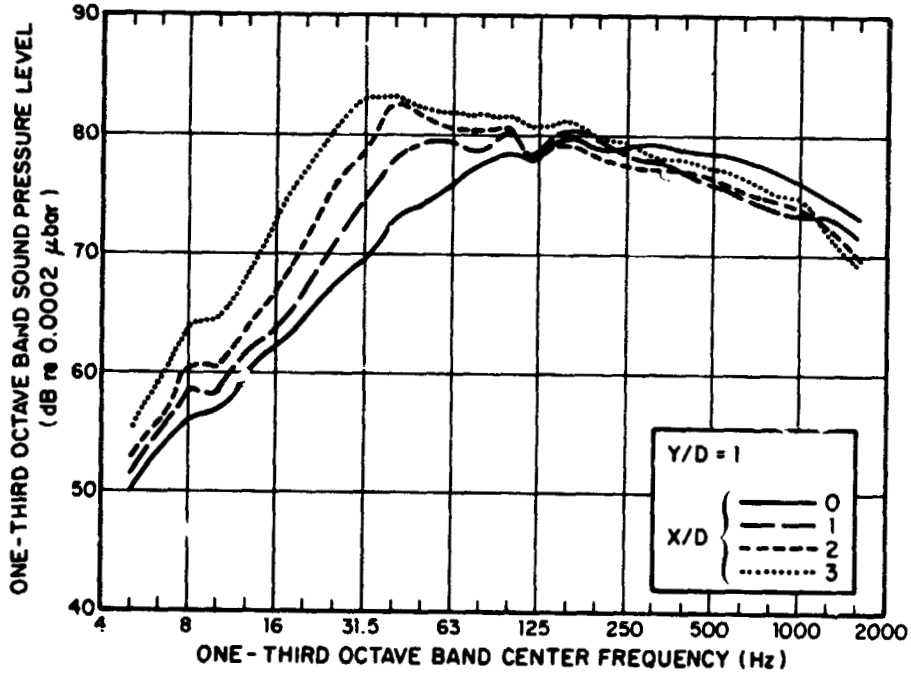

Figure 4.- Sideline noise spectra. Rectangular nozzle; no forward speed; U_J = 244 m/s (800 ft/sec).

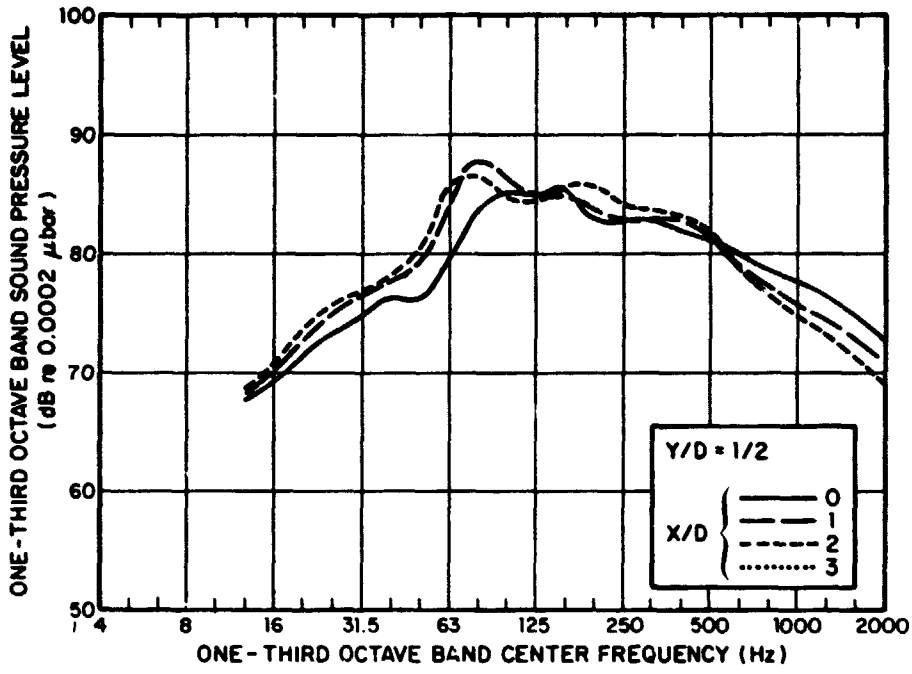

Figure 5.- Flyover noise spectra. Round nozzle; U_J = 244 m/sec (800 ft/sec); U_∞ = 44 m/sec (145 ft/sec).

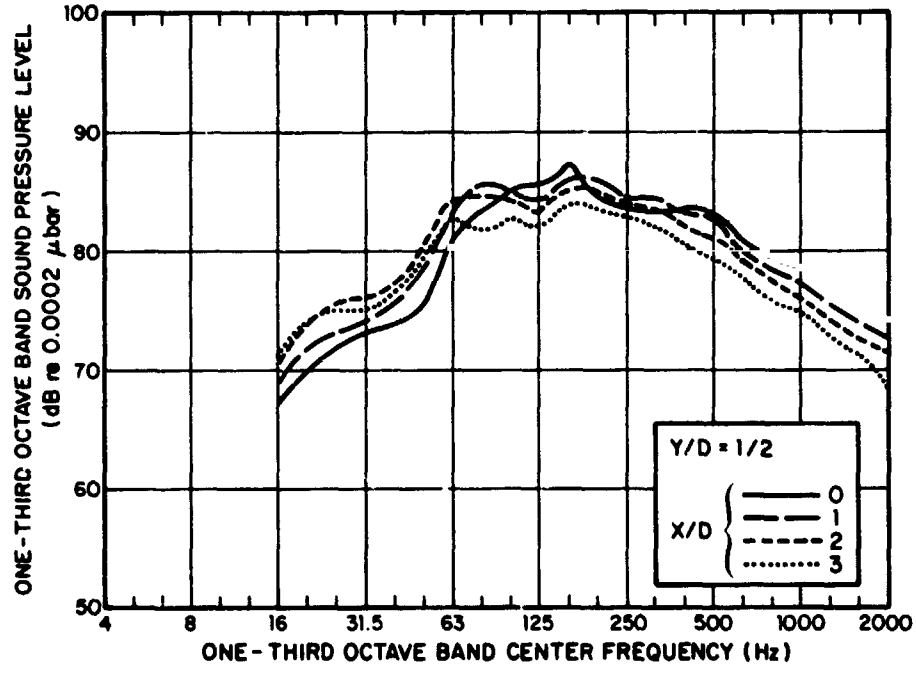

Figure 6.- Flyover noise spectra. Rectangular nozzle; U_J = 244 m/sec (800 ft/sec); U_∞ = 44 m/sec (145 ft/sec).

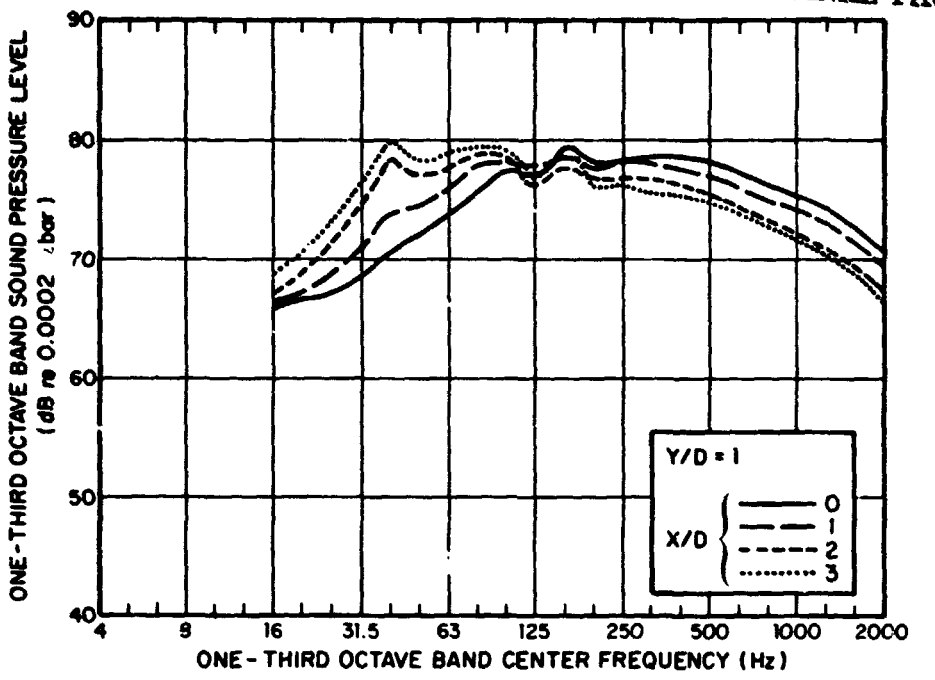

Figure 7.- Sideline noise spectra. Rectangular nozzle; U_J = 244 m/sec (800 ft/sec); U_∞ = 44 m/sec (145 ft/sec).

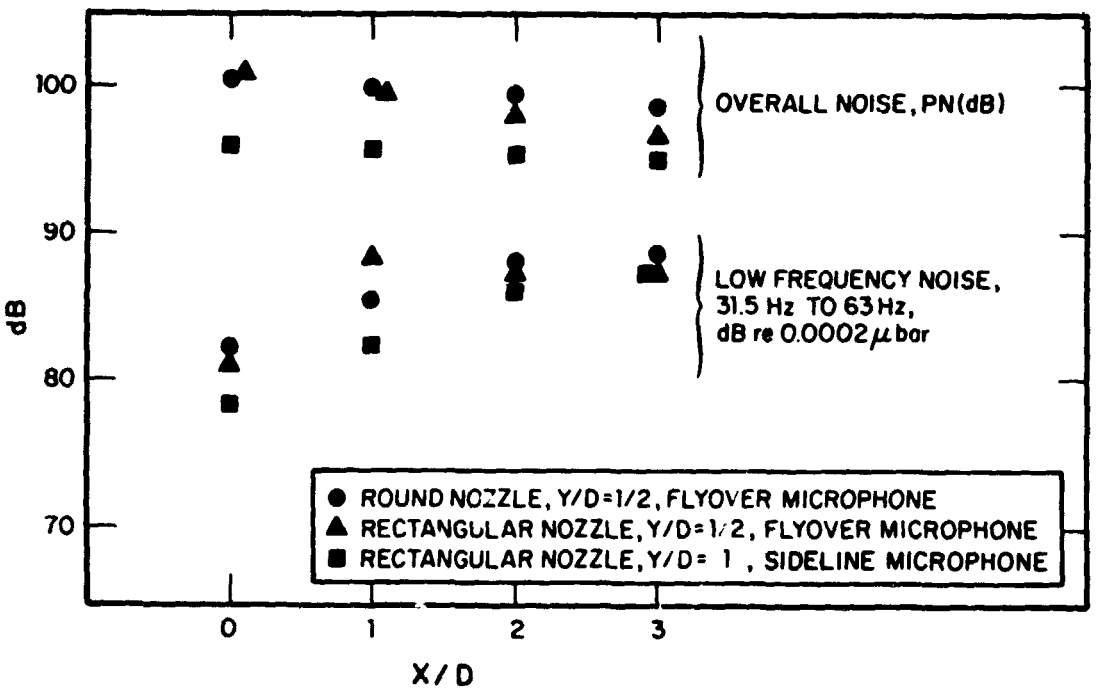

Figure 8.- X/D dependence of overall and low frequency noise; no forward speed.

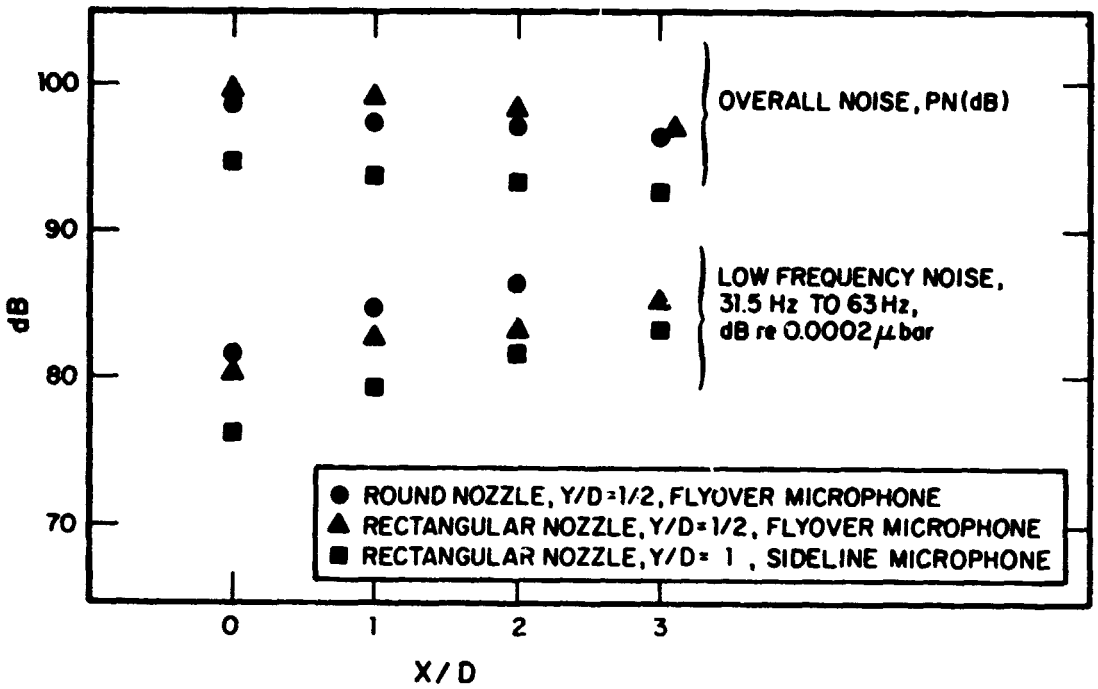

Figure 9.- X/D dependence of overall and low frequency noise; J_∞ = 44 m/sec (145 ft/sec).

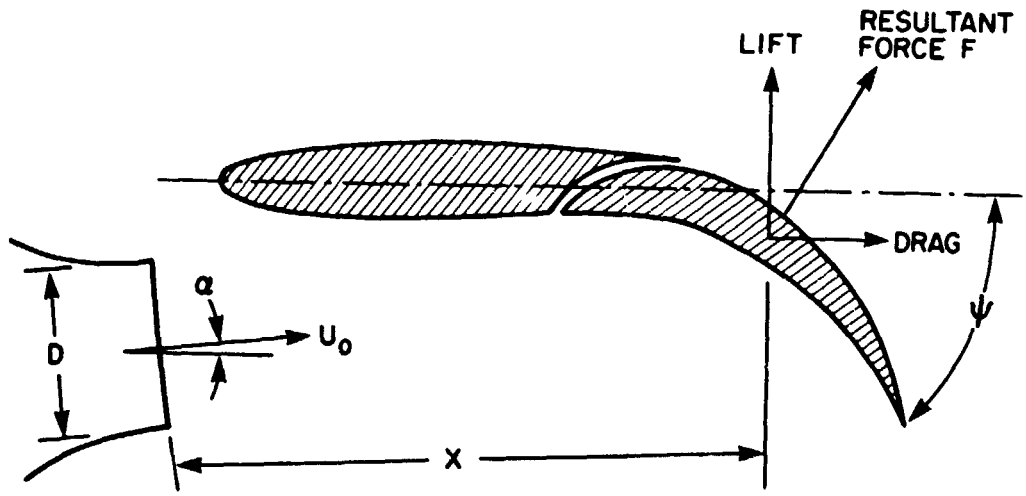

Figure 10.- Externally blown flap as a smoothly faired corner.

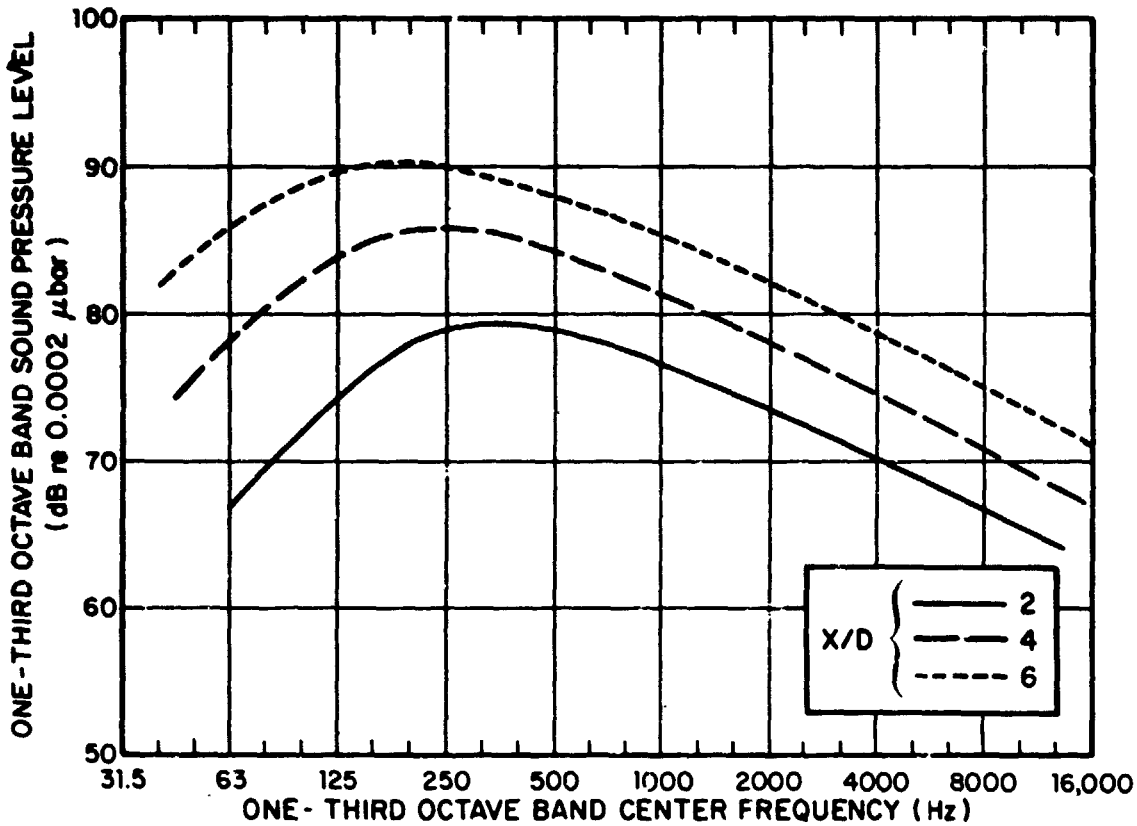

Figure 11.- Estimated noise from fluctuations in gross turning forces.

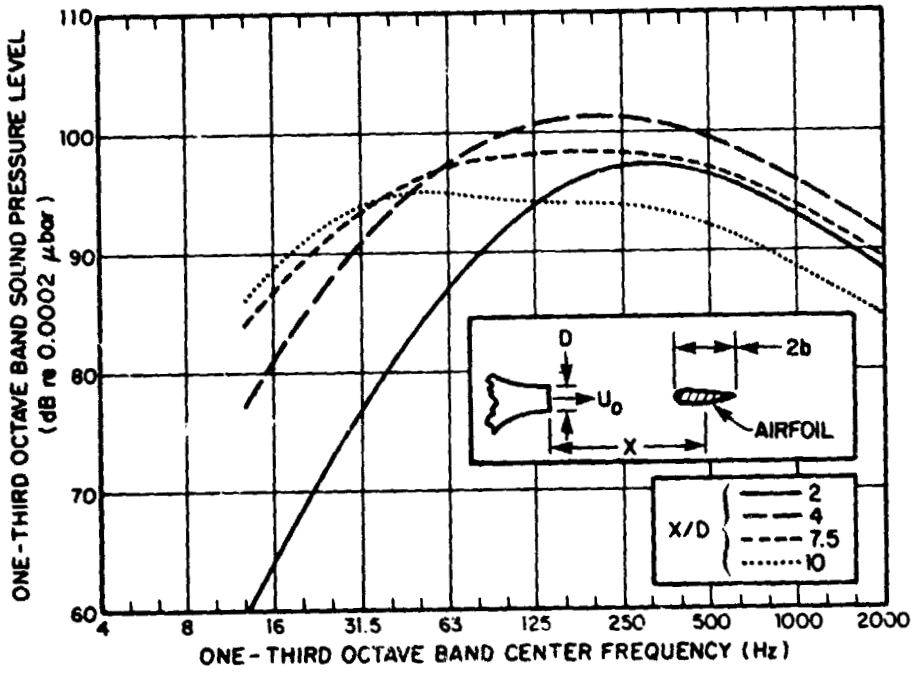

Figure 12.- Estimated noise from fluctuating lift at leading edge.

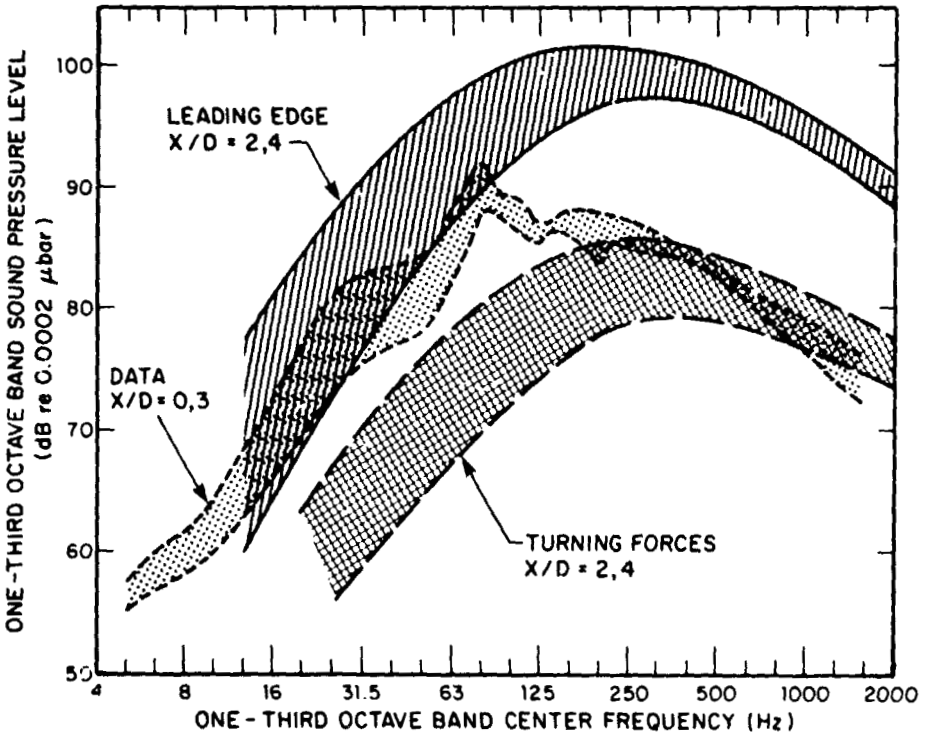

Figure 13.- Comparison of estimated noise and experimental data.

N78-24066

OVERVIEW OF THE QCSEE PROGRAM

Carl C. Ciepluch
NASA Lewis Research Center

INTRODUCTION

The objective of the QCSEE (Quiet, Clean Short-Haul Experimental Engine) Program is to develop propulsion system technology for future powered-lift short-haul aircraft. As the title of the program indicates, one of the specific objectives of the program is to develop technology that will permit the development of lower noise propulsion systems. Low noise is particularly important for short-haul aircraft because, by their very nature, these aircraft will operate out of small airports where the close surrounding community can be more easily disturbed. A second specific objective is to develop technology which will allow the production of propulsion systems that produce very low exhaust emissions. Because of the prospect of stringent future government regulations in this regard, it is important to minimize the emissions of future propulsion systems. And, finally, the QCSEE Program has the objective of providing acceptable propulsion system performance. This is a difficult task because low noise requirements generally result in performance penalties. However, it is a very important objective because of the recent interest in energy conservation and the need to provide a propulsion approach that will result in an economically viable short-haul aircraft.

In this paper an overview of the QCSEE Program is presented. Included in the overview will be a description of the technical requirements and the design features and characteristics of the two engines in the program. Finally, the progress made to date in the program will be reviewed.

Inasmuch as this paper is an overview of the QCSEE Program, the information presented is limited. For further details on the acoustic design of the engines, the reader is referred to reference 1. Further information concerning other areas of the QCSEE design can be found in reference 2.

POWERED-LIFT CONCEPTS

In the QCSEE Program propulsion technology applicable to two powered-lift concepts is being investigated. The externally blown flap is one concept being investigated (see fig. 1). The propulsion system for this concept is installed under the wing (UTW) in much the same manner as it is in many conventional aircraft. The second approach, commonly referred to as the upper surface blown flap powered-lift concept, is illustrated in figure 2. Here, the propulsion system is installed in an unconventional manner: the engines are mounted over

the wing (OTW). These alternative approaches have their advantages and disadvantages. The UTW concept, being more conventional, is simpler from both an aerodynamic and mechanical installation standpoint. But the OTW powered-lift concept offers the advantage of lower aircraft noise: The wing surface chields ground observers from much of the noise emanating from the aft end of the engine and also the powered-lift generated noise.

PROPULSION SYSTEM REQUIREMENTS

The general technical requirements established for the QCSEE engines are listed in table I. As shown, the noise limits set for the engines are quite low. In regard to exhaust pollutants, the engines are being designed to meet the proposed EPA 1979 emission standards that are intended to apply to conventional types of aircraft. This is because of the absence of any specific proposed standards for the short-haul, powered-lift type of aircraft. The thrust requirements are primarily a result of the desire to provide technology in the 88 960-N (20 000 lb) thrust class of engine and the use of the F101 engine core which generally has the capability for this thrust class.

Another challenging requirement of the QCSEE engines is the high installed thrust-to-weight ratios. One of the important aspects of the program is to reduce the installation thrust and weight penalties. To illustrate the improvement in thrust-to-weight ratio being sought, the thrust-to-weight ratio of the CF-6 engine used in the DC-10 is about 3.5. And finally, we have set relatively short dynamic response times for the QCSEE engines because short response time is required in short-haul, powered-lift propulsion systems.

UTW PROPULSION SYSTEM

A cross section of the UTW propulsion system, which also identifies the advanced technology features incorporated, is shown in figure 3. (For further detailed engine design information consult ref. 2.) As mentioned earlier, the F-101 engine core is used. The F-101 engine is being developed by the General Electric Company for use in the Air Force B-1 bomber. The engine core will employ a modified, preflight rating test (PFRT) combustor. In order to meet the stringent pollution goals in the program, a double annular, dome combustor is being adapted to the F-101 combustor envelope. This adaptation will be evaluated in combustor rig tests. The double annular, dome combustor concept is one of the more successful types that are undergoing development in the NASA Clean Combustor Program (ref. 3).

One significant feature of the engine is the variable pitch fan, which is attractive for lower pressure ratio fans because it results in a lighter weight, thrust reversing system than that obtained with the conventional target type of thrust reverser. It also offers other advantages, such as increased thrust response and improved engine performance and reduced noise under some operating conditions. A significant number of components of the engine are built of light-

weight composite materials. They include the fan frame, fan blades and the nacelle. The use of composite materials in these components is expected to reduce their weight by some 25 to 30 percent below that of conventional metal components. These lightweight composite materials are important factors in obtaining the high propulsion system thrust-to-weight ratios that are a goal of the QCSEE Program.

The engine also incorporates lightweight, speed reduction gears between the low pressure turbine and the fan. Because of the relatively low pressure ratio fan and corresponding low tip speed, the use of reduction gears reduces the overall weight of the engine by significantly reducing the size and weight of the turbine. A unique high Mach number inlet is used to suppress fan inlet noise. In addition, acoustic wall treatment, which employs a number of advanced suppression concepts, is located in the inlet, the aft fan duct walls and the core nozzle. The acoustic design of the engine is described in more detail in reference 1.

And finally, the engine is controlled by an engine-mounted digital electronic control. This advanced control technique is ideal for the complex control problem involved in the UTW engine. In all, four variable engine components must be controlled. They include the usual fuel valve and the variable compressor stators as well as the variable pitch fan and the variable area exhaust nozzle.

OTW PROPULSION SYSTEM

A cross section of the OTW propulsion system is shown in figure 4. The significant differences between it and the UTW propulsion system are (1) a fixed-pitch higher pressure ratio fan, (2) a combined core and fan flow exhaust nozzle, and (3) a target-type thrust reverser. The target-type thrust reverser is used in this engine because the higher fan pressure ratio results in a lighter weight system and the OTW installation lends itself to the upward and forward discharge of the engine exhaust which is advantageous. The combined flow exhaust nozzle permits configuring for good powered lift in OTW installations. The digital control contains an advanced feature, which is referred to as the "failure indication and corrective action system", that allows the control to function in the event that one or more of the engine sensors fail. This feature will enhance digital control system reliability. The engine also uses the high Mach number inlet, reduction gears, and a composite material fan frame much the same as the UTW engine.

ENGINE CHARACTERISTICS

Table II shows some UTW and OTW engine characteristics at takeoff. As can be seen, both engines have high bypass ratios. These bypass ratios are about twice that of current modern engines. The high bypass ratio is a consequence of the low fan pressure ratios. Low fan pressure ratios are necessary to re-

duce the combined noise of the engine and that generated by the powered lift. The moderately higher fan pressure ratio of the OTW engine is a result of the noise shielding benefits of the OTW type of installation. Higher fan pressure ratios result in increased performance and accordingly decreased fuel consumption in a flight application. Higher overall pressure ratios can be obtained by the addition of booster stages and their incorporation would also improve performance. Doing this is not a technically difficult task; however, it is expensive and, accordingly, it was not attempted in the QCSEE Program.

PROGRAM SCHEDULE

A schedule of program milestones is shown in figure 5. The major part of the program is being done by private companies under contract to the NASA Lewis Research Center. The prime contractor, the General Electric Co., is designing, fabricating, and testing two QCSEE engines. As indicated in figure 5, the design work is complete, the UTW engine assembly is nearing completion, and the assembly of the OTW engine has begun. The first of the UTW engine tests will begin in June. The program is about a month behind schedule. Following testing of both engines, they will be delivered to Lewis near the end of 1977. NASA tests will include acoustic evaluation of the engines with wing and flap sections installed to simulate the powered-lift condition, and additional evaluation of the control system and the engine altitude performance.

A photograph of the composite fan frame prior to assembly into the engine is shown in figure 6. The frame is 1.98 m (78 in.) high and weighs about 217.5 kg (480 lb). In the photo the fan outlet guide vanes (viewing upstream) can be seen along with the core flow passage towards the center of the frame. The frame is constructed primarily of graphite fibers in an epoxy resin matrix.

APPLICATION OF ADVANCED TECHNOLOGY

The QCSEE Program is investigating a broad range of advanced propulsion technologies. Although the main thrust of the program is directed toward powered-lift aircraft applications, many of the technology elements can be applied to other types of airplanes. (See table III.) Thus the technology developed in the program is expected to have the potential for wide application to future propulsion systems.

CONCLUSIONS

The QCSEE Program has progressed through the design phase and is well into the fabrication phase of the two engines in the program. In the near future the first engine will be tested. A wide range of advanced propulsion system technologies are being investigated. These new technologies can be grouped into the areas of noise, emissions, and performance. Although the program is directed toward providing propulsion technology for powered-lift, short-haul

aircraft, many of the technology elements in the program can be applied to other types of aircraft.

REFERENCES

1. Loeffler, Irvin J.; Smith, Edward B.; and Sowers, Harry D.: Acoustic Design of the QCSEE Propulsion Systems. Powered-Lift Aerodynamics and Acoustics, NASA SP-406, 1976. (Paper no. 21 of this compilation.)

2. Quiet Clean Short-Haul Experimental Engine (QCSEE). Preliminary Analyses and Design Report. Volumes I and II. (R74AEG479, General Electric Co.; NAS 3-18021.) NASA CR-134838 and NASA CR-134839, 1974. (FEDD distribution.)

3. Bahr, D. W.; and Gleason, C. C.: Experimental Clean Combustor Program. Phase 1. (GE-74AEG380, General Electric Co.; NAS 3-16830.) NASA CR-134737, 1975.

TABLE I. - QCSEE REQUIREMENTS

NOISE at 152.4-m (500-ft) sideline and 400 300 N (90 000 lb) thrust		
Takeoff and approach - EPNdB	95	
Reverse thrust - PNdB	100	
Pollution	EPA 1979 emission levels	
Thrust, N(lb)		
Forward -	Uninstalled	Installed
UTW	81 400 (18 300)	77 400 (17 400)
OTW	93 400 (21 000)	90 300 (20 300)
Reverse	35% of forward thrust	
Thrust-to-weight ratio:		
UTW	6.2	4.3
OTW	7.4	4.7
Dynamic response:		
Approach to takeoff thrust, sec	1.0	
Reverse thrust, sec	1.5	

TABLE II. - TAKEOFF ENGINE CHARACTERISTICS

	UTW	OTW
Bypass ratio	12.1	10.1
Fan pressure ratio	1.27	1.34
Fan tip speed, m/sec (ft/sec)	289 (950)	354 (1162)
Overall pressure ratio	14.3	17.3
Thrust, N (lb)	77 400 (17 400)	90 300 (20 300)

TABLE III. - APPLICATION OF QCSEE ADVANCED TECHNOLOGY

Technology area	Type of aircraft		
	Powered-lift short haul	Conventional short haul	Long haul
Powered-lift aerodynamics and acoustics	✓		
High bypass ratio	✓	✓	
Variable pitch fan	✓	✓	
Reduction gears	✓	✓	✓
Noise reduction	✓	✓	✓
Emissions reduction	✓	✓	✓
Variable fan nozzle area	✓	✓	✓
Composite material frame	✓	✓	✓
Composite material blades	✓	✓	✓
Composite material nacelle	✓	✓	✓
Digital electronic controls	✓	✓	✓

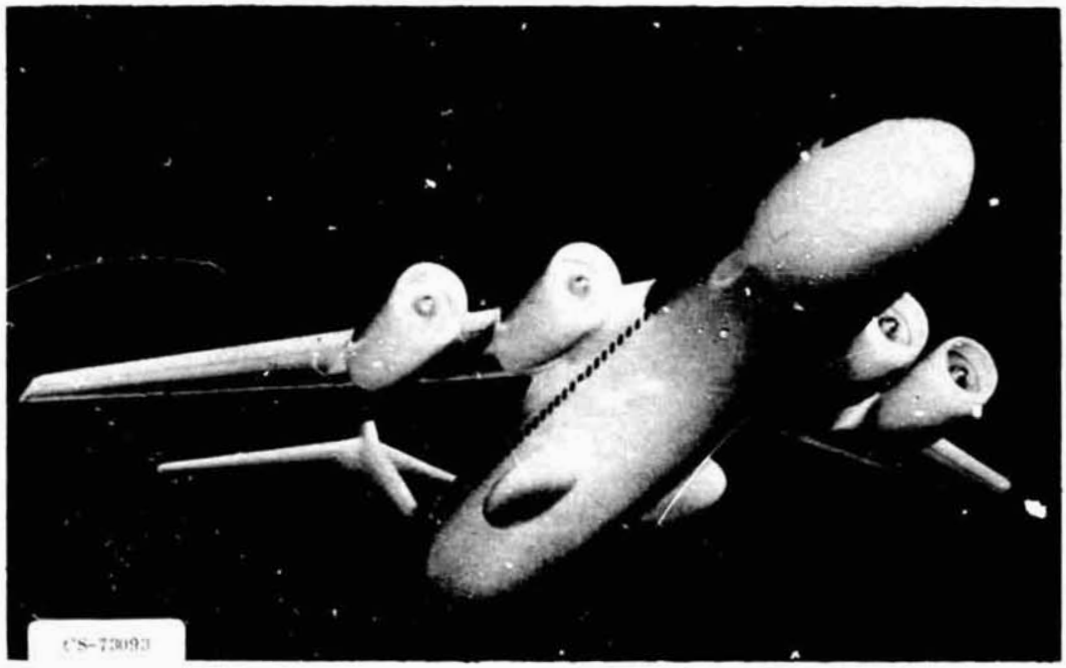

Figure 1.- Conceptual UTW short-haul aircraft.

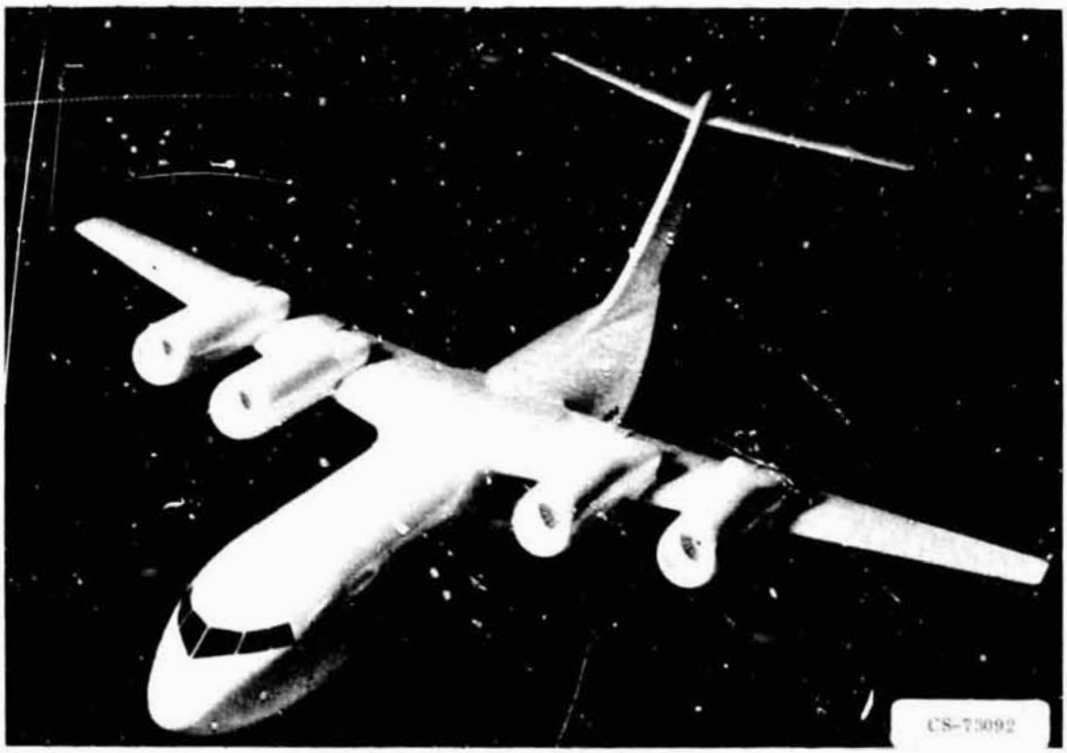

Figure 2.- Conceptual OTW short-haul aircraft.

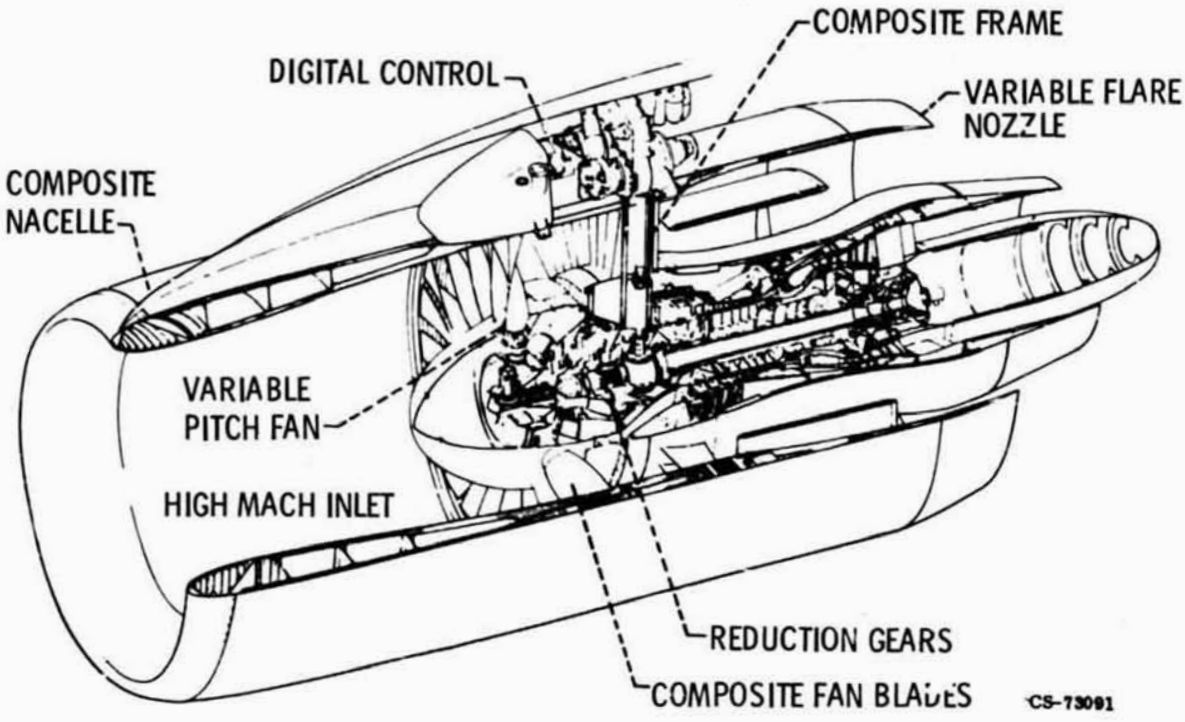

Figure 3.- QCSEE UTW engine.

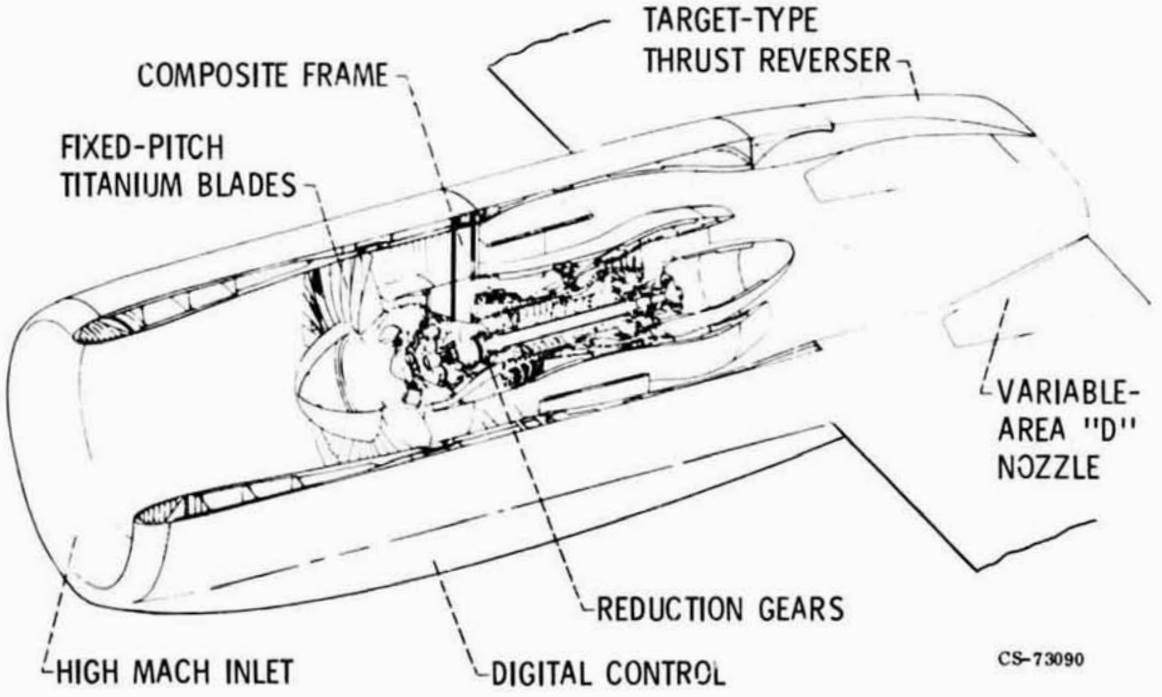

Figure 4.- QCSEE OTW engine.

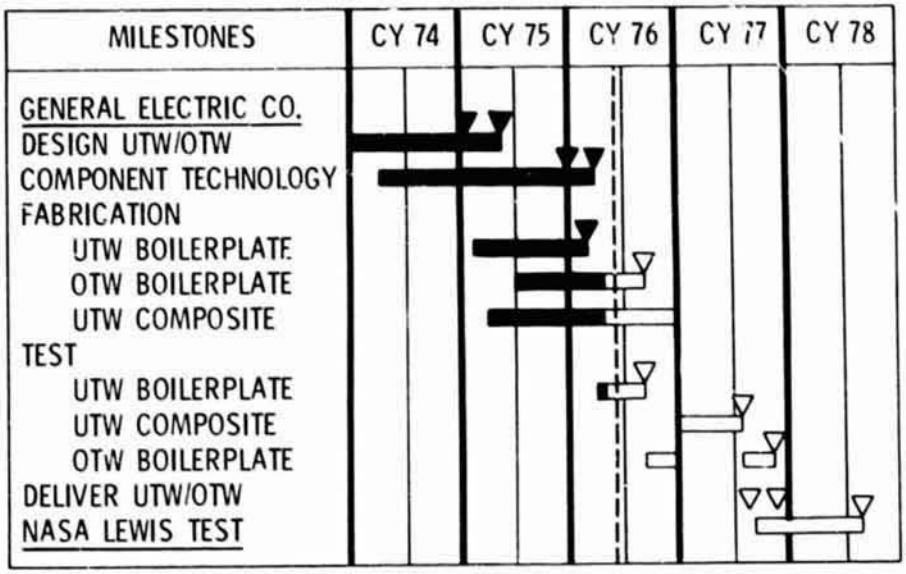

Figure 5.- QCSEE Program schedule.

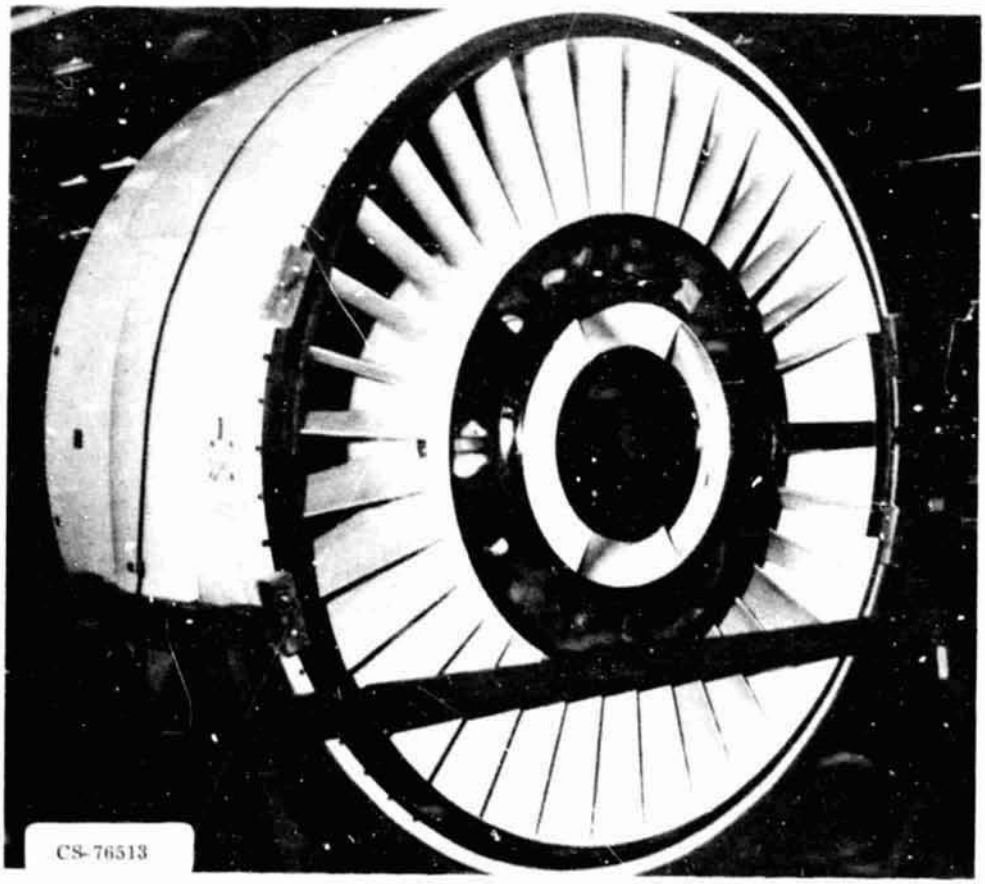

Figure 6.- Composite material fan frame.

ACOUSTIC DESIGN OF THE QCSEE PROPULSION SYSTEMS

Irvin J. Loeffler
NASA Lewis Research Center

Edward B. Smith and Harry D. Sowers
General Electric Company

SUMMARY

Acoustic design features and techniques employed in the Quiet Clean Short-Haul Experimental Engine (QCSEE) Program are described. The role of jet/flap noise in selecting the engine fan pressure ratio for powered-lift propulsion systems is discussed. The QCSEE acoustic design features include a hybrid inlet (near-sonic throat velocity with acoustic treatment); low fan and core pressure ratios; low fan tip speeds; gear-driven fans; high- and low-frequency "stacked" core noise treatment; multiple-thickness treatment; bulk absorber treatment; and treatment on the stator vanes. The QCSEE designs represent an anticipated acoustic technology improvement of 12 to 16 PNdB relative to the noise levels of the low-noise engines used on current wide-body commercial jet transport aircraft.

INTRODUCTION

The overall objective of the Quiet Clean Short-Haul Experimental Engine (QCSEE) Program is the development of propulsion system technology suitable for future powered-lift, short-haul aircraft. One of the program's major objectives is the development of technology for producing very low propulsion system noise without excessive performance penalties. The program includes the design, fabrication, and static ground testing of two different engines for externally blown-flap (EBF) systems: an under-the-wing (UTW) design, and an over-the-wing (OTW) design. (The designation EBF is sometimes used in reference to a UTW configuration and USB (upper-surface blowing) in reference to an OTW configuration.)

This paper presents a discussion of acoustic design features and techniques employed in the QCSEE program. It emphasizes the unique problems of designing low-noise engines for powered-lift propulsion systems in general. No attempt is made to present a detailed analysis and documentation of the QCSEE engine acoustic designs. Details of the preliminary acoustic design effort are provided in references 1 and 2. Further acoustic design and analysis reports will follow completion of engine testing in 1977.

NOISE GOALS

The very stringent noise goals of the QCSEE program present a formidable challenge in aircraft engine design. Not only are the noise goals far more severe than current levels, but a commercial transport employing QCSEE engines must meet these goals without allowance for the additional noise associated with a powered-lift system and with engines sufficiently powerful to allow takeoff and landing on a runway only 610 m (2000 ft) in length. Furthermore, the noise goals are to be achieved without serious penalties in engine performance, size, weight, and cost.

The QCSEE noise goals for both the UTW and OTW powered-lift aircraft with four QCSEE engines producing 400 kN (90 000 lbf) of thrust are illustrated in figure 1. With the engines at takeoff thrust and the aircraft at the altitude at which maximum noise is produced (approx 61 m (200 ft)), the 152.4-m- (500-ft-) sideline noise goal is 95 EPNdB. The same goal applies at approach, with the engines producing 65 percent of takeoff thrust. After the airplane has landed on the runway and the engines are producing reverse thrust equal to 35 percent of takeoff thrust, the noise goal is 100 PNdB.

The acoustic analysis and design effort to achieve these stringent noise goals includes the following elements:

(1) Identification and assessment of noise sources

(2) Minimizing source noise

(3) Application of efficient suppression concepts

The unrestricted pursuit of the last two elements could lead to unacceptable penalties in engine aerodynamic performance, weight, size, cost, and operating economy. In a commercially viable powered-lift propulsion system, each noise source must be reduced only to a near-optimum level relative to an established noise goal in order to produce a "balanced acoustic design."

ACOUSTIC DESIGN OF BASIC ENGINE

The UTW and OTW engine parameters associated with the acoustic design are listed in table I. As discussed subsequently, a judicious trade-off between acoustic design and engine performance was involved in selecting some of these parameters.

The major noise sources for the QCSEE engines are called out on the sketch of the UTW powered-lift system in figure 2. The single-stage fan generates tones and broadband noise that are radiated out through the inlet in the forward direction and also out through the fan exhaust passage to the rear. The broadband noise from the combustor is radiated rearward. The turbine generates both tones and broadband noise that are propagated through the core exhaust

duct. The only remaining major noise source is a combination of the engine jet noise and the noise associated with the interaction of the jet and the flap surfaces during the production of powered lift, commonly referred to as jet/flap noise.

From prediction equations and correlations and the engine design parameters of table I, noise spectra at takeoff, approach, and reverse thrust as radiated in the forward and aft quadrants from an aircraft in flight must be established for each of the major noise sources. In the example plot of figure 3, the major source spectra for the UTW propulsion system aft noise on takeoff are presented. Plots of this type provide an indication of the amount of suppression required to achieve a balanced acoustic design or, if some suppression requirements are excessive, the need to select another set of design parameters to achieve a better-balanced design.

Figure 3 shows that the jet/flap spectrum is essentially broadband noise that dominates the very low-frequency end of the spectrum. The noise from this source, as shown by the spectrum, falls off rapidly at higher frequencies, of the order of 5 dB per octave. The fan noise radiated rearward includes the blade passing frequency (BPF) tone, which lies in the 1/3-octave band centered at 1000 Hz; the second harmonic of the BPF tone, which lies in the 2000-Hz band; and the fan broadband noise. Dominating the spectral region between the jet/flap noise peak and the fan noise peak is the broadband noise of the combustor, with a peak at about 400 Hz. The combustor noise falls off very rapidly below and above its peak frequency. The broadband noise generated by the low-pressure-fan drive turbine actually peaks at about 8000 Hz on takeoff, but because the high frequencies are reduced by atmospheric attenuation, the propagated turbine noise is represented by the curve with the peak at about 5000 Hz, as shown in figure 3.

Minor noise sources were also considered in the acoustic design. These include compressor noise radiated through the inlet, mechanical noise from the reduction gears, and noise generated by flow over acoustically treated surfaces and airfoils. None of these sources was strong enough to add significantly to the overall engine noise level.

Jet/Flap Noise

Although jet/flap interaction noise is generated entirely outside the engine, this noise source is controlled primarily by engine design parameters. Numerous attempts have been made to reduce jet/flap noise by modifying the wing/flap geometry, by employing porous or compliant flap surfaces or edges, and by relocating the engine relative to the flap system. Such efforts, to date, have produced only small reductions in jet/flap noise without lift/drag or thrust-turning efficiency penalties. The flap noise, however, is very sensitive to the velocity of the flow impinging upon the wing/flap system. Hence, the most effective way to reduce the jet/flap noise to any required level, after adopting a preferred configuration, is to reduce the fan and core jet velocities by selecting an engine cycle with suitable fan and core pressure ratios.

Correlations of jet/flap noise experimental results for both model and engine tests showed that the overall sound pressure level (OASPL) from this source varies as V^6, where V is the effective engine exhaust velocity at the engine nozzle exit (ref. 3). For unmixed fan and core flows the effective velocity was obtained from a V^6 weighting of the separate velocities. A later correlation and analysis (ref. 4) resulted in a V^6 relation for OTW jet/flap noise and a $V^{6.7}$ dependency for UTW jet/flap noise.

The sensitivity of jet/flap noise to fan pressure ratio is indicated in figure 4. Effective perceived noise level (EPNL) values for the QCSEE UTW and OTW engine cycles are plotted against fan pressure ratio. The QCSEE UTW jet/flap noise design levels for takeoff and approach were set 3.5 dB below the prediction of reference 3 to allow for advances in UTW flap noise technology corresponding to 1980 engine technology. For a similar reason, the OTW design levels were set 2.5 dB below the reference 3 prediction.

The OTW jet/flap noise curve is approximately 4 EPNdB lower than the UTW curve for a given fan pressure ratio. This is due to the high-frequency portion of the OTW jet/flap noise being shielded to some extent from an observer below and to the side of an aircraft by the presence of the wing. Consequently, for a given jet/flap noise level, the engine can have a higher fan pressure ratio for an OTW system than for a UTW system. This gives the OTW system a possible advantage in size, weight, and performance over the UTW system for a given noise goal.

The levels of figure 4 are based on QCSEE engine cycles and takeoff flap settings. As shown, the QCSEE fan-pressure-ratio design points were set such that the jet/flap noise levels are about 3 EPNdB below the total system noise goal of 95 EPNdB. This arrangement allows the engine and jet/flap noise sources to make approximately equal contributions to the total system noise level and produces a balanced design. Allowing the jet/flap noise to go to levels nearer 95 EPNdB would unduly penalize the engine performance by requiring correspondingly lower engine noise levels. For example, if the jet/flap noise were set at 94.5 EPNdB, a 2.5-EPNdB increase, the engine noise limit would be 85.5 EPNdB, a 6.5-EPNdB decrease. Clearly, if two noise sources are difficult to control or suppress, a balanced design requires that neither be allowed to impose unrealistic levels upon the other.

In accordance with this rationale and engine cycle analyses, the UTW fan pressure ratio was set at 1.27 and the OTW fan pressure ratio was set at 1.34.

Fan Noise

The engine design parameters that influence fan noise are labeled in the sketch of the UTW engine system shown in figure 5. Based on correlations of forward-radiated fan noise with fan tip speed, the lowest UTW and OTW fan tip speeds consistent with engine cycle requirements were selected. The selected QCSEE UTW fan tip speed was 290 m/sec (950 ft/sec), and the OTW value was 315 m/sec (1150 ft/sec). These tip speeds are also low enough to prevent

serious inlet noise problems from multiple pure tones caused by interaction of shock waves from the rotor-blade leading edges. The estimated inlet noise levels were substantiated by UTW model fan tests.

A low fan pressure ratio, important in achieving low jet/flap noise, is also important in producing low fan noise. Aft-radiated fan noise for the UTW and OTW engines was estimated by scaling measured acoustic data from full-scale fans and adjusting for pressure ratio, tip speed, and weight flow.

The UTW engine rotor/stator spacing of 1.5 rotor tip chords provides for relatively weak rotor wakes interacting with the stators. An even larger spacing would increase engine length without a proportionate reduction in rotor/stator interaction noise.

The shorter OTW rotor tip chord would require a smaller rotor/stator spacing distance than the UTW spacing distance to provide a spacing of 1.5 rotor tip chords. However, to reduce program costs through commonality of design, tooling, and fabrication, the OTW fan frame was designed with the same spacing distance and basic dimensions as the UTW fan frame. The resultant OTW rotor/stator spacing of 1.93 rotor chords was accepted instead of a smaller spacing for economic considerations.

Another means of minimizing rotor/stator interaction noise is to use a vane/blade ratio (number of stator vanes divided by number of rotor blades) that will cut off the blade-passing-frequency tone, the fundamental tone of the fan. With a vane/blade ratio slightly in excess of 2, the rotor/stator interaction noise does not propagate out the inlet duct, according to the Tyler and Sofrin theory (ref. 5). However, the QCSEE UTW vane/blade ratio was not selected for BPF tone cutoff. It was selected instead to minimize propagation of the second harmonic of the BPF tone (2xBPF) according to the theoretical analysis of Mani (ref. 6). In figure 6 the predicted UTW fan exhaust noise spectrum is shown by two curves: one labeled "actual", and the other labeled "noy-weighted." In the actual curve, the BPF tone lies in the 1/3-octave band with a center frequency at 1000 Hz and has a value of about 86 dB, which is about 2.5 dB higher than the second harmonic tone. However, after noy-weighting (adjusting for human annoyance as a function of frequency), the second harmonic tone level is about 5.5 dB greater than the BPF tone. Hence, it was preferable to favor reduction of the second harmonic in the selection of the vane/blade ratio. The concept by Mani was verified in scale-model fan tests with a closely spaced rotor/stator (ref. 7), where the aft-radiated second harmonic tone was 3 to 6 dB lower for near-optimum than for nonoptimum vane/blade combinations. The effect was measured at a rotor/stator spacing of 0.5 but not at 1.5. The effect may have been masked at the larger spacing by rotor inflow turbulence noise, which is believed to be higher in ground tests than in flight situations. Thus, the benefit might be realized in a flight situation, where inflow turbulence is reduced (ref. 8).

The OTW fan, with a vane/blade ratio of 1.18, was also not designed to cut off the fan fundamental tone. Suppression of the fan BPF tone was preferred to the mechanical design and economic compromises necessary to achieve cutoff. The fan noise, both forward and aft, exceeds that of the UTW engine.

The over-the-wing mounting arrangement provides shielding for the fan, combustor, and turbine noise in the aft direction, but not forward. Thus, the OTW engine is forward-noise dominated and requires more inlet and less aft acoustic suppression than the UTW engine.

The variable-pitch fan (to permit thrust reversing) and the adjustable exhaust nozzle of the QCSEE UTW propulsion system provide a potential acoustic benefit. By permitting a variety of combinations of blade angle, nozzle area, and fan speed at takeoff and approach thrust requirements, these devices provide considerable flexibility in optimizing acoustic and fan performance tradeoffs.

Combustor and Turbine Noise

Since both QCSEE engines were designed around an existing General Electric engine core, core noise control was limited to determining combustor and turbine source characteristics and suppression requirements. The core noise was measured and extrapolated to QCSEE conditions. The combustor and turbine spectra are presented in figure 3 for the UTW propulsion system at takeoff as radiated in the aft quadrant.

Compressor Noise

Compressor noise estimates indicate this source to be relatively low. In addition, the second- and third-stage tones are above 10 kHz and fall into the low noy-weighted region and also into the high atmospheric attenuation region. The first-stage fundamental tone is at 8 kHz for the takeoff condition. Again acoustic suppression will be relied upon to control any compressor noise that may be present.

Reduction Gear Noise

Extrapolations of gear noise data from lower horsepower gear noise tests revealed that gear noise levels would not contribute significantly to the total system noise levels. However, using reduction gears does offer a significant acoustic advantage.

The low fan pressure ratio of the QCSEE engines permitted the selection of a low fan tip speed for low noise. The reduction gear provided high fan drive turbine speeds, reducing turbine size and weight and shifting the turbine noise spectrum to higher frequencies, which are less annoying and more highly attenuated by the atmosphere. This effect is illustrated in figure 6.

Flow Noise, Splitter Noise, and Strut Noise

From theoretical and experimental studies, working models for predicting flow noise, strut noise, and splitter trailing-edge noise have been formulated. Since these noise sources are a strong function of flow velocity, the aft duct flow path has been designed to limit the average duct Mach number to 0.47 for both QCSEE engines. This is expected to keep these sources well below the suppressed fan exhaust noise.

ENGINE ACOUSTIC SUPPRESSION

Two different kinds of suppression are employed in the QCSEE program: acoustically treated liners for the flow passages, and the sonic inlet effect. The types of acoustic treatment used in the two QCSEE engines are illustrated in figure 7. The single-degree-of-freedom (SDOF) design employs the conventional honeycomb material bonded between a base plate and a perforated facesheet adjacent to the flow path. A typical suppression curve for this design is shown in the figure. This treatment is used in the fan inlets, the fan exhaust passages, the fan frame, the stator vanes, the UTW nozzle cowl flaps, and the fan exhaust duct splitter.

The stacked SDOF design is employed in the core noise treatment. Suppression of QCSEE core noise presents a severe problem in acoustic treatment design. The core noise consists of high-frequency broadband noise from the fan-drive turbine and low-frequency broadband noise from the combustor, as shown in figure 3. Because of the short length of the core duct, a "stacked treatment" concept was investigated and adopted for both QCSEE engines. In the compact stacked treatment design, high-frequency treatment consisting of small-hole perforated facesheet over honeycomb is placed along the core exhaust walls. The much thicker low-frequency combustor treatment is placed behind the thin turbine treatment. The rather large resonator cavities are connected to the exhaust passage by a series of tubes passing through the thin treatment. The tubes also extend inward into the resonator cavities, increasing the effective cavity depth. This permits tuning at the very low frequencies (400 or 500 Hz), which normally require much deeper cavities than the 7.5 or 10 cm (3 or 4 in.) available in the core region. The core treatment also has to be designed to withstand high exhaust temperatures of about 810 K (1000° F) and the associated differential thermal expansion during engine startup and shutdown.

The suppression spectrum of the stacked SDOF core treatment is illustrated below the sketch in figure 7. Two peaks, one for low frequency and one for high frequency, are shown, and have been verified by component hot-flow-duct tests.

Bulk absorber treatment is also illustrated in figure 7. This treatment has demonstrated better suppression characteristics than SDOF treatment, based on engine and scale-model tests. The suppression curve is similar to that of the SDOF design, but the peak attenuation is higher and the bandwidth greater

than for a typical SDOF design of equal treatment area. Recent progress by the General Electric Co. in resolving contamination and degradation problems for bulk absorbers has resulted in the development of a Kevlar bulk absorber treatment material that is considered to be flightworthy. Bulk absorber treatment is used in one of the fan inlet designs.

The basic UTW and OTW engine acoustic hardware includes a "boilerplate nacelle" that will accommodate nine interchangeable acoustic panels. In addition to panels for the hard-wall configuration, treated panels for the basic UTW acoustic treatment are to be fabricated. A second treatment will be fabricated if engine acoustic tests indicate a need to adjust the suppression spectrum of the basic treatment. This will be done by designing and fabricating one to six new panels from stockpiled materials to replace corresponding panels in the basic treatment. In a similar manner, an initial-test OTW treatment made up of UTW elements will be modified if needed to satisfy the QCSEE noise goals. The basic construction of these panels is the conventional perforated aluminum facesheet bonded to aluminum honeycomb. An alternate inlet design uses specially treated Kevlar bulk absorber material instead of the honeycomb. A flightworthy composite nacelle that incorporates the best acoustic design and in which the acoustic treatment is integrated into the nacelle load-carrying structure will also be tested on the UTW engine.

In figure 8, curves representing the total system noise (unsuppressed and suppressed) were added to the major noise source spectral plots of figure 3. The curve labeled "total suppressed" becomes relatively flat when no weighted, representing a balanced acoustic design that satisfies the QCSEE UTW takeoff noise goals. A rough indication of suppression requirements is shown by the extent to which each source must be reduced to reach a position well below the total suppressed curve. As shown, considerable suppression of the fan exhaust noise is required in the region of 500 to 10 000 Hz, as much as 20 dB at some frequencies. For the combustor and turbine, on the other hand, suppression is required for less than two octaves, with peak requirements of the order of 5 or 6 dB.

The location and extent of acoustic suppression used in the UTW engine are shown schematically in figure 9. The QCSEE hybrid inlet with a throat Mach number of 0.79 at takeoff was combined with three different thicknesses of acoustic wall treatment to provide 12 to 13 PNdB of suppression. Thus, the hybrid inlet provides very high suppression without the use of inlet acoustic splitters. Based on UTW fan model tests, at takeoff conditions the near-sonic inlet provides about 10 PNdB of suppression and the wall treatment supplies the other 3 PNdB. At approach, the inlet Mach number is less than 0.6, and only the wall treatment is effective. Approach suppression was measured at about 6 PNdB. The wall treatment also provides about 4 PNdB of suppression in the reverse-thrust mode. Hybrid inlet design for powered-lift propulsion systems is discussed in the paper by R. Luidens (ref. 9).

Fan exhaust duct suppression includes multiple-thickness wall treatment on inner and outer walls, a 1.02-m- (40-in.-) long splitter, and treatment in the fan frame, on the pressure side of the stator vanes, and on the nozzle cowl flaps. The fan inlet and fan exhaust treatments have several thicknesses and

are tuned to several different peak frequencies to more nearly match the desired suppression spectrum. The effectiveness of stator vane treatment has not yet been established. The locations of the compressor inlet, turbine, and combustor treatments are also shown in figure 9.

Suppression for the OTW engine is shown in the cross section of figure 10. Comparing figures 9 and 10 reveals the commonality of acoustic and mechanical design for the UTW and OTW engines. With only minor exceptions, the OTW initial-test treatment is the same as that of the UTW engine. The 102-cm (40-in.) splitter was shortened to 76.2 cm (30 in.) by the removal of a specially designed tailpiece. The fan frame treatment is tuned for the OTW BPF tone, and the OTW uses no fan nozzle treatment. The engine acoustic test program was designed to take full advantage of the acoustic hardware commonality of the two QCSEE engines.

Treatment depth, porosity, and tuning frequency for the fan inlet and exhaust acoustic treatments are presented in table II.

Predicted suppression levels for the UTW and OTW propulsion systems on takeoff, approach, and reverse thrust for each noise source are given in table III. At takeoff, which is the most difficult condition with respect to the QCSEE noise goal, the predicted UTW suppression values are 12.3 PNdB for the inlet, 13.4 PNdB for the fan exhaust, 5.1 PNdB for the combustor, and 5.8 PNdB for the turbine. Predicted OTW inlet suppression on takeoff is 12.9 PNdB; the predicted fan exhaust suppression is 12.8 PNdB. Combustor and turbine suppression values are the same as those for the UTW system.

PROPULSION SYSTEM NOISE LEVELS

Current estimates of QCSEE propulsion system noise levels are plotted in bar-graph form in figure 11. In the takeoff mode of operation the UTW jet/flap noise level is about 92 EPNdB, which is 3 EPNdB below the noise goal, as originally planned. The engine noise level is about 2 EPNdB below the jet/flap level as well as 2 EPNdB below the allowable engine noise level. The total system noise is about 1.5 EPNdB below the UTW takeoff noise goal, and it may be possible to remove some of the engine acoustic treatment and still satisfy the noise goal. This will be determined after the results of the initial suppressed engine tests are obtained. The predicted UTW approach noise is well below the QCSEE noise goal and thus presents no problem. The suppression required at takeoff provides this margin at approach.

At takeoff the OTW engine and jet/flap noise levels are nearly equal, as designed; and the predicted system level just meets the noise goal. The OTW system approach condition was obtained primarily by reducing the fan speed. The engine noise and the jet/flap noise are both greatly reduced. The system noise is more than 4 EPNdB below the approach limit and presents no particular problem.

Current predictions indicate that neither engine is likely to meet the reverse-thrust noise goal of 100 PNdB. The QCSEE UTW model fan in reverse pitch was noiser than was indicated by earlier tests of model and full-scale reverse-pitch fans. Based on the UTW model tests, the UTW system reverse-thrust noise level will be about 104 PNdB. It is anticipated that by operating the engine at a more optimum blade angle, the reverse-thrust noise level can be lowered. This will be determined during engine tests.

The reverse-thrust noise characteristics of the OTW nozzle are compromised by a variety of other requirements for this nozzle. The D-shaped OTW nozzle must provide flow attachment on the upper wing and flap surfaces; variable exhaust areas for cruise, takeoff, and approach; and acceptable cruise drag and must also serve as a quiet thrust reverser. These conflicting design requirements produce a complex mechanical, aerodynamic, and acoustic design problem. The current OTW design does not represent an optimum acoustic or aerodynamic design. Future development beyond the QCSEE engine tests is required. On the basis of 1/6th-scale thrust reverser model tests, the predicted total system noise level is 104 PNdB.

Although higher than the noise goal, the QCSEE reverse-thrust noise levels are lower than current CTOL engine reverse-thrust levels. Furthermore, since in reverse-thrust operation, the noise source is on the airport runway, the noise footprint does not extend far beyond the airport as it does in the case of takeoff and approach noise footprints. Hence, a severe compromise of other engine requirements to achieve low reverse-thrust noise is probably not desirable.

It is of interest to compare the noise levels of aircraft using QCSEE engines with the noise levels of aircraft that use current high-bypass-ratio, low-noise engines. This task is somewhat complicated by differences in the noise-goal measurement locations, differences in aircraft flight profiles, and the powered-lift aspect of the QCSEE application. So QCSEE was compared with other engines under static ground test conditions, which is a relatively straightforward exercise. The results are shown in table IV. Measured noise levels were adjusted to the same thrust level on a 61-m (200-ft) sideline without jet/flap noise. The current high BPR engines, as represented by the CF6-50 or CF6-6 engines with bypass ratios of 4 and 6, respectively, were used as a reference. Sideline noise levels of aircraft with these engines are about 11 EPNdB better than the FAA FAR 36 requirements (ref. 10). The QCSEE OTW engine, with a bypass ratio of 10, represents a 12-PNdB improvement: 6 PNdB from source noise reduction, and 6 PNdB from suppression improvement. Te QCSEE UTW engine, with a bypass ratio of 12, is 16 PNdB quieter than the CF6 engines, with source noise reduced by 10 PNdB and suppression, as for the OTW engine, improved by 6 PNdB over the CF6 engines. Thus the two QCSEE engines represent an engine acoustic technology level as much 12 to 16 PNdB better than that of the low-noise engines employed on current wide-body jet transport aircraft. However, some of the low-noise techniques used by the QCSEE engines may be inappropriate for some conventional commercial aircraft.

Of course, the design of viable aircraft propulsion systems involves the consideration of many more criteria than acoustics. For example, aircraft

economics is very important. And, although much effort has been put into reducing the performance penalty associated with the low noise levels obtained in the QCSEE propulsion systems, the penalties have not been completely eliminated. Because of the continuing public interest in reducing aircraft noise levels, the extent to which the new technology will be applicable to new aircraft will depend on the direction of future noise regulations, which will be a function of the trade-off between public acceptance and aircraft economics.

CONCLUSIONS

For powered-lift propulsion systems with stringent noise goals the engine cycle is significantly influenced by the jet/flap noise source such that low fan pressure ratios are required. In addition, engine design parameters must be chosen to generate low noise levels, where possible at frequencies that are easily attenuated and are least annoying to an observer.

The Quiet Clean Short-Haul Experimental Engine (QCSEE) designs employ hybrid inlets in which suppression is provided by a combination of sonic inlet effect and acoustic wall treatment. Core-noise, high-temperature acoustic treatment includes both low- and high-frequency suppression in a unique "stacked treatment" design. Multiple-thickness acoustic suppression is used in fan inlet and exhaust passages. Acoustic treatment is provided in the fan frames, on the stator vanes, and on the under-the-wing (UTW) nozzle cowl flaps. The QCSEE composite nacelle acoustic treatment is integrated into the nacelle load-carrying structure.

Current predictions indicate that the two QCSEE engines will meet the specified noise goals on takeoff and approach. However, in the reverse-thrust mode both engines are estimated to be about 4 PNdB over the goal.

The QCSEE designs are estimated to be as much as 12 to 16 PNdB below the noise levels of the low-noise engines used on current wide-body commercial jet transport aircraft.

REFERENCES

1. Quiet Clean Short-Haul Experimental Engine (QCSEE) - Preliminary Analyses and Design Report Volume I. NASA CR-134838, 1974. (FEDD distribution.)

2. Quiet Clean Short-Haul Experimental Engine (QCSEE) - Preliminary Analyses and Design Report Volume II. NASA CR-134839, 1974. (FEDD distribution.)

3. Clark, Bruce J.; Dorsch, Robert G.; and Reshotko, Meyer: Flap Noise Prediction Method for a Powered Lift System. AIAA Paper 73-1028, Oct. 1974.

4. Dorsch, Robert G.; Clark, Bruce J.; and Reshotko, Meyer: Interim Prediction Method for Externally Blown Flap Noise. NASA TM X-71768, 1975.

5. Tyler, J. M.; and Sofrin, T. G.: Axial Flow Compressor Noise Studies. SAE Trans., vol. 70, 1962, pp. 309-332.

6. Mani, R.: Discrete Frequency Noise Generation from an Axial Flow Fan Blade Row. ASME Paper 69-GE-12, June 1969.

7. Stimpert, D. L.; and McFalls, R. A.: Demonstration of Short-Haul Aircraft Aft Noise Reduction Techniques on a Twenty Inch (50.8 cm) Diameter Fan. Volume I - An Early Domestic Dissemination Report. NASA CR-134849, 1975.

8. Feiler, C. E.; and Merriman, J. E.: Effects of Forward Velocity and Acoustic Treatment on Inlet Fan Noise. AIAA Paper 74-946, Aug. 1974.

9. Luidens, R. W.: Inlet Technology for Powered-Lift Aircraft. Powered-Lift Aerodynamics and Acoustics, NASA SP-406, 1976. (Paper no. 23 of this compilation.)

10. Noise Standards: Aircraft Type and Airworthiness Certification. Federal Aviation Regulations, pt. 36, FAA, June 1974.

TABLE I. - QCSEE DESIGN PARAMETERS

[Speed, 41 m/sec (80 knots); altitude, 61 m (200 ft).]

Parameter	Under-the-wing engine	Over-the-wing engine
Fan pressure ratio	1.27	1.34
Fan tip speed, m/sec (ft/sec)	290(950)	350(1150)
Inlet Mach number (throat)	0.79	0.79
Number of fan blades	18	28
Number of stator vanes	33(32 + pylon)	33
Engine weight flow (corrected), kg/sec (lb/sec)	405(894)	405(894)
Blade passing frequency, Hz	920	1760
Vane/blade ratio	1.83	1.18
Rotor/stator spacing, rotor tip chords	1.5	1.93
Bypass ratio	12.1	10.2
Gross thrust (SLS uninstalled), kN (lbf)	81.40(18 300)	93.41(21 000)
Fan exhaust velocity, m/sec (ft/sec)	198(649)	231(757)
Core exhaust velocity, m/sec (ft/sec)	238(784)	
Fan exhaust area, m^2 (in^2)	1.615(2504)	1.747(2708)
Core exhaust area, m^2 (in^2)	0.348(540)	
Fan diameter, cm (in.)	180.4(71)	180.4(71)
Fan rotating speed, rpm	3089	3778

TABLE II. - FAN INLET AND EXHAUST DUCT ACOUSTIC TREATMENT

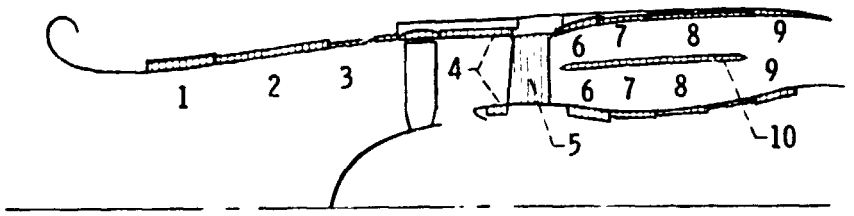

Section	Cavity depth		Porosity, percent	Forward thrust	Reverse thrust
	cm	in.		Design frequency, Hz	
1	3.81	1.5	10	1000	1600
2	1.90	.75		1600	2500
3	1.27	.5		2000	3150
4	5.08	2.0		1000	----
5	.76	.3		4000	----
6	5.08	2.0	22	1250	----
7	2.54	1.0	15.5	2000	----
8	1.90	.75	15.5	2500	----
9	2.54	1.0	15.5	1600	----
10	1.27	.5	11.5	2500	----

TABLE III. - PREDICTED COMPONENT NOISE SUPPRESSION

FOR BOILERPLATE NACELLE

[Sideline distance, 152.4 m (500 ft).]

Acoustic treatment on-	Engine	Takeoff	Approach	Reverse thrust
		Noise suppression, ΔPNdB		
Fan inlet	Under the wing	12.3	6.3	4.3
	Over the wing	12.9	7.7	7.7
Fan exhaust	Under the wing	13.4	13.4	9.3
	Over the wing	12.8	12.8	12.8
Combustor	Both	5.1	5.1	5.1
Turbine	Both	9.8	9.8	9.8

TABLE IV. - ENGINE NOISE COMPARISON

[61-m-(200-ft-) sideline maximum perceived noise level; thrust, 100 kN (22 500 lbf).]

Engine class	Engine designation	Bypass ratio	Source noise reduction, ΔPNdB	Suppression improvement, ΔPNdB	Total noise reduction, ΔPNdB
Current high bypass ratio	CF6-50	4	Ref.	Ref.	Ref.
	CF6-6	6	Ref.	Ref.	Ref.
QCSEE fixed pitch	QCSEE OTW	10	6	6	12
QCSEE variable pitch	QCSEE UTW	12	10	6	16

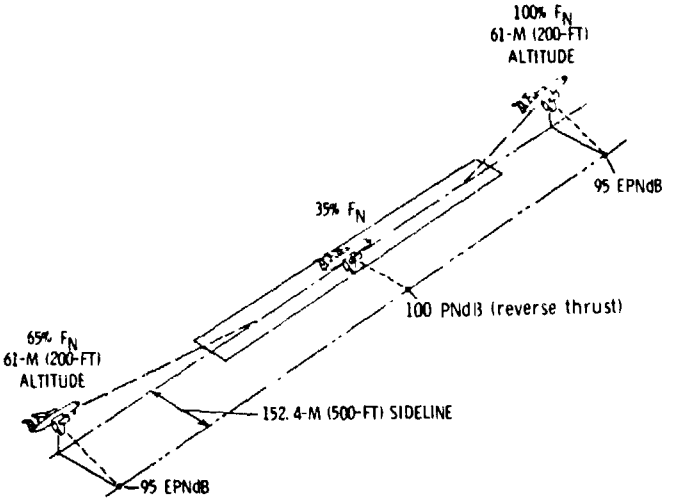

Figure 1.- QCSEE noise goals. Number of engines, 4; takeoff thrust, F_N, 400 kN (90 000 lb).

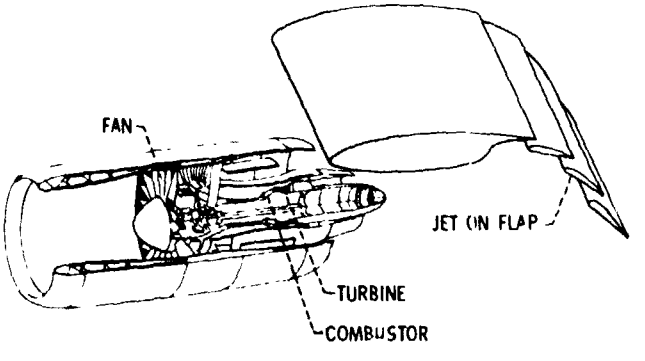

Figure 2.- Major noise sources - under-the-wing engine.

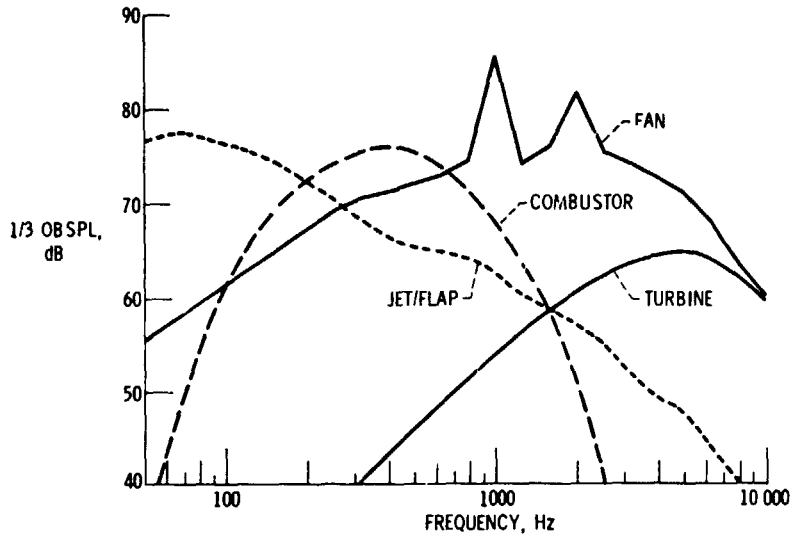

Figure 3.- Takeoff spectra - single under-the-wing engine. Maximum aft acoustic angle, 120°; sideline distance, 152.4 m (500 ft).

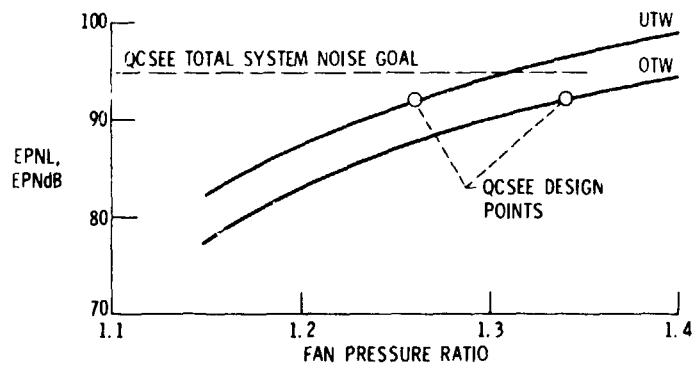

Figure 4.- Effect of jet/flap noise on fan-pressure-ratio selection - four-engine aircraft. Altitude, 61 m (200 ft); sideline distance, 152.4 m (500 ft).

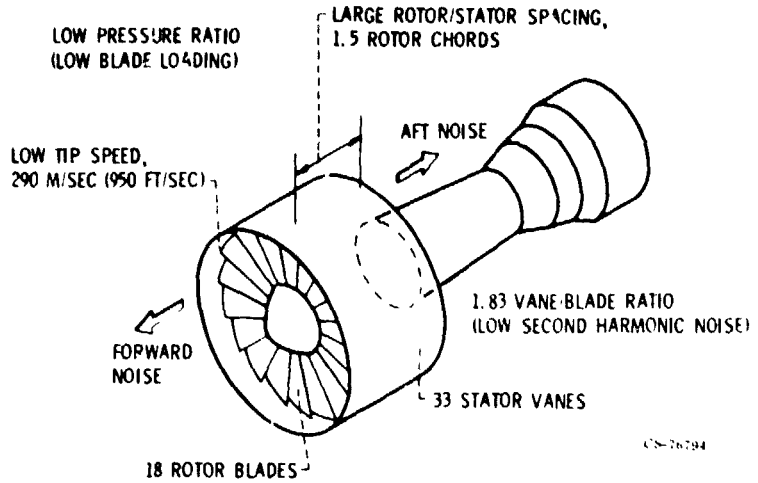

Figure 5.- Low fan source noise - under-the-wing engine.

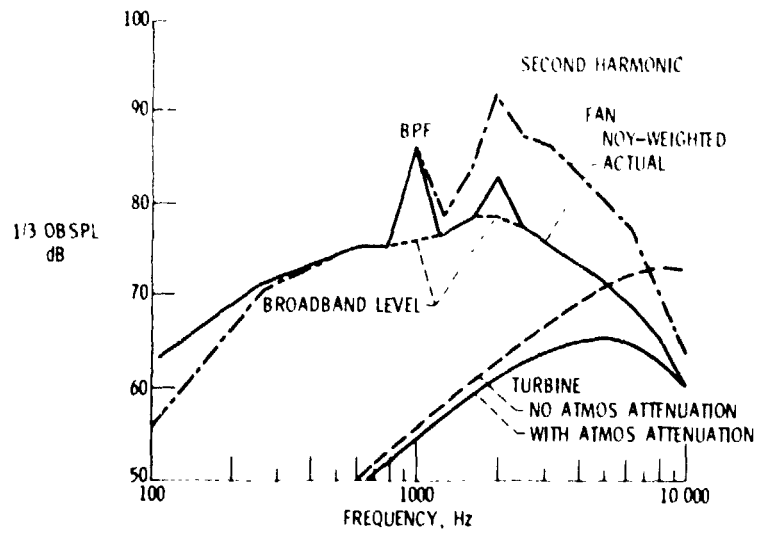

Figure 6.- Frequency effects on perceived sideline noise - under-the-wing fan and turbine exhaust spectra. Sideline distance, 152.4 m (500 ft); altitude, 61 m (200 ft).

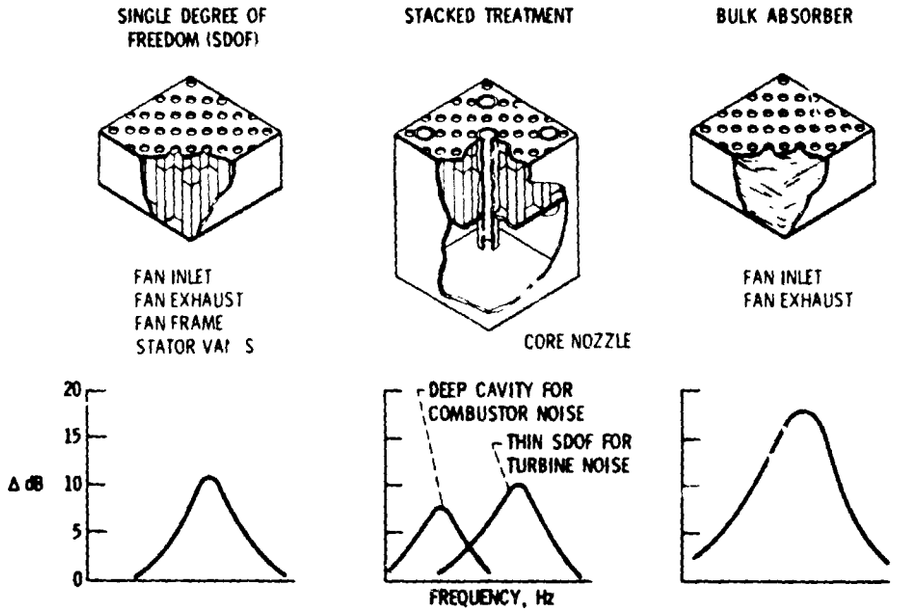

Figure 7.- Types of acoustic treatment for QCSEE engines.

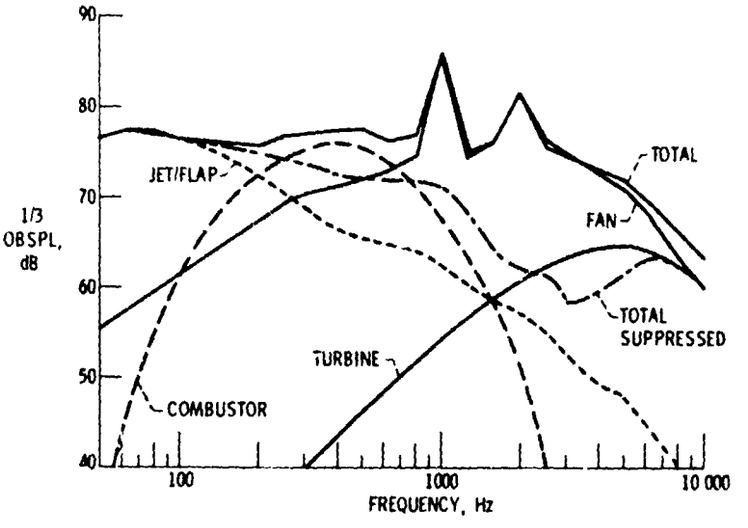

Figure 8.- Takeoff spectra including total and total suppressed noise - single under-the-wing engine. Maximum aft acoustic angle, 120°; sideline distance, 152.4 m (500 ft).

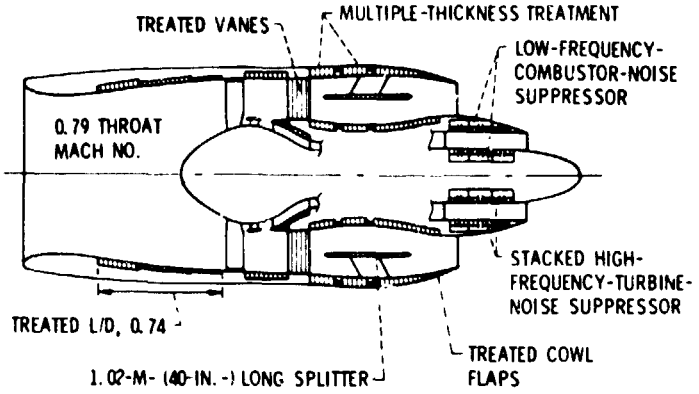

Figure 9.- Acoustic suppression - under-the-wing engine. (Treated L/D is ratio of length of treatment to diameter.)

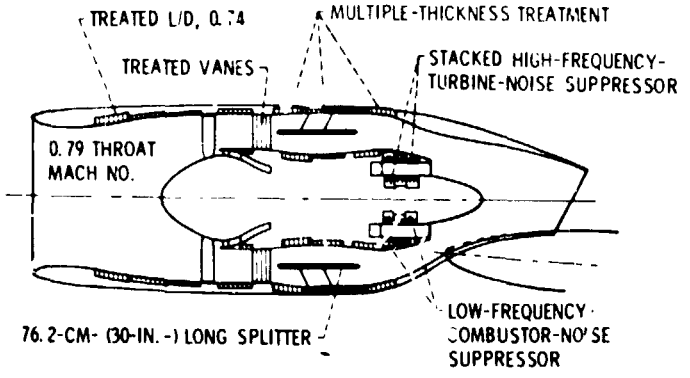

Figure 10.- Acoustic suppression - over-the-wing engine.

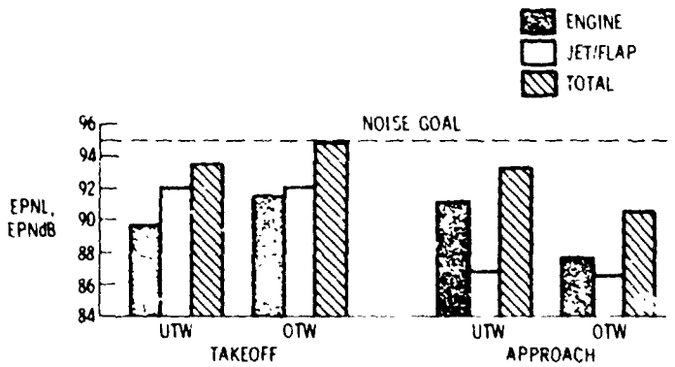

Figure 11.- QCSEE system noise status. Sideline distance, 152.4 m (500 ft).

INLET/NACELLE/EXHAUST SYSTEM INTEGRATION FOR THE QCSEE PROPULSION SYSTEMS

John T. Kutney
General Electric Company

SUMMARY

The QCSEE UTW and OTW propulsion systems provide advanced technology by the introduction of the integrated engine/nacelle installation. This technology is a critical ingredient in achieving the objectives of high installed performance and high installed thrust to weight ratio for the extremely low noise, low fan pressure ratio short haul propulsion systems. The key features of the integrated propulsion systems are discussed in this paper including the high Mach number, fixed geometry supersonic inlet, the variable area nozzles, thrust reversing systems and aircraft accessory location. The roles and interplay of each element are discussed and comparisons made with conventional state-of-the-art technology.

INTRODUCTION

The General Electric Company is currently under contract to NASA to develop, design, build and test two engine systems complete with inlet, ducting and nacelles for future short haul powered-lift aircraft that may enter service in the 1980's. The two engine systems are the under the wing (UTW) based on the principle of the externally blown flap (EBF) STOL aircraft similar to the YC15, and the over the wing (OTW), based on the principle of the upper surface blowing (USB) STOL aircraft similar to the YC14. The General Electric task was to develop the complete propulsion system, integrating all aspects of engine cycle, structure, acoustics, and aerodynamics into a balanced design to meet the program objectives. To assist in this task, Douglas, Boeing and American Airlines were subcontractors to the General Electric Company with the general assignment of reviewing program plans, installation features and performance characteristics. In particular, Douglas was funded for specific assistance in the high Mach inlet design based on their data base and Boeing provided guidance for the OTW exhaust system internal and external aero line definitions.

The General Electric Company design approach provided the first application of the integrated engine/nacelle propulsion system. Some of the key aerodynamic elements of this system, the inlet and exhaust systems, involved advancements in propulsion design technology not normally found in conventional designs. Extensive analysis and component testing were required to provide the timely solution for the best overall design. These tests were conducted

at the NASA Lewis and Langley wind tunnel facilities.

A description of the integrated propulsion system and the role played by the key components is presented in this paper as well as the significant results from the experimental programs.

DISCUSSION

The extremely low noise goals of the QCSEE program present a major challenge in the aerodynamics of nacelle integration in order to provide propulsion systems with minimum performance penalties. The magnitude of the task is vividly portrayed by reference to Figure 1. This analysis illustrates the sea level takeoff thrust per unit frontal area as a function of the fan pressure ratio. The analysis is presented relative to todays CTOL high bypass ratio systems with a nominal fan pressure ratio of 1.6. The figure shows that the QCSEE UTW propulsion system with its fan pressure ratio of 1.25 has a decrease in thrust per unit frontal area relative to the reference CTOL system of 85% and the QCSEE OTW with its fan pressure ratio of 1.35 is in the order of 65%. This perspective portrays the significant need to achieve the lowest installed diameter and length practical with the system requirements.

INLET SELECTION

The inlet is the single largest component of the nacelle installation and has particular significance because it generally defines the nacelle maximum diameter.

The QCSEE UTW and OTW propulsion systems employ a high (0.79) throat Mach number fixed geometry inlet system. Figure 2 illustrates the comparison of the QCSEE high Mach inlet and nacelle and conventional design low Mach inlet of 0.6 The low Mach inlet results in a nacelle diameter 9% larger and a nacelle cowl 10% longer. The low Mach inlet which is representative of conventional state-of-the-art of design technology does indeed define the maximum nacelle diameter and plays a large role in defining the overall nacelle length.

The QCSEE M=.79 throat inlet, however, with its reduced throat area does not set the maximum nacelle diameter since the inlet internal and external geometry diameter design results in a diameter less than that for the integrated nacelle structure.

For the QCSEE propulsion system, the inlet must also provide by its design a large measure of front end noise suppression to meet the low noise goals and also achieve a much higher angle of attack for aircraft operation. The 0.79 throat Mach number inlet with its near sonic flow characteristics is able to achieve its significant front end noise suppression in an inlet length to diameter ratio of 1.0 compared to a 20% increase for the low Mach inlet.

Numerous aero/acoustic tests have demonstrated the significant front end noise suppression of near sonic inlets. The QCSEE propulsion systems are the first to use this characteristic in a practical propulsion design which meets all the QCSEE program objectives.

The QCSEE inlet was designed for a throat Mach number of 0.79 because this was the highest Mach number practical considering inlet engine matching requirements. Typical subsonic inlet performance characteristics follow the recovery/Mach number relationship shown on Figure 3. These data obtained at static conditions show a precipitous fall off in recovery at a Mach number of 0.82. The Mach number of 0.79 was selected by consideration of tolerances required for engine airflow variation, transient engine operational requirements, throat corrected flow variations due to aircraft operational effects and inlet manufacturing tolerances, and then backing off from the limit value of 0.82.

In addition to the required integration for noise and minimum diameter, the QCSEE inlet had another most stringent requirement.

The QCSEE inlet system needed to operate at unusually high angles of attack because of anticipated STOL airplane characteristics and crosswind conditions. The angle of attack condition defined by the NASA requirement was satisfactory engine operation to 50 degrees angle of attack at 80 knots forward velocity. This compares to the more normal maximum angles of attack of conventional CTOL aircraft of 20 to 22 degrees. The NASA defined crosswind requirement was for satisfactory engine operation with 35 knots crosswind at 90 degrees. This is consistent with conventional CTOL type operation.

The selected QCSEE inlet geometry as demonstrated in a scale model verification test program did achieve the desired inlet recovery versus Mach number characteristics. The detailed lip geometry and diffuser shape to achieve the non-separated flow with its attendant low distortion characteristics at the high angles of attack required by QCSEE received much attention in the scale model program. The test data show that the selected QCSEE inlet does not have separation and resultant high distortion until approximately 63 degrees, well beyond the 50° requirement. This assures the engine/airframe compatibility.

The ability of the QCSEE UTW engine/propulsion system to achieve the relatively high takeoff throat Mach number for a fixed geometry inlet is a significant advancement in aero/acoustic integration as evidenced by the flight placard airflow characteristics shown on Figure 4. This analysis portrays the resultant throat Mach number of conventional CTOL systems and the QCSEE UTW system at the takeoff, maximum climb, cruise and approach conditions. The conventional aircraft propulsion system is shown to have its highest throat Mach number at maximum climb conditions and, due to its fixed geometry fan and non-variable nozzle, the Mach number at takeoff and approach falls to 0.57 and .40, respectively. As a result, the CTOL system has no inherent accelerating flow noise suppression benefit at the critical takeoff and approach conditions. The present QCSEE design estimate for the inlet/nozzle/cycle match results in the relatively high inlet throat Mach number of 0.71 at approach conditions also producing some noise suppression. This is made possible by the unique aerothermodynamic UTW engine cycle operating characteristics with the UTW variable pitch fan and variable exhaust fan nozzle.

CONFIGURATION DESCRIPTION

The UTW propulsion system is shown on Figure 5 as it would be installed on a typical EBF aircraft wing arrangement. The overall nacelle geometry is shown to be compatible with the aircraft pylon, wing and nacelle location requirements. The major nacelle components consist of the high Mach inlet, upper pylon mounted accessories, fan duct, the multi-function flare nozzle, core cowl and plug. All nacelle components are axisymmetric and have acoustic treatment as an integral part of the structural walls. The inlet is not drooped as is the case on most CTOL aircraft because the inlet location is far enough forward of the wing to be out of the upwash flow field. The nacelle maximum diameter is 200 cm (78.7 in) with an overall length of 536 cm (211 in). Attention is directed to the accessory pylon location. This upper pylon location does not produce any unusual maintenance problems for the high wing aircraft but does provide a reduced projected frontal area by allowing the accessories to fit within the silhouette of the pylon. The upper accessory location shortens configuration hardware (tubes, ducts, cables, wires, etc.) since there is a minimum distance from the engine to the engine accessories and then on to the aircraft interconnect points. The upper accessory location eliminates the characteristic lower bulge which results in local supervelocities and attendant lower static pressures and hence downward force and loss of aircraft lift. In addition, the accessory sidewise bulge in the pylon is located in front of the wing for a favorable impact on overall aircraft area ruling. The upper pylon accessory location eliminates the need for fan casing hardware on the typical bottom mounted accessory arrangement and permits integration of the fan cowl into the engine structure. This permits thinner nacelle walls - approximately 10 cm (4 in) all around compared to 25 cm (10 in) on the top and sides of the CF6 and 50 cm (20 in) on the bottom of the CF6/DC10 nacelle.

The conventional bottom - mounted accessory arrangement is shown in Figure 6. The nacelle structure is no longer symmetrical and a potential drag producing fairing is required to cover the accessories. In order to maintain low boattail angles, the fairing must be extended aft of the normal nacelle exit with potential negative impact on internal flow characteristics.

EXHAUST SYSTEM

The requirement for low fan pressure ratio to achieve low noise introduces another installation design complexity in the exhaust system. These low pressure ratio systems require variable area exhaust nozzles with the cruise area being reduced relative to takeoff area in order to maintain fan efficiency and increase altitude cruise thrust. The QCSEE UTW engine cycle requires an area increase of 31% while the OTW needs 21% as shown on Figure 7. Conventional CTOL systems being in the higher fan pressure ratio range of 1.5 and over do not employ variable area nozzles.

The QCSEE UTW propulsion system employs a 4 flap arrangement as shown on Figure 8. The 4 flaps are arranged to provide the 31% area change required for takeoff to cruise operations while maintaining acceptable low boattail angles for cruise conditions. In addition, these flaps are actuated outward to pro-

vide the flow inlet for reverse mode operation for the variable pitch UTW fan. Testing at NASA Lewis during wind on conditions has demonstrated recovery levels during reverse tests of 95% at simulated aircraft landing conditions and low pressure distortion levels of 7% at the fan face. This UTW multi-function exhaust system was designed to fit within the overall nacelle envelope defined for the integrated propulsion system.

The QCSEE OTW exhaust system had the additional requirements of efficient flow turning for the over the wing nacelle arrangement (the target was 60° of turning for approach conditions), exit area variability of 21% and a thrust reverser producing 35% reverse thrust.

Since the QCSEE OTW effort involved the development of a ground test engine only, and the nacelle integration with the wing would need to be very intimately tailored to the fuselage and wing flow field, the design thought process specifically excluded any detailed external and internal aerodynamic iterations and no plans were put into place for tradeoff studies or wind tunnel cruise drag investigations. Overall general guidance on the nozzle geometry was received from the Boeing Company.

The QCSEE OTW exhaust system was developed with the assistance of the NASA Langley Dynamic Stability Branch. The aft views on Figure 9 show the means of achieving the required 21% area variation. Two side doors are opened up for takeoff mode and the doors closed for the cruise mode to provide continuous flow surfaces. The side doors provide the required 21% area change and in addition, enhance the sidewise flow spreading characteristics to achieve the desired jet turning for USB Propulsive Lift Systems. The detailed internal and external contours of the nozzle are called out on Figure 10. The combination of the nacelle lines produces a very significant impingement angle of the flow on the wing surface resulting in 59 degrees of jet turning and efficiency of 87%.

The manner in which the nozzle integrates with the overall OTW nacelle and the target type thrust reverser is shown on Figure 11. The reverser geometry was also developed at NASA Langley. The reverse thrust objective of 35% was achieved. The combination of the nacelle duct area and reverser location does restrict the reverse airflow to about 85% of the forward mode level. However, under these conditions, the QCSEE OTW engine has adequate stall margin for satisfactory engine operation in the reverse mode for ground test purposes.

CONCLUDING REMARKS

The QCSEE integrated propulsion system design provides technology advancements in the areas of the high Mach fixed inlet, integrated low drag nacelle with unique upper pylon accessories, and variable area nozzle arrangements. These components have been integrated to fully meet the objectives of the QCSEE short haul transport requirements. The inlet, cycle and exhaust system, nozzle and reverser for both the UTW and OTW are matched efficiently to provide a balanced aero/acoustic design.

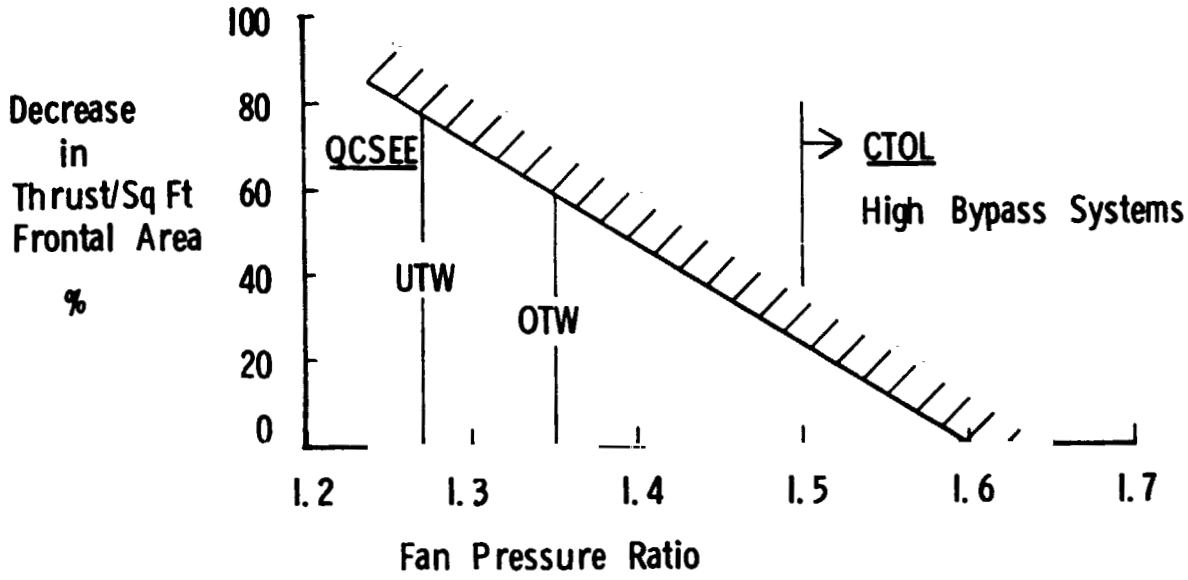

Figure 1.- Effect of fan pressure ratio on thrust per square foot of frontal area.

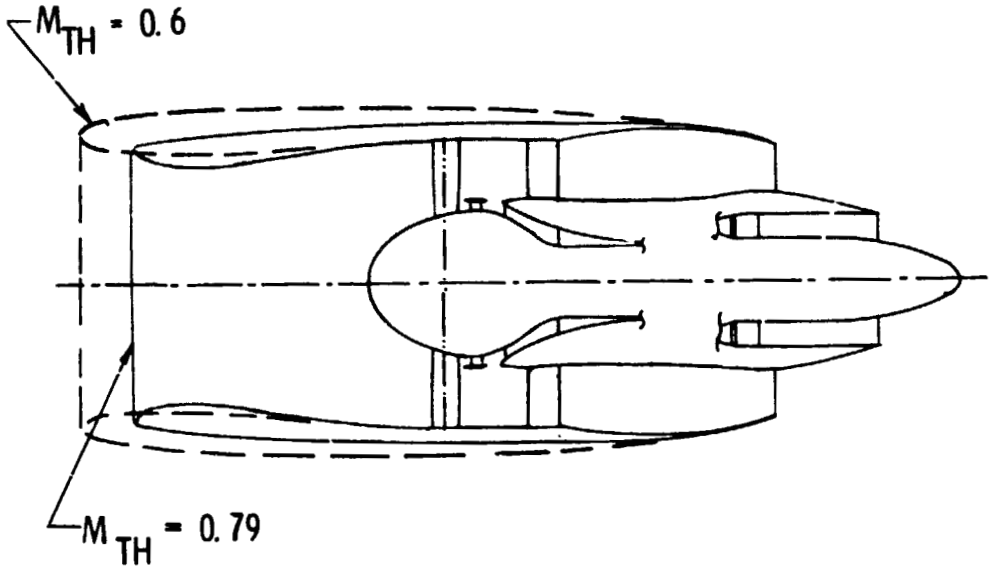

LOW MACH NUMBER INLET: Nacelle Diameter = 9% Larger

Nacelle Cowl = 10% Longer

Figure 2.- Nacelle comparison of high throat Mach number with low throat Mach number.

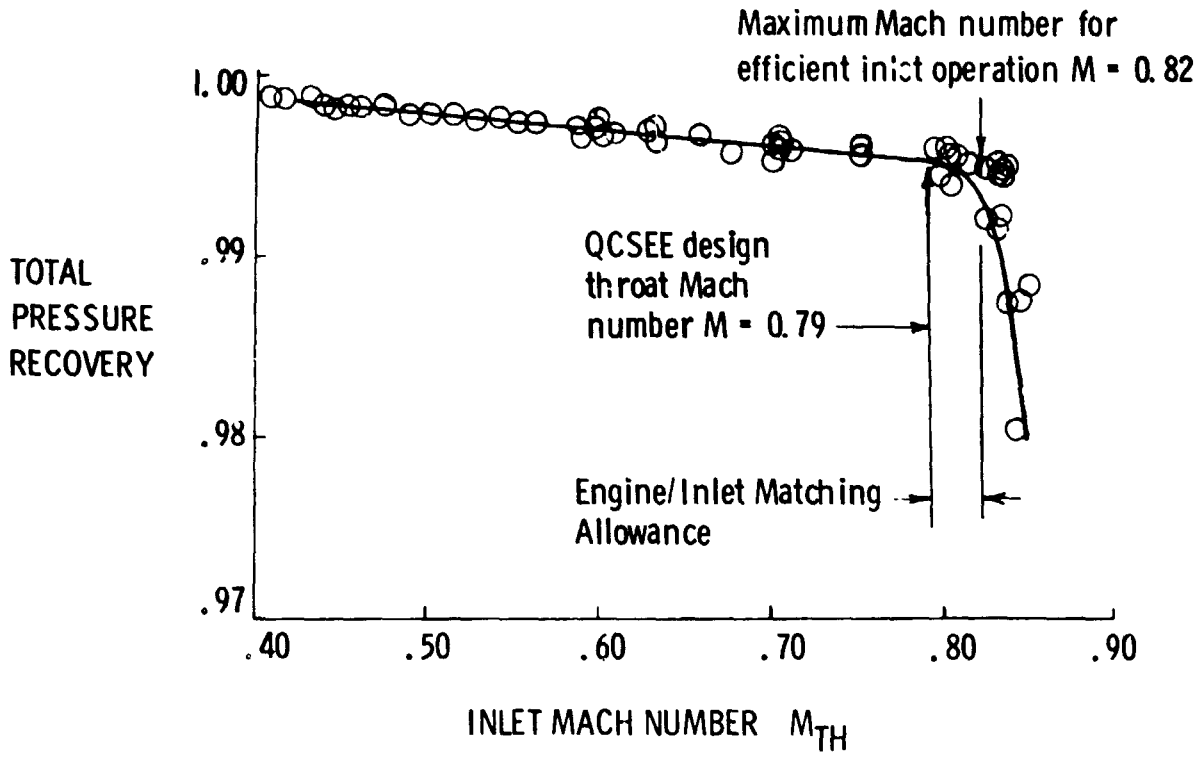

Figure 3.- Inlet throat Mach number selection.

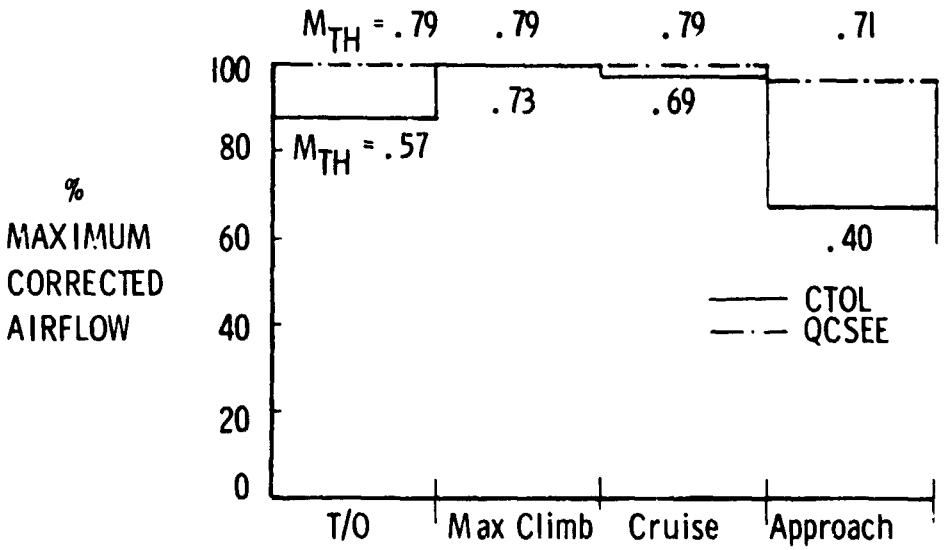

Figure 4.- Flight placard airflow characteristics for QCSEE UTW and CTOL aircraft.

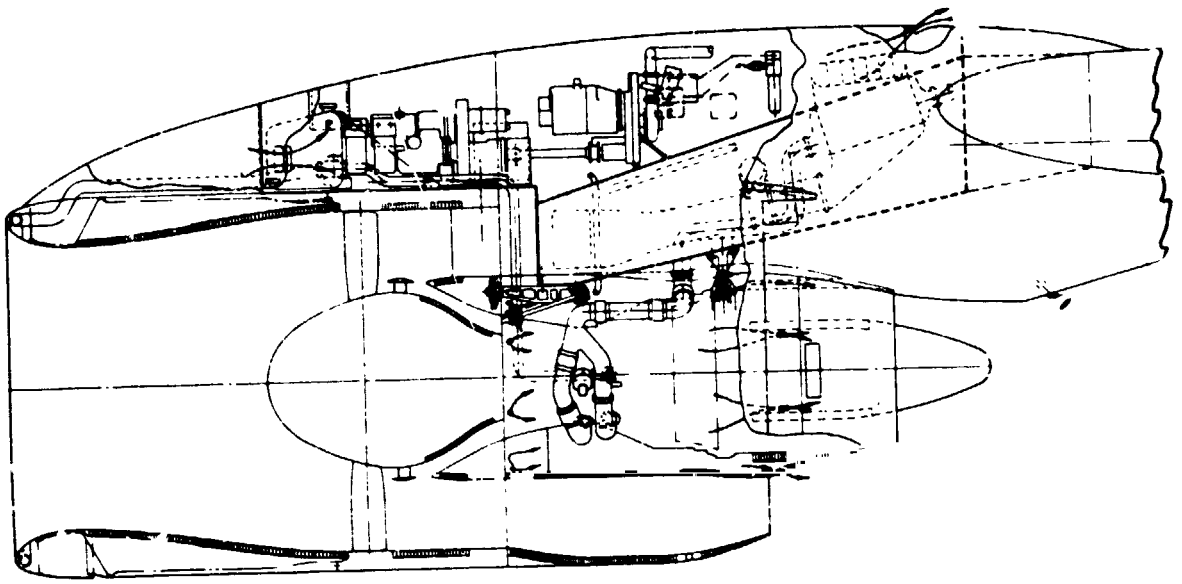

Figure 5.- QCSEE UTW baseline propulsion system, upper pylon accessories.

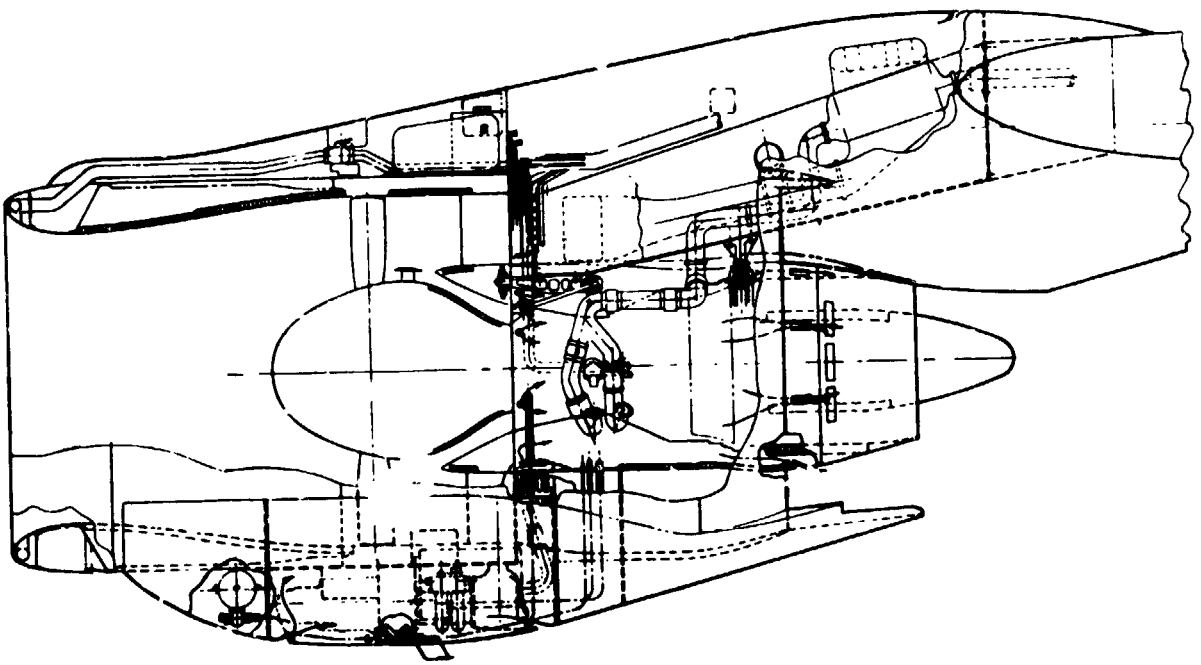

Figure 6.- QCSEE UTW study propulsion system, bottom mounted accessories.

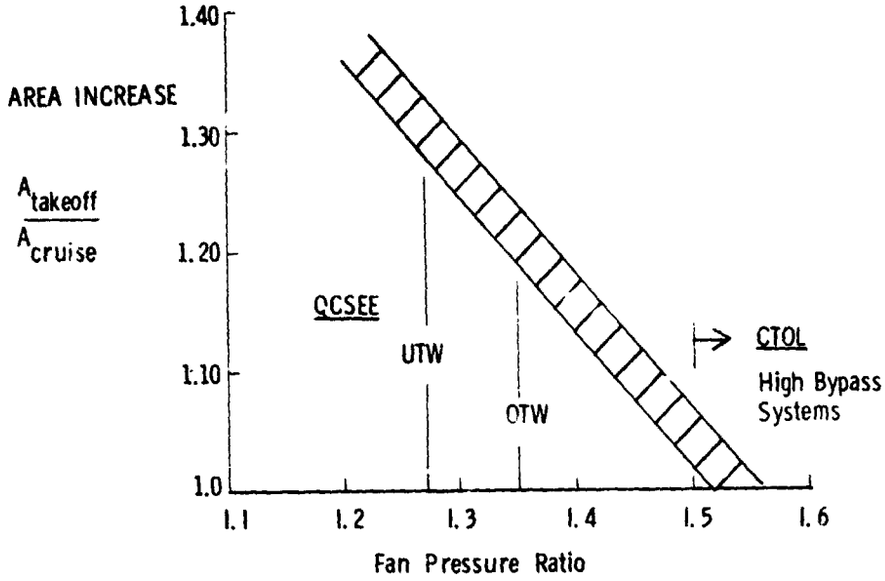

Figure 7.- Effect of fan pressure ratio on nozzle area to maintain fan efficiency at cruise.

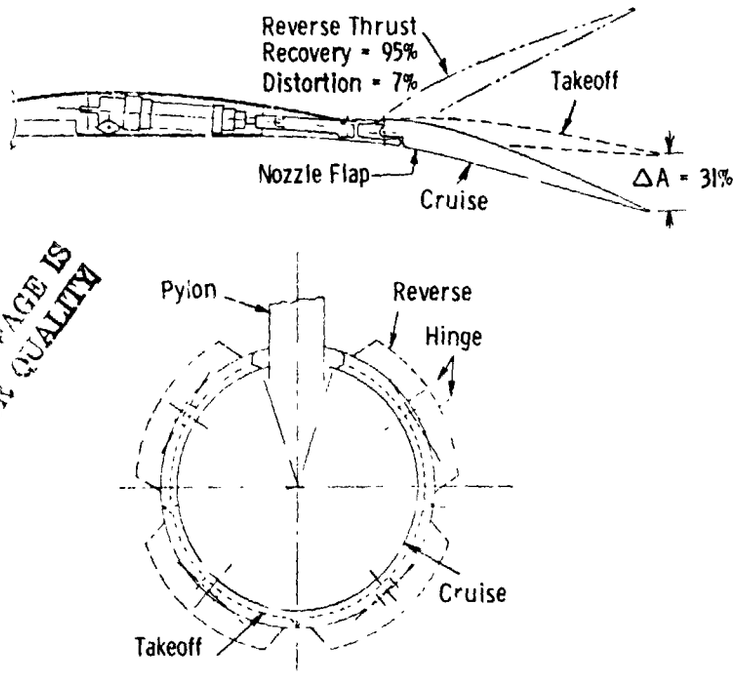

Figure 8.- Exhaust nozzle for QCSEE UTW.

Figure 9.- Exhaust nozzle for QCSEE OTW aft view.

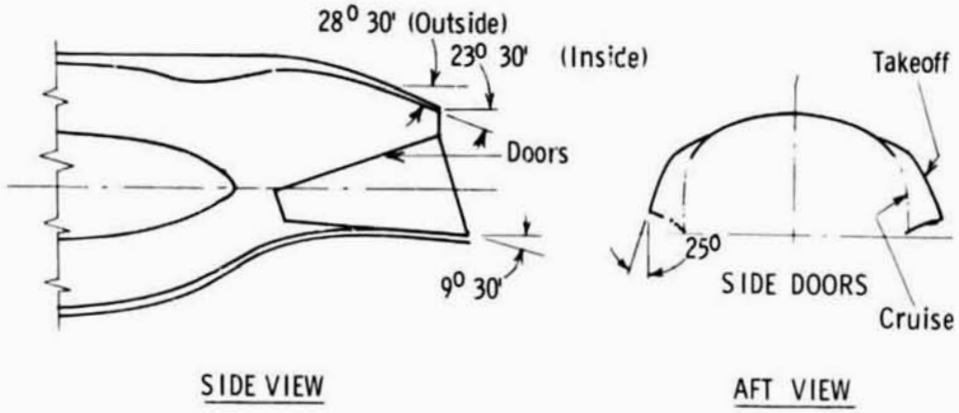

Jet Turning Angle = 59°, Efficiency = 87%

Takeoff to Cruise

Nozzle Area Change = 21%

Figure 10.- QCSEE OTW exhaust nozzle.

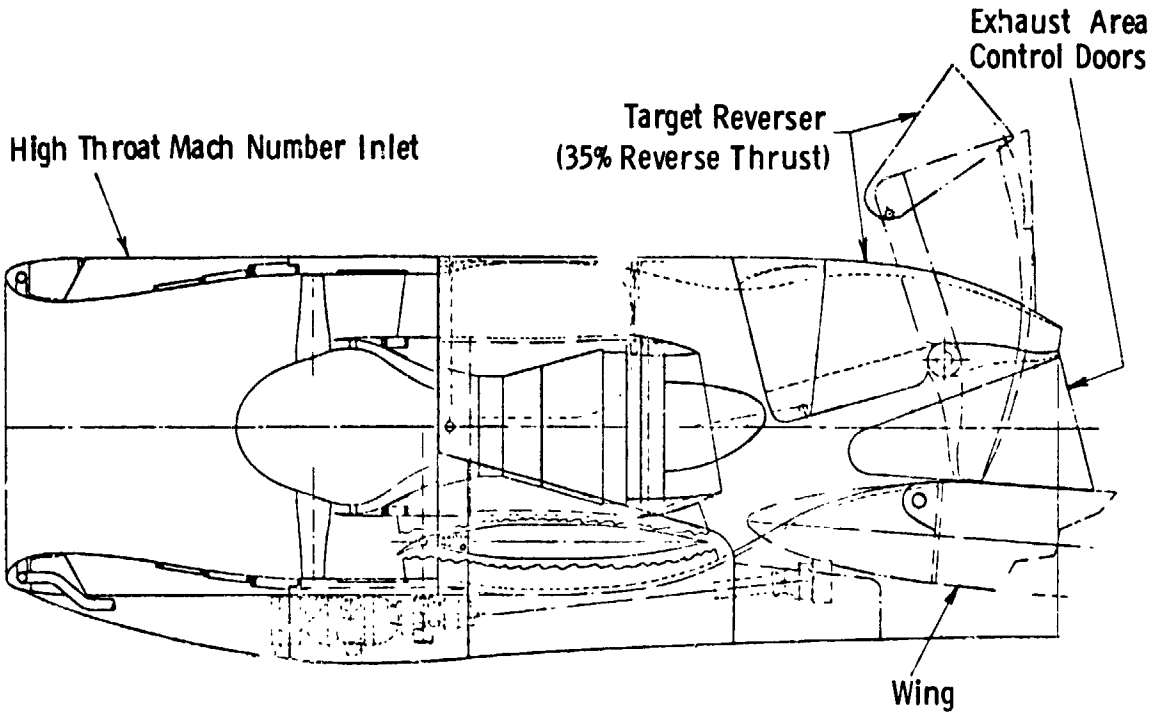

Figure 11.- QCSEE OTW nacelle - sideview variable nozzle and thrust reverser.

N78-24069

INLET TECHNOLOGY FOR POWERED-LIFT AIRCRAFT

Roger W. Luidens
NASA Lewis Research Center

23

SUMMARY

The concepts, analytical tools, and experimental data available for designing inlets for powered-lift airplanes are discussed. It is shown that inlets can be designed to meet noise, distortion, and cruise drag requirements at the flight and engine operating conditions of a powered-lift airplane. The penalty in pressure recovery for achieving the required noise suppression was 0.3 percent.

INTRODUCTION

Discussed in this paper are some of the concepts, analytical tools, and experimental data that form the technology base for designing inlets for powered-lift aircraft. While the objective of the paper is to discuss technology, the QCSEE inlet design problem is used as a focal point of the discussion. Inlets for powered lift differ from conventional subsonic inlets largely because the requirements imposed on them are more stringent. The requirements for the QCSEE (quiet, clean, short-haul experimental engine) inlet are shown in figure 1: (1) The inlet must also provide to the fan a low-distortion airflow at a high pressure recovery. High pressure recovery is more important to a low fan pressure ratio powered-lift engine like QCSEE than the current higher fan pressure ratio engines. Good inlet aerodynamic performance, in general, means no ... flow separation can occur for any of the flow conditions to which the ... may be subjected, namely, static conditions, which may set the design of the top region of the lip; a 15-m/sec (30-kn), 90° crosswind, which may set the design of the side of the inlet; and an 41-m/sec (80-kn), 50° upwash, which controls the design of the bottom region of the lip. This last condition greatly exceeds that for conventional aircraft. (2) As discussed in the preceding paper (ref. 1), the inlet must yield greater noise suppression than conventional inlets. This may be achieved by wall treatment, a high throat Mach number, or a combination of these two approaches. (3) The inlet should have low drag. Again, when the powered-lift engines like QCSEE have a lower fan pressure ratio, the fan and, thus, the inlet diameter are relatively large so the inlet drag is a greater fraction of the engine thrust. Designing for a low cruise drag is thus of greater importance. Similarly, when the airplane is climbing out after takeoff, the failure of an engine should not result in excessive drag related to inlet aerodynamics.

368

PAGE INTENTIONALLY BLANK

SYMBOLS

a/b	lip internal fineness ratio, ratio of ellipse semimajor to semiminor axis
A_h	area circumscribed by inlet highlight
A_m	maximum inlet frontal area
A_0	cross-sectional area of free-stream tube of air entering inlet
CR	contraction ratio
d_f	fan diameter
b	honeycomb backing depth
l	length of inlet
l_a	length of acoustic treatment
M_f	axial Mach number at the fan face
M_{max}	maximum Mach number
M_0	free-stream Mach number
M_t	average throat Mach number
q_t	dynamic pressure corresponding to the average throat Mach number
r_f	fan radius
r_h	radius to the highlight
r_t	throat radius
V_0	free-stream velocity
V_t	average throat velocity
α	inlet flow angle of attack due to upwash
α_{sep}	separation flow angle
ΔP	total pressure loss
θ_{max}	diffuser maximum wall angle
σ	open area ratio
ψ	crosswind flow angle

Boundary-layer properties determined from such analyses (ref. 9) are shown in figure 4. The results are shown for the internal surface of the windward side of the inlet as suggested by the lower sketch.

In the figure the local skin friction coefficient is plotted versus the surface distance from the inlet stagnation point. A zero value for the local friction coefficient indicates separation. Beginning with the zero angle of attack case, the boundary layer, starting at the stagnation point on the inlet lip, is first laminar. In the laminar region the skin friction drops rapidly with increasing surface distance to the first minimum which occurs on the inlet lip. Then, transition from laminar to turbulent boundary layer takes place and the local skin friction increases. Next, in the region of fully developed turbulent flow, the friction coefficient reaches a second minimum part way down the diffuser.

The two minima are locations of potential separation. As the angle of attack is increased from 0 to 20°, the skin friction at the second minimum goes to zero, indicating separation in the inlet diffuser. When the angle of attack is increased to 40°, the diffuser separation moves upstream slightly. At a 50° angle of attack the skin friction at the first minimum has gone to zero, and the separation has jumped to the lip. This, of course, precedes and thus engulfs the diffuser separation.

Flow separation in general depends on such factors as surface roughness, free-stream turbulence, and the size of the inlet. The diffuser separation depends also on the diffuser shape, including the maximum wall angle θ_{max} and the condition of the boundary layer entering the diffuser (ref. 10). The influence of these factors is currently being investigated.

Effect of separation location on total pressure loss. - The location of the flow separation within the inlet affects the amount of total-pressure loss it causes as shown in figure 5 (ref. 9). The ordinate is the total-pressure loss coefficient $\Delta P/q_t$ (where ΔP is equal to 1 minus the pressure recovery and q_t is the dynamic pressure corresponding to the average throat Mach number). The abscissa is again the surface location on the inlet. Note that lip separation causes much larger losses than diffuser separation. Also, large flow distortions are usually associated with lip separation. To emphasize the importance of lip separation, fan blade failures have been observed for a model fan when it was subjected to several repetitions of separated lip flow. Because of its grave consequences, the following discussion deals with lip separation.

Separation Bounds

Returning to figure 4, the angle of attack at which the flow first separates from the lip, 50° in figure 3, is called the lip separation angle. The data of figure 4 are for an inlet at one flow condition (V_0 = 80 kn, M_t = 0.50). The lip separation angle for an inlet can be determined for a wide range of free-stream velocities and throat Mach numbers. The separation angle presented as a function of an appropriate independent variable is called the inlet separation bound.

Local surface Mach numbers less than unity. - Figure 6 considers cases (ref. 11) where the throat Mach numbers are sufficiently low that the flow can be considered incompressible; i.e., the local surface Mach numbers never exceed unity. The results are plotted as separation angle α_{sep} versus throat to free-stream velocity ratio, the parameter suggested in the discussion of figure 3. This plot fairly well collapses the data over the complete angle of attack range from zero to 180°. (Similar results are shown in ref. 12.)

Several of the QCSEE inlet operating conditions are shown in figure 6. As can be seen, the region of primary interest to powered lift is that for separation angles less than 90°. Also, it can be judged by the location of the requirements relative to the separation bound that the 50° flow angle at 80 knots is the more difficult condition; and it is the one that will be used in subsequent examples.

Local surface Mach numbers greater than unity. - The inlet throat Mach number affects the separation bounds as shown in figure 7, which is a plot of separation angle versus throat Mach number (ref. 13). The data are for a constant free-stream velocity of 80 knots so that an increasing throat Mach number corresponds also to increasing V_t/V_0 as indicated by the second abscissa. For values of throat Mach numbers less than about 0.60, the curve is rising and concave upward as were the previous cases for low throat Mach numbers. For higher values of throat Mach number, the local surface Mach number exceeds unity, and the curve becomes concave downward with the separation angle finally decreasing with increasing throat Mach number. This kind of separation is associated with shock - boundary-layer interaction on the lip as depicted in the sketch for $M_{max} > 1.0$ (fig. 7). A more detailed analysis of inlet separation is given in reference 14. The throat Mach number thus has a strong effect on separation angle.

Note that the choking flow limit occurs for an average throat Mach number of less than unity. The reasons for this will be shown shortly.

Effect of lip contraction ratio. - Figure 8, which repeats the coordinate system and data of the previous figure but adds the data for both a larger and smaller inlet contraction ratio (ref. 13), shows the effect of increasing contraction ratio (increasing lip thickness) is to increase the separation angle.

Also shown in the figure is the QCSEE operating region of 50° at 80 knots for airflows (throat Mach numbers) from flight idle to full throttle. A critical condition is that of flight idle at a 50° upwash. The inlet with the 1.37 contraction ratio does not meet the requirements at flight idle or at takeoff; the inlet with a 1.46 contraction ratio satisfied the full range of conditions.

Having defined an inlet that satisfies the condition of no lip separation, we turn next to the subject of noise suppression.

Noise Suppression

Fan noise characteristics. - To understand the acoustic results, it is

necessary to understand two characteristics of the fan noise listed and illustrated in figure 9, its radial and angular distribution. (1) Radial distribution of intensity: Noise generated by the fan tends to be greatest toward the fan tip or near the duct wall. (2) Acoustic ray directions: As suggested by the sketch, sound waves can have velocity components in the radial and circumferential directions as well as the axial direction. When significant radial and circumferential components exist, the axial component may be considerably less than the speed of sound. These nonaxial components are related to what acousticians call acoustic modes. The propagation of these modes upstream in the inlet duct is influenced by the duct geometry and the flow Mach number.

Suppression methods: Two sound suppression methods are also listed and illustrated in figure 9, acoustic wall treatment, and high throat Mach number. (1) Wall treatment: The sound, as it proceeds up the inlet duct, can be absorbed by wall acoustic treatment. This can be especially effective when the sound is concentrated near the wall as in the case illustrated. (2) High throat Mach number: There are two aspects of this topic to be considered. (a) Because the axial component of the sound wave is generally less than the speed of the sound, a throat Mach number (the ratio of the flow velocity to the speed of sound) less than unity will choke off the propagation of the sound wave out of the inlet. (b) Even for throat Mach numbers significantly less than one, the local Mach numbers near the wall can approach or exceed one as illustrated by the throat Mach number profile in figure 9. This profile is due to the wall curvature in the lip and throat regions. Again, because the noise is concentrated near the wall and has an axial velocity less than the speed of sound, these high local Mach numbers can be very effective in reducing the noise.

As was seen in figure 7, the choking weight flow limit is less than that corresponding to an average throat Mach number of unity. The nonuniform velocity profile across the throat plane shown in figure 9 is the reason for this. An average throat Mach number of unity can occur only for a uniform throat velocity profile.

Inlet acoustic performance: The acoustic performance of two inlets is shown in figure 10. Although the data of figure 10 are new, some of the results are similar to those that may be found in references 15 to 22. The plot shows the reduction in sound pressure level (SPL) of the source noise in the one-third octave band, containing the blade-passage frequency (BPF). This is plotted versus the average throat Mach number. The lower curve is for a hard wall or untreated inlet. Noise suppression starts at a throat Mach number of about 0.60. The suppression then increases rapidly with increasing throat Mach number. The suppression starts at such a low throat Mach number because of the source noise characteristics and throat Mach number profile previously described. If the noise source had been a simple plane wave normal to the inlet axis and if the throat velocity profile had been flat, little or no suppression would have occurred until the average throat Mach number was unity, and at that condition the noise would have been choked off abruptly.

The upper curve is for an inlet with the same geometry as the hard wall inlet but with the walls acoustically treated with honeycomb covered by a perforated plate as illustrated in figure 9. The honeycomb has a backing depth h

of 1.5 percent of the fan diameter, and the face plate has a 6.2 percent open area. An 8- to 9-dB suppression results at the lower throat Mach numbers. The incremental suppression contributed by the treated wall decreases when the throat Mach numbers become high enough to also cause suppression. The reduced effectiveness of the treatment may be due to the higher velocities over its surface. This is an area as yet not fully understood. Acoustic results similar to those shown have also been obtained at static conditions for a model of the QCSEE inlet.

Shown on the ordinate are the QCSEE inlet suppression requirements, in decibels, of perceived noise level, PNdB. The ΔPNdB and ΔSPL are about the same if the source noise has a dominant fan tone as is the case here. The approach noise suppression of 8 PNdB, which is required at the lower throat Mach numbers that will occur during this maneuver, can be achieved by the wall treatment alone. The 13 PNdB required for takeoff can be achieved at a high throat Mach number for the hard wall inlet, or by the treated wall inlet at a slightly lower throat Mach number.

Inlet aerodynamic performance. - The pressure recovery for the same two inlets is shown versus the average throat Mach number in figure 11. In general, the pressure recovery decreases with increasing throat Mach number. For Mach numbers below 0.7 this is primarily a friction loss as suggested by the fact that the dashed curve, representing a constant total-pressure loss coefficient $\Delta P/q_t$, fits the data. The combination of the physical roughness associated with the porosity of the treated wall and the "pumping" in and out due to the noise causes the effective wall friction of the treated wall to be about 8 percent more than the hard wall. Large total-pressure losses occur precipitously near the choking flow limit. These large losses occur at a lower throat Mach number for the treated inlet. The inlet is entering supercritical operation here. The losses are associated with the occurrence of a region of local supersonic flow and weak shocks which produce a rapid growth in the boundary-layer thickness. The measured boundary-layer profiles, however, indicate that flow separation has not yet occurred for any of the data points in the figure.

The curves are labeled to show where 13-dB suppression is obtained. The treated inlet shows a small advantage in pressure recovery over the hard wall inlet to achieve the required suppression. The higher pressure recovery is 0.990. If no noise suppression had been required, a hard wall inlet could have been designed with a throat Mach number of perhaps 0.6, where the pressure recovery is 0.993. Thus, 0.3 percent pressure recovery loss is chargeable to achieving the required inlet noise suppression using a high throat Mach number inlet with acoustic wall treatment. This corresponds to less than 1.0 percent loss in takeoff thrust for an engine like QCSEE with a 1.27 fan pressure ratio at takeoff.

The results shown are for zero angle of attack. The effect of angle of attack on the aeroacoustic performance of treated wall inlets remain to be determined.

Thus far we've discussed the procedure for selecting an inlet design to avoid separation and to achieve the desired noise suppression. We turn finally to considerations of the inlet drag.

Inlet Drag

Cruise drag. - As shown in figure 12, there are three potential sources of drag to be considered: additive drag, pressure drag, and friction drag. The additive drag on the streamline approaching the inlet will be cancelled by the lip suction thrust if the external frontal area of the inlet $A_m - A_h$ is an appropriate fraction of the spillage frontal area $A_h - A_0$ as discussed in reference 23, for example. Pressure drag can be reduced by shaping the external contour to avoid shock-boundary layer interaction at cruise speed. In the case of QCSEE the cruise Mach number is 0.72. At this Mach number the additive and pressure drags can be made essentially zero by proper design.

The friction drag is unavoidable and depends on the inlet wetted area and hence its length and diameter. For powered-lift inlets that require a high degree of suppression like the QCSEE inlet, a significant factor in determining the inlet length is the length of acoustic treatment required. Also, this treatment must be in a region of local Mach number low enough to be acoustically effective. The lip and throat region then add to the length. The required treatment length makes the diffuser wall angles small enough to prevent diffuser separation due to a high θ_{max} from being a problem. For the QCSEE inlet, the total length to fan diameter ratio turns out to be about one.

The maximum diameter of the inlet is determined by a sequence of factors that are only briefly reviewed here: the fan annulus area, the flow rate through the fan (the fan face Mach number), the throat Mach number for noise suppression, the contraction ratio for the 50° upwash, and the external lip thickness determined to avoid additive drag.

For the QCSEE inlet it was found that the lip shape selected to meet the most difficult flow condition, i.e., an 80-knot, 50° upwash at flight idle, could be applied all around the inlet and still result in a nacelle thickness over the fan that is only 10 percent of the fan radius. This thickness is also about the minimum required for the nacelle structure. With a circumferentially uniform lip the entire inlet can be built axisymmetrically. This has the advantage of simplicity. Because the lip was designed for the most difficult flow condition, the less difficult conditions, like the crosswind requirements, are automatically satisfied. An inlet like the one shown is thus a low-cruise-drag inlet that meets all the noise and flight requirements that have been specified.

An important overall observation is that the high throat Mach number desired for noise suppression is consistent with the thick lip that is desired for high upwash angle tolerance and a thin nacelle thickness over the fan for low cruise drag. In contrast, an inlet designed for a throat Mach number of 0.6 would have had a larger maximum diameter and would not have met the noise suppression requirements.

Engine-out drag. - It is desirable to maintain a low engine drag in event of an engine failure during climbout following takeoff because this helps maintain a safe climb angle and minimizes undesirable rolling and yawing moments. The fan, when it is powered, sucks air into the inlet so that capture

stream tube at climbout is larger than the engine inlet. But, if the fan is unpowered due to engine failure, the fan offers a resistance to the flow of air through the nacelle so some of the air spills around the inlet. The streamline pattern then becomes similar to that shown for cruise, and the potential for inlet drag exists in the additive drag on the approaching streamline. The additive drag can be low if the spillage is low. A high throat Mach number inlet tends to reduce the inlet highlight area and this is in the direction of reducing the spillage. Furthermore, the high lip thickness, which was selected to achieve a high upwash angle tolerance, presents a large lip frontal area on which to generate leading edge thrust to offset the additive drag. Thus the high throat Mach number inlet described should have a low engine-out drag.

With regard to the air spillage, feathering the fan blades, as can be done with a variable pitch fan, produces lower resistance to internal flow than a fixed pitch fan and thus reduces the airflow spillage around the inlet lip. Thus, from the point of view of achieving a low engine-out inlet drag, the variable pitch fan may have an advantage over the fixed pitch fan.

An interesting aspect of high throat Mach number inlets not discussed in this paper is throat Mach number control to maintain suppression. This topic is discussed in reference 24.

CONCLUDING REMARKS

Some of the concepts, analytical tools, and experimental data available for designing inlets for powered-lift aircraft have been discussed. It has been shown that inlets can be designed that meet the noise, distortion, and cruise drag requirements at the flight and engine operating conditions that occur for a powered-lift airplane. The penalty in pressure recovery for achieving the required noise suppression was 0.3 percent.

The effect of high flow velocities on wall treatment on noise suppression is one area that can use more detailed study.

There are also some inlet characteristics that remain to be explored such as (1) the effect of the nonaxisymmetric internal boundary layer due to the inlet upwash angle on the fan source noise and on the suppression characteristics of wall treatment and (2) the effect of the inlet upwash angle on the directivity of the noise propagating from the inlet.

It's expected that some of the acoustic technology that has been developed can be applied to quieting current conventional airplanes and that some of the inlet flow analysis methods and data can be applied to the design of high angle of attack inlets for VTOL airplanes such as the inlet for a tilt nacelle and the inlet for a fan in wing or pod.

REFERENCES

1. Loeffler, Irvin J.; Smith, Edward B.; and Sowers, Harry D.: Acoustic Design of the QCSEE Propulsion Systems. Powered-Lift Aerodynamics and Acoustics, NASA SP-406, 1976. (Paper no. 21 of this compilation.)

2. Albers, James A.; and Miller, Brent A.: Effect of Subsonic Inlet Lip Geometry on Predicted Surface and Flow Mach Number Distributions. NASA TN D-7446, 1973.

3. Stockman, N. O.: Potential Flow Solutions for Inlets of VTOL Lift Fans and Engines. Analytical Methods in Aircraft Aerodynamics. NASA SP-228, 1970, pp. 659-681.

4. Stockman, Norbert O.; and Button, Susan L.: Computer Programs for Calculating Potential Flow in Propulsion System Inlets. NASA TM X-68278, 1973. (See also NASA Tech Brief B75-10018.)

5. Albers, James A.; Stockman, Norbert O.; and Hirn, John J.: Aerodynamic Analysis of Several High Throat Mach Number Inlets for the Quiet Clean Short-Haul Experimental Engine. NASA TM X-3183, 1975.

6. Albers, James A.; and Gregg, John L.: A Computer Program to Calculate Laminar, Transitional, and Turbulent Boundary Layers for Compressible Axisymmetric Flow. NASA TN D-7521, 1974. (See also NASA Tech Brief B74-10129.)

7. Albers, J. A.; and Stockman, N. O.: Calculation Procedures for Potential and Viscous Flow Solutions for Engine Inlets. Eng. Power, vol. 97, ser. A, no. 1, Jan. 1975, pp. 1-10.

8. Stockman, N. O.: Potential and Viscous Flow in VTOL, STOL, or CTOL Propulsion System Inlets. AIAA Paper 75-1186, Sept. 1975.

9. Felderman, E. John; and Albers, James A.: Comparison of Experimental and Theoretical Boundary-Layer Separation for Inlets at Incidence Angle at Low-Speed Conditions. NASA TM X-3194, 1975.

10. Povinelli, L. A.: An Experimental and Analytical Investigation of Axisymmetric Diffusers. AIAA Paper 75-1 1.

11. Tyler, R. A.; and Williamson, R. G.: An Experimental Investigation of Inclined Compressor Inflow. AIAA Paper 65-707, Oct. 1965.

12. Luidens, Roger W.; and Abbott, John M.: Incidence Angle Bounds for Lip Flow Separation of Three 13.97-Centimeter-Diameter Inlets. NASA TM X-3351, 1976.

13. Miller, Brent A.; Dastoli, Benjamin J.; and Wesoky, Howard L.: Effect of Entry-Lip Design on Aerodynamics and Acoustics of High Throat-Mach-Number Inlets for the Quiet, Clean, Short-Haul Experimental Engine. NASA TM X-3222, 1975.

14. Jakubowski, A. K.; and Luidens, R. W.: Internal Cowl-Separation at High Incidence Angles. AIAA Paper 75-64, Jan. 1975.

15. Miller, Brent A.; and Abbott, John M.: Aerodynamic and Acoustic Performance of Two Choked-Flow Inlets Under Static Condition. NASA TM X-2629, 1972.

16. Miller, Brent A.; and Abbott, John M.: Low-Speed Wind-Tunnel Investigation of the Aerodynamic and Acoustic Performance of a Translating-Centerbody Choked-Flow Inlet. NASA TM X-2773, 1973.

17. Klujber, F.: Results of an Experimental Program for the Development of Sonic Inlets for Turbofan Engines. AIAA Paper 73-222, Jan. 1973.

18. Klujber, F.; Bosch, J. C.; Demetrick, R. W.; and Robb, W. L.: Investigation of Noise Suppression by Sonic Inlets for Turbofan Engines. Vol. I: Program Summary. (D6-40855, Boeing Commercial Airplane Co.; NAS3-15574) NASA CR-121126, 1973.

19. Abbott, John M.; Miller, Brent A.; and Golladay, Richard L.: Low-Speed Wind-Tunnel Investigation of the Aerodynamic and Acoustic Performance of a Translating-Grid Choked-Flow Inlet. NASA TM-X2966, 1974.

20. Groth, H. W.: Sonic Inlet Noise Attenuation and Performance with a J-85 Turbojet Engine as a Noise Source. AIAA Paper 74-91, Jan. 1974.

21. Abbott, J. M.: Aeroacoustic Performance of Scale Model Sonic Inlets. AIAA Paper 75-202, Jan. 1975.

22. Hickcox, T. E.; Lawrence, R. L.; Syberg, J.; and Wiley, D. R.: Low Speed and Angle of Attack Effects on Sonic and Near-Sonic Inlets. (D6-42392, Boeing Commercial Airplane Co.; NAS3-18035) NASA CR-134778, 1975.

23. Hancock, J. P.; and Hinson, B. L.: Inlet Development for the L-500. AIAA, June 1969.

24. Miller, B. A.: Experimentally Determined Aeroacoustic Performance and Control of Several Sonic Inlets. AIAA Paper 75-1184, Sept.-Oct. 1975.

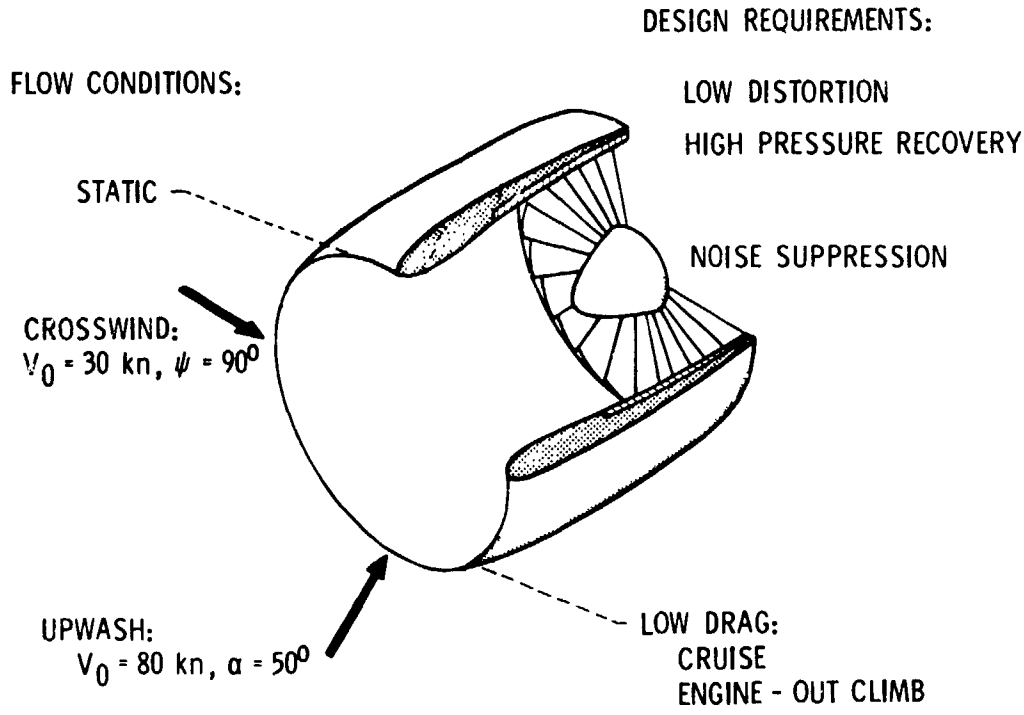

Figure 1.- QCSEE inlet requirements.

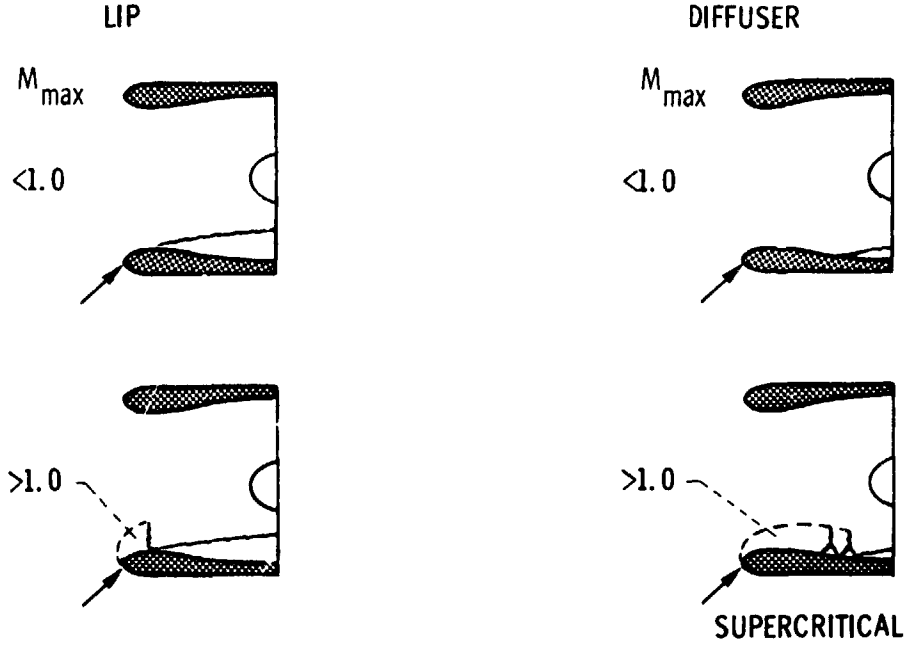

Figure 2.- Kinds of separation.

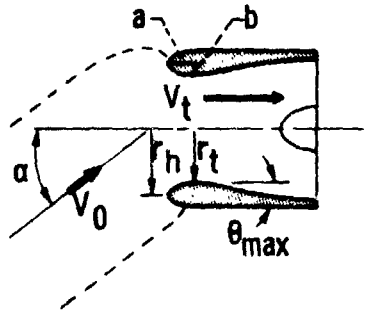

GEOMETRIC	FLOW
a/b	α
θ_{max}	M_t
$CR \equiv (r_h/r_t)^2$	V_t/V_0

Figure 3.- Separation parameters.

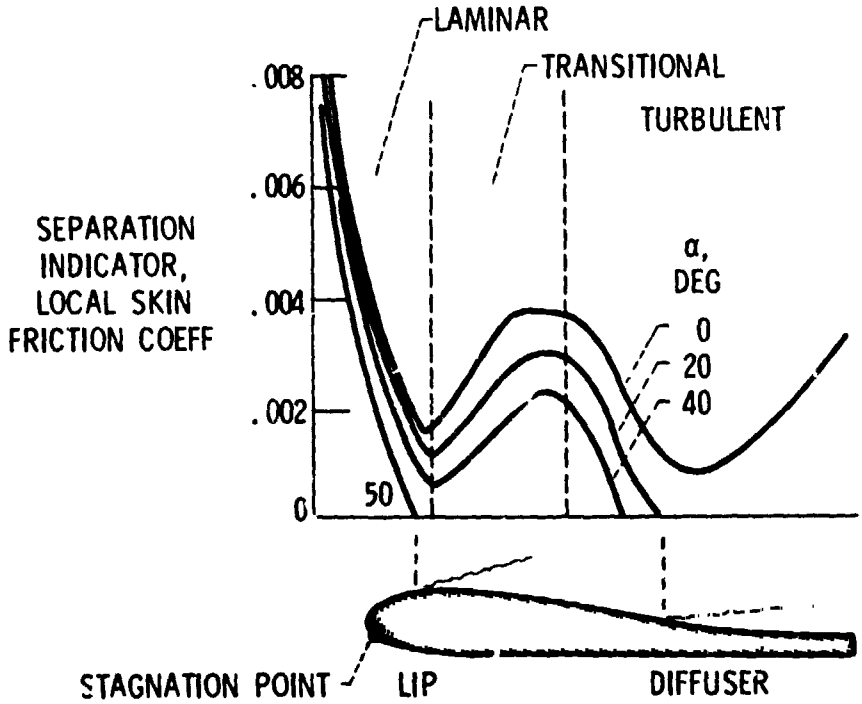

Figure 4.- Boundary-layer analysis of inlet separation. V_0 = 80 kn; M_t = 0.50.

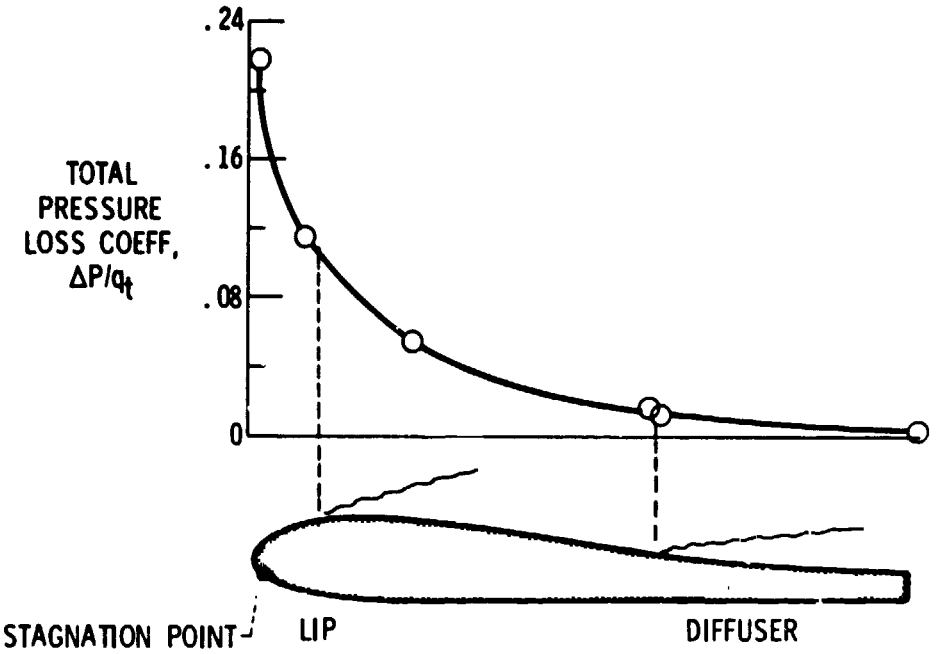

Figure 5.- The variation of inlet total-pressure loss with separation location.

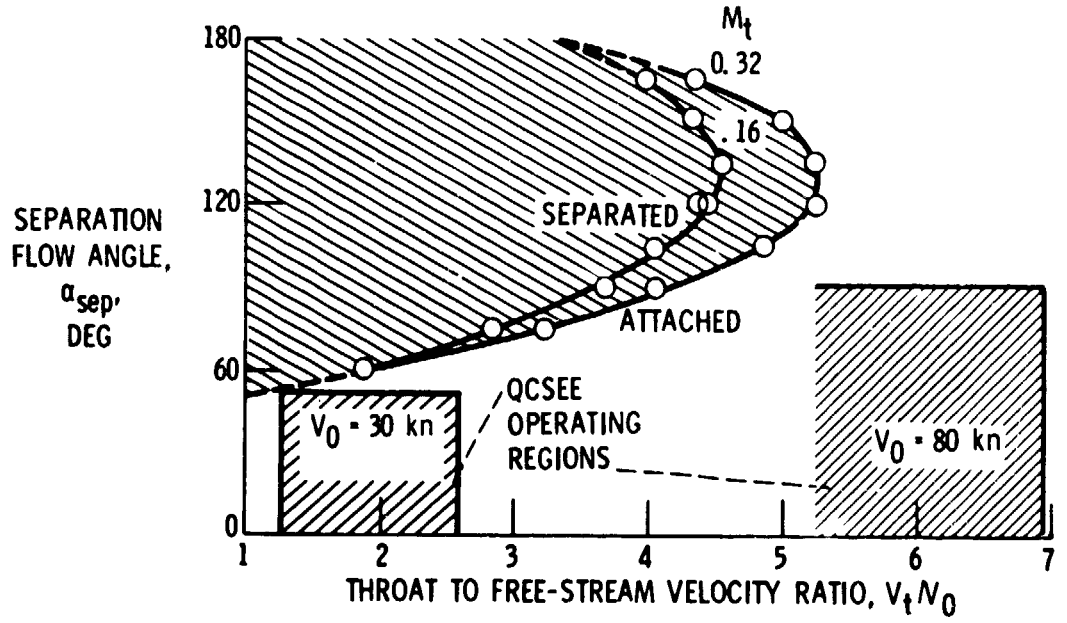

Figure 6.- Lip separation bound, $M_{max} < 1$. CR = 1.30.

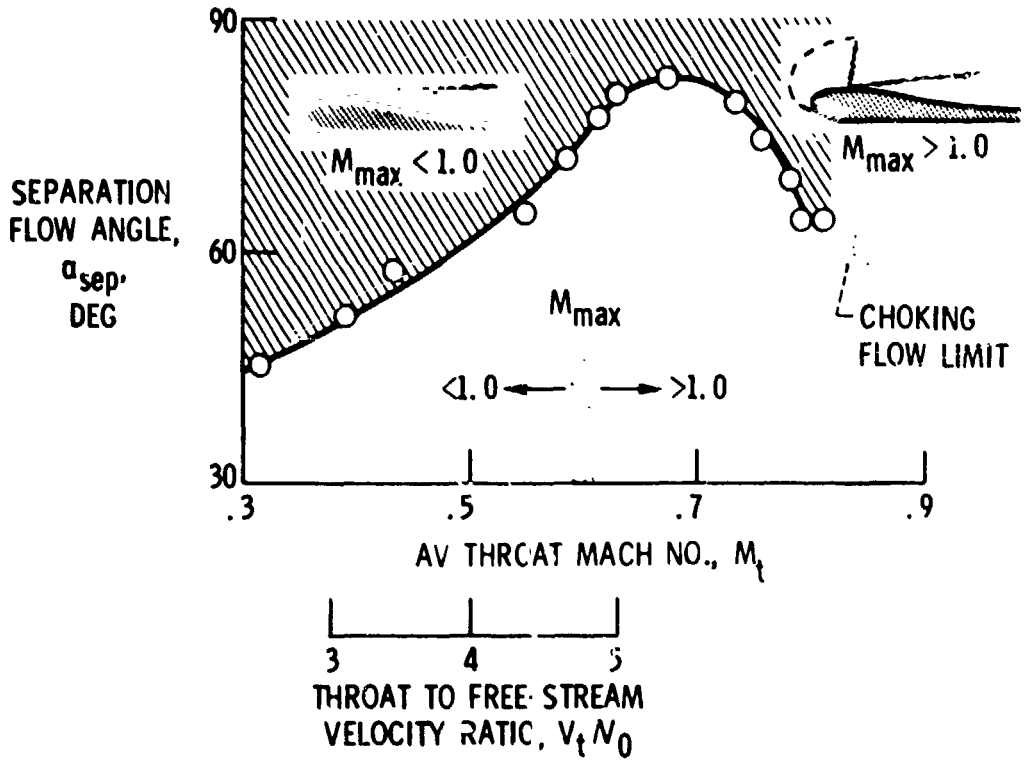

Figure 7.- Lip separation bound. CR = 1.46; V_0 = 80 kn.

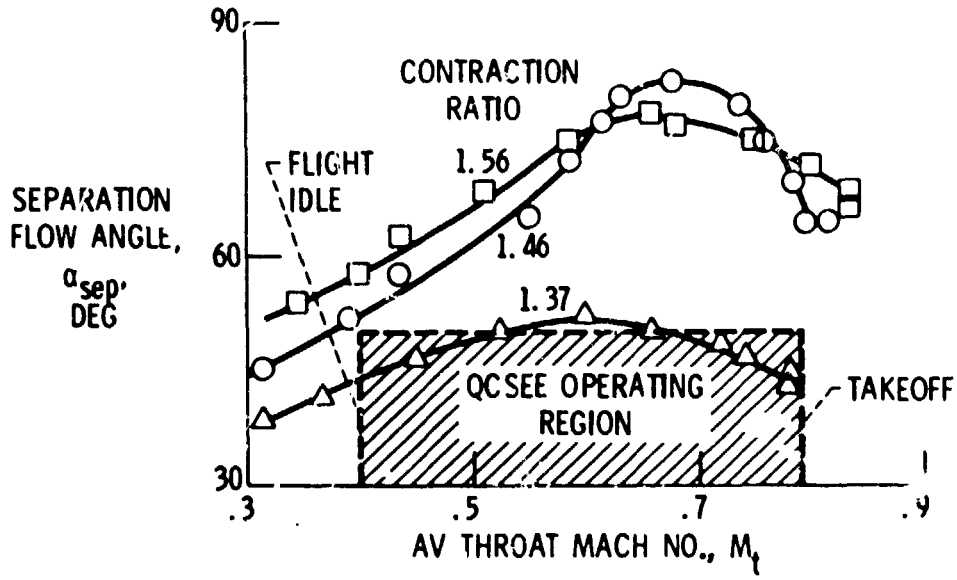

Figure 8.- The effect of contraction ratio on lip separation bounds. V_0 = 80 kn.

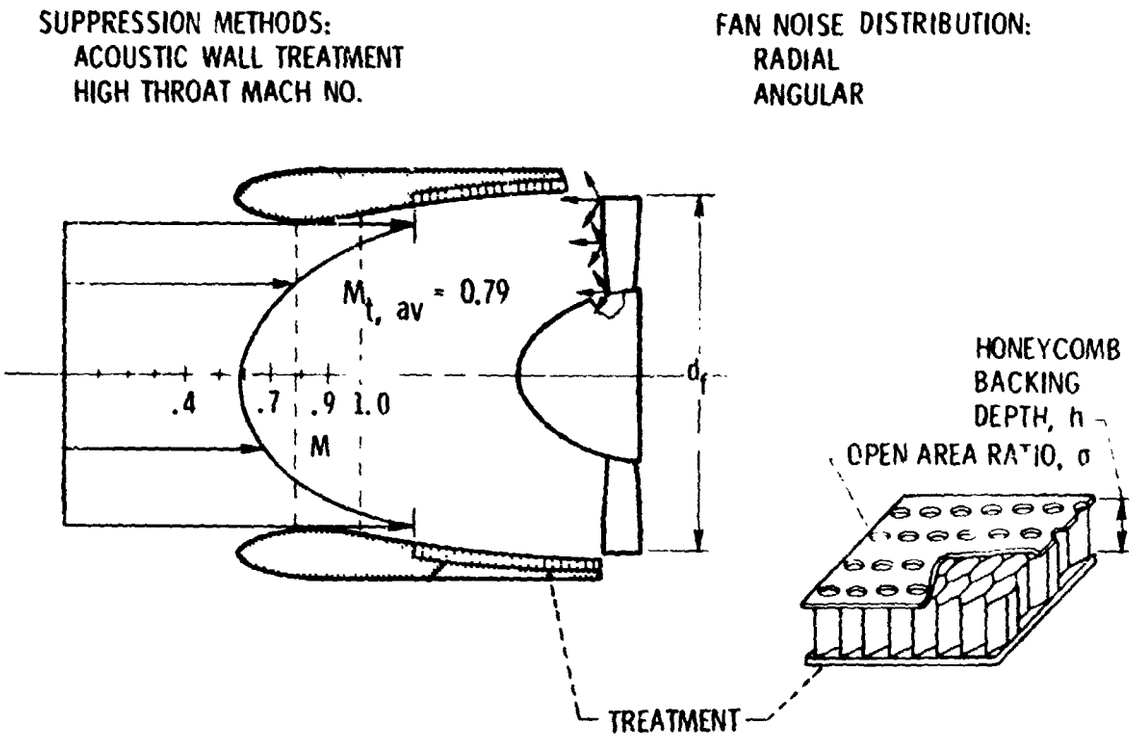

Figure 9.- Inlet noise suppression concepts.

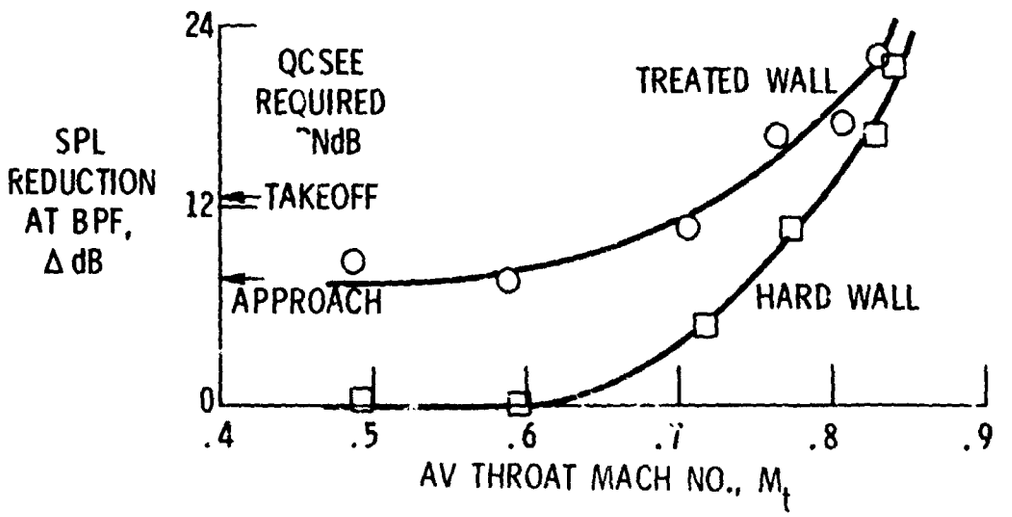

Figure 10.- Inlet acoustic performance. CR = 1.34; l_a/d_f = 0.83; σ = 6.2%; h/d_f = 1.5%; V_0 = 80 kn; α = 0°.

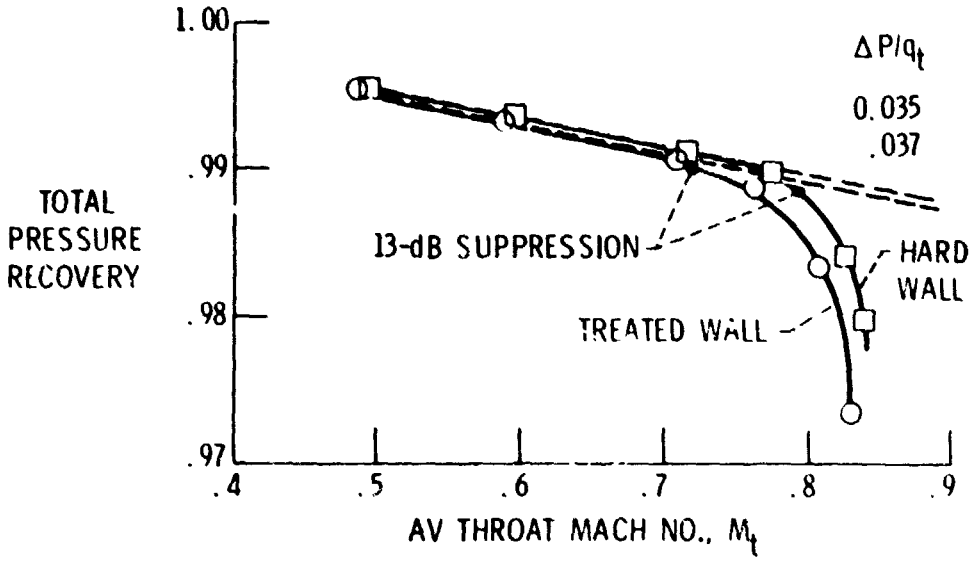

Figure 11.- Inlet aerodynamic performance. CR = 1.34; l_a/d_f = 0.83; σ = 6.2%; h/d_f = 1.5%. V_0 = 80 kn; α = 0°.

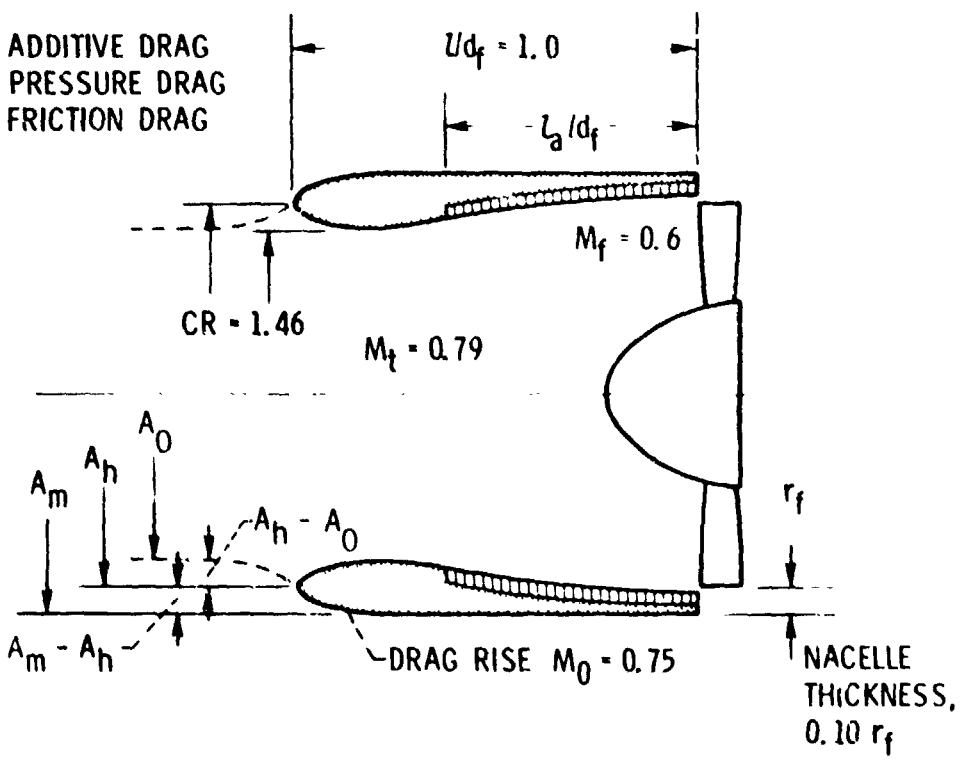

Figure 12.- Inlet drag considerations.

REVERSE-THRUST TECHNOLOGY FOR VARIABLE-PITCH FAN PROPULSION SYSTEMS

David A. Sagerser, John W. Schaefer, and Donald A. Dietrich
NASA Lewis Research Center

SUMMARY

During the past several years, a number of tests have been conducted to develop the technology necessary to meet the unique reverse-thrust performance requirements of a variable-pitch fan propulsion system. Areas that have been investigated include the losses and distortion associated with the air entering the fan and core compressor from the rear of the engine, the direction of fan blade pitch rotation for best reverse-thrust aeroacoustic performance, and engine response and operating characteristics during forward- to reverse-thrust transients. The test results of several scale fan models as well as a full-size variable-pitch fan engine are summarized. More specifically, these tests have shown the following: A flared exhaust nozzle makes a good reverse-thrust inlet, acceptable core inlet duct recovery and distortion levels in reverse flow were demonstrated, adequate thrust levels were achieved, forward- to reverse-thrust response time achieved was better than the goal, thrust and noise levels strongly favor reverse through feather pitch, and finally, flight-type inlets make the establishment of reverse flow more difficult.

INTRODUCTION

The short field lengths envisioned for short-haul aircraft operation have made reverse-thrust performance a critical part of the propulsion system's design requirements. The conventional approach to providing reverse thrust in turbofan engines is to use target or cascade thrust reversers to redirect the engine exhaust flow in a forward direction. Considerable study in recent years has been directed toward an alternate approach to reverse thrust - the variable-pitch fan.

Noise requirements for short-haul aircraft dictate that a low pressure ratio, high bypass ratio fan be used especially for an under-the-wing engine installation. For such requirements, engines designed with variable-pitch fans for reverse thrust have been shown (refs. 1 and 2) to be superior to those with fixed pitch fans and conventional reversers. The primary advantage is lower propulsion system weight. An added benefit is faster response times in forward thrust which are important for approach waveoff maneuvers. The faster forward thrust response times are a result of a variable-pitch fan's ability to provide approach thrust at high fan speeds (ref. 1). Because of these advantages, a variable-pitch fan was incorporated in the under-the-wing engine of NASA's Quiet Clean Short-Haul Experimental Engine (QCSEE) Program.

Obtaining reverse thrust with a variable-pitch fan engine involves a new mode of engine operation. In normal forward-thrust operation engine air enters the inlet, passes through the engine, and is exhausted out the rear as shown in the upper half of figure 1. In reverse thrust the fan blade pitch is changed so that the fan air flows in the opposite direction. Air must be drawn from the rear of the engine; the air is required to turn 180° from its original direction, as shown in the lower half of figure 1. Part of this air must turn nearly 180° again to supply the engine core. The rest of the air passes through the fan and is exhausted out the inlet. Requiring the air to follow this difficult path and operating the engine during the forward to reverse thrust transition raises a number of design questions:

(1) What nozzle shape is required to minimize the pressure losses and distortion in reverse thrust?

(2) Will pressure recovery and distortion levels into the core compressor be satisfactory?

(3) In which direction should the fan blade pitch be changed for adequate reverse-thrust levels?

(4) Can the forward to reverse-thrust transition be accomplished in the required time without engine operational problems?

(5) What effect will a flight-type inlet have on reverse-thrust operation?

A number of tests have been conducted over the past several years to answer these questions. The results of some of these investigations are discussed in this report to provide an overview of reverse-thrust technology for variable-pitch fan propulsion systems. To add perspective to the test results, the reverse-thrust requirements are discussed first.

REVERSE-THRUST REQUIREMENTS

Reverse-thrust regulations for short-haul aircraft have not been established. However, based on a number of aircraft systems studies, reverse-thrust objectives have been defined for QCSEE. They are compared to typical reverse thrust characteristics for conventional engines in table I. The reverse-thrust level for QCSEE, 35 percent of takeoff thrust, is required for landing on icy runways or in the event of brake failure (as described in ref. 3). Although the QCSEE objective falls on the low side of the range for conventional aircraft, the resulting aircraft deceleration is comparable to conventional aircraft because QCSEE is designed for an aircraft with a high thrust-weight ratio.

The forward- to reverse-response time objective, or time to reverse, for QCSEE is considerably more stringent than for conventional aircraft because of the short field operation. However, the time to reverse for conventional aircraft is longer mostly because of the time required to increase the engine speed from a near flight idle condition at the initiation of reverse thrust to the design reverse-thrust condition. Thus, some reverse thrust is being generated during most of that time.

Operating an engine in reverse thrust at low forward velocities can result in exhaust gas reingestion, foreign object damage from the reverse jet impinging

on the ground, and the impingement of hot exhaust gases on aircraft structures. Because of this, reverse-thrust operation is usually prohibited below certain forward velocities. A comparison of the minimum forward-velocity limits (table I) shows that the QCSEE objective is more stringent than conventional aircraft, again because of the short field operation.

The importance of low noise in all phases of short-haul operation resulted in a reverse-thrust noise objective for QCSEE. For 108 400 newtons of reverse thrust a maximum noise level of 100 PNdB on a 152.4-meter sideline has been established.

AIR INTAKE CHARACTERISTICS

Exlet Performance

To assist the flow of air into the rear of the engine during reverse thrust, the fan nozzle can be opened to form a flared shape, called an "exlet," as shown in figure 1. A number of scale exlet models were tested (refs. 4 and 5) to determine what geometry results in the lowest total pressure loss and distortion level. The exlet configurations tested covered flare angles θ from 0° to 60°, contraction ratios A_T/A_E from 1.4 to 2.8, and ducts with and without simulated acoustic splitters.

The results, along with geometric definitions, are summarized in figure 2 for freestream velocities V_∞ of 0 and 41.2 meters per second and a fan duct Mach number M_d of 0.4. The results indicate that a flare angle of 30° gave the highest pressure recovery. At flare angles other than 0°, the data fell in a relatively narrow band showing relative insensitivity to contraction ratio and the presence of an acoustic splitter. A flare angle of 0° represents a nozzle in a forward thrust position and would not normally be considered for reverse thrust operation except in the event of a nozzle actuator failure. In general, the exlet tests showed that the total pressure recovery was high when the sharp turn the flow must make around the exlet lip is considered. However, test data shown in figure 2 are for smooth axisymmetric exlets and constant fan duct Mach number. Therefore, the effects of differences in these characteristics should also be considered.

Exlet shapes with V notches which more accurately represent a variable area nozzle were also tested. These tests showed that for a configuration similar to the QCSEE nozzle the presence of notches would reduce recovery about 0.5 percent (ref. 5).

The fan duct Mach number has an effect on recovery, but to a lesser extent than the free-stream velocity (ref. 4). For example, changing the duct Mach number from 0.4 to 0.5 reduced recovery less than 0.5 percent.

Distortion levels in the fan duct were also measured. For the exlet geometries tested in reference 5 (except for the 0° flare), the distortion levels

were less than 7 percent. Such levels were considered acceptable for an engine like QCSEE.

Core Inlet Duct Performance

Like the exlet, the core inlet duct offers a similar sharp turn for the air to negotiate. But in terms of pressure loss, this turn is more severe. The Mach number of the flow at the beginning of the turn is three or four times that for the exlet. Also, the flow must pass through the fan stators and, depending on the core inlet design, the core inlet guide vanes. The losses in the fan stators are expected to be low. However, these stators impart a swirl to the reverse flow which will result in an unfavorable incidence angle on the core inlet guide vanes. This in turn could result in more significant losses.

Core inlet recovery test data for two engine configurations are presented in figure 3 from tests described in reference 6 and from an unpublished investigation by J. W. Schaefer of Lewis Research Center. The first engine configuration shown in figure 3 is the full-size Q-fan T-55 engine and the second one shown is a scale model (50.8-cm fan diameter) of the QCSEE engine. Both sets of data show that core-inlet total pressure recovery is a function of fan duct Mach number.

The importance of core inlet recovery is shown by the core limit lines on this figure. These points are operating conditions where further increases in reverse thrust level cannot be achieved without exceeding a core operational limit. For the Q-fan T-55, the core operational limit is the compressor speed; for the QCSEE engine, the calculated core limit is the turbine inlet temperature.

The solid symbols in figure 3 show the point where the required reverse-thrust level is obtained. In both cases the core recovery is adequate to meet the required reverse-thrust level.

As can be seen from figure 3, both sets of data are adequately represented by the same loss coefficient line of 1.5, even though the core inlet duct configurations are different. The Q-fan T-55 splitter lip is more rounded than the sharp lip of the QCSEE model which would suggest higher losses for the QCSEE model. However, the core inlet guide vanes of the Q-fan T-55 are located in the core inlet duct and are subject to unfavorable incidence angles. The QCSEE core inlet guide vanes are external to the core duct which allows most of the core flow to bypass them in reverse thrust. Apparently, these configuration differences have offsetting effects which result in similar loss characteristics.

Distortion levels at the compressor face were also measured during the reverse-thrust tests of the Q-fan T-55 and QCSEE models (refs. 6 and 7). For the Q-fan T-55, the reverse-thrust distortion level (combined radial and circumferential) was about the same as for the forward-thrust level. This unexpected result may be partially attributed to the inlet guide vanes which are located in the core inlet duct. This location may help to make the core flow more uniform. Results of QCSEE scale model tests indicated the reverse-thrust

distortion to be higher than in forward thrust but acceptable for full-scale engine operation.

FAN DESIGN AND OPERATION

A basic concern for the operation of a variable-pitch fan is the direction in which the fan blade pitch should be changed to develop reverse thrust. The two possible ways are illustrated in figure 4. A cross section of two fan blades shown in their normal forward-thrust position is at the top of this figure. From this position, the blades can be turned through flat pitch, a condition of zero lift, to the reverse-thrust position as shown on the left of figure 4. Two things should be noted for this approach. First, adjacent blade leading and trailing edges must pass each other during the transition through flat pitch. This requires that the blade solidity be less than one at all radii. This can limit fan performance, especially at the hub. Second, while the blade leading edge remains the same relative to the airflow, the blade camber is wrong for reverse-thrust operation.

The alternate approach is to turn the blades through feather pitch, passing through a stall condition. This is shown on the right side of figure 4. In this case, blade camber is correct in the reverse position, but the leading and trailing edges are reversed. During the transition the flow over the blades separates or stalls. The flow then reattaches in reverse thrust and moves in the opposite direction relative to the blade. With this approach the blade solidity may exceed one, although the blade twist and camber will still limit the hub solidity to some extent.

Thrust

To determine which approach is best, both steady-state reverse thrust performance and transient operating characteristics must be considered. A comparison of static reverse-thrust levels at nominal reverse-thrust blade angles is shown in figure 5. The data are from tests of the Q-fan T-55 and QCSEE scale model (unpublished Lewis data and ref. 6). Both tests were conducted with similar flight-type inlets. In all cases the reverse-thrust data are presented relative to the design takeoff thrust level. The design takeoff condition, however, was never achieved in tests of the Q-fan T-55 due to a core horsepower limitation. The fan was designed for a higher horsepower model of the T-55 than what was tested. This horsepower limited to some extent the maximum reverse thrust attained. Reverse-thrust levels for the Q-fan T-55 are direct force measurements while reverse-thrust levels for the QCSEE model are calculated from measured pressures and temperatures.

As shown in this figure, reverse-thrust levels exceeding the 35-percent goal can be achieved through feather pitch before reaching the core limiting conditions. By comparison, reverse-thrust levels through flat pitch are less than half of those through feather pitch and, even at the fan limits, are considerably less than the goal.

Noise

Noise is another factor to consider when deciding which way to change fan blade pitch for reverse thrust. Unsuppressed reverse-thrust noise level data (unpublished Lewis data) for the Q-fan T-55 are compared in figure 6. The noise data show that reverse through flat pitch is a considerably noisier way to achieve reverse thrust.

Transient Performance

The data that have been discussed so far have all been at steady-state conditions. Critical to which way blade pitch should be changed and to the whole issue of achieving reverse thrust with a variable-pitch fan engine is the performance of the engine during the forward- to reverse-thrust transition. Tests to determine transient performance have been conducted with the Q-fan T-55 both at Hamilton Standard and NASA Lewis test facilities (unpublished Lewis data and ref. 8). A photograph of this engine at NASA Lewis is shown in figure 7. The results of these tests are discussed by comparing a representative example of a through flat pitch and through feather pitch transient.

Considering first reverse through flat pitch transients, time histories for fan blade angle, thrust, fan speed, and fan blade stress are shown in figure 8 for a representative transition from a landing approach to a reverse-thrust condition, In this figure the transient is initiated at time equals zero. The blade pitch was changed at a rate of about 100° per second starting from the design angle in forward thrust and moving to the reverse angle, 80° in the flat pitch direction. The throttle was held constant in this transient. Thrust, presented as a percent of measured takeoff thrust, responds to the blade angle change and falls off smoothly. The final reverse-thrust level is reached in somewhat less than 1 second. The fan speed during this time accelerates quickly as the load in the fan blades is reduced. As the blade loading increases again in reverse thrust, the fan speed peaks and then converges on the final reverse-thrust value. Fan blade vibratory stresses gradually build up during the transient and reach a level slightly over twice that in forward thrust. This level is well within the limits of normal blade design.

The primary operational problem encountered in the reverse through flat pitch transients is that the fan tends to overspeed. There are two ways to help reduce this effect. First, the transient can be initiated at a reduced fan speed to allow more overspeed margin as was done in the example of figure 8. This could reduce the engine's forward-thrust response time for waveoff manuevers. Second, starting from a higher initial fan speed, the fuel flow can initially be cut back in an attempt to reduce the available engine power while the fan blades pass through flat pitch. This requires careful control of the fan blade pitch and engine throttle during the transient to reach the reverse blade position with the fan speed at the desired level.

A somewhat different sequence of events occurs during a reverse through feather pitch transient which is shown in figure 9. The transient was initiated from the same approach thrust level as the transient in figure 8 but at

a higher fan speed for better waveoff response capability. The fan blade pitch was changed, in the feather pitch direction, at about 130° per second. This change initially increases the aerodynamic loads on the blades. As this happens, the fan speed is lowered as the fan rotational energy is converted into a thrust increase. The throttle in this case was immediately reset to the final reverse-thrust level. As the blade pitch continues to change, the fan eventually stalls and the thrust falls suddenly to zero. This unloads the blades to some degree and causes the fan speed to increase. Shortly after the blades reach their reverse position, the flow reattaches and reverse thrust is obtained. The final reverse-thrust level is reached about 1 second after the transient was initiated.

During the transient, the fan blade stresses build up and peak as the blade stalls. A second peak, generally somewhat higher than the first, occurs as flow reattaches to the blades in the reverse direction. These stress peaks, while high relative to forward-thrust levels, did not limit the transient tests of the Q-fan T-55. Even though these results are encouraging, further tests of higher pressure ratio variable-pitch fans, such as QCSEE, are needed before more general conclusions can be drawn.

INLET BACKPRESSURE

Tests of the Q-fan T-55, as well as the QCSEE scale model, showed that a flight-type inlet can produce a backpressure on the fan which tends to prevent the establishment of reverse flow. This can occur when the fan is started from rest with the blades initially in a reverse position or, more importantly, during a forward to reverse transient through feather pitch. This effect can be explained by noting that when the fan is stalled, flow in the duct is primarily tangential and tends to rotate with the fan. When the fan is unstalled and producing reverse thrust, the flow is nearly axial. Photographs of tufts in the fan inlet in figure 10 show the stalled and unstalled flow fields.

In order for the swirling flow in the stalled condition to be exhausted out the smaller diameter throat of the inlet, the flow velocity must increase to conserve angular momentum. Since the static pressure at the front of the inlet is ambient, a higher than ambient pressure at the fan face is implied. The fan must, therefore, overcome this backpressure to clear stall. The magnitude of the backpressure will depend on the inlet geometry.

Test data showing this effect are presented in figure 11 for the Q-fan T-55 at a reverse through feather blade angle. Wall static pressures divided by ambient pressure are compared for a bellmouth and a flight-type inlet both in stalled and unstalled conditions for the same fan speed. Of primary interest is the static pressure at the fan face. As can be seen from figure 11, a higher pressure does exist with the flight-type inlet in a stalled condition. The nearly identical static pressures for the two configurations in the unstalled condition demonstrated that the inlet backpressure effect is due to more than just the one-dimensional difference in throat areas.

A technique to overcome the effect of inlet backpressure and promote quick establishment of reverse flow was demonstrated during reverse through feather transient tests of the Q-fan T-55 (unpublished Lewis data). With this technique, the fan blades are moved beyond the final reverse position, held there for a short period of time, and then returned. This temporarily reduces the angle of attack on the blades which allows reverse flow to be established. This technique was shown to be effective without increasing response time.

CONCLUDING REMARKS

The tests conducted to develop reverse-thrust technology for variable-pitch fan engines have done much to demonstrate the viability of this approach for powered-lift propulsion systems. More specifically, these tests have shown the following:

1. A flared exhaust nozzle is an acceptable reverse thrust inlet.
2. Acceptable core inlet duct recovery and distortion levels in reverse flow have been demonstrated.
3. Adequate reverse-thrust levels can be achieved.
4. Forward- to reverse-thrust response times better than the goal have been demonstrated without any significant operational problems.
5. Thrust and noise levels strongly favor reverse through feather pitch.
6. Flight-type inlets make the establishment of reverse flow more difficult, but moving the fan blades beyond their normal reverse thrust position for a short period of time was effective in overcoming inlet backpressure.

Areas where variable-pitch fan technology for reverse thrust needs to be expanded include the following:

1. Effect of forward velocity on the establishment of reverse flow especially with flight-type inlets
2. Fan blade stress levels for higher pressure fans during reverse through feather transients
3. Aircraft installation effects - flap-exlet interaction and reverse-jet ground impingement

REFERENCES

1. Neitzel, R.; Lee, R.; and Chamay, A. J.: QCSEE Task 2: Engine Installation Preliminary Design. (General Electric Co.; NAS 3-16726.) NASA CR-134738, 1973. (FEDD distribution.)

2. Helms, H. E.: Quiet Clean STOL Experimental Engine Study Program, Task 1 - Parametric Propulsion Systems Studies. (Detroit Diesel Allison; NAS 3-16727.) NASA CR-135015, 1976. (FEDD distribution.)

3. Howard, D. F.; et al.: Quiet Clean Short-Haul Experimental Engine, Preliminary Under the Wing Flight Propulsion System Analysis Report. (General Electric Co.; NAS 3-18021.) NASA CR-134868, 1976. (FEDD distribution.)

4. Dietrich, Donald A.; Keith, Theo G.; and Kelm, Gary G.: Aerodynamic Performance of Flared Fan Nozzles Used as Inlets. NASA TM X-3367, 1976.

5. Vier, W. F.: Quiet, Clean Short-Haul Experimental Engine (QCSEE) Test Results from a 14 cm Inlet for a Variable Pitch Fan Thrust Reverser. (General Electric Co.; NAS 3-18021.) NASA CR-134867, 1975. (FEDD distribution.)

6. Giffin, R. G.; et al.: Quiet Clean Short-Haul Experimental Engine, Aerodynamic and Aeromechanical Performance of a 50.8 cm (20 Inch) Diameter 1.34 Pressure Ratio Variable Pitch Fan with Core Flow. (General Electric Co.; NAS 3-18021.) NASA CR-135017, 1976. (FEDD distribution.)

7. Demers, W. J.; et al.: Testing of the Hamilton Standard Q-Fan Demonstrator. (Hamilton Standard; NAS 3-16827.) NASA CR-121265, 1973.

8. Demers, W. J.; et al.: Hamilton Standard Q-Fan Demonstrator Dynamic Pitch Change Test Program. (Hamilton Standard; NAS 3-18513.) NASA CR-134861, 1976.

TABLE I. - REVERSE-THRUST REQUIREMENTS

	QCSEE objectives	Conventional engine characteristics
Reverse-thrust level, percent takeoff thrust	35	35 to 50
Time to reverse, sec	1.5	5 to 10
Minimum forward-velocity operating limit, m/sec	5.1	15 to 30
Noise (152.4 m sideline PNdB; reverse thrust, 108 400 N)	100	--------

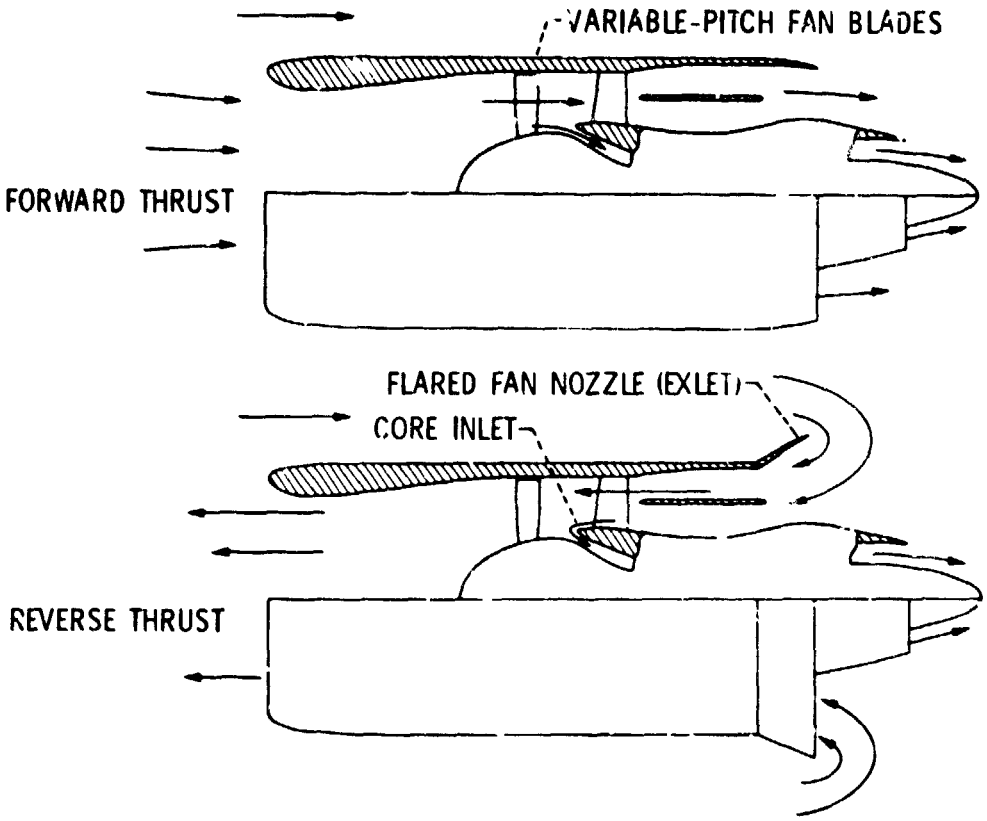

Figure 1.- Variable-pitch fan engine operation.

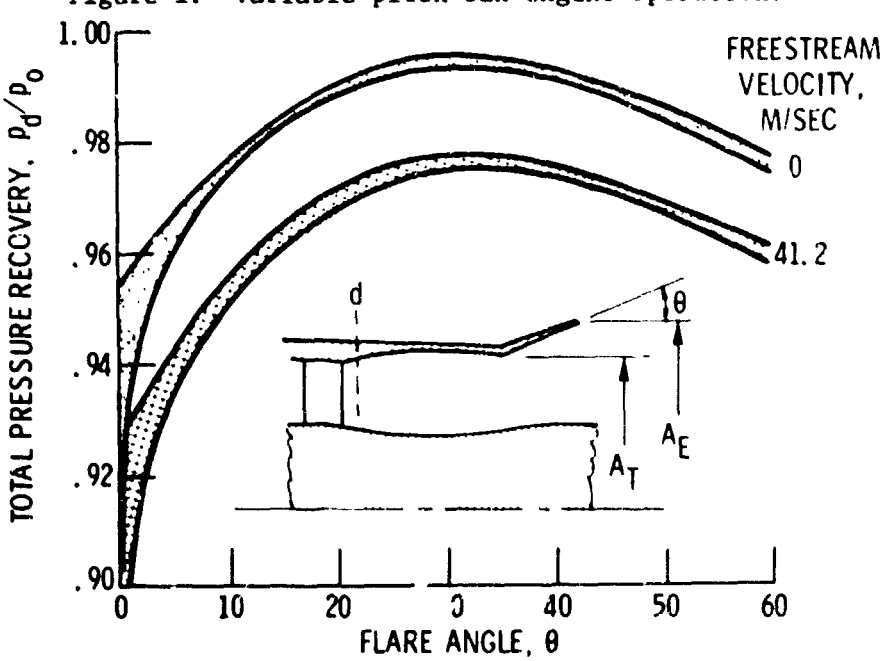

Figure 2.- Exlet performance. Fan duct Mach number, M_d, 0.4; contraction ratios, A_E/A_T, 1.4 to 2.8; p_d, duct total pressure; p_o, ambient pressure.

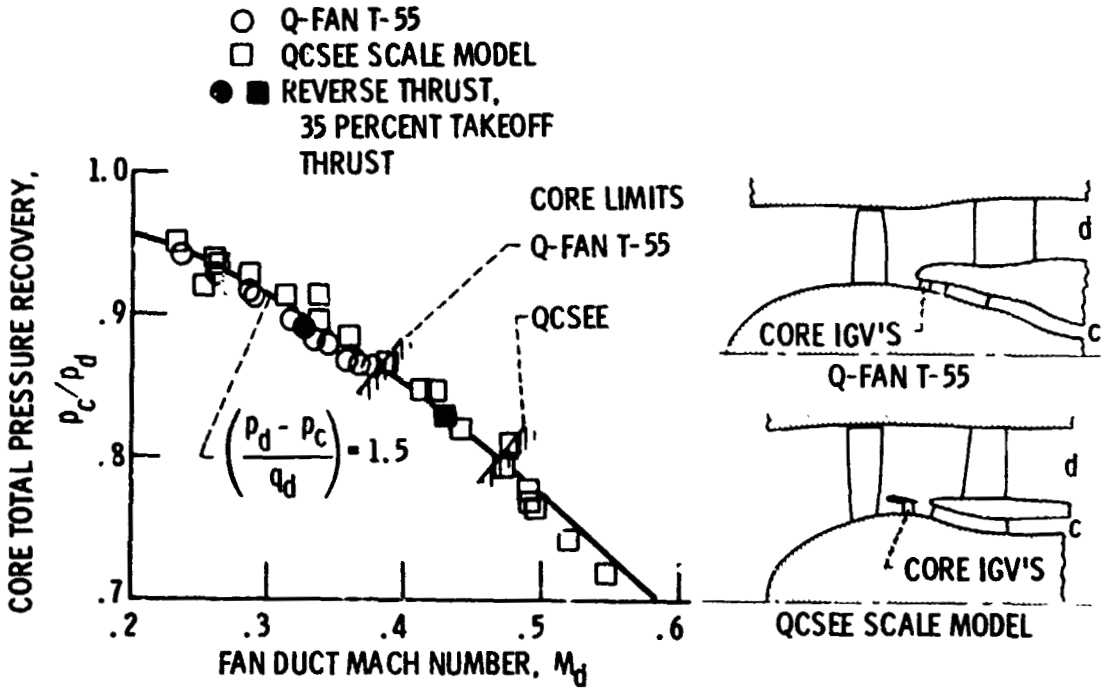

Figure 3.- Core inlet performance. p_c, core total pressure; p_d, duct total pressure; q_d, duct dynamic pressure.

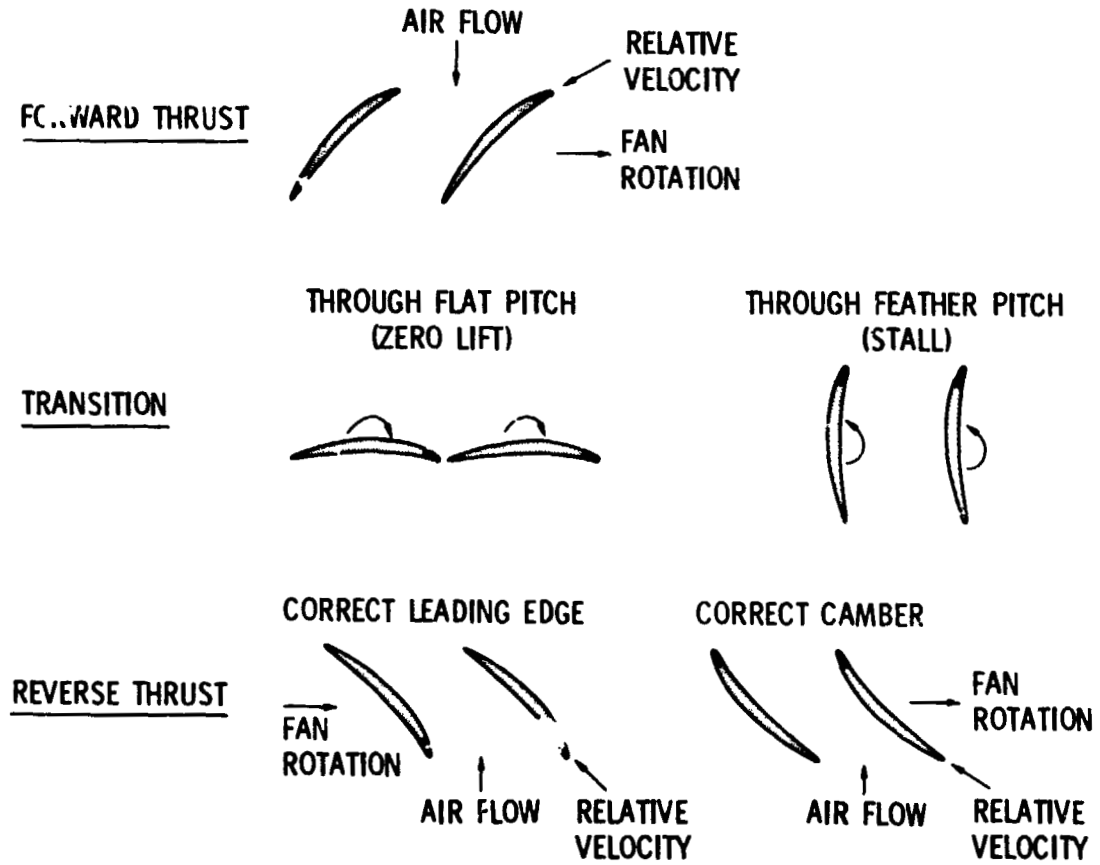

Figure 4.- Reverse pitch alternatives.

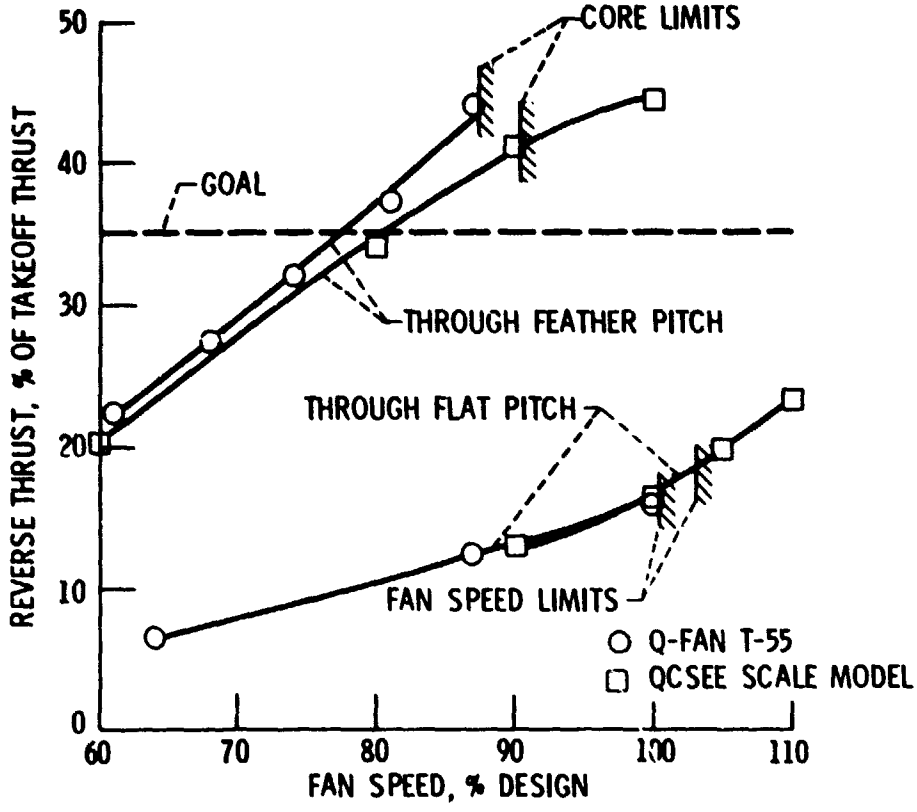

Figure 5.- Static reverse thrust.

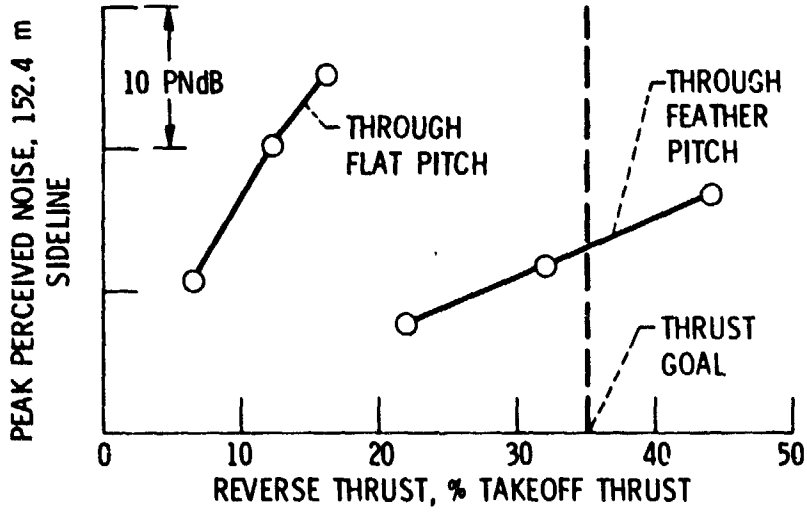

Figure 6.- Unsuppressed reverse-thrust noise for Q-fan T-55.

Figure 8.- Forward- to reverse-thrust transient through flat pitch.

Figure 7.- Q-fan T-55 engine at NASA Lewis Research Center.

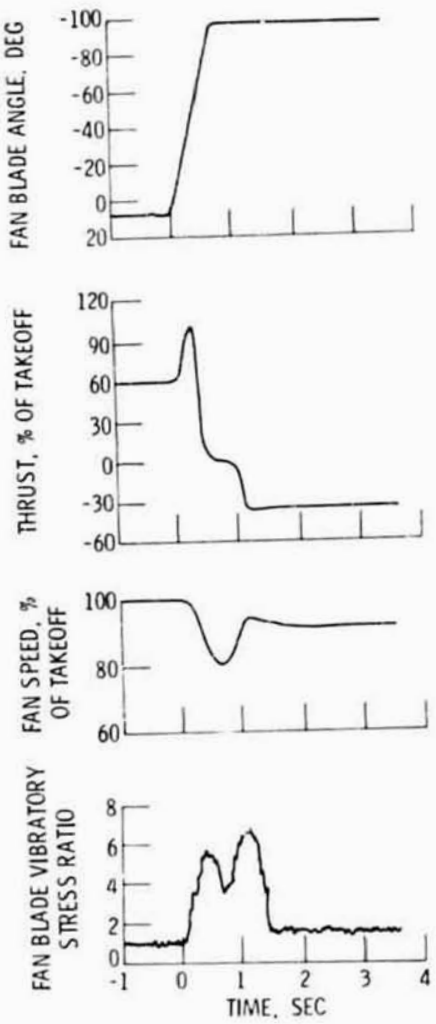

Figure 9.- Forward- to reverse-thrust transient through feather pitch.

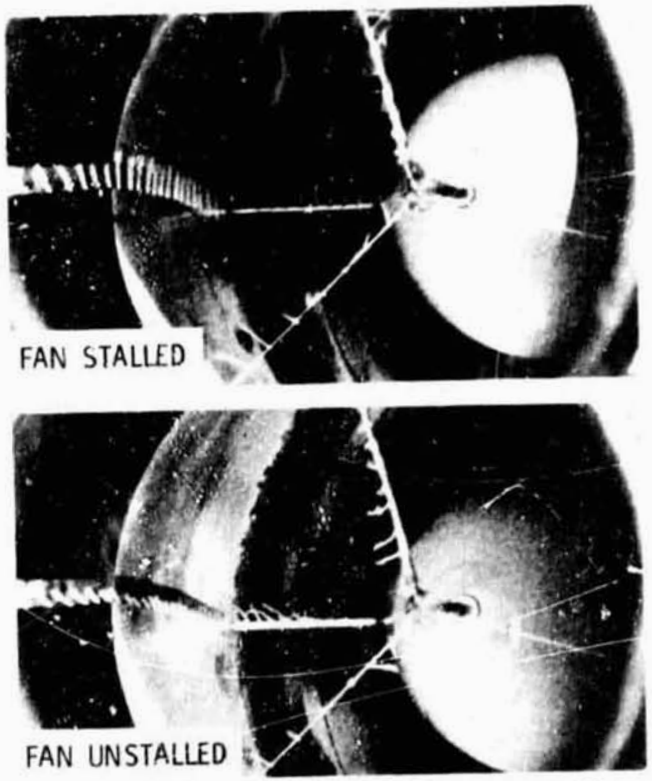

Figure 10.- Inlet reverse-thrust flow of Q-fan T-55 engine.

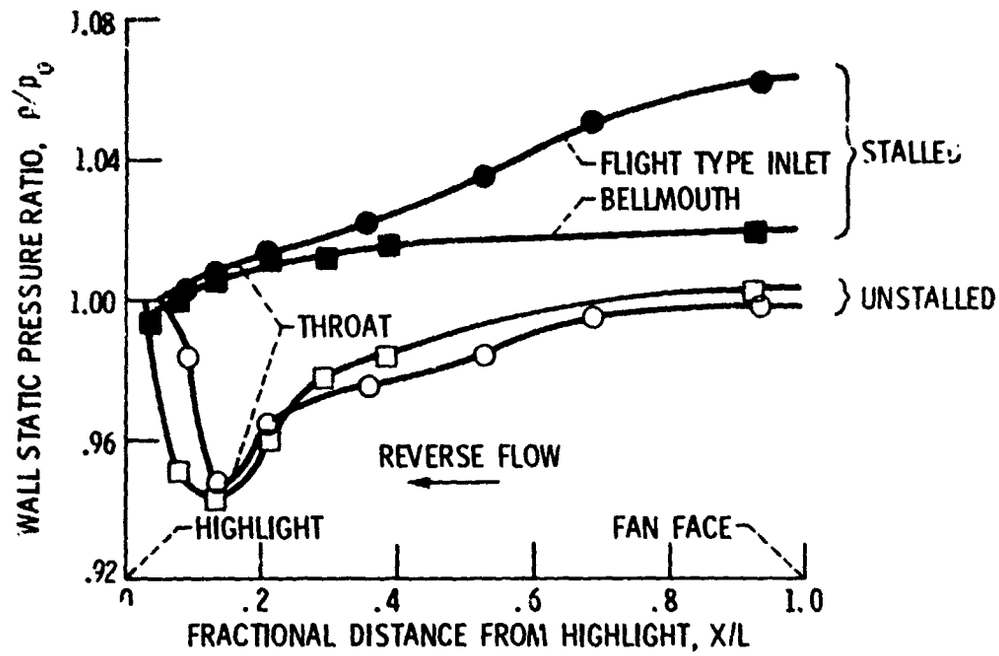

Figure 11.- Inlet backpressure of Q-fan T-55. Fan speed, 76 percent of takeoff; p, static pressure; p_o, ambient pressure; x, distance from inlet highlight; L, inlet length.

ACOUSTICS AND AERODYNAMICS OF OVER-THE-WING THRUST REVERSERS

Dale L. Stimpert and Robert C. Ammer
General Electric Company

ABSTRACT

As part of the Quiet Clean Short-Haul Experimental Engine (QCSEE) program, model tests were conducted to determine the effects of thrust reverser geometric parameters on noise and reverse thrust. The acoustic tests used a 1/6 scale model thrust reverser while the aerodynamic performance tests used a 1/12 scale model reverser. Parameters which were varied in both tests include blocker spacing, blocker height, lip angle, and lip length. The impact of these parameters on peak sideline noise and reverse thrust performance is presented.

25

INTRODUCTION

Commercial CTOL jet transports, although certified to stop without thrust reversers, do employ thrust reversers to decelerate the aircraft, to decrease wear on brakes, and to improve stopping on icy or wet runways. It is anticipated that future STOL aircraft will rely heavily on some type of thrust reversers to help decelerate the aircraft for the short (610 to 914 meter, 2000 to 3000 foot) runways into which they operate. It is also anticipated that future STOL aircraft will have to meet very stringent reverse thrust noise goals in addition to the noise goals at takeoff and approach which are currently being proposed.

As part of the Quiet Clean Short-Haul Experimental Engine (QCSEE) program currently underway at General Electric Company and which is sponsored by NASA Lewis Research Center, two engines for STOL aircraft are being built using advanced technology. Design rationale and background information for these engines are presented in Reference 1. Each engine has a different mode of thrust reversal. The Under-The-Wing (UTW) engine utilizes variable pitch fan blades to achieve reverse thrust. On the second QCSEE engine - an Over-The-Wing (OTW) ergine version - reverse thrust will be achieved by deploying a target type thrust reverser which captures the fan and core exhaust flows and directs the jet upward and forward from the wing upper surface as shown in Figure 1. The OTW installation offers some unique advantages relative to the UTW installation which makes it attractive to STOL applications. The advantages include elimination of ground induced reingestion and incidence of foreign object damage, upward reverser discharge to provide an additional force on the landing gear for higher braking forces, and unobstructed interaction between freestream airflow and the wing flap system for aircraft landing configuration drag.

This paper is concerned with the design parameters which are important in selecting an OTW target reverser as demonstrated by model tests conducted under the QCSEE OTW thrust reverser development program. The design parameters were investigated from the viewpoint of aerodynamic performance and acoustics.

Three model test programs were utilized in studying target reverser design criteria. Initial tests by NASA Ames Research Center provided noise and performance data on a 1/3 scale model. Further acoustic testing under the QCSEE program was conducted at the General Electric Company Jet Engine Noise Outdoor Test Stand (JENOTS) using a 1/6 scale model of the OTW thrust reverser. It had provisions to vary target reverser parameters such as blocker spacing, blocker height, lip length, and lip angle. No thrust measurements were taken with these tests; however, airflow and pressure data were obtained. Also under the QCSEE program, reverse thrust aerodynamic performance was investigated on a 1/12 scale model at NASA Langley Research Center where thrust and performance were monitored for various target reverser geometries.

OTW TARGET REVERSER DESIGN CRITERIA

Design of a target thrust reverser for a STOL aircraft must consider two disciplines - aerodynamics and acoustics. The aerodynamic design must incorporate the thrust reverser into the nacelle in a manner which least compromises the forward flight performance. The upper portion of Figure 1 is a schematic of an OTW type thrust reverser shown stowed for forward thrust operation while the lower schematic shows the target actuated for reverse thrust. Target area or size relative to the nozzle area is determined by the reverse thrust level required. The effective discharge area of the thrust reverser must be sized to ensure that engine stall margin and turbine operating temperature limits are maintained for satisfactory engine operation.

Acoustically, the noise from other constituents such as fan inlet, fan exhaust, core, and turbine must be considered relative to the thrust reverser levels. Figure 2 compares the reverser noise constituents for a highly suppressed STOL-type aircraft engine. The reverser noise is a major contributor to the total system noise and thus is a prime candidate for noise reduction studies. The other sources, except fan inlet noise, are redirected by the target reverser and combine with the reverser noise to give the maximum sideline noise at a forward angle. Figure 3 compares forward thrust jet noise levels to the redirected thrust reverser PNL directivities and shows that not only is there a redirection of the noise into the forward quadrant, but also an increase in the peak level.

Since the reverser noise is a major constituent, techniques of lowering reverser noise should be evaluated. One means is to simply reduce the reverser pressure ratio which drops the jet velocity. This method offers the most potential. A second possibility is to vary reverser geometry.

The ultimate goal of the model tests and investigations of reverser design parameters is to obtain design information which will permit a given level of reverse thrust to be achieved at the lowest sideline noise consistent with engine performance requirements.

ACOUSTIC TEST RESULTS

The model used for investigating reverser geometric variations on noise was a 1/6 scale model of the QCSEE OTW engine. Detailed analysis of the results will be reported in a contractor report at a later date. The test vehicle included a forward thrust nozzle and a target reverser with provisions for varying blocker spacing, blocker height, lip length, and lip angle. Figure 4 shows the reverser model as installed at the General Electric Company JENOTS test site. The design parameters in nondimensional form are defined in Figure 5 along with the range of each variable which was investigated.

Of the four parameters investigated, lip angle and blocker height variations had minimal effect on the farfield noise signature of the thrust reverser. Their effect was individually less than 1 PNdB over the range of each variable.

Both blocker spacing and lip length variation resulted in significant changes in noise. Figure 6 shows the effect of blocker spacing on peak sideline noise at three reverser pressure ratios where pressure ratio is the charging station (see Figure 5) total pressure divided by ambient. There are two effects which must be considered when examining Figure 6, the noise generated within the reverser and that generated external to the reverser. The latter is equivalent to jet noise generation caused by turbulent mixing of the jet with ambient air. The primary means of reducing this type of noise is to reduce the pressure ratio across the reverser which reduces the velocity. Figure 7 represents data taken at constant blocker spacing from Figure 6 and shows the variation of target reverser noise as a function of velocity. The peak sideline PNL varies with the 6th power of velocity, hence any reduction of the operating pressure ratio of the reverser has a significant reduction in noise level. This is consistent with the results observed in Reference 2. Also shown in Figure 7 are peak sideline PNL's scaled from noise tests of a similar target thrust reverser at NASA Ames Research Center. These levels agree with the 6th power dependency on velocity.

Noise generated within the reverser is associated with the turning losses and interaction of the flow with the target. In the limit, if the flow is reversed slowly at low velocities with no pressure losses, then the reverser noise would be equivalent to that of a redirected forward thrust nozzle at the same pressure ratio. Figure 3 has shown this not to be the case. The geometric shape of the reverser elements used to capture the flow influences the internal noise generation. If Figure 6 is examined at constant pressure ratio, spacing is seen to have a direct effect upon the

internal noise generation. Closer spacing produces less noise because there is a reduction in airflow (backpressure effect) at a given pressure ratio and hence a reduction in the velocity hitting the target. Therefore, a low noise target reverser will be one which maintains as low as possible velocity into the reverser consistent with fan exhaust duct flowpath requirements.

Lip length effects on noise are presented in Figure 8. At constant lip length, L/D_{TH}, the dependence on velocity is similar to that shown at constant blocker spacing. Longer lips increase noise; but, as will be discussed later, improve the level of reverse thrust achieved. Thus, a trade must be made between desired performance and acoustic consideratons in choosing the optimum lip length for a given reverser.

AERODYNAMIC RESULTS

Aerodynamic tests on a 1/12 scale model target thrust reverser and forward thrust nozzle were conducted at NASA Langley Research Center in support of the QCSEE OTW design studies. Results will be reported in a contractor report at a later date. The exhaust system was designed to meet the QCSEE OTW engine area requirements in forward thrust, to have excellent jet/flap flow turning characteristics during low speed aircraft operation, and to provide a viable thrust reversing system for use during the landing roll. Encompassed in the reverser test matrix were not only the reverser geometric parameters of blocker spacing, blocker height, lip angle, and lip length that were tested acoustically at JENOTS but also blocker door inclination angle, side skirt geometry, and side skirt rotation angle. The parameters are defined in Figure 9 which is a schematic of the 1/12 scale Langley aerodynamic model. Generally, only the parameters common to both model tests are discussed in this paper.

Primary considerations in target reverser design (or any reverser design) are to efficiently turn the exhaust flow in the direction required to achieve the objective thrust level and to achieve an acceptable engine operating condition for both the forward and reverse thrust modes. Referring to Figure 9, the backpressure effects or stall margin on the engine are controlled primarily by the spacing of the target from the charging station plane. Blocker spacing was investigated to establish the airflow matching characteristics (airflow in reverse divided by forward thrust airflow at a given pressure ratio, W_{REV} W_{FWD}), and the effect on reverse thrust. Reverse thrust is defined as the ratio of the reverse thrust divided by the forward thrust at takeoff, $F_{REV}/F_{FWD\ T/O}$. Figure 10 shows that an increase in blocker spacing results in a decrease in the level of reverse thrust achieved. An increase in the airflow was observed with the increased blocker spacings indicating less backpressure effect and increased stall margin on the engine. This airflow increase is attributed to higher blocker target spillage rate out the sides.

Lip geometry of a target reverser can be either fixed or articulated upon reverser deployment through some appropriate kinematic arrangement. Lip length has a significant effect on reverser thrust as shown in Figure

11. While gains in reverse thrust are evident all the way to $L/D_{TH} = 0.8$, mechanical design constraints on an engine configuration would probably not permit such long lengths. The airflow ratio remains relatively constant for the variations in lip length shown. A favorable change in reverse thrust was achieved by increasing the blocker inclination angle and modifying the side skirt geometry as presented in Figure 11. An obvious and beneficial result is that for a given lip length, a level of reverse thrust can be achieved at a lower pressure. It was shown earlier that lower pressure ratios result in lower reverser noise; therefore, judicious selection of blocker inclination angle and side skirt geometry has potential in lowering reverser noise levels.

Other reverser parameters such as blocker height and lip angle had little significant effect on the target reverser airflow capacity. Blocker height variations did not achieve any significant reverse thrust change; however, a favorable increase in reverse thrust was observed by decreasing the lip angle (or increasing flow turning) from 0.61 radians (35°) to 0.44 radians (25°).

Peak sideline noise was shown to vary with the sixth power of reverser velocity; therefore, low noise can most easily be obtained by meeting the desired level of reverse thrust at as low a reverser pressure ratio as possible. The variation of noise with reverse thrust is shown in Figure 12 for a given nominal configuration. Reverser geometric changes shift the curve up or down but generally keep the same slope.

CLOSING REMARKS

In the design of a target reverser system applicable to an OTW STOL aircraft installation, consideration must be given to acoustics, aerodynamic performance, and mechanical constraints.

Peak sideline noise increased and reverse thrust decreased with increased blocker spacing. This implies that close spacing is desirable. However, a spacing should be chosen consistent with retaining sufficient stall margin on the engine and yet coming closest to meeting the thrust and acoustic objectives.

Both reverse thrust and peak sideline noise increase with longer lip lengths. This necessitates a trade between thrust and acoustics to meet a given noise level; however, lip stowage limitations preclude use of excessively long lips.

The trends and tradeoffs discussed in this paper were evaluated and factored into the design of the QCSEE OTW target thrust reverser. However, acoustic model tests were conducted prior to the aerodynamic model tests and since the aerodynamic model included variations such as blocker inclination angle, side skirt geometry, actuator arm, and side skirt angle which were not evaluated by acoustic tests at JENOTS, acoustic model data on the final

design were not obtained. Lack of time and monetary considerations precluded model testing of this final design. Both noise and aerodynamic performance will be measured on the full scale QCSEE engine when it is tested late this year.

NOMENCLATURE

Symbol or Abbreviation	Definition
D_{TH}	Charging station height
$F_{FWD\ T/O}$	Forward thrust at takeoff power setting
F_{REV}	Reverse thrust
H_B	Blocker height
L	Blocker lip length
PNL	Perceived noise level, PNdB
P_0	Ambient pressure
P_T	Charging station total pressure
V	Velocity
W_{FWD}	Forward thrust airflow as a function of pressure ratio
W_{REV}	Reverse thrust airflow as a function of pressure ratio
α	Blocker inclination angle
β	Lip angle

REFERENCES

1. Adamson, A.P., "Quiet Clean Short-Haul Experimental Engine (QCSEE) Design Rationale," SAE paper 750605, May 1975.

2. Stone, J.R., and Gutierrez, O.A, "Noise of Model Type Thrust Reversers for Engine Over-The-Wing Applications," NASA TM X-71621, November 1974.

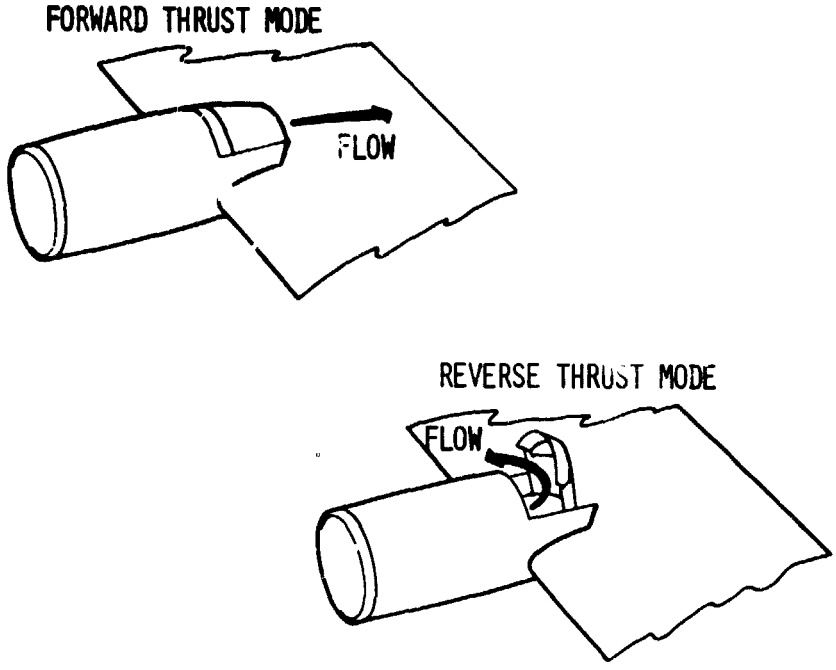

Figure 1.- OTW forward and reverse thrust schematics.

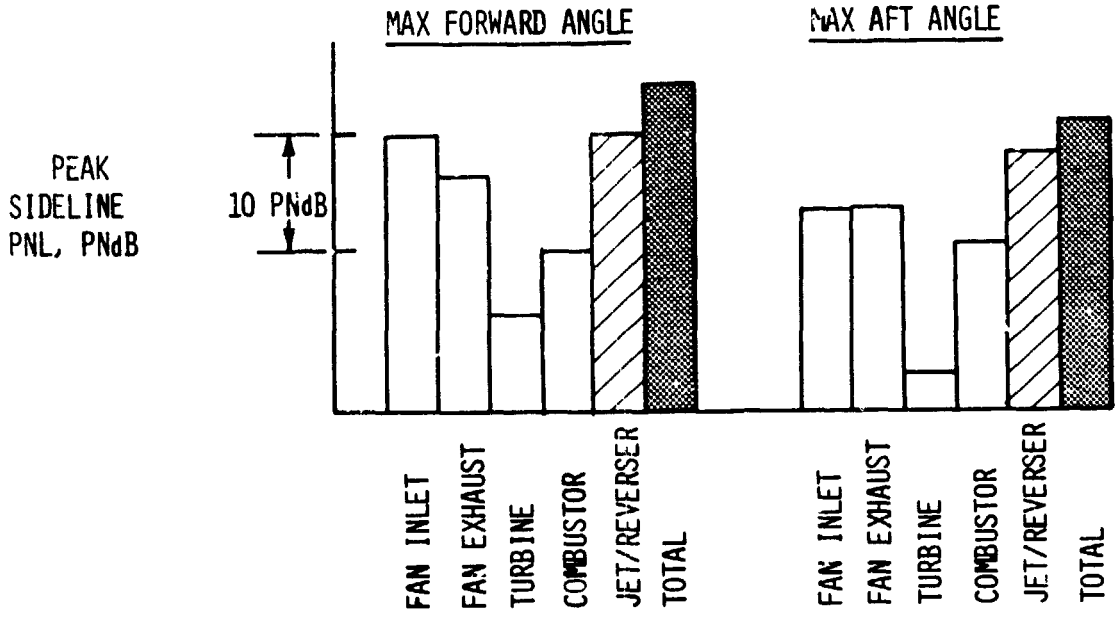

Figure 2.- Reverse thrust constituent noise levels. 152.4 m (500 ft) sideline; suppressed engine.

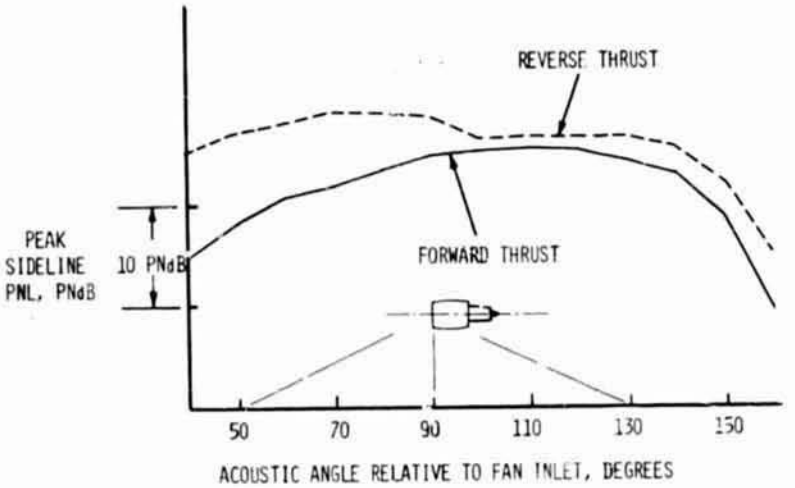

Figure 3.- Reverse and forward thrust PNL directivities. 1.30 pressure ratio; 152.4 m (500 ft) sideline.

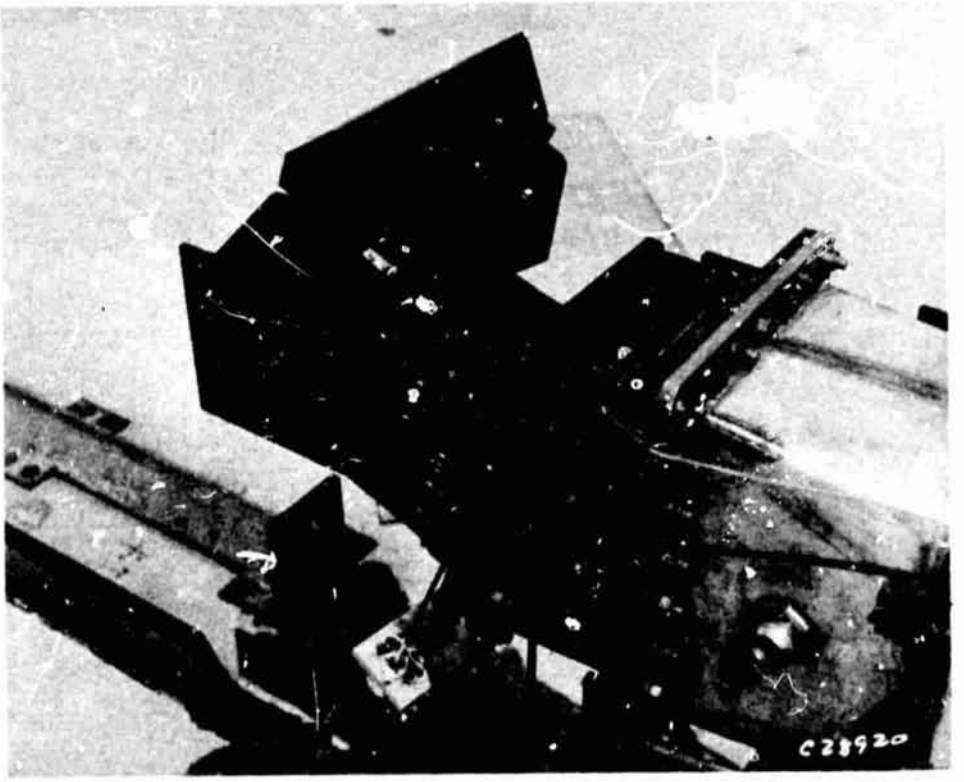

Figure 4.- Acoustic thrust reverser model.

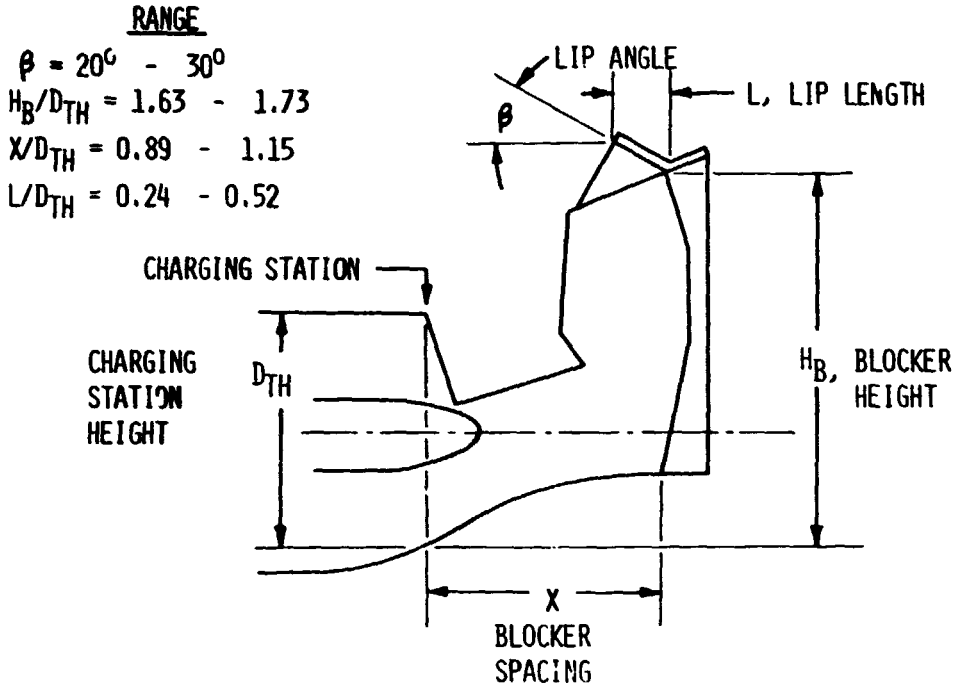

Figure 5.- Acoustic model thrust reverser parameters.

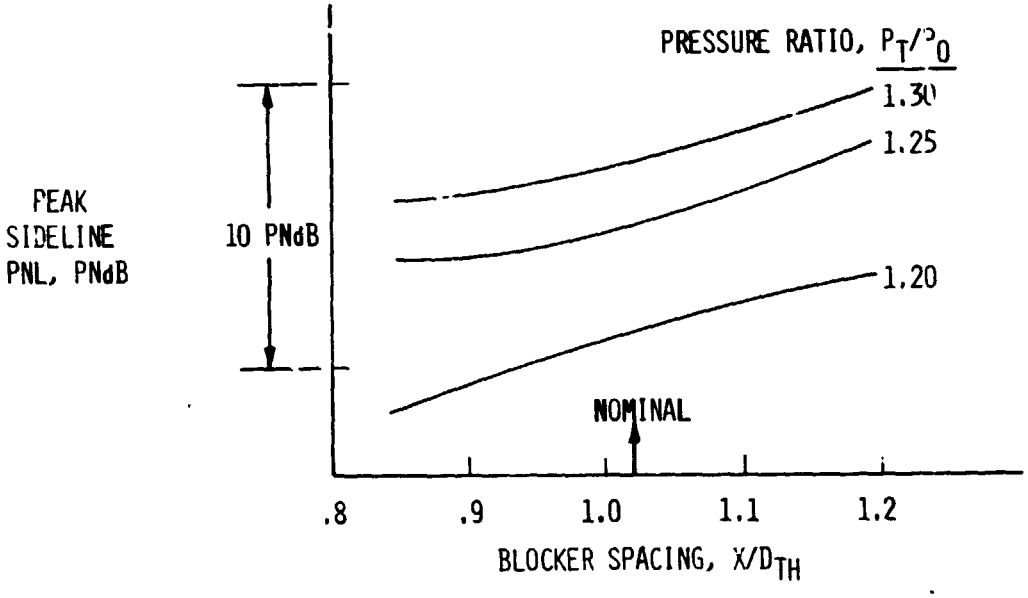

Figure 6.- Blocker spacing effect on peak sideline noise. 152.4 m (500 ft) sideline.

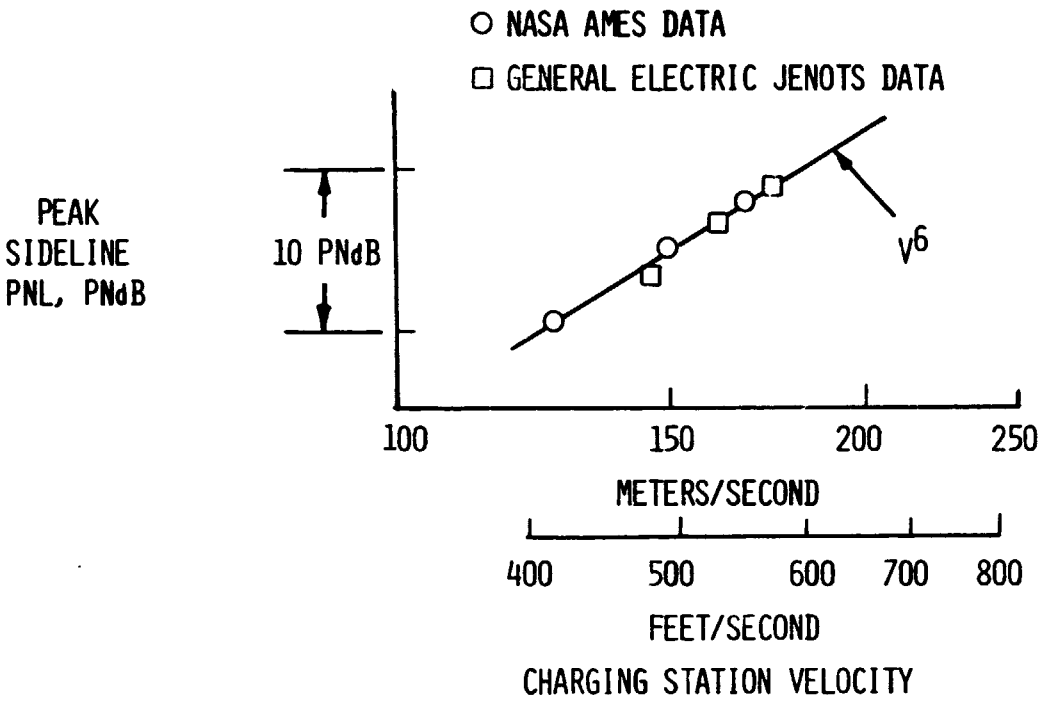

Figure 7.- Charging station velocity effect on target reverser noise. 152.4 m (500 ft) sideline.

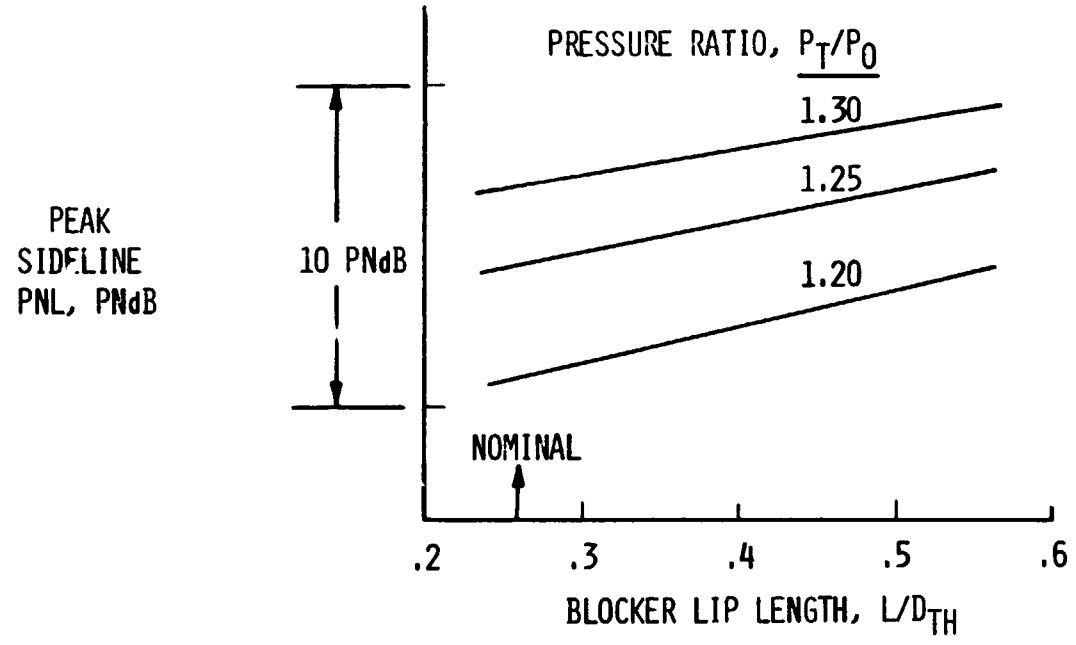

Figure 8.- Blocker lip length effect on peak sideline noise. 152.4 m (500 ft) sideline.

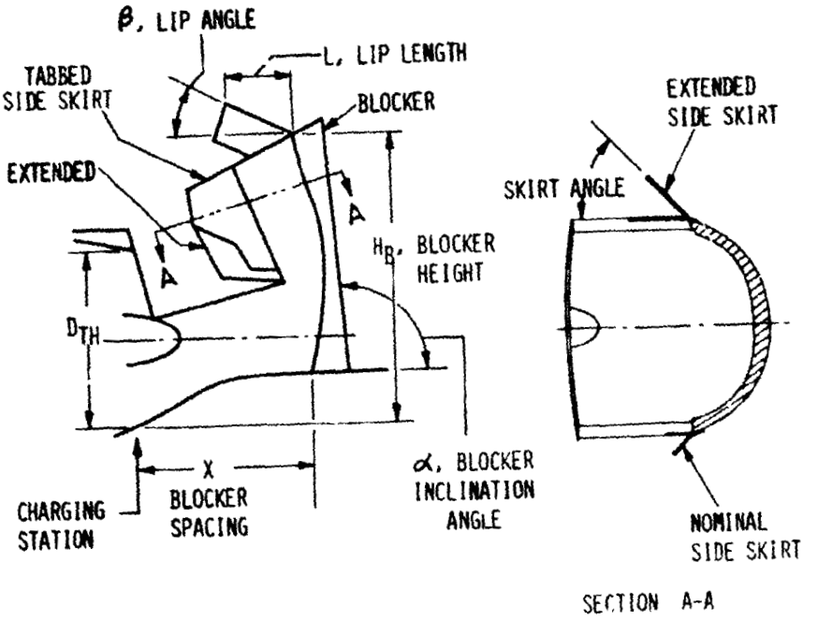

Figure 9.- Aerodynamic thrust reverser model.

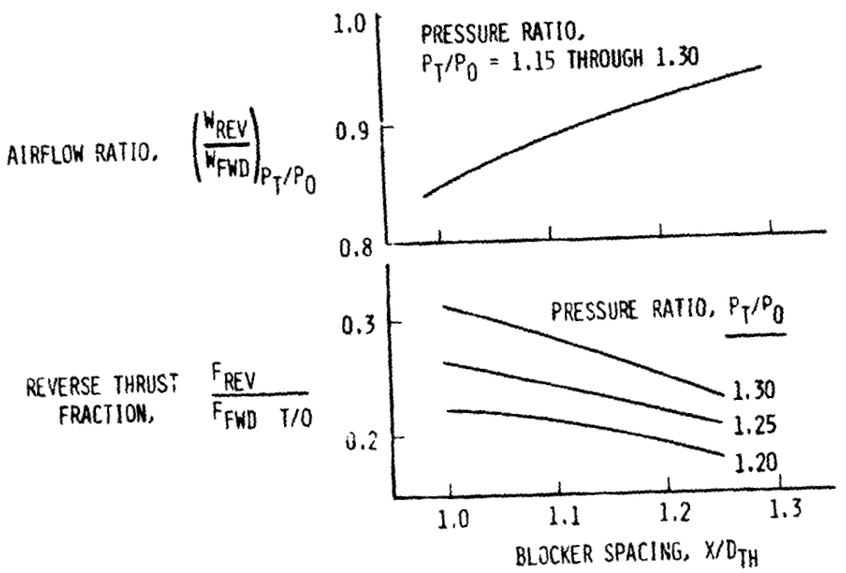

Figure 10.- Blocker spacing effect on flow and reverse thrust.

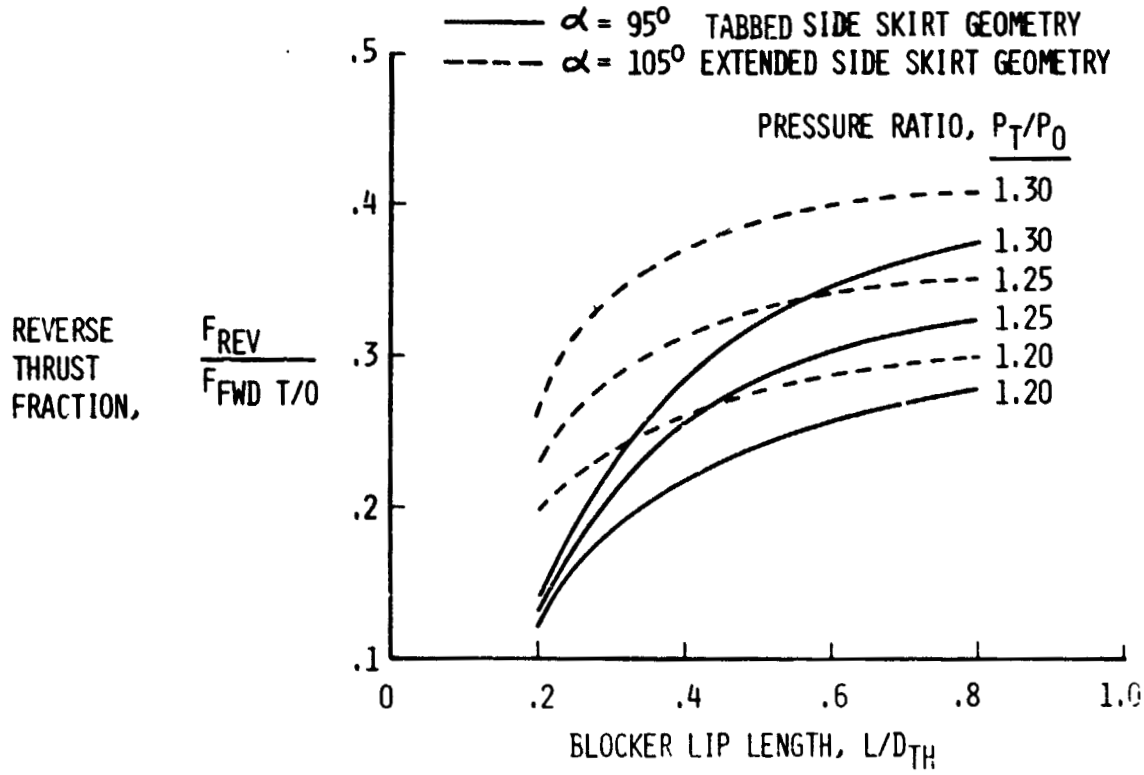

Figure 11.- Blocker lip length effect on reverse thrust.

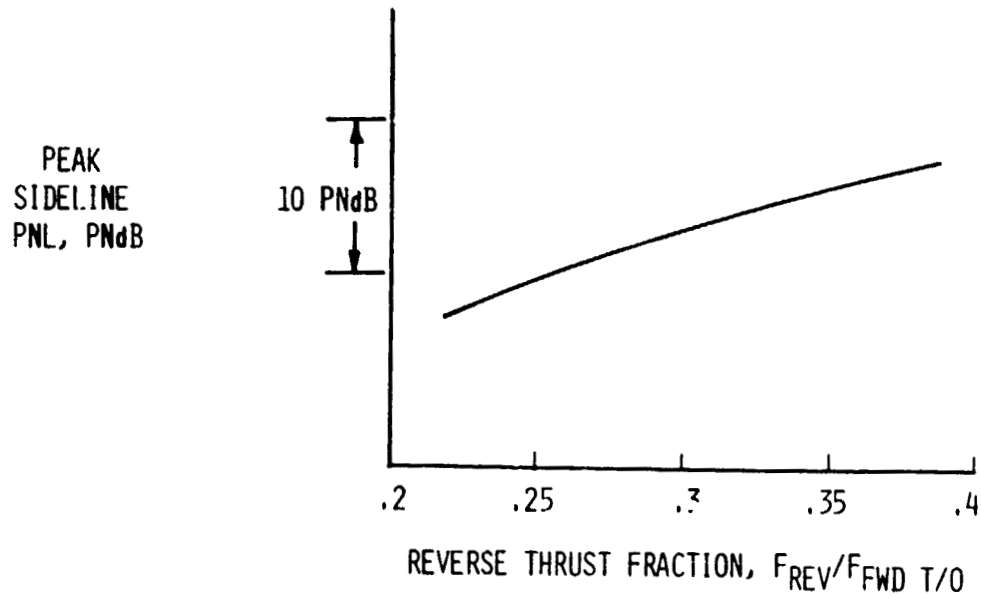

Figure 12.- Peak sideline PNL variation with reverse thrust.

MEASURED AND CALCULATED STEADY AERODYNAMIC LOADS ON A LARGE-SCALE UPPER-SURFACE BLOWN MODEL

Boyd Perry III
NASA Langley Research Center

Michael R. Mendenhall
Nielsen Engineering and Research, Inc.

SUMMARY

This paper presents static aerodynamic loads measurements from wind-tunnel tests of a full-scale upper-surface blown jet-flap configuration. The measured loads are compared with calculations using a recently developed method for predicting longitudinal aerodynamic characteristics of upper-surface blown jet-flap configurations.

INTRODUCTION

The performance and stability and control of upper-surface blown (USB) jet-flap configurations have been well documented. (See refs. 1 to 9.) These results have usually been presented as force and moment coefficients over the range of variables investigated, and most early models were small-scale and powered with compressed-air simulated engines. Some information has been published concerning detailed wing and flap load distributions. (See refs. 9 to 11.)

The development of analytical methods for predicting USB performance and loads has lagged behind the experimental work by 2 or 3 years. Such methods, which treat the aerodynamic interaction between lifting surfaces and the high-velocity exhaust wake, are now beginning to appear in the literature. (See refs. 12 to 14.)

In this paper, results of a loads investigation on a full-scale USB configuration powered with turbofan engines (presented previously in ref. 9) are presented. In addition, comparisons are made with calculated results based on an analytical method presently being developed under contract (which is an extension of the method of ref. 14). Measured wing and flap loads data are presented for parametric variations in angle of attack, flap deflection angle, and engine power setting, and for one engine inoperative.

SYMBOLS

Measurements and calculations were made in U.S. Customary Units and are presented in both the International System of Units (SI) and U.S. Customary Units.

a' location of leading edge of Krueger flap projected onto wing reference plane and expressed as a fraction of local wing chord

b' location of trailing edge of USB flap, double-slotted flap, or aileron, projected onto wing reference plane and expressed as a fraction of local wing chord

b wing span, m (ft)

C_p pressure coefficient, $\frac{p - p_\infty}{q_\infty}$

C_μ static thrust coefficient, $\frac{T}{q_\infty S}$

c local wing chord, m (ft)

c_n section normal-force coefficient, $\int_{a'}^{b'} \Delta C_p \, d\left(\frac{x}{c}\right)$

h initial height of rectangular vortex ring

l initial width of rectangular vortex ring

p local static pressure, N/m^2 (lb/ft^2)

p_∞ free-stream static pressure, N/m^2 (lb/ft^2)

q_∞ free-stream dynamic pressure, N/m^2 (lb/ft^2)

S wing area, m^2 (ft^2)

T static thrust force, N (lb)

x chordwise coordinate, m (ft)

y spanwise coordinate, m (ft)

z vertical coordinate, m (ft)

α angle of attack, deg

δ_a aileron deflection, deg

δ_f deflection of USB and double-slotted flap (deflected together), deg

Abbreviations:

BLC	boundary-layer control
USB	upper-surface blown

DESCRIPTION OF INSTRUMENTED MODEL

The model used in these tests is shown in the Langley full-scale tunnel in figure 1. The model had a wing span of 10.7 m (35.0 ft) and was equipped with two JT15D-1 turbofan engines (with nominal bypass ratio of 3.3). The high-lift system consisted of leading-edge Krueger flaps extending from the engine nacelles to the wing tips, leading-edge blowing boundary-layer control (BLC), upper-surface blown (USB) flaps extending from the fuselage to approximately 40 percent of the semispan, double-slotted flaps extending from approximately 40 percent to approximately 70 percent of the semispan, ailerons (capable of symmetrical deflection) extending from approximately 70 percent of the semispan to the wing tip, and aileron blowing BLC. The exhaust nozzle had an aspect ratio of 6.0 and a deflector attached to it to improve the spreading and turning of the jet exhaust. The right side of the model was instrumented with static pressure orifices at the eight spanwise stations indicated by the dashed lines in figure 1(a). A total of 270 pressure orifices were located on portions of the fuselage, wing, leading-edge Krueger flap, USB flap, double-slotted flap, and aileron. No static pressure orifices were located on the nacelle.

Chordwise sections taken at stations A, B, and C in figure 1(a) are shown in figure 1(b). The three sections are taken through the center of the engine, the double-slotted flap, and the aileron, respectively. Note that flap and aileron deflection angles are defined with respect to the wing reference plane indicated by the center line. A flap deflection of 32° and a symmetrical aileron deflection of 20° corresponds to a typical take-off configuration. A flap deflection of 72° and a symmetrical aileron deflection of 50° corresponds to a typical landing configuration.

ANALYTICAL PREDICTION METHOD

An analytical method, presently being developed under a NASA contract, was used to predict the static aerodynamic loads and the longitudinal aerodynamic characteristics of the USB configuration shown in figure 1. The method uses potential flow models to represent the lifting surfaces and engine wake and predicts the interference between these surfaces and the engine wake. The lifting surfaces are represented by a nonplanar vortex lattice and the engine by an expanding rectangular vortex "ring" model. Figure 2 illustrates the aerodynamic paneling scheme used to model the wing, flaps, and aileron. The shaded panels in figure 2 are those which receive direct interference from the engine wake. Figure 3 illustrates the simulated shape and location of the engine exhaust wake and the wake center line. The shape of the wake was empirically

tailored to the USB configuration of figure 1; that is, the width was determined by measuring the width of soot deposits from photographs in reference 9, and the height was determined from velocity profiles in reference 11 (which used the same engine and wing-flap as ref. 9). The rectangular vortex rings are normal to the wing and flap surfaces, resulting in a jet which is tangent to those surfaces. The wake center line moves aft at a constant y-station (see axis system in fig. 3) and it leaves the trailing edge of the last flap tangent to that surface. It then returns to the free-stream direction via a parabolic path at a distance equal to approximately 1 root chord downstream.

There are some limitations of the analytical prediction method which prevent complete simulation of the physical properties of the USB model. For example, the method cannot simulate either the exhaust nozzle deflector or leading-edge and aileron blowing BLC. In addition, there is no provision in the computer program for eliminating the contributions to the normal-force coefficient from that portion of the wing under the nacelles.

RESULTS AND DISCUSSION

Experimental Data

Figure 4 contains chordwise pressure distributions at a high thrust coefficient for the landing flap deflection. Shown is a portion of the nacelle and the upper surface of the wing and USB flap taken along chordwise section A of figure 1(a). The lines normal to the surface of the wing and flap indicate the location of static pressure orifices and the magnitudes of the pressures. The solid curve represents the wind-on condition (wind velocity was approximately 14 m/sec (45 ft/sec) at sea level), and the dashed curve represents the wind-off condition. Both distributions have the same general shape with about a 20-percent difference in magnitude. In both distributions the peak pressures occur at the knee of the flap. Also shown in the figure is a region of positive pressures at the point of exhaust impingement on the upper surface of the wing. The shapes of these pressure distributions are very similar to those shown in reference 10 and to those obtained in recent static tests of another large-scale USB model, in which peak pressures also occur at the knee of the flap.

Figures 5 to 8 contain plots of section normal-force coefficient c_n as a function of nondimensional semispan position $\frac{y}{b/2}$ for the present tests. Note that the location of the exhaust nozzle is identified in each of these figures. Since no pressure orifices were located on the nacelles, c_n does not include contributions from the nacelles. A common characteristic in figures 5 to 8 is the "dip" in the normal-force coefficient distributions. The dip occurs inboard of the nozzle center line and is due to positive pressures on the wing upper surface in the region of exhaust impingement. The positive pressures result in significantly lower section normal-force coefficients relative to adjacent spanwise stations, which have smaller positive pressures.

In figures 5 to 8, values of both section normal-force coefficient c_n and angle of attack α for constant values of thrust coefficient C_μ were obtained by interpolation of the basic corrected data.

Effect of engine thrust coefficient.- Figure 5 shows spanwise normal-force coefficient distributions for thrust coefficients of 0, 2.15, and 3.93. The angles of attack were 9.63°, 8.62°, and 7.95°, respectively (the difference in α has a negligible effect on the comparison). Examination of figure 5 indicates that from the fuselage center line to approximately 80 percent of the semispan the normal-force coefficients increased with increasing thrust coefficient. At the nozzle center line the normal-force coefficient for maximum thrust was an order of magnitude greater than that for zero thrust. Outboard, near the tip and well removed from the influence of the engine exhaust, the section normal-force coefficients for the two power-on conditions approached a common value, indicating that c_n is independent of C_μ near the tip.

Effect of angle of attack.- Figure 6 shows spanwise normal-force coefficient distributions for angles of attack of -1.3°, 8.5°, 18.3°, and 28.3°. This plot indicates that from the fuselage center line to a position slightly outboard of the nozzle, the spanwise normal-force coefficient is primarily dependent on the engine exhaust and shows little dependence on angle of attack. However, outboard of the nozzle the normal-force coefficient increases with increasing angle of attack as might be expected.

Effect of flap deflection angle.- Figure 7 shows spanwise normal-force coefficient distributions for flap deflection angles of 72° and 32°. The angles of attack were 8.48° for $\delta_f = 72°$ and 8.03° for $\delta_f = 32°$ (the difference in α has a negligible effect on the comparison). Examination of figure 7 indicates that the normal-force coefficients are consistently larger for the 72° flap setting than for the 32° flap setting. From near the tip to well within the spanwise extent of the exhaust nozzle, the normal-force coefficients for the 72° setting are consistently approximately twice as large as those for the 32° setting. Also of interest are c_n variations from the midpoint of the exhaust nozzle to slightly outboard of the exhaust nozzle. For the 72° flap deflection, maximum values of c_n occurred within the spanwise extent of the exhaust nozzle; for the 32° flap deflection, maximum values of c_n occurred outboard of the exhaust nozzle. The locations of these maximum values indicate that there was more spanwise spreading of the high-velocity exhaust for the smaller flap deflection angle than for the higher flap deflection angle.

Effect of one engine inoperative.- Figure 8 shows spanwise normal-force coefficient distributions on the right wing of the model for both engines operating, right engine only, left engine only, and both engines inoperative. The normal-force coefficient distributions for both engines operating and right engine only are very similar, with maximum variations in the region behind the exhaust nozzle. The spanwise normal-force coefficient distributions for left engine only and both engines inoperative are almost identical, indicating that there is very little lift carryover for this model. This result is not in agreement with results from other USB configurations with one engine inoperative (for example, see ref. 10). One reason for the absence of lift carryover for

the present model could be severe flow separation on the fuselage due to the interference between the fuselage and nacelles (ref. 9). It is believed that a leading-edge Krueger flap between the fuselage and nacelles could provide attached flow in this region and therefore provide better flow conditions for lift carryover with one engine inoperative, as indicated by some unpublished data recently obtained.

Analytical Comparison

Some preliminary analytical results obtained by using the prediction method mentioned previously are presented in this section of the paper and compared with experimental data. Figure 9 contains comparisons of experimental and analytical spanwise normal-force coefficient distributions at three power settings for a flap deflection of 72°. Measurements were made at 8 spanwise locations, and analytical calculations were performed at 16 locations. For $C_{\mu} = 0$ (in the upper left side of fig. 9) there is good agreement between predicted and measured results outboard of the nozzle. The predicted loads are too high in the nozzle region. As stated previously, some of this difference may be explained by the lifting surface model in the current program. The wing in the nacelle region is represented with a vortex-lattice arrangement and is allowed to carry loads as if the nacelle were not present. Therefore, this procedure must be permitting too much load to be carried by the wing in this region. For power-on conditions (in the lower left and lower right sides of fig. 9) the theoretically predicted normal-force coefficient distributions show reasonably good agreement with the experimental results. The peak loads for both theoretical and experimental results occur within the spanwise extent of the exhaust nozzle; however, the theoretical peak loads are approximately 20 percent higher. Part of this difference is due to the static pressure differences just mentioned. Another factor contributing to the difference is that the actual flow is highly complex in this region, with areas of positive and negative pressures on the wing upper surface. The analytical prediction method cannot simulate this effect. Outboard, near the wing tip and away from the influence of the engine exhaust, the theoretical and experimental results agree more closely.

CONCLUDING REMARKS

Static pressures were measured on the fuselage, Krueger flap, wing, upper-surface blown (USB) flap, double-slotted flap, and aileron of a large-scale USB model equipped with turbofan engines. Section normal-force coefficients were determined from static pressure data. The power-on section normal-force coefficients directly behind the exhaust nozzle were about an order of magnitude larger than the power-off coefficients at the same location. The section normal-force coefficients were insensitive to angle of attack within the spanwise extent of the exhaust nozzle, but very sensitive to both flap deflection angle and thrust coefficient. Greater spanwise spreading was observed with the flaps deflected for the take-off configuration (32°) than for the landing configuration (72°). For one engine inoperative, there was very little lift carryover across the fuselage for this model.

Some experimental data were compared with analytical results of a method presently being developed under contract. Preliminary results from this method indicate that the analytically predicted shape of the spanwise distribution of section normal-force coefficients is correct, but the magnitudes are approximately 20 percent high for the power-on conditions.

REFERENCES

1. Phelps, Arthur E.; Letko, William; and Henderson, Robert L.: Low-Speed Wind-Tunnel Investigation of a Semispan STOL Jet Transport Wing-Body With an Upper-Surface Blown Jet Flap. NASA TN D-7183, 1973.

2. Phelps, Arthur E., III; and Smith, Charles C., Jr.: Wind-Tunnel Investigation of an Upper Surface Blown Jet-Flap Powered-Lift Configuration. NASA TN D-7399, 1973.

3. Aoyagi, Kiyoshi; Falarski, Michael D.; and Koenig, David G.: Wind Tunnel Investigation of a Large-Scale Upper Surface Blown-Flap Transport Model Having Two Engines. NASA TM X-62,296, 1973.

4. Aoyagi, Kiyoshi; Falarski, Michael D.; and Koenig, David G.: Wind Tunnel Investigation of a Large-Scale Upper Surface Blown-Flap Model Having Four Engines. NASA TM X-62419, 1975.

5. Carros, Robert J.; Boissevain, Alfred G.; and Aoyagi, Kiyoshi: Aerodynamic Characteristics of a Large-Scale Hybrid Upper Surface Blown Flap Model Having Four Engines. NASA TM X-62460, 1975.

6. Smith, Charles C., Jr.; Phelps, Arthur E., III; and Copeland, W. Latham: Wind-Tunnel Investigation of a Large-Scale Semispan Model With an Unswept Wing and an Upper-Surface Blown Jet Flap. NASA TN D-7526, 1974.

7. Parlett, Lysle P.: Free-Flight Wind-Tunnel Investigation of a Four-Engine Sweptwing Upper-Surface Blown Transport Configuration. NASA TM X-71932, 1974.

8. Phelps, Arthur E., III: Wind-Tunnel Investigation of a Twin-Engine Straight-Wing Upper-Surface Blown Jet-Flap Configuration. NASA TN D-7778, 1975.

9. Staff of Langley Research Center: Wind-Tunnel Investigation of the Aerodynamic Performance, Steady and Vibratory Loads, Surface Temperatures and Acoustic Characteristics of a Large-Scale Twin-Engine Upper-Surface Blown Jet-Flap Configuration. NASA TM X-72794, 1975.

10. Smith, Charles C., Jr.; and White, Lucy C.: Pressure Distribution of a Twin-Engine Upper-Surface Blown Jet-Flap Model. NASA TM X-71937, 1974.

11. Shivers, James P.; and Smith, Charles C., Jr.: Static Tests of a Simulated Upper Surface Blown Jet-Flap Configuration Utilizing a Full-Size Turbofan Engine. NASA TN D-7816, 1975.

12. Lan, C. Edward; and Campbell, James F.: Theoretical Aerodynamics of Upper-Surface-Blowing Jet-Wing Interaction. NASA TN D-7936, 1975.

13. Lan, C. Edward: A Theoretical Investigation of Over-Wing-Blowing Aerodynamics. NASA CR-144969, 1976.

14. Mendenhall, M. R.; Perkins, S. C., Jr.; Goodwin, F. K.; and Spangler, S. B.: Calculation of Static Longitudinal Aerodynamic Characteristics of STOL Aircraft With Upper-Surface-Blown Flaps. NASA CR-137646, 19[illegible].

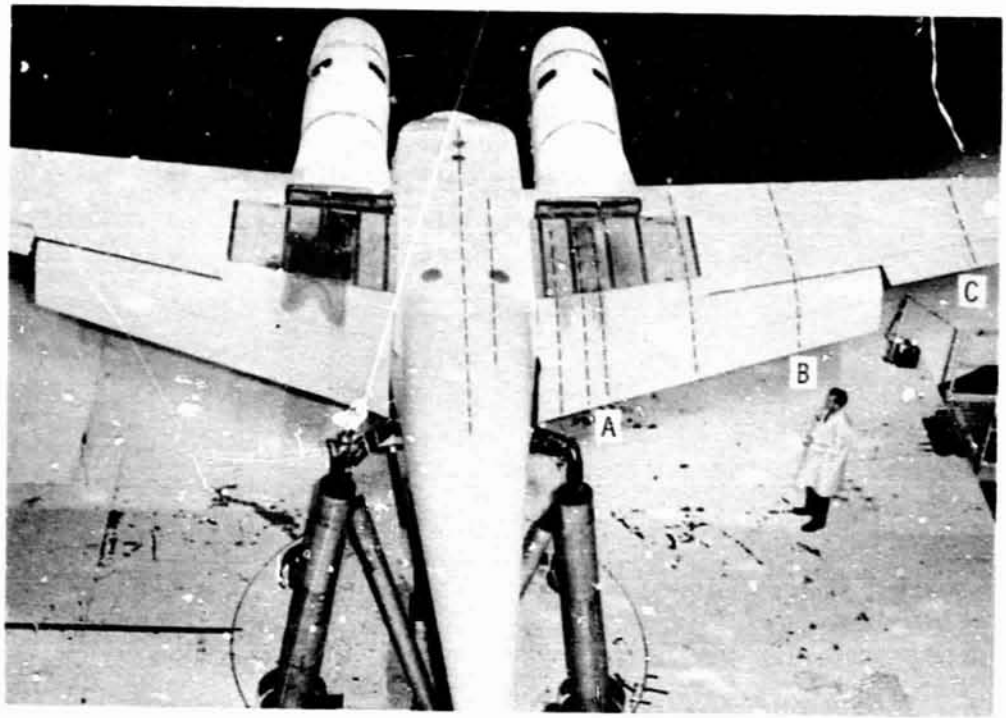

(a) Model in Langley full-scale tunnel.

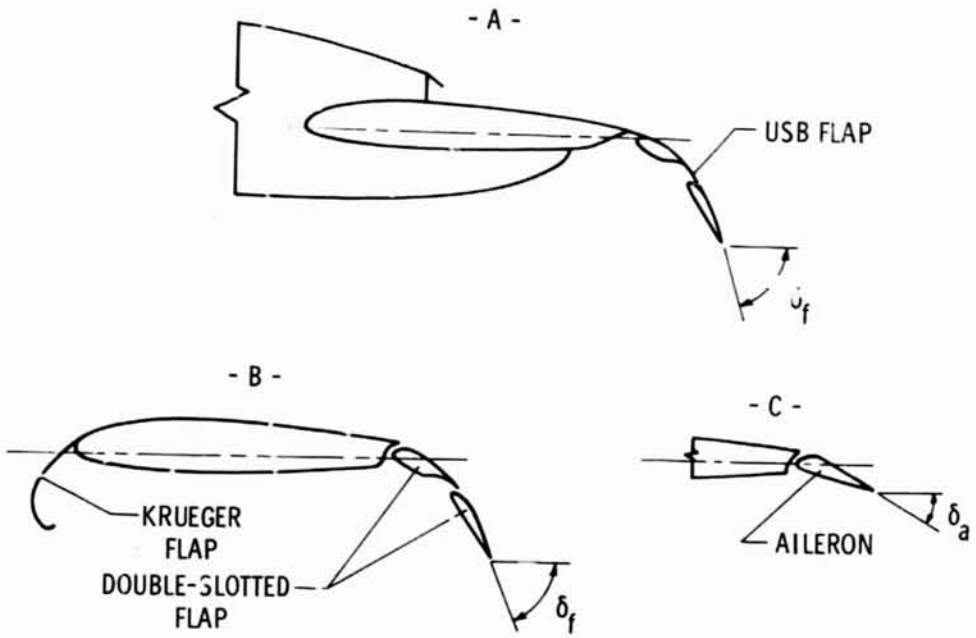

(b) Chordwise sections.

Figure 1.- Test configuration.

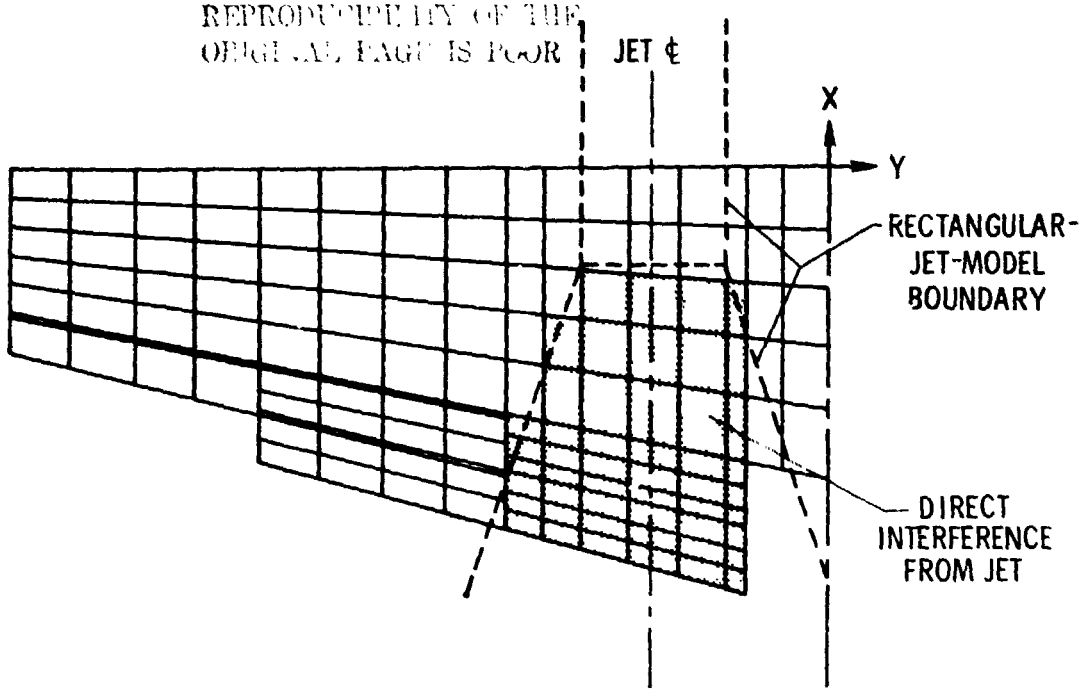

Figure 2.- Vortex-lattice layout.

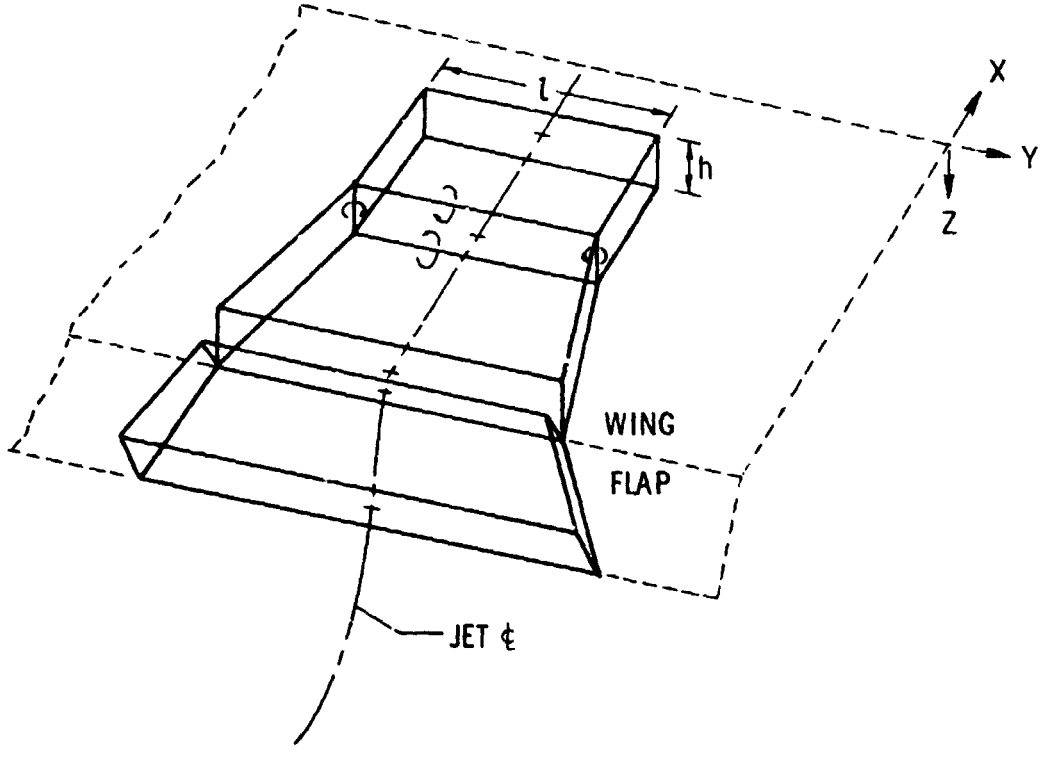

Figure 3.- Rectangular vortex ring jet model.

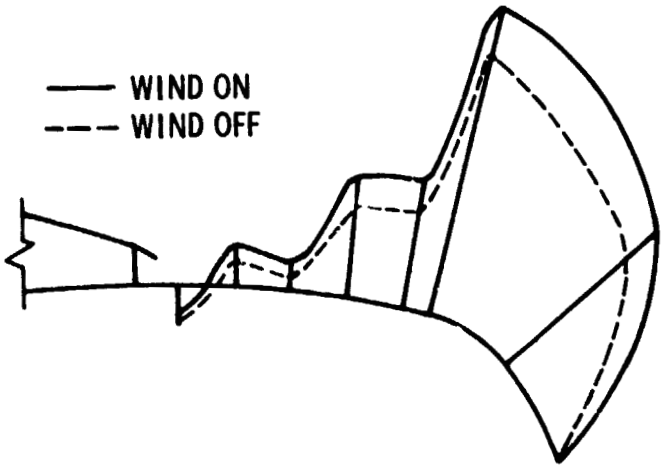

Figure 4.- Chordwise static pressure distributions along engine center line. $C_\mu = 3.93$; $\delta_f = 72^\circ$.

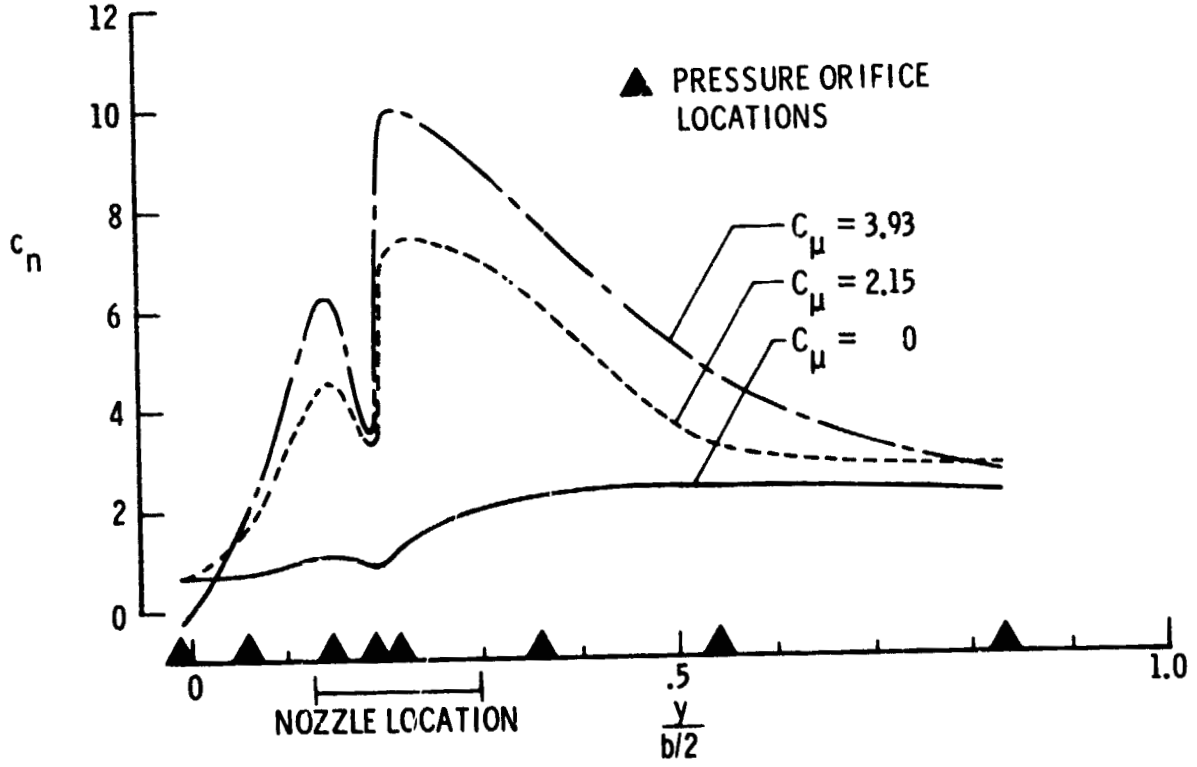

Figure 5.- Effect of thrust coefficient on spanwise loads. $\alpha = 10^\circ$ (nominal); $\delta_f = 72^\circ$; $\delta_a = 50^\circ$.

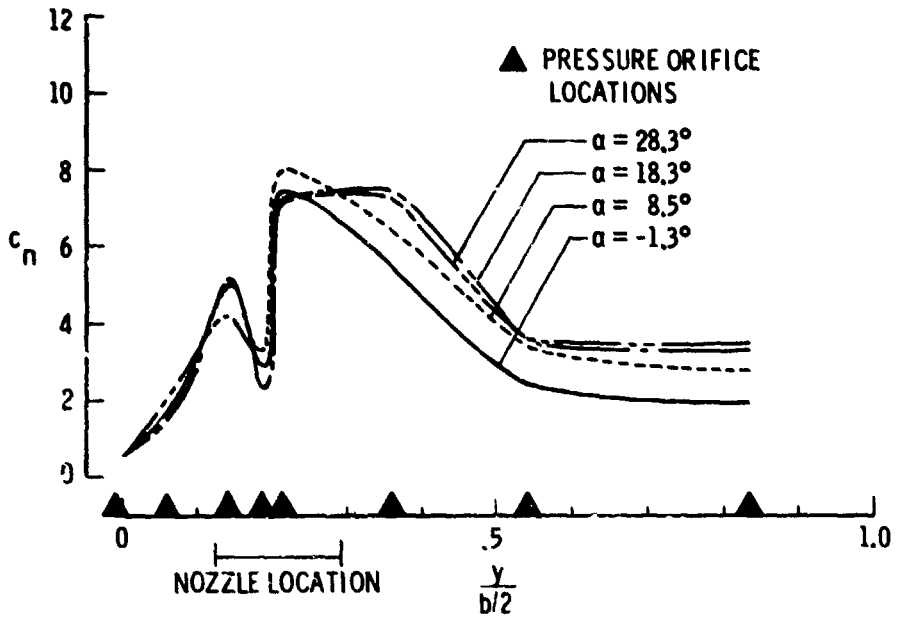

Figure 6.- Effect of angle of attack on spanwise loads. $C_\mu = 2.5$; $\delta_f = 72^\circ$; $\delta_a = 50^\circ$.

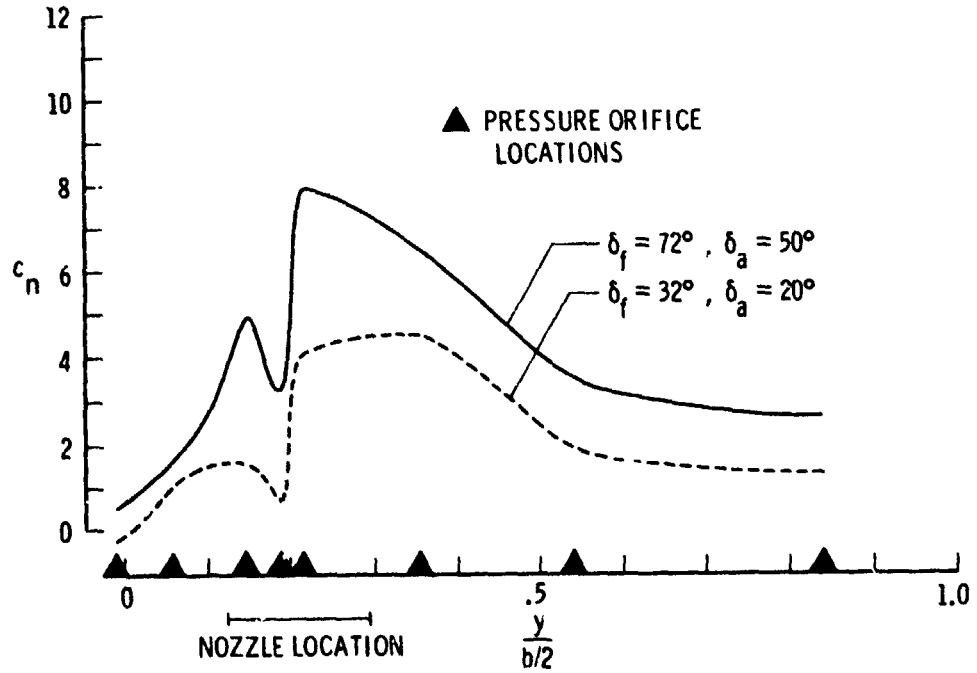

Figure 7.- Effect of flap deflection on spanwise loads. $C_\mu = 2.5$; $\alpha = 10^\circ$ (nominal).

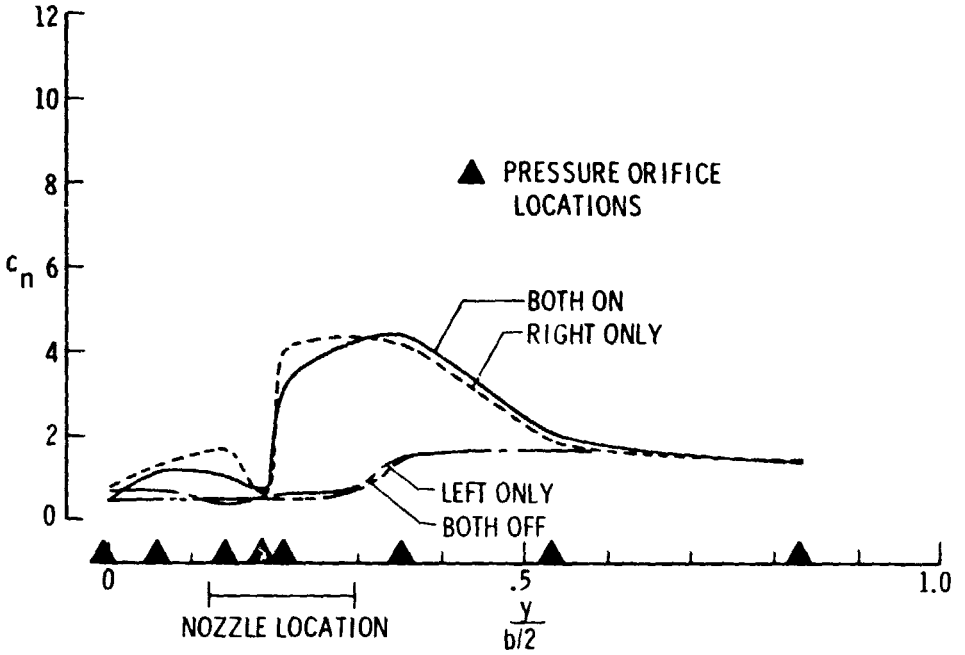

Figure 8.- Effect of one engine inoperative on spanwise loads on right wing. $\alpha = 10^{o}$ (nominal); $\delta_f = 32^{o}$; $\delta_a = 20^{o}$; $C_\mu = 1.0$ per engine.

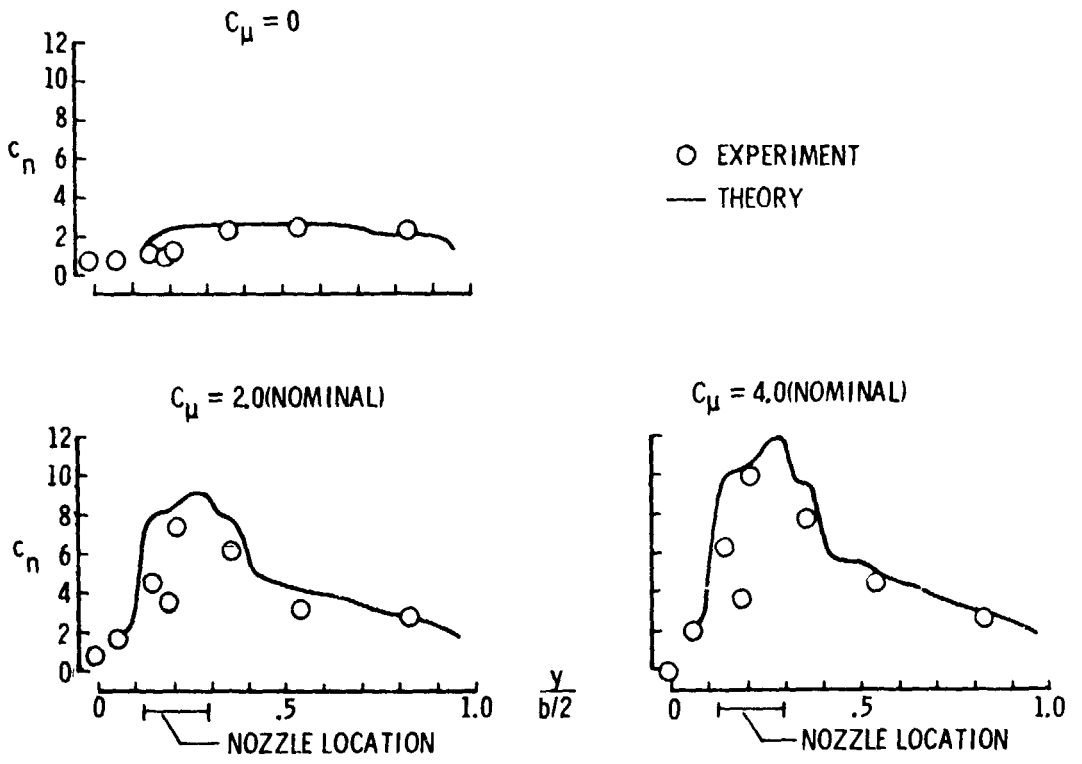

Figure 9.- Measured and calculated spanwise loads. $\alpha = 10^{o}$ (nominal); $\delta_f = 72^{o}$; $\delta_a = 50^{o}$.

ACOUSTIC-LOADS RESEARCH FOR POWERED-LIFT CONFIGURATIONS

James A. Schoenster, Conrad M. Willis,
James C. Schroeder, and John S. Mixson,
NASA Langley Research Center

SUMMARY

Intense noise sources are associated with the impingement of the jet engine exhaust on the wing and flap surfaces of powered-lift configurations. These noise sources may cause excessive noise inside the aircraft or may induce early acoustic fatigue failure. A current research program is aimed at determining the acoustic loads on the aircraft surfaces due to the impingement noise for use in studies of acoustic fatigue and interior noise control and at developing methods for predicting the loads. The research program includes acoustic-loads measurements on a variety of configurations including small-scale models, large-scale models, and flight vehicles. Companion analytical studies seek to develop and verify scaling laws for prediction of flight values from scale-model tests. Data presented from large-scale model tests with jet engines having thrusts of 9 kN (2000 lb) and 36 kN (8000 lb) include acoustic loads for an externally blown wing and flap induced by a TF34 jet engine, an upper surface blown (USB) aircraft model in a wind tunnel, and two USB models in static tests. Comparisons of these results with results from acoustic-loads studies on configurations of other sizes are made and the implications of these results on interior noise and acoustic fatigue are discussed.

INTRODUCTION

Two of the powered-lift configurations receiving considerable attention for use in short take-off and landing (STOL) aircraft are the externally blown flap (EBF) system and the upper-surface blown (USB) system. To obtain the additional lift, both these configurations require the jet engine exhaust to impinge directly on the wing-flap structures of the aircraft. The effects of this impingement are (1) to increase the overall fluctuating loads on the aircraft above the level normally encountered by conventional aircraft and (2) to concentrate the peak levels of these fluctuating loads at lower frequencies than normally encountered. The results of these high levels and the low-frequency content are (1) to increase the potential of sonic fatigue and (2) to induce high acoustic levels in the interior of the aircraft. The extent of these problems in powered-lift aircraft is shown in figures 1 and 2. Figure 1, taken from reference 1, shows that sonic fatigue failures of small secondary structures have occurred for a wide variety of sources when levels exceed 130 dB. Above this level, special design considerations are needed to minimize the potential of failure. Figure 2, taken from reference 2, illustrates the potential interior noise problems of STOL aircraft. Figure 2(a) shows the external noise

spectrum for a USB take-off configuration. Figure 2(b) indicates the current technology of aircraft sidewall noise reduction. Figure 2(c) shows the resulting USB interior noise spectrum based on the data in figures 2(a) and (b). Also shown, for reference purposes, in figure 2(c) are spectral data measured during cruise conditions on CTOL aircraft. These predictions indicate that in the lower frequency range, interior noise levels are 25 dB above those for current cruise aircraft - a considerably noisier interior environment.

Because of these potential problem areas, a program designed to develop techniques for predicting fluctuating loads on STOL aircraft was established at Langley Research Center. The effects of these predicted loads could then be incorporated in the design of the aircraft to prevent many problems that otherwise would require modifications after the aircraft was built. It was believed that the use of models would be the best approach. Shown in figure 3 is an outline of the program which developed. To aid in determining scaling laws and prediction methods, three types of models were selected for investigation: small-scale models, large-scale models, and flight vehicles. Langley has directly supported or conducted in-house tests on all three types of models for both the EBF configuration and the USB configuration.

SYMBOLS

d	jet nozzle exit diameter, m
f	frequency, Hz
M_j	Mach number of the jet at the nozzle exit
p_{rms}	root-mean-square value of the fluctuating pressure, Pa
q_o	dynamic pressure of the jet at the nozzle exit, Pa
U_0	velocity of the jet at the nozzle exit, m/sec

ABBREVIATIONS

AMST	advanced medium short take-off and landing transport
BBN	Bolt Beranek and Newman
EBF	externally blown flap
FPL	fluctuating pressure level
OA	overall
OAFPL	overall fluctuating pressure level

PSD power spectral density

SPL sound pressure level

USB upper-surface blown

EBF FLUCTUATING-LOADS STUDIES

Shown in figure 4 are photographs of the test configurations being used to study the EBF fluctuating loads. At the lower left is the Bolt Beranek and Newman (BBN) EBF small-scale model. Data from this model have been reported in reference 3. In the middle photograph is the TF34 engine (36 kN (8000 lb) thrust) EBF model which was tested at the NASA Lewis Research Center. Preliminary data from this test have been reported in references 4 and 5. Shown at the top of the figure is the Douglas AMST YC-15 aircraft. The YC-15 is currently undergoing flight evaluation tests by the U.S. Air Force, and in the spring of 1976, fluctuating-loads data were obtained on the wing, flap, and fuselage. In addition, Langley Research Center in cooperation with the Air Force Flight Dynamics Laboratory has obtained data on the structural response of the fuselage sidewall and on interior noise levels of this aircraft. These data are not currently available for publication.

Overall fluctuating pressure levels (OAFPL), in decibels referenced to 20μPa, measured on the TF34 EBF model are shown in table I. Shown in schematic view are the engine, the wing, and the flap settings for typical take-off (flap angles of 0°, 20°, and 40°) and landing (flap angles of 15°, 35°, and 55°) configurations. Listed in the table are measurements obtained at flap locations on a vertical plane through the engine center line. The measurements cover a range of jet exhaust Mach numbers from 0.33 to 0.59. The highest levels were 163 dB for the take-off flap setting and 162 dB for the landing flap setting. However, in all cases, the table shows levels equal to or exceeding 143 dB, clearly above the level indicated in figure 1 for the onset of acoustic fatigue problems.

Although the BBN small-scale model is not an exact replica of the TF34 model, it is approximately a 1/20-scale model. Nondimensionalized data from both models obtained at transducer locations 2 and 5 (see sketch in table I) for both a take-off configuration and a landing configuration are shown in figure 5. The frequency scale is nondimensionalized by using the nozzle exit diameter and nozzle exit jet velocity as parameters. This normalized value is called the Strouhal number. The mean-square fluctuating pressure levels in 1/3-octave bandwidths and normalized to the jet dynamic pressure at the exit are plotted in decibels on the vertical scale. Data from the models collapse very well for both flaps in the take-off configuration and for the aft flap in the landing configuration (figs. 5(a), (b), and (d)). Normalized amplitudes are well within 5 dB of each other and the peak response generally occurs at a Strouhal number between 0.4 and 0.5. The peak response is at a somewhat lower Strouhal number (0.27) on the aft flap in the take-off configuration for the small-scale model (fig. 5(b)). For the forward flap in the landing configuration (fig. 5(c)), the TF34 data follow the same trend as the data in the other parts of figure 5; but the small-

scale model data indicate a lower overall level and a much flatter spectrum, without a clearly definable frequency of peak response.

These data indicate that techniques using scaled geometry and the jet nozzle exit dynamic pressure, velocity, and diameter as parameters are sufficient to predict the loads on the flaps. However, some questions concerning the effects of temperature and noncircular nozzle exits still remain.

USB FLUCTUATING-LOADS STUDIES

Shown in figure 6 are photographs of the test configurations being used to study the USB fluctuating loads. Data on the fluctuating loads of each of these configurations have been or will be obtained. Starting at the upper left is an Aero Commander aircraft modified by the installation of over-the-wing JT15D engines (9 kN (2000 lb) thrust). Below that is a full-scale boilerplate model of the Aero Commander wing and flap, mounted upside down, also with a JT15D engine. In the lower left corner is a small-scale model of the boilerplate model using a cold air jet. Tests of the small-scale model are being conducted at the University of Virginia as part of a NASA study grant on powered-lift configurations. Results of these efforts are presented in reference 6.

At the upper right corner is an artist's sketch of the Boeing AMST YC-14. During the Air Force flight evaluation tests, the Boeing Company will obtain data on both the fluctuating loads and the interior noise levels for NASA. These tests are currently scheduled to start in the summer of 1976. Immediately below the YC-14 is a sketch of the YC-14 ground test rig. The Boeing Company, under contract to NASA, conducted tests on a full-scale mockup of the YC-14 using a combination of actual aircraft components and boilerplate components. Preliminary results from this test are reported in reference 7. Below the Boeing model is a photograph of the YC-14 scale model at Langley. Results on the USB static performance of the 1/4-scale model were presented in reference 8.

Wing Flap Loads

An example of the type of data obtained on the loads is shown in figure 7. The pressure spectra on the wing of the YC-14 scale model during engine run-up are shown in a "three-dimensional" format. A continuing spectral analysis, from 0 to 7 kHz in 20-Hz bandwidths, is performed while the engine thrust is increased from the value at idle speed (about 1100 N) to maximum thrust (7500 N). Each subsequent analysis is plotted just below the preceding one to form the picture shown in figure 7(b). This type of analysis presents a visual display of the continuous change in spectra with engine thrust. The fan tones and a compressor tone are clearly visible as peaks in the spectral curve, increasing in frequency as the thrust increases. Over the frequency range displayed, it may also be seen that with the exception of the engine tones, the spectra do not show any activity above 2 kHz. Below 2 kHz, the spectra vary as the thrust of the engine increases, and in figure 7(a) the section of the spectra shown by the dashed loop in figure 7(b) is expanded by analyzing the same data with a

4-Hz bandwidth over a frequency range of 0 to 500 Hz. Using this narrower band analysis shows that the frequency of the first peak in the response curve increases from about 100 Hz to 270 Hz for an increase in thrust from idle to maximum thrust. (See dashed lines in fig. 7(a).) Because the frequencies of peak response increase with thrust, a normalization such as Strouhal number would appear to be a reasonable approach to nondimensionalizing the frequency scale.

However, the problem may not be as straightforward as that for the EBF configurations. Shown in figure 8 are the fluctuating pressures along the projection of the engine center line for the USB boilerplate model of the Aero Commander. The OAFPL in decibels are shown at the right of the figure, with the maximum level of 156 dB occurring not in the impinged area, but somewhat downstream on the wing. Shown at the left of the figure are the power spectral densities of the fluctuating pressures associated with those overall levels. The 0 dB points on the vertical scale for each of the plots have been displaced so that the various spectra would not overlap. It may be observed that the spectra vary with the location on the wing or flap. At the impinged area (151 dB OAFPL), there are two peaks in the spectra: one at about 250 Hz. the other at 1700 Hz. Data from measurement locations downstream on the flap show a single peak emerging in the spectra and the frequency of this peak response decreasing. Near the flap trailing edge, the frequency of the peak response is 40 Hz. To normalize these data, it is apparent that the engine nozzle exhaust parameters would not be sufficient to collapse the levels and frequencies completely. Also, perhaps because of the nonsymmetrical shape of the nozzle, there appear to be at least two sources influencing the shape of the spectra at the impinged area. Continuing studies of the small-scale models should provide answers to some of these questions.

The studies on the Aero Commander model provided data on the structural response of a representative airframe structure. Although the structure of this model has been reinforced to support the engines and withstand the loads, it is clearly not a boilerplate model. Data reported in reference 9 showed rms levels as high as 38g occurring on panel sections in response to the flow over the upper surface of this structure. Shown in figure 9 are the responses of some of the main support structure in the area immersed in exhaust flow. The data are shown in terms of power spectral density plots of the pressure or acceleration. The two pressure spectra, one on the wing and one on the aft flap are similar to those reported in figure 8. The accelerations on the wing show several peak responses over the entire frequency range, although the maximum response is in the lower frequency range, where the pressure levels are the highest. An overall rms level of 4g was measured. The accelerometer on the flap was mounted on the flap track, a section of support structure connected all the way back to the wing. The acceleration spectrum also has several peaks with an overall rms level of 15g. Although the structure is responding very strongly to the excitation, in general the frequencies of peak responses in the wing do not match the frequencies of peak responses in the flap. This would indicate that the resonant responses of the structure are very localized and are not major overall vibration modes of the wing-flap system.

Fuselage Loads

The scale model of the YC-14 includes a section of fuselage. Shown in figure 10 are photographs of a tuft flow visualization pattern on this fuselage section. It should be noted that vortex generators to aid flow turning are installed. In figure 10(a), the engine is off and the tufts are hanging downward. In figure 10(b), the engine is running with an average jet exhaust velocity of 366 m/s. Along the bottom of the fuselage the tufts are almost horizontal; in the middle they are spinning around, as indicated by the blurred image; along the fairing they follow flow lines parallel to the flap contour; and on the top there is no indication of flow at all. In figure 11, the fluctuating pressure spectra at several locations on the fuselage are shown. The OAFPL's range from a high of 160 dB on the fairing section of the fuselage just off the trailing edge of the flap to a low of 144 dB on the top of the fuselage. This low measurement occurred in an area in which the tufts indicate no flow. The differences between the locations in the flow and the one location outside the flow may be better seen by looking at the spectra. Shown are the fluctuating levels, in decibels, analyzed by a constant-bandwidth filter having a nominal 20-Hz bandwidth. All the measurements made where the tufts indicate surface flow follow the same trend. Although the levels vary, all the spectra maximize at frequencies below 120 Hz. The measurements from the transducers located below the fuselage fairing have relatively flat responses below 120 Hz, whereas the measurements from the transducers on the upper sections of the fuselage peak at about that frequency. Above 120 Hz, the spectra all decrease at an approximate slope of 6 dB per octave. The spectrum measured outside the flow region had different characteristics. First, the peak in the response curve occurs at a somewhat higher frequency, centering at about 160 Hz; and the spectrum decreases at a much flatter slope, with levels above 1000 Hz actually higher than those measured by the two adjacent transducers. These data indicate that the higher levels and the lower frequencies are directly related to the exhaust flow; but even where there is no exhaust gas flow, acoustic levels are very high.

Although the conditions are not matched, the spectra in the exhaust gas flow areas shown here are very similar to the predicted spectra shown in figure 2, both in shape and level. This similarity indicates that the interior noise levels will be as high as predicted under some circumstances and that new techniques will have to be developed to help reduce these levels to current commercial aircraft levels.

CONCLUDING REMARKS

Measurements have been obtained from several EBF and USB test configurations ranging from small-scale models to large, full-scale models using actual jet engines. Data from these models are being evaluated at present, and initial results indicate that the anticipated high levels and low frequencies actually occur and will likely require special design considerations. The use of small-scale models to aid in predicting the loads and frequencies looks very promising, but additional development is still necessary and investigation into modeling is continuing.

Because initial predictions, partially supported by ground-test loads data, indicate high interior noise levels in powered-lift aircraft, Langley Research Center has extended its fluctuating-loads program into interior noise studies. Currently, measurements are being obtained on the AMST aircraft to aid in studies of sources and transmission paths of cabin interior noise in STOL aircraft.

The AMST flight test program, by obtaining measurements during actual operational conditions, should provide definitive data for evaluating the capabilities of scale-model prediction methods.

REFERENCES

1. Lansing, Donald L.; Mixson, John S.; Brown, Thomas J.; and Drischler, Joseph A.: Externally Blown Flap Dynamic Loads. STOL Technology, NASA SP-320, 1972, pp. 131-142.

2. Darton, C. Kearney: Interior Noise Consideration for Powered-Lift STOL Aircraft. NASA TM X-72675, 1975.

3. Hayden, Richard E.; Kadman, Yoram; and Chanaud, Robert C.: A Study of the Variable Impedance Surface Concept as a Means for Reducing Noise From Jet Interaction With Deployed Lift-Augmenting Flaps. NASA CR-112166, 1973.

4. Schoenster, James A.: Acoustic Loads on an Externally Blown Flap System Due to Impingement of a TF-34 Jet Engine Exhaust. NASA TM X-71950, 1974.

5. Mixson, John S.; Schoenster, James A.; and Willis, Conrad M.: Fluctuating Pressures on Aircraft Wing and Flap Surfaces Associated With Powered-Lift Systems. AIAA Paper 75-472, Mar. 1975.

6. Morton, J. B.; Haviland, J. K.; Catalano, G. D.; and Herling, W. W.: Investigations of Scaling Laws for Jet Impingement. Powered-Lift Aerodynamics and Acoustics, NASA SP-406, 1976. (Paper no. 28 of this compilation.)

7. Sussman, M. B.; Harkonen, D. L.; and Reed, J. B.: USB Environment Measurements Based on Full-Scale Static Engine Ground Tests. Powered-Lift Aerodynamics and Acoustics, NASA SP-406, 1976. (Paper no. 30 of this compilation.)

8. Hassell, James L., Jr.: Results of Static Tests of a 1/4-Scale Model of the Boeing YC-14 Powered-Lift System. Powered-Lift Aerodynamics and Acoustics, NASA SP-406, 1976. (Paper no. 3 of this compilation.)

9. Staff of Langley Research Center: Wind-Tunnel Investigation of the Aerodynamic Performance, Steady and Vibratory Loads, Surface Temperatures and Acoustic Characteristics of a Large-Scale Twin-Engine Upper-Surface Blown Jet-Flap Configuration. NASA TM X-72794, 1975.

TABLE I.-- OVERALL FLUCTUATING SURFACE PRESSURE LEVELS ON TF34 EBF MODEL

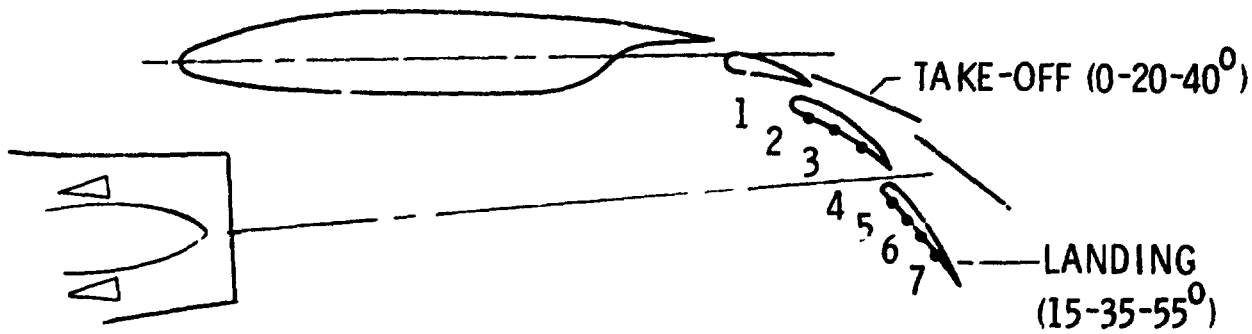

Transducer	OAFPL, dB (ref. 20 μPa), at Mach number of -									
	0.33	0.45	0.51	0.57	0.59	0.33	0.44	0.49	0.55	0.59
	Take-off flaps (0°-20°-40°)					Landing flaps (15°-35°-55°)				
1	149	155	156	158	159	150	156	158	160	(162)
2	151	157	159	160	161	148	154	156	159	160
3	152	158	160	162	(163)	148	153	155	157	159
4	149	154	156	159	160	(146)	152	153	156	157
5	145	150	152	155	156	147	152	154	156	156
6	(143)	148	150	152	153	148	154	155	156	157
7	144	149	151	---	154	148	153	155	157	157

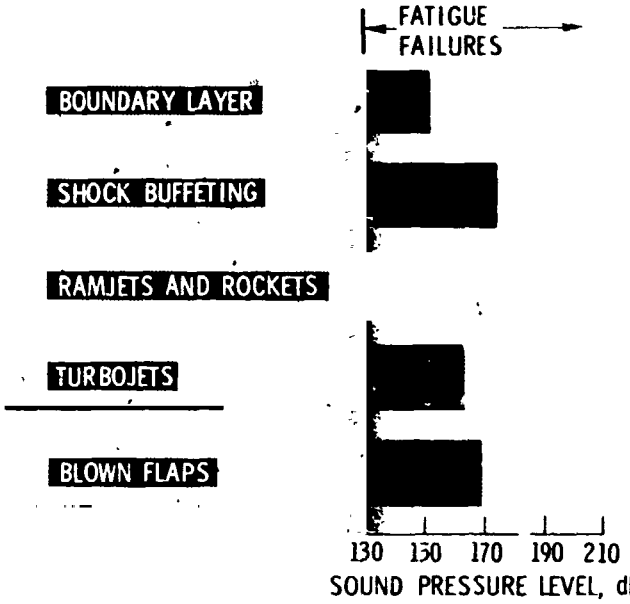

Figure 1.- Sound pressure levels of acoustic loading on aircraft structures (from ref. 1).

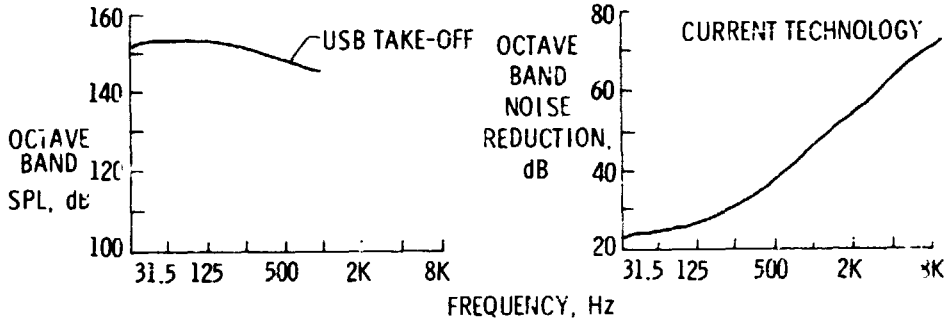

(a) External noise spectra.

(b) Sidewall noise reduction - current technology.

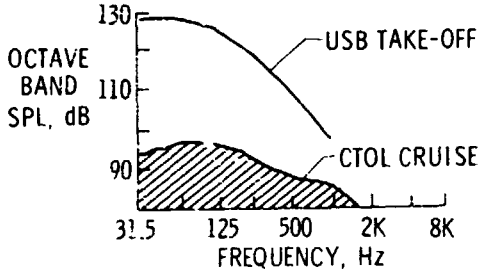

(c) Interior noise spectra.

Figure 2.- Estimated USB noise spectra (from ref. 2).

SCALING LAWS AND PREDICTION METHODS

SMALL-SCALE MODELS	LARGE-SCALE MODELS	FLIGHT TESTS
EBF MODEL (BBN)	TF34 EBF	AMST YC-15 (DOUGLAS) EBF
USB MODEL (U. VA.)	MODIFIED AERO COMMANDER-USB	AMST YC-14 (BOEING) USB
	BOILERPLATE MODEL-USB	
	YC-14 GROUND TEST-USB	
	YC-14 SCALE MODEL-USB	

Figure 3.- Program for development of prediction methods for fluctuating loads.

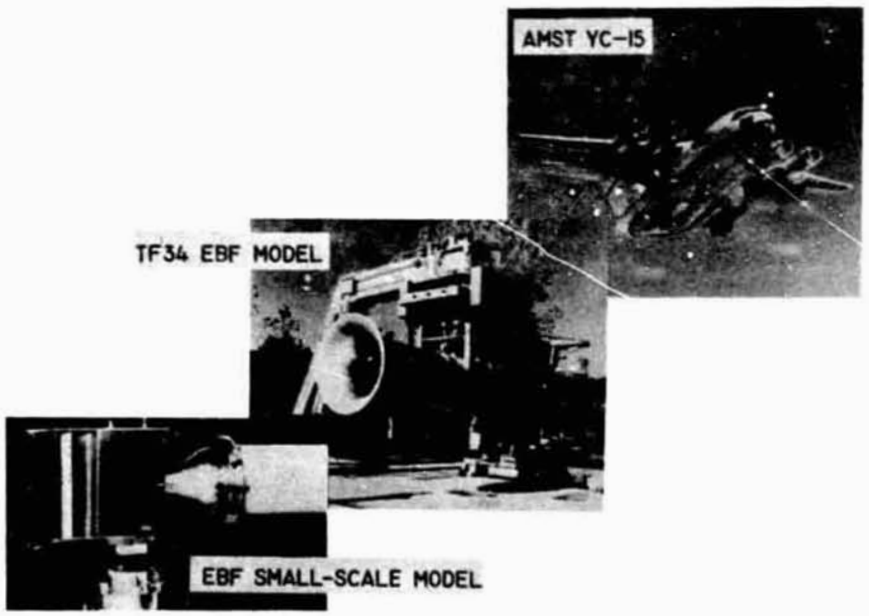

Figure 4.- Test configurations for EBF fluctuating-loads studies.

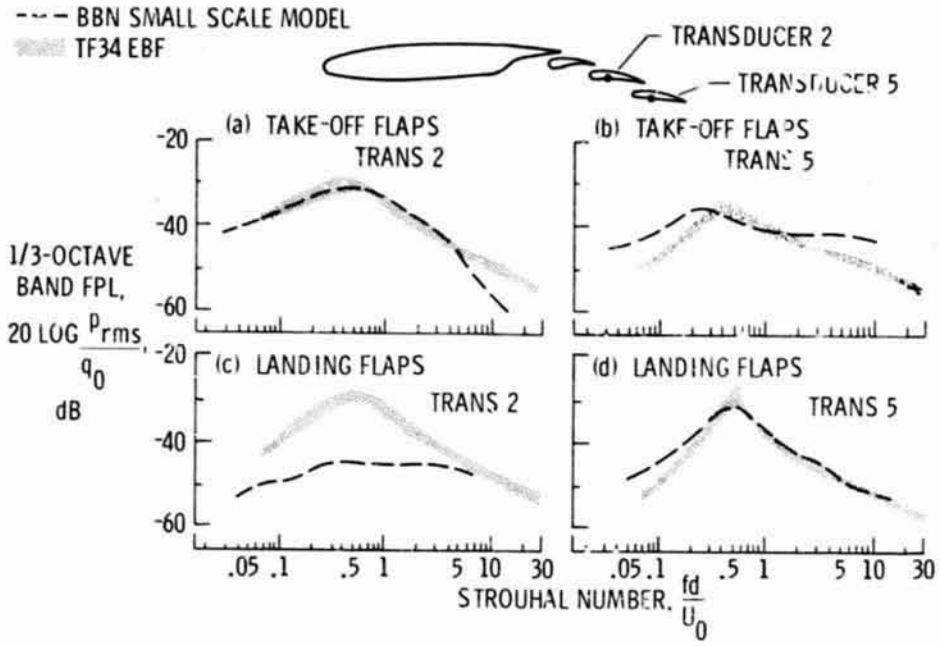

Figure 5.- Comparison of the fluctuating pressures on large- and small-scale EBF models.

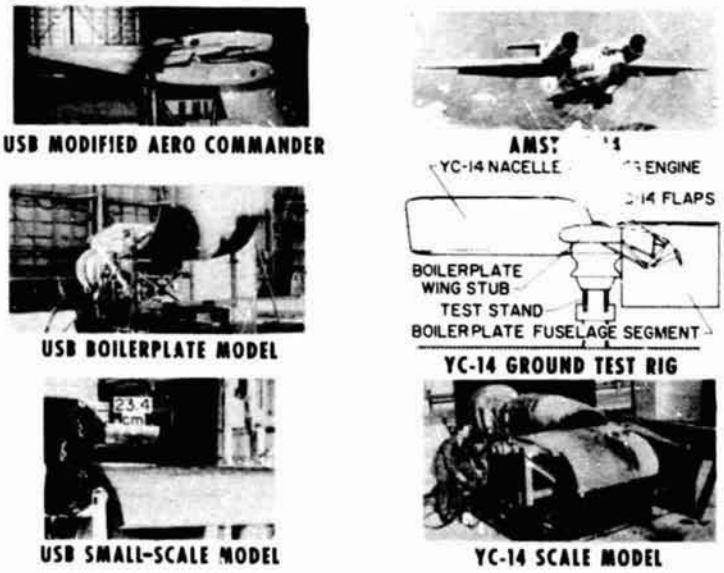

Figure 6.- Test configurations for USB fluctuating-loads studies.

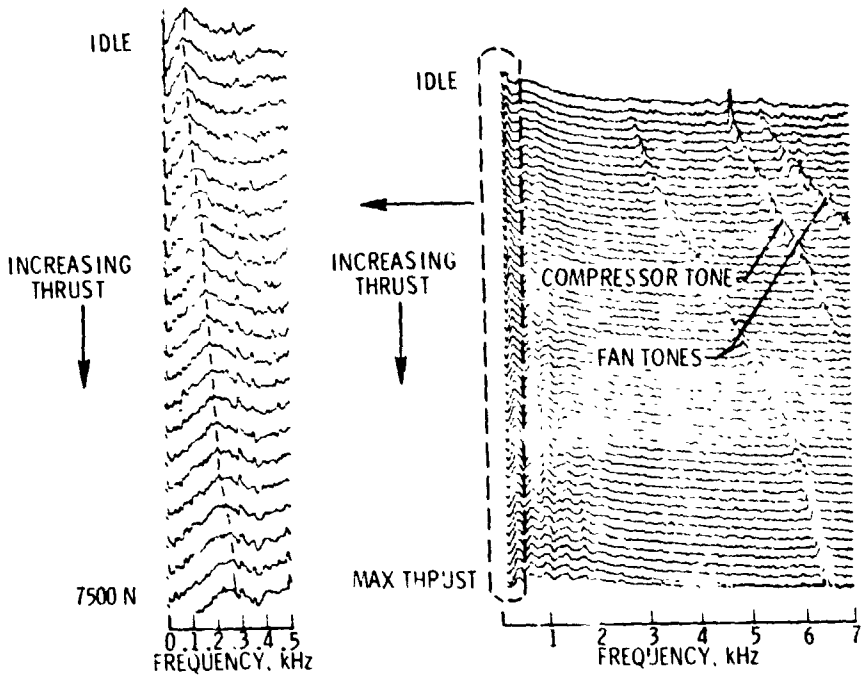

(a) 4-Hz bandwidth analysis.

(b) 20-Hz bandwidth analysis.

Figure 7.- Pressure spectra on wing of YC-14 scale model during engine run-up.

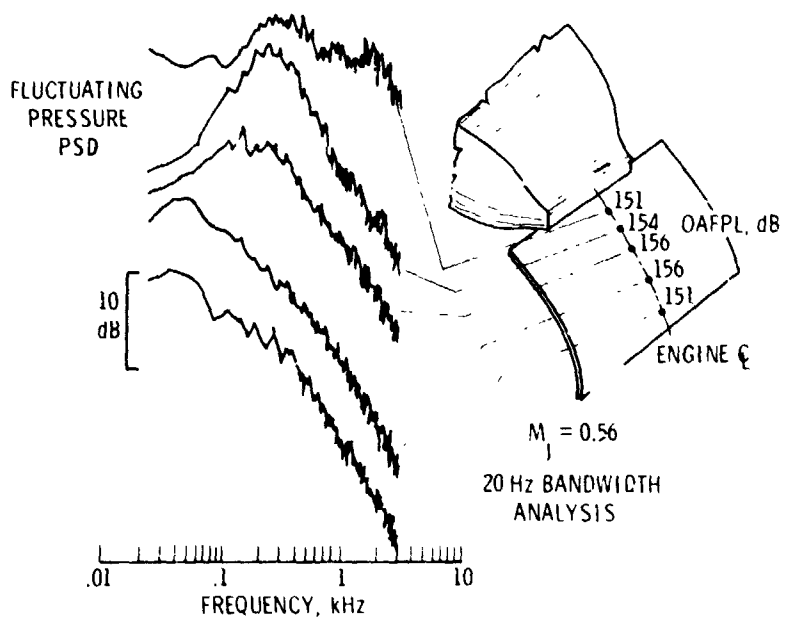

Figure 8.- Pressure spectra along engine center line of USB boilerplate model.

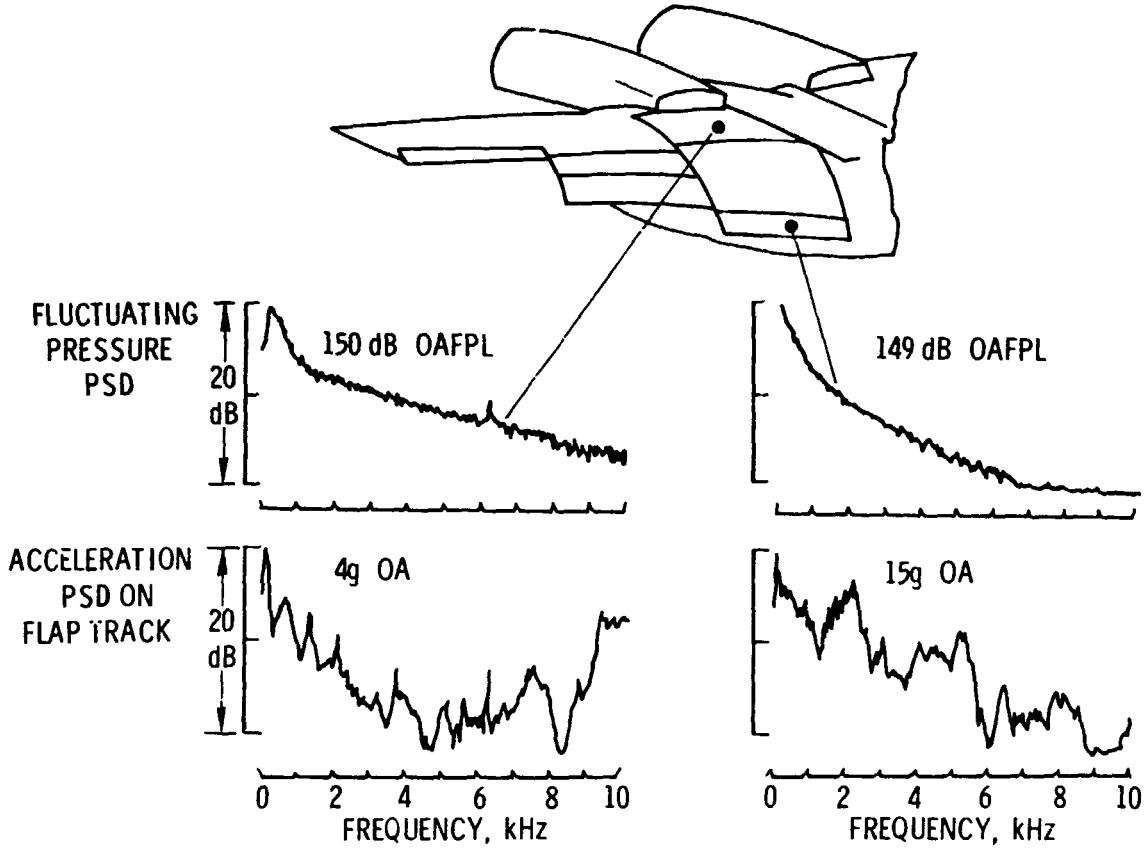

Figure 9.- Loads and response of wing and flap of USB modified Aero Commander.

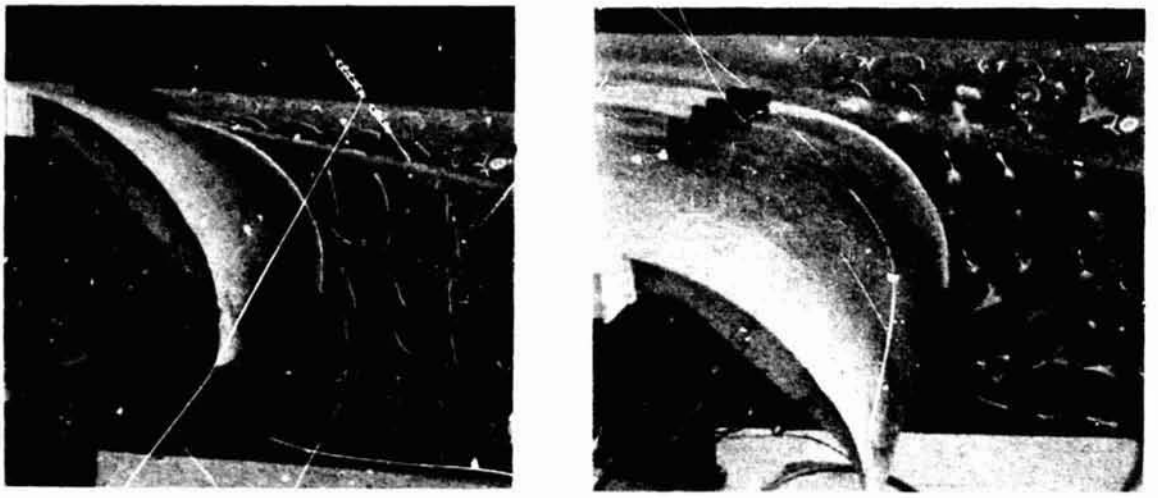

(a) Jet velocity: 0.

(b) Jet velocity: 366 m/s.

Figure 10.- Tuft flow patterns on fuselage surface of YC-14 scale model.

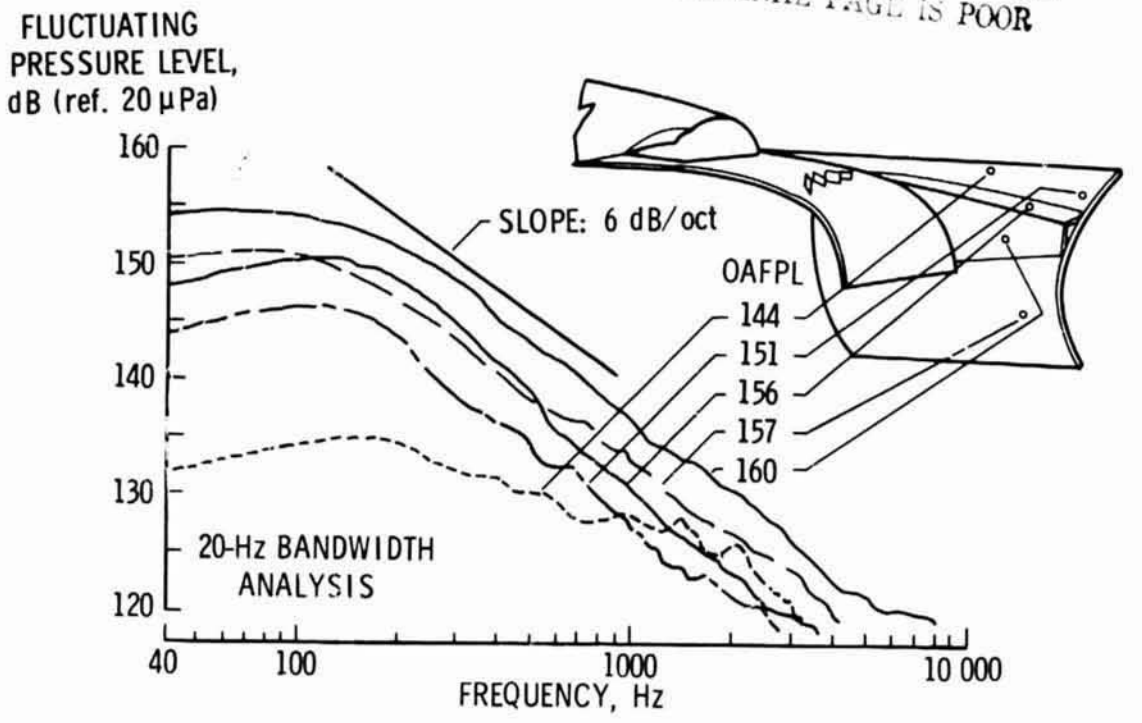

Figure 11.- Fluctuating pressures on fuselage sidewall of YC-14 scale model.

N78-24074

INVESTIGATIONS OF SCALING LAWS FOR JET IMPINGEMENT

J.B. Morton, J.K. Haviland, G.D. Catalano, and W.W. Herling
University of Virginia

SUMMARY

Current developments in upper surface blowing and in externally blown flap configurations have promoted interest in the effects of jet flows on flap or wing surfaces and in the loadings induced on them. The present investigation has been concerned with the scaling laws involved in relating model studies to full-size configurations. As a first step, the statistical properties of tangential flows over surfaces were investigated by two techniques. In one, a laser-Doppler velocimeter (LDV) was used in a smoke-laden jet to measure one-point statistical properties, including mean velocities, turbulent intensities, intermittencies, auto-correlations, and power-spectral densities. In the other technique, free-stream and surface pressure probes connected to 1/8 inch microphones were used to obtain single-point rms and 1/3-octave pressures, as well as two-point cross-correlations, the latter being converted to auto-spectra, amplitude ratios, phase lags, and coherences. The results of these studies supported the vortex model of jets, gave some insights into the effects of surface impingement, and confirmed that jet diameter and velocity are the scaling parameters for circular jets, while Reynolds number is relatively unimportant. Effects of jet Mach number could not be studied due to limitations on flow velocities. Addition investigations were made with a 1/4 scale model of the Langley static thrust stand, with a rectangular nozzle in an upper surface blowing configuration. It was found that there are at least two effective diameters; the one corresponding to the highest frequency peaks in the pressure spectrum appears to be either the hydraulic depth or the minor rectangular dimension. This decays in about five lengths, but does contribute to structural loads. The effective diameter corresponding to the lower peak, which persists for a longer distance, appears to be in agreement with a value given in the literature for far-field noise. There is also some evidence of a third spectral peak at an even lower frequency, corresponding to an effective diameter equal to the major rectangular dimension. Initial surface pressure measurements have been used to obtain dimensionless spectra for comparison with full-scale test data, and agreement has been sufficiently good to support the idea of using low Mach number models for this purpose. However, these spectra are dependent on the acoustical pressure spectra in the nozzle to an as yet undetermined extent, so that it may become necessary to simulate the engine spectra to obtain reliable results.

28

444
PAGE INTENTIONALLY BLANK

INTRODUCTION

The principal goal of this investigation is to determine the scaling laws for the dynamic pressures induced on wing surfaces or flaps of STOL aircraft due to jet impingement. To achieve this goal, the investigators have used an approach which has combined theoretical considerations, basic studies of jet flows, and direct scale model tests on a known configuration. This paper is divided into three sections. The first presents a brief discussion of the literature, and of some of the theoretical considerations which might lead to a method of scaling. The second presents a basic study of the flow in a circular jet blowing over an airfoil surface, using a laser-Doppler velocimeter. The third presents some initial results from a 1/4 scale model of the upper surface blowing facility at Langley, which uses a JT15D-1 engine. Another major effort in this program, now completed (ref. 1), has been an investigation of the flow from a circular jet, which has involved measurement of the fluctuating pressures in the free flow and in the flow impingement on a flat plate.

DISCUSSION

Literature Review

In reviewing the literature, one finds that the single most important contribution to the understanding of jet flows is the replacement of the "classical" jet model shown in figure 1a by the vortex model shown in figure 1b. Early investigators, such as Powell (ref. 2), Bradshaw, Ferris and Johnson (ref. 3), and Mollo-Christensen (ref. 4) had realized that the jet turbulence was structured, while Davies (ref. 5), Crow and Champagne (ref. 6), and Lau, Fisher and Fuchs (ref. 7), to name just a few, contributed to the identification of the vortex structure. Whereas these investigators worked mainly on measuring overall flow statistics, many others attempted flow vizualization. Also, by examining instantaneous signals from pressure transducers, Laufer, Kaplan, and Chu (ref. 8) showed that pairs of vortices tend to coalesce into single vortices, as shown in figure 1b. Recently, Lau and Fisher (ref. 9) have argued the case for the 'probable flow', in contrast to the 'idealized flow', both shown in figure 1b.

It is difficult to construct a satisfactory analytical model of the jet structure. However, Batchelor and Gill (ref. 10) showed that the vortex tube which emerges from a jet is unstable, and that this could trigger the formation of vortices. Widnall and Sullivan (ref. 11) showed that individual vortices are unstable, develop lobes, and ultimately break up. Also, Davies et al. (ref. 12) constructed a computer model in which the vortex tube emerging from the jet was represented by small, closely spaced vortices, and showed that these combine into larger vortices, just as the observed vortex tube instability would indicate.

The vortices present in the jet contribute to the characteristic jet spectrum, which peaks at a Strouhal number (frequency f times jet diameter D divided by jet velocity U_J) of between 0.3 and 0.4, so that one might expect this frequency to show up in the dynamic pressures exerted during impingement. There have been some full-scale studies of the effects of jet engines in externally blown flaps and in upper surface blowing configurations (refs. 13-15), and of small cold jets impinging on flat plates (refs. 1, 16-18), which substantiate this.

Since it is known that far-field radiated jet noise originates in the turbulent jet structure, one might well expect some relationship between the jet noise spectrum and the distribution of vortices in the jet. In fact, the noise spectrum in a stationary jet at about 30° to the axis, where it is a maximum, also exhibits a peak at a Strouhal number of around 0.3. The literature on jet noise is extensive, and a good account of it is given by Stone (ref. 19). It is unfortunate that the accepted method of non-dimensionalizing jet noise is to refer it back to the values obtained at 90° where the spectral peak occurs at a Strouhal number of around 1.0, because there are several examples of spectra for slot nozzles, representing upper surface blowing configurations (refs. 20, 21). These show secondary peaks at much lower Strouhal numbers in the 90° case, but there is no information on how these peaks shift as the angle is reduced to 30°.

Theoretical Considerations

The scaling laws for fluid flows are well-known, and it is quite clear that an adequate job of scaling a jet impingement configuration could be done if the correct Reynolds number and Mach number could be obtained, if the internal noise spectra could be scaled, and if the core air were preheated to produce the correct temperature ratio. Then the spectra of pressure coefficients (i.e., fluctuating pressures divided by jet dynamic pressure) as functions of the Strouhal number would be identical for the model and for the full-scale article. Nevertheless, it is virtually impossible to achieve scaling to this extent. Therefore, let us consider to what extent these hypothetical requirements can be relaxed.

First, consider the Reynolds number. Several investigators have reported no apparent effect of Reynolds number above about 10^4, because, although viscosity may play a part in tripping the initial instability which causes the vortex tube to roll up, subsequent behavior of the jet appears to be dominated by the vortex structure, which causes the potential core to disappear in only five jet diameters.

Second, consider the Mach number. It seems inevitable that, once a Mach number of one is reached in the jet, shock formation phenomena will play some part. However, most investigators into jet noise (see, for example, ref. 19) have reported minimal compressibility effects, although there are kinematic effects which play a part in the correction for angle to the jet axis. Also, a small Mach number dependent effect on pressure coefficients was noted in a full-scale upper surface blowing test (ref. 15).

If the effect of Reynolds number is negligible and the effect of Mach number is minimal, it should be possible to design quite simple scale model tests for the determination of dynamic loads on typical STOL configurations, such as in upper-surface blowing and in blown-flap arrangements. One merely has to design a scale model, and to interpret the results in terms of pressure coefficients referenced to jet dynamic pressure and to Strouhal number.

However, two difficulties remain. First, it is not possible to model a fan jet engine correctly with cold air, unless there is 100% mixing ahead of the exit nozzle, because the different densities of the hot and cold air make it impossible to scale both dynamic pressure (dynamic scaling) and jet velocities (kinematic scaling) at the same time. Second, it may be difficult to scale internal engine noise spectra adequately.

LASER VELOCIMETER MEASUREMENTS

Discussion

A discussion of the development of LDV techniques for the measurement of instantaneous velocity components in a smoke laden jet is given in reference 22. Using these techniques, the following can be found; mean velocity components, turbulence intensities, velocity auto-correlations, and velocity power-spectral densities. Also, the presence or lack of smoke laden air at a given point can be used for intermittency measurements. A light scattering technique is also used to measure concentration of smoke. When this concentration is correlated with velocity, useful information about the structure of the jet can be obtained.

The purpose of the laser-Doppler-velocimeter (LDV) experiment was to determine the effects of an airfoil on the flow field of an axisymmetric jet as well as to study the implications of the vortex model of the near field of a free jet. The positioning of the airfoil relative to the exit plane of the jet in figure 2 corresponds to the upper surface blowing configuration. The arrows are scaled to the local velocity vectors obtained by LDV measurements and can be seen to follow the surface contour.

A jet with a contraction ratio of 14 to 1 over a length of 159 mm and an exit plane diameter of 21.4 mm is used to generate a flat velocity profile at its exit plane. The airfoil is composed of two sections, a flat surface 178 mm wide and 75 mm long, and a curved portion with a radius of curvature of 65 mm sweeping out an arc of 70 degrees. This airfoil is a scaled down model of the actual airfoil surface which had been used in the upper surface blowing investigation at NASA-Langley. The ratio of the dimensions of full-scale configuration to the model used in this investigation is about 12 to 1.

The jet and airfoil were placed inside a 203 mm by 305 mm wind tunnel, where a uniform flow was maintained. The exit Reynolds number of the jet was 22 600 while the ratio of the exit velocity U_J of the jet to that of the parallel secondary flow U_{FS} in the wind tunnel was 5.16 to 1.

Mean Velocities

In figure 3, mean velocity profiles for the longitudinal component are presented for three downstream locations (X/D = 2,3,4) and at one vertical position (Z/D = 0.5) for flow fields with and without flap. The ratio of the local excess velocity, $U - U_{FS}$, to the excess core velocity, $U_J - U_{FS}$, is plotted versus lateral distance, Y/D (non-dimensionalized by the diameter of the jet) from the centerline of the jet, where U_{FS} is the free stream velocity of the wind tunnel flow. Two observations can be made concerning the comparison of the flows. With the airfoil present, there is a noticeable increase in the width of the velocity field at each downstream location. Secondly, the maximum velocity at the centerline (Y/D = 0) of the profiles decays much more rapidly. When X/D equals 4 in the freely expanding coflowing jet, the maximum value of mean velocity has decayed to approximately .95 of its exit plane value. However, with the airfoil surface positioned in the flow field, the ratio, $(U - U_{FS})/(U_J - U_{FS})$, has a maximum of approximately .55.

A comparison of lateral mean velocities V for both flow fields in figure 4 indicates once again an increase in the width of the velocity field with the airfoil present. Also, the maximum value of the ratio, $V/(U_J - U_{FS})$, has approximately doubled when X/D equals 4 and Z/D equals 0.5. Profiles of mean velocity in the vertical direction W for the same downstream location (X/D = 4), but different vertical positions (Z/D = 0.5 and 0.185) are also presented in figure 4. When Z/D equals 0.5, the maximum value of the ratio, $W/(U_J - U_{FS})$, is obtained at the centerline of the profile. This is in contrast to the data presented for Z/D equal to 0.185. In this profile, $W/(U_J - U_{FS})$ remains relatively small and constant in the central region of the velocity field and reaches a maximum when Y/D approximately equals 0.90. This fact might indicate that the jet is rotating or rolling up as it spreads out over the surface of the airfoil.

Turbulent Intensities

The axial and radial distributions of the turbulence intensities in terms of the core velocity $u_{rms}/(U_J - U_{FS})$ are plotted versus radial position at the vertical location where Z/D equals 0.50 in figure 5. Once again examination of the comparative profiles yields two observations. First, with the airfoil present, the turbulent velocity field is significantly wider. Second, the potential core region of the axisymmetric jet is broken up much sooner. The turbulent intensities have actually more than doubled in the central regions of the profiles where X/D equals 3 or 4. Thus, the turbulent velocity field is quite dramatically affected by the inclusion of the airfoil surface in the flow.

Concentration-Velocity Correlation

The concentration-velocity correlation coefficient was also measured in the freely expanding jet. It is defined as follows:

$$r_{u\theta} = \frac{\overline{u\theta}}{u_{rms}\,\theta_{rms}}$$

where u is the fluctuating velocity and θ is the fluctuating part of the concentration, both measured at the same point and time in the flow. The three profiles shown in figure 6 are taken where X/D equals 2, 4 and 8.

The significance of the concentration-velocity correlation is that it indicates how closely the passive admixture field is related to the velocity field as one moves downstream. A zero correlation indicates that the fluctuations in the concentration field are totally independent of the turbulent velocity fluctuations, as is the case for the profile taken where X/D equals 2, near the centerline. Though both θ_{rms} and u_{rms} are small in the potential core, they are not negligible. The existence of θ_{rms} at the exit plane is probably due to imperfect seeding. Out from the centerline of the jet, $r_{u\theta}$ initially becomes negative, then changes sign, and eventually reaches a maximum value at an R/D approximately equal to one half. Vortices, which would entrain "clean" air from outside the jet and would then accelerate the entrained air, would give rise to concentration velocity correlations of the shape shown where X/D equals 2. As the potential core breaks up further downstream, the concentration and velocity fluctuations would become more highly dependent in the center region of the jet, as is the case. Thus, the results shown are entirely consistent with the vortex model.

QUARTER-SCALE MODEL STUDY

Discussion

In the study reported in reference 1, unsteady pressure measurements were made in the free flow of a circular jet and of the surface pressures due to the impingement of this jet on a flat surface. All measurements were made with 1/8 inch (3.2 mm) B & K microphones which were connected by plastic tubing to surface probes or to miniature total or static free-flow probes. Instrumentation included mean total velocity, and rms or 1/3 octave spectra of static pressures. Also, two-point auto- and cross-correlations were obtained which were later converted into power spectra, relative amplitudes and phases, and coherences. Considerable emphasis was placed on the measurements of transfer functions for the probes. Although techniques for correction by computer were demonstrated, the necessary calibration equipment was not available at the time, so that corrections had to be made by hand where necessary.

Measurements made in the circular jet supported the vortex model, and were in general agreement with other results reported in the literature when they were expressed in dimensionless form using the jet diameter and velocity as scaling parameters. No dependency on Reynolds number could be seen, and no attempt was made to determine Mach number effects.

During the investigation of the rectangular jet described in the following paragraphs, frequent comparisons are made with the results on circular jets. One question of particular interest is, what form do the vortices take, and what are their characteristic dimensions?

Test Apparatus

A quarter scale model of the nozzle and airfoil used in test on the static thrust stand at Langl. (ref. 14) was built in order to make a direct evaluation of the use of scaling laws in conjunction with low Mach number models The test apparatus used is shown in figure 7. The scaled nozzle is attached to an adapter section leading from a plenum chamber. Two inlets to the plenum chamber are intended for the core and fan air to simulate the JT15D-1 engine. However, the inner nozzle for the core jet has not been installed to date. Initial testing was carried out with two blowers supplying a pressure of 8.25 cm of water (630 N/m^2) which results in a 32 m/s jet. Later, one of the two mufflers was used with one blower, the other inlet being used for a speaker to provide excitation of the pl chamber. With one blower and muffler, the flow velocity fell to 22 m/.

Instrumentation used was the same as that developed for the earlier circular jet study (ref. 1). Free stream probes were of 1.3 mm outside diameter, with four 0.5 mm holes 12.7 mm from the rounded end. The internal diameter was stepped up to 3.2 mm and connected by up to 3 meters of plastic tubing to the 1/8 inch (3.2 mm) B & K microphones. Surface probes were flush mounted holes, 1.0 mm in diameter. It was necessary to correct for probe respons when measuring spectra, particularly with the 3 m tubing, but this response cancelled out when relative amplitudes, phase lags, and coherences were measured.

Correlation Coefficients

In the previous circular jet study of the variation of the correlation coefficient between a probe on the centerline, and a probe at a radial position R, the correlation was found to drop to a minimum when R/D approached one half, so that the probe was behind the jet lip, and then to increase again as R/D increased further. This was attributed to the irregular passage of vortex filaments over the probe when it was located behind the jet lip. The results of a similar study 17 cm behind the exit plane of the rectangular nozzle are shown in figure 8. One probe was placed as indicated in the figure by "ref", and the second was moved to the positions indicated. When the probe was moved vertically in the direction of the smaller dimension, the correlation coefficient became a minimum behind the lower lip, and then increased beyond it. This behavior, which was accentuated when the airfoil was installed, was taken to indicate that vortex filaments were breaking from the lower lip. When the probe was displaced horizontally, the correlation at a given distance was somewhat less, although it again improved with the airfoil installed. The latter behavior was consistent with the idea that vertical vortex filaments might be passing at random, and that they could be parts of vortices whose dimensions would be of the order of the minor nozzle dimension. Another indication of the

presence of vortex filaments had been found in the circular jet study to be a peak in the rms pressure as the jet was traversed. A similar traverse of the rectangular nozzle (no figure) shows peaks behind the upper and lower lip, except that the peak behind the upper lip disappears when the airfoil is installed. This could be explained in terms of horseshoe vortices attached to the airfoil.

Phase and Coherence Plots

Three phase lag and coherence plots are shown in figure 9 for two of the locations covered in the correlation study, one of them in the free jet with the airfoil removed. The coherence has much the same significance as correlation, except for being frequency dependent. The phase lag is a direct measure of convection velocity between two points. Thus, in the examples shown in figure 9, the small phase lags indicate that the pressure disturbances arrive at the two probes almost simultaneously. It should be noted that the coherence between two vertically displaced probes is much higher with the airfoil present than in the free jet, and also much higher than for two horizontally displaced probes.

Other phase lag plots (not shown) were obtained with the probes displaced axially and were used to calculate convection velocities. It was found that these velocities were between 0.3 and 0.4 of jet velocity up to 100 Hertz, and that they increased to between 0.6 and 0.7 of jet velocity at higher frequencies. In contrast, convection velocities in the circular jet were constant between 0.6 and 0.7 of jet velocity over the entire frequency range. This could be explained on the basis that the lower frequency disturbances in rectangular jets are associated with large vortices which expand outside the jet flow, and therefore convect more slowly. On the other hand, vortices in the circular jets remain equal to the jet diameter.

One-Third-Octave Spectra

The development of 1/3-octave spectra (referenced to jet dynamic pressure) along the jet centerline, both in the free jet and with the airfoil installed, is shown in figure 10. One can interpret the peaks in the spectra as resulting from disturbances at a Strouhal number of 0.3, but related to vortices of a corresponding effective diameter. Thus, with the flow velocity at 30.8 m/s, the 315 Hertz peak, which decays in 200 mm from the exit plane, could relate to an effective diameter of 29 mm, close to the minor nozzle dimension of 42 mm. The 100 Hertz peak, which persists out beyond 300 mm, could relate to an effective diameter of 92 mm. Stone (ref. 19) suggests an effective diameter D_e of

$$D_e = D_a^{0.6}\, D_h^{0.4}$$

where D_a ($\sqrt{4A/\pi}$) is the diameter based on area, and D_h (4A/P) is the hydraulic depth.

In these equations A is the nozzle area, and P is its perimeter. For the 234 mm by 42 mm rectangular nozzle, D_a is equal to 112 mm and D_h is equal to 71 mm, so that D_e works out to be 93 mm, which is consistent with the 100 Hertz peak. A persistent lower peak also observed at 40 Hertz could relate to an equivalent diameter of 231 mm, close to the major dimension of 234 mm, but this peak could also have been tripped by noise known to be present in the plenum chamber.

Jet Excitation

Because it was suspected that some of the disturbances might be induced by blower noise present in the plenum chamber, a muffler was added, and a speaker was installed for excitation of the plenum chamber. The muffler was found to eliminate disturbances above 50 Hertz, but was noisy at 40 Hertz due to the formation of internal vortices by the 152 mm ducts which were used. The alternate muffler, shown in figure 7, eliminated the 40 Hertz noise but was relatively ineffective at higher frequencies.

The results of exciting the plenum chamber at 1/3-octave band center frequencies are shown in figure 11 in decibels referenced to the levels at the exit plane with the blower running to provide an airflow. When the blower was turned off, the measured level at the exit plane was unchanged, indicating that the pressures measured at the exit were purely acoustic. However, as the probe was moved away from the exit, the pressures increased with the blower on while the acoustic pressures dropped with the blower off. This indicated that the pressure disturbances measured in the jet were attached to vortices which had been tripped by acoustic excitation of the plenum. Measured levels were 15 to 20 decibels above background levels. The rate of buildup was greatest at 160 Hertz, corresponding to an effective diameter of 41 mm in the 22 m/s flow, i.e., the minor dimension, as stated before.

Surface Pressure Measurements

One-third-octave surface pressure measurements were made on the 1/4 scale model for comparison with power-spectral density plots of surface pressures on the full-scale article. The effective diameter D_e was chosen as the scaling dimension, because it has already been recommended for far-field noise (ref.18), and because it appears to relate to the most persistent peak in the static pressure spectra. The spectra were non-dimensionalized as follows:

Strouhal No.

$$St = f D_e/U_J$$

Dimensionless spectral density from power spectral density PSD(f)

$$LDPSD(f) = 10 \log_{10} (PSD(f)\ U_J/q^2 D_e) \text{ decibels}$$

where f is the frequency, U_J the jet velocity, and q is the jet dynamic

pressure.

Dimensionless spectral density from 1/3-octave level L_i

$$LDPSD_i = L_i - 10 \log_{10} f_i + 6.4 - 10 \log_{10} (q^2 D_e / p_{ref} U_J) \text{ decibels}$$

where f_i is the 1/3-octave center band frequency, and p_{ref} is the reference pressure for sound pressure level. A table of the values of the relevant scaling dimensions used is given below.

Table of Scaling Dimensions

	D_e (m)	U (m/s)	q (Pascals)
Model	0.0934	21.6	285.8
Full-scale	0.357	277.4 (910 fps)	22 320 (3.237 psi)

Plots of the dimensionless spectral densities are shown in figure 12 for both the model and the full-scale article. Agreement between the two appears to be as good as might be expected in view of the lack of a core nozzle in the model, and in view of the lack of any attempt to scale internal engine noise in the model. The frequenc peaks at the intermediate points are in quite good agreement with the full scale results. Predicted peak frequencies based on the nozzle dimensions, the effective diameter D_e, and the hydraulic depth D_h are shown in the figure.

CONCLUDING REMARKS

Laser Velocimeter Measurements

The investigation of the effect of an airfoil on the flow from a circular jet showed the following: The jet tends to spread faster in the lateral direction along the airfoil. The potential core region is smaller and pulled down towards the airfoil. And turbulent intensities are increased at least for several diameters downstream.

The investigation of velocity-concentration correlations in the free jet gave results that are consistent with the vortex model of the near field.

Quarter-Scale Model Study

The quarter-scale model study resulted in the following conclusions. There is evidence of a vortex-like structure in a free rectangular jet; however, vortices of several dimensions appear to be present, the smaller vortices dying out faster than the larger ones.

For a short distance from the exit, the pressure spectrum peaks at a frequency whose Strouhal number, based on the minor rectangular dimension or on the hydraulic depth, is about 0.3. However, this decays about five of these dimensions downstream, and is replaced by a lower peak which appears to be based on an effective diameter, as defined in the literature for far-field noise (Westley et al., AGARD-CP-113). These peaks are accentuated when excited by a speaker in the plenum chamber. There may be a low frequency peak, based on the major rectangular dimension, but this was not confirmed.

Airfoil surface pressures can be scaled by reducing them to pressure coefficients based on jet dynamic pressure, and the corresponding frequencies can be scaled by reducing them to Strouhal numbers based on any suitable reference length. However, to facilitate comparisons between nozzles of different shapes, it might be better to use the above-mentioned effective nozzle diameter.

Evidence available to date, but not substantiated further in this study, indicates that the effect of jet Reynolds number is negligible, while the effect of Mach number is certainly small, although not well understood at present.

The effect of the internal noise spectrum of the jet engine is probably of sufficient importance that it will have to be accounted for to some extent.

REFERENCES

1. Schroeder, J. C. and Haviland, J. K.: "Fluctuating Pressures in Flow Fields of Jets", NASA TM X-71979 (1976).

2. Powell, Alan: J. Acoust. Soc. Am. 36, 177-195 (1964).

3. Bradshaw, P.; Ferris, D. H.; and Johnson, R. F.: J. Fluid. Mech. 19, 591-624 (1964).

4. Mollo-Christensen, Eric: J. Appl. Mech. 89, 1- (1967).

5. Davies, P. O. A. L.: J. AIAA 4, 1971-1978 (1966).

6. Crow, S. C. and Champagne, F. H.: J. Fluid Mech. 48, 3, 547-591 (1971).

7. Lau, J. C.; Fisher, M. J.; and Fuchs, H. V.: J. Sound Vibr. 22, 4, 379-406 (1972).

8. Laufer, J.; Kaplan, R. E.; and Chu, W. T.: AGARD-CP-131, March (1974).

9. Lau, J. C. and Fisher, M. J.: J. Fluid Mech. 67, 2, 299-337 (1975).

10. Batchelor, G. K. and Gill, A. E.: J. Fluid Mech. 14, 529-551 (1962).

11. Widnall, S. E. and Sullivan, J. P.: Proc. R. Soc. Lond. 332, 335-353 (1973).

12. Davies, P. O. A. L.: AIAA Paper 75-441 (1975).

13. Schoenster, J. A.: "Acoustic Loads on an Externally Blown Flap System Due to Impingement of TF-34 Jet Engine Exhaust", NASA TM X-71950 (1974).

14. Shivers, J. P. and Smith, C. C., Jr.: "Static Tests of a Simulated Upper Surface Blown Jet-Flap Configuration Utilizing a Full-Size Turbofan Engine", NASA TN D-7816 (1975).

15. Mixson, J. S.; Schoenster, J. A.; and Willis, C. M.: AIAA Paper 75-472 (1975).

16. Foss, J. F. and Kleis, S. J.: "The Oblique Impingement of an Axisymmetric Jet", Division of Engineering Research, Michigan State University, Second Annual Report, to NASA Lewis Research Center, December (1972). [Available as NASA CR-134961 AR-2.]

17. Strong, D. R.; Siddon, T. E.; and Chu, W. T.: "Pressure Fluctuations on a Flat Plate With Oblique Jet Impingement", Institute of Aerospace Studies, University of Toronto, Technical Note No. 107, February (1967). [Also NASA CR-839.]

18. Westley, R.; Woolley, J. H.; and Brosseau, P.: "Surface Pressure Fluctuations From Jet Impingement on an Inclined Flat Plate." Symposium on Acoustic Fatigue, AGARD-CP-113, May 1973, pp. 4-1-4-17.

19. Stone, J. R.. "Interim Prediction Method for Jet Noise", NASA TM X-71618 (1974).

20. Reshotko, M.; Olsen, W. A.; and Dorsch, R. G.: "Preliminary Noise Tests of the Engine-Over-the-Wing Concept. I. 30° - 60° Flap Position", NASA TM X-68032 (1972).

21. Stone, J. R. and Gutierrez, O. A.: "Small-Scale Noise Tests of a Slot Nozzle with V-Gutter Target Thrust Reverser", NASA TM X-2758 (1973).

22. Catalano, G. D.; Morton, J. B.; and Humphris, R. R.: "An Experimental Investigation of an Axisymmetric Jet in a Coflowing Airstream". AIAA J., vol. 14, no. 9, Sept. 1976. (To be published.)

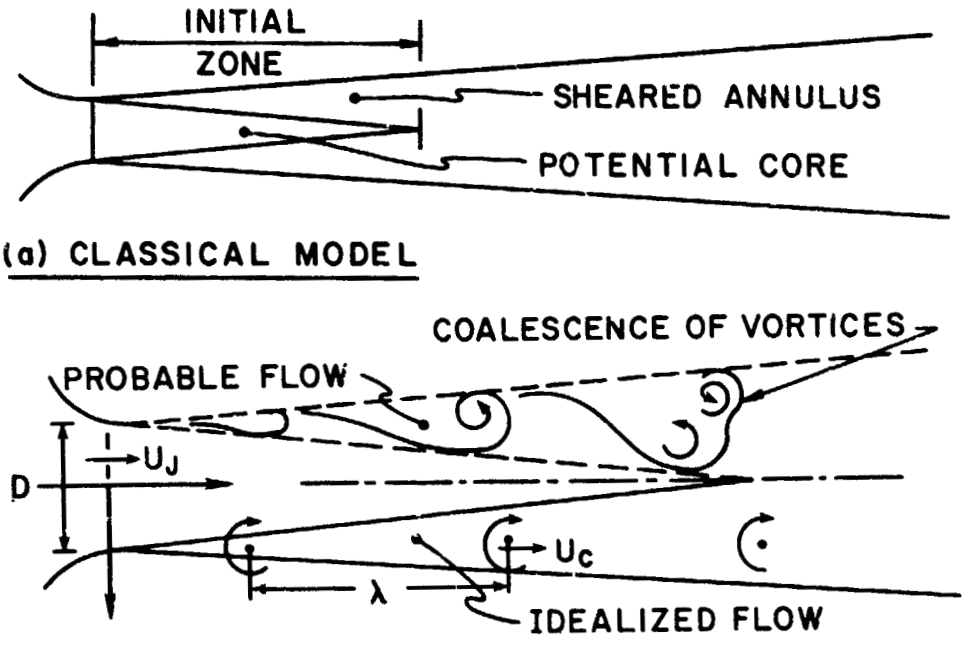

Figure 1.- Current models of the structured turbulence in circular jets. (U_c is the convection velocity of the vortices.)

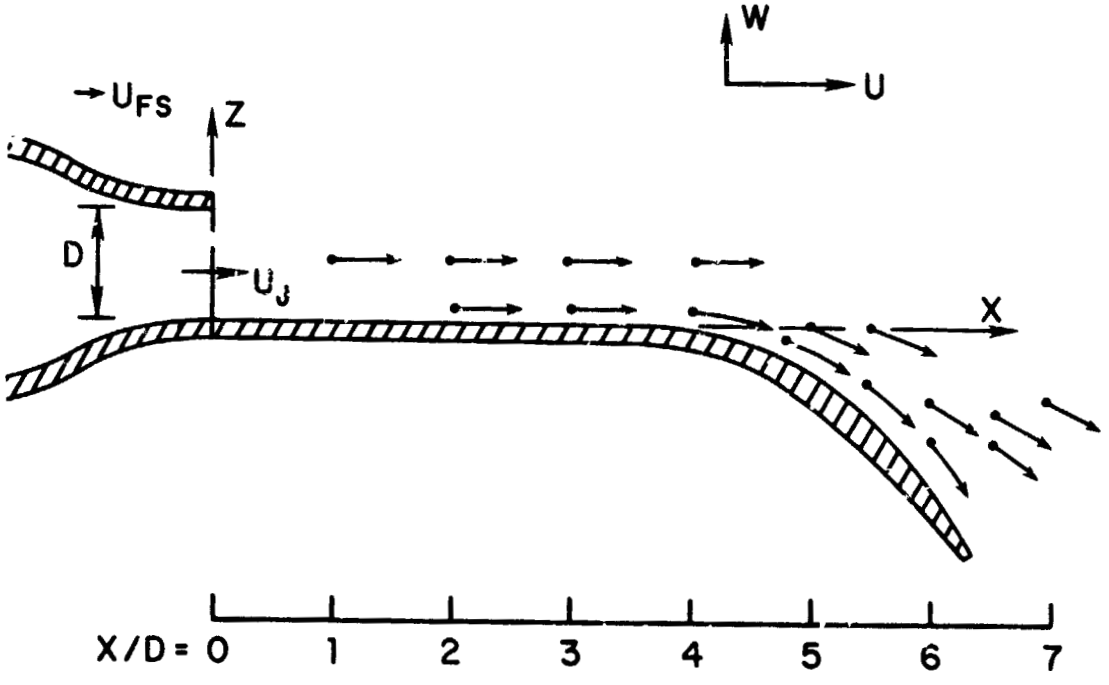

Figure 2.- Vectorial diagram of the mean velocities in the X-Z plane. Circular jet over airfoil, using LDV.

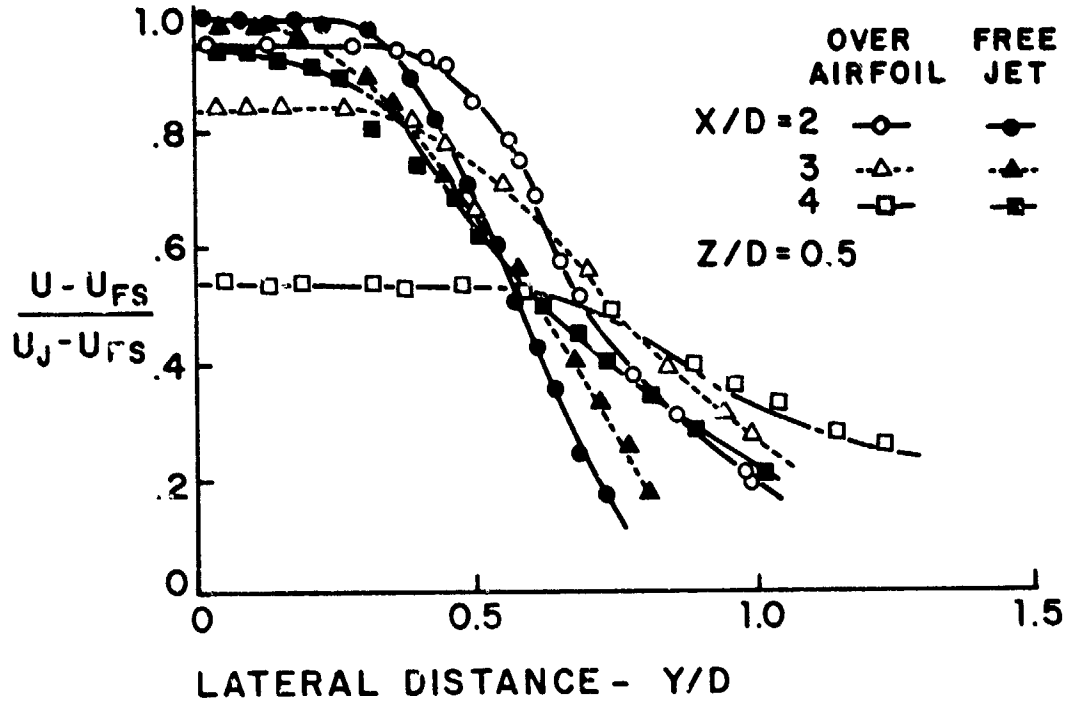

Figure 3.- Profiles of the axial (U) components of the mean velocity. Circular jet over airfoil, using LDV.

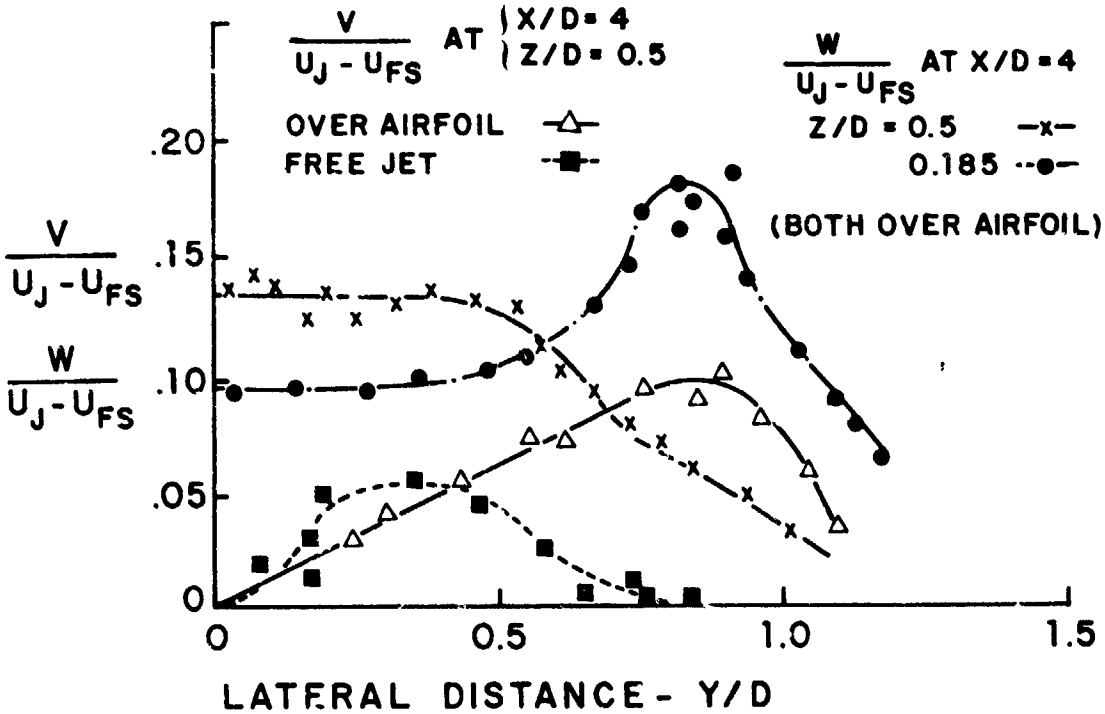

Figure 4.- Profiles of the horizontal (V) and vertical (W) components of the mean velocity. Circular jet over airfoil, using LDV.

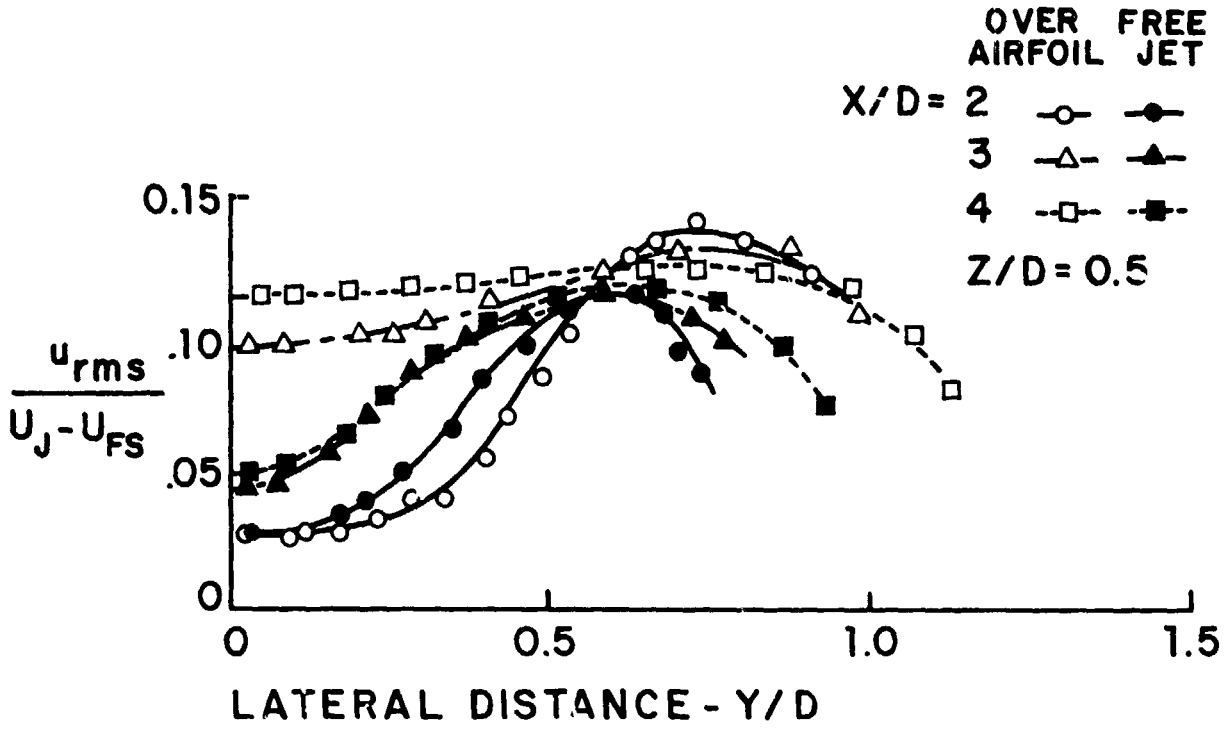

Figure 5.- Profiles of the axial (U) components of turbulence intensity. Circular jet over airfoil, using LDV.

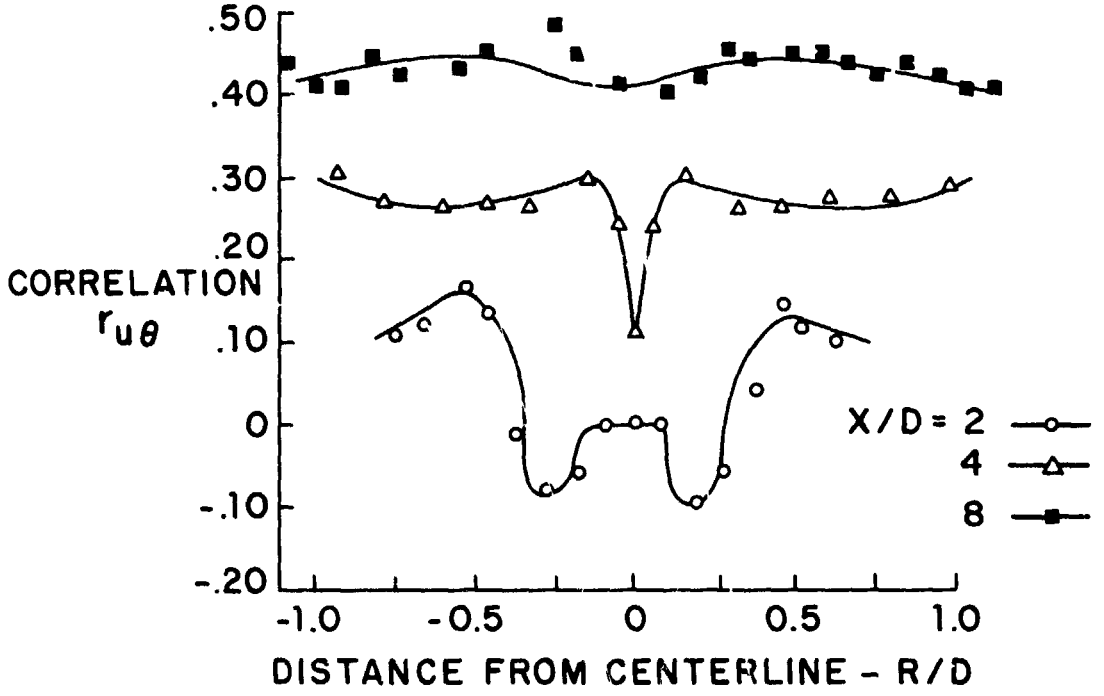

Figure 6.- Profiles of the concentration-velocity correlation coefficient. Free circular jet, using LDV.

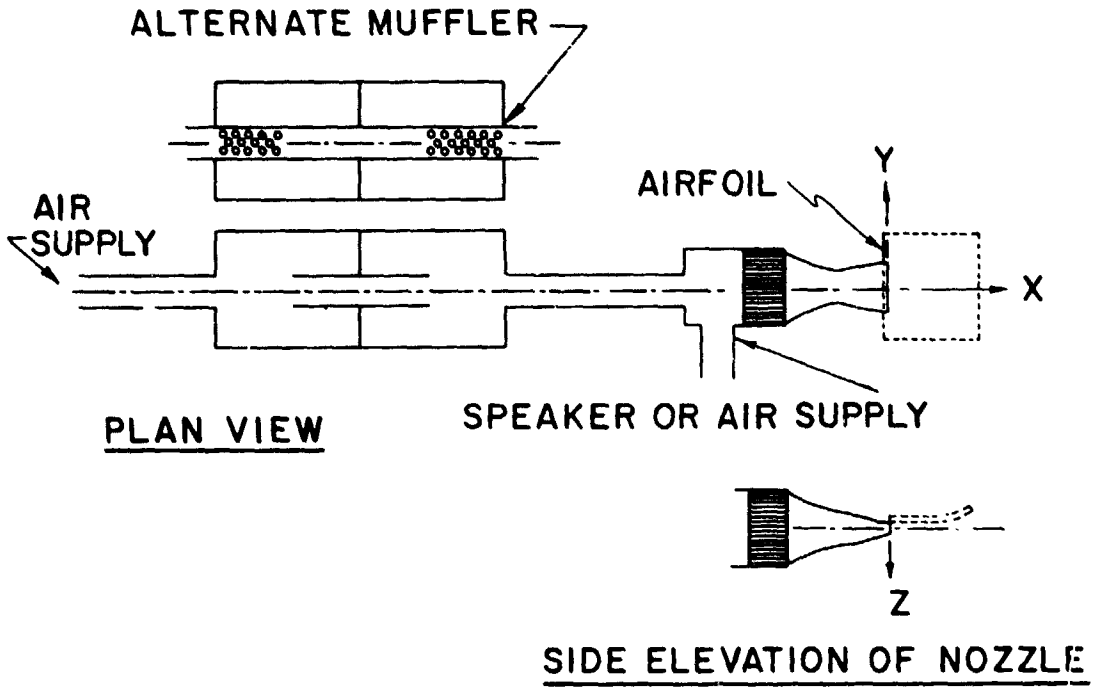

Figure 7.- Schematic of quarter-scale model of upper surface blowing configuration.

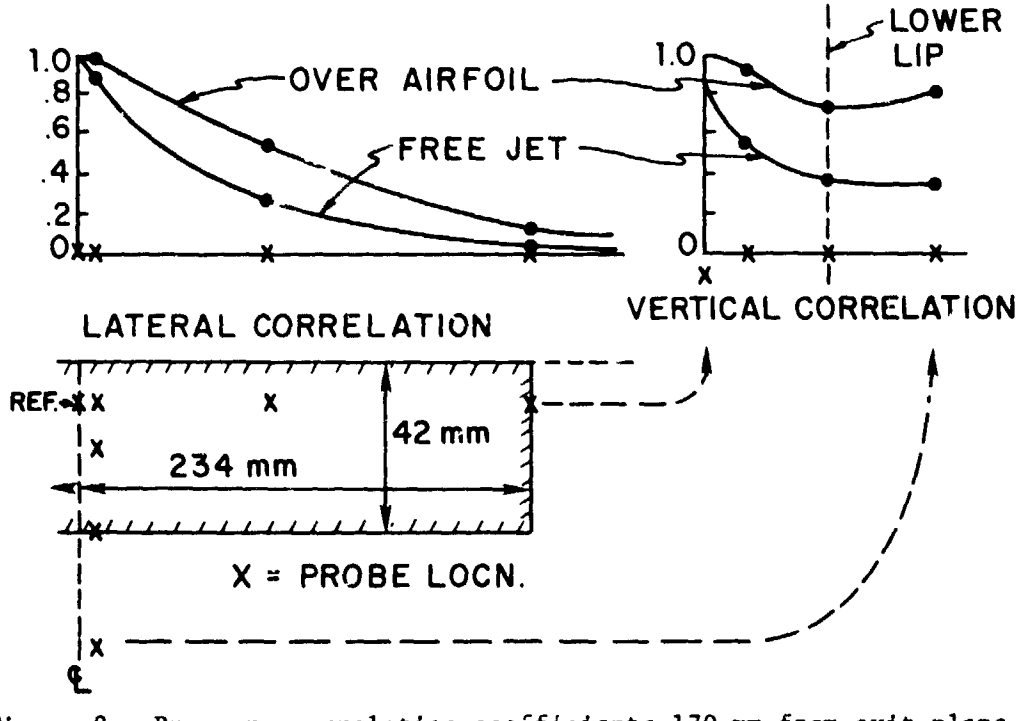

Figure 8.- Pressure correlation coefficients 170 mm from exit plane of quarter-scale model rectangular jet, both free and blowing over airfoil.

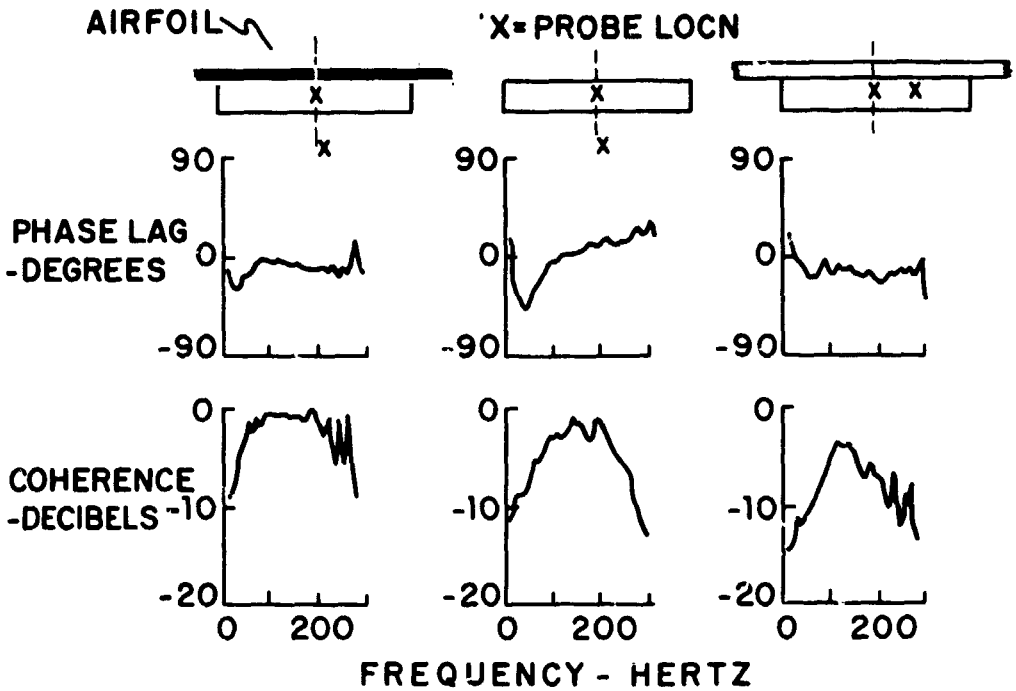

Figure 9.- Phase and coherence plots 220 mm from exit plane of quarter-scale model rectangular jet, both free and blowing over airfoil.

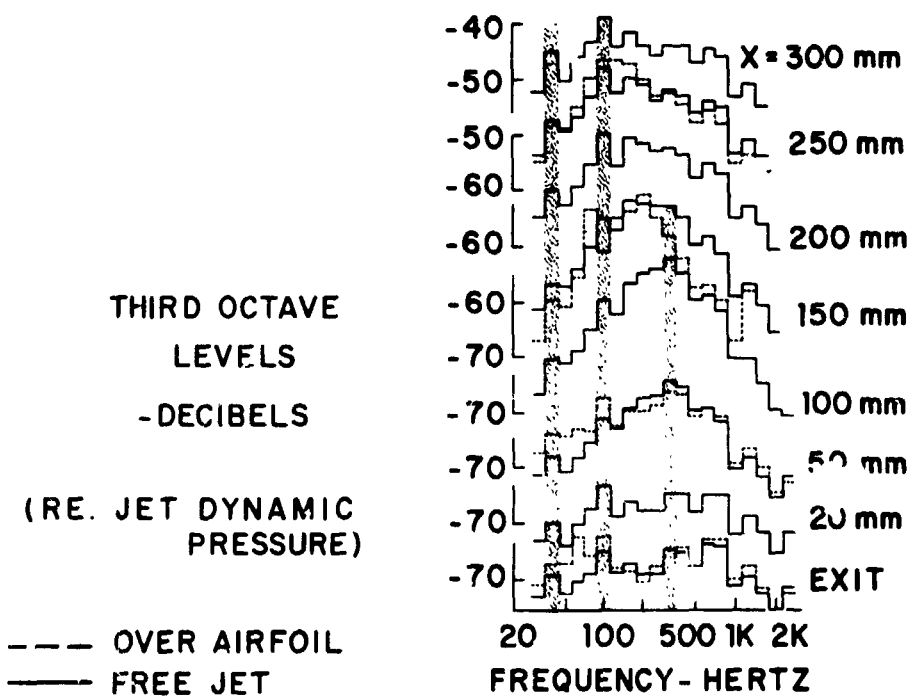

Figure 10.- Growth of 1/3-octave pressure levels in quarter-scale model rectangular jet, both free and blowing over airfoil.

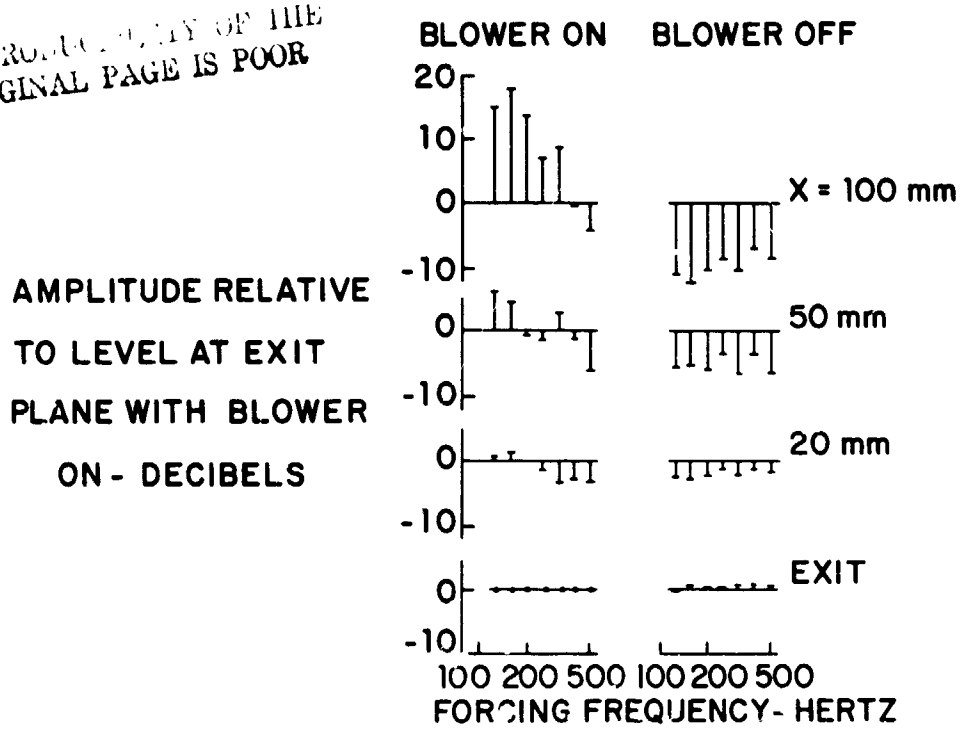

Figure 11.- Effect of forcing separate 1/3-octave band center frequencies in rectangular jet blowing over airfoil, compared with acoustical levels without airflow. Quarter-scale model.

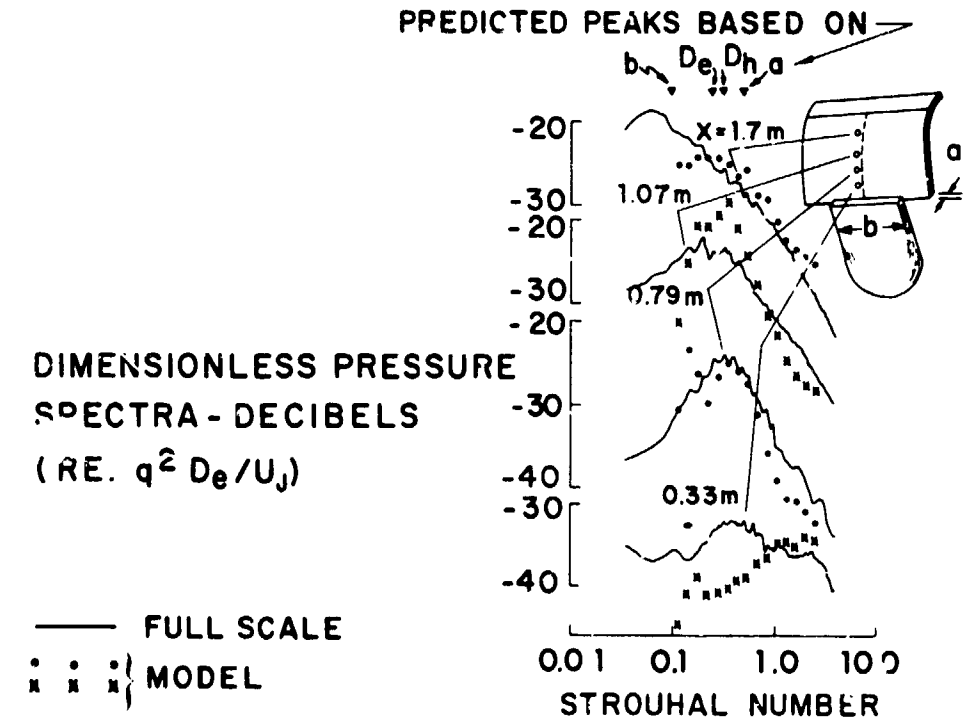

Figure 12.- Comparison of nondimensional power-spectral densities of static pressure spectra. Quarter-scale model vs. full-size configuration.

NASA PARTICIPATION IN THE AMST PROGRAM

Earl J. Montoya
NASA Dryden Flight Research Center

Alan E. Faye, Jr.
NASA Ames Research Center

INTRODUCTION

During the past 10 to 15 years, NASA research programs related to propulsive-lift aircraft technology have been directed toward expanding the technology data base which the aircraft industry designers may use for application to short-haul transport aircraft designs (ref. 1). These NASA research programs have resulted in development of such propulsive-lift concepts as the augmentor wing, externally blown flap, and upper-surface blown flap, which can produce more than twice the amount of usable aircraft lift coefficient for landing compared with the more conventional, non-powered-lift aircraft configurations (refs. 2 to 4). The improved take-off and landing performance inherent in these propulsive-lift aircraft concepts has been stated as a national asset, since short-haul transports employing these concepts will be able to operate from short runways with highly maneuverable, steep, and curved flight paths that could satisfy domestic and foreign market needs and, at the same time, could result in reduced community noise exposure (refs. 5 and 6).

With the advent of the U.S. Air Force Advanced Medium STOL Transport (AMST) Prototype Program early in 1973, the upper-surface blown flap concept was selected by The Boeing Company (ref. 7) to be applied to their YC-14 AMST prototype (fig. 1), while the externally blown flap concept was selected by the Douglas Aircraft Company (ref. 8) to be applied to their YC-15 AMST prototype (fig. 2). The Air Force AMST Program marks the first industrial application of several NASA propulsive-lift concepts to full-scale, mission-oriented transport aircraft (fig. 3). The AMST Program also provides the opportunity for full-scale flight validation of the propulsive-lift research which has been accomplished over the years through relatively small-scale experimental programs and through analytical techniques by NASA and the aerospace industry.

When it became apparent that NASA participation with the Air Force in the AMST Prototype Program could satisfy a number of the NASA objectives relative to civil short-haul transport technology needs, a Memorandum of Understanding was constituted in February 1973 by the Air Force and NASA. This Memorandum provides for NASA to conduct flight research experiments concurrent with the Air Force on noninterference or complementary bases during the Prototype Flight Test and Evaluation Program. The Memorandum further states that NASA will provide technical and facility support to the Air Force as needed, and that one or more of the prototype aircraft could possibly be made available to NASA subsequently for continued flight research.

29

C-6

To structure and conduct an integrated NASA AMST Experiments Program, representatives from NASA Ames, Dryden, Langley, and Lewis Research Centers; NASA Headquarters; FAA; and the Air Force Flight Dynamics Laboratory have been meeting periodically to develop the set of flight experiments currently implemented and being conducted during the Air Force Flight Test and Evaluation Program on the YC-14 and YC-15. These representatives are also developing another set of follow-on flight experiments which are proposed to be implemented and conducted subsequently. The NASA AMST Experiments Program is intended to be a cooperative program between NASA and other government participants and the aircraft industry.

This paper discusses the objectives of the NASA AMST Experiments Program and describes several of the NASA experiments as they are currently being implemented and conducted on the YC-14 and YC-15 prototype aircraft. A brief description of the proposed future NASA AMST Experiments Program is included. This discussion is confined to those NASA experiments related to powered-lift aerodynamics and acoustics.

SCHEDULE OF EXPERIMENTS

Agreement in the USAF/NASA Memorandum of Understanding and the USAF AMST Program schedule has resulted in the following general NASA schedule of experiments involving AMST:

	AIRCRAFT	TEST PERIOD	USAF PROGRAM	NASA PROGRAM
CURRENT	DOUGLAS YC-15	AUG. 1975 - AUG. 1976	PROTOTYPE FLIGHT TEST AND EVALUATION	NONINTERFERENCE EXPERIMENTS
CURRENT	BOEING YC-14	AUG. 1976 - AUG. 1977	PROTOTYPE FLIGHT TEST AND EVALUATION	NONINTERFERENCE EXPERIMENTS
FUTURE	COMPETITION WINNER: YC-14 OR YC-15	OCT. 1977 - 1981	FULL-SCALE DEVELOPMENT	LIMITED NONINTERFERENCE EXPERIMENTS
FUTURE	COMPETITION LOSER: YC-14 OR YC-15	OCT. 1977 - OCT. 1982	POSSIBLE COEXPERIMENTERS WITH NASA	MAJOR EXPERIMENTS PROGRAM

Both current and future NASA AMST experiments are shown. Current experiments include

(1) YC-15 flight experiments over the period August 1975 to August 1976.

(2) YC-14 flight experiments over the period August 1976 to August 1977.

Future experiments utilize either or both YC-14 and YC-15 aircraft over the period October 1977 through October 1982. These two time periods encompass the period of the Air Force AMST Prototype Flight Test and Evaluation Program (August 1975 to August 1977) and the Air Force AMST Full-Scale Development Program scheduled to begin October 1977. During this latter Air Force Program period of full-scale development, NASA expects to conduct many of the major candidate experiments requiring at least one and possibly two dedicated AMST prototype aircraft to be made available by the Air Force. Additional minor experiments on a noninterference basis are planned to be conducted on the full-scale development prototype aircraft selected by the Air Force.

NASA AMST EXPERIMENT OBJECTIVES

The NASA AMST experiment objectives in the areas of powered-lift aerodynamics and acoustics are

(1) The full-scale flight validation of predictive methods based on small-scale experimental investigations and analytical techniques

(2) Development through flight research of a better understanding of aerodynamic and/or acoustic characteristics in areas where predictive methods don't exist or the phenomena have been too complex to model

(3) Full-scale proof-of-concept through flight research of methods for improving aerodynamic efficiency and reducing the effects of the acoustic environment

Several conference papers (refs. 9 to 12) are authored by NASA or NASA-sponsored AMST experimenters who have proposed flight and ground experiments to be conducted on both the YC-14 and the YC-15. These experiments will satisfy some of the NASA AMST objectives just described. The current (ongoing) AMST experiments fall into three broad experiment categories:

(1) Aeroacoustic and thermal load environments

(2) Noise sources affecting exterior fuselage structure, interior fuselage noise, and far-field noise environments

(3) Propulsive-lift aerodynamics

These experiments are intended to satisfy as many of the NASA experiment objectives as could be reasonably accommodated by the flight hardware and flight test time available in keeping with the USAF/NASA Memorandum of Understanding.

Specifically, small-scale experimental data have been obtained which indicate that jet propulsive-lift systems produce local flows which can subject wing, flap, and fuselage structures to severe environments involving aeroacoustic and thermal loads. These propulsive-lift environments are expected to be more severe in magnitude than currently experienced in conventional jet-powered

transports and must be understood if efficient aircraft structural designs are to be realized. Further, there is a need to understand the mechanisms by which noise is generated in propulsive-lift systems, the propagation of this noise into the fuselage interior and the exterior far field, and methods by which noise can be attenuated. Finally, full-scale propulsive-lift aerodynamic characteristics in the dynamic flight environment must be examined to validate predictive methods based on wind tunnels, static test rigs, and analytical models.

KEY TECHNOLOGY AREAS

Experiments in the current Prototype Program are very similar for both the AMST YC-14 and YC-15 because

(1) Both the upper-surface blown flap and the externally blown flap propulsive-lift concepts encompass key technology areas which generally tend to be quite common.

(2) Experiments which tend to develop data in key technology areas generally had to be performed equally on both the YC-14 and YC-15 because of the competitive nature of the AMST program. This was necessary to avoid NASA-generated data that might unbalance the competition.

The key technology areas that are being addressed in these experiments are as follows:

- Structures and materials subjected to loads in the extreme aero-thermal-acoustic-vibration jet STOL environment
- External and internal acoustics
- Noise source identification
- Flow turning efficiency of engine effluence
- High-lift ground-effects aerodynamics
- Powered-lift configuration aerodynamics

The experimental investigations into these technology areas can generally be summed up by three broad experiment categories: (1) internal/external noise experiments, (2) flap loads/acoustics/inlet experiments, and (3) special or opportunity-type experiments.

Commonality to both the YC-14 and YC-15 exists for the first two stated experiment categories as shown in the following:

Common to YC-14 and YC-15:

Internal/external acoustics

Flap and inlet aerothermodynamic loads and acoustics

Unique to individual aircraft:

Targets of opportunity (e.g., ground crew noise)

Special tests identified during flight test program (e.g., ground effects)

Since the NASA YC-15 flight experiments have been completed, a brief discussion of only the NASA YC-15 flight experiments in these categories is included. However, similar NASA flight experiments are essentially planned for the YC-14 for the fall of 1976. The YC-14 static ground-test experiment completed in February 1976 for NASA to support the YC-14 flight tests is discussed briefly here and in detail in reference 9.

YC-15 Experiments

Internal and external noise environment measurements were conducted on the YC-15. Transducer locations on the YC-15 fuselage for the interior/exterior acoustics experiments are shown in figure 4. There were 8 accelerometers and 21 microphones in this installation. The ground and flight tests for this experiment were conducted in March 1976.

Flap loads/acoustics/inlet investigation experiments were conducted during early May 1976. The instrumentation on the starboard flap area was primarily for sensing aeroacoustic loads and for measuring the thermal environment. Flap instrumentation locations are shown in figure 5. Instrumentation for the engine inlet acoustics in the right inboard nacelle (engine 3) consisted of three static pressure transducers and five dynamic pressure transducers (microphones), as shown in figure 6, along with one exterior fuselage microphone.

As mentioned before, both the exterior/interior noise experiment and the flap loads/acoustics/inlet experiment will essentially be repeated with the YC-14 aircraft in the early fall of 1976.

Special or opportunity experiments have been planned for both the YC-14 and YC-15. In some cases these experiments have been implemented on the YC-15. Examples of this type of experiment include

(1) Engine noise investigations in the vicinity of the ground crew. Microphone positions for investigating engine noise in the vicinity of the ground crew are shown in figure 7.

(2) Flyover (far-field) noise measurements performed by the USAF Aerospace Medical Research Laboratory (AMRL).

(3) Ground-effects tests. The profile of a typical ground-effects test is shown in figure 8.

(4) NASA pilot evaluations (10 hours maximum).

YC-14 Experiments

The YC-14 experiments include integrated flight and static ground-test experiments wherein NASA was able to piggyback experiments on a planned test by Boeing of actual aircraft propulsive-lift hardware at their static test facility at Tulalip, Washington. The Tulalip ground test was a special set of experiments conducted with full-scale YC-14 hardware prior to flight tests. Figure 9 indicates the full-scale hardware tested at Tulalip. Since the Tulalip tests are discussed in detail in reference 9, only the following brief summary is presented.

The Tulalip tests permitted NASA to achieve the following objectives:

(1) To provide full-scale static measurements that could be compared with 1/4-scale static measurements of an identical configuration made by members of Langley Research Center

(2) To provide the data base required to correlate static measurements with flight measurements to assess the effects of the flight environment

(3) To assess the adequacy and location of research instrumentation to be installed in the flight vehicle

Future Experiments

There have been about 50 experiments of varying degrees of complexity proposed for the AMST. These proposed experiments have been compiled into a list, which is considered a "living list," since experiments will be modified, deleted, and added with time and as the AMST program unfolds. Examples of proposed future NASA experiments for the AMST program are as follows:

Ames Research Center

Prediction of the performance, stability, and control characteristics of STOL aircraft

Investigation of powered-lift STOL wake turbulence

Military/civil commonality in avionics design for short-haul air transportation

Validation of tentative airworthiness criteria for certification of powered-lift transports

Certification of powered-lift transports incorporating advanced guidance and augmentation devices

Langley Research Center

Acoustic loading and fatigue for STOL aircraft structure

Ride quality - vibration and noise measurements in the AMST

Lewis Research Center

Measurement of upwash angles at engine inlet

Forward velocity effects on fan and jet/flap interaction noise

Forward velocity effects on thrust reverser noise

Instrumentation, dedicated flight time, and aircraft modification requirements for the proposed experiments range from simple to extensive. An example of an experiment requiring extensive aircraft modifications is the possible flight testing of the Quiet Clean Short-Haul Experimental Engine (QCSEE) on the AMST.

CONCLUDING REMARKS

As discussed in this paper, the major element of NASA participation in the Air Force AMST Prototype Program is the conduct of flight research experiments on the AMST prototype aircraft, the Boeing YC-14 and Douglas YC-15. These experiments cover the broad range of technical disciplines that includes aerodynamics, propulsion, acoustics (including community noise and human factors), structures (including structural environment), stability and control, avionics and flight control systems, handling qualities, operating systems, and certification criteria. This paper has been limited to a discussion of the categories propulsive-lift aerodynamics and acoustics of flight experiments. As many NASA flight experiments as can be accomplished without interference to the basic Air Force AMST Prototype Program Objectives are currently being pursued by the NASA experimenters. Follow-on NASA flight experiments are being defined to be implemented subsequently, when one or more of the AMST prototype aircraft should be available for additional NASA flight research.

It is anticipated that the results of these flight experiments will provide the aircraft industry with additional needed technology that contributes to economical, safe, efficient STOL transport aircraft for both civil and military missions.

REFERENCES

1. STOL Technology. NASA SP-320, 1972.

2. Koenig, David G.; Corsiglia, Victor R.; and Morelli, Joseph P.: Aerodynamic Characteristics of a Large-Scale Model With an Unswept Wing and Augmented Jet Flap. NASA TN D-4610, 1968.

3. Campbell, John P.; and Johnson, Joseph L., Jr.: Wind-Tunnel Investigation of an External-Flow Jet-Augmented Slotted Flap Suitable for Application to Airplanes With Pod-Mounted Jet Engines. NACA TN 3898, 1956.

4. Phelps, Arthur E.; Letko, William; and Henderson, Robert L.: Low-Speed Wind-Tunnel Investigation of a Semispar STOL Jet Transport Wing-Body With an Upper-Surface Blown Jet Flap. NASA TN D-7183, 1973.

5. Savin, Raymond C.; Galloway, Thomas L.; Wilcox, Darrell E.; Kenyon, George C.; Ardema, Mark D.; and Waters, Mark H.: Summary of Recent Short-Haul Systems Studies. NASA TM X-3010, 1975.

6. Parametric Study of STOL Short-Haul Transport Engine Cycles and Operational Techniques To Minimize Community Noise Impact. MDC-J4437 (Contract NAS 2-6994), Douglas Aircraft Co., June 1974. (Available as NASA CR-114759.)

7. Wimpress, John K.: Upper Surface Blowing Technology as Applied to the YC-14 Airplane. [Preprint] 730916, Soc. Automot. Eng., Oct. 1973.

8. Heald, Ervin R.: External Blowing Flap Technology on the USAF/McDonnell Douglas YC-15 (AMST) Program. [Preprint] 730915, Soc. Automot. Eng., Oct. 1973.

9. Sussman, M. B.; Harkonen, D. L.; and Reed, J. B.: USB Environment Measurements Based on Full-Scale Static Engine Ground Tests. Powered-Lift Aerodynamics and Acoustics, NASA SP-406, 1976. (Paper no. 30 of this compilation.)

10. Schoenster, James A.; Willis, Conrad M.; Schroeder, James C.; and Mixson, John S.: Acoustic-Loads Research for Powered-Lift Configurations. Powered-Lift Aerodynamics and Acoustics, NASA SP-406, 1976. (Paper no. 27 of this compilation.)

11. Perry, Boyd, III; and Mendenhall, Michael R.: Measured and Calculated Steady Aerodynamic Loads on a Large-Scale Upper-Surface Blown Model. Powered-Lift Aerodynamics and Acoustics, NASA SP-406, 1976. (Paper no. 26 of this compilation.)

12. Hassell, James L., Jr.: Results of Static Tests of a 1/4-Scale Model of the Boeing YC-14 Powered-Lift System. Powered-Lift Aerodynamics and Acoustics, NASA SP-406, 1976. (Paper no. 3 of this compilation.)

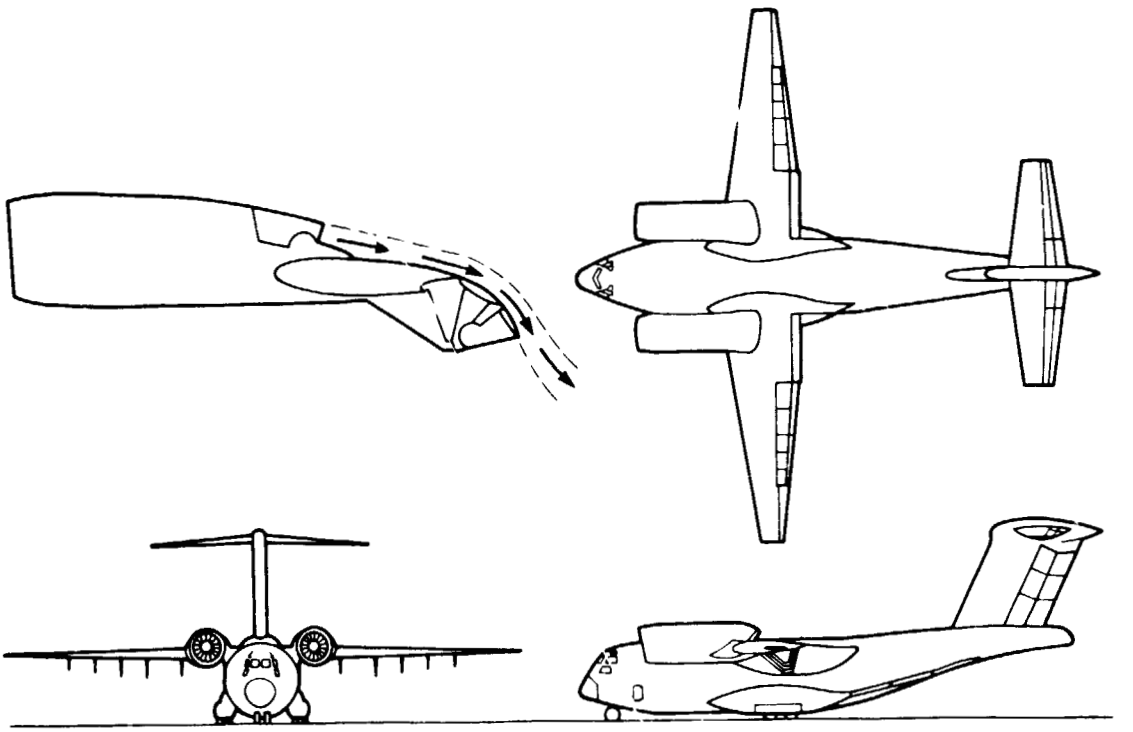

Figure 1.- USAF/Boeing YC-14 AMST prototype — upper-surface blown flap.

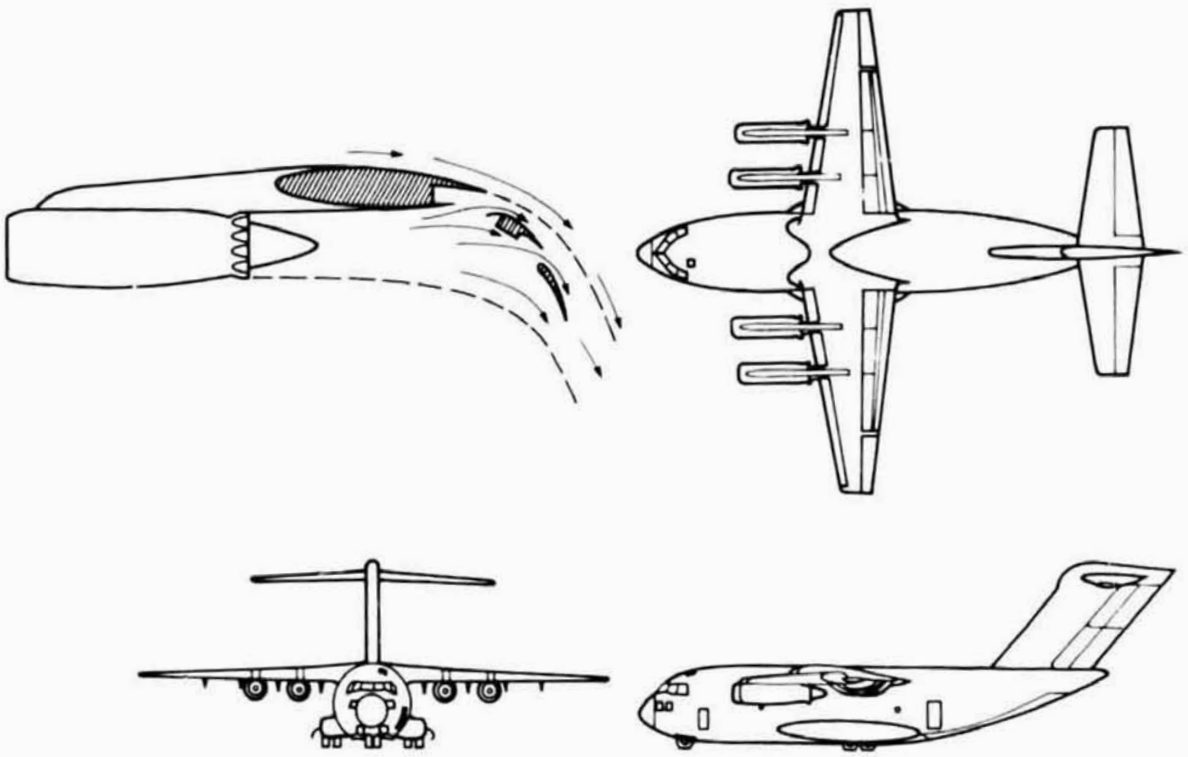

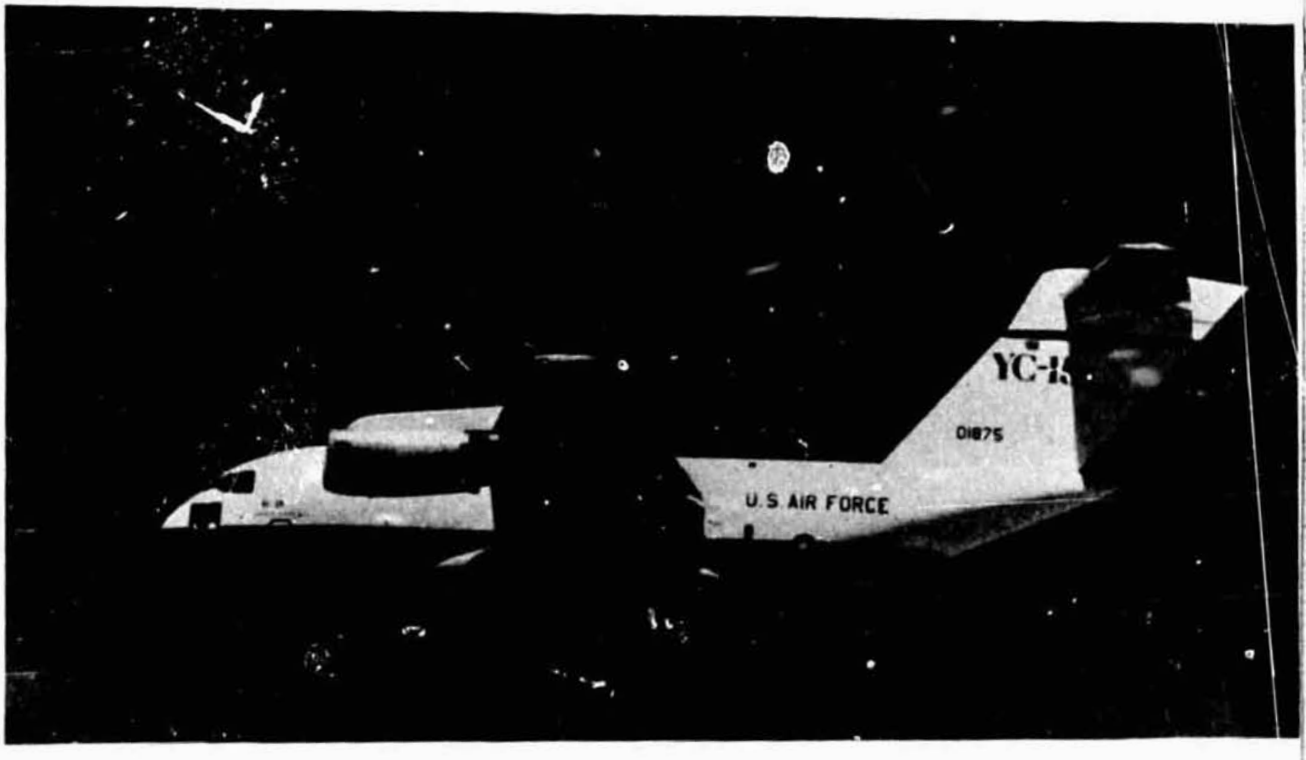

Figure 2.- USAF/Douglas YC-15 AMST prototype — propulsive-lift externally blown flap.

CAPABILITY: TAKEOFF AND LAND FROM 6096 m (2000 ft) RUNWAY WITH 12 247 kg (27 000 lb) PAYLOAD

BOEING YC-14

POWERED-LIFT

UPPER-SURFACE BLOWING

2 - CF6-50 ENGINES

FIRST FLIGHT: AUGUST 1976

DOUGLAS YC-15

POWERED-LIFT

EXTERNALLY BLOWN FLAP

4 - JT8D-17 ENGINES

FIRST FLIGHT: AUGUST 1975

Figure 3.- USAF advanced medium STOL transport (AMST) aircraft.

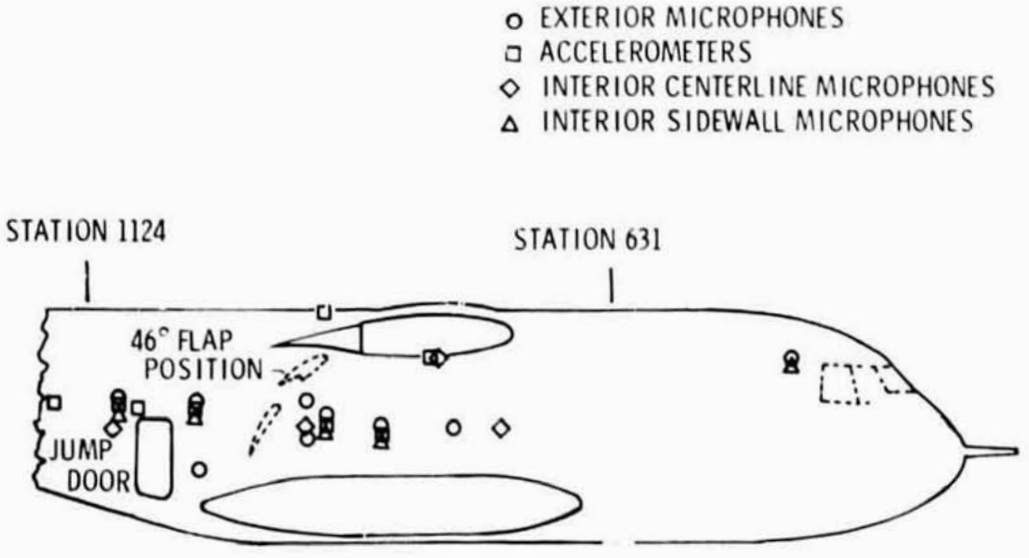

Figure 4.- Transducer locations on YC-15 fuselage.

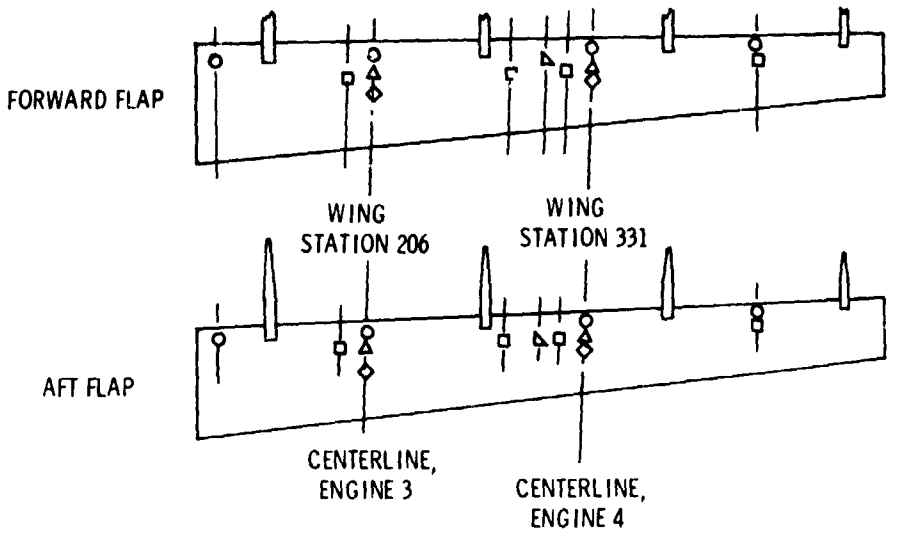

- ○ ACCELEROMETER
- □ ACCELEROMETERS, STATIC AND DYNAMIC PRESSURE TRANSDUCERS, AND THERMOCOUPLES (LOWER SURFACE)
- ◇ STATIC, DYNAMIC, AND TOTAL PRESSURE TRANSDUCERS AND THERMOCOUPLES (LOWER SURFACE)
- △ STATIC AND DYNAMIC PRESSURE TRANSDUCERS AND THERMOCOUPLES (UPPER AND LOWER SURFACES)
- ◺ ABSOLUTE PRESSURE TRANSDUCERS (INSIDE FLAP)

Figure 5.- Flap instrumentation locations.

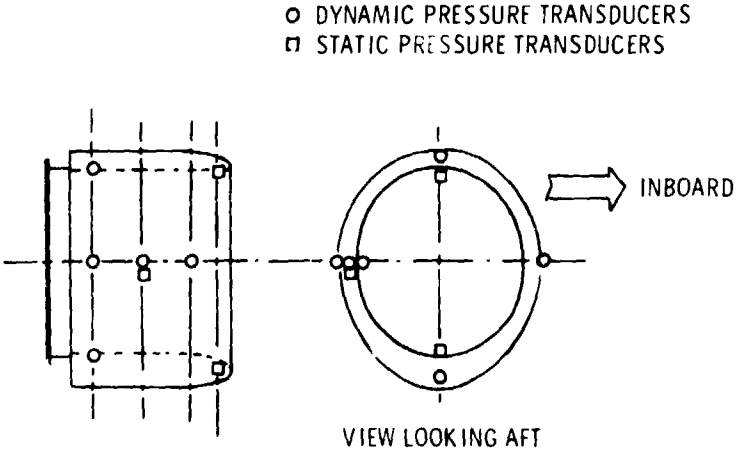

Figure 6.- Engine inlet instrumentation.

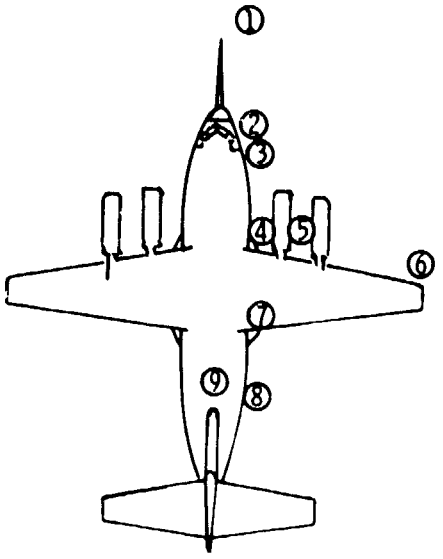

MICRO-PHONE	HEIGHT, cm	HEIGHT, in.	POSITION
1	163	64	6.1 m (20 ft) FORWARD OF NOSE
2	163	64	FORWARD DOOR
3	76	30	FORWARD LANDING GEAR
4	163	64	INBOARD ENGINES
5	163	64	BETWEEN ENGINES
6	163	64	OUTBOARD OF WING
7	76	30	MAIN LANDING GEAR
8	163	64	AFT CREW DOOR
9	163	64	INSIDE AIRCRAFT ON CENTERLINE

Figure 7.- Microphone positions for investigating engine noise in vicinity of ground crew.

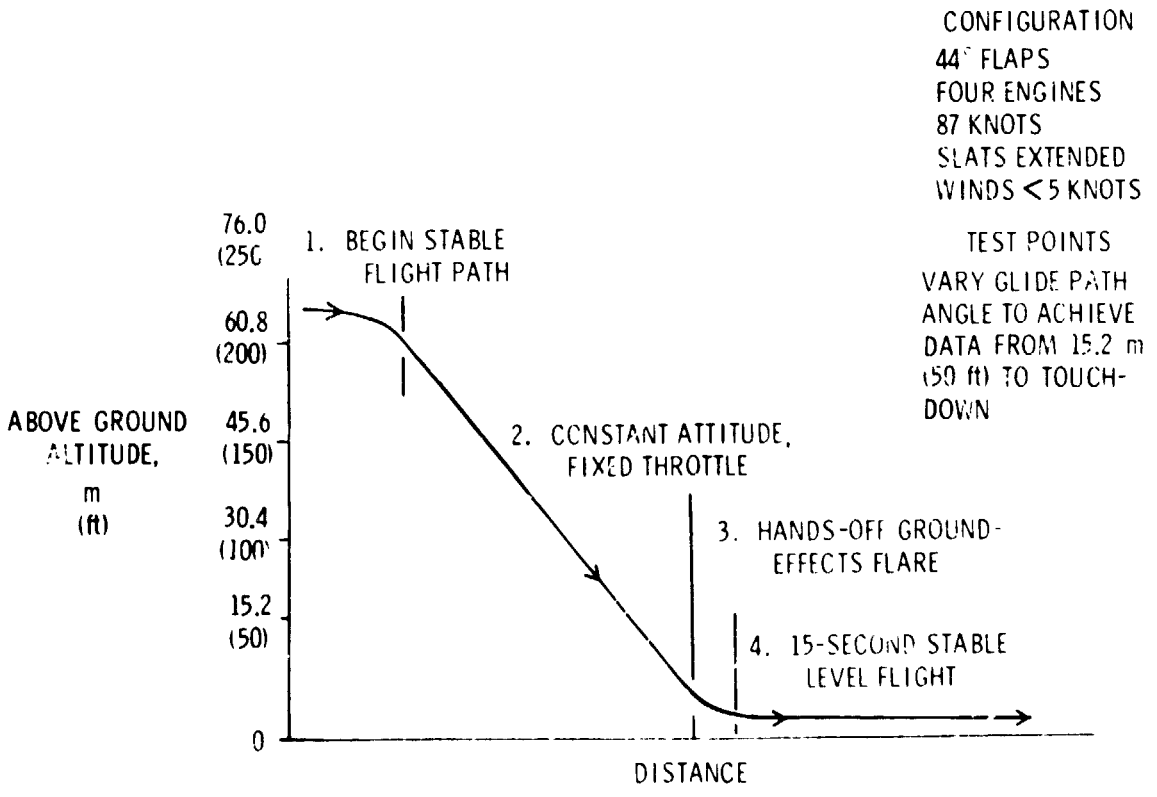

Figure 8.- Typical YC-15 ground-effects test.

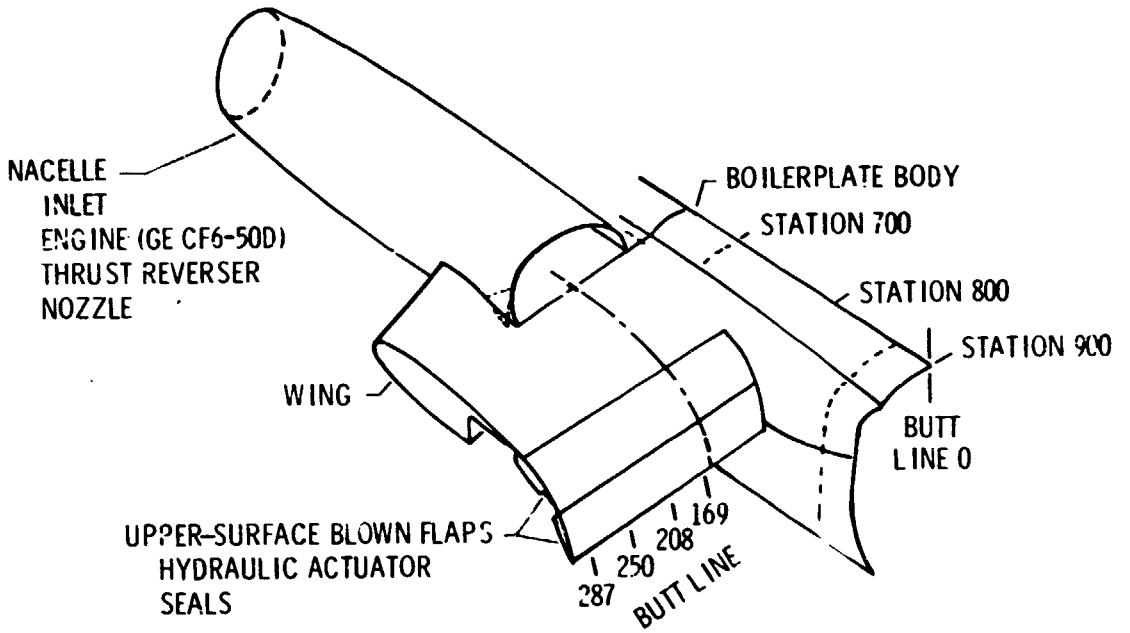

Figure 9.- Full-scale YC-14 hardware used in Tulalip ground test.

N78-24076

USB ENVIRONMENT MEASUREMENTS BASED ON FULL-SCALE STATIC ENGINE GROUND TESTS

M.B. Sussman, D. L. Harkonen and J. B. Reed
The Boeing Company

SUMMARY

Flow turning parameters, static pressures, surface temperatures, surface fluctuating pressures and acceleration levels were measured in the environment of a full-scale upper surface blowing (USB) propulsive-lift test configuration. The test components included a flightworthy CF6-50D engine, nacelle and USB flap assembly utilized in conjunction with ground verification testing of the USAF YC-14 Advanced Medium STOL Transport propulsion system. Results, based on a preliminary analysis of the data, generally show reasonable agreement with predicted levels based on model data. However, additional detailed analysis is required to confirm the preliminary evaluation, to help delineate certain discrepancies with model data and to establish a basis for future flight test comparisons.

INTRODUCTION

Recently for both military and commercial powered-lift airplane concepts, attention has been directed to the use of upper surface blowing (USB) for propulsive lift. The present USB technology base has been developed through extensive model- and small-scale tests of general research configurations and is currently being applied to the USAF YC-14 Advanced Medium STOL Transport (AMST). Results of these small-scale studies have provided an initial understanding of such key powered-lift technology areas as: achievement of adequate structures in areas subject to the difficult environment of the engine exhaust; definition of the external and internal acoustic environment; achievement of adequate exhaust flow turning at low speed; and integration of the engine exhaust system with the airframe. Further progress is anticipated through development of a data base of full-scale hardware and comparison of this data with the model measurements.

The National Aeronautics and Space Administration (NASA) has undertaken, in conjunction with broad base technology development, some large-scale USB technology efforts which will be valuable in defining successful design approaches. In particular, NASA is participating with the U.S. Air Force to develop technology during both full-scale ground and flight testing associated with the USAF YC-14 prototype airplane development. Another notable example is the recently initiated NASA Quiet Short-Haul Research Airplane (QSRA) program.

The present program, an integrated ground and flight test technology program to study the USB environment, has been undertaken by NASA as part of their AMST efforts. The program was structured to utilize prototype YC-14 airplane hardware and to accomplish all measurements on a piggyback, noninterference basis.

It was planned that the ground test hardware would incorporate, where possible, instrumentation identical to that designated for the subsequent flight test. The combined ground/flight test program was then planned in an integrated framework.

The general objectives of the program were the following:

- To achieve the planning, design and fabrication of certain modifications required of the YC-14 prototype airplane no. , to permit subsequent flexibility for flight test experiments of interest to the NASA

- To accomplish early, full-scale engine ground test of the critical aerodynamic and structural technologies unique to the USB concept using a test article (including engine/nacelle/wing flap/body section) of which significant portions are actual flightworthy, YC-14 prototype airplane hardware instrumented for ground test identically to the flight test vehicle

- To accomplish initial flight testing of the structural and acoustic technology items for which these instrumentation modifications have been incorporated

- To integrate the ground and flight test programs in order that: (1) certain complex flight instrumentation systems are thoroughly checked out in the ground test prior to flight; and (2) that costs are reduced through the use of common design efforts and instrumentation

The present paper provides results together with a preliminary analysis of the full-scale engine static ground test. The results are preliminary in that plans call for future detailed analysis of the ground test data together with acquisition of and comparative analysis with flight results, testing for which is planned for August, 1976.

DESCRIPTION OF THE GROUND TEST

The NASA-funded ground test efforts were accomplished as part of the basic YC-14 program engine verification test conducted at the Boeing Tulalip test facilities from December 1975 to February 1976.

Testing was accomplished on a specially constructed engine test stand which features a considerably open support structure to provide sufficient clearance for a full-scale USB installation including nacelle, USB flaps and simulated fuselage segment (fig. 1). A photograph of the test rig is given in figure 2. The entire test article was installed on top of a specially designed six-component force balance which provided strain-gauged-flexure outputs proportional to forces in the thrust, lift and side directions together with moments about the three principal axes. Two of the five CF6-50D engines designated to support the YC-14 flight test program were used, consecutively, during the ground test. Similarly, airplane flightworthy nacelle and USB flap hardware were incorporated as major elements of the ground test configuration. To help relate the test geometry to that of the flight vehicle, figure 3 shows the features of the no. 1 prototype airplane as visible during airplane final assembly in Seattle.

The technical objectives of the NASA-funded portion of the ground test are summarized in figure 4. Principal test parameter variations related to the NASA measurements included the following: engine power setting, angle of USB flap deployment, position of USB mixed-flow nozzle auxiliary bleedoff door, position of USB flap vortex generators. In addition, related to the basic YC-14 program development objectives, variations of engine bleed flow rates, level of thrust reverser and bellmouth/flight-inlet engine intake configurations were tested. These latter measurements are beyond the scope of the present paper. Also, the reader is directed to references 1 through 4 for information related to design and development of the YC-14 USB installations.

INSTRUMENTATION

Approximately 150 channels of instrumentation were incorporated to assess the USB environment for the NASA-funded measurements. The approximate sensor locations for the static pressures, surface air temperatures, microphones, and accelerometers are shown in figure 5. The first two of these groups were treated as steady state measurements, whereas the latter two measurements were handled as instantaneous or high frequency data. Test objectives call for maximum commonality between flight and ground test instrumentation. The following were two exceptions to this commonality: (1) Provisions for four additional microphones, located on and near the wing-body fairing were added for the ground test, (2) Static pressures were measured only on the USB flap/wing upper surface. Flight test static pressure measurements will include undersurface measurements.

In addition to the NASA instrumentation, extensive instrumentation of the engine, outdoor environment, and other pertinent test information was made available by the YC-14 program. Of particular interest is that instrumentation associated with the engine operation which includes: shaft speeds, exhaust stream charging pressures and temperatures, primary and secondary airflows and others. Instrumentation was also provided for model overall thrust, lift and pitching moment forces.

Conventional type transducers were used for measurement of the various steady state parameters of interest. The flight inlet, the fan duct, and nozzle ramp area sound level were measured internally by flush-mounted microphones, Photocon no. 524. The upper wing surface sound levels were measured by flush-mounted Kulite miniature microphones. The flap area sound levels were measured by flush-mounted Photocon no. 765 and 524 microphones. The body area sound levels were measured by flush-mounted microphones including Photocon no. 524 and B & K no. 4134 types. Endevco Accelerometers model no. 2229C were principally used for the flap vibration measurements. These are a microminiature design with flat charge and voltage response over a broad temperature range.

All steady state performance data were acquired through a Beckman 210 Digital Data system. This is a high-speed, high-accuracy data acquisition system which contains a stable dc amplifier for each analog channel. Microphone and accelerometer measurements were acquired on separate wide band FM tape recorders outfitted with appropriate individual channel signal conditioning. The systems provided flat response through a frequency range of 20 to 10 000 Hz for the microphones and 5 to 2500 Hz for the accelerometers.

NASA-LANGLEY GROUND TEST

It should be noted that a contractually unrelated but coordinated static ground test program has been undertaken at NASA-Langley. The Langley testing used a 0.25 scale test article with identical USB nozzle/flap/fuselage geometry together with a United Aircraft of Canada JT15D engine (see fig. 6). It is intended that subsequent scale effect assessments will include comparisons with the Langley 0.25 scale program. Such comparisons are beyond the scope of this paper.

PRINCIPAL TEST RESULTS

Preliminary results and conclusions, developed during a two month posttest documentation period, are summarized below. These are subject to modification upon further detailed data reduction and analysis.

Flow Turning

Figure 7 summarizes the USB nozzle/flap flow turning results for the two flaps-down configurations tested. Flow turning angle as measured by the lift and thrust components of the six-component force balance is plotted against fan pressure ratio for both the full-down (41°/70°) and intermediate (31.5°/54°) flaps. The numbers in parentheses refer to the incremental rotation from flaps-up of the main and aft flap segments respectively. Figure 8 provides additional information on the flow turning results in terms of a polar plot. The axial and vertical force balance readings are normalized by the ideal thrust computed from the actual primary and secondary stream airflows and nozzle pressure ratios determined by internal pressure rakes upstream of the mixed flow exhaust nozzle. The data illustrates that as turning is increased, the ratio of total resultant force to the ideal thrust decreases. This is due primarily to the increased scrubbing losses incurred on the USB flap system as additional USB flap area is wetted. Key results of the flow turning assessment from the data given here and other data provided in Boeing document D748-10113-1 "YC-14 Ground and Flight Experiments for NASA-Ground Test Final Report" April 1976 were these:

- Flow turning angles of between 60° and 63° were achieved for full-down flaps. A preliminary comparison of these values with Boeing 1/15-scale model measurements shows good agreement, with the full-scale turning angles exceeding the model measurements by about 2-1/2°. This level of turning was accomplished after flap-to-flap and flap-to-fuselage sealing procedures used for the ground test were brought up to design standards. Flow turning angles of about 50° to 52° were obtained for the intermediate flap setting. The takeoff configuration (flaps up, nozzle door open) produced about 13° of turning. Preliminary comparison shows good agreement with Boeing model data.

- Retraction of the vortex generators and closure of the auxiliary nozzle door (both failure conditions for airplane operation with USB flaps deployed) exacted flow turning penalties, relative to the design condition, of about 11° and 16° respectively for full-down flaps.

- All flow turning measurements were performed with the test article installed at a fixed height above ground (engine $\mathcal{L}$ height = 5.8 m) duplicative of installation during airplane

taxi. Existing *model* data suggests the presence of "ground effect" impacting the data by loss of several degrees of flow turning and between 3% to 10% of resultant thrust when compared to free field measurements. Resultant velocity coefficients of about 0.75 and 0 78 were measured at Tulalip for the full-down and intermediate flaps cases, respectively. (The Boeing velocity coefficient parameter accounts for internal duct and mixing losses, nozzle losses and losses associated with flow turning and scrubbing over the USB flap and fuselage surfaces.) The reader is cautioned that certain of the instrumentation supporting the measured velocity coefficients are currently under review and accordingly are subject to some minor changes.

Pressure Environment

Figure 9 is representative of the pressure distribution data acquired during the testing. Both chordwise and spanwise pressure profiles are shown in this particular comparison which illustrates the loss of suction pressure over the aft portion of the USB flap system upon retraction of the vortex generators(VG). Assessment of all the pressure distribution data provides the following principal results:

- All pressure profile data were quite orderly and consistent in reflecting the integrated changes in flow turning recorded by the force balance instrumentation. Increased flow turning due to improvements in flap sealing was evidenced primarily by increased suction pressures on the aft USB flap segment

- A drop in the chordwise suction pressure profile between the main and aft USB flap, initially attributed to flap-to-flap seal leakage, was subsequently judged to be primarily a result of local surface curvature changes

- Detailed comparisons of the full-scale pressure distributions with model data have not been made. However, preliminary review suggests that the aft flap suction pressures do not exhibit close agreement with the available model data and further evaluation of these data are recommended

Temperature Environment

Figure 10 provides a comparison of temperature distribution contours (based on model data) used for design requirements for the intermediate flap setting at an engine fan pressure ratio of 1.52. This condition provided the highest measured full-scale flap temperature (155.6°C) of any of the test conditions run. As noted on the figure, an adjustment to the measured full-scale levels of approximately 44°C has been applied to bring these temperatures to a common reference level of maximum takeoff power on a hot day (39.4° C ambient). The primary conclusions drawn from these and other temperature measurements (not shown) are as follows:

- Maximum flap temperatures tend to occur somewhat outboard of the engine centerline on the aft USB flap. Decreasing power setting tends to shift the line of peak temperatures slightly inboard

- **Maximum measured internal, upper-surface nozzle temperature was 251.7° C which occurred in the flaps-up, door-open (i.e., takeoff) configuration at an engine power setting corresponding to fan pressure ratio = 1.71**

- **Recorded fuselage temperatures were generally quite cool with the highest level exceeding ambient by only ≈ 28° C. These levels were recorded at the most downstream portion of the simulated fuselage section**

- **Preliminary comparison with model data from two sources indicates fair agreement in both temperature level and distribution. The full-scale temperature distribution tended to show peak temperatures somewhat further inboard than the most recent model data.**

Acoustic Environment

Figures 11 to 13 are representative summaries of the fluctuating pressure (i.e., acoustic) data. Figure 11 gives overall fluctuating pressure level trends against a calculated, average mixed flow jet velocity for various geometric groups of microphones. The maximum recorded dB level on the flaps was on the order of 165dB. This level was also reached by certain fuselage microphones which were in the vicinity of the flap trailing edge region. Figures 12 and 13 give a representation of the frequency distribution of the acoustic energy as defined by 1/3-octave band analysis. The principal features of this acoustic data and the other data analyzed to date can be summarized as:

- Overall fluctuating pressures on the wing/flap/fuselage in excess of 160 dB tend to be contained within the flow-scrubbed regions on the USB flaps or the adjacent fiberglass fairing between the wing and fuselage

- Overall fluctuating pressure levels on the fuselage itself tend to remain less than 155-dB (fuselage section below the fiberglass fairing) or less than 150 dB (fuselage section above the fiberglass fairing)

- Overall fluctuating pressure levels measured in the fan duct and on the nozzle wall did not exceed 155 dB

- Preliminary comparisons of overall sound pressure level between full-scale and Boeing 1/8-scale model data show quite good agreement with respect to the wing and fuselage regions; measurements in the USB flap region agree reasonably well

- 1/3-octave band spectral analysis shows low frequency activity in the neighborhood of 80 to 100 Hz corresponding to a Strouhal number of approximately 0.35. Peak energy in this frequency is measured on the fuselage region near the flap trailing edge, on the flaps and on the wing trailing edge panel. Activity in this Strouhal number range is consistent with previous model-scale investigations of near-field acoustic measurements for USB propulsive lift installations and is associated with the jet/wing-surface interaction shear regions

- An indication that fuselage microphones near the flaps are directly exposed to the flow scrubbing is that higher levels of low frequency activity (approximately 10 dB) are measured than in more distant regions. The level of activity in the frequency band of 30 to 50 Hz is slightly higher than indicated by model data but detailed assessment must await a narrow band analysis

- Another apparent peak in the spectra is in the 300- to 400-Hz range corresponding to a Strouhal number of approximately 1.5. This frequency band is predominant in nozzle, wing, and flap regions and is associated with the exhaust-jet/ambient-air shear regions. This pattern of acoustic energy is also consistent with observations of previous model experiments

- Retraction of the vortex generators at full-down flaps and high power setting produced a considerable (approximately 5 dB) decrease of noise in the neighborhood of 90 to 100 Hz. This characteristic was noticeable in both the wing and nozzle microphone measurements

- Engine fan tone noise is evident in the high frequency end of the spectrum (1500 to 5000 Hz) for measurements in the fan duct and in the nozzle wall region and is also prominent in some of the wing microphone data. However, the levels tend to be considerably less evident downstream of the wing in the flap and fuselage regions where the broad band noise of the jet mixing region determines the noise level at these higher frequencies

Acceleration Environment

Figures 14 to 16 are representative summaries of the USB flap acceleration data for the flaps down test condition analyzed. Figure 14 gives overall vibration levels in g's rms for several chordwise locations at the spanwise position of the outboard hinge fitting. The direction of the accelerometer sensor is indicated by the arrows. Figure 15 gives the results of an engine-off test where the installed flaps were subjected to inputs from an electromagnetic shaker over a range of frequencies from 0 to 500 Hz. The engine-off tests were intended to help interpret the resulting engine-on accelerometer measurements in terms of the flap-assembly natural modes. Figure 16 gives frequency spectra for several accelerometers illustrating the variation in energy distribution with downstream location. The primary features of this data and the other accelerometer data analyzed to date are summarized below:

- Only a small portion of the acquired accelerometer data was able to be analyzed in the allotted time. However, all of the data examined appeared to be orderly and self-consistent with respect to power setting, geometric location and expectations based upon the engine-off, shake test

- Overall vibration levels of 3 to 4 g's rms (parallel) and 7 to 9 g's rms (transverse to the flap chord) were measured on both flaps at the inboard and outboard attachment points of the primary flap structural components. Higher overall levels of 14 and 38 g's rms were measured normal to the skin of the aft flap downstream of the hinge arm support structure but at the same spanwise location. One accelerometer, on an aft flap skin panel outboard of the hinge arm, measured 56 g's rms

- Numerous frequency peaks are evident in the various spectra examined. The most dominant activity appeared to take place in 3 separate frequency ranges: 20 to 30 Hz, 90 to 110 Hz and 250 to 350 Hz

- The 20- to 30-Hz activity is evident in both the main and aft flaps for those accelerometers located at the principal attachment points of the primary flap structural components. This suggests that the activity is associated with a response mode of the overall flap assembly

- The 90- to 110-Hz activity is also visible in many of the accelerometers but tends to be dominant in the aft flap sensors. This vibration activity is increased the higher the power setting and the further downstream on the flap the measurement is made. These characteristics together with the trend of increasing overall rms acceleration level in the downstream direction suggest a pitching-motion-type flap response at this frequency

- Activity in the 250- to 350-Hz range is dominant in the acceleration response of the sensor located on one of the upper surface, aft flap skin panels and was judged to be primarily panel response

- Vibration activity in the frequency bands noted above is consistent with USB exhaust jet pressure fluctuations determined by acoustic microphone measurement and associated with various of the noise source shear regions typical of a USB installation as discussed previously

- The above conclusions are based on a preliminary examination of portions of the available data. Additional detailed data analysis could be profitable pursued to: (1) complete analysis of data not yet examined, and (2) extend comparisons with the acoustic measurements to more fully understand the nature of the fluctuating loads and the flap response

Instrumentation Verification

All of the steady state pressure and temperature instrumentation as well as the high frequency accelerometers performed well during the ground test and with the possible exception of some minor location changes are considered satisfactory for flight testing. Of the 36 microphone installations, all but the 7-USB flap upper surface measurements were considered satisfactory for flight. Problems with the latter microphone installations (see fig. 17) during the first part of the ground test were attributed to a combination of: microphone quality control and mechanical construction of the special cable and cable connectors. Subsequent vendor refurbishment and onsite repairs provided satisfactory measurements during the remainder of the ground test. However, in view of the decreased instrumentation accessibility and the increased cost of flight test delays, it has been recommended that the flap microphone installations be reevaluated and compared with alternate installations.

FOLLOW-ON DATA ANALYSIS

Based upon the preliminary data analysis, recommendations for detailed analysis of this ground test data are deemed appropriate. The principal elements of these recommendations include:

- Further analysis of the full-scale Tulalip data to include additional test conditions not yet analyzed
- Additional interpretation of the data by integrated assessment of the microphone, accelerometer and steady state measurements
- Extending comparisons of the full-scale data to those of Boeing 1/16-scale and NASA-Langley 1/4-scale JT15D static tests in order to assess scaling relationships

CONCLUDING REMARKS

Conclusions based upon the preliminary data analysis are given in figure 18. In summary, all of the principal objectives of the ground test measurements have been accomplished. The material and data developed will provide a sound basis for both: (1) extending the preliminary analysis presented herein to help evaluate scaling relationships, and (2) serving as a guide for accomplishing satisfactory flight test measurements.

REFERENCES

1. J. K. Wimpress, "Upper Surface Blowing Technology as Applied to the YC-14 Airplane," SAE Paper 730916, October, 1973.
2. H. Skavdahl, T. Wang and W. J. Hirt, "Nozzle Development for the Upper Surface Blown Jet Flap on the YC-14 Airplane," SAE Paper 740469, April, 1974.
3. F. W. May and G. E. Bean, "Aerodynamic Design of The Boeing YC-14 Advanced Medium STOL Transport (AMST)," AIAA Paper no. 75-1015, August, 1975.
4. C. A. Grotz, "Development of the YC-14 Propulsion System," AIAA Paper no. 75-1314, September, 1975.

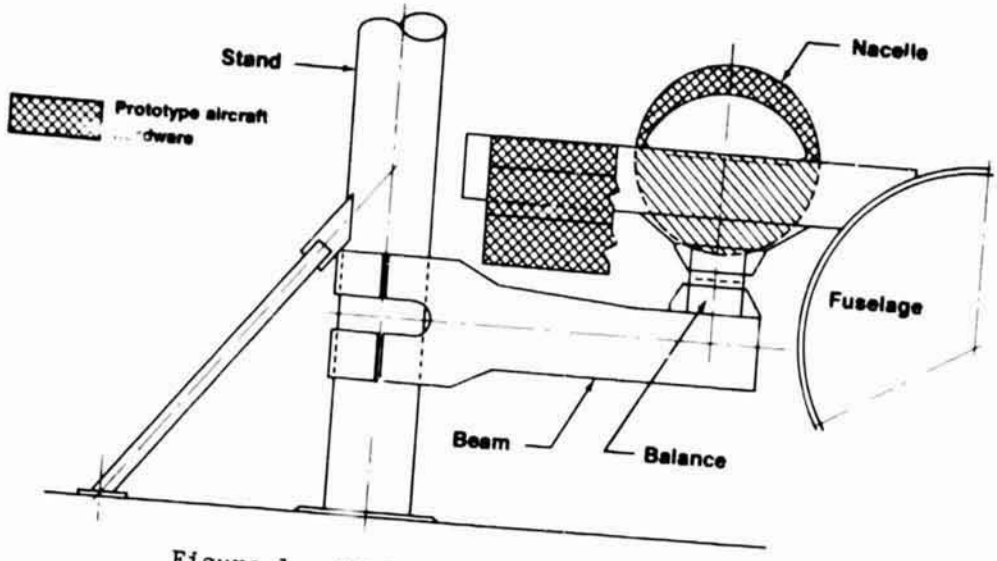

Figure 1.- YC-14 ground test installation.

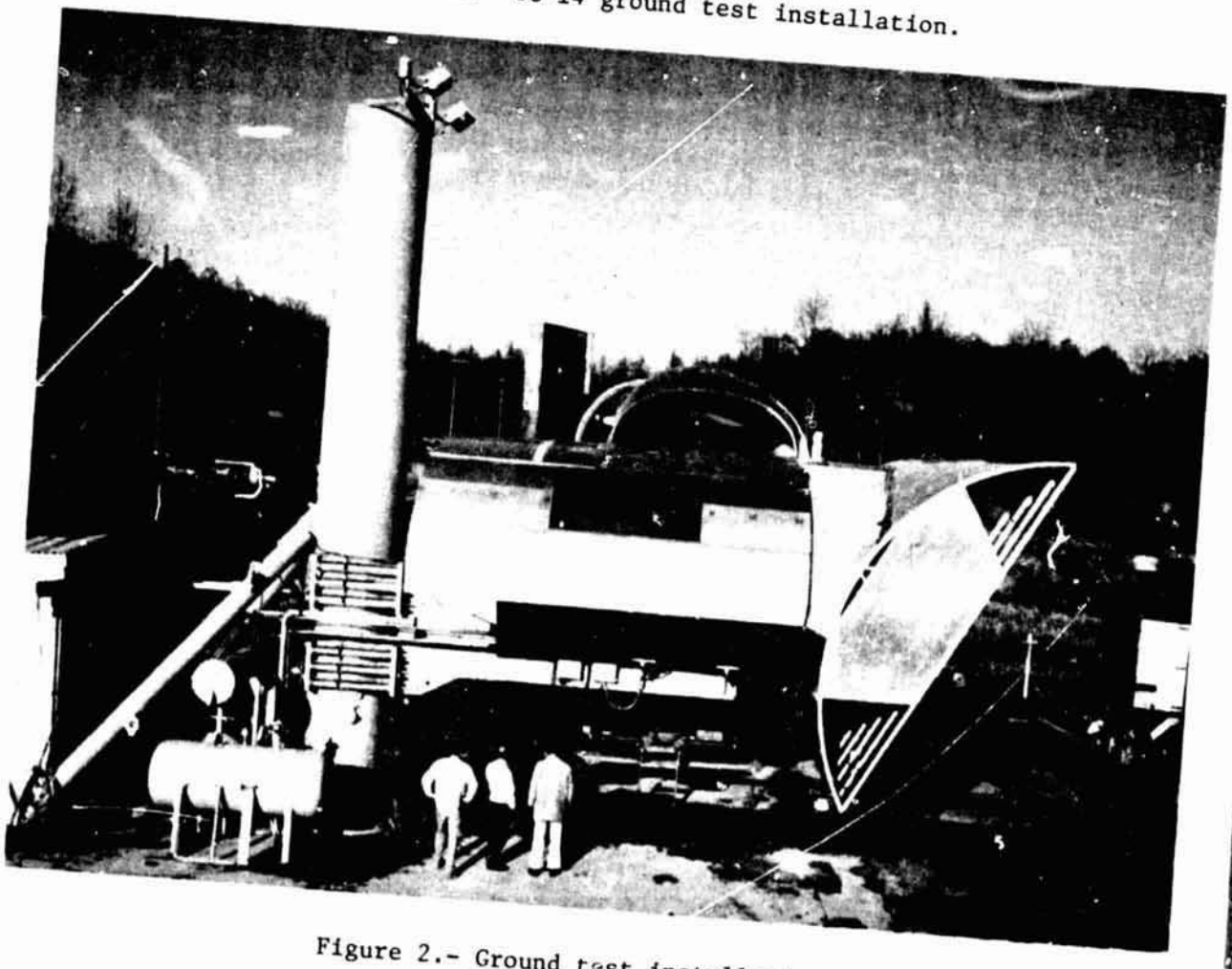

Figure 2.- Ground test installation.

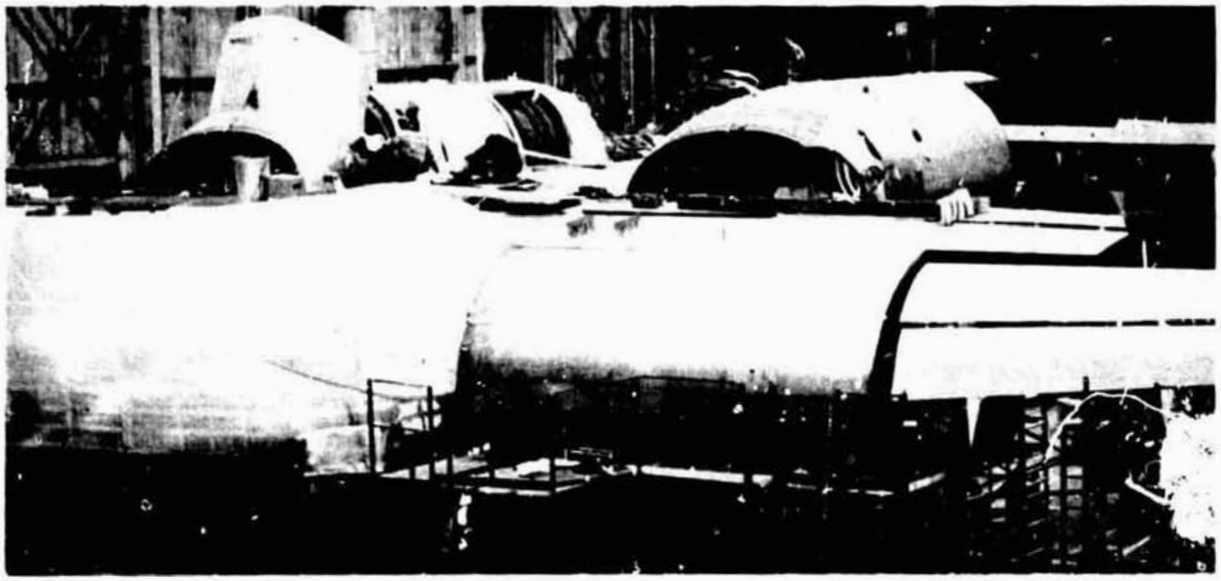

Figure 3.- YC-14 prototype no. 1 - final assembly, February 1976.

1. Assess USB structural environment
   Pressure, thermal, fatigue loads
2. Assess USB flap structural response
3. Identify USB noise sources
   Near-field assessment
4. Assess static aerodynamic flow turning
5. Assess fuselage noise environment
6. Assess nacelle acoustics
7. Develop preflight instrumentation verification
8. Develop data for ground/flight correlation
9. Develop data for scaling correlations

Figure 4.- Ground test technical objectives.

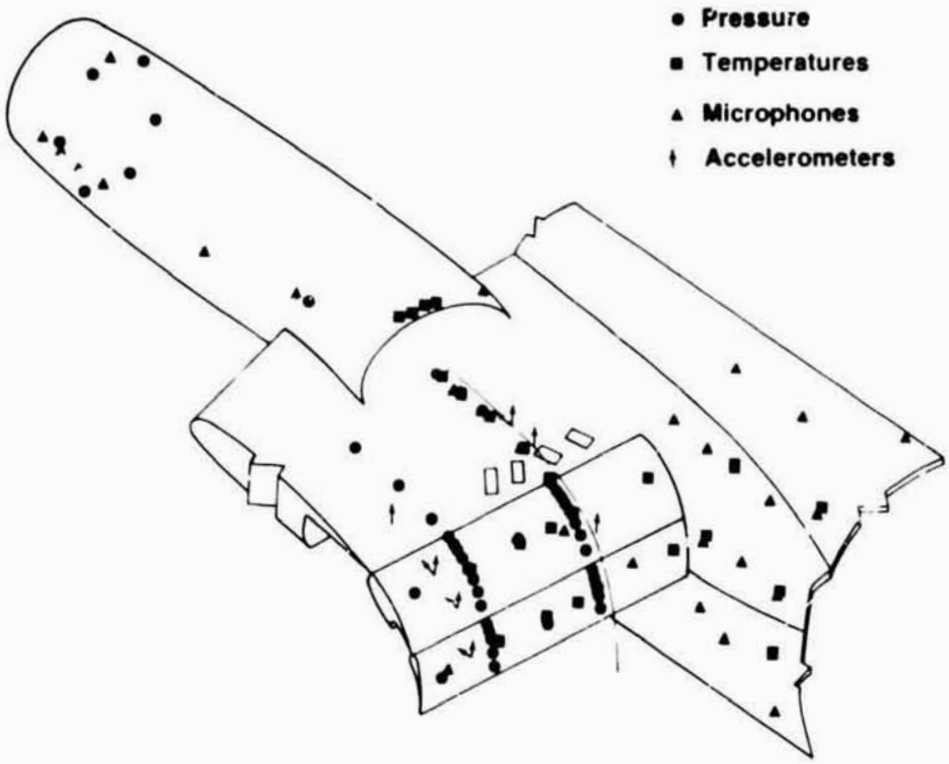

Figure 5.- Ground test instrumentation.

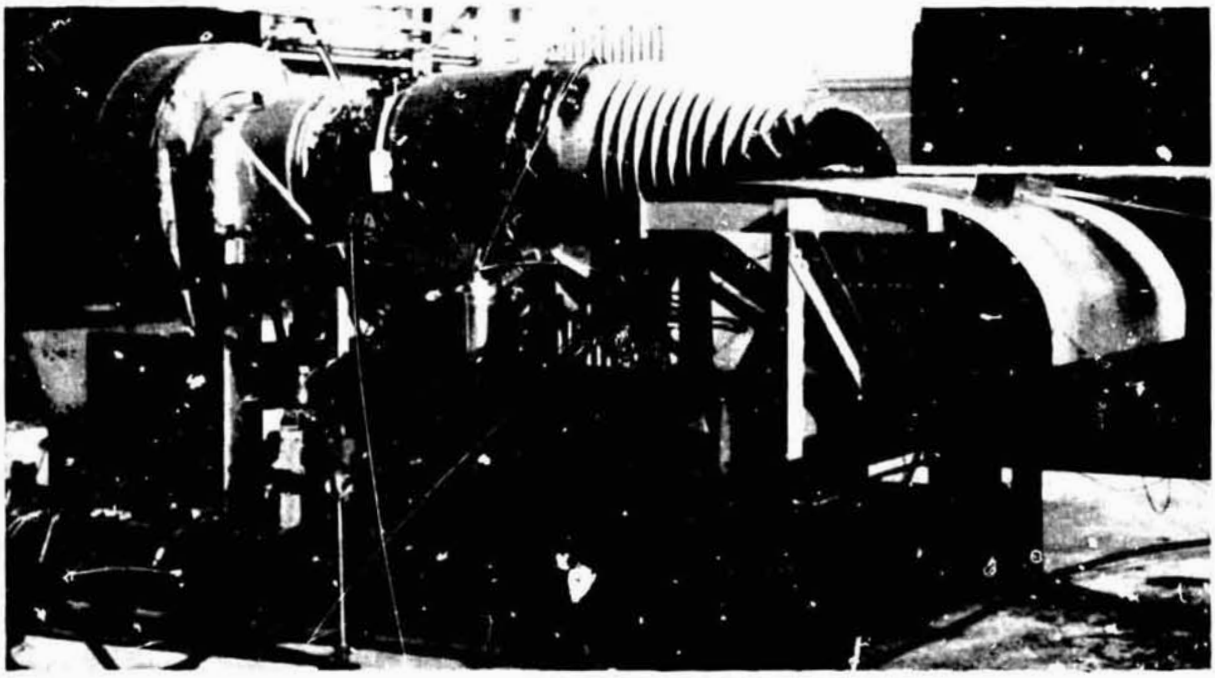

Figure 6.- NASA Langley JT15D static test rig.

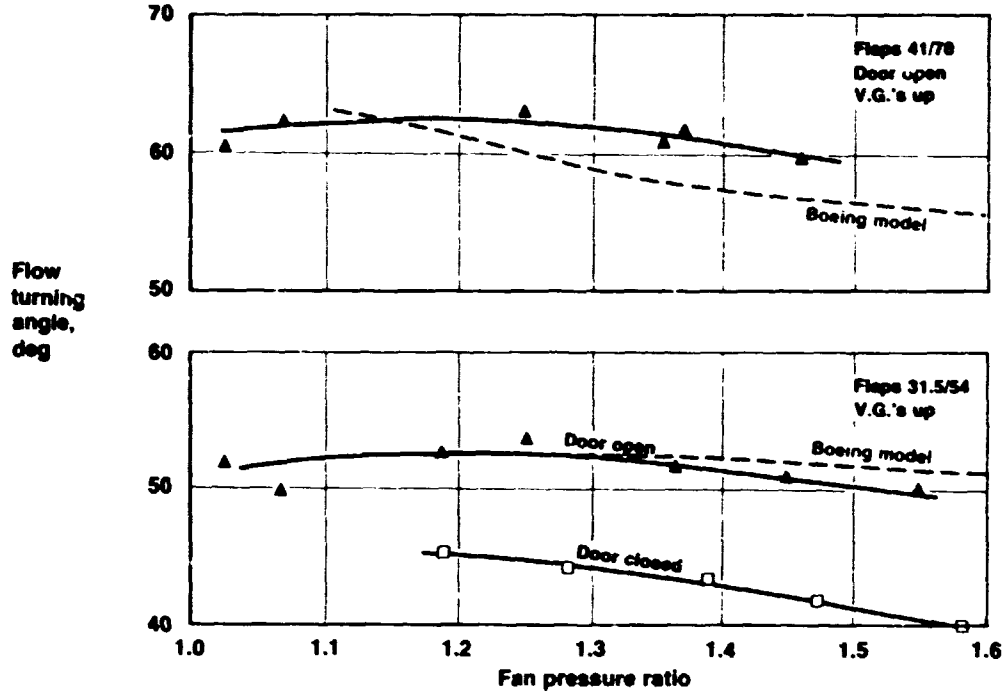

Figure 7.- Static flow turning data - intermediate and full-down USB flaps.

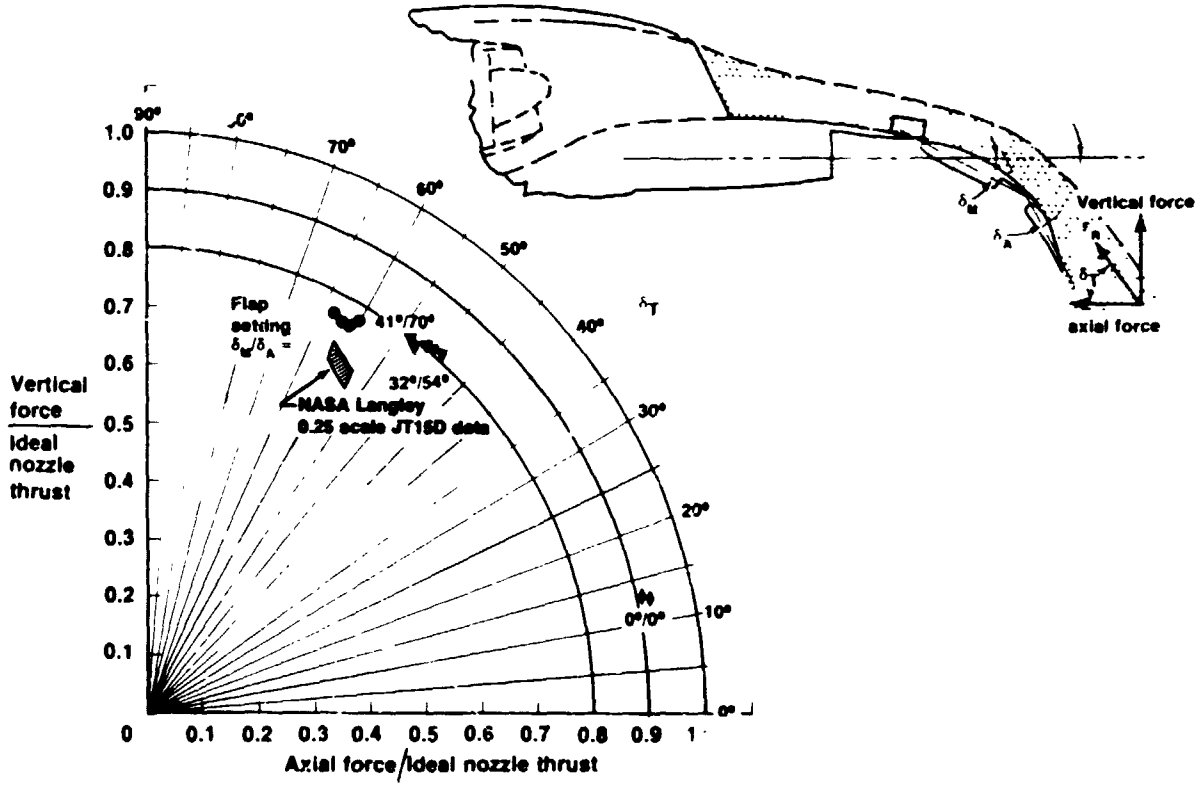

Figure 8.- USB flap static turning performance.

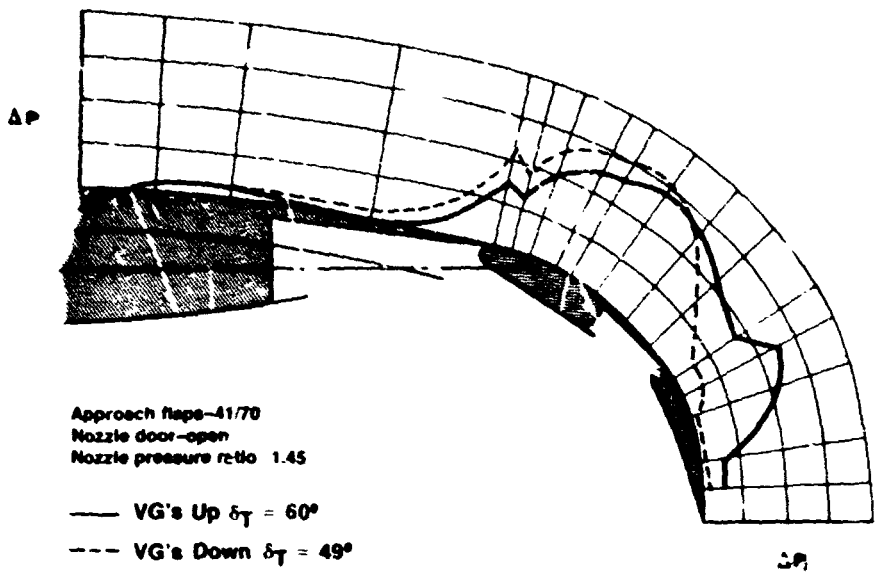

Figure 9.- Chordwise upper surface pressures along engine centerline.

°F	°C	°F	°C
50	10.0	260	126.7
80	26.7	273	133.9
103	39.4	299	148.4
173	78.3	300	148.9
175	79.5	305	151.7
180	82.2	312	155.6
188	86.7	344	173.4
200	93.3	390	198.9
208	97.8	393	200.6
209	98.3	400	204.5
219	103.9	405	207.2
240	115.6	415	212.8
256	124.5	450	232.2

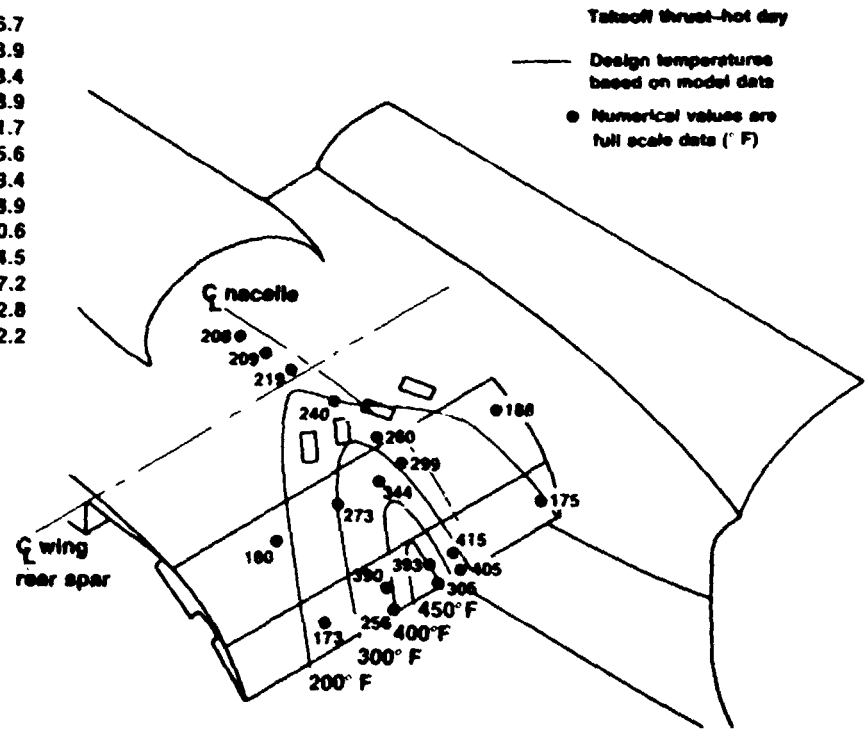

Figure 10.- USB flap temperature distributions.

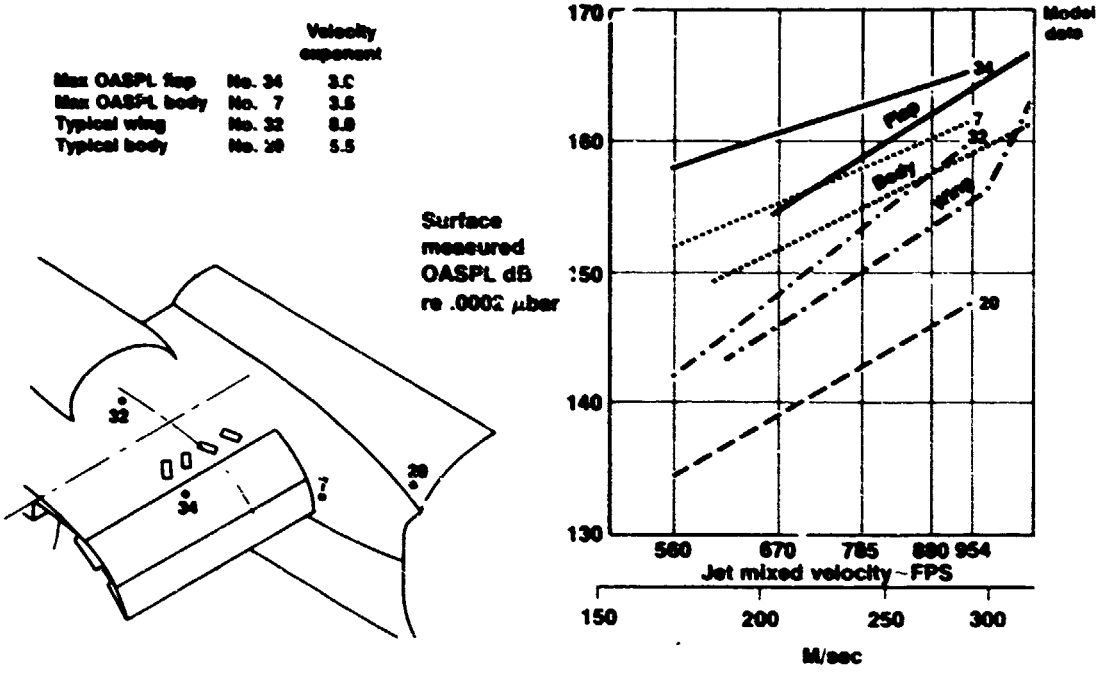

Figure 11.- Surface measured fluctuating pressures.

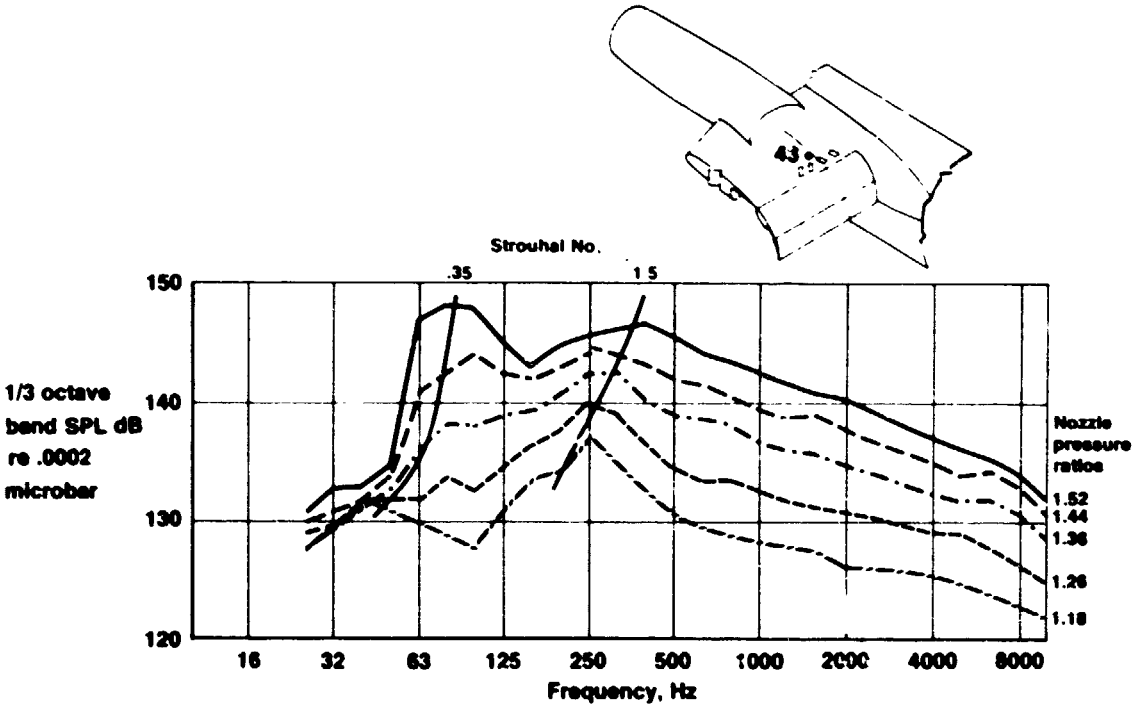

Figure 12.- Typical 1/3-octave band spectra.

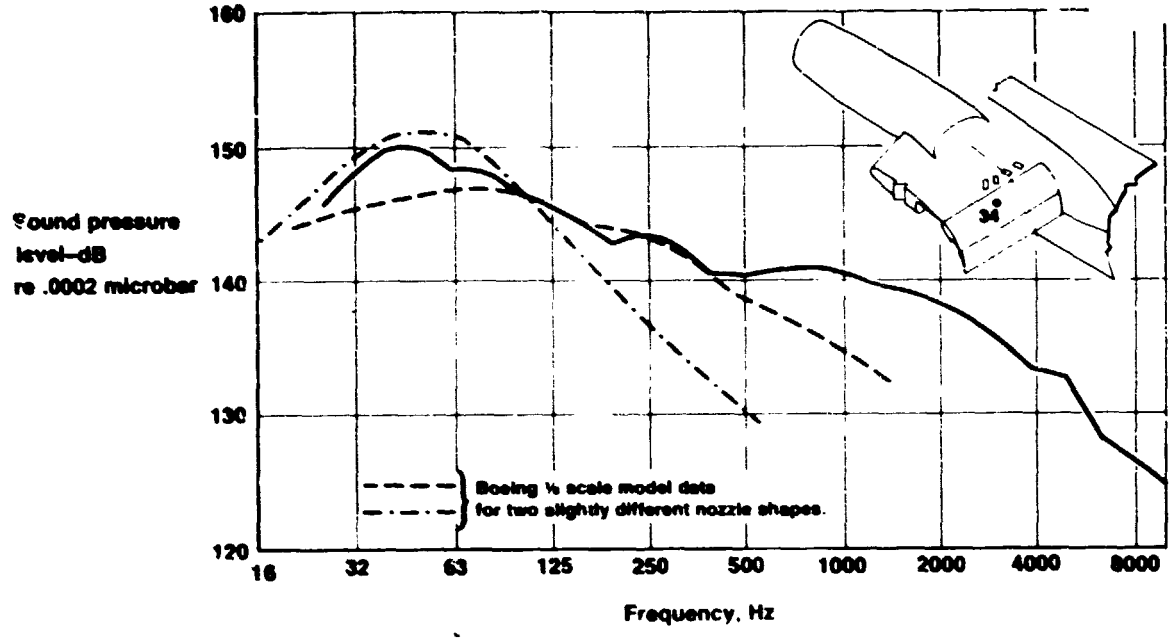

Figure 13.- Typical 1/3-octave band spectra.

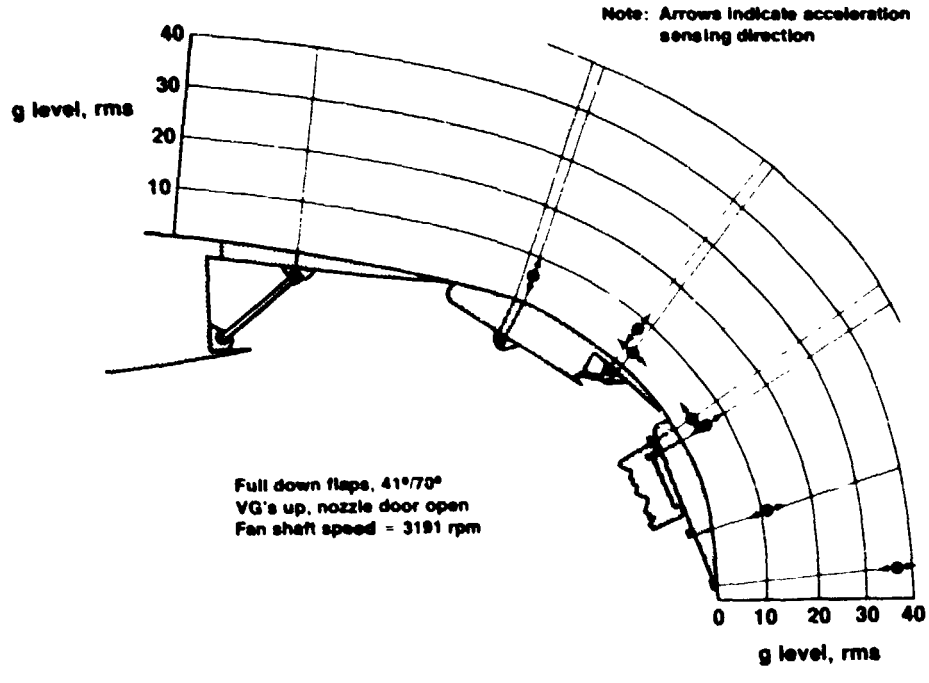

Figure 14.- Flap overall rms acceleration levels.

Frequency sweep results	
Noticeable responding frequencies Hz	Test engineer comments
25.4	–
56	–
62	–
89	–
128	Large resonance
161	–
181	Trailing edge
196	Small peak
196	Small peak
218	Fitting on trailing edge in resonance
278	Small peak
288	Very small
304	Very small
319	Stronger peak
361	Small peak
392	Large resonance

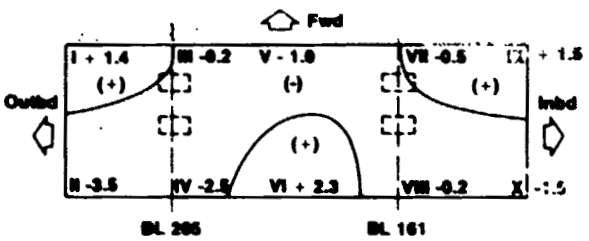

Figure 15.- Typical results of engine-off shake test.

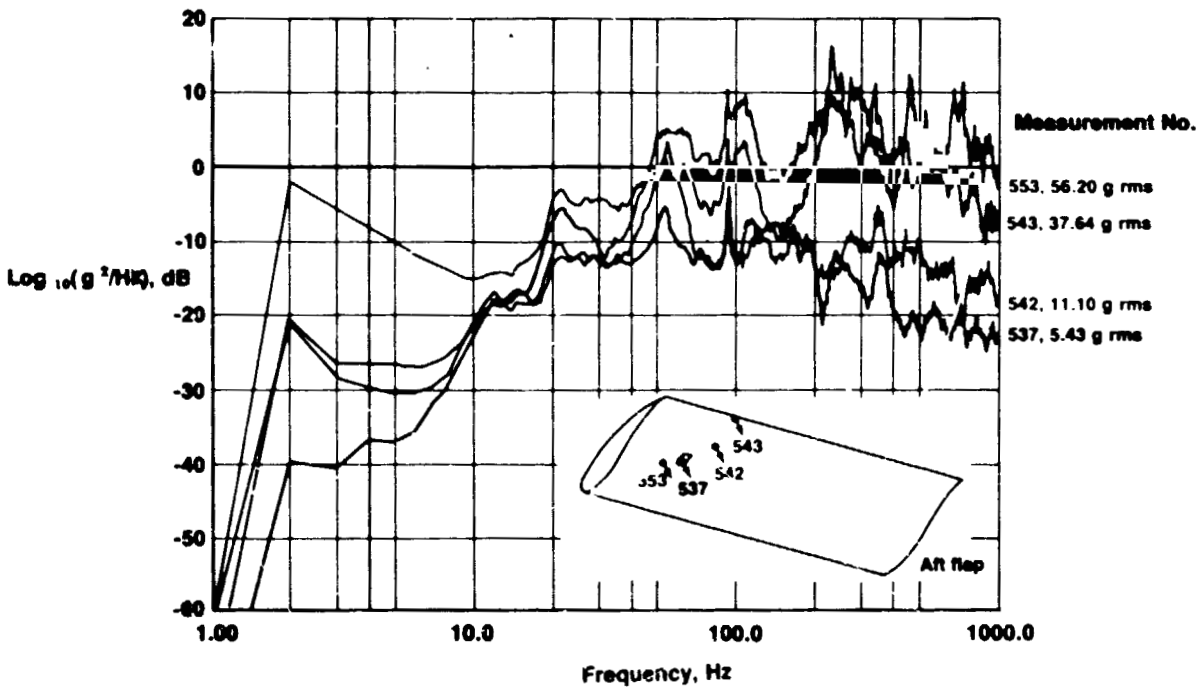

Figure 16.- Vertical acceleration spectra, flaps $41^{o}/70^{o}$.

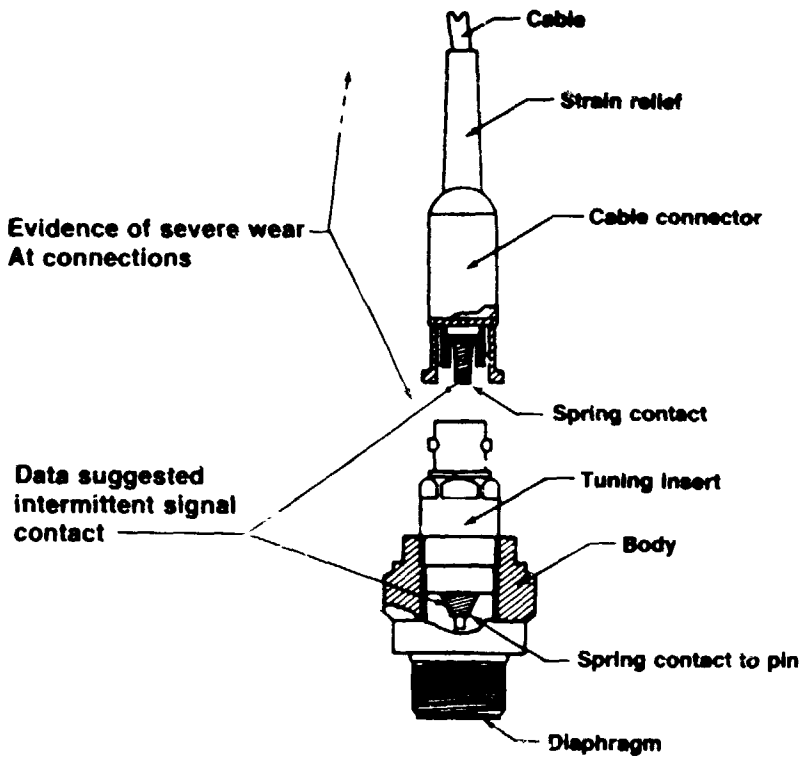

Figure 17.- Microphone description and problem areas.

- Full-down flap turning angles of about 62° agreed well with Boeing model data
- Static pressure data confirmed force balance measurement trends; however agreement with model data was not satisfactory and further study is recommended
- Maximum (adjusted) flap temperature was 211.1° C and agreed well with model data
- Maximum (adjusted) surface acoustic levels of
  -165 dB on the USB flaps and adjacent fairing
  -155 dB on the fuselage and within the nacelle
  agreed well with model data
- Acoustic spectra showed activity at Strouhal no's of about 0.3 and 1.5 giving good agreement with model data
- Flap acceleration levels and spectra are interpretable in terms of the imposed acoustic pressure field and flap vibration modes established during engine-off shake tests

Figure 18.- Conclusions based on preliminary analysis.